CHARACTERIZATION OF THE LOCAL STRUCTURE AND COMPOSITION OF LOW DIMENSIONAL HETEROSTRUCTURES AND THIN FILMS

by

JEFFREY DITTO

A DISSERTATION

Presented to the Department of Chemistry and Biochemistry
and the Graduate School of the University of Oregon
in partial fulfillment of the requirements
for the degree of
Doctor of Philosophy

June 2016

DISSERTATION APPROVAL PAGE

Student: Jeffrey Ditto

Title: Characterization of Local Structure and Composition of Thin Films

This dissertation has been accepted and approved in partial fulfillment of the requirements for the Doctor of Philosophy degree in the Department of Chemistry and Biochemistry by:

George Nazin	Chairperson
David C. Johnson	Advisor
Shannon Boettcher	Core Member
Benjamin McMorran	Institutional Representative

and

Scott L. Pratt	Dean of the Graduate School

Original approval signatures are on file with the University of Oregon Graduate School.

Degree awarded June 2016

DISSERTATION ABSTRACT

Jeffrey Ditto

Doctor of Philosophy

Department of Chemistry and Biochemistry

June 2016

Title: Characterization of Local Structure and Composition of Thin Films

The observation of graphene's extraordinary electrical properties has stirred great interest in two dimensional (2D) materials. The rapid pace of discovery for low dimensional materials with exciting properties continue with graphene allotropes, multiple polymorphs of borophene, germanene, and many others. The future of 2D materials goes beyond synthesis and characterization of free standing materials and on to the construction of heterostructures or sophisticated multilayer devices. Knowledge about the resulting local structure and composition of such systems will be key to understanding and optimizing their performance characteristics.

2D materials do not have a repeating crystal structure which can be easily characterized using bulk methods and therefore a localized high resolution method is needed. Electron microscopy is well suited for characterizing 2D materials as a repeating coherent structure is not necessary to produce a measureable signal as may be the case for diffraction methods. A unique opportunity for fine local scale measurements in low dimensional systems exists with a specific class of materials known as ferecrystals, the rotationally disordered relative of misfit layer compounds. Ferecrystals provide an excellent test system to observe effects at heterostructure interfaces as the whole film is

composed of interdigitated two dimensional layers. Therefore bulk methods can be used to corroborate local scale measurements.

From the qualitative interpretation of high resolution scanning transmission electron microscope (STEM) images to the quantitative application of STEM energy dispersive X-ray spectroscopy (EDX), this thesis uses numerous methods electron microscopy. The culmination of this work is seen at the end of the thesis where atomically resolved STEM-EDX hyperspectral maps could be used to measure element specific atomic distances and the atomically resolved fractional occupancies of a low dimensional alloy. These local scale measurements are corroborated by additional experimental data. The input of multiple techniques leads to improved certainty in local scale measurements and the applicability of these methods to non-ferecrystal low dimensional systems.

CURRICULUM VITAE

NAME OF AUTHOR: Jeffrey Ditto

GRADUATE AND UNDERGRADUATE SCHOOLS ATTENDED:

University of Oregon, Eugene, Oregon
Pacific Lutheran University, Tacoma, Washington

DEGREES AWARDED:

Doctor of Philosophy, Chemistry, 2016, University of Oregon
Master of Science, Chemistry, 2009, University of Oregon
Bachelor of Art, Chemistry, 2008, Pacific Lutheran University

AREAS OF SPECIAL INTEREST:

Materials characterization
Electron microscopy
Focused ion beam microscopy and fabrication
Energy dispersive X-ray spectroscopy

PROFESSIONAL EXPERIENCE:

Research Assistant, University of Oregon, 2009-2014

GRANTS, AWARDS, AND HONORS:

Outstanding Accomplishment Award, Non-tenure-track faculty,
University of Oregon VPR's office, 2013

PUBLICATIONS:

Prabhakaran, V., Mehdi, B. L., Ditto, J., Engelhard, M. H., Wang, B., Gunaratne, K. D., Johnson, D. C., Browning, N. D., Johnson, G., Laskin, J., Nature Communications 2016, 7, 11399

Westover, R. D., Mitchson, G., Ditto, J., Johnson, D. C., Eur. J. Inorg. Chem. 2016, 8, 1225–1231

Westover, R. D., Atkins, R. A., Falmbigl, M., Ditto, J., Johnson, D. C, Journal of Solid State Chemistry 2016, 236, 173-185

Fairley, K., Merrill, D. R., Woods, K. N., Ditto, J., Xu, C., Oleksak, R., Gustafsson, T., Johnson, D., Garfunkel, E. L., Herman, G. S., Johnson, D. C., Page, C. J., ACS Appl. Mater. Interfaces 2016, 8, 667-672

Hite, O., Nellist, M., Ditto, J., Falmbigl, M., Johnson, D. C., J. Mater. Res 2015, 31 (7), 886-892

Falmbigl, M., Hay, Z., Ditto, J., Johnson, D. C., J. Mater. Chem. C 2015, 3, 12308-12315,

Alemayehu, M., Falmbigl, M., Ta, M., Ditto, J., Medlin, D., and Johnson, D., Angew. Chem. Int. Ed. 2015, 54, 15468-15472

Mitchson, G., Falmbigl, M., Ditto, J., Johnson, D., Inorg. Chem. 2015, 54, 10309-10315

Bauers, S. R.; Moore, D. B.; Ditto, J.; Johnson, D.C, J. Alloys Compd. 2015, 645, 118–124

Regus, M., Mokovsky, S., Polesya, S., Kuhn, G., Ditto, J., Schürmann, U., Jacquot, A., Bartholomé, K., Näther, C., Winkler, M., König, J., Böttner, H., Kienle, L, Johnson, D. C., Ebert, H., Bensch, W., Journal of Solid State Chemistry 2015, 230, 254-265

Westover, R.D., Ditto, J., Falmbigl, M., Hay, Z. L., Johnson, D.C., Chem. Mater. 2015, 27 (18), 6411-6417

Wood, S.R., Merrill, D. R., Falmbigl M., Moore, D., Ditto, J., Esters, M., Johnson, D.C., Chem. Mater. 2015, 27 (17), 6067-6076

Ditto, J., Merrill, D.R., Medlin, D.L., and Johnson D.C., Microsc. Microanal. 2015, 21, Suppl 3, 1327-1328

Kienle, L., Dankwort, T., König, J., Winkler, M., Hansen, A., Koch, C., Ditto, J., Johnson, D. C., and Bensch, W., Microsc. Microanal. 2015, 21, Suppl 3, 1823-1824

Falmbigl, M., Putzky, D., Ditto, J., Johnson, D.C., Journal of Solid State Chemistry 2015, 231, 101-107

Falmbigl, M., Putzky, D., Ditto, J., Esters, M., Bauers, S., Ronning, F., Johnson, D. C., ACS Nano 2015, 9 (8), pp 8440–8448

Merrill, D., Sutherland, D., Ditto, J., Bauers, S., Falmbigl, M., Medlin, D., Johnson, D., Chem. Mater. 2015, 27, 4066-4072

Merrill, D.R., Moore, D., Ditto, J., Sutherland, D., Falmbigl, M., Winkler, M., Pernau H., and Johnson, D.C., Eur. J. Inorg. Chem. 2015, 83-91

Hansen, A.L., Dankwort, T., Winkler, M., Ditto, J., Johnson, D.C., König, I.D., Bartholomé, K., Kienle, L., Bensch, W., Chemistry of Materials, 2014, *26*, pp 6518–6522

Mahaney, W.C., Krinsley, D.H., Allen, C.C.R., Ditto, J., Langworthy, K., Batchelor, A.D., LeCompte, M., Milner, M.W., Hart, K., Kelleher, B.P., Hancock, R.G.V., Geomicrobiology Journal 2015, *32*, 27-41

Westover, R., Atkins, R. A., Ditto, J., and Johnson, D.C., Chemistry of Materials, 2014, *26*, 3443–3449.

Alemayehu, M., Mitchson, G., Ditto, J., Hanken, B., Asta, M., Johnson, D. C., Chemistry of Materials 2014 26, 1859–1866.

Dorn, R., Krinsley, D., Langworthy, K., Ditto, J., and Thompson, T., Aeolian Research 2013, 10, 61-76

Krinsley, D., Ditto, J., Dorn, R., and Thompson, T., Physical Geography 2013. 34, 159-173

Mahaney, W.C., Krinsley, D.H., Allen, C.C.R., Langworthy, K., Ditto, J. and Milner, M.W., 2012, J. of Geology, 120, 591-602

Ditto, J., Krinsley, D., and Langworthy, K., Scanning 2012, 34, 279-283 + Front Cover

Dorn, R., Krinsley, D. and Ditto, J., J. Geology 2011, 120, 14

Krinsley, D., Dorn, R.I., DiGregorio, B., Langworthy, K, and Ditto, J., Geomorphology 2012 138, 339-351

Mahaney, W.C., Krinsley, D.H., Kalm, V., Langworthy, K. and Ditto, J., J. Advanced Microscopy Research 2011, 6, 177-185

Langworthy, K, Ditto, J., Hartfield, C., Krinsley, D., Microscopy and Microanalysis 2011, 17(S2), 640-641

Cotten, M., Fu, R., Gordon, E., Daza, E., Kozlova, A., Hibbard, D., Taylor, M., Ditto, J., Truong, M., Biophysical Journal 2009, 96, Issue 3, 390a

ACKNOWLEDGMENTS

I sincerely appreciate the support and guidance of my advisor, Dr. David Johnson who made every effort to create educational opportunities for me. I could not have ask for a more supportive mentor. I am very greatful for the help of Dougas Medlin and our lengthy technical discussions about data analysis. Much of the work in this thesis benefited greatly from the support of Nigel Browning, access to instrumentation through the PREMIER Network and the Chemical Imaging Intiative, at Pacific Northwest National Laboratory. Special thanks are due to my colleagues Sage Bauers, Suzannah Wood, Dr. Dan Moore, Dr. Matthias Falmbigl, Marco Esters and Kyle Hite for making my time in the laboratory entertaining and educational. I owe a great deal of gratitude to Devin Merril for his help and synthesis of multiple samples for my research. It has been a great pleasure working with Gavin Mitchson and I am thankful for the intellectual contributions and effort he contributed to my projects. I thank Robert Fischer for his friendship, kindness, and flexibility with instrument scheduling. I thank Joshua Razink for his training, knowledge, and time having thoughtful discussions about topics relating to my thesis. I also thank my committee members, Dr. George Nazin, Dr. Shannon Beotcher, and Dr. Benjamin McMorran for their time and feedback.

I owe much appreciation to my parents and my sister for their encouragement and support of my decision to continue my education. I thank David Krinsley for sharing his thoughtful advice and experience as I navigate my life and future career. I would like to express the upmost appreciation for Alecia Chang and her family. Their unending support, friendship, and faith in me has been a major source of motivation.

I acknowledge funding from National Science Foundation under grant DMR-1266217 and support from the National Science Foundation through CCI grant number CHE-1102637. Some of the data was collected in collaboration with Sandia National Laboratories, a multi-program laboratory managed and operated by Sandia Corporation, a wholly owned subsidiary of Lockheed Martin Corporation, for the U.S. Department of Energy's National Nuclear Security Administration under contract DE-AC0494AL85000. I also acknowledge support through the Collaborative Access Team (CAT): Pooled Resources for Electron Microscopy Informatics, Education and Research (PREMIER) Network Program and the Chemical Imaging Initiative at Pacific Northwest National Laboratory (PNNL) and the Environmental Molecular Sciences Laboratory, a national scientific user facility sponsored by DOE's Office of Biological and Environmental Research at PNNL. PNNL is a multiprogram national laboratory operated by Battelle for DOE under Contract DE-AC05-76RL01830.

I dedicate this dissertation to my family, my friends, and a lifetime of discovery together.

TABLE OF CONTENTS

Chapter Page

I. INTRODUCTION 1

II. TWO AXIS TILTING FOR FOCUSED-ION-BEAM PREPARATION OF INHOMOGENEOUS MATERIALS FOR STEM 20
II.1.Introduction 20

II.2. Instruments Used 23

II.3.Wedge Pre-Milling and Sample Thinning 23

II.4.In-situ Rocking Angle Methods 26

II.5. Conclusions 34

III. CHARGE TRANSFER BETWEEN PBSE AND NBSE2 IN $[(PbSe)_{1.14}]_m(NbSe_2)_1$ FERECRYSTALLINE COMPOUNDS 35

III.1. Authorship statement 35

III.2. Introduction 35

III.3. Experimental Section 37

III.4. Results and Discussion 40

IV. SYNTHESIS OF $([SnSe]_{1.16-1.09})([Nb_xMo_{1-x}]Se_2)_1$ FERECRYSTAL ALLOYS 58

IV.1. Authorship statement 58

IV.2. Introduction 58

IV.3. Experimental 61

IV.4. Results and Discussion 63

IV.5. Conclusion 77

V. INFLUENCE OF DEFECTS ON THE CHARGE DENSITY WAVE OF $([SnSe]_{1+\delta})_1(VSe_2)_1$ FERECRYSTALS 79

V.1. Authorship statement 79

V.2. Introduction 79

V.3. Result and Discussion 81

V.3.1. Synthesis and Structural Properties 81

V.3.2. Specific Heat 89

V.3.3. Transport Properties 91

V.4.Conclusions 95

V.5. Methods 96

VI. INFLUENCE OF INTERSTITIAL V ON STRUCTURE AND PROPERTIES OF FERECRYSTALLINE $([SnSe]_{1.15})_1(V_{1+x}Se_2)N$ FOR N=1,2,3,4,5, AND 6 99

VI.1. Authorship statement 99

VI.2. Introduction 99

VI.3. Experimental Detail 101

VI.4. Results and Discussion 102

VI.4.1. Structure and Composition 102

VI.4.2. Electrical Properties 111

VI.5. Conclusion 115

VII. PHASE WIDTH OF KINETICALLY STABLE $([PbSe]_{1+y})_1(TiSe_2)_1$ FERECRYSTALS AND THE EFFECT OF PRECURSOR STRUCTURE ON ELECTRICAL PROPERTIES 117

VII.1. Authorship statement 117

VII.2. Introduction 117

VII.3. Experimental Details 119

VII.4. Results and Discussion 120

VII.5. Conclusion 131

VIII. MODIFYING A CHARGE DENSITY WAVE TRANSITION BY MODULATION DOPING: FERECRYSTALLINE COMPOUNDS ($[Sn_{1-x}Bi_xSe]_{1.15})_1(VSe_2)_1$ WITH $0 \leqq X \leqq 0.66$ 133

VIII.1. Authorship statement 133

VIII.2. Introduction 133

VIII.3. Experimental 135

VIII.4. Results and Discussion 137

VIII.4.1.Electrical Properties 148

VIII.5. Conclusion 153

IX. THE SYNTHESIS, STRUCTURE, AND ELECTRICAL CHARACTERIZATION OF $(SnSe)_{1.2}TiSe_2$ 154

IX.1. Authorship statement 154

IX.2. Introduction 154

IX.3. Experimental Section 156

IX.4. Results and Discussion 157

IX.4.1. Structural Analysis 158

IX.4.2. Electrical Characterization 167

IX.5. Conclusions 175

X. TUNING ELECTRICAL PROPERTIES THROUGH CONTROL OF $TiSe_2$ THICKNESS IN $(BiSe)_{1+\delta}(TiSe_2)_N$ COMPOUNDS 176

X.1. Authorship statement 176

X.2. Introduction 176

X.3. Experimental 178

X.4. Results and Discussion 180

X.5. Electrical Properties 184

X.6. Conclusions 191

XI. TRANSPORT PROPERTIES OF VANADIUM DISELENIDE MONOLAYERS SEPARATED BY BILAYERS OF BISE 200

XI.1. Authorship statement 200

XI.2. Introduction 200

XI.3. Experimental Section 202

XI.4. Results and Discussion 204

XI.6. Conclusions 213

XII. ANTIPHASE BOUNDARIES IN THE TURBOSTRATICALLY DISORDERED MISFIT COMPOUND $(BiSe)_{1+\delta}NbSe_2$ 215

XII.1. Authorship statement 215

XII.2. Introduction 215

XII.3. Experimental 219

XII.4. Results and Discussion 221

XII.5. Conclusions 233

XIII. DESIGNED SYNTHESIS OF NEW VAN DER WAALS HETEROSTRUCTURES: THE POWER OF KINETIC CONTROLS 235

XIII.1. Authorship statement 235

XIII.2.Communication 235

XIII.3. Experimental Section 246

XIV. KINETICALLY CONTROLLED SITE-SPECIFIC SUBSTITUTIONS IN HIGHER ORDER HETEROSTRUCTURES 247

XIV.1. Authorship statement 247

XIV.2. Introduction 247

XIV.3. Experimental 250

XIV.4. Result and Discussion 251

XIV.4.1. Structural Properties 253

XIV4.2. Electrical Transport Properties 259

XIV.5. Conclusions 265

XV. THE SYNTHESIS OF MULTI-CONSTITUENT HETEROSTRUCTURES FROM DESIGNED AMORPHOUS PRECURSORS 266

XV.1. Authorship statement 266

XV.2.Communication 266

XV.3. Experimental Section 275

XVI. SYNTHESIS AND CHARACTERIZATION OF QUATERNARY MONOLAYER THICK $MoSe_2$/SnSe/$NbSe_2$/SnSe HETEROJUNCTION SUPERLATTICES 276

XVI.1. Authorship statement 276

XVI.2. Introduction 276

XVI.3. Experimental 279

XVI.4. Results and Discussion 281

XVI.5. Conclusion 291

XVII. SYNTHESIS OF A FAMILY OF $([SnSe]_{1+\delta})m([\{Mo_xNb_{1-x}\}Se_2]_{1+\gamma})_1$ $([SnSe]_{1+\delta})_m(\{Nb_xMo_{1-x}\}Se_2)_1$ HETEROJUNCTION SUPERLATTICES (WHERE m = 0, 1, 2, 3 AND 4) 292

XVII.1. Authorship statement 292

XVII.2. Introduction 292

XVII.3. Experimental Section 295

XVII.4. Results and Discussion 296

XVII.5. Conclusion 308

XVIII. SELF-ASSEMBLY OF DISIGNED PRECURSORS: A ROUTE TO CRYSTALLOGRAPHICALLY ALIGNED NEW MATERIALS WITH CONTROLLED NANOARCHITECUTURE 310

XVIII.1. Authorship statement 310

XVIII.2. Introduction 310

XVIII.3. Modulated Elemental Reactants 314

XVIII.3.1. Single Component Systems 317

XVIII.4. Two Component Systems 321

XVIII.5. Adding Additional Complexity 327

XVIII.5.1. Preparing Random Alloys 328

XVIII.6. Ordered ABAC Alloys 335

XVIII.7. Electrical Properties 341

XVIII.8. Summary and Conclusions 344

XIX. NON-UNIFORM COMPOSITION PROFILES IN INORGANIC THIN FILMS FROM AQUEOUS SOLUTIONS 347

XIX.1. Authorship statement 347

XIX.2. Introduction 347

XIX.3. Experimental 350

XIX.4. Results and Discussion 353

XIX.5. Summary 362

XX. LOW VOLTAGE PATTERING OF HafSOx: EFFECTS OF VALTAGE ON RESOLUTION, CONTRAST, AND SENSITIVITY 365

XX.1. Authorship statement 365

XX.2. Introduction 365

XX.3. Experimental 365

XX.4. Results and Discussion 371

XX.5. Conclusion 379

XXI. HAADF STEM SIGNAL INTENSITY ANALYSIS METHOD FOR EXTRACTING STRUCTURAL INFORMATION FROM COMPLEX THIN FILMS 381

XXI.1. Authorship statement 381

XII.2. Introduction 381

XXI.3. Experimental 383

XXI.4. Results and Discussion 385

XXI.5. Summary 397

XXII. ELEMENT SEGREGATION IN 2D HETEROSTRUCTURES $[(Pb_{1-x}Sn_x)_{1+\delta}]_n(TiSe_2)_1$ QUANTIFIED BY STEM-EDX 399

REFERENCES CITED 416

LIST OF FIGURES

Figure Page

I.1: A drawing demonstrating the micromechanical cleavage technique first described in 2004[1] to generate free standing two dimensional layers of graphene from graphite. There have since been numerous observations of 2D crystals as a result of this synthetic method. Quick identification of resulting monolayers is achieved by deposition onto a silicon substrate with 300 nm SiO_2 on the top surface and observation in a reflected light microscope 2

I.2. Images and corresponding drawing of an alloy ferecrystal. The surface plane of the substrate and layered films oriented vertically showing $(MX)_{1+\delta}TX$ and $(MX)_{3+\delta}TX$ stacking motifs. The white scale bar is 2 nanometers. (a) A STEM image showing resolved atomic planes of a $(Pb_xSn_{1-x}Se)_{m+\delta}TiSe_2$ alloy ferecrystal, (b) a corresponding composite EDX map showing distributions of Ti (blue), Pb (red), Sn (green), and Se (cyan), and (c) a not to scale cartoon model of the image demonstrating rotational disorder (Sn and Pb are both represented by the red positions). The [110] orientation of $(Pb_xSn_{1-x}Se)$ is seen in the HAADF while the rest of the layers exhibit off zone axis rotation. 5

I.3. (a) simulated TEM images with varying defocus and thickness that can be correlated to experimental data. (b) An experimental image with regions that correspond to both simulated images of VSe_2 and VSe. (c) Simulated overlays indicate a combination of simulations from the two materials appears to match the experimental data. 7

I.4. High angle annular dark-field (HAADF) STEM images of a structurally unsolved $(LaSe)_{1+\delta}(V_xSe_y)_n$ system. (a) High resolution images showing an oriented grain of the layer of interest interdigitated with off zone axis layers of LaSe. (b) A high magnification cropped portion of the images in (a) with a drawing of the observed structure. 9

I.5.A basic electron ray diagram of a STEM instrument showing different hardware elements used for STEM imaging. 10

I.6. A Bohr model of an atom showing examples of electron energy transitions for different shells (K, L, M, N), their corresponding principal quantum numbers (n= 1, 2, 3, 4) and the potential energy transitions that release the characteristic X-rays used for energy dispersive X-ray spectroscopy. 12

I.7. A high quality EDX intensity profile of a single repeat of a $[(Pb_{0.37}Sn_{0.63}Se)_{1.17}]_3(TiSe_{2.00})$ ferecrystal demonstrating non-zero peak intensity in regions illustrating the presence of delocalization effects. A thermodynamic argument from knowledge about ferecrystals and misfit layer

compounds can be used to suggest that Ti would not be present in areas outside of the central peak in the image. 14

I.8. A diagram illustrating the process of using element specific signals from EDX hyperspectral data to produce images that deconvolute otherwise overlapped elements in the image. Guassian peak fitting of extracted intensity profiles from the individual images allows the measurement of element specific interplanar distances. 15

I.9. Scanning electron microscope and focused ion beam microscope (SEM-FIB) images demonstrating the in-situ lift-out method for TEM sample preparation. The white scale bars are all 10 um. (a) A carbon protecting layer is deposited using electron beam induced deposition (EBID). (b) Additional carbon is grown using ion beam induced deposition (IBID) and the material on either side of a lamella is cut out using ion beam sputtering. (c) A micromanipulator probe is attached to the sample using IBID, the lamella is cut free from the substrate and lifted out. (d) The lamella is then deposited onto a transmission electron microscope grid using IBID and the micromanipulator probe is cut free. (e) The sample is thinned using ion beam sputtering until thin enough to be electron transparent. 16

I.10. Images showing the Gaussian profile of the low-voltage ion beam at different vacuum levels. Lines were cut into a silicon substrate using a 5kV accelerating voltage gallium focused ion beam using the same dwell times. The trenches were backfilled and coated with a organometallic platinum protecting layer and cut in cross-section to be viewed at 45 degrees using the electron beam. The voids in the backfill of the trenches are an artifact of the mean induced deposition methods. 17

II.1.Curtaining artifacts and their removal (a) SEM micrograph of a partially thinned lamella for TEM lifted out from a rock varnish coating in a polished geological thin section. Curtain artifacts parallel to the incident ion beam can be seen propagating from pores and inhomogeneity in the sample. (b) The sample was rotated 90 degrees *ex-situ* and reloaded into the FIB so that the majority of artifacts could be polished away. Artifacts are then created in the new incident FIB direction. Multiple iterations can produce lamellas with minimal artifacts. (c) A low magnification bright field STEM image taken on an FEI Helios Nanolab 600 Dual-Beam at 30kV demonstrating smooth preparation of a 25x25 um lamella from a highly porous and inhomogeneous sample, where bright areas indicate low density or natural pores in the sample 22

II.2. A demonstration of the benefits of wedge pre-milling. (a) SEM images taken of a silicon lamella exhibit thickness contrast at 5kV that suggests the very top and very bottom of the sample are thinnest. The contrast is the result of additional secondary electron generation on the back side of the lamella as it gets thinner. (b) Illustrates a two dimensional cross-section of the thickness

profile of the lamella throughout the wedge premilling process. (c) When lower tilts are used the lamella has more parallel side walls however the protecting layer quickly degrades and limits the sample thickness that can be achieved. 24

II.3. Scanning electron microscope images of the lamella thinning process using wedge pre-milling. (a) Comparison images of the same lamella demonstrating the difference in translucent appearance at 5kV and 2kV. As the sample becomes thinner, it is often advantageous to use lower imaging voltage on the electron column to increase thickness contrast. (b) SEM micrographs of the final thinning steps demonstrating how thickness contrast can be used to target a specific thickness. The numbers reported here were measured using electron energy loss thickness measurements. (c) A 2D illustration of the lamella during thinning demonstrates the inevitable variation in thickness of the lamella. The green arrows indicate the incident direction of the ion beam probe. 25

II.4. A simulated chamber camera view (not to scale) demonstrating how samples are mounted to a pretilted TEM half grid for rocking angle thinning in a FIB-SEM: (a) shows a wafer substrate attached to an SEM stub, a micromanipulator probe lifting a lamella from the substrate, and a FEI row holder for TEM grids attached to a 45° stub. (b) To mount the lift-out sample to the pretilted grid, the stage is tilted 45°. (c) The stage is rotated 180° and tilted 7° so that the protective cap is normal to the Ga^+ ion column which is 52° from the electron column for thinning the lamella. 26

II.5.With the TEM half grid pre-tilted, stage rotation can be used for a second tilt axis relative to the ion beam while thinning a lamella for TEM, which enables rocking angle methods to remove curtaining artifacts. 28

II.6. Scanning electron microscope images demonstrating the rocking angle methods used to produce TEM samples with minimal artifacts. (a-c) Rocking angle methods are achieved by orienting the lamella so that the rotational axis of the stage can be used to tilt the sample relative to the ion beam. (d) Demonstrates the improvement in FIB induced artifacts by rocking the sample. Numerous voids that are native to the sample are visible throughout a large and smooth 10x10 µm lamella. 29

II.7. A view of the back-side of the pretilted lamella during rocking angle thinning. (a) An SEM micrograph of the back side of the lamella with visible curtaining artifacts. A magnified and contrast/brightness adjusted image of the cross-section is shown to the right. (b) The same view with magnified image after thinning the sample using rocking angle methods. (c) A drawing of the stage orientation from which the micrographs were taken. 31

II.8: Removal of inhomogeneities in a film (a) An ADF-STEM image nanoscale curtains often seen when preparing samples with an electron beam induced deposition (EBID) platinum protecting layer. ADF-intensity (counts) extracted

from the layer of interest (a lanthanum zirconium oxide film deposited from aqueous precursors) is shown below the image. The native oxide [110] silicon lattice of the substrate below the film and the EBID platinum at the top of the image are both visible. (b) ADF-STEM images from the same sample after additional thinning of the sample using rocking angle methods. Note the thickness related slope in contrast. 32

II.9: Distinguising curtaining from other effects (a) a low magnification image of a rotationally disordered two dimensional laminate system, $(SnSe)_{1.2}(TiSe_2)$, deposited over the native oxide of silicon. (b) A graph showing lateral intensity profiles extracted from parallel areas in the overview image. The blue profile, extracted from the silicon substrate region of the image, demonstrates the uniform thickness of the lamella. The red profile, extracted from the $(SnSe)_{1.2}(TiSe_2)$ region of the image exhibits intensity changes relating to composition and crystallographic orientation rather than curtaining. (c) A high magnification image showing [110] silicon dumbbells in the bottom of the image and regions of crystallographically oriented $(SnSe)_{1.2}(TiSe_2)$ demonstrating that the sample was preserved by the FIB preparation and thin enough for high resolution imaging 33

III.1. X-ray reflectivity data of the precursors designed to form ([Pb|Se]1+δ)m(Nb|Se)1. The numbers to the right of the scans indicates the number of Pb:Se. and Nb:Se repeats deposited in each sample. The calibration results in one crystallographic unit of each structure per bilayer deposited. 43

III.2. Diffraction patterns of $([PbSe]_{1.14})_m(NbSe_2)_1$ compounds. The compounds are crystallographically aligned with the *c*-axis normal to the sample substrate. (*) Symblolizes a *k*α Si peak from substrate at 32° and a *k*β Si at 64°. Peaks marked with (#) on the (1,1) diffraction pattern at 23° and 46° are traces of a ternary phase of the structure. All the diffraction maxima can be indexed as 00*l* reflections as indicated above each peak. 45

III.3. HAADF-STEM image of $([PbSe]_{1.14})_2(NbSe_2)_1$ compounds. The bright spots represent the lead selenide layers and the darker spots represent the NbSe2 layers. 46

III. 4. Measured resistivity of $([PbSe]_{1.14})_m(NbSe_2)_1$ for variable temperatures showing an increase in resistivity as a function of *m*.. 47

III. 5. Two potential band alignment between the conduction band and the valence band of $NbSe_2$ and PbSe where (a) represents no charge transfer and (b) represents charge transfer... 49

III. 6. Parallel Resistor Model of $([PbSe]_{1.14})_m(NbSe_2)_1$.. 50

III. 7. Experimental resistivity of a single $NbSe_2$ layer as a function of temperature derived from the data in Figure 4 using Equation 7. The values of *m* and *n* in $([PbSe]_{1.14})_m(NbSe_2)_1$ for each data set are indicated in parenthesis..... 52

III. 8. Hall coefficients of $([PbSe]_{1.14})_1(NbSe_2)_1$ as a function of temperature... 53

III. 9. Carrier concentration of $([PbSe]_{1.14})_1(NbSe_2)_1$ as a function of temperature as derived from hall coefficient..... 54

III. 10. Experimental carrier concentration for a single $NbSe_2$ layer as function of temperature..... 55

III. 11. Experimental mobility of $([PbSe]_{1.10})_m(NbSe_2)_1$ as a function of temperature for varying *m* layers. 56

III. 12. Theoretical DFT calculation of $([PbSe]_{1.14})_m(NbSe_2)_1$ predicting charge transfer between PbSe and $NbSe_2$... 57

IV.1. Schematic of the synthesis scheme for $([SnSe]_{1.16-1.09})_1([Nb_xMo_{1-x}]Se_2)_1$ alloy ferecrystals. On the left is the as-deposited amorphous precursor. On the right is the ferecrystal alloy after self-assembly... 60

IV.2. (a) Nb/Mo ratios of PVD source vs. the first resulting ferecrystal sample. (b) Sample Nb/Mo ratio change vs. number of depositions for PVD sources with different initial Nb content... 66

IV.3. (a) Grazing incidence XRD patterns of $(SnSe)_{1.13}(Nb_{0.51}Mo_{0.49})Se_2$ annealed at 300, 350, 400, 450, 500, and 550 °C for 20 min. (b) Intensity of the (002) diffraction peaks with temperature..... 67

IV.4. (a) Out-of-plane X-ray diffraction patterns showing shift in the (004) peak with changes in dichalcogenide composition. (b) Plot of *c*-lattice parameter vs. x for $(SnSe)_{1.16-1.09}(Nb_xMo_{1-x})Se_2$ alloys.... 68

IV.5. In-plane (*hk0*) X-ray diffraction pattern of $(SnSe)_{1.13}(Nb_{0.51}Mo_{0.49})Se_2$. Indices for the cubic SnSe are given in bold, while those of the hexagonal $(Nb_{0.51}Mo_{0.49})Se_2$ are given in italic.... 70

IV.6. (a) In-plane X-ray diffraction patterns showing shift in the (110) peak of the dichalcogenide with changes in Mo/Nb ratio. (b) Plot of dichalcogenide *a*-lattice parameter vs. x for $(SnSe)_{1.16-1.09}(Nb_xMo_{1-x})Se_2$ alloys..... 72

IV.7. (a) Plot of rock salt *a*-parameter vs. x for $(SnSe)_z(Nb_xMo_{1-x})Se_2$ alloys. (b) Misfit parameter (z) vs. x for $(SnSe)_z(Nb_xMo_{1-x})Se_2$ alloys..... 73

IV.8. STEM image of $(SnSe)_{1.13}Nb_{0.51}Mo_{0.49}Se_2$..... 74

IV.9. 2D X-ray diffraction pattern of $(SnSe)_{1.13}Nb_{0.51}Mo_{0.49}Se_2$ ferecrystal. 75

IV.10. Resistivity vs. temperature for $(SnSe)_{1.16\text{-}1.09}(Nb_xMo_{1\text{-}x})Se_2$ ferecrystals with x = 0, 0.35, 0.54, 0.76 and 1... 76

IV.11. (a) Room Temperature conductivity vs. x for $(SnSe)_{1.16\text{-}1.09}(Nb_xMo_{1\text{-}x})Se_2$ alloys compared to literature values for $(Nb_xMo_{1\text{-}x})Se_2$ TMD alloys. (b) Room Temperature carrier concentration vs. x for $(SnSe)_{1.16\text{-}1.09}(Nb_xMo_{1\text{-}x})Se_2$ alloys... 77

V. 1. *c*-axis lattice parameters and deposition rates as a function of the measured Sn/V-ratio for all $([SnSe]_{1+\delta})_1(VSe_2)_1$ compounds. 82

V. 2. Specular X-ray diffraction of selected samples covering the investigated range of different Sn/V ratios. Only 00*l* reflections are observed. $^+$denotes Si-substrate peaks. 83

V. 3. HAADF-STEM image of the sample with a Sn/V-ratio of 1.37. The partial replacement of the dichalcogenide layer by SnSe-layers is observed. The stacking defects (b) and respective crystallographic orientations of the constituent layers (c) are highlighted. 85

V. 4. HAADF-STEM image of the compound with a Sn/V-ratio of 0.89. The partial replacement of the SnSe-layers by VSe_2 layers is observed (a). The stacking defects (b) and respective crystallographic orientations of the constituent layers (c) are highlighted. 86

V. 5. Rietveld refinement results for a substitution model, where one of the constituent layers is partially replaced by the other one for two compounds with Sn/V-ratios of 1.23 and 0.89 respectively. The refinement reveals interplanar distances along the *c*-axis. The error in all distances is below 0.005 nm..... 87

V. 6: In-plane X-ray diffraction patterns for three compounds with Sn/V-ratios of 0.89, 1.17, and 1.37, respectively. The *hk*0 indices of the rocksalt and dichalcogenide structures are provided and the (420) peak of the SnSe constituent is magnified to highlight the presence of two different lattice dimensions for the Sn-rich sample. 89

V. 7: a) Heat capacity (C_p) of $([SnSe]_{1.15})_1(VSe_2)_1$, compared to single crystalline VSe_2[6] as a function of temperature. The red dashed lines indicate the classic Dulong-Petit value for vibrations. The inset shows a discontinuity at 102 K, which is attributed to the charge density wave transition. The magnitude of the jump in C_P corresponds to an electronic Sommerfeld value of the normal state of $\gamma_n = 12 mJmol^{-1}K^{-1}$. b) C_p/T vs. T^2 for $([SnSe]_{1.15})_1(VSe_2)_1$ below 10 K including a least squares fit (blue dashed line) to the polynomial equation given in the Figure..... 91

V. 8: Electrical resistivity as a function of temperature for selected samples..... 92

V. 9: Carrier concentration as a function of temperature for selected samples..... 94

VI. 1. a) High-angle X-ray diffraction patterns of $([SnSe]_{1.15})_1(V_{1+x}Se_2)_3$ collected at different temperatures. Selected Bragg reflections for the sample annealed at 400°C are provided. The asterisk marks stage or substrate peaks. b) EPMA results as a function of temperature for $([SnSe]_{1.15})_1(V_{1+x}Se_2)_3$. Please note that the data points plotted at 0°C correspond to the unannealed precursor. 104

VI. 2. a) High-angle X-ray diffraction patterns of $([SnSe]_{1.15})_1(V_{1+x}Se_2)_n$ with n = 1 - 6 and a VSe_2 thinfilm. Selected Bragg reflections for all compounds are provided. The asterisk marks a substrate peak. b) *c*-lattice paramter for $([SnSe]_{1.15})_1(V_{1+x}Se_2)_n$ as a function of the number of VSe_2-layers (n) for as deposited and annealed (400°C, 20 min) compounds. 106

VI. 3. In-plane X-ray diffraction patterns of $([SnSe]_{1.15})_1(V_{1+x}Se_2)_n$ with n = 1 -6 and a $V_{1+x}Se_2$ thin film. The Bragg reflections for the SnSe and the $V_{1+x}Se_2$ constituent are provided for the (1,1) compound and the (0,1) compound, respectively. 108

VI. 4. Rietveld refinement results for $([SnSe]_{1.15})_1(V_{1+x}Se_2)_n$ with n = 2 and 3. The interlayer distances along the *c*-axis are provided. The error for all distances is < 0.001 nm. The structural schematics show full occupation of the interstitial V-position. 108

VI. 5. HAADF-STEM images of $([SnSe]_{1.15})_1(V_{1+x}Se_2)_6$. a) an overview displaying the intended layering sequence and highlighting the presence of rotational disorder between the constituents, b) displaying an area of 6 consecutive layers of $V_{1+x}Se_2$, where interstitial V-atoms are observed. The stick and ball models of the corresponding VSe_2 and VSe structures[10, 25] with projections along the [110] direction are provided. 110

VI. 6. a) Electrical resistivity as a function of temperature for $([SnSe]_{1.15})_1(V_{1+x}Se_2)_n$ with n = 1 - 6 and a $V_{1+x}Se_2$ thin film. b) Detailed view of the compounds with n = 3 - 6 and a $V_{1+x}Se_2$ thin film. For comparison the data of single crystalline bulk VSe_2 [14] are plotted. 112

VI. 7. Hall coefficient as a function of temperature for $([SnSe]_{1.15})_1(V_{1+x}Se_2)_n$ with n = 1 - 6 and a $V_{1+x}Se_2$ thin film. For comparison the data of single crystalline bulk VSe_2 [14] are plotted. 113

VII.1. Low-angle diffraction patterns collected from samples. Data from the Moore 1:1 compound are shown as the bottom curve in each. (a) Set A. The first loss of intensity near the critical angle is a substrate artifact. The critical angle is taken

from the second loss. (b) Set B. The apparent amplitude difference is due to the stacking. The range of normalized data is comparable for all samples... 123

VII.2. High angle specular diffraction patterns collected from samples in (a) set A and (b) set B. Data from the Moore 1:1 compound are shown for comparison as the bottom curve in each pane. The apparent difference in scales is due to a reduced range in the pane with fewer curves... 126

VII.3. Sample resistivity values cluster in two regions for the two sample sets and trend with Pb/Se ratio. The line is provided as a guide to the eye... 127

VII.4. Variable temperature resistivity data for select ferecrystal samples from set A. Curvature is very similar in all cases, with the value differences in magnitude roughly scaling with carrier concentration 128

VII.5. Carrier concentration as a function of temperature for a subset of samples. The gentle change is typical of a metallic band structure 129

VII.6. Room temperature carrier density plotted against Seebeck coefficients for all samples. The solid curves indicate the expected relationship for different effective masses assuming a single rigid parabolic band. 131

VIII. 1 Specular X-ray diffraction of ([Sn0.4Bi0.6Se]1+d)1(VSe2)1 at temperatures indicated above the X-ray patterns with intensity plotted on a log scale to highlight weak reflections. AD means ''as deposited''. 139

VIII. 2 Specular X-ray diffraction patterns of ([Sn1−*x*Bi*x*Se]1+d)1(VSe2)1 compounds with different Bi-contents. The intensity is plotted on a log scale to highlight weak intensity reflections 140

VIII. 3 The *c*-axis lattice parameter as a function of Bi-content for([Sn1−*x*Bi*x*Se]1+d)1(VSe2)1 compounds 142

VIII. 4 In-plane X-ray diffraction patterns of ([Sn1-*x*Bi*x*Se]1+d)1(VSe2)1 compounds with $0 \le x \le 0.57$. The dashed vertical lines highlight the peak shift observed for the (110) reflection of the VSe_2 constituent and the (220) reflection on the rock salt constituent. The asterisk marks a stage peak 143

VIII. 5 In-plane area/f.u. for both constituents of ([Sn1-*x*Bi*x*Se]1+d)1(VSe2)1 as a function of *x* 144

VIII. 6 (a) Structural schematic and refinement model with the distances between the atomic planes along the *c*-direction of the ferecrystalline superlattice. (b) Change of the interplanar distances as a function of Bi-content from Rietveld refinements 146

VIII. 7 STEM images of ([Sn0.6Bi0.4Se]1+d)1(VSe2)1 showing (a) an overview of the sample along the *c*-direction, and (b) distinct crystallographic orientations in diff erent layers highlighting the rotational disorder 147

VIII. 8 Resistivity of ([Sn1−*x*Bi*x*Se]1.15)1(VSe2)1 compounds as function of temperature. The inset displays the temperature dependence of the residual resistivity ratio (RRR). 149

VIII. 9 Hall coeffi cient, *R*H, of ([Sn1−*x*Bi*x*Se]1.15)1(VSe2)1 as function of temperature. For comparison the Hall coefficient for bulk 1T-VSe2 is plotted.. 149

VIII. 10 Seebeck coefficient, s, at room temperature for ([SnSe]1.15)*m*(VSe2)1 compounds as function of x..... 150

IX.1: 00*l* Diffraction as a function of annealing temperature (offset for clarity). Observed superlattice maxima are indexed for the pattern at the optimum temperature (350°C).. 159

IX.2: A diffraction pattern of sample A (a) displaying Kiessig fringes to more than 15° 2θ (b). The Parratt relationship is inset. Superlattice maxima are indexed, * denotes substrate or stage peaks. 163

IX.3: (a) Low magnification HAADF-STEM images displaying alternating layers of SnSe and $TiSe_2$ throughout the entirety of the film. (b) Bulk structures for the constituent compounds. (c) High magnification HAADF-STEM displaying two unique lattices intergrown. Crystal faces and structure representations are specified for hexagonal $TiSe_2$ and square-basal SnSe, as seen with other ferecrystal systems.. 165

IX.4: Rietveld refinement of sample A. The red dots represent the measured pattern, the black line the modeled intensity, the blue line the difference between experimental and calculated intenstity, and the blue ticks indicate the Bragg positions (only 00l). Spacings between interatomic planes in the c direction are also given.. 167

IX.5: Temperature dependent resistivity for the compounds synthesized from modulated elemental reactants. 170

IX.6: Temperature dependent Hall coefficient for the compounds synthesized from modulated elemental reactants. 171

IX.7: (a) Calculated carrier concentration (n_e) and (b) electron mobility (μ_e) based on a single band model, as a function of temperature. 172

IX.8: Proposed band structures of the constituent materials (left and right) and the ferecrystal product (center)... 174

X.1. A series of 00l diffraction patterns for a precursor designed to form $(BiSe)_{1+\delta}(TiSe_2)_2$ collected as a function of annealing temperature (offset for clarity). All films were annealed for 30 minutes at the temperature indicated by the scan and the scans are offset by arbitrary amounts. The y-axis is log intensity to make weak reflections more apparent. 181

X2. X-ray diffraction patterns of $[(BiSe)_{1+\delta}]_1(TiSe_2)_n$ (1-n) samples. Compounds are crystallographically aligned with the c-axis normal to the substrate so all maxima can be indexed as 00l reflections. Diffraction patterns were collected using two different wavelengths and are shown as log intensity versus Q to make weak reflections visible. The scans are offset by arbitrary amounts. The asterisk (*) indicates peaks from the silicon substrate... 182

X.3. Temperature-dependent resistivity of the $[(BiSe)_{1+\delta}]_1(TiSe_2)_n$ (1-n) ferecrystalline compounds is compared to the published temperature dependent resistivity for the ferecrystal $(BiSe)_{1.15}TiSe_2$,[12] and MLC $(BiSe)_{1.13}TiSe_2$ and $(BiSe)_{1.15}(TiSe_2)_2$.[14].. 184

X.4.Temperature-dependent a) Hall Coefficients, b) carrier concentrations, and c) mobilities. a) Temperature-dependent Hall Coefficients for the ferecrystalline compounds $[(BiSe)_{1+\delta}]_1(TiSe_2)_n$ (1-n) are compared to the previously published ferecrystal $(BiSe)_{1.15}TiSe_2$.[12] b) Temperature-dependent carrier concentration calculated using a single band model for the ferecrystalline compounds $[(BiSe)_{1+\delta}]_1(TiSe_2)_n$ (1-n) including previously published $(BiSe)_{1.15}TiSe_2$.[12] c) Temperature-dependent mobilities calculated using a single band model for synthesized from the ferecrystals including previously published $(BiSe)_{1.15}TiSe_2$.[12].. 186

X5. In-plane (hk0) diffraction pattern of $[(BiSe)_{1+\delta}]_1(TiSe_2)_n$ (1-n) samples displaying Bragg peaks and associated indices from the independent lattice structures of both constituents. Diffraction patterns shown in q-space because they were collected using two different wavelengths, graphed using log intensity to make weak reflections visible and offset by arbitrary amounts. All films were annealed for 30 min at 350 °C. 184

X.6. Cross Sectional HAADF-STEM images: a) a full film cross-section showing alternating BiSe and $TiSe_2$ layers in $(BiSe)_{1.14}(TiSe_2)_2$ and rotational disorder between constituent layers, b) higher magnification image of a region of the $(BiSe)_{1.14}(TiSe_2)_2$ sample showing the 1-T polymorph of the $TiSe_2$ layer, c) higher magnification image of a region of the $(BiSe)_{1.15}(TiSe_2)_3$ with a grain boundary in the $TiSe_2$ layer, and d) a higher magnification image of a region of the $(BiSe)_{1.14}(TiSe_2)_4$ showing the 1T polymorph of the $TiSe_2$ layer and the rotational disorder between constituents.. 194

X.7. High magnification cross sectional HAADF-STEM image of $(BiSe)_{1.14}(TiSe_2)_2$ showing the Bi-Bi bonded pairs resulting from the anti phase boundary are most visible along the (110) zone axis (rock salt setting) of the BiSe... 195

X.8. Models for the refined atomic plane positions in $(BiSe)_{1+\delta}(TiSe_2)_2$, $(BiSe)_{1+\delta}(TiSe_2)_3$, and $(BiSe)_{1+\delta}(TiSe_2)_4$. The dashed lines indicate the unit cell. The models for the Rietveld refinement of 00l diffraction patterns were based on the constituents BiSe and $TiSe_2$ as determined by hk0 diffraction. For each compound Bi is puckered toward the dichalcogenide. 197

X.9. Area X-ray diffraction data for $(BiSe)_{1.14}(TiSe_2)_2$ and $(BiSe)_{1.14}(TiSe_2)_4$ compounds indicate turbostratic disorder..... 197

XI.2. A series of diffraction scans collected as a function of annealing temperature, as indicated at the right side of the scans. All of the diffraction peaks from the sample can be indexed as (00*l*) reflections and the (004) reflection is indexed in the figure. Diffraction artifacts from the stage and Si substrate are marked with * symbols..... 206

XI.3: Rietveld refinement of the $[(BiSe)_{1+\delta}]_1[VSe_2]_1$ heterostructure determine the position of atomic planes along the c-axis. The model to the right shows projected positions of the atoms onto the c-axis and their relative distances..... 208

XI.4. (a) Representative cross section HAADF-STEM images of the $[(BiSe)_{1+\delta}]_1[VSe_2]_1$ heterostructure. (b) Appearance of anti-phase boundaries apparent in BiSe bilayer... 209

XI.5. Resistivity data as a function of temperature for the $[(BiSe)_{1+\delta}]_1[VSe_2]_1$ heterostructure compared to that reported for VSe_2[12] and $[(SnSe)_{1.15}]_1(VSe_2)_1$.[15].. 210

XI.6. Hall coefficients as a function of temperature for the $[(BiSe)_{1+\delta}]_1[VSe_2]_1$ heterostructure compared to that reported for VSe_2[12] and $[(SnSe)_{1.15}]_1(VSe_2)_1$.[15].. 211

XII. 7. Out-of-plane XRD pattern (Cu K_α source) for representative sample (red circles), calculated pattern from Reitveld refinement (black line), and difference between the experimental and simulated patterns (blue line). The numbers in parenthesis indicate the (00*l*) plane contributing to the observed reflection. The schematic represents the refined structure, with blue lines indicating a plane of Se atoms, red lines a plane of Nb atoms, and green lines a plane of Bi atoms. Dimensions in the schematic are given in nm..... 224

XII. 8. In-plane XRD scan from Sample B. Peaks corresponding to the BiSe phase are labeled in green boldface. Peaks corresponding to the $NbSe_2$ phase are labeled in black italics. The broad reflections at angles greater than 75 °2θ were not used to determine in-plane lattice parameters... 226

XII. 9. Representative cross-sectional HAADF-STEM image. The colored boxes in the upper left corner indicate which layers correspond to which constituent. The indices refer to the zone axis of the grain to the right of the indices in that layer 228

XII. 10. A 110 zone axis (relative to a face centered cubic unit cell) showing antiphase boundaries approximately every 1.52 nm. The scale bar represents 2.5 nm. The colored image below the HAADF-STEM image shows an idealized structural model. The red arrows indicate the observed antiphase boundaries..... 229

XII. 11. Temperature-dependent electrical resistivities for four different Bi-Nb ferecrystals (measured in this work) and for the Bi-Nb misfit layered compound measured by Zhou and coworkers.[10] The error bars due to uncertainty in the measurements are about the size of each data point in the figure. 231

XII. 12. Temperature-dependent Hall coefficients for four different Bi-Nb ferecrystals (measured in this work) and for the Bi-Nb misfit layer compound measured by Zhou and coworkers.[10] 233

XIII. 1. Structural information for the VSe_2–$GeSe_2$ heterostructures. a) Energetic requirements and reaction pathway for the formation of the VSe_2(m)–$GeSe_2$(n) heterostructures where m = 2–4 and n = 1–2. b) Specular X-ray diffraction patterns of VSe_2(m)–$GeSe_2$(n). c) In-plane X-ray diffraction patterns of VSe_2(3)–$GeSe_2$(1) and VSe_2(3)–$GeSe_2$(2). d) Rietveld refinement of VSe_2(3)–$GeSe_2$(2), the error of atomic plane distances is below 0.002 nm 238

XIII. 2. STEM image and an EDX map of the (3,1) heterostructure. a) STEM image of the VSe_2(3)–$GeSe_2$(1) compound with VSe_2 corresponding to the bright layers and $GeSe_2$ corresponding to the dark layers. b) EDX map of the area highlighted by the yellow square in (a). Ge red, V green. 239

XIII. 3. Superlattice structural representation and HAADF-STEM image of the (3,1) heterostructure. a) Two structural units of the VSe2(3)–GeSe2(1) compound highlighting rotational disorder indicated by white marks. b) HAADF-STEM image of VSe2(3)–GeSe2(1) with all the 20 consecutive structural units of the (3,1) compound. The highlighted areas labeled 4a, 4c, and 4d refer to the close up images in Figure XIII. 4.. 240

XIII. 4. HAADF-STEM images of the (3,1) heterostructure. a) A monolayer $GeSe_2$ structure with a section that contains the $GeSe_2$ structure shown. b) An enlargement of Figure XIII. 4a illustrating the [100] orientation of the $GeSe_2$ structure. An enlargement of Figure XIII. 3b where the same (c) or different (d) VSe_2 orientations are observed.. 242

XIII. 5. Electrical transport properties of VSe2(m)–GeSe2(n) where m = 2–4 and n = 1 or 2. a) Temperature- dependent resistivity. Note: the break in the y-axis. b) Temperature dependent Hall coefficient. Note: the scale change in the y-axis. c) Hall coefficient at 95K as a function of n/m ratio. 245

XIV.1: The evolution of the diffraction pattern during the self assembly of an as-deposited precursor designed to nominally form $(Pb_{0.5}Sn_{0.5}Se)_{1+\delta}TiSe_2$. The 00*l* indices for the superlattice reflections are given above the 350°C scan... 253

XIV.2: (a) The 00*l* diffraction pattern of the five $(Pb_xSn_{1-x}Se)_{1+\delta}TiSe_2$ compounds prepared in this investigation (offset for clarity), the peaks can be indexed to the superlattice (out-of-plane) structure. (b) A close up of the (007) and (008) reflections, showing the systematic shift in the position of the reflections and the systematic change in the intensity of the (007) reflection of the different compounds as x is varied. The inset shows the change in the lattice parameter as a function of composition. 254

XIV.3: (a) In-plane diffraction patterns of the five $(Pb_xSn_{1-x}Se)_{1+\delta}TiSe_2$ compounds prepared in this investigation. All peaks can be indexed to *hk*0 reflections of the constituent structures. (b) A close up of two reflections that clearly show the rectangular in plane distortion of the rock salt constituent as it becomes more Sn rich. 257

XIV.4: In-plane area of the PbxSn1-xSe constituent unit cell and the calculated misfit parameter, which results from the incommensurate constituent lattices. The error for both data sets is smaller than the markers for each point. 258

XIV.5: (a) HAADF-STEM data of a representative region (x = 0.26) showing superlattice structure. Visible zone axes are labeled for each constituent and (b) the corresponding EDX map, with Se-Ti-Se trilayers clearly visible. 259

XIV.6: top - EDX map for the x = 0.70 sample with the Se signal removed for clarity. The bottom three graphs provide integrated intensity profiles for the three alloy compounds. Pixel resolution varies depending on the magnification used for the profile, but the compositionally distinct layers are clearly resolved for all three samples. 261

XIV.7: Temperature dependent resistivity. The magnitudes of the resistivity for all compounds fall within the range expected from sample to sample variation. The (A) and (B) labels for the two x = 0 data sets refer to two separate preparations of nominally the same sample, as previously reported.. 262

XIV.8: Carrier concentration calculated from the Hall coefficient, assuming a single band model 263

XIV.9: Hall mobility calculated from resistivity and carrier concentration. The magnitude of the mobility either remains constant or increases for the mixed cation compounds, providing the first direct evidence for the conduction mechanism in the compounds. 264

XV.1. a. Out-of-plane (00l) diffraction patterns for compounds with different layering schemes. Indices are shown in parentheses above for selected reflections 270

XV.2 In- plane (*hk*0) diffraction patterns for compounds with different layering schemes. Indices are shown in parentheses above for selected reflections..... 271

XV.13: HAADF-STEM of the m = 1, n = 3 compound at low (a) and high (b) magnification, where the expected crystal faces for the constituents are observed. The EDS mapping data and the corresponding integrated profile can be found in pane c 273

XV.4: The calculated number of unique compounds based on the number of constituent layers, and the number of layers in the unit cell 274

XVI.1. (a) Synthesis schematic for $(SnSe)_{1+\delta}(MoSe_2)_{1+\gamma}(SnSe)_{1+\delta}(NbSe_2)_1$. The as deposited precursor is depicted on the left with the self-assembled ferecrystal on the right..... 279

XVI.2. Specular XRD patterns of $(SnSe)_{1+\delta}([Mo_xNb_{1-x}]Se_2)_{1+\gamma}(SnSe)_{1+\delta}$ $([Nb_xMo_{1-x}]Se_2)$ annealed at temperatures ranging from 300 to 500 °C. The (00*l*) indices are shown above the scan taken after annealing at 450°C.. 282

XVI.3. (a) Change in the intensity of the (004) reflection with temperature. (b) Change in the FWHM of the (004) reflection with temperature..... 283

XVI.4. Rietveld refinement of the $(SnSe)_{1+\delta}([Mo_xNb_{1-x}]Se_2)_{1+\gamma}(SnSe)_{1+\delta}$ $([Nb_xMo_{1-x}]Se_2$. Experimental data are in black and the fit to the data in red with the residuals below in blue. The inset shows the structure and distances obtained from the fit..... 285

XVI 5. (a) STEM image of $(SnSe)_{1+\delta}([Mo_xNb_{1-x}]Se_2)_{1+\gamma}(SnSe)_{1+\delta}([Nb_xMo_{1-x}]Se_2)$. (b) Expansions of different layers within part a showing the local coordination of the layers. (c) HAADF Intensity line profile for $(SnSe)_{1+\delta}([Mo_xNb_{1-x}]Se_2)_{1+\gamma}(SnSe)_{1+\delta}$ $([Nb_xMo_{1-x}]Se_2$ film..... 286

XVI.6. EDX line scan of $(SnSe)_{1+\delta}([Mo_xNb_{1-x}]Se_2)_{1+\gamma}(SnSe)_{1+\delta}([Nb_xMo_{1-x}]Se_2)$. The Mo-K line (red), Nb-K line (blue) and the Sn-L line (purple dashed) are shown. Selenium omitted for clarity..... 287

XVI.7. (a) In-plane (*hk*0) XRD pattern of $(SnSe)_{1+\delta}([Mo_xNb_{1-x}]Se_2)_{1+\gamma}(SnSe)_{1+\delta}$ $([Nb_xMo_{1-x}]Se_2)$ compared to the $(SnSe)_{1.16}NbSe_2$ and $(SnSe)_{1.09}MoSe_2$ parent compounds. Indices for the SnSe are given in bold, while those of the TSe_2 (where T = Mo and/or Nb) are given in italics. (b) Expansion of the TSe_2 110 region.. 288

XVI.8. (a) Electrical resistivity vs. temperature of $(SnSe)_{1.16}([Mo_{0.9}Nb_{0.1}]Se_2)_{1.06}$ $(SnSe)_{1.16}([Nb_{0.9}Mo_{0.1}]Se_2)$ (green circles), $(SnSe)_{1.03}MoSe_2$ (blue triangles), $(SnSe)_{1.13}$ $([Nb_{0.5}Mo_{0.5}]Se_2)$ (black squares) and $(SnSe)_{1.16}NbSe_2$ (red diamonds). (b) Normalized room temperature (red squares) and 45K (blue squares) resistivity vs. x for the $(SnSe)_z$ $(Nb_xMo_{1-x})Se_2)$ ferecrystal alloys compared to the $(SnSe)_{1+\delta}([Mo_xNb_{1-x}]Se_2)_{1+\gamma}(SnSe)_{1+\delta}$ $([Nb_xMo_{1-x}]Se_2)$ (green circles)..... 290

XVII.1. Illustration of the change in the dichalcogenide separation through modification of the stacking sequence of $([SnSe]_{1+\delta})_m([\{Mo_xNb_{1x}\}Se_2]_{1+\gamma})_1([SnSe]_{1+\delta})_m(\{Nb_xMo_{1-x}\}Se_2)_1$ ferecrystals (with m = to 0 - 4).. 294

XVII.2. Locked-coupled (00*l*) XRD patterns of $([SnSe]_{1+\delta})_m([\{Mo_xNb_{1-x}\}Se_2]_{1+\gamma})_1$ $([SnSe]_{1+\delta})_m(\{Nb_xMo_{1-x}\}Se_2)_1$ ferecrystals (with m = to 0 - 4)... 298

XVII.3. HAADF-STEM images of $([SnSe]_{1+\delta})_m([\{Mo_xNb_{1-x}\}Se_2]_{1+\gamma})_1$ $([SnSe]_{1+\delta})_m(\{Nb_xMo_{1-x}\}Se_2)_1$samples with m = 2 and 4. Se_2 Different orientations of the individual constituents are highlighted... 299

XVII.4. In-Plane (*hk*0) XRD $([SnSe]_{1+\delta})_m([\{Mo_xNb_{1-x}\}Se_2]_{1+\gamma})_1([SnSe]_{1+\delta})_m$ $(\{Nb_xMo_{1-x}\}Se_2)$ ferecrystals (with m = to 0-4) compared to the $([SnSe]_{1.16})_1(NbSe_2)_1$ and $([SnSe]_{1.09})_1(MoSe_2)_1$ parent compounds. Insets show the expansion of the TSe_2 110 and SnSe 310/130 regions.. 300

XVII.5. TSe_2 *a*-axis lattice parameter is graphed versus the number of SnSe bilayers. The Mo-rich constituent is given by blue triangles, the Nb-rich constituent by red circles. The red and blue horizontal lines depict the *a*-parameters of the $SnSe_{1.16}NbSe_2$ and $SnSe_{1.09}MoSe_2$ parent compounds respectively..... 302

XVII.6. Resistivity vs. temperature for the $([SnSe]_{1+\delta})_m([\{Mo_xNb_{1-x}\}Se_2]_{1+\gamma})_1$ $([SnSe]_{1+\delta})_m(\{Nb_xMo_{1-x}\}Se_2)_1$ compounds with m = 0-4. The inset shows the resistivity ratio ρ/ρ_{295K}... 303

XVII.7. (a) Room temperature resistivity and normalized room temperature resistivity (b) vs. the number of SnSe layers in $([SnSe]_{1+\delta})_m([\{Mo_xNb_{1-x}\}Se_2]_{1+\gamma})_1([SnSe]_{1+\delta})_m(\{Nb_xMo_{1-x}\}Se_2)_1$ compounds with m = to 0-4. (b) Normalized room temperature resistivity (red squares)... 304

XVII.8. Temperature dependent Hall coefficients measured for the $([SnSe]_{1+\delta})_m$ $([\{Mo_xNb_{1-x}\}Se_2]_{1+\gamma})_1([SnSe]_{1+\delta})_m(\{Nb_xMo_{1-x}\}Se_2)_1$ compounds with *m* = to 0-4.. 305

XVII.9. Temperature dependent carrer concentrations calculated using a single band model for the $([SnSe]_{1+\delta})_m([\{Mo_xNb_{1-x}\}Se_2]_{1+\gamma})_1([SnSe]_{1+\delta})_m(\{Nb_xMo_{1-x}\}Se_2)_1$ compounds..... 306

XVII.10. Holes per Nb with increasing numbers of SnSe layers for the $([SnSe]_{1+\delta})_m([\{Mo_xNb_{1-x}\}Se_2]_{1+\gamma})_1([SnSe]_{1+\delta})_m(\{Nb_xMo_{1-x}\}Se_2)_1$ (red squares) compared to the $([SnSe]_{1.16})_m(NbSe_2)_1$ (black circles)... 307

XVII.11. Band alignment diagram of the $NbSe_2$ (green), SnSe (blue), and $MoSe_2$ (red) systems..... 308

XVIII.1. Schematic of a layered precursor showing the interdiffusion of the layers to form an amorphous intermediate and the subsequent nucleation of the targeted compound. 315

XVIII.2. The blue box shows the thinnest structural units of three representative binary constituents, the outside two with a transition metal dichalcogenide structure (TSe2 and T'Se2) and the middle one a rock salt structure (MSe) with two (001) planes. The second row in the red box displays the three simplest binary heterostrutures, (MSe)1(TSe2)1, (TSe2)1(T'Se2)1 and(MSe)1(T'Se2)1. The top row shows the three compounds with the next smallest repeating units, A1B2, A2B2 and A2B1, illustrating how the constituents can be assembled with different individual thicknesses and, for thicker repeats, different orders of assembly. The bottom row contains a schematic of compounds where the dichalcogenides have been allowed to form the compound (MSe)1(T1 - *x*T'*x*Se2)1 (green box). The thickness of each constituent can be controlled as shown in the top row for the pure dichalcogenides. The image on the bottom left (orange box) shows an ordered alloy, where the three components form the (MSe)1(TSe2)1(MSe)1(T'Se2)1 compound. The A, B, and C components can be combined in different thicknesses and sequences to make a very large number of unique nanoarchitectures. (For interpretation of the references to color in this figure legend, the reader is referred to the web version of this article.)..... 316

XVIII.3. Diffraction pattern of NbSe2 formed at 400 °C by annealing a precursor containing Nb/Se elemental bilayers. The y *axis* is log intensity to highlight low intensity diffraction maxima. Only the 00*l* reflections are observed due to the textured nature of the product. Substrate peaks are indicated with an asterisk..... 318

XVIII.4. The intensity of the first observed 00*l* reflection of NbSe2, formed at 400 °C, as a function of time that the shutter was open depositing Nb at a constant rate. The maximum in the intensity corresponds to the precursor with a 1:2 ratio of Nb to Se.. 319

XVIII.5. An XRR pattern of a sample containing 58 repeating NbSe2 trilayers, formed at 400 °C, from a precursor containing 58 repeating Nb–Se bilayers in the repeating precursor. 320

XVIII.6. Specular diffraction scans of $[(SnSe)_{1.15}]_1(VSe_2)_1$, $[(SnSe)_{1.16}]1(NbSe_2)_1$, $[(SnSe)_{1.09}]_1(MoSe_2)_1$, and $[(SnSe)_{1.15}]_1(TaSe_2)_1$. All of the diffraction peaks are 00lreflections, and the indices for each reflection are indicated above the scan of the $[(SnSe)_{1.15}]_1(VSe_2)_1$ sample. All samples were annealed at 400 °C for 20 min. 322

XVIII.7. In-plane diffraction scans of $([SnSe])_{1.15})_1(VSe_2)_1$, $([SnSe])_{1.16})_1(NbSe_2)_1$, $([SnSe])_{1.09})_1(MoSe_2)_1$, and $([SnSe])_{1.15})_1(TaSe_2)_1$. All of the diffraction peaks can be indexed as (*hk*0) reflections of the two constituents. The indices for each reflection are indicated above the scan of the $([SnSe]_{1.15})_1(VSe_2)_1$ sample. 323

XVIII.8. Cross sectional HAADF STEM image of $([SnSe]_{1.15})_1(VSe_2)_1$..... 325

XVIII.9. The number of possible structural isomers for a given AmBn stoichiometry are given in each of the boxes. The shading of the boxes reflects the rapid increase in the number of isomers as m and n increase.... 327

XVIII.10. The difference between the initial source composition and the composition of the first sample made from that source, showing the preferential deposition of Mo.... 329

XVIII.11. Plot of the change in the composition of samples as samples are sequentially made from a specific source. The samples become more Nb rich as the source becomes depleted in Mo..... 330

XVIII.12. The change in the atomic percent of Ta in a sample containing an alloyed $(Ta_{1-x}V_x)Se_2$ layer graphed versus the change in the percent of time the shutter of Ta was open divided by the total time that the shutters of Ta and V were opened.... 331

XVIII.13. Specular X-ray diffraction scans of a series of (SnSe)1 þδ(TaxV1 - x)Se2 com- pounds formed at 400 °C. The diffraction peaks shift slightly to lower angles as x is increased, indicating an increase in the c-axis lattice parameter. The 00lindices are shown above the top diffraction scan.... 332

XVIII.14. The calculated c-axis lattice parameter for a series of (SnSe)1 þ δ(TaxV1 - x)Se2 compounds plotted as a function of x. The linear increase in the c-axis lattice parameter with increasing x is expected from Vegard's law..... 332

XVIII.15. In-plane X-ray diffraction scans of a series of (SnSe)1 þ δ(TaxV1 - x)Se2 com- pounds formed at 400 °C. The diffraction peaks shift as x is increased,

indicating changes in the a-axis lattice parameter of both constituents. The (hk0) indices are shown above the top diffraction scan with the indices for SnSe indicated in bold.... 334

XVIII.16. The calculated a-axis lattice parameter for the $(Ta_xV_1 - x)Se_2$ constituent plotted as a function of x. The linear increase in the a-axis lattice parameter with increasing x is expected from Vegard's law due to the larger size of Ta relative to V. The small a-axis lattice parameter for x ¼ 1 results from a change from octahedral coordination for x ¼ 0.8 to trigonal prismatic coordination when x ¼ 1.... 334

XVIII.17. The calculated a-axis lattice parameter for the SnSe constituent plotted as a function of x..... 335

XVIII.18. A graph of the Mo to Nb ratio as a function of the time the Mo shutter was open while the Nb shutter time was held constant. The dotted green line describes the misfit between the NbSe2 and the MoSe2 constituents and the intercept with the experimental line provides the time the Mo shutter needs to be held open to achieve this composition. 337

XVIII.19. A comparison of the diffraction patterns of $(SnSe)_{1 þ δ}(Ta_{0.5}V_{0.5})Se_2$ and $(SnSe)_{1 þ δ}(VSe_2)_{1 þ γ}(SnSe)_{1 þ δ}TaSe_2$ formated at 400 °C. The doubling of the number of reflections results form a doubling of the *c*-axis lattice parameter 338

XVIII. 20. In-plane diffraction of the nominally (SnSe)1 þδ(VSe2)1 þ γ(SnSe)1 þ δTaSe2 compound (green) to determine the extent of intermixing. The indices of the (hk0) reflections are given above the top diffraction scan, with those in bold the indices for SnSe reflections and those in italic for the dichalcogenide constituents. The pattern of the (SnSe)1þ δ(VSe2)1þ γ(SnSe)1þ δTaSe2 (blue) is provided for comparison. (For interpretation of the reference to color in this figure legend, the reader is referred to the web version of this article.)..... 339

XVIII. 21. High resolution HAADF STEM image of the nominal (SnSe)1 þ δ(VSe2)1 þ γ(SnSe)1 þδTaSe2 compound shows the local structure. The different zone axes in different layers result from rotational disorder which is typical for layered compounds prepared using the MER technique. 339

XVIII. 22. EDX maps of a region the $[(SnSe)_{1.15}]_1([Ta_xV_{1-x}]Se_2)_1[(SnSe)_{1.15}]_1([V_yTa_{1-y}]Se_2)_1$ compound. The data is consistent with the HAADF STEM images, with alternating layers of SnSe and the transition metal dichalcogenide. The vanadium and tantalum intensities oscillate out of phase with one another, suggesting alternating layers of a tantalum rich and a vanadium rich dichalcogenide.... 340

XVIII. 23. EDX line scans of$[(SnSe)_{1.15}]_1([Ta_xV_{1-x}]Se_2)_1[(SnSe)_{1.15}]_1([V_yTa_{1-y}]Se_2)$ compound. The out of phase oscillation of the Ta and V layers indicates alternating V and Ta rich dichalcogenide layers..... 341

XVIII. 24. Electrical transport properties of the $(SnSe)_{1+\delta}(Ta_xV_{1-x})Se_2$ compounds as a function of x. (a)Temperature dependent resistivity. (b) Room temperature resistivity as a function of x. (c) Temperature dependent Hall coefficient. 344

XVIII. 25. Temperature dependent resistivity of the $[(SnSe)_{1.15}]_1([Ta_{0.3}V_{0.7}]Se_2)_1[(SnSe)_{1.15}]_1([V_{0.3}Ta_{0.7}]Se_2)_1$ compound and the related compounds$[(SnSe)_{1.15}]_1(VSe_2)_1$,$[(SnSe)_{1.15}]_1(TaSe_2)_1$and $[(SnSe)_{1.15}]_1([Ta_{0.5}V_{0.5}]Se_2)_1$..... 344

XIX.1. XRR patterns of 4-coat films of $InGaO_x$, AlO_x, and HafSOx without peroxide (top to bottom, respectively). The patterns are offset for clarity..... 355

XIX.2. (a) A schematic representation of two simple structures of a 4-coat stack, one in which each coat is homogeneous and one where each coat has the identical inhomogeneous electron density. (b) The simulated XRR data for the two cases shown in (a)..... 355

XIX.3. The raw and modeled XRR data of a 4-coat multilayer of HafSOx without peroxide annealed at 180 °C for 1 minute..... 356

XIX.4. XRR data for a single coat film without peroxide annealed at 180 °C for 1 minute. The data was modeled as a homogeneous single layer and as a bilayer with a thin, dense surface layer and a less dense bulk layer separated by a density gradient. The addition of the surface 'crust' improved the agreement between the model and the data, especially in the first three observed minima in the XRR pattern..... 357

XIX.5. XRR data for a single coat film containing peroxide annealed at 80 °C for 1 minute. The data was modeled as a homogeneous single layer and as a bilayer consisting of a thin, dense surface layer and a less dense bulk layer separated by a density gradient. The addition of the surface 'crust' improved the agreement between the model and the data, especially with respect to the minima in the XRR pattern between 0.8 and 2 degrees.. 359

XIX.6. (a) HAADF-STEM image of the cryo-FIB cross-section of a single layer HafSOx film containing peroxide annealed at 80 °C for 1 minute, and (b) the heavy atom density profile of the film obtained by integrating the intensity of the pixels in the boxed region in (a)... 360

XIX.7. (a) MEIS data collected on a HafSOx film containing peroxide annealed for 3 minutes at 80 °C (blue), 5 minutes at 150 °C (red) and 5 minutes at 300 °C (black). (b) An expansion of the Hf area, which visually demonstrates the total

film thickness decreases with increasing annealing temperature while the average density increases. The peak at 125 keV indicates that all of the films have a surface layer with higher Hf density... 362

XX.1. SEM image of an example dose array 371

XX.2. a) Plotted contrast curves for varying accelerating voltages and b) the dependence of contrast and d_{100} on accelerating voltage. c) Modeled interaction volumes for the corresponding voltages showing the retraction of the "tear drop" to the film... 372

XX.3. Simulated normalized PSFs for 2, 5, 6, 10, 20, and 30 keV primary beam energies in a 22 nm thick HafSOx resist... 374

XX.4. Simulated and experimental sensitivity enhancement as a function of beam energy, relative to 30 keV. For the experimental data points, the error bars reflect the uncertainty in the calculation of d_{100}. For the simulated data points, the error bars reflect the sensitivity of the model to small changes in film thickness and composition relative to the assumed values..... 374

XX.5. SEM images of patterned 9 nm lines at 10 keV... 376

XX.6. STEM cross-section images of high resolutions lines patterned using 10 keV primary beam energy... 377

XX.7. Percentage of total energy deposited in the resist as a function of radius from the beam irradiation spot for HafSOx films of different thicknesses..... 379

XXI. 14. Representative HAADF STEM image from the $[(SnSe)_{1.16}]_2(MoSe_2)_{1.06}[(SnSe)_{1.16}]_2(NbSe_2)_1$ heterostructure. The $MoSe_2$ and $NbSe_2$ monolayers cannot be visually distinguished from one another, and are labeled as TSe_2 using red and purple boxes. The SnSe layers are indicated in green. Zone axes in selected regions are labeled for each constituent. The yellow box marks the region selected for analysis..... 386

XXI. 15. Horizontal intensity deviation analysis. (a) Shows the raw horizontal intensity deviation profile and 155-pixel running median smoother. (b) Shows the resulting background subtracted horizontal intensity deviation profile, in which the running median values have been subtracted from the raw profile. (c) Shows the distribution of intensity deviations relative to the mean. (d) Shows how the distribution width (standard deviation) depends on the box size that is scanned across image 388

XXI. 16. Vertical intensity deviation analysis. (a) Shows the raw vertical intensity deviation profile and 155-pixel running median smoother. (b) Shows the resulting background subtracted vertical intensity deviation profile, in which the

running median values have been subtracted from the raw profile. (c) Shows the distribution of intensity deviations relative to the mean after background subtraction. For comparison, the horizontal distribution is the same as shown in Figure XXI. 35c. (d) Shows how the distribution width (standard deviation) depends on the box size that is scanned vertically across image 390

XXI. 17. a) Atomic plane z-coordinates determined using HAADF STEM data. The uncertainty in the atomic plane positions comes from the 95% confidence interval from the combined image measurements. The Sn and Se layers in the SnSe layers could not be distinguished in the HAADF images. b) Refined atomic plane z-coordinates obtained after performing a Rietveld refinement of diffraction data using the coordinates in (a) as a starting point..... 391

XXI. 18. Representative HAADF STEM image from an amorphous solution-cast four layer LZO film. The red box represents the region of the image that was used for analysis 394

XXI. 19. Horizontal and vertical intensity deviation analysis for LZO film using scanned boxes. (a) Background-subtracted horizontal intensity deviation profile. (b) Background-subtracted vertical intensity deviation profile. (c) Horizontal and vertical deviation distributions. (d) Effect of box size on distribution width for horizontal and vertical deviation profiles. The vertical distribution widths have been scaled down to match the range of horizontal distribution widths for convenient comparison. 396

XXII.1. (a) EDX map of this area indicating the non-uniform distribution of Pb and Sn in the 6 rock salt atomic planes. (b) Integrated intensity of the respective elemental signals smoothed with a 5 pixel moving average showing the average distribution of elements. (c) HAADF STEM image of a rock salt hexalayer surrounded by $[(Pb_xSn_{1-x}Se)_{1+\delta}]_1(TiSe_2)_1$ layers. (d) Bar graph indicating the quantified atomic ratio of Pb/Sn for the different atomic layers with error bars indicating the 99% confidence interval for each of the measurements. The ratios were determined using 6 different spectrum images and the average measured composition for the layers indicated 401

XXII.2. Left: The calculated energy difference between computational models having Pb or Sn segregated to the interface as a function of composition of the $[(Pb_x\ Sn_{1-x}Se)]_3$ layer. A positive energy difference indicates the preference of Pb segregation to the interface. The blue curve is for vacuum isolated 6 layer thick rock salt structured layers and Sn segregation to the interface is thermodynamically preferred. Repeating the calculation now with a $TiSe_2$ layer between the rock salt layers (red curve), reverses this tendency and Pb preferentially occupies the interface as seen in the experimental data. The extremums are the pure PbSe and SnSe phases. Right: Schematic structures of 3 precursors with different initial distributions of Pb and Sn. The structures on the right would be expected if diffusion is limited and kinetics dominates. The

structure on the left would be expected if the segregation lead to the surface is thermodynamically driven and accessible under the annealing conditions 405

XXII.3. (3a) A representative HAADF-STEM image and the corresponding EDX map (inset) for the heterostrucure formed from the disperse precursor (center precursor in the schematic on the right in **Figure XXII.**2). Crystallographic alignment of the expected phases is observed. (3b) The integrated EDX intensity profile of the heterostrucure formed from the precursor with Pb in the middle layer. After annealing, all precursors exhibited approximately the same intensity profile indicating that the same compositional heterostructure is forming with Pb at the interface. (3c) HAADF-STEM average intensity plot..... 407

XXII.4. Determining the global structure of complex layered 2D materials is best achieved through a combination of inputs from theory, microscopy, and XRD... 414

LIST OF TABLES

Table Page

III.1. A summary of the lattice parameter and FWHM of the 00*l* peaks for samples prepared with different Pb:Se bilayer thicknesses 42

V. 1. Deposition parameter ratio and the resulting composition determined by EPMA, precursor repeat thickness, *a*- and *c*-axis lattice parameters of the constituents and the respective $([SnSe]_{1+\delta})_1(VSe_2)_1$ superlattice and the calculated misfit parameter, δ..... 84

V. 2. Room temperature resistivity (ρ_{RT}), temperature at ρ_{min} (T_{min}), ρ_{max}/ρ_{min}, carriers/V-atom at room temperature ($n_{V,RT}$), carriers quenched in the CDW transition/V-atom (n_{CDW}), and carrier mobility at room temperature (μ_{RT}) for compounds with different Sn/V-ratios 94

VI.1. *a*-lattice parameters of the constituents, misfit parameter (δ), *c*-lattice parameter of the superlattice, *c*/*a*-ratio (a-lattice of the $V_{1+x}Se_2$ constituent) , Sn/V-ratio (EPMA, normalized to a (1,1) composition) and off-stoichiometry (x) of $V_{1+x}Se_2$ calculated from EPMA results for a thin film $V_{1+x}Se_2$ and the ferecrystalline compounds $([SnSe]_{1.15})_1(V_{1+x}Se_2)_n$ with $n = 1 – 6$..... 106

VI.2. Electrical resistivity ratio, carrier concentration at room temperature, carriers/V-atom at RT and RT carrier mobility for $([SnSe]_{1.15})_1(V_{1+x}Se_2)_n$ with $n = 1 – 6$, a $V_{1+x}Se_2$ thin film, and bulk VSe_2 [14]..... 113

VII.1. Summary of all samples as well as data from the previously reported 1:1 compound. Samples from the first deposition cycle, set a, were deposited in order from a1 to a9. Samples from the second deposition, set b, were deposited in order from b1 to b4. 122

VIII.1. Bismuth content (from EPMA) (*x*), *c*-axis lattice parameter, (Bi + Sn)/V-ratio (from EPMA), *a*-axis lattice parameters of the two constituents and calculated misfit parameter for $([Sn_{1-x}Bi_xSe]_{1+d})_1(VSe_2)_1$ compounds..... 142

IX.1. Table of samples synthesized during the calibration process that displayed superlattice diffraction maxima. Composition is reported from EPMA and represents global film composition. The composition of the superstructure is given by the in-plane packing density of each constituent (calculated from in-plane lattice parameters below). Samples given in bold (A-E) are considered representative of the title compound. 162

IX.2. Refinement parameters for interatomic plane spacing along the c-axis associated with the fit plotted in Figure IX.4 168

IX.3. Electrical properties of TiX_2 based compounds are shown. Those given in bold are compounds synthesized from modulated elemental reactants. 169

X.1. Lattice parameters and misfit parameters for the (BiSe)1+δ(TiSe2)n compounds investigated. 184

X.2. Seebeck Coefficients of (BiSe)1+δ(TiSe2)n at room temperature. 191

X.3. Bi/Ti Ratio Measured by EPMA and Calculated from Misfit Parameter (δ). 197

XII.1. Sample numbers, annealing conditions, lattice parameters, and Bi/Nb atomic ratios for four different Bi-Nb ferecrystals 221

XII.2. Refinement parameters for Rietveld refinement conducted on Sample 2 in space group $P\bar{3}m1$. 224

XIV.1: A summary of the measured composition and lattice parameter for the targeted $(Pb_xSn_{1-x}Se)_{1+\delta}TiSe_2$ compounds. The measured oxygen content partially results from the SiO_2 layer on the top of the substrate and is not used in calculating x. 256

XIV.2: In-plane lattice parameters for both constituents of $[(Pb_xSn_{1-x}Se)_{1+\delta}]TiSe_2$ and the calculated misfit parameter (1+δ). 257

XV.1. Lattice Parameters obtained from the in and out of plane diffraction measurements 270

XVII.1. The precursor structure, targeted structure and elemental ratios, both targeted and measured, of the $([SnSe]_{1+\delta})_m([MoSe_2]_{1+\gamma})_1([SnSe]_{1+\delta})_m(NbSe_2)_1$ compounds 297

XVII.2. The lattice parameters and formulas estimated from in-plane X-ray diffraction for the $([SnSe]_{1+\delta})_m([MoSe_2]_{1+\gamma})_1([SnSe]_{1+\delta})_m(NbSe_2)_1$ compounds. 299

XVIII.1. A summary of the different families of compounds that have been prepared utilizing the MER technique 326

XXII.1. Atomic plane Z-coordinates relative to Ti atomic plane and atomic plane occupancies determined from analysis of HAADF and EDS data (initial Z's and Occ's) and values obtained from a Rietveld refinement of X-ray diffraction data using the initial Z's and Occ's as model inputs. The refinements were conducted using space group *P -3 m 1* with the mirror plane halfway through the hexalayer. HAADF initial occupancies were estimated from the measured compound stoichiometry. For ease of comparison, Occupancies of Pb and Sn are expressed as fraction of nearest Se plane

occupancy, assuming full Se occupancy. Both refinements converged to a *c* axis lattice parameter of 2.3862(2) nm, which is consistent with the 2.38(1) nm determined from both HAADF and EDS data. For further refinement details, the reader is referred to the supplemental information 410

CHAPTER I

INTRODUCTION

The realization that free standing monolayers of van der Waals layered materials could be mechanically exfoliated from bulk parent compounds[1,2] followed by observation of graphene's extraordinary electrical properites[3] has stirred great interest in two dimensional (2D) materials. The micromechanical cleavage method concept is illustrated in Figure I.1. The same exfoliation techniques lead to the observation of molybdenum disulfide monolayers which were found to be direct bandgap semiconductors[4] and recent incorporation into high performance photodetector devices[5]. The rapid pace of discovery for low dimensional materials with exciting properties continue with graphene allotropes[6], multiple polymorphs of borophene[7], germanene[8], and many others[9].

Highly enabling for these advances was the observation by Blake *et al.* that monolayers of graphene could be visualized in a reflected light microscope when deposited on a silicon wafer with 300nm of SiO_2 using white light filtered in the λ=500-600 nm range[10]. It is the combination of these two developments, the use of micromechanical cleavage and reflected light microscopy that enabled research ultimately leading to the Nobel Prize in Physics awarded to Andre Geim and Konstantin Novoselov in 2010. It is surprising that high resolution methods such as atomic-force, scanning-tunneling, and electron microscopes were incapable of this achievement due to restrictions in throughput and the ability to distinguish monolayers from thicker stacks. Atomic structure and composition are much more challenging on the monolayer scale,

however. Methods in transmission electron microscopy provide a reasonable avenue for further advancement in our knowledge of two dimensional systems.

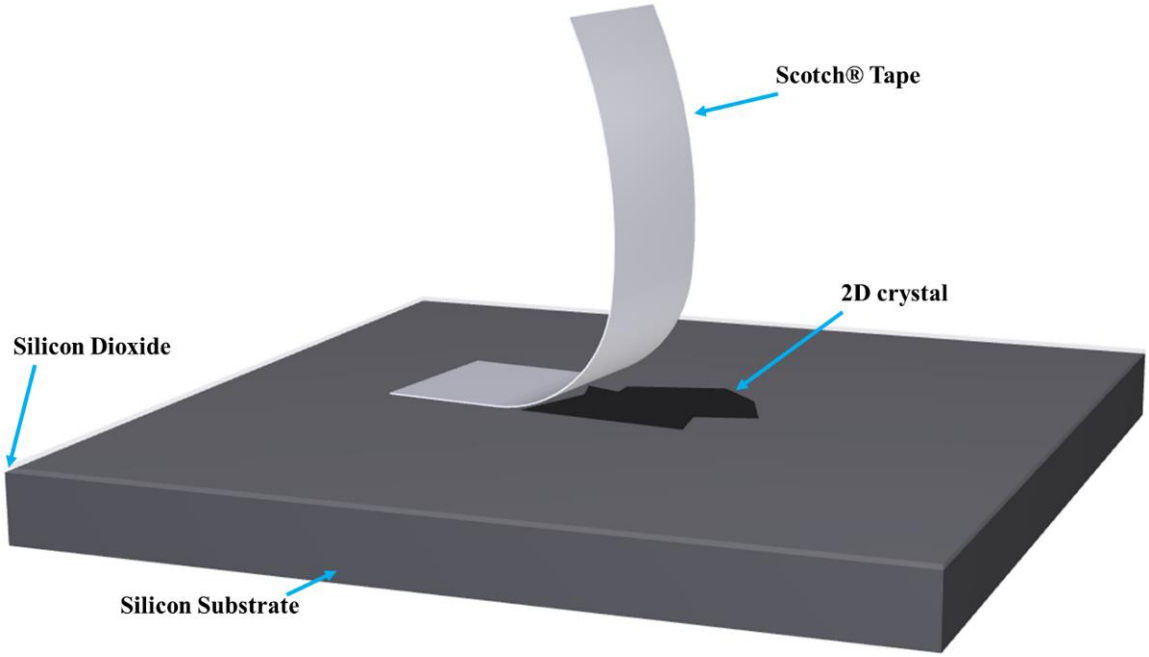

Figure I.1: A drawing demonstrating the micromechanical cleavage technique first described in 2004[1] to generate free standing two dimensional layers of graphene from graphite. There have since been numerous observations of 2D crystals as a result of this synthetic method. Quick identification of resulting monolayers is achieved by deposition onto a silicon substrate with 300 nm SiO_2 on the top surface and observation in a reflected light microscope.

Moving beyond synthesis and characterization of free standing materials, one could imagine the integration of these materials into heterostructures or sophisticated devices[11]. The first demonstration of a multilayer van der Waals heterostructure incorporated graphene layers spaced 20-30 nanometers apart by hexagonal boron nitride crystals[12]. A vertical graphene-based field-effect tunneling transistor was recently prototyped which achieved high ON-OFF ratios, a common critique of graphene's potential incorporation into field-effect transistors[13]. Two-dimensional transition metal dichalcogenides (TMDs) provide complementary materials to graphene for future devices

such as MoS_2 with a nonzero bandgap. Integrated circuits using bilayer MoS_2 based transistors have been demonstrated[14].

It was first proved that the concept of 2D superlattices and heterostructure devices manually assembled can be atomically sharp and clean by using focused ion beam sample preparation followed by transmission electron microscopy in 2012[15]. These first cross-sectional images provided confirmation that the layers were atomically sharp. No local structure or compositional information was obtainable from the relatively poor quality images, however. Prior analysis of 2D materials took place in plan-view[16–18] which is less practical for analysis of heterostructure systems where the layers are superimposed. Thorough characterization of the resulting structure and composition at the atomic scale of low dimensional systems remains a crucial challenge for the future of nanomaterials and heterostructures.

Often, electron microscopy is employed for characterization of interfaces[19,20], grain boundaries[21], and structural defects[22] for example. Electron microscopy is a well suited characterization method for low dimensional systems as a repeating structure is not necessary to produce a measureable signal. Low dimensional materials do not have a large volume that is easily probed with X-ray diffraction (XRD) as is often pursued for 3D crystals[23]. Incidentally, aberration corrected scanning transmission electron microscopes (STEM) are commercially available which achieve sub-angstrom (ångström, Å) resolution[24] and offer a capable method for directly resolving 2D systems[25].

A unique opportunity for fine local scale measurements exists with a specific class of materials known as ferecrystals, the rotationally disordered relative of misfit

layer compounds[26]. Ferecrystals provide an excellent test system to observe effects at heterostructure interfaces as the whole film is composed of interdigitated two dimensional layers. Therefore bulk methods can be used to corroborate local scale measurements. On the flip side, ferecrystals are not crystals and precise single crystal solutions are not achievable using XRD. Electron microscopy can be used to confirm the general coordination of the atoms and observe local structure and layering motifs that occur. The use of high resolution images has therefore been catalytic in providing feedback for the advancement of this class of materials in recent years.

Ferecrystals are synthesized using the modulated elemental reactant (MER) synthesis method[27]. Amorphous precursors are deposited at room temperature with the appropriate precursor thickness and composition for a targeted material and post annealed at low temperature. Typical stoichiometry of targeted compounds can be complicated but have a general chemical formula of $[(MX)_{1+\delta}]_m(TX_2)_n$ where M is Sn, Pb, Sb, Bi, or a rare earth metal, X is a chalcogenide, and T is Ti, V, Nb, Ta, or Cr. The two constituents, MX and TX_2, have differing *a* and *b* lattice parameters which is expressed by a misfit parameter, $1+\delta$. It has been shown that the nanostructure of the deposited precursor is preserved in the final products[28–30] allowing non-thermodynamic layering schemes to be grown. The kinetically trapped structure of the composition-targeted compound is well oriented relative to the plane of substrate but exhibits a degree of rotational disorder around the c axis (Figure I.2). Merrill *et al.* published a thorough article describing the broader context of ferecrystals as model thermoelectric materials[26].

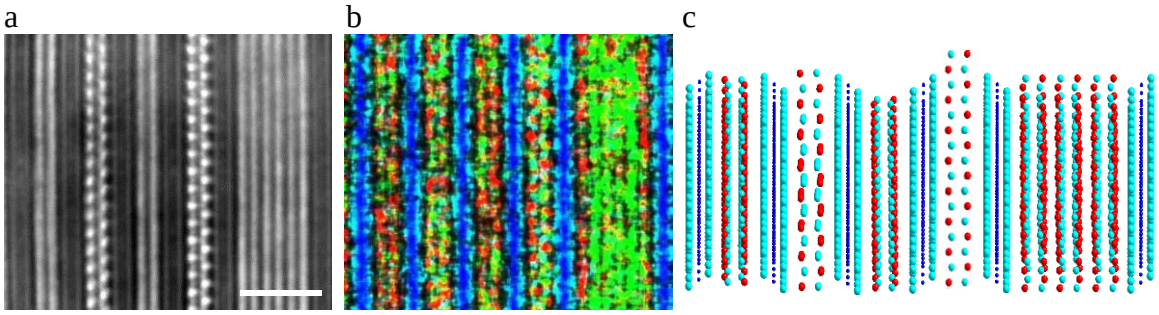

Figure I.2. Images and corresponding drawing of an alloy ferecrystal. The surface plane of the substrate and layered films oriented vertically showing $(MX)_{1+\delta}TX$ and $(MX)_{3+\delta}TX$ stacking motifs. The white scale bar is 2 nanometers. (a) A STEM image showing resolved atomic planes of a $(Pb_xSn_{1-x}Se)_{m+\delta}TiSe_2$ alloy ferecrystal, (b) a corresponding composite EDX map showing distributions of Ti (blue), Pb (red), Sn (green), and Se (cyan), and (c) a not to scale cartoon model of the image demonstrating rotational disorder (Sn and Pb are both represented by the red positions). The [110] orientation of $(Pb_xSn_{1-x}Se)$ is seen in the HAADF while the rest of the layers exhibit off zone axis rotation.

To characterize ferecrystals and two dimensional materials in the electron microscope, one can use the conventional projected parallel beam mode or, with the same instrument, in a scanning converged probe mode. There is often confusion about the differences between these two imaging modes, conventional transmission electron microscopy (TEM) and scanning transmission electron microscopy (STEM). Practically speaking, STEM is a directly interpretable imaging mode and TEM imaging often requires image simulation to interpret images at the atomic scale. The following provides an example of the applications of both techniques and the justification for the use of STEM throughout this thesis.

TEM is a coherent imaging mode so that the incident electron beam is approximately parallel rather than converged. After passing through the sample, the electron beam is scattered into multiple beams that can be projected onto a charge

coupled device (CCD) camera[31] to generate an electron diffraction image. If the same beams are magnified and focused (superimposed) onto the CCD camera, a phase contrast image is generated (if more than one post specimen beam is projected, phase contrast is present). To achieve high resolution in TEM, most (if not all) of the beams are used producing indirectly interpretable fringes. Solving for the structure that produced the observed fringes in the image requires simulation[32,33] of potential solutions and comparison of resulting images to experimental data.

Figure I.3 demonstrates the application of conventional TEM and multislice simulation on a ferecrystal system, $(LaSe)_{1+\delta}(V_xSe_y)_n$. Quantitative electron probe microanalysis suggested that the material was deficient in selenium for the targeted $(LaSe)_{1+\delta}(VSe_2)_2$ layers but sharp XRD peaks suggested that a crystalized material was formed. In order to identify the resulting V and Se containing layer, TEM was attempted on a 300kV Tecnai TEM. Focal series images were compared to focus/thickness maps of the two potential materials TiSe or $TiSe_2$ (Figure I.3a). The resulting images indicated that the structure was neither VSe nor VSe_2. This analysis did not conclusively solve the structure however elements of both of the simulated structures appeared to create a reasonable match for the experimental data when combined (Figure I.3c).

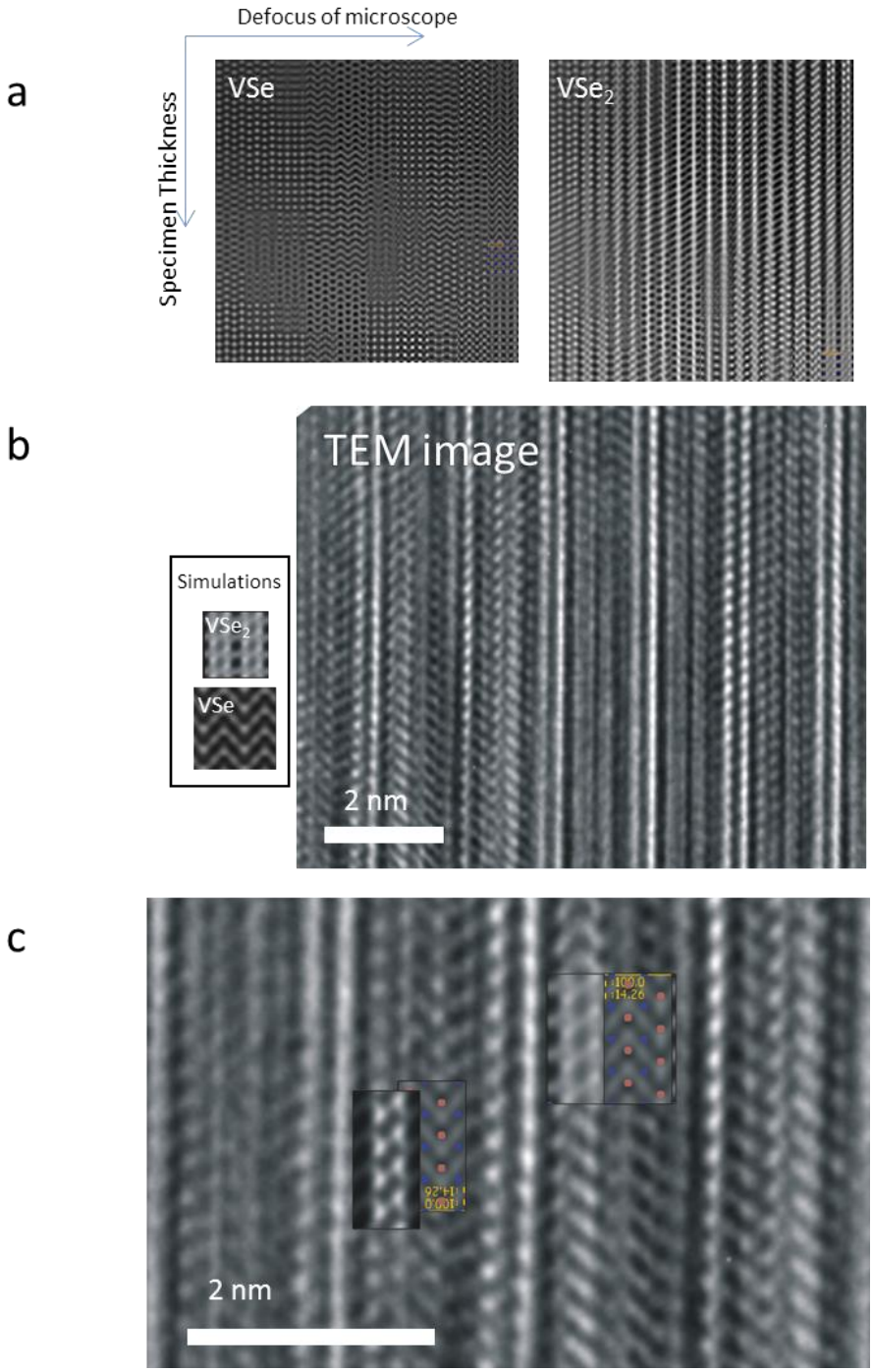

Figure I.3. (a) Simulated TEM images with varying defocus and thickness that can be correlated to experimental data. (b) An experimental image with regions that correspond to both simulated images of VSe_2 and VSe. (c) Simulated overlays indicate a combination of simulations from the two materials appears to match the experimental data.

Subsequent to the TEM imaging and simulation of the $(LaSe)_{1+\delta}(V_xSe_y)_n$, a similar sample was imaged using STEM mode for the $(LaSe)_{1+\delta}(VSe_2)_4$ targeted system (Figure I.4). Given that STEM contrast is directly interpretable, it is immediately apparent that the sample has VSe_2-like layers with interstitial V atoms. Upon closer inspection the interstitial atoms are spaced regularly in the crystal and can be described by a normal unit cell. These results suggest that the V_xSe_y layer has a chemical formula of V_3Se_4. This is consistent with the TEM simulations with a high degree of certainty. Also apparent in the images is a zig-zag staggering of the selenium atoms in the selenium planes and AB plane offsets of the V atoms. The simplicity and level of detail that can be observed in STEM images justifies the use of STEM for the remainder of this thesis.

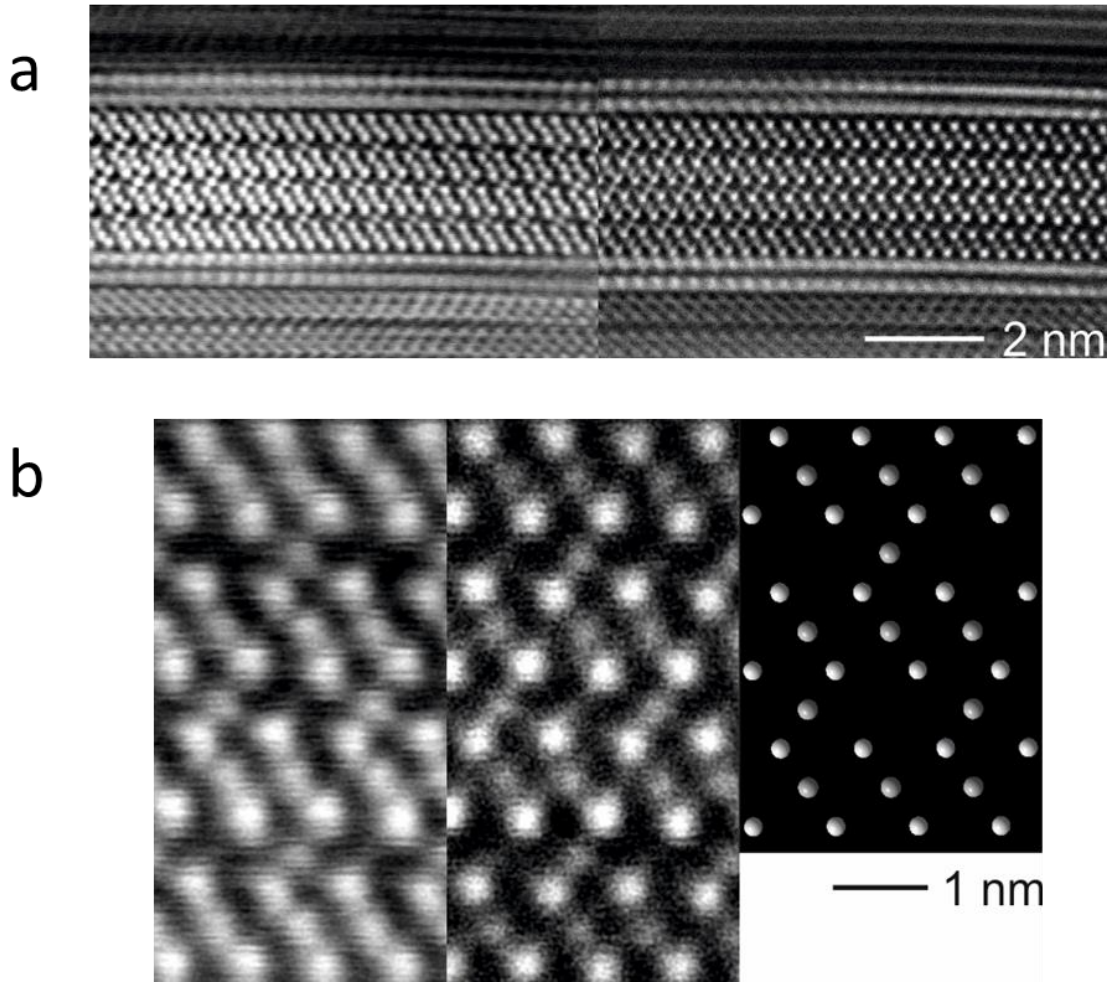

Figure I.4. High angle annular dark-field (HAADF) STEM images of a structurally unsolved $(LaSe)_{1+\delta}(V_xSe_y)_n$ system. (a) High resolution images showing an oriented grain of the layer of interest interdigitated with off zone axis layers of LaSe. (b) A high magnification cropped portion of the images in (a) with a drawing of the observed structure.

Scanning transmission electron microscopy (STEM) is an electron beam imaging mode that scans a focused electron probe across a sample and collects scattered electrons (dark-field) and transmitted electrons (bright-field) into a post specimen detector. As shown in the electron ray diagram in Figure I.5, multiple electromagnetic lenses are used to focus an accelerated electron probe at the specimen plane. An aperture is used to cut

out electrons with aberrations that would lead to significant blurring of the probe. Scan coils are used to scan the probe over the sample in a raster pattern. Typically post specimen projection lenses are used to manipulate the magnification of the projected converged beam pattern to effectively change the length between the sample and the detectors, referred to as “camera length”.

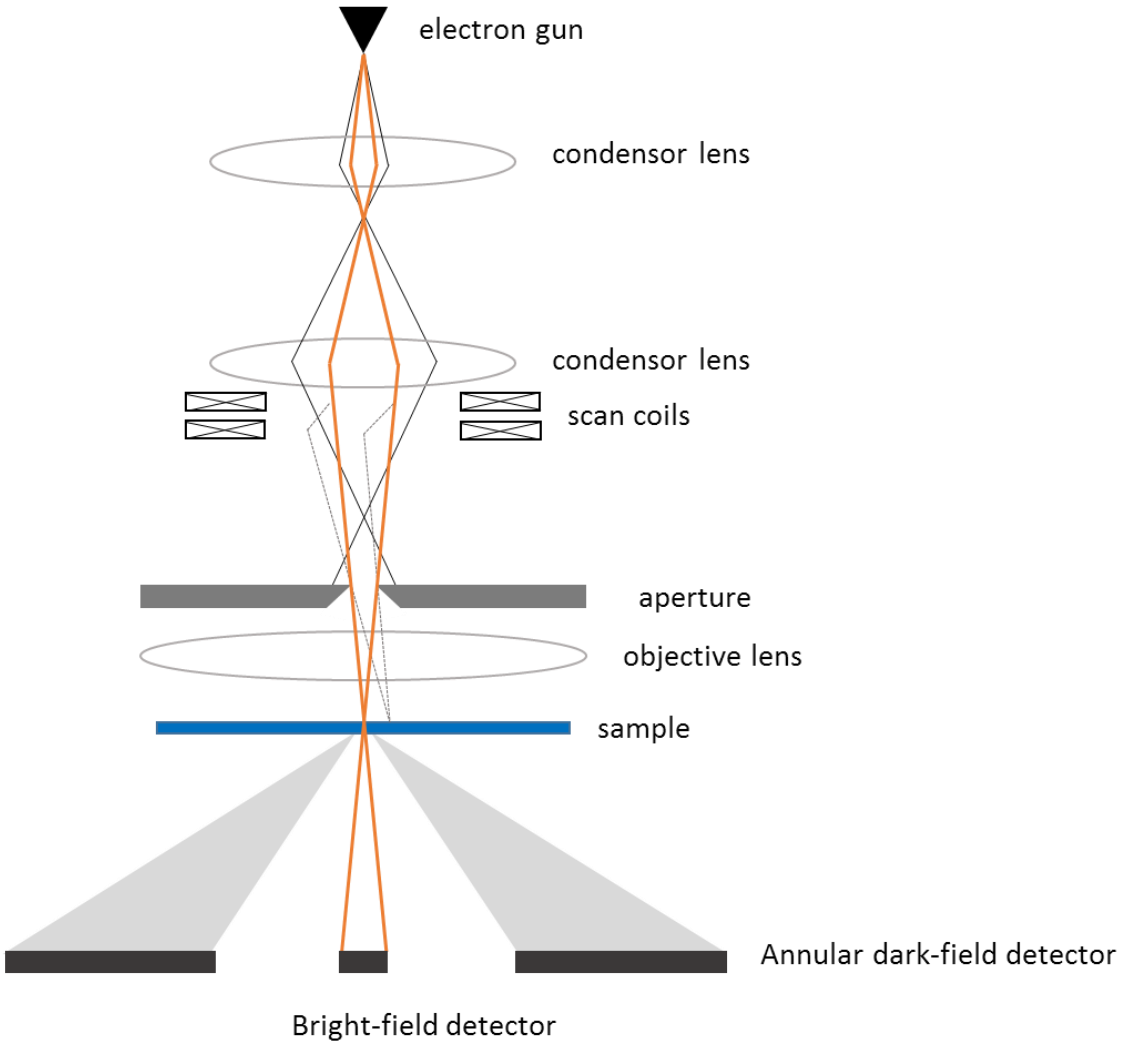

Figure I.5 A basic electron ray diagram of a STEM instrument showing different hardware elements used for STEM imaging.

Unlike aberration free light microscope lenses which can reach wavelength limited resolution, electromagnetic lenses used in electron microscope imaging resolution suffers from spherical aberrations where off axis rays are focused/defocused differently from rays that are closer to being on axis. As demonstrated by the black rays in Figure I.5, the further off axis the ray is, the more forcefully the ray is bent back toward the central axis of the beam. Using a smaller aperture size is one method to effectively reduce aberrations in the final probe. The tradeoff is that a small aperture reduces probe current and ultimately signal generated for imaging and spectroscopic analysis. Spherical aberration correctors exist which greatly improve resolution with higher probe convergence angles and coherent electron current for high resolution STEM[24]. A combination of aberration corrected and uncorrected STEM are used throughout this thesis.

Inelastic scattering events between the incident electron beam and the specimen lead to secondary electron emission and X-ray emission. To generate X-rays, the high energy incident beam penetrates the outer conducting and valance bands of the atoms and transfers at least enough energy to eject an inner-shell electron. The ground state of the atom is recovered when the hole is filled with an electron from an outer shell. This relaxation releases an X-ray of energy characteristic of the specific transition that took place and is different for each element. Using an X-ray detector in the STEM column, we can collect spectra of the characteristic X-rays and map the composition of the specimen.

To picture the X-ray generation process it is helpful to imagine the Bohr Theory for atomic structure which describes electrons encircling the nucleus. Quantum theory describes electron shells which are quantized into finite energy values determined by the

number of protons in the nucleus. The principal quantum number (n=1, 2, 3, etc..) describes these shells that were originally labeled K, L, M, N, and O in the early days of X-ray spectroscopy and the labels have since stayed. In EDX, the characteristic X-rays are the differences in energy between two shells, the energy of the ejected electron and the original energy state of the relaxed electron. As seen in Figure I.6, the labeling for these transitions work so that if a K-shell electron hole is filled by an L shell electron, a K_α X-ray is emitted. If the hole is filled by an M shell electron, a K_β X-ray is emitted.

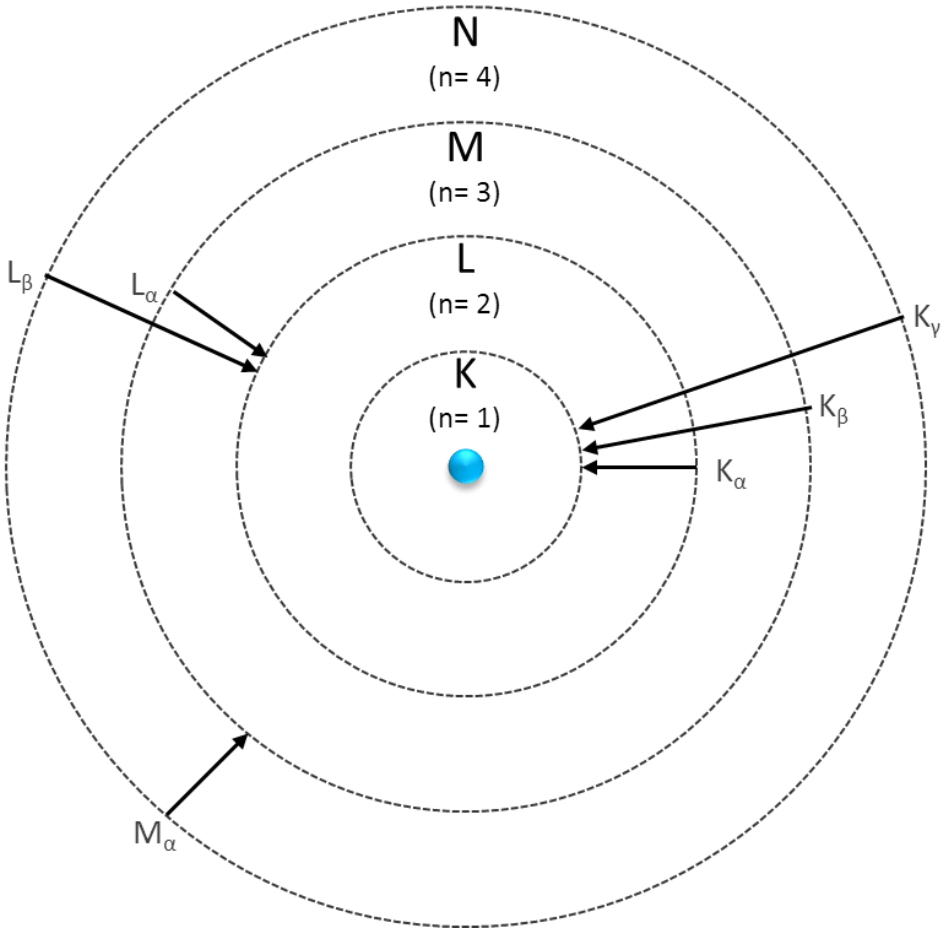

Figure I.6. A Bohr model of an atom showing examples of electron energy transitions for different shells (K, L, M, N), their corresponding principal quantum numbers (n= 1, 2, 3, 4) and the potential energy transitions that release the characteristic X-rays used for energy dispersive X-ray spectroscopy.

The relative intensities of X-ray peaks can be compared to quantify the composition of the specimen. Quantitative EDX is a relatively simple to do using the Cliff-Lorimer ratio technique[34]. It is assumed that the specimen is thin enough that absorption and fluorescence can be ignored and the ratio of the compositions of a binary system (element A and B) is related to the ratio of EDX peak intensities by a Cliff-Lorimer factor (k-factor), k:

$$\frac{C_A}{C_B} = k_{AB}\frac{I_A}{I_B}$$

Where the C is the concentration and I is the intensity of the peak after background subtraction. Background subtractions are accomplished by simply doing a linear subtraction of the average intensity on either side of the peak. The k-factor is determined experimentally using standards with known composition. Additionally k-factors from two different standards with elements AB and BC can be used to relate AC using the following relationship:

$$k_{AB} = \frac{k_{AC}}{k_{BC}}$$

This strategy can be applied generally until the resolution of the analyzed areas approaches atomic column resolution. Atomic scale EDX intensity takes place over the top of delocalized intensity which relates to the beam broadening as it propagates through the sample[35–37]. This can be seen clearly in Figure I.7 collected from ferecrystals where a single columns of titanium are spaced 2.37 nm apart. To effectively threshold intensity,

Gaussian peak fitting is used to extract localized intensity relating to the atomic column[38,39] and the rotational disorder avoids nonlinear channeling effects[40].

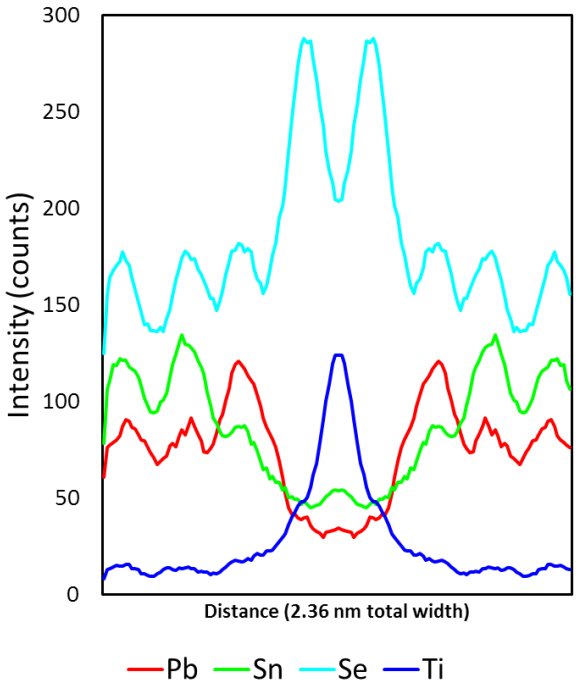

Figure I.7. A high quality EDX intensity profile of a single repeat of a $[(Pb_{0.37}Sn_{0.63}Se)_{1.17}]_3(TiSe_{2.00})$ ferecrystal demonstrating non-zero peak intensity in regions illustrating the presence of delocalization effects. A thermodynamic argument from knowledge about ferecrystals and misfit layer compounds can be used to suggest that Ti would not be present in areas outside of the central peak in the image.

Since the first demonstration of atomically resolved energy dispersive x-ray spectroscopy (EDX) using a scanning transmission electron microscope (STEM) in 2010[36], theory based simulations established that EDS hyperspectral maps could be used to measure atomic distances. That is, EDX is an incoherent imaging mode and signal intensity corresponds directly to the structure of the sample[36]. In addition to using extracting quantifiable intensities from atomic columns, Gaussian peak fitting provides a

sub pixel estimate of the peak position. An illustration of this process is shown in Figure I.8.

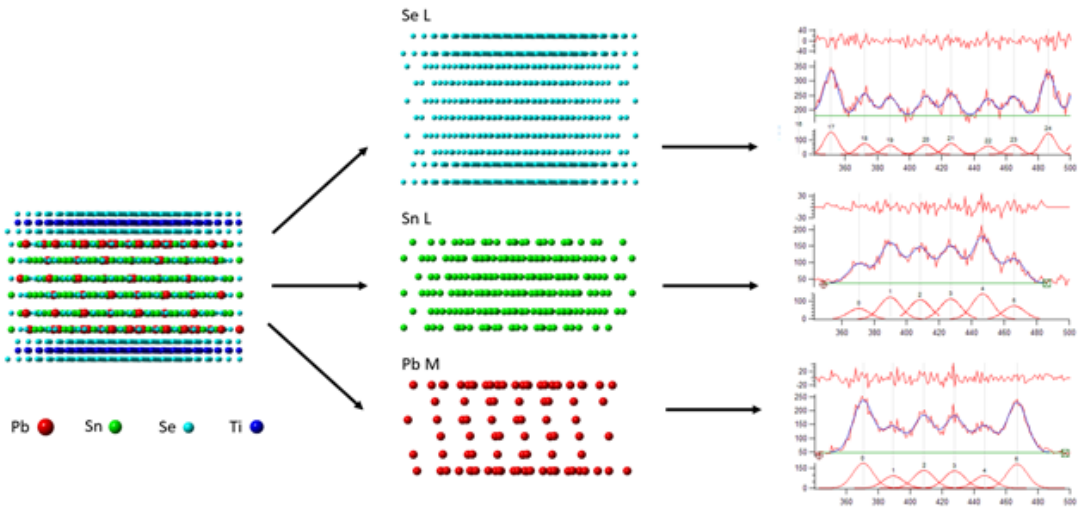

Figure I.8. A diagram illustrating the process of using element specific signals from EDX hyperspectral data to produce images that deconvolute otherwise overlapped elements in the image. Guassian peak fitting of extracted intensity profiles from the individual images allows the measurement of element specific interplanar distances.

A major limitation of STEM imaging is the necessity for a thin specimen. Sample preparation is often the biggest challenge in obtaining high resolution and artifact free images. FIB instruments have been used for many years to produce site-specific samples for transmission electron microscopy (TEM)[41] and have continued to gain in popularity in many areas of research. FIB instruments are usually equipped with scanning electron microscopes and micromanipulators to accommodate in situ lift-out techniques for reliable and fast sample preparation. This means a site-of-interest can be identified, cut free and transferred directly to a TEM half-grid (see Figure I.9).

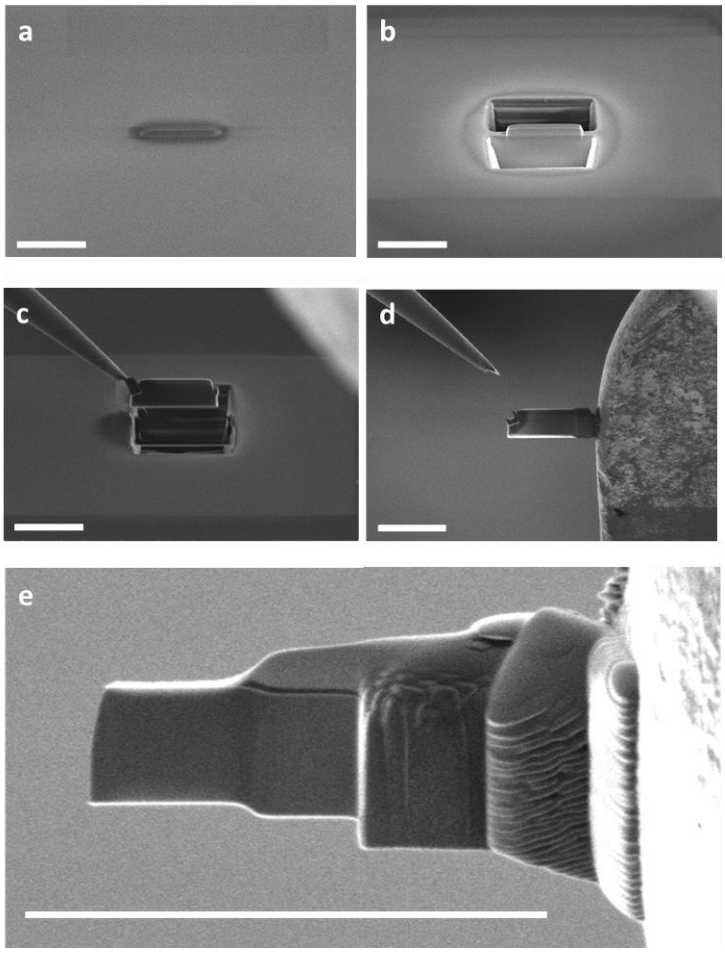

Figure I.9. Scanning electron microscope and focused ion beam microscope (SEM-FIB) images demonstrating the in-situ lift-out method for TEM sample preparation. The white scale bars are all 10 um. (a) A carbon protecting layer is deposited using electron beam induced deposition (EBID). (b) Additional carbon is grown using ion beam induced deposition (IBID) and the material on either side of a lamella is cut out using ion beam sputtering. (c) A micromanipulator probe is attached to the sample using IBID, the lamella is cut free from the substrate and lifted out. (d) The lamella is then deposited onto a transmission electron microscope grid using IBID and the micromanipulator probe is cut free. (e) The sample is thinned using ion beam sputtering until thin enough to be electron transparent.

FIB techniques and instrumentation have advanced dramatically[42] and a typical high quality preparation can be reliably completed in less than one or two hours. Ion beam fabrication of TEM lamellas can produce specimens as thin or thick as the application requires. Typically samples between 10 and 30 nanometers are optimal for

high-resolution TEM (HRTEM), scanning transmission electron microscopy and electron energy loss spectroscopy (EELS). In some cases, thicker samples (50-70 nanometers) are helpful to increase interactions for energy dispersive x-ray spectroscopy (EDX).

Preserving the native structure of crystalized samples and to minimize the presence of implanted gallium (Ga^+, the most commonly used ion species) requires the use of low accelerating voltages. At low voltage, the probe resolution becomes chromatic aberration limited and the tails of Gaussian shaped probe become highly significant. These effects are exacerbated by the mean free path of the ions in vacuum. Figure I.10 below presents experimental data demonstrating the distribution of ions in a 5kV gallium ion probe and the effects of vacuum level. The profile of the beam effectively dictates the profile of the cross-section the FIB cuts. The Gaussian slope achieved at high voltage is effectively approximated to a straight line with the bottom and the top of a multiple µm cut varying by only a few nanometers. The difference changes to 10s to 100s of nanometers at low voltage leading to samples with varying thickness.

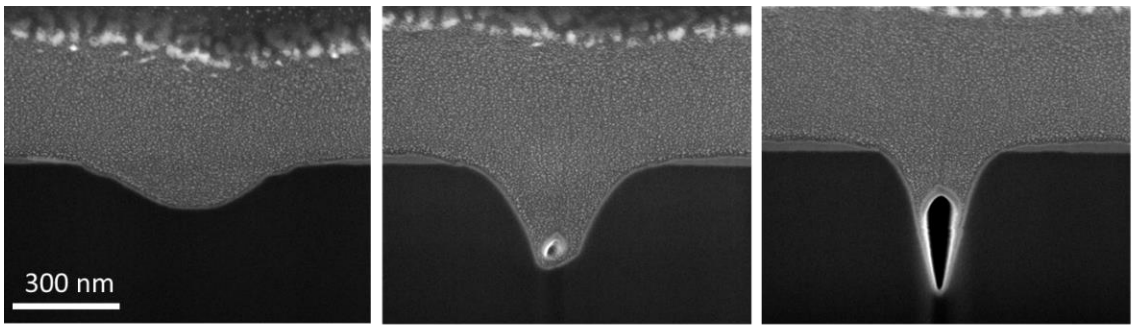

Figure I.10. Images showing the Gaussian profile of the low-voltage ion beam at different vacuum levels. Lines were cut into a silicon substrate using a 5kV accelerating voltage gallium focused ion beam using the same dwell times. The trenches were backfilled and

coated with a organometallic platinum protecting layer and cut in cross-section to be viewed at 45 degrees using the electron beam. The voids in the backfill of the trenches are an artifact of the mean induced deposition methods.

Throughout this thesis, methods described by Schaffer *et al.* providing sample thinning methods that optimize for increased beam tails at low voltage during lamella preparation are used[43]. These methods are highly relevant as TEM technology continues to make substantial progress with the development of Cs correctors which push the scanning transmission electron microscope (STEM) resolution of the microscope to sub-Angstrom levels[44,45] and make atomic resolution compositional mapping possible[46]. Additional details about unique strategies for thin lamella preparation used in this thesis will be described in chapter 2.

In the following chapters I take prerequisite steps for implementation of electron microscopy and energy dispersive X-ray spectroscopy (EDX) to characterize heterostructures at the atomic scale. Unique methods for sample preparation and sample thinning are described in chapter 2 which enable the production of virtually artifact free samples for STEM. Given that the super lattice of the ferecrystal can be seen in the STEM when oriented in cross-section to the AB plane of the crystal, valuable confirmation of models calculated using XRD in chapters 3-8 were provided. Chapters 9-12 provide examples where structures were found using STEM revealed new information that was not detectable by XRD and changed the course of understanding about the materials. In chapter 13, the targeted structure did not form however XRD indicated the presence of a well ordered system. STEM was used to provide a starting model for the XRD interpretations. In chapters 14-18, alloy systems and multi component systems were synthesized where STEM-EDX was used to characterize the local distributions of

elements. In chapter 19, low dose STEM was used to identify the presence of inhomogeneity in beam sensitive solution cast amorphous film. In chapter 20, the dose dependent exposure of an electron beam resist was increased by using inverse methods realized in chapter 16 to avoid exposure of the system for imaging. Chapter 21 describes a methods to analyze signal in STEM from complex thin films. All of this work leads to the capstone of this thesis, chapter 22, where STEM-EDX is used qualitatively to confirm expected structures and quantitatively to determine the composition of an alloy heterostructure system, the local atomic plane compositions, and the element specific interatomic distances.

CHAPTER II

TWO AXIS TILTING FOR FOCUSED-ION-BEAM PREPARATION OF INHOMOGENEOUS MATERIALS FOR STEM

II.1.Introduction

Focused-ion-beam (FIB) instruments provide a number of advantages as a tool to prepare site-specific lamellas for transmission electron microscopy (TEM) of integrated circuits [1]. Polished silicon wafers also make ideal specimens for FIB TEM sample preparation because they are smooth and homogenous. FIB produced lamella have been used in high-resolution TEM (HRTEM), atomic resolution scanning transmission electron microscopy (STEM), energy dispersive x-ray spectroscopy (EDX) and electron energy loss spectroscopy (EELS) studies and an ideal lamella has a large area of constant thickness. FIB instruments equipped with scanning electron microscopes (SEM) and micromanipulators to accommodate *in situ* lift-out techniques enable particularly fast and reliable lamella preparations. A site-of-interest can be identified, cut free and transferred directly to a TEM grid, as first described almost two decades ago [2].

The same techniques can, in principle, be used to prepare lamellae of any material. However, FIB sputtered lamellae from samples with inhomogeneity, porosity or rough surfaces often exhibit artifacts that resemble the topology of a theater curtain, referred to as "curtaining" [3]. Figure II.1a shows a partially thinned lamella with such curtaining artifacts. One approach to reduce curtaining effects utilizes a low sputter yield protecting layer, that casts a smooth shadow over the cross-section of the sample and protects the surface [4]. The protective cap can also be the substrate itself when the lamella is flipped upside down relative to the ion beam prior to thinning steps, often referred to as

backside milling [5,6] or shadow FIB geometry [7,8]. Broad beam ion polishing methods have historically also produced curtaining artifacts similar to those seen in FIB cross-sections. To reduce or eliminate these artifacts, ion beam etching systems use a rocking motion along the axis normal to the polished surface to alternate the direction which the beam hits the sample [9,10]. Similar approaches to reduce curtaining have been demonstrated recently for xenon plasma focused ion beam systems for cutting large cross-sections with high current beams [11,12].

Rocking angle methods are less accessible tor TEM lamella preparation using FIB *in situ* lift-out as most FIB systems have a single tilt axis on the stage and cannot rock the sample and perform the necessary tilts to make a uniformly thick sample. The cross-sections of fib cuts are often more trapezoidal than rectangular [13,14] so tilting the sample < 4 degrees to expose the cross-section face of sample to the beam is necessary. One can manually rock the sample along a second tilt axis (Figure II.1) using similar methods to those mentioned by Ishitani *et al.* [3], however, venting the chamber and manually rotating the sample is time consuming [15]. A second tilt axis normal to the cross-section surface is needed to rock the sample *in-situ*, as recently developed by Hitachi which includes an automated anti curtaining effect (ACE) procedure [16].

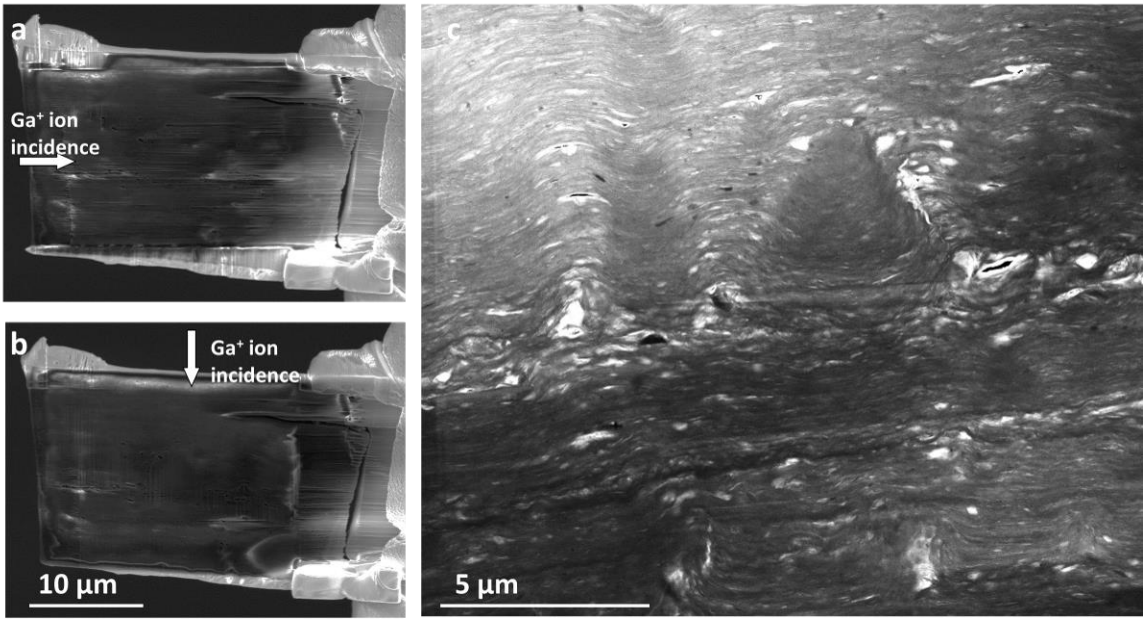

Figure II.1. Curtaining artifacts and their removal (a) SEM micrograph of a partially thinned lamella for TEM lifted out from a rock varnish coating in a polished geological thin section. Curtain artifacts parallel to the incident ion beam can be seen propagating from pores and inhomogeneity in the sample. (b) The sample was rotated 90 degrees *ex-situ* and reloaded into the FIB so that the majority of artifacts could be polished away. Artifacts are then created in the new incident FIB direction. Multiple iterations can produce lamellas with minimal artifacts. (c) A low magnification bright field STEM image taken on an FEI Helios Nanolab 600 Dual-Beam at 30kV demonstrating smooth preparation of a 25x25 um lamella from a highly porous and inhomogeneous sample, where bright areas indicate low density or natural pores in the sample.

Most existing FIB instruments, however, do not have this capability, which led us to develop the *in-situ* process for rocking angle ion polishing technique described in this paper. We demonstrate here that this approach works to prepare TEM lamella without curtaining effects for a variety of samples, including geological samples containing sub-millimeter coatings. Silica glaze [17], heavy metal skins [18], and manganiferous rock varnish [19] are just a few of the many different types of rock coatings [20], and samples with these natural features have taken on increasing importance in recent years because of their utility in understanding the conservation of ancient monuments such as Petra, Jorda [21], in the decay or preservation of historic buildings [22], in assessing potential Earth analogs for

coatings on Mars [23], in understanding the effects of heavy-metal pollution [24], and in evaluating the stability of earth surfaces [25,26]. We demonstrate the utility of our approach in this paper using a variety of different samples - porous ceramics, yttria stabilized zirconia, an amorphous solution deposited inorganic film and a nanolaminated heterostructure. A platinum e-beam deposited protective layer on the surface of specimens, notorious for initiating curtain artifacts, was used for all of these samples.

II.2. Instruments used

TEM lamellas were prepared using *in situ* lift-out methods on both a FEI Helios Nanolab 600 Dual-Beam FIB (Sidewinder ion column) and an FEI Helios Nanolab 600i Dual-Beam FIB (Tomahawk ion column). Annular dark field STEM (ADF-STEM) images (Figure II.II.6) were taken on an FEI Titan 80-300 at 300 kV and 240 mm camera length. High angle ADF-STEM (HAADF-STEM) images (Figure II.6) were taken on a probe aberration corrected FEI Titan 80-300 at 300kV and 120mm camera length. Bright field STEM images (Figure II.1c) were taken on an FEI Helios Nanolab 600 at 30kV. 3D CAD drawings were made using Geomagic Design™ version: 2015.0.1. A Gatan Digital Micrograph version 2.31.734.0 extracted intensity profiles.

II.3. Wedge pre-milling and sample thinning

Wedge pre-milling methods described by Schaffer *et al.* provide a strategy for consistent ultrathin (≤15 nm) lamella preparation and preservation of beam induced protecting layers that are often degraded by large beam tails present during low voltage thinning. Using higher tilts (>3°) during the initial stages of sample thinning removes bulk material that is challenging to remove during low voltage thinning and often results in loss of protecting layers before the whole lamella is thin.

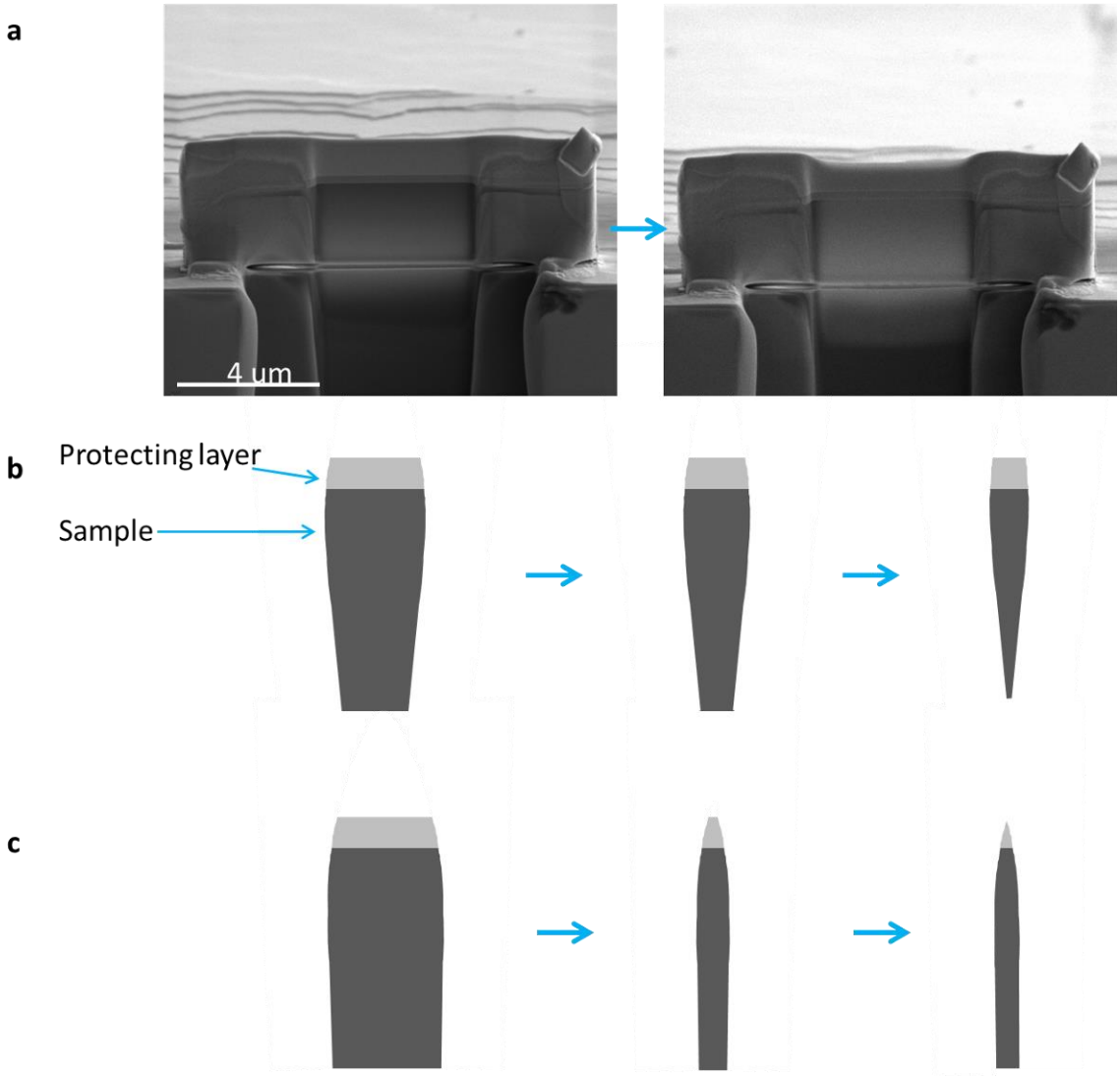

Figure II.2. A demonstration of the benefits of wedge pre-milling. (a) SEM images taken of a silicon lamella exhibit thickness contrast at 5kV that suggests the very top and very bottom of the sample are thinnest. The contrast is the result of additional secondary electron generation on the back side of the lamella as it gets thinner. (b) Illustrates a two dimensional cross-section of the thickness profile of the lamella throughout the wedge premilling process. (c) When lower tilts are used the lamella has more parallel side walls however the protecting layer quickly degrades and limits the sample thickness that can be achieved.

Thickness contrast can be used to observe the uniformity of a sample and, with experience, relative contrast changes can be used to estimate and target a specific sample thickness. Figure II.3 demonstrates the changes in contrast when one uses 5kV and 2kV electron beam accelerating voltages and the changes in contrast as the thickness of the

sample decreases. As the sample becomes thinner, lower voltage is needed to increase sensitivity to relative variations in thickness.

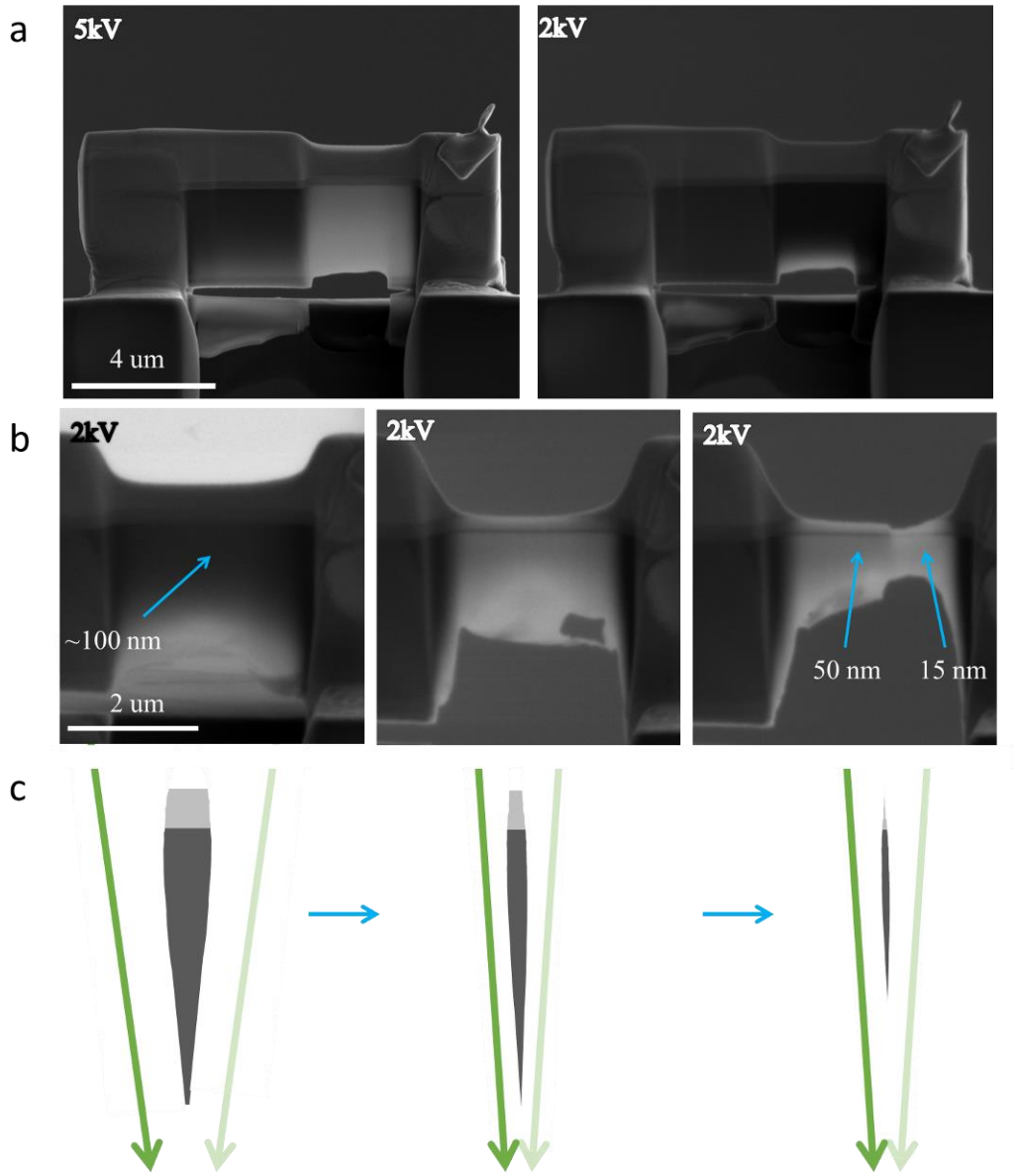

Figure II.3. Scanning electron microscope images of the lamella thinning process using wedge pre-milling. (a) Comparison images of the same lamella demonstrating the difference in translucent appearance at 5kV and 2kV. As the sample becomes thinner, it is often advantageous to use lower imaging voltage on the electron column to increase thickness contrast. (b) SEM micrographs of the final thinning steps demonstrating how thickness contrast can be used to target a specific thickness. The numbers reported here were measured using electron energy loss thickness measurements. (c) A 2D illustration of the lamella during thinning demonstrates the inevitable variation in thickness of the

lamella. The green arrows indicate the incident direction of the ion beam probe. Fabricating samples that are ultrathin for a large area (> 1 um^2) is not achievable without the pre-milling steps.

II.4. In-situ rocking angle methods

TEM samples were prepared using *in situ* lift-out methods and transferred to TEM half grids loaded into the FEI row holder mounted on a 45° pretilted sample holder using conductive double sided carbon tape as demonstrated in Figure II.4. The stage was tilted to 45° so that the half grid mounting posts were vertical prior to welding the sample. Wedge pre-milling methods [27] produced (30kV and 1 nA) large and uniformly thin samples lamellas ~300 nm thick.

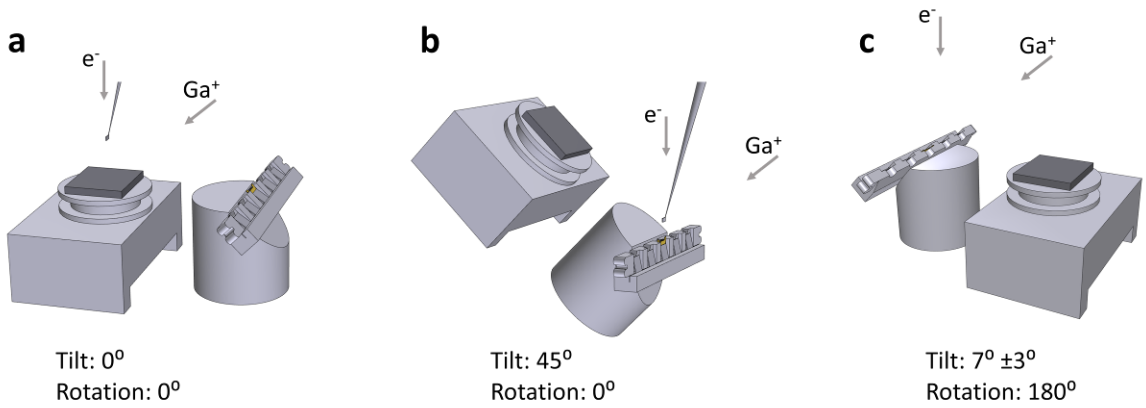

Figure II.4. A simulated chamber camera view (not to scale) demonstrating how samples are mounted to a pretilted TEM half grid for rocking angle thinning in a FIB-SEM: (a) shows a wafer substrate attached to an SEM stub, a micromanipulator probe lifting a lamella from the substrate, and a FEI row holder for TEM grids attached to a 45° stub. (b) To mount the lift-out sample to the pretilted grid, the stage is tilted 45°. (c) The stage is rotated 180° and tilted 7° so that the protective cap is normal to the Ga^+ ion column which is 52° from the electron column for thinning the lamella.

At low accelerating voltages (usually 5kV) on the Ga^+ column, samples are thinned using standard methods [27] (between ±2° and ±4°) until curtain artifacts are observed using the SEM. The stage is then rotated 10 to 20° to "tilt" the lamella along a second tilt axis relative to the ion column (Figure II.5). Using either scan rotation or

rotating the FIB pattern area is necessary to align the pattern used for thinning.

Typically we use a single slow raster pattern (referred to as a “cleaning cross-section” in the FEI software) and raster the ion beam many times over the cross-section to thin the sample. When previous curtaining artifacts are mostly removed and new artifacts start to appear, the stage is then rotated 10 to 20° in the other direction. Multiple iterations and careful monitoring are typically needed to mitigate curtaining artifacts. Often three orientations were used, normal, positive and negative stage rotations in addition to <4° stage tilts to make uniformly thick lamellae. Strict recipes were not used for these procedures, as adaptations must be made for different material types and sample geometries.

Our method relies on the SEM to qualitatively track artifacts in addition to sample thickness. SEM micrographs of the rocking angle procedure can be seen in Figure II.6. The curtaining artifacts are clear in the SEM micrographs and it is ideal to progressively reduce the amount of FIB exposure at each sample orientation so that the artifact depth approaches zero when the sample is thin.

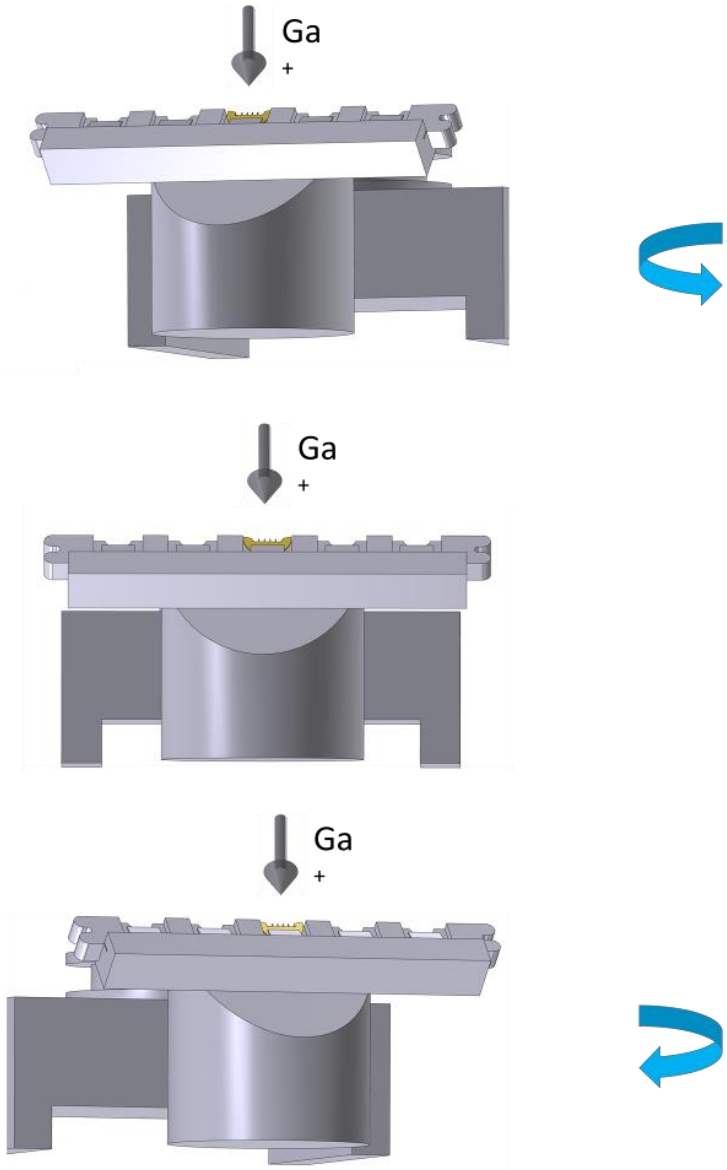

Figure II.5. With the TEM half grid pre-tilted, stage rotation can be used for a second tilt axis relative to the ion beam while thinning a lamella for TEM, which enables rocking angle methods to remove curtaining artifacts.

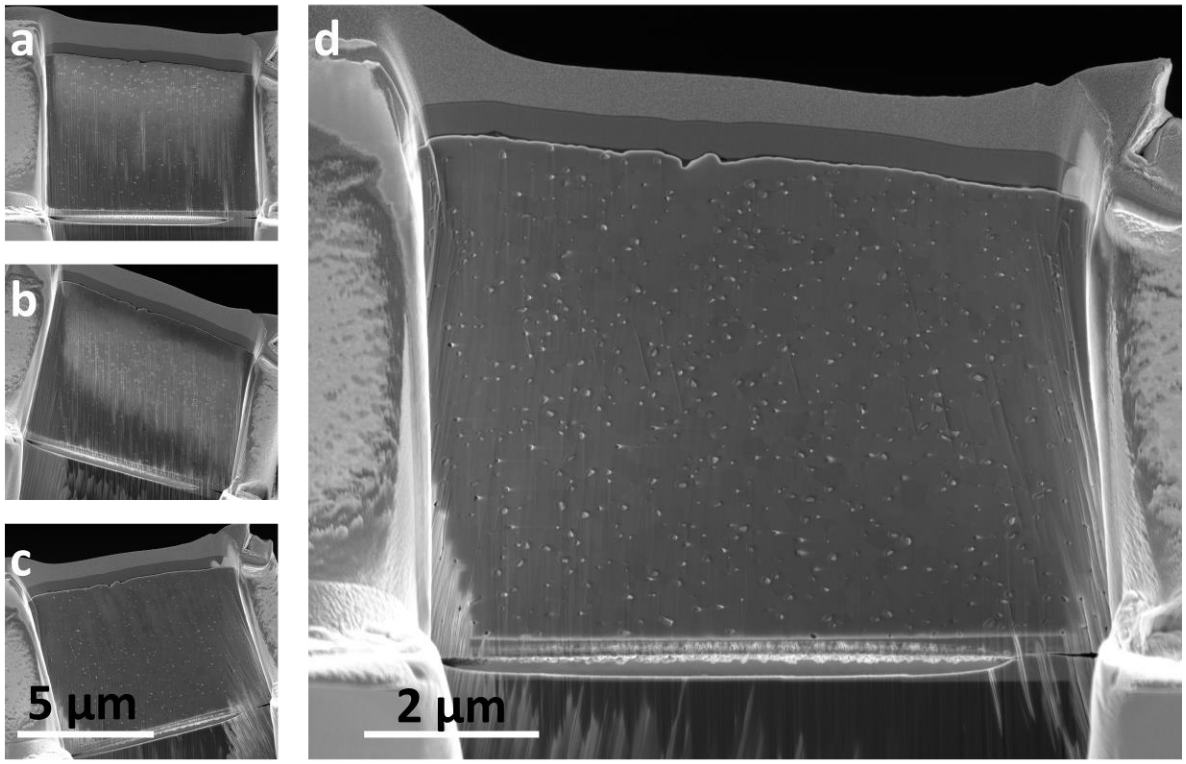

Figure II.6. Scanning electron microscope images demonstrating the rocking angle methods used to produce TEM samples with minimal artifacts. (a-c) Rocking angle methods are achieved by orienting the lamella so that the rotational axis of the stage can be used to tilt the sample relative to the ion beam. (d) Demonstrates the improvement in FIB induced artifacts by rocking the sample. Numerous voids that are native to the sample are visible throughout a large and smooth 10x10 µm lamella.

With a pretilted half grid as described above, however, it is difficult to view the cross-section of the sample from the backside to monitor the curtain artifacts using the SEM column. As demonstrated in Figure II.5, it is possible to image the backside cross-section at a steep angle by rotating the stage 180° and tilting the stage to the highest angle allowed (57° on the FEI Helios 600 at the cross-point of the SEM and FIB). To save the time of performing this procedure, care should be taken to treat both sides of the lamella equally so that the artifacts on the visible side of the lamella are representative of both

sides. This example demonstrates the ability of this method to prepare large, uniform lamellae without curtaining effects.

We have observed that curtaining artifacts are more of a problem at the lower accelerating voltages on the ion column. In addition to lower sputter yields, low voltage probes (and probe tails) are much larger. Both of these characteristics likely contribute to the introduction of curtaining artifacts. Our typical thinning strategy removes all of the material in the outermost plane of the cross-section before stepping the beam into the sample. The shape of the probe, therefore, determines the profile of the cross-section face. At lower voltages, low sputter yield requires much longer dwell times, that are not always used. Beam-raster stepping into the sample before all of the material is removed can cause severe curtain artifacts, even at higher voltages. The same problem is present with large beam tails. The tails will start milling material in the next row. This is often why smaller apertures are helpful in the final cleaning steps in FIB cross-sectioning, as the probe and probe tails are smaller and unlikely to propagate artifacts.

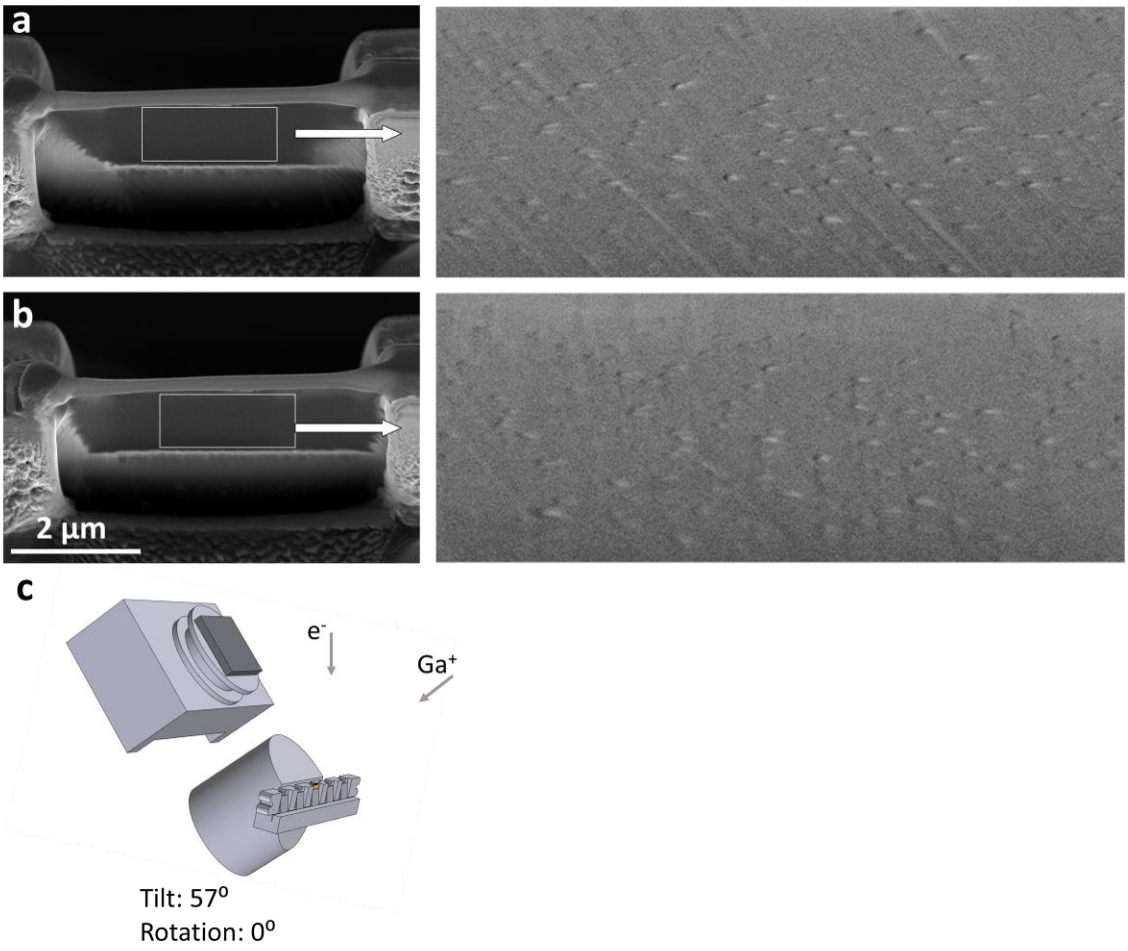

Figure II.7. A view of the back-side of the pretilted lamella during rocking angle thinning. (a) An SEM micrograph of the back side of the lamella with visible curtaining artifacts. A magnified and contrast/brightness adjusted image of the cross-section is shown to the right. (b) The same view with magnified image after thinning the sample using rocking angle methods. (c) A drawing of the stage orientation from which the micrographs were taken.

The rocking angle methods described above can be used in wide range of different sample types, and are particularly advantageous when the aim of an investigation is to determine the extent of inherent sample inhomogeneity using either HAADF STEM intensities or STEM EDX techniques. One example is the study of segregation of ions during spin coating of inorganic thin films from aqueous solutions. Understanding how to control compositional inhomogeneity and/or density variations in

the films by changing processing conditions requires knowledge of local composition and density; this makes it critical that the lamella preparation not introduce artifacts. FIB instruments are commonly equipped with a platinum precursor gas injector make Pt a logical choice for a protecting layer for lamella preparation. However, e-beam deposited Pt films typically propagate curtaining artifacts into the lamella being prepared. As seen in Figure II.8a, curtain artifacts dominated the relative intensity and disrupted statistical analysis of inhomogeneities in a film. The same lamella polished using the rocking angle methods described herein and reimaged (Figure II.8b) has a smooth and linear background provided an easily removable background intensity for quantification. [28].

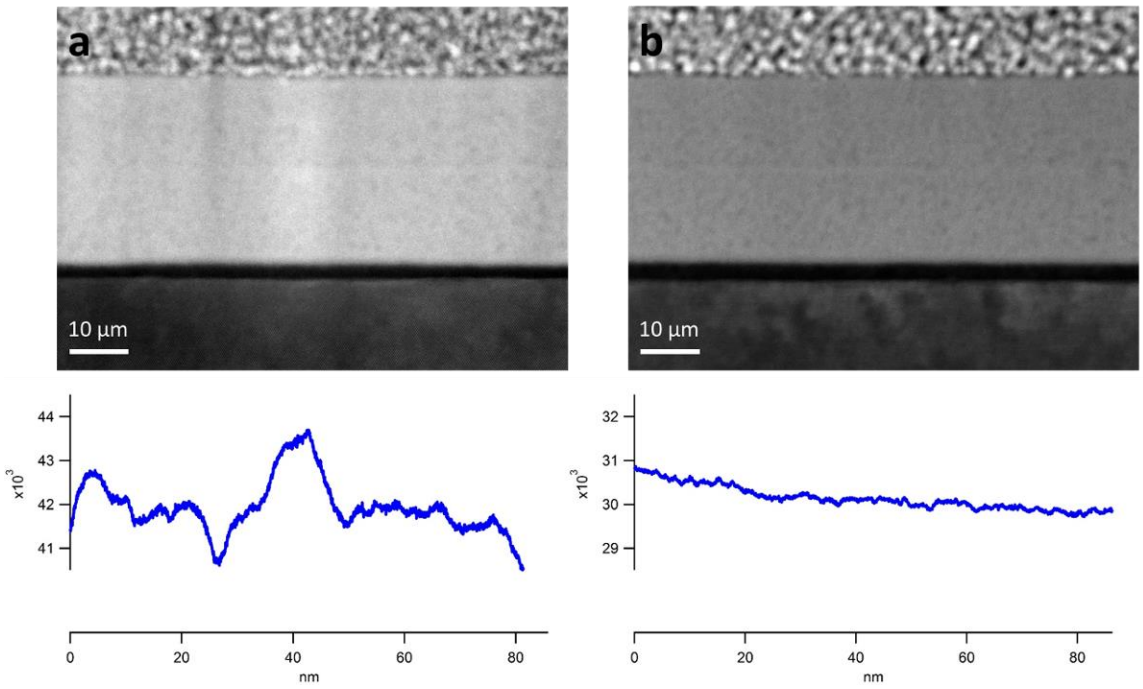

Figure II.8. Removal of inhomogeneities in a film (a) An ADF-STEM image nanoscale curtains often seen when preparing samples with an electron beam induced deposition (EBID) platinum protecting layer. ADF-intensity (counts) extracted from the layer of interest (a lanthanum zirconium oxide film deposited from aqueous precursors) is shown below the image. The native oxide [110] silicon lattice of the substrate below the film and the EBID platinum at the top of the image are both visible. (b) ADF-STEM images from the same sample after additional thinning of the sample using rocking angle methods. Note the thickness related slope in contrast.

Images of a layered chalcogenide heterostructure, $(SnSe)_{1.2}(TiSe_2)$, taken on a lamella prepared using the approach described herein (Figure II.9) illustrates the detection of pseudo-curtaining effects. A low magnification image shown in Figure II.7a has intensity variations that could be interpreted as curtain artifacts. However, as seen in Figure II.7b, the intensity variations do not continue into the silicon substrate, indicating that the cause of the variation is not due to thickness effects. Lateral intensity variations are mostly dominated by diffraction contrast in the STEM image relating to vertical columns of the film that are tilted slightly off axis from the substrate. These slight tilts may result from stacking defects near the bottom of the film. Rotational disorder leads to some regions that are oriented on a crystallographic zone axis where diffraction contrast is the strongest, also leading to intensity changes. Figure II.9c shows a high magnification image of a well oriented region of the film and increased HAADF- intensity throughout the oriented area relative to the off axis areas of the film.

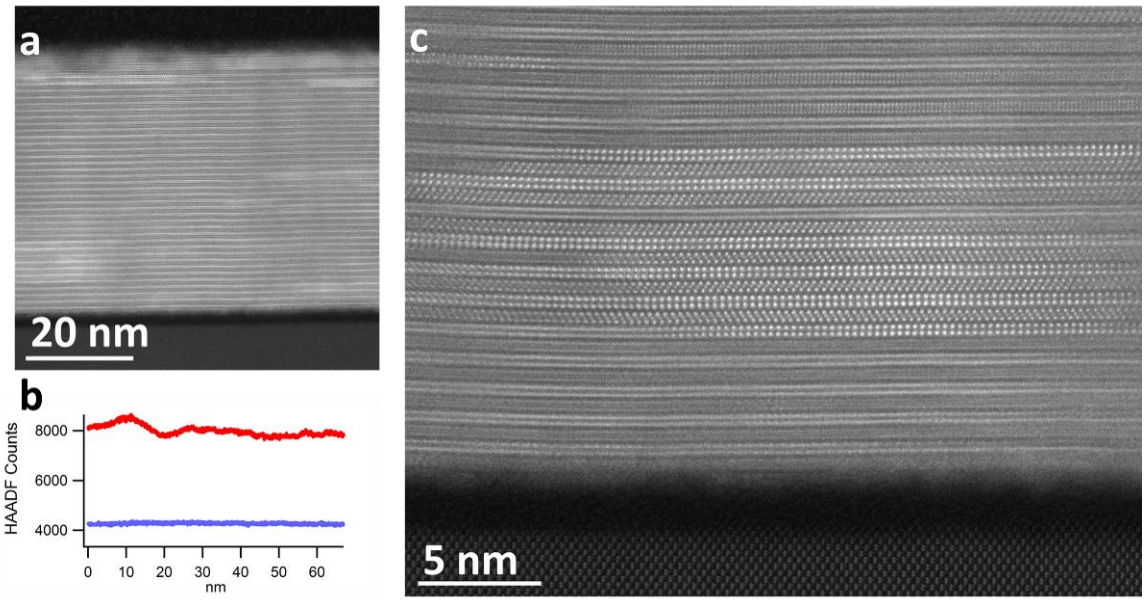

Figure II.9. Distinguising curtaining from other effects (a) a low magnification image of a rotationally disordered two dimensional laminate system, $(SnSe)_{1.2}(TiSe_2)$, deposited over

the native oxide of silicon. (b) A graph showing lateral intensity profiles extracted from parallel areas in the overview image. The blue profile, extracted from the silicon substrate region of the image, demonstrates the uniform thickness of the lamella. The red profile, extracted from the $(SnSe)_{1.2}(TiSe_2)$ region of the image exhibits intensity changes relating to composition and crystallographic orientation rather than curtaining. (c) A high magnification image showing [110] silicon dumbbells in the bottom of the image and regions of crystallographically oriented $(SnSe)_{1.2}(TiSe_2)$ demonstrating that the sample was preserved by the FIB preparation and thin enough for high resolution imaging.

II.5.Conclusions

In this paper we present a rocking angle polishing method that can be applied to remove curtaining artifacts for TEM lamella preparation using FIB instruments that do not have a second tilt axis normal to the cross-section surface. Pretilting the TEM half grid used for *in situ* lift-out preparations allows the use of the rotational axis of the stage to rock the sample relative to the ion beam. These methods can be applied to prepare large areas at low voltage with minimal artifacts, making this an ideal approach for TEM sample preparation of a broad range of materials.

CHAPTER III

CHARGE TRANSFER BETWEEN PbSe AND $NbSe_2$ IN $[(PbSe)_{1.14}]_M(NbSe_2)_1$ FERECRYSTALLINE COMPOUNDS

III.1. Authorship statement

In the following chapters (III-VIII), I prepared samples using a focused ion beam using methods described above and performed high resolution scanning transmission electron microscopy for qualitative investigation of synthetic products. In this work, atomic resolution Z-contrast images provided climactic final data for these papers and provided necessary confirmation of X-ray diffraction results.

The following chapter was published in Chemistry of Materials in 2014, volume 26, pages 1859-1866. Matti Alemayehu is the first author and synthesized the materials. I performed STEM work used for structural interpretations.

III.2 Introduction

Rational design of new molecules with desired properties requires an understanding of the interactions between different structural components in order to predict properties and reactivity. Organic chemists, for example, use charge donating and withdrawing groups to systematically control electrostatics and bonding affinity of compounds and hence tailor chemical reactivity. A classic example is benzene, where electron-withdrawing groups deactivate the ring towards an electrophilic substitution and increase the reactivity of the ortho and para position of the ring. The concept of charge transfer is central to chemists understanding reactivity in both chemical and biochemical

reactions and hence is used both in the design of synthesis routes to targeted molecules and to tailor the activity of molecules.

In solid-state inorganic chemistry, the concept of charge transfer is used to understand intercalation and de-intercalation reactions, where an intercalating alkali metal atom donates its valence electron to the host structure, as it becomes a cation. More subtle charge transfer phenomena, analogous to that used in molecular chemistry between nominally uncharged, has been hindered by the inability to prepare series of structurally related compounds and observe trends in physical properties or chemical reactivity. In the misfit layered compounds with formula $[(MX)_{1+\delta}]_m(TX_2)_n$[1–5] that contain layers of a metal dichalcogenide (TX_2: T = Ti, V, Nb, Ta, Cr; X = S, Se) alternating with layers of a rock salt (MX: M = Sn, Pb, Bi, RE; X = S, Se), for example, charge transfer between the MX and TX_2 constituents has been proposed as a potential mechanism to explain both electrical and magnetic properties. This charge transfer has been relatively easy to confirm in the case of $[(REX)_{1+\delta}]_m(TX_2)_n$[1–5] compounds, where the magnetic moment of the RE ion can be used to infer the valence state. For compounds such as $[(SnX)_{1+\delta}]_m(TX_2)_n$ or $[(PbX)_{1+\delta}]_m(TX_2)_n$, however, valence electron counts would imply little or no charge transfer. There is still continuing debate as to the extent of charge transfer in these compounds, and whether charge transfer between constituents or entropic contributions from cation disorder stabilize the high temperature formation of these compounds.[3,7] Since typically only the $n = m = 1$ compound can be prepared via traditional high temperature synthesis techniques, investigating systematic changes in properties as a function of *n* and *m* to probe the extent of charge transfer has not been possible.

The MER method has recently been used to prepare a large number of $[(MX)_{1+\delta}]_m(TX_2)_n$ compounds with precise control over the value of *m* and *n* in the final self- assembled product.[1,6–10] These initial reports focused on details of the synthesis approach and on the structure of the new compounds, describing structural changes in the constituents as *m* and *n* are varied. The precise control resulting from this synthesis approach permits, for the first time, the formation of many systematic series of compounds for a given $MX-TX_2$ system to probe structure-composition-property relationships. We report here the synthesis and structure of the first six compounds in the $[(PbSe)_{1.14}]_m(NbSe_2)_1$ series and the results of our investigation of the electrical transport properties of $[(PbSe)_{1.14}]_m(NbSe_2)_1$ compounds where we use the systematic changes in measured properties to infer the extent of charge transfer between the lamella of PbSe and the lamella of the metal dichalcogenide layer. Band structure calculations show systematic distortions in the PbSe structure as a function of *m*, also seen in the reported STEM image, and an overlap of the PbSe valence band with empty states in the $NbSe_2$ conduction band, supporting charge transfer between the constituents.

III.3. Experimental Section

The compounds $[(PbSe)_{1.14}]_m(NbSe_2)_1$ where $1 \leq m \leq 6$ were synthesized using the MER technique, as originally described by Noh, *et al*[4,6] and subsequently optimized by Lin[1] and Atkins[9], using a custom-built physical vapor deposition system.[12] The system uses quartz crystal monitors to control the deposition source rates and provides thickness and rate feedback information to a LabVIEW computer program, which controls shutters that are located above each elemental source. Lead (Pb) and niobium (Nb) were deposited at a rate of 0.04 nm/sec and 0.02 nm/sec respectively, using electron beam sources, while

selenium was evaporated from an effusion cell held at a temperature that yielded a rate of 0.05 nm/sec. The substrates were mounted on a motorized stage that rotates to move samples to different sources. This system allows deposition of a precise amount of material and the generation of the elemental layer sequences required to prepare the title compounds. All samples were simultaneously deposited onto Si (100) wafers and fused quartz substrates. The samples deposited onto Si (100) substrates were used for X-ray measurements. The quartz substrates were shadow masked to form films in the shape of a cross optimized for measurement of electrical properties using the Van der Pauw method. The quartz-substrate films were used for electrical resistivity and Hall effect measurements to ensure an insulating substrate. The as-deposited films were annealed at 450 °C for one hour in a nitrogen atmosphere (less than 0.6 ppm O_2) to form the targeted compounds.

Low-angle X-ray reflectivity (XRR) and high angle X-ray diffraction (XRD) measurements were performed using a Bruker AXS D8 Discover X-Ray diffractometer with Cu $K\alpha_1$ radiation, Göbel mirror and Bragg-Brentano optics geometry. For low angle and high angle analysis anti-scatter slit sizes of 0.1 mm-0.6 mm and 0.6 mm-1.0 mm were used respectively. Each sample was individually aligned to the center of the goniometer, and the alignment was confirmed by ensuring that the specular maximum occurred at equal incident and exit angles at several different angles. The procedures for identifying the individual layer thicknesses from XRR patterns prior to annealing and XRD patterns post annealing have been previously described.[4,7]

The atomic composition of the $([PbSe]_{1.14})_m(NbSe_2)_1$ nanolaminate precursors were determined by using electron probe microanalysis (EPMA). 8 mm square samples

deposited on silicon wafers were glued on to an aluminum block for the analysis. Elemental Pb, Nb, Se, Si and the compound MgO were used as standards for the quantification of the characteristic radiation of each element found in the samples. Since the samples each contain a known number of repeats of Pb-Se and Nb-Se bilayers, the variation of the total composition of the samples as a function of the number of Pb-Se bilayers was used to extract the Pb/Se and Nb/Se ratios in each of the bilayers and the Pb/Nb ratio between them.

Electrical resistivity and Hall effect were measured using a van der Pauw sample geometry. Indium contacts were made to the four corners of the cross patterns deposited onto quartz. Current was sourced through two neighboring contacts using a Keithely 220 programmable current source, and the potential difference between the remaining two contacts was measured using a Keithely 2181A nanovoltmeter. All eight combinations were measured and resistivity was determined by using equation (1).

$$r = \frac{\rho d}{\ln 2} \frac{R_{AB,CD} + R_{CB,DA}}{2} f, \quad (1)$$

where f is given as the symmetry of the sample. The measurements were performed from 22 K to 295 K on a custom-built measurement system. Data was collected approximately every 15 K during both heating and cooling after the instrument had stabilized the temperature to within 0.1 % of the targeted value. A Cernox SD-1070 resistance temperature sensor mounted on the Cu block below the sample was used to determine the sample temperature. For the resistivity measurement, several different current values were used, and the slope of current versus voltage was used to determine the resistance. For Hall measurements, a constant current of 0.100 A was applied, and the magnetic field

dependence of the voltage perpendicular to the current flow was obtained. Magnetic fields were provided by a Varian V-7405 electromagnet. The Hall coefficient was obtained from the slope of the voltage versus field measurement. A custom LabView program controls both the resistivity and Hall measurement sequences.

III.4 Results and Discussion

While the thickness and composition of the Pb-Se and Nb-Se elemental precursor bilayers required to prepare $[(PbSe)_{1.14}]_m(NbSe_2)_n$ ferecrystal compounds were previously determined[7], the deposition system used in this study still needed to be calibrated. Briefly, several binary Pb-Se and Nb-Se samples were made containing approximately 50 repeats with a fixed Se thickness and varying metal thicknesses. The compositions of the samples were determined using EPMA, and the ratio of the metal layer to selenium layer required to obtain a 1:1 ratio of Pb:Se and 1:2 ratio of Nb:Se was interpolated from a graph of composition as a function of the thickness of the metal layer. For subsequent samples, metal to selenium ratios yielding a ~5% excess of selenium were used to compensate for Se lost during the annealing process. The next step was to determine the deposition parameters required to prepare samples with the desired misfit parameter. For $[(PbSe)_{1+\delta}]_m(NbSe_2)_n$ misfit layered compounds, two different values of δ have been reported, 0.10[3] and 0.14[5]. We prepared a series of samples with a fixed Pb:Se repeating layer and a layer of Nb:Se of varying thickness maintaining the Nb:Se ratio at the calibrated value. The measured Nb:Pb ratio of these samples was graphed versus the thickness of the Nb layer and the thickness of the Nb:Se layer required to obtain a desired Pb/Nb ratio could be determined by interpolation. We initially targeted the misfit value of 1.10 and prepared a series of samples with fixed Pb:Se, Nb:Se and Pb:Nb ratios

containing the repeat layer sequence Pb:Se:Nb:Se with different total repeat layer thicknesses. These $[(PbSe)_{1.10}]_1[NbSe_2]_1$ precursors were annealed as described in the literature[1] and the diffraction quality of the samples were used to determine the optimum repeat layer thicknesses.

A set of precursors were prepared for the compounds $[(PbSe)_{1.10}]_m(NbSe_2)_1$ using the initial deposition parameters that produced the optimal $[(PbSe)_{1.10}]_1[NbSe_2]_1$ diffraction pattern and annealed at 450 °C for 1 hour. As summarized in the first set of samples in Table III.1, the average thickness of the two 001 planes of crystalline PbSe formed per elemental Pb:Se bilayer deposited in each of these samples was 0.607 nm and samples with larger *m* values were found to have broader diffraction peak widths, low intensities and few high order Bragg diffraction maxima. This suggests that while the compounds could be made, the initial deposition parameters were not optimum. The thickness of the two crystalline 001 planes of PbSe in the known misfit compounds was found to be between 0.612 nm and 0. 614 nm,[3,5] suggesting that there was a deficit of PbSe in the precursors. This was confirmed by TEM and STEM cross-sections of these initial samples, which contained many defects and regions with thinner than expected PbSe layer thickness. This was especially true in samples with larger *m*, because if there is a deficit in each elemental Pb:Se bilayer deposited, then the deficit relative to an amount to form an integer number of crystalline 001 planes increases as *m* is increased.

Table III.1. A summary of the lattice parameter and FWHM of the 00*l* peaks for samples prepared with different Pb:Se bilayer thicknesses.

	Pb:Se thickness 0.607 nm		Pb:Se Thickness 0.611 nm		Pb:Se Thickness 0.612 nm	
m	*c*-axis (nm)	FWHM	*c*-axis (nm)	FWHM	*c*-axis (nm)	FWHM
1	1.24(1)	0.25(1)	1.24(1)	0.27(1)	1.25(1)	0.19(1)
2	1.85(1)	0.32(1)	1.85(1)	0.25(1)	1.86(1)	0.23(1)
3	2.46(1)	0.41(1)	2.46(1)	0.25(1)	2.48(1)	0.21(1)
4	3.07(1)	0.38(1)	3.07(1)	0.37(1)	3.09(1)	0.32(1)
5	3.68(1)	0.40(1)	3.68(1)	0.40(1)	3.72(1)	0.36(1)
6	4.27(1)	0.35(1)	4.29(1)	0.39(1)	4.30(1)	0.40(1)

To further optimize the deposition parameters for the targeted compounds, several sets of $[(PbSe)_{1.14}]_m(NbSe_2)_1$ precursors were prepared where the thickness of the Pb:Se bilayer was systematically increased. The diffraction patterns after annealing were examined to determine which Pb:Se bilayer thickness produced the samples with the best diffraction patterns. Table III.1 contains a summary this data. As we increased the thickness of the elemental Pb:Se bilayer deposited in each set of samples, the average thickness of the two crystalline 001 planes of PbSe per Pb:Se bilayer increased and the average line width of the Bragg diffraction maxima decreased, most prominently for small values of *m*. This suggests that the correct value of δ is larger than 0.10 and close to 0.14. The set of samples in the third column of Table III.1 resulted in the samples with the most number of observable 00l reflections and the narrowest line widths, especially for the m=1-4 samples.

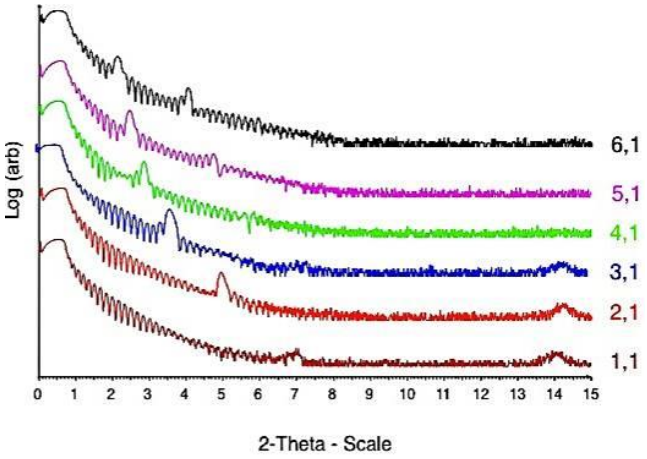

Figure III.1. X-ray reflectivity data of the precursors designed to form $([Pb|Se]_{1+\delta})_m(Nb|Se)_1$. The numbers to the right of the scans indicates the number of Pb:Se. and Nb:Se repeats deposited in each sample. The calibration results in one crystallographic unit of each structure per bilayer deposited.

Annealed samples from the set of samples in the third column of Table III.1 were used in the reported electrical measurements. The low angle diffraction patterns of each of these precursors are shown in Figure III.1. The diffraction patterns contain Bragg maxima from the modulation of the elements in the precursor and Kiessig[11] fringes from the interference between the front and back of the films. The thickness of the repeating sequence of Pb:Se and Nb:Se bilayers in each of the precursors was extracted from the position of the Bragg maxima and the slope of the linear fit thickness versus *m* indicates that each Pb-Se bilayer in the as-deposited films is 0.612 nm thick. The intercept indicates that the single Nb-Se bilayer in the as deposited films is 0.631 nm thick. Clear and well-defined Kiessig[11] fringes extend to 5° 2θ in most of the samples. Based on the relationship derived by Parratt [12] between film roughness and the maximum angle the Kiessig fringes occur,

$$D_t = \frac{\lambda}{4(q_i^2 - q_c^2)^{1/2}}, \quad (2)$$

the relative smoothness of the samples can be extracted, where Δt is the film roughness, λ is the x-ray wavelength (Cu Kα), θ_i is the maximum angle the fringes are observed at, θ_c is the critical angle. Estimating that the Kiessig [11] fringes extend out to at least 5° 2θ in the diffraction patterns in Figure III.1., we calculate that the average film thickness variation is approximately 0.18 nm, reflecting the quality of the as deposited precursor films.

The precursors of the samples listed in Table III.1 were heat-treated at 450 °C for 1 hour, as suggested by prior reports in the literature, to self-assemble each of these target compounds.[11] The resulting diffraction patterns (Figure III.2. contains those from column 3 of Table III.1.) contain well-defined Bragg reflections that can all be indexed as *00l* reflections. The *c*-axis lattice parameters increase linearly with increasing number of Pb:Se bilayers present in the repeating unit of the precursor. The average thickness of the two 001 planes of the distorted PbSe rock salt layer that form from each PbSe bilayer, determined from the slope of a plot of the c-axis lattice parameter versus *m*, varies depending on the thickness of the Pb:Se bilayer in the precursor. For the first set of samples the average increase was 0.607 nm and the $NbSe_2$ layer thickness was 0.632 nm. For the last set of samples, whose high angle diffraction patterns are shown in Figure III.2., the average thickness of the two crystalline 001 planes of PbSe formed per Pb:Se bilayer is 0.612 nm and the $NbSe_2$ layer thickness is 0.630 nm. This average thickness for two crystalline 001 planes of PbSe is similar to that determined for other misfit compounds containing PbSe[3] and is within the range for the bulk PbSe.[5] The Se-Nb-Se

trilayer thickness is smaller than that determined for other misfit compounds containing $NbSe_2$[5] and ~ 0.02 nm smaller than the lattice parameters measured for the different polytypes found for bulk $NbSe_2$.[18] The variation of the c-lattice parameters as a function of precursor structure suggests that these compounds readily form with relatively large concentrations of defects.

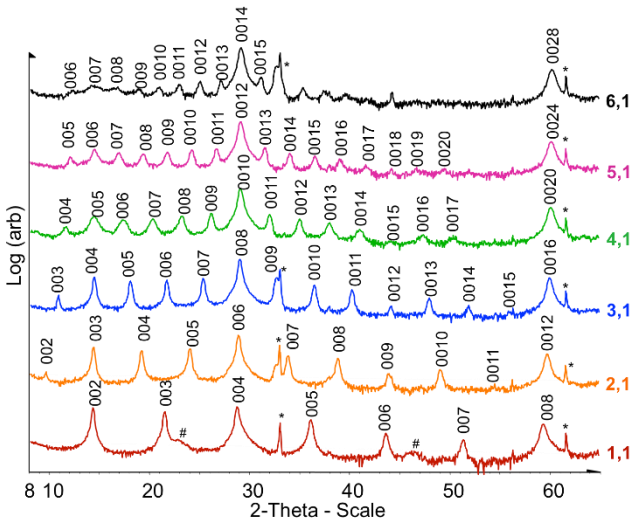

Figure III.2. Diffraction patterns of $([PbSe]_{1.14})_m(NbSe_2)_1$ compounds. The compounds are crystallographically aligned with the *c*-axis normal to the sample substrate. (*) Symblolizes a *k*α Si peak from substrate at 32° and a *k*β Si at 64°. Peaks marked with (#) on the (1,1) diffraction pattern at 23° and 46° are traces of a ternary phase of the structure. All the diffraction maxima can be indexed as 00*l* reflections as indicated above each peak.

HAADF-STEM images of a (2,1) sample from the sample whose diffraction patterns is shown in Figure III.2. is shown in Figure III.3. The STEM image contains a repeating structure of 4 PbSe 001 planes and one Se-Nb-Se trilayer throughout the field of view examined, reflecting the long range order along the c axis of the structure resulting in the diffraction pattern. The interfaces between the PbSe and $NbSe_2$ layers are abrupt. Visible in the expanded image are chevrons for $NbSe_2$ trilayers oriented along the

100 zone axis indicating that the coordination of the Nb atom is trigonal prismatic. The central PbSe region within the expanded image is oriented along a 100 zone axis. Other zone axis orientations are visible in the main image. The appearance of atomic columns localized within constituent layers with a coherence length of few nanometers and the variation of this alignment between layers indicates a turbostratic disorder between adjacent layers of PbSe-$NbSe_2$.

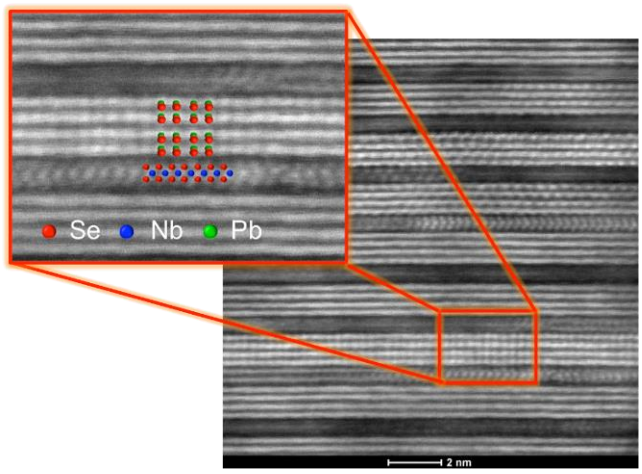

Figure III.3. HAADF-STEM image of $([PbSe]_{1.14})_2(NbSe_2)_1$ compounds. The bright spots represent the lead selenide layers and the darker spots represent the NbSe2 layers.

Figure III.4 contains temperature dependent resistivity data for the series of (*m*,1) samples with the highest quality diffraction patterns. The resistivity systematically increases as *m*, the thickness of the PbSe layer increases. The samples with *m* = 1,2 and 3 exhibit a nearly linear decrease in the resistivity with decreasing temperature, which is characteristic of a metallic material. The samples with *m* = 4, 5 and 6 have a slight upturns at low temperatures suggesting electron localization, perhaps related to the higher disorder reflected in the broader diffraction maxima and lack of higher angle reflections in these samples. These changes as m increases perhaps reflect the changes in the

coupling of the lattice vibrations between the PbSe and $NbSe_2$ constituents. The bilayer of PbSe in the (1,1) structure is considerably distorted from the bulk rock salt structure, while the PbSe structure of the (6,1) is much more like that of the bulk. The slopes of the resistivity at high temperature are approximately a factor of 2 smaller than reported for crystalline $[(PbSe]_{1+\delta}]_1(NbSe_2)_n$ misfit compounds where n = 1,2 and 3.

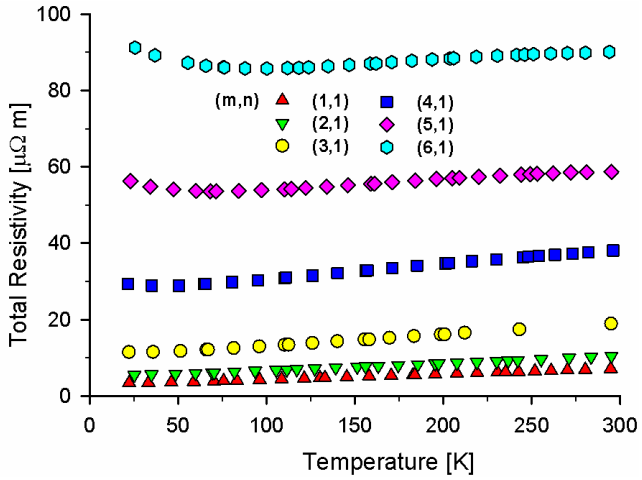

Figure III.4. Measured resistivity of $([PbSe]_{1.14})_m(NbSe_2)_1$ for variable temperatures showing an increase in resistivity as a function of *m*.

The room temperature resistivity of the (1,1) sample is similar to that reported previously for the (1,1) ferecrystal[11] and sits between measured values for the (1,1) crystalline misfit layered compound, being slightly higher in resistivity than reported by Wiegers[3] and an order of magnitude lower in resistivity than reported by Oosawa[5]. The temperature-dependence of the resistivity of our (1,1) sample is very similar to the temperature-dependent resistivity observed by Heideman, *et al.*[11], but has a factor of 2 weaker temperature-dependence than that observed by Oosawa, *et al* [5]. The differences between the electrical properties reflect that the ferecrystal is a different polymorph than the crystalline misfit compound. The observed differences are similar in magnitude to

differences seen between different polymorphs of $NbSe_2$ itself. Somewhat surprising is that the turbostratically disordered polymorph has a similar conductivity to the highest reported conductivity for the crystalline analog, as the disorder might have been expected to decrease the mean free path. The difference in the temperature dependence suggests reduced electron-phonon scattering, which reflects the reduction in organized vibrations due to the disorder in the ferecrystal.

Prior electrical conductivity data for NbX_2 misfit compounds were interpreted as though conduction was through a NbX_2 band formed by the d_z^2 orbitals of niobium.[3] XPS investigations suggested that there was a small amount of charge transfer from the MX to the TX_2, which would create holes in the MX valence band that would contribute to the conductivity.[2] Conduction is still described as being dominated by the NbX_2 constituent, as the holes created from charge transfer of MX to TX_2 were expected to have smaller mobility than the carriers in the TX_2 bands. [2] For charge transfer to occur between the MX and TX_2 layer, the Fermi level of the TX_2 layer has to be lower in energy than the Fermi level in MX. Two potential energy band alignments are described in Figure III.5, where the band alignment shown in Figure III.5 (a) would result in no charge transfer while the band alignment shown in Figure III.5(b) would result in charge transfer from PbSe to $NbSe_2$.

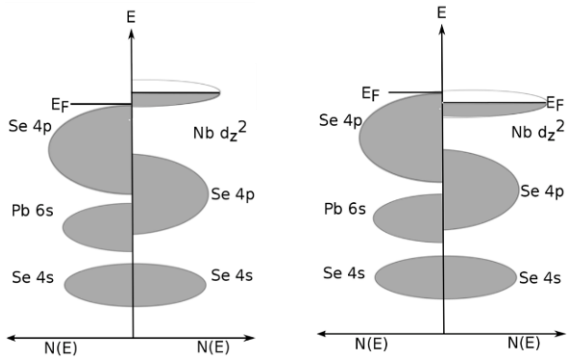

(a) (b)

Figure III.5. Two potential band alignment between the conduction band and the valence band of $NbSe_2$ and PbSe where (a) represents no charge transfer and (b) represents charge transfer.

The systematic decrease in conductivity as *m* is increased supports the idea that the $NbSe_2$ layer dominates the conduction. Simplistically, increasing the number of semiconducting PbSe layers while maintaining a single metallic $NbSe_2$ layer would decrease the number of carriers per unit volume, increasing the resistivity. A simple model treating the constituent layers as resistors in parallel (figure III.6) can be used to estimate the increase in resistivity due to increasing the number of PbSe layers. This model ignores any interaction between the layers such as charge transfer or interface effects (case a in Figure III.5b), but it provides a useful starting point to understand the trends in the measured resistivity.

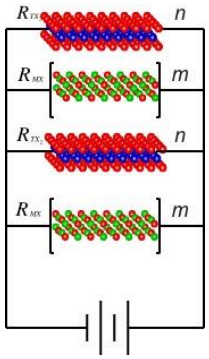

Figure III.6. Parallel Resistor Model of $([PbSe]_{1.14})_m(NbSe_2)_1$

If each repeating unit of the ferecrystal is comprised of *m* layers of PbSe and *n* layers of $NbSe_2$ and there are *k* repeating units in the overall structure, the equivalent circuit resistance, R_{eff}, will be:

$$\frac{1}{R_{eff}} = k\left(\frac{m}{R_{PbSe}} + \frac{n}{R_{NbSe_2}}\right), \quad (3)$$

Where R_{PbSe} and R_{NbSe2} are the resistances of a single layer of PbSe and single layer of $NbSe_2$ respectively. If

$$R_{PbSe} >> R_{NbSe_2}, \quad (4)$$

then

$$R_{eff} = \left(\frac{1}{nk}\right)R_{NbSe_2}, \quad (5)$$

To convert resistance into resistivity, we use the relationship between the resistance and resistivity of a thin sheet of total thickness D_0 [13], where $D_0 = k\,(md_{PbSe} + nd_{NbSe2})$. After simplifying, equation 6 is obtained.

$$r_{eff} = \left(\frac{md_{PbSe} + nd_{NbSe_2}}{n}\right)\frac{r_{NbSe_2}}{d_{NbSe_2}}, \quad (6)$$

If we further assume

$$d_{PbSe} \gg d_{NbSe_2}$$

which is reasonable as d_{PbSe} = 6.12 and d_{NbSe2}=6.30, a 2.5% difference, then Equation (6) simplifies to:

$$r_{eff} = \frac{r_{NbSe_2}(m+n)}{n}, \quad (7)$$

Using Equation 7 we can calculate the resistivity of the single layer of $NbSe_2$ in each of the compounds measured. If the assumptions in the model are correct, the resistivity of all of the $NbSe_2$ layers would be the same. If ignoring charge transport through the PbSe is a poor approximation, the calculated resistivity of the $NbSe_2$ layer might be expected to decrease. If there is significant charge transfer between the PbSe and $NbSe_2$ and the mobility of carriers in the PbSe are much lower than the carriers in $NbSe_2$, then the calculated resistivity per $NbSe_2$ layer might be expected to increase.

Figure III.7 plots the resistivity of the single $NbSe_2$ layer for each of the different samples calculated using equation 7 and the data shown in Figure 4. Instead of being the same for each compound as predicted by the model with its assumptions, the calculated resistivity of the $NbSe_2$ layer in each of the compounds systematically increases as *m* increases. Since the conductivity is proportional to both the carrier concentration and mobility, the resulting decrease in carrier concentration could result from a decrease in carrier concentration, or mobility, or a combination of both.

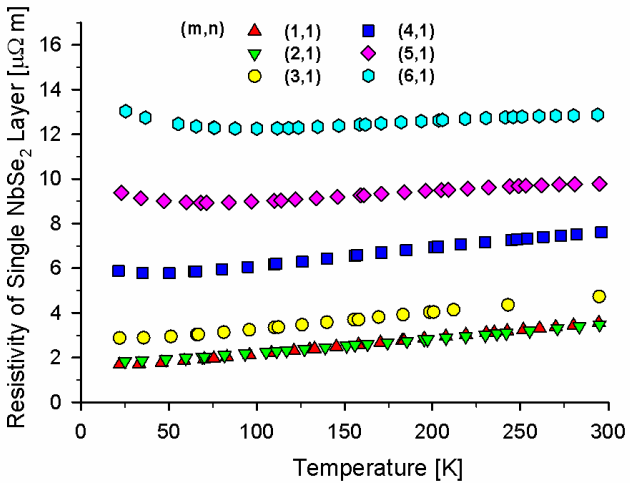

Figure III.7. Experimental resistivity of a single $NbSe_2$ layer as a function of temperature derived from the data in Figure 4 using Equation 7. The values of *m* and *n* in $([PbSe]_{1.14})_m(NbSe_2)_1$ for each data set are indicated in parenthesis.

To gain more insight into the reasons for the change in resistivity in this series of compounds, the Hall coefficient for each of the $([PbSe]_{1.14})_m(NbSe_2)_1$ compounds was measured as a function of temperature (Figure III.8). The Hall coefficients for all of the samples are positive, suggesting that holes are the majority charge carriers. This strongly suggests that the band alignment between the PbSe and $NbSe_2$ constituents are such that charge transfer occurs from PbSe to $NbSe_2$ leading to a more than half filled conduction band in $NbSe_2$ in agreement with prior literature reports on crystalline PbSe-$NbSe_2$ misfit layered compounds, which also had positive Hall coefficients.[5,14] There is also a systematic increase in the Hall coefficient as *m* is increased, suggesting that the average carrier concentration is decreasing as *m* increases.

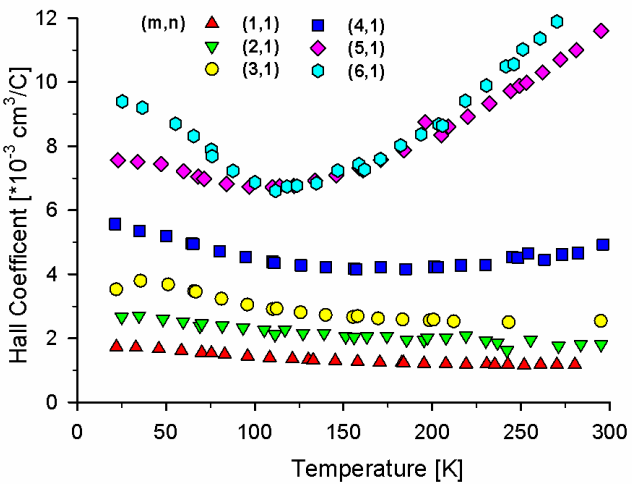

Figure III.8. Hall coefficients of $([PbSe]_{1.14})_1(NbSe_2)_1$ as a function of temperature.

The carrier concentration for each sample was calculated from the Hall coefficients assuming that only a single band contributes to the measured Hall voltage. While this is a significant simplification, the resistivity data suggests that the $NbSe_2$ bands dominate the conductivity and is consistent with the practice of prior researchers investigating misfit compounds.[3] The resulting single band carrier concentrations are graphed in Figure III.9, and show a systematic decrease in carrier concentration with increasing number of PbSe layers. This is consistent with the idea that adding layers of PbSe, which are semiconducting with a low carrier concentration, is essentially diluting the average carrier concentration and increasing the resistivity as *m* is increased. The carrier concentrations for the *m* = 1,2 and 3 samples are close to being temperature independent. For *m* = 4, 5 and 6, the carrier concentrations increase slightly as temperature is raised.

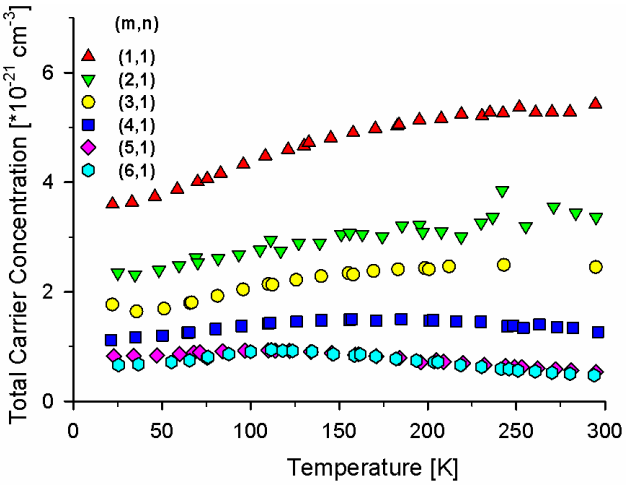

Figure III.9. Carrier concentration of $([PbSe]_{1.14})_1(NbSe_2)_1$ as a function of temperature as derived from hall coefficient

We can calculate a carrier concentration assuming all carriers are within the $NbSe_2$ layer with non-conducting PbSe layers and in the simplest picture one would expect a constant carrier concentration within the $NbSe_2$ layer as PbSe thickness is varied. Figure III.10 contains calculated carrier concentrations assuming all carriers are within the $NbSe_2$ layer. Instead of all samples having a constant carrier concentration, there remains a drop in carrier concentration as *m* is increased by more than a factor of 4 difference between the *m*=1 and *m*=6 compounds. This is consistent with increasing charge transfer from PbSe to $NbSe_2$ as *m* increases.

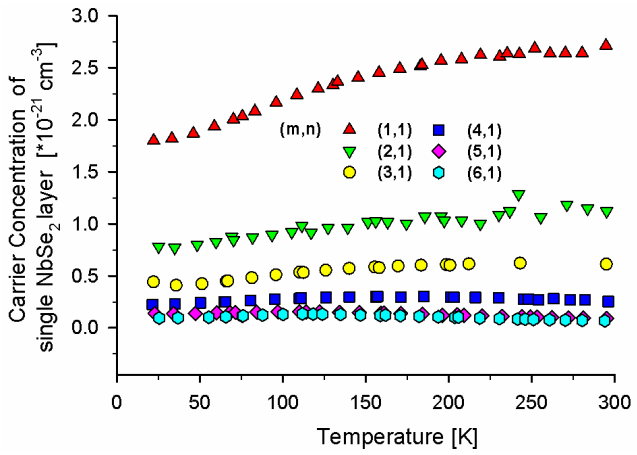

Figure III.10. Experimental carrier concentration for a single $NbSe_2$ layer as function of temperature.

The calculated mobility (Figure III.11) for the different samples are all around 1 $cm^2V^{-1}sec^{-1}$ at room temperature, suggesting that the predominant band that is responsible for the conductivity does not change as a function of *m*. Surprisingly, the room temperature mobility of all of these ferecrystals are about the same and higher than the mobility reported for the crystalline 1:1 misfit compounds. There is also a systematic reduction in the temperature dependence of the mobility. The (1,1) and (2,1) samples' mobility values increase linearly as temperature is lowered, increasing by a factor of 3 between room temperature and 20 K. The mobility of the (5,1) and (6,1) samples initially decrease and are almost temperature independent in the lower temperature range. The magnitude change observed in the resistivity is not accounted by differences in the mobility.

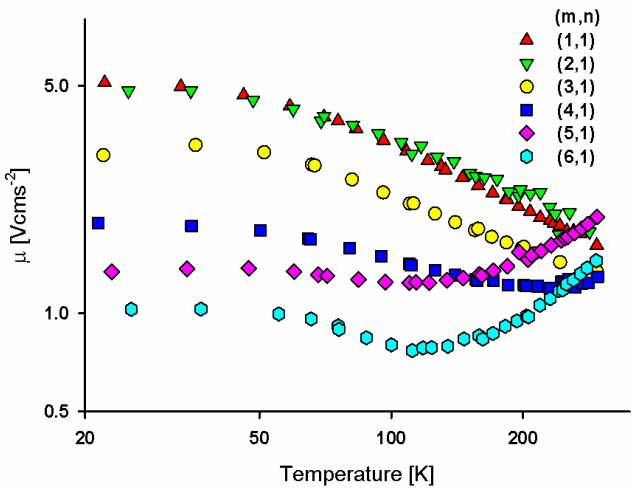

Figure III.11. Experimental mobility of $([PbSe]_{1.10})_m(NbSe_2)_1$ as a function of temperature for varying *m* layers.

One explanation for observed electrical behavior is that although $NbSe_2$ remains the major conduit for conduction, there is charge transfer from the PbSe to the $NbSe_2$. This was suggested by previous researchers when discussing the electrical behavior of misfit compounds and inferred from XPS data. To provide more insight as to the band alignments, density functional theory calculations were performed (Figure III.12). The calculation confirms observed experimental results suggesting that charge transfer from PbSe to $NbSe_2$ occurs. The band calculation for the PbSe shown on the left side of Figure 12 has a full valance band for the PbSe and the expected band gap for this semiconducting compound. The $NbSe_2$ calculation, shown on the right, results in a roughly half filled band consisting of mostly Nb d character. The center of Figure III.12 contains the calculated band diagram of the (1,1) compound using a supercell to approximate the lattice mismatch. The calculation places part of the valence band of the PbSe constituent above the empty states in the NbSe2 conduction band. This results in empty Pb (*p*) and Se (*p*) states and the transfer of electrons to the lower energy d_z^2 band

of the Nb. As the PbSe layer thickness is increased by increasing m, the amount of charge transfer increases.

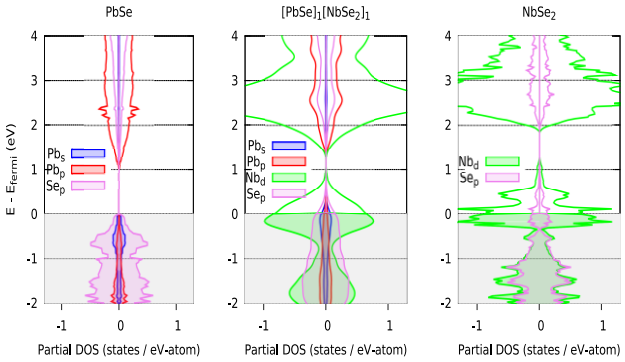

Figure III.12. Theoretical DFT calculation of $([PbSe]_{1.14})_m(NbSe_2)_1$ predicting charge transfer between PbSe and $NbSe_2$.

$[(PbSe)_{1.14}]_m(NbSe_2)_n$ ferecrystals were synthesized using MER technique. Samples were structurally characterized via *00l* diffraction, In-pane diffraction and TEM. The electrical resistivity and hall coefficient of $[(PbSe)_{1.14}]_m(NbSe_2)_n$ ferecrystal thin films were measured from 22 K to 295 K. The measurements were compared to the predictions of a simplistic model that assumes no charge transfer between rock salt and dichalcogenide layers. The simplistic model is inadequate to describe the observed changes in electrical resistivity with increased number of PbSe layers, which suggests there is interlayer charge transfer. An improved understanding of interlayer charge transfer is required in order to more accurately predict the properties of a given ferecrystal material.

CHAPTER IV

SYNTHESIS OF $([SnSe]_{1.16-1.09})([Nb_xMo_{1-x}]Se_2)_1$ FERECRYSTAL ALLOYS

IV.1. Authorship Statement

Chapter III was published in *Chemistry of Materials, volume 26, pages 3443-3449* in 2014. Co-authors Ryan A. Atkins assisted in the synthesis of the initial compounds. I performed microscopy measurements. Richard Westover is the primary author of the manuscript.

IV.2. Introduction

Virtually all solid state synthesis techniques require elevated temperatures to facilitate diffusion and extended times to achieve homogeneity. As a result, conventional high temperature solid state synthesis techniques are limited by thermodynamics to the formation of only the most stable product(s) of a given elemental composition.[1] As the composition becomes more complex, the number of potential products increases and the synthesis becomes increasingly challenging. For example, the formation of quaternary solid state compounds is very difficult because the product must be more stable than all other possible quaternary configurations as well as all possible configurations involving combinations of ternary compounds, binary compounds and the elements.[2,3] In addition, there are kinetic challenges arising from the need for *n* different elements to diffuse to the same location with correct concentrations for the formation of the product.

Misfit layer dichalcogenides are a good example of the limitations of conventional thermodynamic synthesis techniques. Misfit layer dichalcogenides are a

subset of layered materials that can be viewed as composite crystals with the generic formula $[(MX)_z]_m(TX_2)_n$, built from the interleaving of the two independent constituents: a distorted rocksalt MX (M = Sn, La, Pb, Bi; X = S, Se, Te) and a transition metal dichalcogenide TX_2 (T = Mo, Nb, Ti, V, Ta, and Cr) with *z* being the extent of the misfit between the constituents in the *ab*-plane.[4-7] Misfit layer dichalcogenides are conventionally synthesized through mixing of the three constituent elements, or a mixture of binary compounds, sometimes with an excess of the chalcogen, followed by annealing at an elevated temperature, typically 850 to 1100 °C, to allow the elements to mix via diffusion.[7] To obtain single crystals, Schäfer's vapor transport approach is typically used, where a small amount of transport agent is added and the sample is annealed at high temperature with a small gradient in temperature to promote the vapor transport of the elements to a growing crystal.[8] As a result of the high temperatures, only thermodynamically stable products are likely to be accessible and stable under the reaction conditions, greatly limiting the number of different compounds that can be formed. For example, while one might expect compounds with different values of *m* an *n* to be kinetically stable, only compounds where *m* and *n* are equal to 1 have been reported, except for a few instances where compounds with *n* equal to 2 or 3 have been more stable.[4,9] In addition, while Kalikhman *et al*[10-12] and others[13,14] have synthesized alloys of several transition metal dichalcogenides, (including $(Nb_xMo_{1-x})Se_2$, $(Ta_xMo_{1-x})Se_2$ and $(Ta_xW_{1-x})Se_2$), controlled alloying of misfit layer dichalcogenides has not been reported to our knowledge. The lack of ability to prepare even these simple solid-solution derivatives of known compounds makes developing an understanding of structure-property relationships challenging as concepts cannot be tested.

Recently, our group described a synthetic method by which numerous metastable $[(MX)_z]_m(TX_2)_n$ compounds, known as ferecrystals, could be synthesized. Ferecrystals are structurally similar to misfit layer dichalcogenides, but lack the long range order of true crystsls due to substantial rotational disorder between subsequent layers referred to as turbostratic disorder.[15-23] In the formation of these metastable compounds, physical vapor deposition is used to form an amorphous modulated precursor, as shown in Figure IV.1, with local composition and layer thicknesses closely mimicking the desired product. Self-assembly into the desired product is observed upon mild annealing. The use of modulated precursors minimizes diffusion lengths, allowing the formation of kinetically trapped metastable products where the final product contains the nanostructure of the initial precursor. This approach results in a much greater synthetic scope than conventional methods allow, with reports of new $[(MX)_z]_m(TX_2)_n$ compounds in which *m* and *n* were independently varied between 1 and 16.

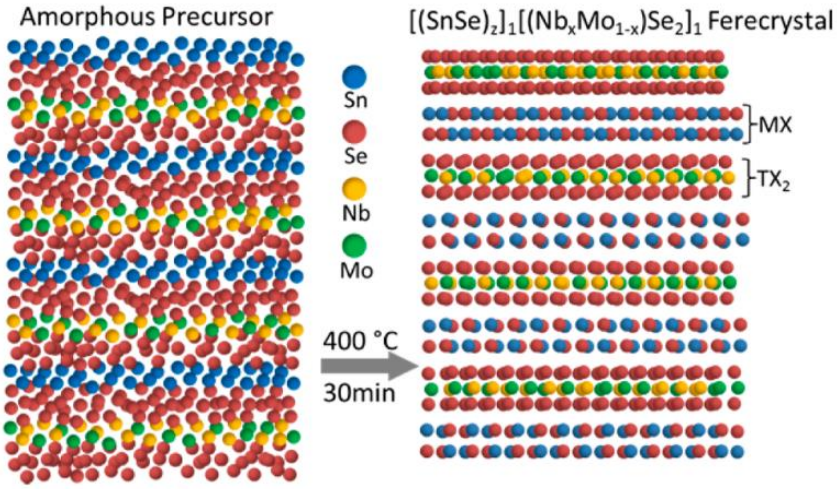

Figure IV.1. Schematic of the synthesis scheme for $([SnSe]_{1.16\text{-}1.09})_1([Nb_xMo_{1\text{-}x}]Se_2)_1$ alloy ferecrystals. On the left is the as-deposited amorphous precursor. On the right is the ferecrystal alloy after self-assembly.

The expansion of this method through the formation of modulated precursors with mixed metal layers, as shown in Figure IV.1, might allow the synthesis of quaternary $([MX]_z)_m([T_xT'_{1-x}]X_2)_n$ compounds with controlled compositions. We tested this idea using Nb and Mo as the transition metals because they are among the most common elements used for dichalcogenide alloys in literature[10-14] and their similarities in size and vapor pressure cause them to behave similarly in physical vapor deposition. In addition, the substitution of Nb acts as a p-type dopant in $MoSe_2$, allowing the addition of Nb to be tracked electrically as well as structurally and compositionally. We anticipated that this might hold true in our study. Herein we report the first synthesis of $(SnSe)_{1.16-1.09}(Nb_xMo_{1-x})Se_2$ compounds with x = 0, 0.26, 0.49, 0.83, and 1. Varying Mo/Nb ratios alters the structure of the materials, as shown in X-ray diffraction studies, with lattice parameters of the alloys following linear trends between those of the parent systems as predicted by Vegard's law.[24,25] Electrical transport properties of alloy materials were seen to trend between the metallic $(SnSe)_{1.16}NbSe_2$ and semiconducting $(SnSe)_{1.09}MoSe_2$ parent compounds with each Nb atom providing slightly less than one hole carrier in the $MoSe_2$ host.

IV.3. Experimental

$(SnSe)_{1.16-1.09}(Nb_xMo_{1-x})Se_2$ with x = 0, 0.26, 0.49, 0.83, and 1 were formed from designed modulated precursors prepared using the modulated elemental reactant technique in a custom built physical vapor deposition vacuum system. A more detailed description of this synthesis technique has been published previously.[23] A dual turbo and cryo pump vacuum system allowed depositions at pressures as low as 10^{-8} torr. Mo (99.95% purity), Nb (99.8% purity), Sn (99.999% purity) and Se (99.5% purity) acquired

from Alfa Aesar were used as elemental sources. In order to prepare refractive metals for evaporation as received, Mo and Nb pieces were loaded into a custom built, water cooled copper hearth and placed into a hermetically sealed chamber and purged with He at 8 L/min for 20 min. After purging, to remove remaining oxygen, oxophillic Ti was arc-melted by energizing a W electrode to 20 kV for 30 s. Samples were then arc melted to create dense pieces of suitable size. For alloy materials, Nb and Mo were added in desired stoichiometric amounts and then arc-melted.

Compositions of the arc-melted alloy sources and the resulting ferecrystal samples were determined by electron probe micro-analysis (EPMA) on a Cameca SX-100. Accelerated voltages of 10, 15 and 20 keV were used to collect intensities. This technique has been described previously in the literature.[26] Composition was then calculated from the film and substrate, or from the alloy source, as a function of accelerating voltage.

Metal sources were evaporated at rates of approximately 0.2 Å/s for Mo and Nb and 0.4 Å/s for Sn, using Thermionics 3 kW electron beam guns. Se was evaporated using a custom built Knudsen effusion cell at a rate of about 0.5 Å/s. Rates were monitored and controlled with quartz crystal monitors. Substrates were mounted on a rotating carousel controlled by a custom designed lab view program, which positioned the sample over the desired source. Pneumatically powered shutters between the elemental sources and the substrates controlled the exposure time of the samples to the elemental flux. Repetition of this process allowed the modulated precursors to be built up layer by layer until reaching a desired thicknesses ranging from of 500 to 600 Å.

Total thickness and repeating unit thickness were monitored by high resolution X-ray reflectivity (XRR) and X-ray diffraction (XRD) performed on a Bruker D8

Discover diffractometer equipped with a Cu K_α X-ray source and Göbel mirror optics. Synchrotron X-ray diffraction from the Advanced Photon Source (APS), Argonne National Laboratory (beamline 33BM) was used to determine the *ab*-plane lattice parameters.

TEM cross section lift-out samples were prepared and analyzed at the Center for Advanced Materials Characterization in Oregon (CAMCOR) High-Resolution and Nanofabrication Facility. Scanning Transmission Electron Microscopy (STEM) samples were prepared using an FEI NOVA Nanolab Dual Beam FIB equipped with Side winder ion column and performed on a FEI 80-300 kV Titan equipped with a Fischione Model 3000 Annular Dark Field (ADF) detector.[28,29] All images were collected at 300 kV. Samples for electrical measurements were deposited on quartz slides in a 1 x 1 cm cross pattern defined by a shadow mask. Temperature dependent resistivity and Hall effect measurements were performed using the van der Pauw technique.[27]

IV.4. Results and Discussion

The synthesis of $(SnSe)_{1.16\text{-}1.09}(Nb_xMo_{1-x})Se_2$ alloy ferecrystals begins with the preparation of a series of compositionally modulated precursors with appropriate compositions and thicknesses to enable self-assembly to the desired products. In order to ensure formation of precursors with stoichiometry and nanoarchitecture analogous to the targeted compounds, careful calibration of the deposition times of the constituent elements is required as described previously.[23] To simplify the procedure for the targeted quaternary compounds, calibrations for the parent ternary $(SnSe)_{1.09}(MoSe_2)$ and $(SnSe)_{1.16}NbSe_2$ compounds were used as starting points for the calibrations of the alloy precursors. Briefly, the deposition parameters required to form each binary constituent,

SnSe and TSe_2 (where T = Mo, or Nb) were determined by preparing a series of compounds with fixed metal thickness and varying thickness of selenium. Once the ratio of thicknesses required to obtain the composition of the binary compounds was determined, a series of ternary samples with varying Sn to T ratios were prepared to find the deposition parameters that correspond to the misfit ratio of the desired compound. Finally, the Sn:Se and M:Se thicknesses were scaled simultaneously until the repeat sequence resulted in a single unit cell of the $(SnSe)_y(TSe_2)_1$ after annealing.

Once the calibrations for the parent $(SnSe)_{1.04}(MoSe_2)$ and $(SnSe)_{1.16}NbSe_2$ compounds were complete, substitutions of Mo and Nb allowed the preparation of modulated precursors for the $(SnSe)_{1.16\text{-}1.09}(Nb_xMo_{1-x})Se_2$ alloy compounds. This was accomplished by replacing the pure transition metal sources with alloys of various compositions. Transition metal shutter time was calculated as a function of desired Mo/Nb composition assuming a linear trend between the calibrated times of the parent systems. Electron probe micro-analysis of the Mo/Nb ratios of the samples and alloy sources, shown in Figure IV.2a, indicate that the samples are consistently lower in Mo content than the source. This is likely because the vapor pressure of Mo is slightly lower than that of Nb,[30] resulting in a vapor phase rich in Mo and ultimately in a Mo rich film. In addition, as shown in Figure IV.2b, the more times the source is used the higher the Nb content of the sample because the source becomes depleted in Mo. Similar results have been found by other groups for the deposition of alloys using physical vapor deposition.[31,32]

Once the calibration of the modulated precursors was complete, the annealing conditions were optimized by varying temperature and time and following the evolution

of the X-ray diffraction pattern. As shown in Figure IV.3a, in the as-deposited sample the (001) diffraction peak is visible but no higher order peaks are observed reflecting the disordered state of the as-deposited sample. At 300 °C, peaks that can be indexed as higher order 00*l* reflections start to form as the precursor self assembles. Figure IV.3b graphs the intensity of the (002) reflection as a function of annealing temperature, show ing that the intensity increases until a maximum intensity is reached at 400 °C. Above 400°C, peaks broaden and lose intensity as the targeted compound begins to decompose, indicating the targeted product cannot be prepared via the usual high temperature solid state reaction schemes and that the product is probably metastable. Assuming that the optimal conditions correspond with the maximum diffraction intensity, 400 °C was chosen as the annealing temperature for the alloys. This is the same temperature determined in previous studies for the parent systems.[22]

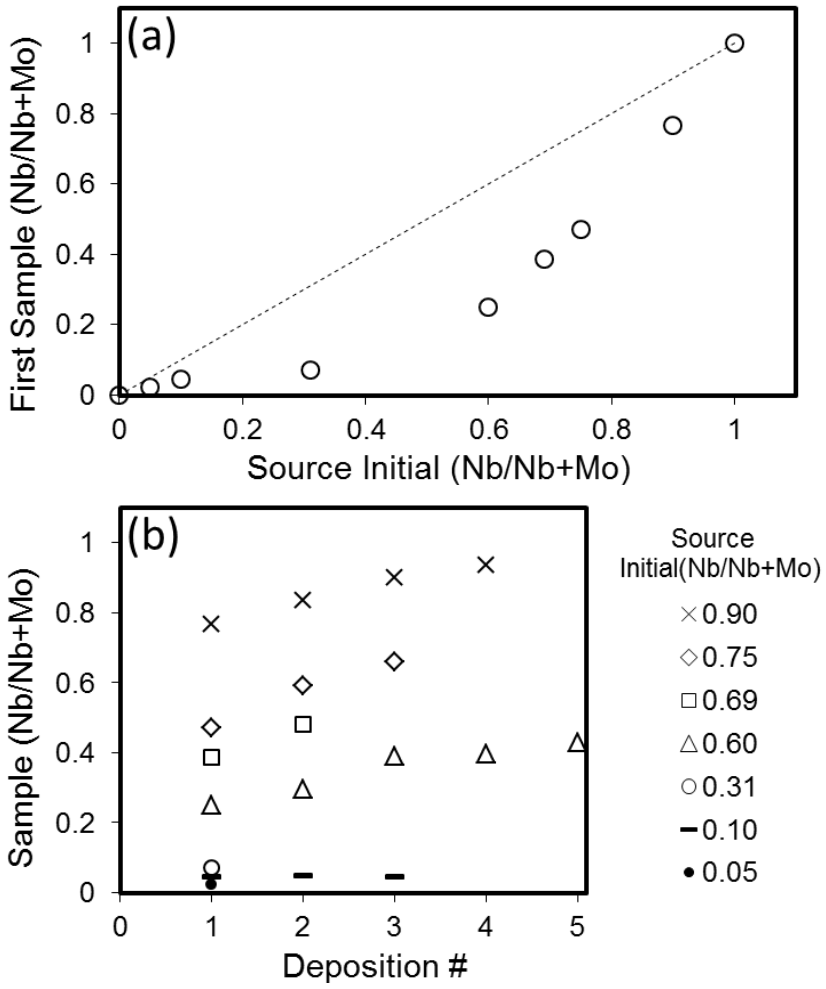

Figure IV.2. (a) Nb/Mo ratios of PVD source vs. the first resulting ferecrystal sample. (b) Sample Nb/Mo ratio change vs. number of depositions for PVD sources with different initial Nb content.

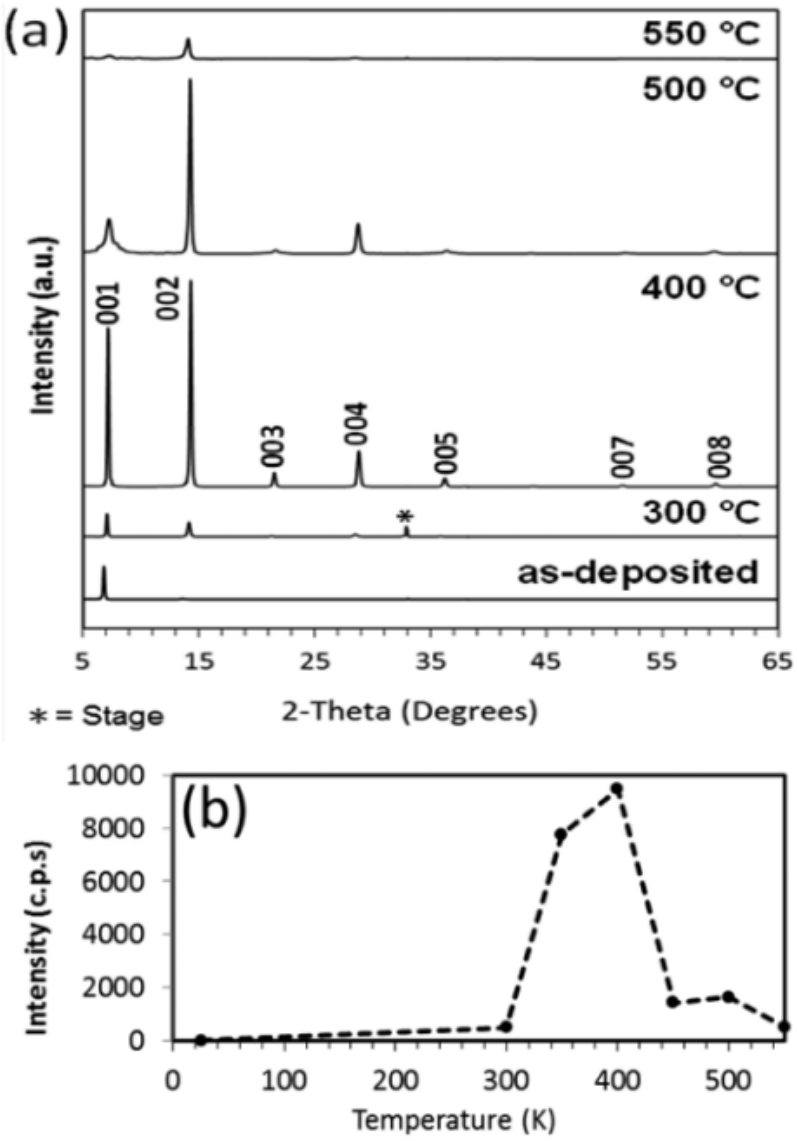

Figure IV.3. (a) Grazing incidence XRD patterns of $(SnSe)_{1.13}(Nb_{0.51}Mo_{0.49})Se_2$ annealed at 300, 350, 400, 450, 500, and 550 °C for 20 min. (b) Intensity of the (002) diffraction peaks with temperature.

To determine the structural evolution of the $(SnSe)_{1.16\text{-}1.09}(Nb_xMo_{1\text{-}x})Se_2$ alloy intergrowths as the Mo/Nb ratio is changed, a number of diffraction experiments were performed. Out-of-plane diffraction patterns, shown in Figure IV.4a, of each of the compounds indicated a systematic shift to higher angles of the *00l* peaks with increasing

Nb content. This is caused by linear decrease in the *c*-lattice parameter of the films as depicted in Figure IV.4b. This decrease in *c*-lattice parameter with increasing Nb occurs despite the fact that Nb is slightly larger than Mo and would be expected to cause an expansion of the lattice parameters as predicted by Vegard's law.[24,25] Comparison with the

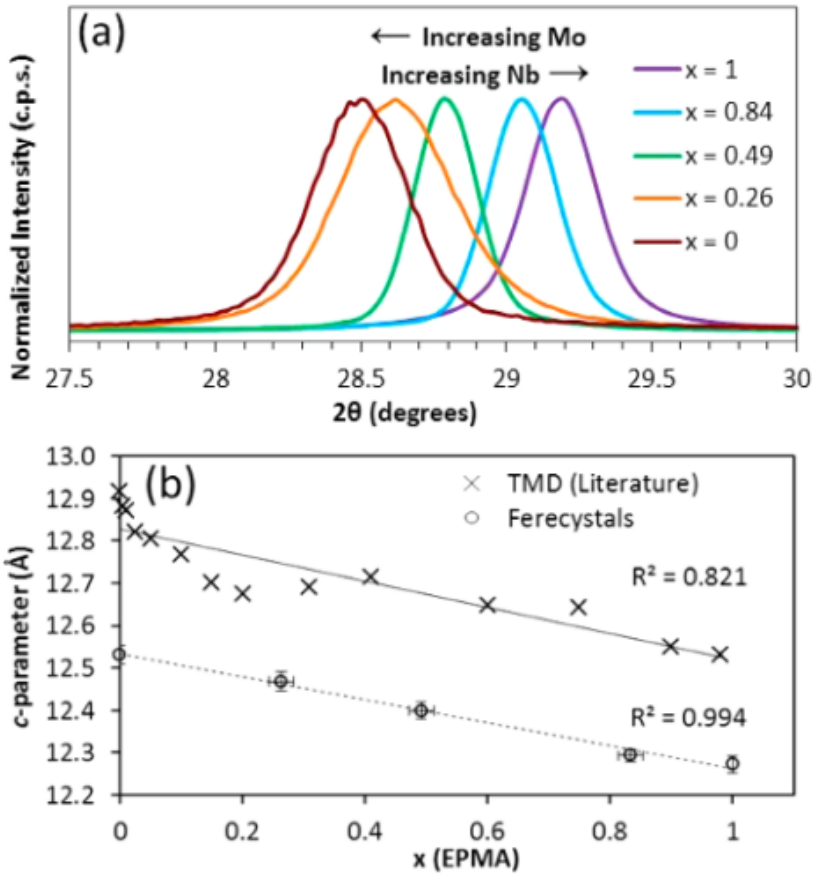

Figure IV.4. (a) Out-of-plane X-ray diffraction patterns showing shift in the (004) peak with changes in dichalcogenide composition. (b) Plot of *c*-lattice parameter vs. x for $(SnSe)_{1.16\text{-}1.09}(Nb_xMo_{1-x})Se_2$ alloys.

$(Nb_xMo_{1-x})Se_2$ TMD alloys, measured by Kalikhman,[10] shows a similar overall trend and slope. The contraction in the c-lattice parameter of the TMD alloys was attributed by Moussa Bougouma *et al*[14] to a reduction of electron density with added Nb causing changes in electrostatic repulsions between the selenium atoms and the transition

metal atom. Deviations from linearity in the $(Nb_xMo_{1-x})Se_2$ TMD systems was attributed, by Kalikhman, to regions of mixed 3R and 2H-TSe_2 phases. The addition of the SnSe layer in the ferecrystals between TSe_2 layers removes this effect, resulting in a more linear trend.

The in-plane (*hk0)* structure of the alloys was investigated from X-ray diffraction scans obtained at the Advanced Photon Source (APS). Figure IV.5 shows a representative in-plane diffraction pattern for the sample $(SnSe)_{1.13}(Nb_{0.51}Mo_{0.49})Se_2$. The diffraction maxima can be indexed as a mixture of cubic SnSe and hexagonal $Nb_{0.51}Mo_{0.49}Se_2$. The values for the $(SnSe)_{1.09}MoSe_2$[22] and $(SnSe)_{1.16}NbSe_2$[6] parent compounds of 6.003(1) Å and 5.928(1) Å respectively. The *a*-lattice parameter of the $Nb_{0.51}Mo_{0.49}Se_2$ was found to be 3.398(4)Å which is also between the literature values for the parent compounds of 3.320(1)Å for the $(SnSe)_{1.06}(MoSe_2)$ and 3.441(1)Å for the $(SnSe)_{1.16}NbSe_2$. Based on the unit cell parameters of the rocksalt and dichalcogenide components, the structural misfit was calculated to be z = 1.13 also falling between the published values of the parent $(SnSe)_{1.09}(MoSe_2)$ and $(SnSe)_{1.16}NbSe_2$ systems.

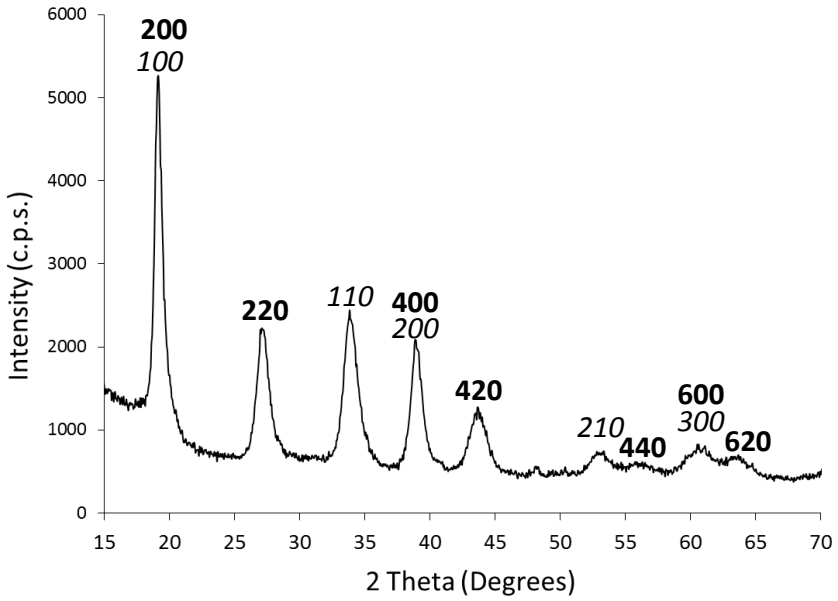

Figure IV.5. In-plane (*hk0*) X-ray diffraction pattern of $(SnSe)_{1.13}(Nb_{0.51}Mo_{0.49})Se_2$. Indices for the cubic SnSe are given in bold, while those of the hexagonal $(Nb_{0.51}Mo_{0.49})Se_2$ are given in italic.

In-plane diffraction patterns of the ferecrystals, shown in Figure IV.6a, exhibit a shift to lower angles of the (110) peaks of the dichalcogenide constituent with increasing Nb content. This is caused by a linear increase in the dichalcogenide *a*-lattice parameter that is very similar to Kalikhman's findings for the $(Nb_xMo_{1-x})Se_2$ TMD systems, as shown in Figure IV.6b. While increasing the Nb content of the alloys causes a decrease in the *c*-lattice parameter of the film, it increases the *a*-lattice parameter of the dichalco genide constituent. The result is an overall decrease in the *c/a* ratio of the unit cell with increased Nb content. Moussa Bougouma *et al*[14] attributed this decrease in *c/a* ratio with increased Nb to a decrease in electron density in the $4dz^2$ of the transition metal. They postulated that this leads to a less pronounced repulsion of the selenium atoms by this non-bonding orbital and a decrease in the *c*-lattice parameter. Further, they attribute the

increase in *a*-lattice parameter to changes in inner shell repulsion with the repulsion of the selenium $3p_x$ and $3p_y$ orbitals stronger than the repulsion of the $3p_z$ orbitals. Structural rearrangement takes place to reduce repulsion of the $3p_x$ and $3p_y$ orbitals resulting in an increase in *a*-lattice parameter and a decrease in *c*-lattice parameter as the Nb/Mo ratio increases. While the *a*-lattice parameter of the dichalcogenide increases with Nb content, the rock salt *a*-lattice parameter, as shown in Figure IV.7a, does not change within error. This supports the view that the substitution of Nb into $(SnSe)_{1.09}(MoSe_2)$ takes place exclusively in the dichalcogenide layer leaving the structure of the rock salt largely unchanged. Changes in the relative *a*-parameters of the dichalcogenide and rock salt layers leads to a linear change in the misfit parameter of the $(SnSe)_{1.16\text{-}1.09}(Nb_xMo_{1-x})Se_2$ alloys as a function of x, varying from 1.09 at x = 0 to 1.16 at x = 1, as shown in Figure IV.7b.

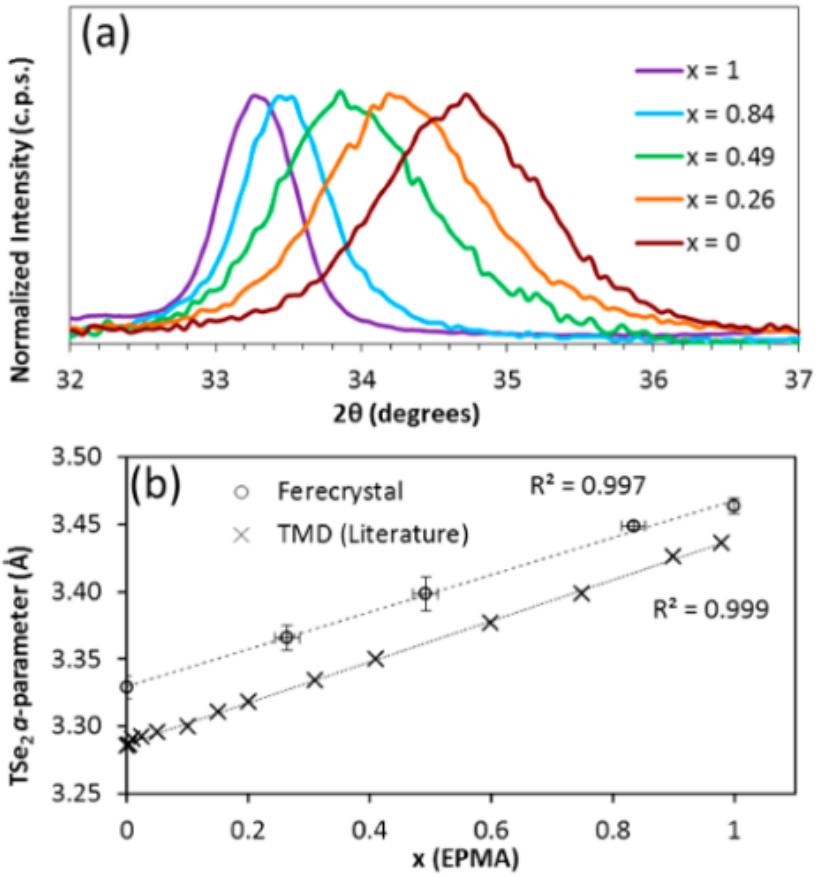

Figure IV.6. (a) In-plane X-ray diffraction patterns showing shift in the (110) peak of the dichalcogenide with changes in Mo/Nb ratio. (b) Plot of dichalcogenide *a*-lattice parameter vs. x for $(SnSe)_{1.16\text{-}1.09}(Nb_xMo_{1\text{-}x})Se_2$ alloys.

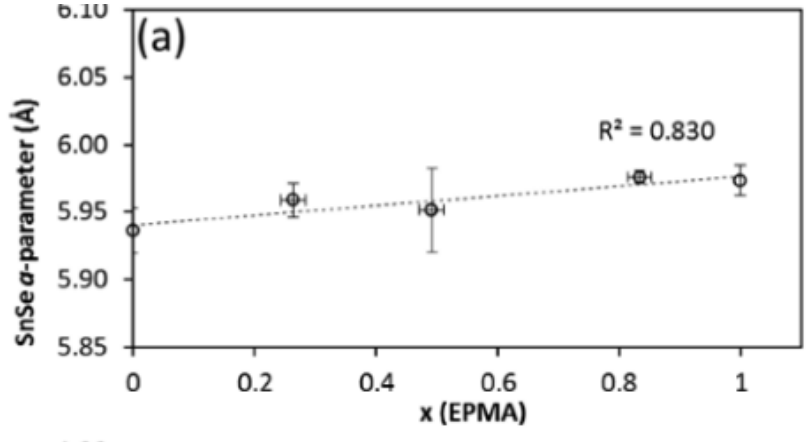

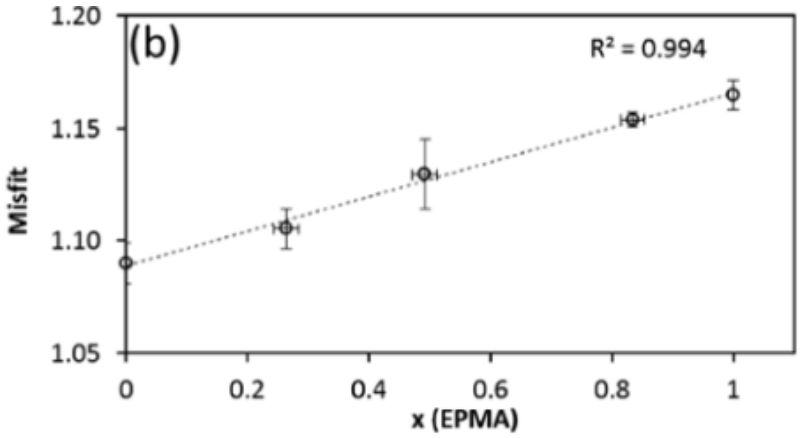

Figure IV.7. (a) Plot of rock salt *a*-parameter vs. x for $(SnSe)_z(Nb_xMo_{1-x})Se_2$ alloys. (b) Misfit parameter (z) vs. x for $(SnSe)_z(Nb_xMo_{1-x})Se_2$ alloys.

High-angle annular dark-field (HAADF) STEM was used to further investigate the structure of the ferecrystal alloys. A Z-contrast STEM image of the $([SnSe]_{1.13})_1(Nb_{0.49}Mo_{0.51}Se_2)_1$ ferecrystal is shown in Figure IV.8. The coordination of the transition metal is clearly trigonal prismatic as can be seen from the chevron structure in the expanded region of Figure IV.8. Distinct alternating parallel layering of SnSe bilayers with $Nb_{0.49}Mo_{0.51}Se_2$ monolayers is observed as expected based on *00l* X-ray diffraction measurements. While several different crystal orientations of the constituent layers can be seen in the image without any relationship between them, a degree of short range order can be seen in the upper left corner of the image, with adjacent SnSe and dichalcogenide layers showing the same orientation in adjacent layers.

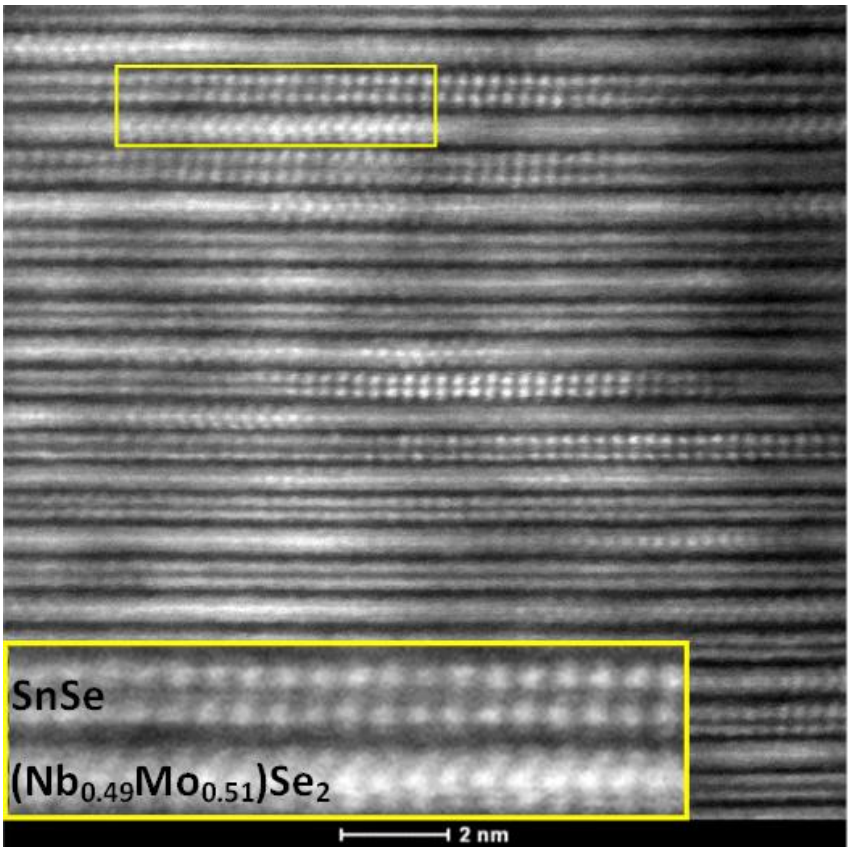

Figure IV.8. STEM image of $(SnSe)_{1.13}Nb_{0.51}Mo_{0.49}Se_2$

In order to further investigate the long range order of the $(SnSe)_{1.16\text{-}1.09}(Nb_xMo_{1-x})Se_2$ alloys, area X-ray patterns were obtained at the Advanced Photon Source (APS). A representative image of the $(SnSe)_{1.13}(Nb_{0.49}Mo_{0.51})Se_2$ ferecrystal is shown in Figure IV.9. Significant broadening of the reflections along the *c*-direction is indicative of a short coherence length in this direction. The lack of long range coherent scattering from the layered constituents is indicative of turbostratic disorder and confirms that only short range order exists between the layers as seen in the STEM image in Figure IV.8**.**

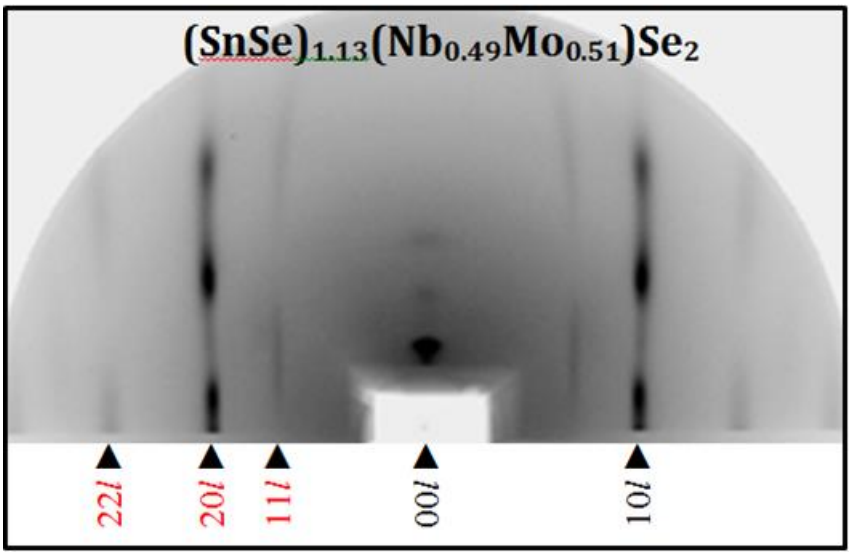

Figure IV.9. 2D X-ray diffraction pattern of $(SnSe)_{1.13}Nb_{0.51}Mo_{0.49}Se_2$ ferecrystal.

To measure electrical transport properties, $(SnSe)_{1.16\text{-}1.09}Nb_xMo_{1\text{-}x}Se_2$ ferecrystals with x = 0, 0.35, 0.54 0.76 and 1 were deposited on quartz slides. X-ray and EPMA analysis confirmed these samples had the same diffraction patterns and compositions as the samples deposited on silicon wafers and discussed earlier. The $(SnSe)_{1.09}MoSe_2$ showed semiconducting resistivity vs. temperature behavior, as shown in Figure IV.10, with a room temperature resistivity ρ = 220 mΩ-cm. This is similar to previously published values for the $(SnSe)_{1.09}MoSe_2$ ferecrystal of ρ = 140 mΩ-cm.[22] The $(SnSe)_{1.16}NbSe_2$ ferecrystal showed metallic resistivity vs. temperature behavior with ρ = 0.35 mΩ-cm at 300K dropping slightly to 0.14 mΩ-cm at 20K. This is a slightly lower resistivity than was reported by Wiegers *et al* for the crystalline misfit layer compound analog.[6] Wiegers reported a ρ = 0.58 mΩ-cm at 300K which dropped to 0.28 mΩ-cm at 4K. The lower resistivity measured for the ferecrystal is surprising, given the extent of turbostratic disorder. This suggests that the rotational disorder is not an effective scatter of the charge carriers. Electrical resistivity vs. temperature behavior of the

$(SnSe)_zNb_xMo_{1-x}Se_2$ alloy ferecrystals, shown in Figure IV.10, was consistent with heavily doped semiconductors becoming more metallic with increased x.

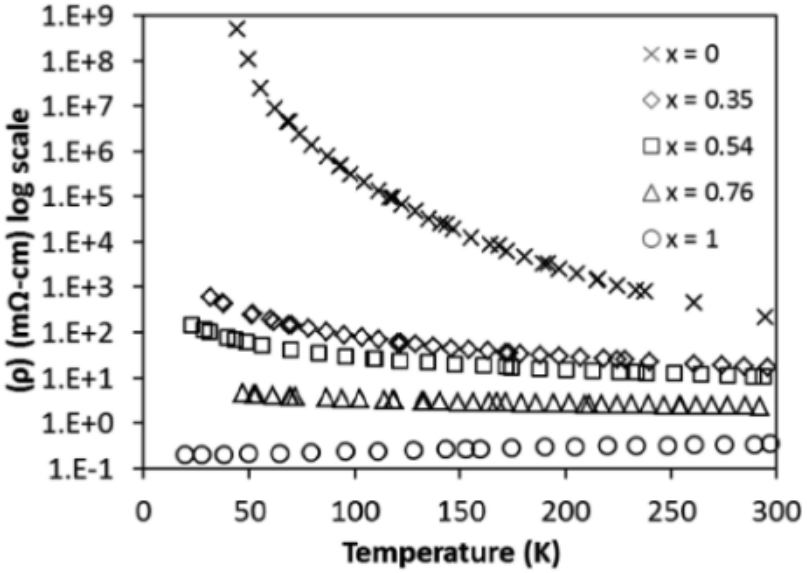

Figure IV.10. Resistivity vs. temperature for $(SnSe)_{1.16-1.09}(Nb_xMo_{1-x})Se_2$ ferecrystals with x = 0, 0.35, 0.54, 0.76 and 1.

The room temperature electrical transport properties of the $(SnSe)_{1.16-1.09}$ $(Nb_xMo_{1-x})Se_2$ alloy ferecrystals exhibit electrical transport properties between those of the $(SnSe)_{1.09}MoSe_2$ and $(SnSe)_{1.16}NbSe_2$ ferecrystals. Electrical conductivity, shown in Figure IV.11a, increases slowly for x between 0 and 0.54, increasing more rapidly as x approaches 1. This is similar to results from the $(Nb_xMo_{1-x})Se_2$ TMD system where Kalikhman[12] attributed it to formation of deep impurity bands which reduce the number of carriers added per Nb to less than 1 for Mo rich $(Nb_xMo_{1-x})Se_2$ alloys. This is supported by the room temperature carrier concentration vs. x of the $(SnSe)_{1.16-1.09}$ $Nb_xMo_{1-x}Se_2$ ferecrystals, calculated from measured Hall coefficients using the single band model.

Figure IV.11b shows that carrier concentrations are consistently lower than the linear slope expected by the addition of a single hole per added Nb atom. Calculations based on unit cell size and the number of Nb atoms per unit cell indicates that the number of holes per Nb drops with additional Mo from 0.98 hole/Nb at x = 1 to 0.25 hole/Nb at x = 0.35.

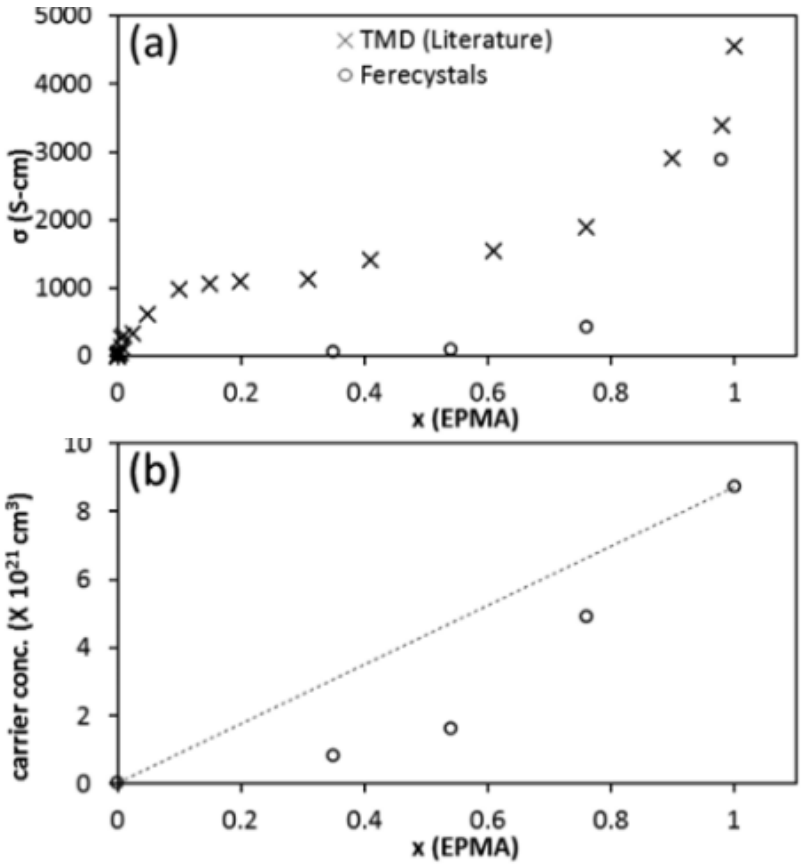

Figure IV.11. (a) Room Temperature conductivity vs. x for $(SnSe)_{1.16\text{-}1.09}(Nb_xMo_{1\text{-}x})Se_2$ alloys compared to literature values for $(Nb_xMo_{1\text{-}x})Se_2$ TMD alloys. (b) Room Temperature carrier concentration vs. x for $(SnSe)_{1.16\text{-}1.09}(Nb_xMo_{1\text{-}x})Se_2$ alloys.

IV.5. Conclusion

The mixed-metal ferecrystal compounds, $(SnSe)_{1.16\text{-}1.09}Nb_xMo_{1\text{-}x}Se_2$ with x = 0, 0.26, 0.49, 0.83, and 1, were successfully produced via adaptation of the modulated elemental reactant method. To our knowledge, this is the first report of a systematic solid solution in misfit compounds and was enabled by the structure and short diffusion lengths

in the designed precursors. Structural changes observed in the alloys, as a function of metallic ratios, were similar to literature observations for the $Nb_xMo_{1-x}Se_2$ system. A linear decrease in the *c*-lattice parameters was observed from 12.53(2)Å for $(SnSe)_{1.09}MoSe_2$, to 12.27(2)Å for $(SnSe)_{1.16}NbSe_2$. A linear increase in the *a*-parameters of the dichalcogenide constituent was observed from 3.329(8)Å for $(SnSe)_{1.09}MoSe_2$, to 3.461(4)Å for $(SnSe)_{1.16}NbSe_2$. Very little change was observed in the *a*-lattice parameter of the rocksalt constituent leading to a linear increase in misfit parameter of the alloys with increased Nb content. STEM imaging and 2D-Xray diffraction confirm structural characteristics similar to misfit layer compounds but also show turbostratic disorder indicative of ferecrystals. Electrical transport properties of these $(SnSe)_{1.16\text{-}1.09}$ $Nb_xMo_{1-x}Se_2$ ferecrystals were found to be between those of the semiconducting $(SnSe)_{1.09}MoSe_2$ and metallic $(SnSe)_{1.16}NbSe_2$ parent compounds but with carrier concentrations and conductivity consistently lower than expected by the addition of a single hole per added Nb atom.

CHAPTER V

INFLUENCE OF DEFECTS ON THE CHARGE DENSITY WAVE OF $([SnSe]_{1+\delta})_1(VSe_2)_1$ FERECRYSTALS

V.1. Authorship Statement

The primary author of the following manuscript is Matthias Falmbigl. For this work, I provided STEM images for structural interpretations and the presence of defects.

V.2. Introduction

The discovery of graphene with it's unique properties[11, 12] has inspired the exploration of many other candidates qualifying as 2 dimensional materials, such as boron nitride [13], transition metal dichalcogenides[14] and halides [15]. In the past decade researchers have found exotic and intriguing properties in these and other 2 dimensional materials offering a wide range of electrical properties from metals to semiconductors and insulators[11, 15, 16, 17] [2011]. The TMDs MoS_2 and WS_2 have attracted much attention due to a change from an indirect to a direct band gap upon reduction of symmetry from 3D to a 2D monolayer[14] and their potential use in optoelectronic and light harvesting applications[18, 19]. Reducing the dimensionality of metallic TMD's with charge density waves has theoretically been predicted to convert 2*H*-$NbSe_2$ from a metal to a semimetal [21], to cause no or only a slight changes in the wave vector for 2*H*-$TaSe_2$ [22], and induce the presence of magnetism in 1*T*-VSe_2 monolayers[20].

In 3D bulk materials the charge density wave transition is strongly influenced and easily suppressed by any defects and impurities[31]. Partial substitution of the transition

metal cation can result in a decrease[25] or an increase of the transition temperature[30], but always leads to a suppression of the charge density wave at higher substitution levels. Recently it has been demonstrated that the charge density wave transition temperature (T_{CDW}) in transition metal dichalcogenides can be modified by varying the thickness of nanosheets without significantly affecting the magnitude of the CDW. Whereas an increase of T_{CDW} upon reducing dimensionality was reported for $TiSe_2$[23], in VSe_2 the transition temperature decreases with smaller thickness [24]. This would imply a destabilization of the CDW state in VSe_2 via reduction of the dimensionality. However, we reported a charge density wave transition for the compound $([SnSe]_{1.15})_1(VSe_2)_1$ with extensive rotational disorder between the SnSe bilayer and VSe_2 trilayer which results in their average structures being independent of one another[7]. Compared to bulk VSe_2 and ultrathin films, the discontinuity in the electrical transport (electrical resistivity and Hall coefficient) is significantly enhanced. Increasing the VSe_2 thickness in $([SnSe]_{1.15})_1(VSe_2)_n$[9] to only two adjacent VSe_2 layers results in bulk-like behavior, suggesting that the phenomenon depends on having only a single, structurally independent VSe_2 layer. Due to the extensive rotational disorder, attempts to find a structural change using electron or X-ray diffraction have been unsuccessful. To our knowledge there is no information on the influence of defects on the charge density wave of structurally independent monolayers of any dichalcogenide.

Here we present specific heat data that clearly show a discontinuity at 102 K, centered within the temperature interval where the electrical resistivity and Hall coefficient both abruptly increase. No hysteresis is observed and the magnitude and temperature dependence of these measurements are similar to previous reports of charge

density wave transitions in transition metal dichalcogenides[6, 26]. The magnitudes of the change in resistivity and carrier concentration in stoichiometric $([SnSe]_{1.15})_1(VSe_2)_1$ are both larger than observed in bulk transition metal dichalcogenides. We find that the charge density wave transition temperature is not modified in $([SnSe]_{1+\delta})_1(VSe_2)_1$ as the Sn/V-ratio is varied between $0.89 \leq \delta \leq 1.37$ even though the average carrier concentration systematically changes. The magnitude of change in both resistivity and Hall coefficient is, however, strongly influenced by the Sn/V-ratio. X-ray diffraction and electron microscopy investigations show that the non-stoichiometry results in partial or complete replacement of one constituent layer by the other, with the density of these stacking defects scaling with the extent of non-stoichiometry. Hence the decline in the magnitude of the change in resistivity is correlated to a change in the volume fraction of independent VSe_2 monolayers and demonstrates that the charge density wave transition in these intergrowth compounds arises from the VSe_2 constituent.

V.3. Result and Discussion

V.3.1. Synthesis and Structural Properties

Details of the calibration process and the determination of the best conditions for the subsequent annealing step are described elsewhere[7, 8]. In contrast to the previous synthesis of stoichiometric compounds of $([SnSe]_{1.15})_m(VSe_2)_n$ [7, 8, 9], for this study the parameters for the amounts of Sn and V deposited onto the Si-wafers were varied systematically in order to obtain precursors with different Sn/V-ratios. To promote the self-assembly of the targeted compounds by annealing at 400°C for 20 minutes the precursor thickness was kept nearly constant for all compounds (see Table V. 1), but the

relative thickness of the constituent layers was varied . The linear dependence of the ratio of the deposition times and the resulting composition is shown in Figure V. 1.

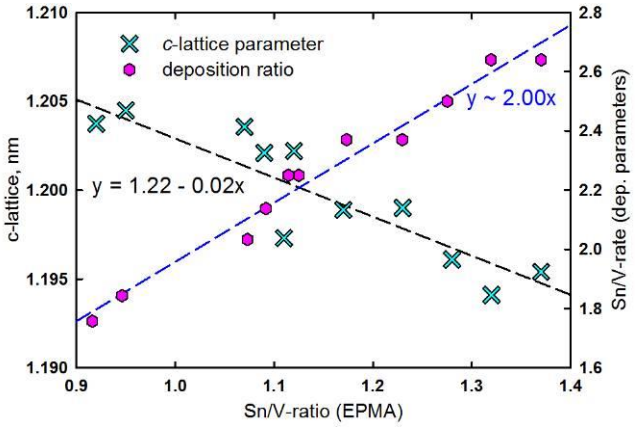

Figure V. 1. *c*-axis lattice parameters and deposition rates as a function of the measured Sn/V-ratio for all $([SnSe]_{1+\delta})_1(VSe_2)_1$ compounds.

The lattice parameters of the compounds also exhibit a linear correlation to the Sn/V-ratio. The difference in the repeat thickness of the superlattice can be explained by the different layer thicknesses along the *c*-direction for the two different constituents, 0.576(1) nm for SnSe[8], and 0.596(1) nm for VSe_2 [9], respectively. For high Sn/V-ratios a substitution of the dichalcogenide by the SnSe constituent is observed (see Figure V. 3) resulting in a slightly smaller average *c*-lattice parameter, than the stoichiometric compounds. The relatively large random scatter of the c-axis lattice parameters around the linear trend is not unexpected, as it depends not only on the total amount of each constituent, but also on the distribution of the constituents throughout the compound as the interlayer distances between the constituents vary significantly from SnSe-SnSe (0.261-0.271 nm[8]) to SnSe-VSe_2 (0.292-0.301 nm[9]) and VSe_2-VSe_2 (0.288-0.289 nm[9]).

The XRD patterns of all samples show Bragg reflections that can be indexed as consecutive 00*l* peaks and the superstructure is formed over a surprisingly wide range of Sn/V-ratios without dramatic changes in the specular X-ray diffraction patterns (Figure V. 2).

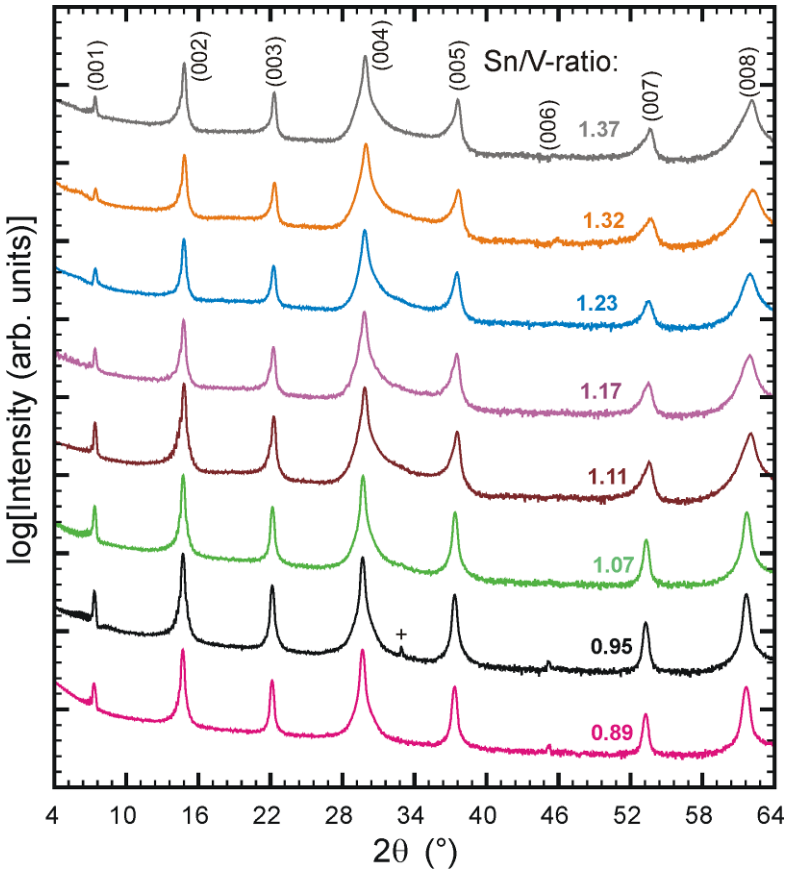

Figure V. 2. Specular X-ray diffraction of selected samples covering the investigated range of different Sn/V ratios. Only 00*l* reflections are observed. $^{+}$denotes Si-substrate peaks.

However, a closer inspection of the diffractograms displayed in Figure V. 2 reveals several distinct features as the Sn/V ratio changes from 0.89 to 1.37: (i) at high V-contents all peaks appear symmetrically shaped, whereas, for Sn-rich compounds the peak width and asymmetry of the Bragg reflections increase, (ii) the (006) reflection is only observed below a Sn/V-ratio of 1.1, (iii) as the Sn-content increases a broad feature

around 30-35° in 2θ raises the background, which might arise from the (400) reflection of bulk SnSe [5] or the presence of amorphous material. These systematic changes confirm that the superlattice is modified as a function of the Sn/V-ratio.

Table V. 1. Deposition parameter ratio and the resulting composition determined by EPMA, precursor repeat thickness, *a*- and *c*-axis lattice parameters of the constituents and the respective $([SnSe]_{1+\delta})_1(VSe_2)_1$ superlattice and the calculated misfit parameter, δ.

Sn/V-ratio, EPMA	**Sn/V-ratio, shutter opening time**	**Precursor-thickness, nm**	**c-axis lattice parameter, nm**	**a-axis lattice parameter (SnSe), nm**	**a-axis lattice parameter (VSe_2), nm**	**misfit, δ**
1.37	2.6	1.30 (5)	1.1954(1)	0.5995(3) 0.5940(1)[1]	0.3413(1)	0.12 0.14[1]
1.32	2.6	1.26(5)	1.1941(3)	-	-	-
1.23	2.4	1.24(5)	1.1990(1)	-	-	-
1.17	2.4	1.29(5)	1.1989(2)	0.59273(4)	0.3408(1)	0.15
1.11	2.3	1.24(5)	1.1973(1)	-	-	-
1.07	2.0	1.29(5)	1.20356(3)	-	-	-
0.95	1.8	1.29(5)	1.20449(5)	-	-	-
0.89	1.7	1.23(5)	1.20446(6)	0.5924(1)	0.3402(4)	0.14

[1]For the sample with a Sn/V-ratio of 1.37 the in-plane X-ray diffraction pattern revealed two different a-axis lattice parameters for the SnSe constituent (see also Figure V. 6).

A direct proof of these observations is shown in the HAADF-STEM images. The results for an extremely Sn-rich compound with a Sn/V-ratio of 1.37 are displayed in Figure V. 3. Although the ideal layering sequence of alternating SnSe bilayers (brighter) and VSe_2 trilayers (darker) is still visible, additional SnSe layers are frequently replacing the VSe_2 constituent (Figure V. 3a). The partial replacement of layers without any obvious interruption or strain was already reported for the $([SnSe]_{1.15})_m(TaSe_2)_n$

ferecrystals[4]. These volume defects occur without deformation of involved or adjacent layers (see Figure V. 3b). However, as can be seen in Figure V. 3a, the thickness of the layers varies between the ideal stacking (1.75 nm for a sequence of SnSe-VSe_2-SnSe) and the defect stacking (1.73 nm for three consecutive SnSe-layers). These values are in excellent agreement with the expected values of 1.748 nm and 1.728 nm, respectively, using the *c*-axis lattice parameters for the two different constituents. It is interesting to note, that most layers of the defect blocks (3 consecutive SnSe-layers) show all the same orientation, corresponding to e. g. the (100) orientation of a rocksalt structured layer. For the VSe_2-layer, several times a (110) orientation indicating an octahedral coordination of the V atom similar to the bulk 1*T*-structure is observed (see Figure V. 3c). An inspection of larger areas of the compound clearly reveals that no long range order between the stacking defects exists.

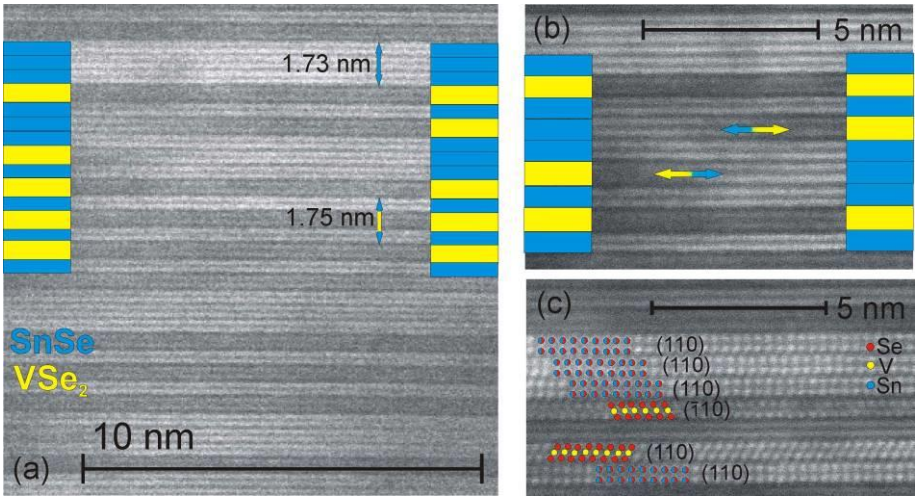

Figure V. 3. HAADF-STEM image of the sample with a Sn/V-ratio of 1.37. The partial replacement of the dichalcogenide layer by SnSe-layers is observed. The stacking defects (b) and respective crystallographic orientations of the constituent layers (c) are highlighted.

In Figure V. 4 HAADF-STEM images of the compound with the highest V-content are displayed. Also here the ideal alternating layering sequence is interrupted by the insertion and substitution of several VSe_2 layers replacing SnSe layers (see Figure V. 4a). The thickness of three consecutive layers of VSe_2 is 1.79(1) nm, which is in good agreement with the sum of three monolayers of 0.596(1) nm reported for $([SnSe]_{1.15})_1(VSe_2)_n$ compounds[9]. In Figure V. 4b a transition from the brighter SnSe layer into the darker dichalcogenide layer is highlighted. Again, this local substitution takes place without any significant distortion around this area. In Figure V. 4c distinct crystallographic orientations of both constituents can be identified.

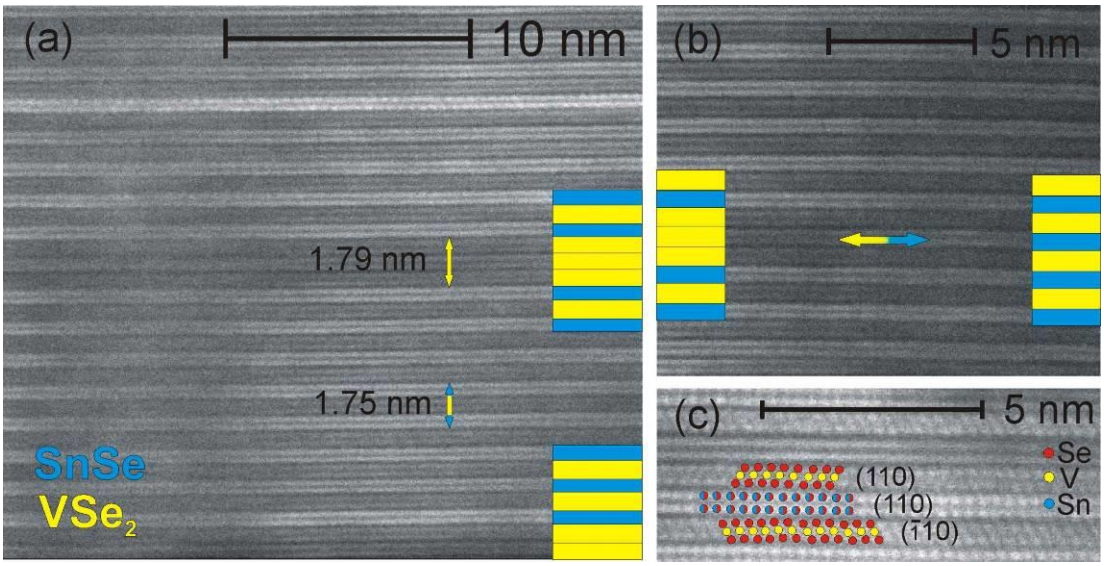

Figure V. 4. HAADF-STEM image of the compound with a Sn/V-ratio of 0.89. The partial replacement of the SnSe-layers by VSe_2 layers is observed (a). The stacking defects (b) and respective crystallographic orientations of the constituent layers (c) are highlighted.

In order to perform Rietveld refinements for these compounds, the information gained from the analysis of the HAADF-STEM images was used to create a layer substitution model. Starting from the ideal (1,1) superstructures partial layer substitution of either the SnSe or the VSe_2 constituent was introduced to mimic the complex scenario

present in these compounds (Figure V. 5). First the ideal (1,1) structure was refined, followed by introducing the substitution model according to the Sn/V-ratio. The distances within two similar layers were constrained to be the same, while only the occupation was refined to keep the number of refinable parameters reasonably low. For both compounds with a Sn/V-ratio of 1.23 and 0.89, respectively, the introduction of the substitution model resulted in a significant lowering of the R-values. The resulting distances in the superlattices along the *c*-axis are plotted in Figure V. 5 and show that the portion representing the ideal stacking sequence is very similar in both cases. One noteworthy result is that the average spacing between the layers is slightly larger in case of the V-rich sample, which can be attributed to the presence of weaker bonding between two VSe_2 layers and VSe_2 and SnSe compared to two consecutive rocksalt structured layers with strong ionic bonding. The model reveals a Sn/V-ratio of 1.21 for the Sn-rich sample, which is in excellent agreement with the EPMA-result of 1.23, however, for the V-rich sample the refinement results in a ratio of 1.1, which is too high compared to 0.89 from EPMA. This might be caused by the non-uniform distribution of the additional VSe_2-layers or the restrictions and limitations of the substitution model.

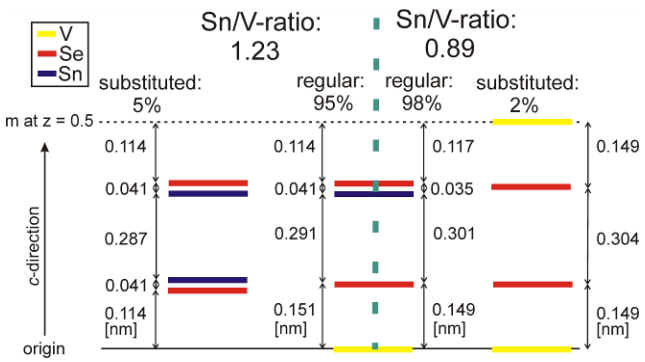

Figure V. 5: Rietveld refinement results for a substitution model, where one of the constituent layers is partially replaced by the other one for two compounds with Sn/V-

ratios of 1.23 and 0.89 respectively. The refinement reveals interplanar distances along the *c*-axis. The error in all distances is below 0.005 nm.

In-plane X-ray diffraction was conducted for three samples with Sn/V-ratios of 0.89, 1.17, and 1.37 respectively. The patterns are displayed in Figure V. 6 and reveal peaks corresponding to the crystal structure of the individual constituents as typically observed for ferecrystalline compounds[10]. The peaks of the SnSe constituent can be indexed to the square basal plane of a rocksalt structure and the peaks attributed to the VSe_2 constituent are consistent with a hexagonal basal plane of the 1*T*-bulk structure[32]. The lattice parameters of the SnSe and VSe_2 constituents are listed in Table V. 1 and are consistent with the ones reported earlier for $([SnSe]_{1.15})_m(VSe_2)_n$ ferecrystalline compounds[7, 8, 9]. One interesting observation is that for the Sn-richest compound each Bragg-peak of the SnSe constituent exhibits a splitting. This clearly points toward the presence of two distinct in-plane parameters for this constituent. Interestingly, the peaks at slightly lower angles corresponding to a larger *a*-axis lattice parameter of 0.5995(3) nm exhibit lower intensity and can thus be attributed to the inserted SnSe, where three or more consecutive layers are present (see Figure V. 3a). Indeed, the in-plane lattice parameter of $([SnSe]_{1.15})_m(VSe_2)_1$ with m = 2 and 3 are slightly increased compared to the compound with only one SnSe layer (m = 1, a = 0.5935(4) nm) and range between 0.59923(7) and 0.59976(2) nm [8]. In general, the in-plane lattice parameters of both constituents increase slightly as the Sn-content is increased (see Table V. 1).

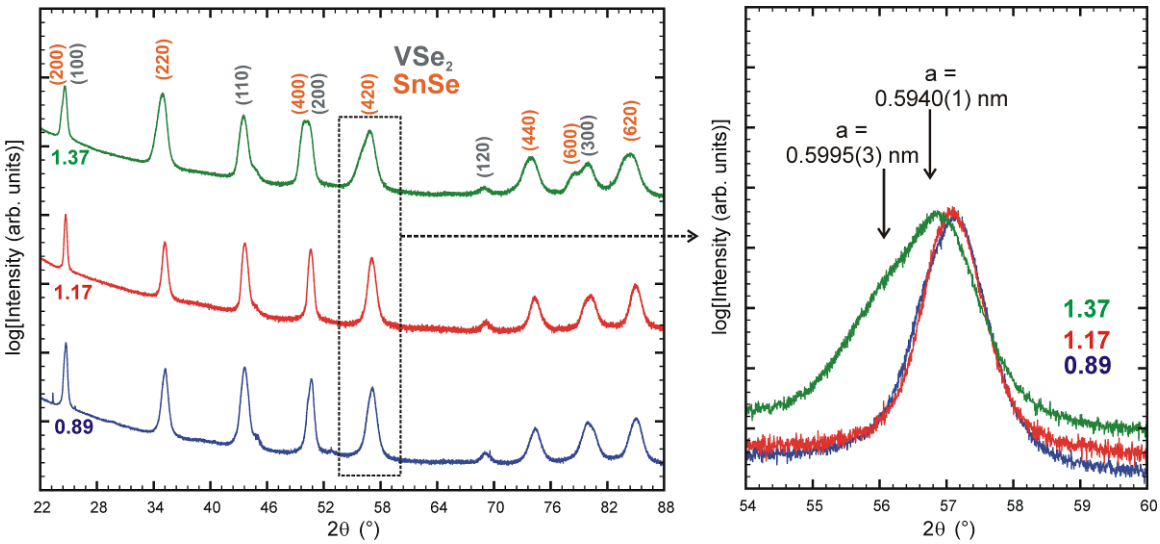

Figure V. 6: In-plane X-ray diffraction patterns for three compounds with Sn/V-ratios of 0.89, 1.17, and 1.37, respectively. The *hk*0 indices of the rocksalt and dichalcogenide structures are provided and the (420) peak of the SnSe constituent is magnified to highlight the presence of two different lattice dimensions for the Sn-rich sample.

V.3.2. Specific Heat

The temperature dependent specific heat of a compound with Sn/V-ratio of 1.17 is displayed in Figure V. 7. Figure V. 7a shows the temperature dependence compared to bulk VSe_2 [6]. In both cases the heat capacity at 200 K remains below the Dulong-Petit value. Similar to the VSe_2, which shows a discontinuity at 110 K[6], a jump in the specific heat at 102 K (see inset Figure V. 7a) is observed for the ferecrystalline compound $([SnSe]_{1.15})_1(VSe_2)_1$. In both cases this anomaly can be attributed to the charge density wave transition. The specific heat below 10 K is plotted as C_P/T vs. T^2 and a least squares fit to the equation given in Figure V. 7b is plotted. The fit reveals an electronic Sommerfeld coefficient (γ) of 24.5 $mJmol^{-1}K^{-2}$ and a Debye temperature of θ_D = 185.5 K, which was calculated according to:

(1) $$\beta = \frac{12nR\pi^4}{5\theta_D^3}$$

where *n* is the number of atoms per formula unit and *R* is the gas constant. This value is slightly smaller than θ_D = 213 K for bulk VSe_2[6] and θ_D ~ 200-300 K for sulfur based misfit layer compounds[27,] [1996Wie]. However, the electronic specific heat is significantly larger than the 7 $mJmol^{-1}K^{-2}$ reported for bulk VSe_2 [6]. This might result from a significant contribution of the SnSe constituent. The ratio of the specific heat jump (ΔC_P) at the CDW transition to the normal state heat capacity γT_C yields,

(2) $$\frac{\Delta C_P(T_C)}{\gamma T_C} \approx 0.71$$

which is significantly smaller than 1.43 predicted by the BCS-theory for superconductors. Applying this weak coupling BCS expression to estimate the normal state density of states results in a value of only 12 $mJmol^{-1}K^{-2}$, which could imply that large portions of the Fermi surface do not contribute in the phase transition or simply that due to the rather broad feature of the transition the jump in specific heat is experimentally significantly underestimated. However, ΔC_P ~ 1.8 $Jmol^{-1}K^{-1}$ is in the same order of magnitude as reported for the transition in bulk $TiSe_2$, where the anomaly is, ΔC_P ~ 1.15 $Jmol^{-1}K^{-1}$ [26]. An estimation of the density of electronic states ($D_\uparrow(E_F)$) removed by the formation of gaps at the Fermi surface can be derived from a BCS like model neglecting any phonon contribution:

(3) $$\Delta C_P = 3 \times 9.4 D_\uparrow(E_F) k_B^2 T_C$$

Applying equation (3) results in $D_\uparrow(E_F) = 0.87 \frac{\text{states}}{\text{eV}} - \text{V atom} - \text{spin}$ (for one spin direction), which is well within the range reported for various transition metal diselenides [26]. The transition is most likely of second order as in two consecutive runs no hysteresis

during cooling or heating was observed. This is consistent with the expected transition from a normal state into the incommensurate CDW-state[25] for a typical CDW unstable layered compound. In general, the anomaly found in the ferecrystalline compound $([SnSe]_{1.15})_1(VSe_2)_1$ exhibits similar features as comparable CDW transitions in single crystalline bulk VSe_2[6] and $TiSe_2$ [26].

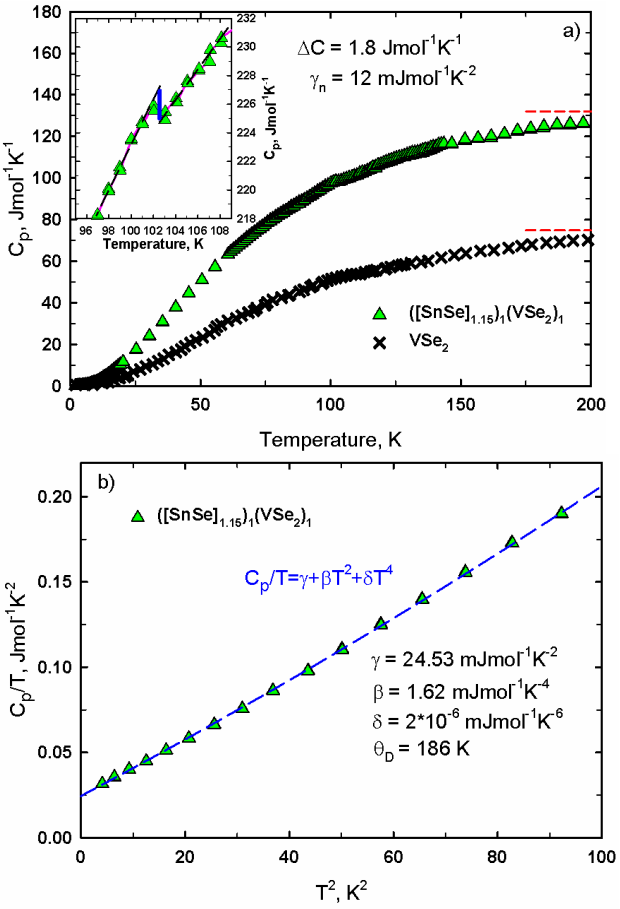

Figure V. 7: a) Heat capacity (C_p) of $([SnSe]_{1.15})_1(VSe_2)_1$, compared to single crystalline VSe_2[6] as a function of temperature. The red dashed lines indicate the classic Dulong-Petit value for vibrations. The inset shows a discontinuity at 102 K, which is attributed to the charge density wave transition. The magnitude of the jump in C_P corresponds to an electronic Sommerfeld value of the normal state of $\gamma_n = 12 mJmol^{-1}K^{-1}$. b) C_p/T vs. T^2 for $([SnSe]_{1.15})_1(VSe_2)_1$ below 10 K including a least squares fit (blue dashed line) to the polynomial equation given in the Figure.

V.3.3. Transport Properties

The electrical resistivity as a function of temperature for compounds with varying Sn/V-ratio is plotted in Figure V. 8. All compounds exhibit a charge density wave transition consistent with the results from the specific heat measurements. A minimum resistivity around 122-127 K, which increases with increasing Sn/V-ratio (see Table 2) is observed. The ρ_{max}/ρ_{min} ratio increases as the compounds become richer in V, and therefore contain a larger number of VSe_2 layers. However, the room temperature resistivity does not exhibit a systematic change, which might arise from slight variations in defect concentration and distribution and/or amount of impurities in different samples.

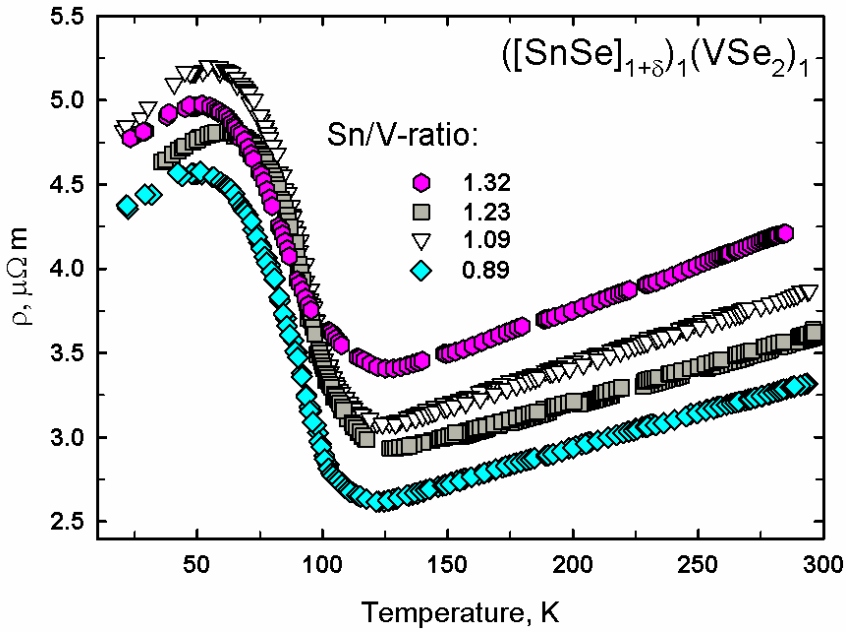

Figure V. 8: Electrical resistivity as a function of temperature for selected samples.

The carrier concentration, which is displayed in Figure V. 9, was calculated from Hall measurements applying the single parabolic band approximation (scattering factor = 1). The Hall coefficient for all compounds was positive in the measured temperature range suggesting holes are the majority carriers, while electrons are found to be the majority carriers in bulk VSe_2. A systematic trend is observed in the magnitude of the Hall

coefficient, with the carrier concentration decreasing as the Sn/V-ratio increases. This is consistent with the structural changes, where more and more metallic VSe_2-layers are replaced by semiconducting SnSe-layers. A dramatic decrease of carrier concentration for all compounds at the charge density wave transition is observed; however, again the magnitude of the change depends on the Sn/V-ratio. Calculating the volume per V-atom of an ideal (1,1) sample using the lattice dimensions given in Table V. 1 yields the number of carriers per V-atom (n_V) listed in Table V. 2 for room temperature and the difference between the maximum and the minimum at the CDW transition. A comparison clearly shows that the change in the Sn/V-ratio is too small to account for the differences observed in the carrier concentration. Whereas the Sn/V-ratio has a ratio of ~1.5 between the Sn- and V-richest samples, the ratio of carriers/V exceeds 3 at room temperature and 5.5 for the carriers quenched during the CDW transition. This observation points toward more complex charge transfer mechanisms depending on the thickness of the SnSe-layer (*m*), which were already reported for $([SnSe]_{1.15})_m(VSe_2)_1$ [8], $([PbSe]_{1.14})_m(NbSe_2)_1$[28], and $([SnSe]_{1.16})_m(NbSe_2)_1$ [29] ferecrystalline compounds and analogous misfit layer compounds [1996Wie]. Interestingly, for samples with a lower Sn/V-ratio than the ideal value of 1.15, the number of carriers quenched during the transition is larger than the room temperature value, maybe indicating that at elevated temperatures minority carriers from the SnSe constituent also contribute to the Hall coefficient.

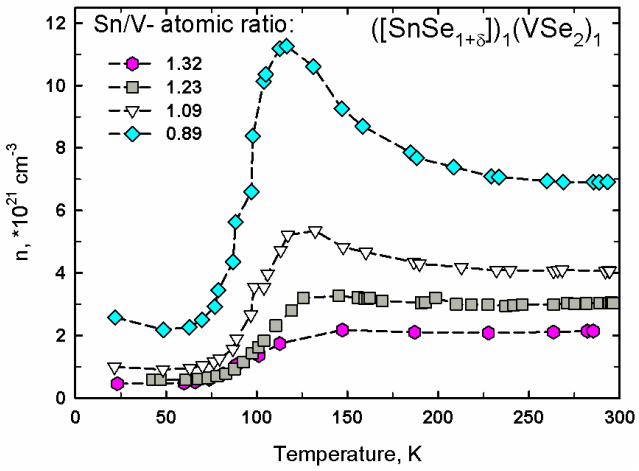

Figure V. 9: Carrier concentration as a function of temperature for selected samples.

The carrier mobility values at room temperature for samples with varying Sn/V-ratio are listed in Table V. 2. The mobility increases as a function of the Sn/V-ratio, which is surprising considering that the more conducting layer is VSe_2 and that with increasing Sn/V-ratio a larger number of SnSe-layers are partially replacing the dichalcogenide layers. This observation might again indicate that the approximation of a single band model is not valid for these complex intergrowth compounds.

Table V. 2. Room temperature resistivity (ρ_{RT}), temperature at ρ_{min} (T_{min}), ρ_{max}/ρ_{min}, carriers/V-atom at room temperature ($n_{V,RT}$), carriers quenched in the CDW transition/V-atom (n_{CDW}), and carrier mobility at room temperature (μ_{RT}) for compounds with different Sn/V-ratios.

Sn/V-ratio	**ρ_{RT}, μΩm**	**T_{min}, K**	**ρ_{max}/ρ_{min}**	**$n_{V,RT}$**	**n_{CDW}**	μ_{RT}, $cm^2V^{-1}s^{-1}$
1.32	4.21	127	1.46	0.26	0.20	6.93
1.23	3.60	127	1.64	0.37	0.32	5.69
1.09	3.87	125	1.67	0.49	0.54	3.95
0.89	3.32	122	1.74	0.84	1.11	2.72

All results clearly demonstrate that the VSe_2 constituent in $([SnSe]_{1+\delta})_1(VSe_2)_1$ ferecrystals causes the charge density wave transition as the magnitude changes systematically with the number of VSe_2 layers in the compounds. However, the results

from an earlier investigation on $([SnSe]_{1.15})_1(VSe_2)_n$ demonstrated that the nature of the transition changes dramatically as soon as adjacent VSe_2 layers are present and the 2-dimensionality is reduced[9] and that spacing out the VSe_2 layers by more than one SnSe-layer also causes changes due to charge transfer between the two constituents, which overall creates a very complex scenario. The volume defects generated by varying the Sn and V content in the compounds don't suppress the charge density wave transition, rather they modify slightly the Fermi level and hence, cause variations in the carrier concentration.

V.4. Conclusions

A series of $([SnSe]_{1+\delta})_1(VSe_2)_1$ compounds with varying Sn/V-ratio was synthesized. The compounds form over a wide compositional range of Sn/V-ratios from $0.89 \leq \delta \leq 1.37$. X-ray diffraction reveals systematic changes in intensity and a slight decrease of the *c*-axis lattice parameter as the Sn/V-ratio is increased. Typical for ferecrystalline compounds, independent in-plane crystal symmetries for both constituents of the intergrowth compound were observed. The *a*-lattice parameter of the VSe_2 constituent increases slightly as the Sn/V-ratio is increased and the SnSe constituent exhibits two individual *a*-lattice parameters for individual and blocks of the rocksalt like layer, when the dichalcogenide layer is replaced or substituted. HAADF-STEM images clearly show the mechanism how the off-stoichiometry is accommodated: partial or full replacement of one layer by the other one without distortion of the surrounding layers. The temperature dependent specific heat shows an anomaly at 102 K, which is attributed to a charge density wave transition consistent with the electrical properties. The features of the anomaly are very similar to the anomalies reported for transition metal diselenides

at the CDW transition. Electrical resistivity of compounds with varying Sn/V-ratio shows that only the magnitude of the CDW transition is influenced by the defects, but the CDW transition temperature is not shifted by the volume defects present in the compounds. The carrier concentration trends with the Sn/V-ratio demonstrating that the VSe_2 constituent mainly contributes to the conduction and the charge density wave of the ferecrystalline compounds. However, the change in magnitude reveals that a more complex mechanism involving charge transfer between the constituents plays a key role.

V.5. Methods

All thin film samples were synthesized using physical vapor deposition (PVD) in a custom-built vacuum deposition chamber[1] at pressures as low as 2×10^{-7} mbar. During the deposition process the low pressure was maintained by a cryogenic absorber pump. Se (Alfa Aesar, 99.999 % purity) was evaporated utilizing an effusion cell and electron beam guns were used to evaporate Sn (Alfa Aesar, 99.98 %) and V (Alfa Aesar 99.7 %). The PVD process was carried out using two different substrates, either (100) oriented Si-wafers for structural characterizations or fused silica for the measurement of electrical properties. Details on the operation of the deposition system and the calibration procedure for the initial precursor films of the desired layered samples are described elsewhere[7, 8]. All samples were annealed on a hot plate inside a glove box under nitrogen atmosphere (< 1 ppm/O_2).

X-ray reflection (XRR) and high-resolution X-ray diffraction (XRD) were performed using a Bruker D8 Discover diffractometer equipped with Cu-K_α radiation. High quality scans for Rietveld refinement were collected using off-specular conditions

(angle offset between θ and 2θ was in all cases 0.2°). The FullProf program package[2] was used for Rietveld refinements. In-plane diffraction of selected samples was performed at the Advanced Photon Source (APS), Argonne National Laboratories, at Beamline 33BM using an incident X-ray beam with $\lambda = 0.12653$ nm.

The chemical composition of the thin film samples was determined using a Cameca SX100 Electron Probe Microanalyzer (EPMA) equipped with 5 wavelength dispersive spectrometers (WDS). A thin film technique applying three different acceleration voltages (10, 15, and 20 kV) described in details elsewhere[3] was utilized for precise compositional analysis.

High resolution scanning transmission electron microscopy (HRSTEM) was carried out on a FEI Titan 80-300 TEM/STEM instrument, using an objective lens c_s-correction and a high angle annular dark field detector (HAADF). The preparation of selected samples for HRSTEM was performed at the Center for Advanced Materials Characterization in Oregon (CAMCOR) of the University of Oregon (UO) utilizing a FEI Helios Nanolab 600 Dual Beam focused ion beam (FIB). After an in-situ lift out the samples were treated by a thinning technique followed by low voltage ion beam polishing.

The sample for the heat capacity measurement was deposited onto PMMA coated Si-wafers and ~5g of the ferecrystalline thin film material were floated off the substrate by dissolving the PMMA in acetone, followed by a drying step. Annealing of the powder was conducted in a Netzsch DSC under N_2-atmosphere.

In order to perform in-plane electrical resistivity and Hall measurements a shadow mask creating a cross pattern was used during deposition. The total film thickness used for the conversion of the measured sheet resistance to electrical resistivity and the Hall-coefficient was evaluated from XRR data and was for all samples about 50 nm. Small Indium pieces were used to electrically contact the samples to Cu-wires. All measurements were carried out in a temperature range between 20 and 295 K and for the Hall measurements magnetic fields up to 1.6 T were applied.

CHAPTER VI

INFLUENCE OF INTERSTITIAL V ON STRUCTURE AND PROPERTIES OF FERECRYSTALLINE $([SnSe]_{1.15})_1(V_{1+x}Se_2)N$ FOR N=1,2,3,4,5, AND 6

VI.1. Authorship Statement

The following manuscript was primarily prepared by Matthias Falmbigl and published in the Journal of Solid State Chemistry in 2015, volume 231, pages 101-107. For this work I completed STEM measurements and confirmed the presence of interstitial vanadium.

VI.2. Introduction

Layered transition metal dichalcogenides (TMD) TX_2 with T being transition metals of group 14, 15, 16 or Sn and X = S or Se qualify due to their structural characteristics as good candidates for intercalation compounds. Whereas within the TX_2 sandwiches strong ionic and/or covalent bonding between the metal and chalcogen atoms is present, only weak van der Waals like cohesive forces hold the individual TX_2 units together. Hence, intercalation of various species such as monoatomic cations, molecular ions and even neutral molecules is possible[1]. A special class of intercalated TMDs are misfit layer compounds, where bilayers of rocksalt-like structured monochalcogenides are inserted into the van der Waals gap of the dichalcogenide, resulting in a general formula of $([MX]_{1+\delta})_m(TX_2)_n$ [1996Wie]. Also, these intergrowth compounds can serve as intercalation hosts and especially Li can be incorporated chemically or electrochemically [19, 20, 21, 22, 23]. Whereas Li readily intercalates into vacant positions between the MX and TX_2 layer in $([MX]_{1+\delta})_1(TX_2)_1$ and $([MX]_{1+\delta})_1(TX_2)_2$ as well as between the two dichalcogenide layers in $([MX]_{1+\delta})_1(TX_2)_2$, Na was successfully intercalated only into the van der Waals gap of $([MX]_{1+\delta})_1(TX_2)_2$ compounds [1993Pow]. Recently, it was

demonstrated that addition of small amounts of Cu promotes the formation of $Cu_x(BiSe)_{1+\delta}(TiSe_2)_2$ due to the tendency of Cu occupying cavities between the two $TiSe_2$ layers[24].

For VSe_2 the tendency to form self intercalated compounds $V_{1+x}Se_2$ is well known, however, the dependency of the lattice parameters of the 1*T*-structure (CdI_2-type) with *c* decreasing and *a* increasing as a function of x[13] is different from the expected behavior of intercalated TMDs, where mainly the *c*-lattice parameter increases upon intercalation [1993Pow]. Moreover, the charged density wave (CDW) transition at 100 K [14]is rapidly suppressed in off-stoichiometric compounds due to additional electrons from the interstitial Vanadium atoms populating the conduction band [13]. Recently, an enhancement of the CDW transition in $([SnSe]_{1.15})_1(VSe_2)_1$ was observed [2] and it was demonstrated that a change in dimensionality for $([SnSe]_{1.15})_1(VSe_2)_n$ with *n* = 1, 2, 3, and 4 is mainly responsible for the pronounced effect in the quasi-2 dimensional ferecrystal $([SnSe]_{1.15})_1(VSe_2)_1$.

In this study we explore the effect of interstitial V-atoms on the structural and electrical properties of $([SnSe]_{1.15})_1(V_{1+x}Se_2)_n$ and a $V_{1.13}Se_2$ thin film. In contrast to bulk $V_{1+x}Se_2$ an expansion of the *c*-lattice parameter is observed and the interstitial V-atoms reside in the van der Waals gap between two TMD-layers. The additional V-atoms have a minor influence on the charge density wave transition of the ferecrystalline compounds. However, the thin film $V_{1.13}Se_2$ shows similar structural and electrical property changes as observed for the bulk compound.

VI.3. Experimental Details

All thin film samples were synthesized using physical vapor deposition (PVD) in a custom-built vacuum deposition chamber [1] at base pressures as low as 10^{-8} mbar. During the deposition process the low pressure was kept by a cryogenic absorber pump. Whereas Se (Alfa Aesar, 99.999 % purity) was evaporated via an effusion cell, electron beam guns were used to evaporate Sn (Alfa Aesar, 99.98 %) and V (Alfa Aesar 99.7 %). The PVD process was carried out on two different substrates, either (100) oriented Si-wafers for structural characterizations or fused silica for the measurement of electrical properties. Details on the operation of the deposition system and the calibration procedure for the initial precursor films of the desired layered samples are described elsewhere [2, 5]. All samples were annealed on a hot plate inside a glove box under nitrogen atmosphere (< 1 ppm/O_2).

X-ray reflection (XRR) and high-resolution X-ray diffraction (XRD) were evaluated using a Bruker D8 Discover diffractometer equipped with Cu-Kα radiation. High quality scans for Rietveld refinement were collected using off-specular conditions (angle offset between θ and 2θ was in all cases 0.2°). The FullProf program package[3] was used for Rietveld refinements. In-plane diffraction of selected samples was performed at the advanced photon source (APS), Argonne National Laboratories, at Beamline 33BM using an incident X-ray beam with λ= 0.11272 nm. The lattice parameters were calculated performing least squares fits to the peak positions utilizing the WinCSD package[8].

The chemical composition of the thin film samples was determined using a Cameca SX100 Electron Microprobe equipped with 4 wavelength dispersive spectrometers. A thin film technique applying three different acceleration voltages (10,

15, and 20 kV) described in details elsewhere[4] was utilized for precise compositional analysis.

High resolution scanning transmission electron microscopy (HRSTEM) was carried out on a FEI Titan 80-300 TEM/STEM instrument with an objective lens c_s-correction and a high angle annular dark field detector (HAADF). The preparation of selected samples for HRSTEM was performed at the Center for Advanced Materials Characterization in Oregon (CAMCOR) of the University of Oregon (UO) utilizing a FEI Helios Nanolab D600 Dual Beam focused ion beam (FIB). After an in-situ lift out the samples were treated by a thinning technique followed by a low voltage ion beam polishing.

In order to perform in-plane electrical resistivity and Hall measurements a shadow mask creating a cross pattern was used on fused silica substrates. The total film thickness used to calculate the sheet resistivity and the Hall-coefficient was evaluated from XRR data and for all samples about 50 nm. Small Indium pieces were used to electrically contact the sample to Cu-wires. All measurements were carried out in a temperature range between 20 and 300 K and for the Hall measurements magnetic fields up to 1.6 T were applied.

VI.4. Results and Discussion

VI.4.1. Structure and Composition

The modulated elemental reactant (MER) method[6] allows synthesizing nanolaminate precursors, which resemble already the intended product closely in layering sequence and composition. To create the desired precursor an extensive multi-step

calibration of the deposition parameters to define stoichiometric ratios between the involved elements and to find the correct total amount of material condensed onto the substrate is required [2013Atk]. In the present study a Sn/V ratio of ~0.95 rather than the ideal ratio of 1.15 was chosen in order to synthesize V-rich compounds. To form the final metastable intergrowth compounds a short annealing duration at moderate temperatures is required. In an earlier investigation the ideal annealing conditions for $([SnSe]_{1.15})_1(VSe_2)_1$ were found to be 400°C for 20 min [2013Atk]. Here, the number of VSe_2-layers (*n*) in $([SnSe]_{1.15})_1(V_{1+x}Se_2)_n$ (short hand notation (1,*n*)) is consecutively increased from 1 to 6 and in addition a thin film sample $V_{1+x}Se_2$ was synthesized in a similar manner. As a change of ideal conditions to form the intended product cannot be excluded, an annealing study for the sample $([SnSe]_{1.15})_1(V_{1+x}Se_2)_3$ was carried out. A sample deposited on a Si wafer was cleaved into several pieces, which were annealed at different temperatures for a duration of 20 min each. Specular diffraction scans were performed for all samples in order to elucidate under which conditions the self-assembly into the superstructure is promoted best. The resulting patterns are plotted in Figure VI. 1a and confirm that an annealing step of 20 min at 400 °C is ideal to form the final intergrowth compound. The Bragg reflections belonging to binary 1*T*-VSe_2 [10] although very broad are clearly visible already after the deposition process. Only at temperatures ≥300°C the superstructure peaks start to grow and the intensity increases at the same time as the full width at half maximum (FWHM) decreases until 400°C. At higher temperatures the compound starts to decompose. The Bragg reflections shift with increasing temperature to higher angles indicating a shrinking of the unit cell. This reduction in size indicating the formation of the final product up to 400 °C is accompanied by a slight decrease in Se-content as

observed by EPMA and displayed in Figure VI. 1b. However, above 400 °C the oxygen content increases significantly and the Se content drops. It is interesting to mention, that the Sn/V ratio remains essentially constant until 450°C. However, at higher temperatures the Sn-content rapidly decreases to 0. This most likely arises from the formation of tin(II)oxide, which sublimates under the open annealing conditions[7]. The peak at 33.0° in 2θ, which is observed in the diffraction pattern collected after the heat treatment at 500°C, can be attributed to the formation of V_2O_3 [9]. Backscattered images of the sample annealed at 600°C combined with EDX-spectra clearly show the presence of V and O in the film with small islands, where V, Se and a smaller amount of O are still present. This observation is corroborated by the diffraction pattern of the sample annealed at 500°C, where the (00*l*) peaks of 1*T*-VSe_2 together with the impurity peak can be observed (see Figure VI. 1a).

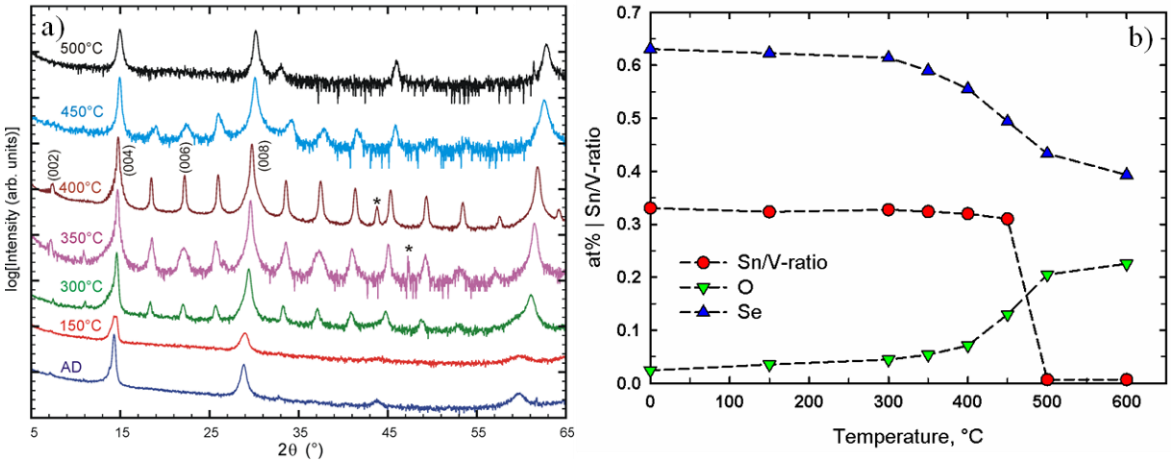

Figure VI. 1. a) High-angle X-ray diffraction patterns of $([SnSe]_{1.15})_1(V_{1+x}Se_2)_3$ collected at different temperatures. Selected Bragg reflections for the sample annealed at 400°C are provided. The asterisk marks stage or substrate peaks. b) EPMA results as a function of temperature for $([SnSe]_{1.15})_1(V_{1+x}Se_2)_3$. Please note that the data points plotted at 0°C correspond to the unannealed precursor.

After defining the ideal annealing conditions a set of precursors $([SnSe]_{1.15})_1(V_{1+x}Se_2)_n$ with n = 1 to 6 was synthesized and subsequently annealed at 400°C for 20 min. The XRD patterns after annealing contain sharp Bragg-reflections, which can all be indexed to (00*l*) reflections of the targeted compounds (Figure VI. 2a). The absence of all other but (00*l*)-reflections arises from the strong preferred orientation of the superstructures parallel to the Si-substrate surface. The *c*-lattice parameters of all $([SnSe]_{1.15})_1(V_{1+x}Se_2)_n$ compounds in as deposited state as well as after annealing are plotted as a function of the number of VSe_2-layers in Figure VI. 2b (see also Table VI. 1). The slope for the as deposited samples reveals an average thickness per V:2Se-layer of 0.667(5) nm, which shrinks upon annealing to 0.605(1) nm corresponding to the thickness of a single VSe_2 layer. Interestingly, this value is significantly larger than the previously reported VSe_2 layer thickness of 0.596(1) nm for the stoichiometric series of $([SnSe]_{1.15})_1(VSe_2)_n$ [26]. This difference can be attributed to the presence of a significant amount of interstitial Vanadium atoms in the present compounds ranging from x = 0.14 to 0.42 as determined by EPMA (Table VI. 1). This expansion along the *c*-axis is contrary to the behavior of bulk $V_{1+x}Se_2$, where the *c*-lattice parameter decreases from 0.611 to 0.596 nm for x = 0 to 0.18 [13] and for x = 0.13 has a value of 0.600 nm. For the thin film $V_{1.13}Se_2$ a *c*-lattice parameter of 0.60795(1) nm close to the bulk value was observed. The intercept of the linear fit of the *c*-lattice parameters as a function of *n* reveals a thickness for the SnSe constituent of 0.592(5) nm, which is slightly thicker than 0.576(2) nm reported for the series of $([SnSe]_{1.15})_m(VSe_2)_1$ [5]. This difference results from the larger distance between SnSe and VSe_2 constituents compared to the distance between two consecutive SnSe-layers [5, 11].

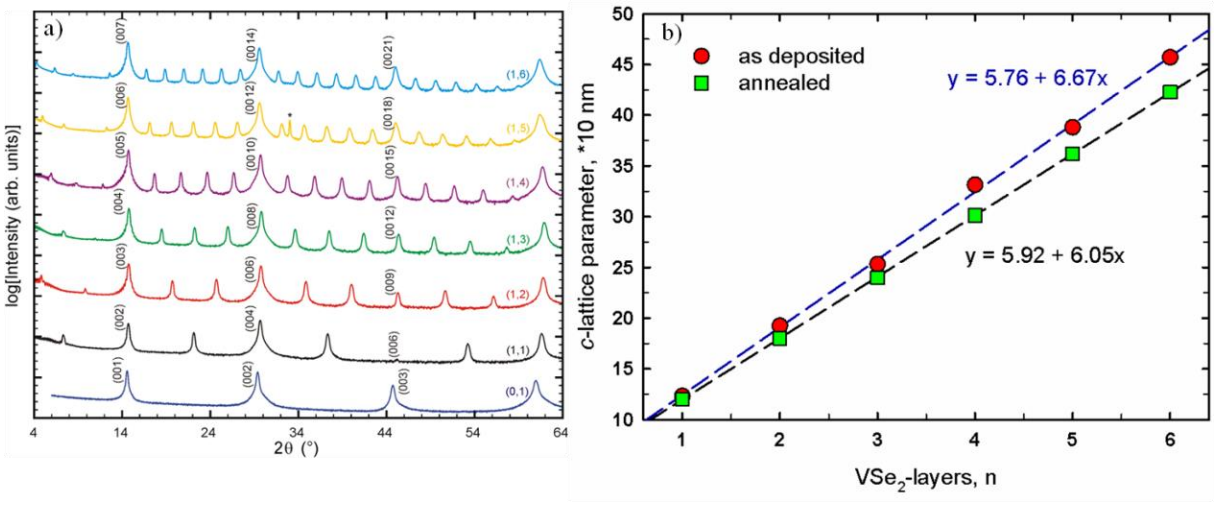

Figure VI. 2. a) High-angle X-ray diffraction patterns of $([SnSe]_{1.15})_1(V_{1+x}Se_2)_n$ with n = 1 -6 and a VSe_2 thinfilm. Selected Bragg reflections for all compounds are provided. The asterisk marks a substrate peak. b) c-lattice paramter for $([SnSe]_{1.15})_1(V_{1+x}Se_2)_n$ as a function of the number of VSe_2-layers (n) for as deposited and annealed (400°C, 20 min) compounds.

Table VI. 1. a-lattice parameters of the constituents, misfit parameter (δ), c-lattice parameter of the superlattice, c/a-ratio (a-lattice of the $V_{1+x}Se_2$ constituent) , Sn/V-ratio (EPMA, normalized to a (1,1) composition) and off-stoichiometry (x) of $V_{1+x}Se_2$ calculated from EPMA results for a thin film $V_{1+x}Se_2$ and the ferecrystalline compounds $([SnSe]_{1.15})_1(V_{1+x}Se_2)_n$ with n = 1 – 6.

compound	***a*-lattice parameter (SnSe), nm**	***a*-lattice parameter ($V_{1+x}Se_2$), nm**	**Misfit parameter δ**	***c*-lattice parameter, nm**	***c*/*a*-ratio**	**Sn/V-ratio**	**$V_{1+x}Se_2$, x**	
(0,1)	n.a.	0.3376(3)	n.a.	0.60795(1)	1.80	n.a.	0.13	
(1,1)	0.59273(4)	0.34082(8)	0.15	1.2030(1)	1.78	0.97	0.23	
(1,2)	0.59419(5)	0.34240(3)	0.15	1.8014(1)	1.76	0.97	0.14	
(1,3)	0.59514(4)	0.34335(3)	0.15	2.400(1)	1.76	0.93	0.22	
(1,4)	0.5917(1)	0.34037(9)	0.15	3.012(1)	1.78	0.91	0.42	
(1,5)	0.5908(1)	0.33985(9)	0.15	3.618(1)	1.78	0.93	0.38	
(1,6)	0.59412(5)	0.34273(4)	0.15	4.228(1)	1.77	0.90	0.28	

The in-plane diffraction patterns of all compounds are displayed in Figure VI. 3. The VSe_2 thin film exhibits only hk0 reflections consistent with the trigonal structure of bulk VSe_2 [10] and has the smallest a-lattice parameter. However, the value is significantly

smaller than expected from the bulk lattice parameter of a = 0.342 nm for nonstoichiometric $V_{1.13}Se_2$ [13]. For all ferecrystalline compounds $([SnSe]_{1.15})_1(V_{1+x}Se_2)_n$ with n = 1 to 6 independent lattice parameters for both constituents are observed. The Bragg reflections corresponding to the SnSe constituent can be indexed to a square basal plane and all a-lattice parameters are close to the values reported for stoichiometric $([SnSe]_{1.15})_m(VSe_2)_1$ ferecrystals[5]. For bulk $V_{1+x}Se_2$ it is well known that the a-lattice parameter increases with increasing x [13]. However, for the present intergrowth compounds no clear trend is observed. The significantly smaller a-lattice parameters of the dichalcogenide constituents for the (1,4) and the (1,5) sample are not related to the Sn/V-ratio, but to the larger off-stoichiometry in the VSe_2 layer (see Table VI. 1). Interestingly, the SnSe in-plane area adjusts to the smaller area of the $V_{1+x}Se_2$ constituent to keep the misfit for all the compounds at 0.15. This large range of the monochalcogenide area adapting to the one of the dichalcogenide is a general characteristic of ferecrystalline compounds [11]. The intensities of the SnSe reflections compared to the $V_{1+x}Se_2$ reflections decrease as expected for increasing n in the $([SnSe]_{1.15})_1(V_{1+x}Se_2)_n$ compounds.

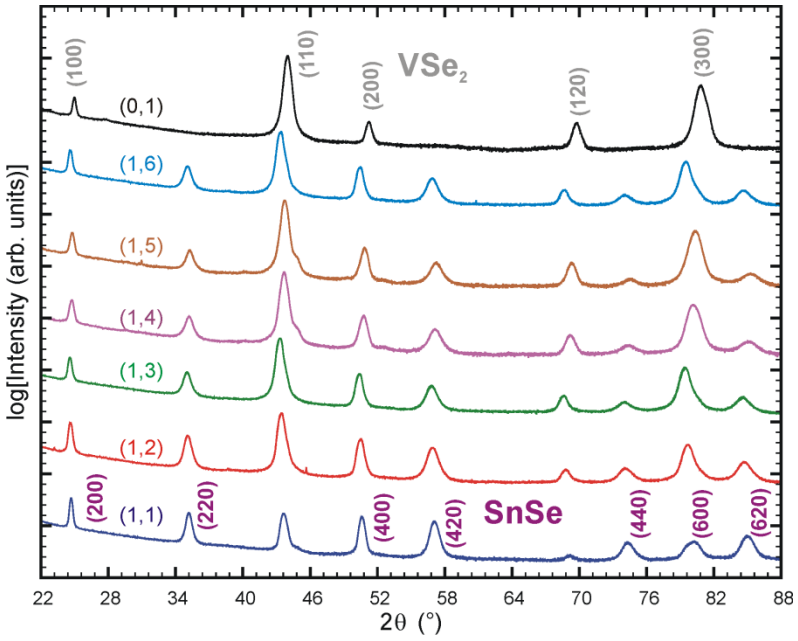

Figure VI. 3. In-plane X-ray diffraction patterns of $([SnSe]_{1.15})_1(V_{1+x}Se_2)_n$ with n = 1 -6 and a $V_{1+x}Se_2$ thin film. The Bragg reflections for the SnSe and the $V_{1+x}Se_2$ constituent are provided for the (1,1) compound and the (0,1) compound, respectively.

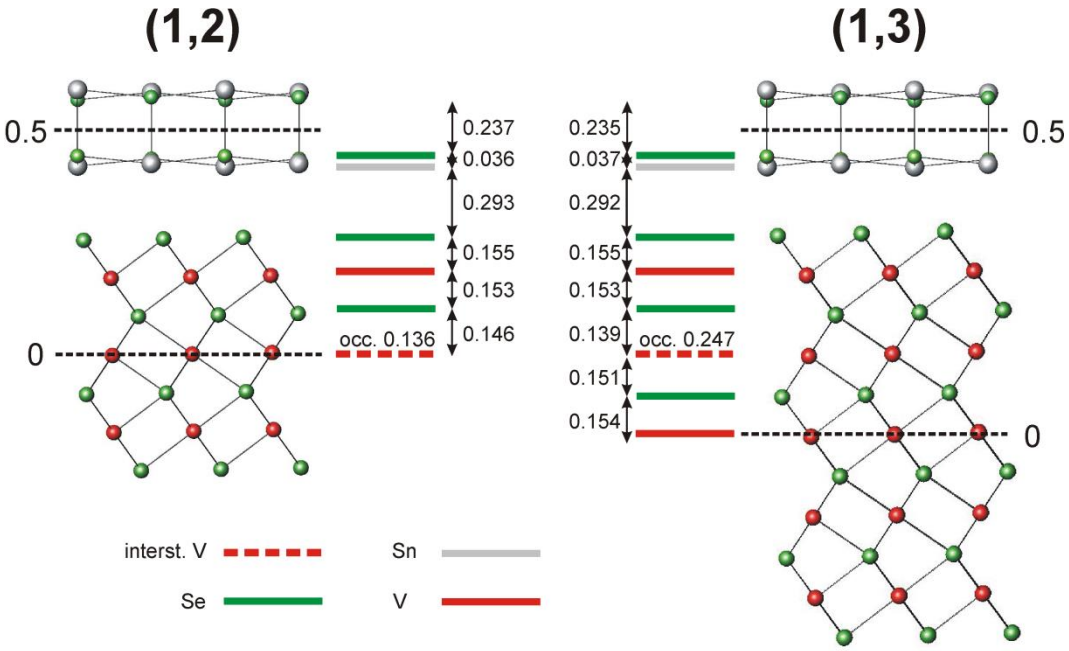

Figure VI. 4. Rietveld refinement results for $([SnSe]_{1.15})_1(V_{1+x}Se_2)_n$ with n = 2 and 3. The interlayer distances along the *c*-axis are provided. The error for all distances is < 0.001 nm. The structural schematics show full occupation of the interstitial V-position.

Rietveld refinements of the 00*l* patterns were conducted for three compounds, the (0,1), (1,2) and (1,3) compound, to unveil the effect of the interstitial V-atoms on the structure along the superlattice direction. For the thin film $V_{1+x}Se_2$ the refinement resulted in a composition of $V_{1.12(1)}Se_2$ in excellent agreement with the EPMA result (Table VI. 1). Similar to the bulk structure[10] the Se-atoms shift away from the center position between the V-layers closer to the interstitial V-atoms by 3 %. (see also Suppl. Inf.). Also for the ferecrystalline compounds $([SnSe]_{1.15})_1(V_{1+x}Se_2)_n$ with n = 2 and 3 the refined occupancy of the interstitial V-atoms matches the EPMA results (Figure VI. 4). During the simultaneous refinement of occupancy and *z*-value of the interstitial V the misfit between the SnSe and the $V_{1+x}Se_2$ constituent were fixed to 1.15 extracted from the in-plane diffraction results. All attempts to introduce interstitial V-atoms in-between the SnSe and VSe_2-layers resulted in slightly negative occupancies. The distance of the interstitial V-atoms to the Se-plane is shorter than the distance between the fully occupied V-position and the Se-layers, which is similar to the behavior observed in the thin film compound and bulk $V_{1+x}Se_2$[10]. For the (1,3) compound the interstitial V-layer resides slightly asymmetric along the superstructure direction as it is shifted closer to the VSe_2-layer adjacent to the SnSe-layer (see Figure VI. 4). In both ferecrystalline compounds the VSe_2-layers exhibit a slight asymmetry, which might affect the transport properties.

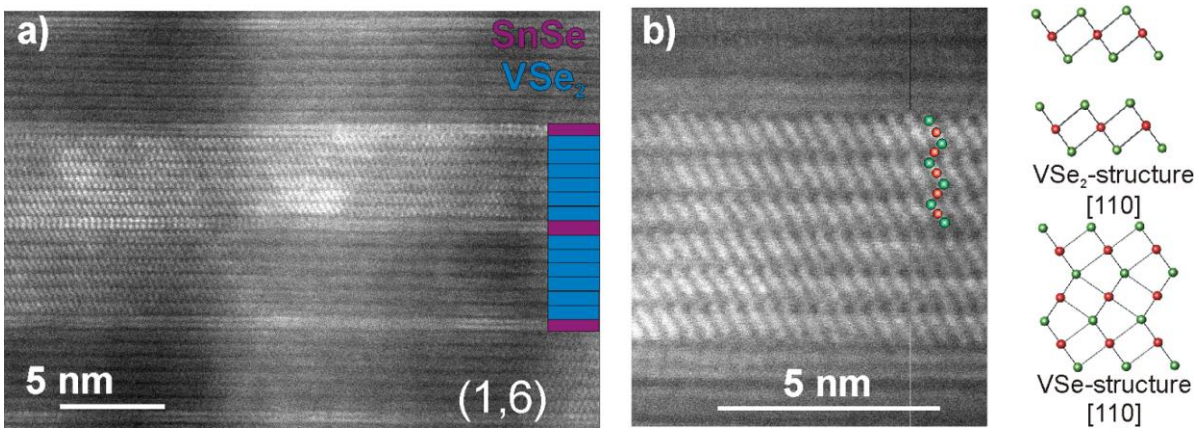

Figure VI. 5. HAADF-STEM images of $([SnSe]_{1.15})_1(V_{1+x}Se_2)_6$. a) an overview displaying the intended layering sequence and highlighting the presence of rotational disorder between the constituents, b) displaying an area of 6 consecutive layers of $V_{1+x}Se_2$, where interstitial V-atoms are observed. The stick and ball models of the corresponding VSe_2 and VSe structures[10, 25] with projections along the [110] direction are provided.

In an earlier report on ferecrystalline compounds it was demonstrated that off-stoichiometry can result in the formation of stacking faults and/or partial replacement of one layer by the other without interrupting the surrounding layers [12]. In particular for the (1,1) compound this defect formation is necessary to accommodate any off-stoichiometry in $([SnSe]_{1+\delta})_1(V_1Se_2)_1$ compounds[11]. In order to confirm the results from Rietveld refinements and rule out the formation of stacking defects for compounds with $n > 1$, HAADF-STEM images were collected. In Figure VI. 5a a cross section of the $([SnSe]_{1.15})_1(V_{1+x}Se_2)_6$ is displayed revealing abrupt interfaces and the intended layering sequence of blocks of 6 consecutive dichalcogenide layers separated by one layer of the SnSe constituent (see also SI for $([SnSe]_{1.15})_1(V_{1+x}Se_2)_3$) and no indication for the presence of stacking faults can be found. For the (1,1) compound no V-atoms were found in the STEM-cross section and the off-stoichiometry results from few stacking faults (see SI). Extensive rotational disorder between the constituents, a typical feature of ferecrystalline compounds [2014Bee], is observed. However, within the VSe_2 blocks the

same crystallographic orientation for each layer as expected for a 1*T*-polytype is observed (see SI). Figure VI. 5b shows a magnified area of one VSe_2 block, where interstitial V-atoms can be observed. The inspection of several images unveils the agglomeration of the interstitial V-atoms in distinct areas, most likely due to the requirement of a small lattice expansion to accommodate the additional V-atoms in the structure. The layers displayed in Figure VI. 5b are comparable to the bulk structure of VSe[25], which is equivalent to a full occupation of the interstitial position in VSe_2 [10], clearly demonstrating the presence of interstitial V-atoms in these compounds.

VI.4.2. Electrical Properties

The electrical resistivity of all compounds as a function of temperature is displayed in Figure VI. 6a. The $V_{1+x}Se_2$ thin film has a similar room temperature resistivity compared to the bulk single crystalline compound [14]. However, the temperature dependence is less pronounced and also the kink at 100 K indicative for the charge density wave transition is hardly visible. This observation is consistent with reports on the effect of non-stoichiometry on the CDW transition in bulk $V_{1+x}Se_2$[13], where already small amounts of interstitial V-atoms cause a suppression of the CDW state. Similarly, also the *c*/*a*-ratio of the thin film compound (1.80) is slightly smaller than the one reported for stoichiometric VSe_2 (1.82) [14]. As already reported previously[26] a change in dimensionality from quasi-2D for the $([SnSe]_{1.15})_1(V_{1+x}Se_2)_1$ compound to 3D as the layer thickness of the dichalcogenide constituent is increased for $([SnSe]_{1.15})_1(V_{1+x}Se_2)_n$ compounds has a dramatic effect on the magnitude of the charge density wave transition (Figure VI. 6). With increasing thickness the CDW transition gets less pronounced and the temperature dependence of the electrical resistivity approaches

the temperature dependence of bulk VSe_2 (Figure VI. 6b). Interestingly, the $([SnSe]_{1.15})_1(V_{1+x}Se_2)_2$ compound exhibits a higher electrical resistivity, whereas upon further increase of the VSe_2-layer thickness a continuous decrease is observed. All ferecrystalline compounds show a significantly smaller temperature dependence of the electrical resistivity compared to the bulk and thin film compounds (see Table VI. 2), which results directly from the rotational disorder between the constituents and thus a reduced scattering of the charge carriers by phonons.

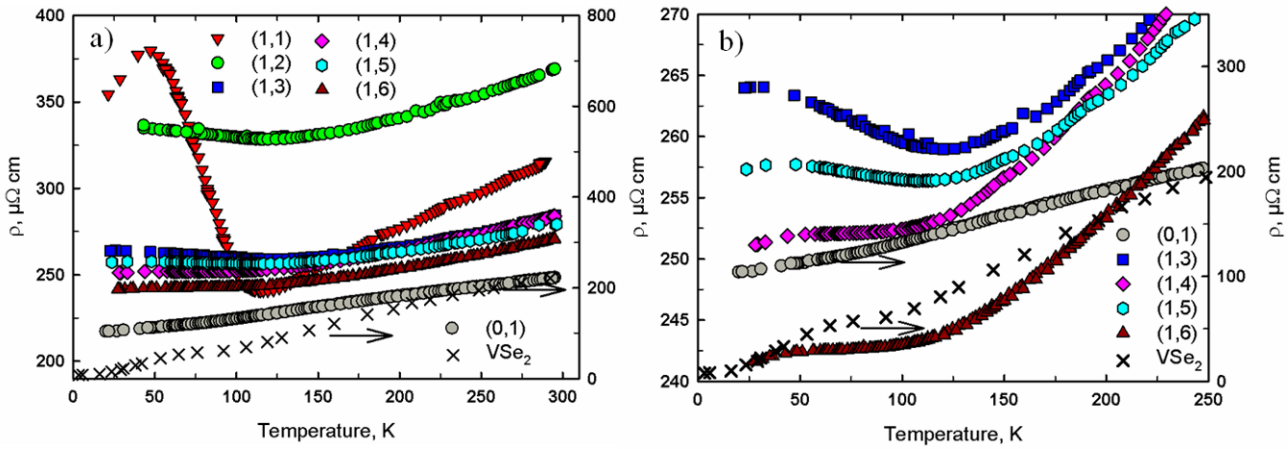

Figure VI. 6. a) Electrical resistivity as a function of temperature for $([SnSe]_{1.15})_1(V_{1+x}Se_2)_n$ with n = 1 - 6 and a $V_{1+x}Se_2$ thin film. b) Detailed view of the compounds with n = 3 - 6 and a $V_{1+x}Se_2$ thin film. For comparison the data of single crystalline bulk VSe_2 [14] are plotted.

The temperature dependent Hall coefficient of all compounds corroborates the results from the electrical resistivity (Figure VI. 7). The $([SnSe]_{1.15})_1(V_{1+x}Se_2)_1$ sample exhibits a distinctly different behavior due to quasi 2-dimensionality[26], which gets rapidly destroyed due to the similar crystallographic orientation of consecutive VSe_2 layers in the 1*T*-polytype. This strong dependence on dimensionality might arise from the unique nature of the charge density wave transition in VSe_2[15, 16]. At the same time the quasi 2-dimensionality in a (1,1) compound also rules out the presence of interstitial V-atoms as

they don't reside between the SnSe and VSe_2 layers. The presence of interstitial V-atoms in the ferecrystalline compounds with $n > 1$ has no considerable effect on the anomaly compared to the stoichiometric compounds[26]. As the thickness of the VSe_2 constituent increases the Hall coefficient decreases and changes sign at temperatures between 4 -20 K for $([SnSe]_{1.15})_1(V_{1+x}Se_2)_n$ with n = 2 and 3, and increases to 60 K for $([SnSe]_{1.15})_1(V_{1+x}Se_2)_6$. Similar to the bulk compound the thin film sample is an n-type conductor. However, the kink at the CDW transition temperature is less pronounced compared to the stoichiometric bulk single crystal [14] and stretched out over a wider temperature range.

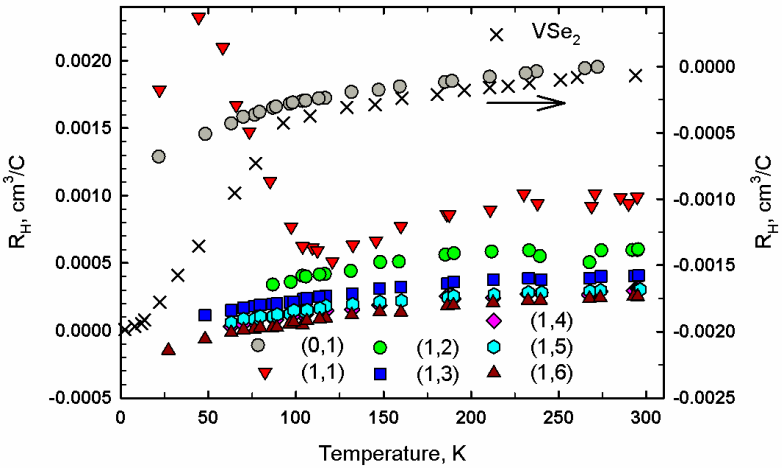

Figure VI. 7. Hall coefficient as a function of temperature for $([SnSe]_{1.15})_1(V_{1+x}Se_2)_n$ with n = 1 - 6 and a $V_{1+x}Se_2$ thin film. For comparison the data of single crystalline bulk VSe_2 [14] are plotted.

Table VI. 2. Electrical resistivity ratio, carrier concentration at room temperature, carriers/V-atom at RT and RT carrier mobility for $([SnSe]_{1.15})_1(V_{1+x}Se_2)_n$ with n = 1 – 6, a $V_{1+x}Se_2$ thin film, and bulk VSe_2 [14].

compound	ρ_{RT}/ρ_{150K}	n_{RT}, $*10^{21}$ cm^3	**Carriers/V-atom**	**Carrier mobility μ, $cm^2V^{-1}s^{-1}$**
(0,1)	1.8	200	10.6	0.14
(1,1)	1.2	6.4	0.6	3.28
(1,2)	1.1	10.4	0.8	1.63
(1,3)	1.1	15.4	1.0	1.42

(1,4)	1.1	20.3	1.1	1.08
(1,5)	1.1	21.2	1.1	1.06
(1,6)	1.1	25.1	1.3	0.92
VSe_2 [14]	2.0	90	5.4	0.31

Applying the single band approximation carrier concentrations and mobilities at room temperature were calculated for all compounds and are listed in Table VI. 2. The carrier concentration of the thin film sample is comparably high, probably due to the presence of interstitial V-atoms, which introduce additional electrons into the conduction band. Even then, the number of 10.6 carriers/V-atom is more than double the number of stoichiometric bulk VSe_2 (5.4 carriers/V-atom), which cannot be explained by the additional electrons from the 0.13 interstitial V-atoms. For the ferecrystalline compounds the carrier concentration increases systematically as a function of *n*. However, comparing the carriers/V-atom based on the composition from EPMA results in an almost constant carrier concentration/V-atom at room temperature for compounds with $n > 3$. Only for the (1,1) and (1,2) compound the carriers/V-atom remain well below 1 indicating the presence of charge transfer between the layers [2014Ale]. Considering not only the lower carrier concentration, but also the opposite sign of the Hall-coefficient revealing holes as the majority carriers at room temperature for all ferecrystals rather than electrons as observed for the bulk and thin film compounds point toward a more complex mechanism than simple charge transfer between the constituents. One possible explanation is a different band splitting induced by a change in the *c*/*a*-ratio of the VSe_2 constituent (see Table VI. 1) in the intergrowth compounds. This ratio is smaller than for the bulk sample and the thin film sample (see Table VI. 1). Theoretical calculations demonstrated that the band structure of VSe_2 is very sensitive to the *c*/*a*-ratio and compared to other 1*T*-

structures is closer to a trigonal prismatic splitting of the *d*-bands [17], where p-type conduction is reported for isovalent 2*H*-$NbSe_2$ and 2*H*-$TaSe_2$ [18]. Such a band splitting could be induced by the interaction between the two constituents in the $([SnSe]_{1.15})_1(V_{1+x}Se_2)_n$ compounds. The (1,1) sample has a significantly higher mobility again indicating a change in dimensionality has a huge effect on the transport properties of the compounds. All ferecrystalline compounds have a higher mobility than the bulk or the thin film sample and the value slightly decreases with increasing VSe_2 thickness. The reduced carrier mobility for the ferecrystalline compounds with $n > 1$ could arise from the slight asymmetry of the VSe_2 constituent along the *c*-direction as well as the presence of interstitial V-atoms, which seems to also decrease the carrier mobility in the thin film compound compared to bulk.

VI.5. Conclusions

A series of ferecrystalline compounds $([SnSe]_{1.15})_1(V_{1+x}Se_2)_n$ with $n = 1 – 6$ and a thin film $V_{1+x}Se_2$ were synthesized utilizing the modulated elemental reactant technique. The presence of interstitial V-atoms ($0.13 \leq x \leq 0.42$) in the thin film sample as well as in the intergrowth compounds with $n > 1$ between two TMD layers was confirmed by Rietveld refinement and careful inspection of HAADF-STEM cross sections. The interstitial V causes an expansion of the VSe_2 constituent along the superlattice direction and the amount also trends with the in-plane lattice parameters of the dichalcogenide. The area of the SnSe constituent adapts to this change in a way to keep the misfit parameter at 0.15 for all compounds. Compared to bulk $V_{1+x}Se_2$ the trend of the lattice parameters as a function of x is reversed. Similar to off-stoichiometry in bulk compounds also the charge density wave transition in the thin film $V_{1.13}Se_2$ is strongly suppressed. In contrast to that

in the intergrowth compounds $([SnSe]_{1.15})_1(V_{1+x}Se_2)_n$ with $n = 1 – 6$ the main cause of the change in the temperature dependence of the electrical resistivity and Hall coefficient is induced by eliminating the quasi 2-dimensionality as soon as *n* exceeds 1. Interestingly, while the carrier concentration increases with increasing VSe_2 layer thickness, the carrier mobility decreases.

CHAPTER VII

PHASE WIDTH OF KINETICALLY STABLE $([PbSe]_{1+y})_1(TiSe_2)_1$ FERECRYSTALS AND THE EFFECT OF PRECURSOR STRUCTURE ON ELECTRICAL PROPERTIES

VII.1.Authorship Statement

The primary author of the following manuscript is Sage Bauers. The paper was published in the Journal of Alloys and Compounds in 2015, volume 645, pages 118-124. For this paper, I performed STEM measurements used to identify local structure and observe local stacking motifs that confirmed XRD results.

VII.2. Introduction

The high temperatures and long times used in most solid state reactions lead to equilibrium products and an equilibrium distribution of defects and impurity atoms.[1] This leads to the common practice of reporting the properties of a new compounds based on the measurement of a single sample, ideally a single crystal that has been structurally characterized. For metallic compounds with a narrow phase width, subsequent reports usually agree with the initial report, as metallic properties are usually not significantly affected by small changes in the concentration of defects or impurities except at low temperatures.[2] For semiconducting compounds properties often vary significantly between preparations, especially preparations from different groups and even when using near equilibrium synthesis conditions, as small differences in impurity levels and/or defects can significantly vary carrier concentration.[2] An especially large variation in properties is typical when there is a range of compositions within which compounds are stable.[2] As the number of elements within a compound is increased or the structure

becomes more complicated, obtaining agreement on properties becomes difficult due to varying distributions of the elements within the ideal composition, impurity atoms, and defects on different crystallographic sites.

The challenges in determining the base properties of ternary intergrowth compounds is especially difficult. An example of this is ternary misfit layer compounds of the form $(MX)_{1+\delta}(TX_2)_n$, which consist of an intergrowth of a rock salt structure, MX, where M = Sn, Pb, Bi, or RE, and a transition metal dichalcogenide, TX_2 where T = Ti, V, Cr, Nb, and Ta. X is either S or Se and δ represents the difference in the area per cation of the two different structures. Electrical properties for nominally the same compound vary considerably from group to group, even for metallic samples. For example, the resistivity of single crystals of $(PbS)_{1.18}TiS_2$ reported by different groups[3] differs by a factor of 5 and the resistivity of $(SmS)_{1.18}TaS_2$ reported by different groups[3] varies by a factor of 7. The differences in properties of these misfit layer compound crystals is thought to be a consequence of different growth conditions used during vapor transport leading to different amounts of incorporated iodine, other impurities and/or defects. Recently a new synthesis approach was shown capable of preparing intergrowth compounds $((MX)_{1+\delta})_m(TX_2)_n$, where m and n can be systematically controlled by design of a precursor. The structures are different from MLC in that there is rotational disorder between constituents and hence no systematic cooperative structural distortion of the constituent layers. The synthesis route to these compounds is kinetically controlled and the kinetics of the formation reaction will determine the concentration and distribution of defects and impurity atoms.

It is important to understand the reproducibility of the kinetically controlled synthesis of these turbostratically disordered misfit layer compounds, or ferecrystals, before considering the difference between compounds with different m and n values, because small deviations in the product could potentially cause the properties to vary more within different preparations of the same compound relative to compounds with different m and n values. Here we investigate two sets of $([PbSe]_{1.16})_1(TiSe_2)_1$ samples prepared from a range of different starting precursors and deposited over several months. Although a large variation of precursors was used, we find that they crystallize to nominally the same product, with a small range of c-axis lattice parameters (defined to be along the stacking direction of the intergrowth). It is difficult to determine the precise composition of the majority compound as different trace amounts of secondary phases may form. We find that electrical behavior in the form of resistivity values, Seebeck coefficients, and carrier densities vary from sample to sample and cluster into discreet regions within deposition cycles. The changes in electrical properties correlate with changes in composition. It will be best to look for trends in properties as m and n are varied by taking advantage of the higher level of repeatability within samples prepared in the same deposition cycle.

VII.3. Experimental Details

Thin films of the amorphous precursor were deposited on silicon and quartz substrates using a custom built physical vapor deposition system.[4] Selenium was deposited using an effusion cell, whereas lead and titanium were deposited using electron beam guns. The thickness of each elemental layer was monitored using quartz crystal microbalances. Background pressure inside the chamber during film deposition was

maintained between 5 x 10^{-8} and 5 x 10^{-7} torr for all reported samples. A typical deposition produced a thin film that was approximately 50 nm thick, which consisted of repetitions of the layer sequence Ti – Se – Pb - Se. A second set of samples, prepared much later than the first set, was made with a total thickness of 35 nm. The precursor was calibrated to contain an excess of 2% Se, as this has previously been shown to produce samples with more intense diffraction patterns.[5] The thickness of each layer in the repeating sequence was calibrated via a method described previously such that each layer self assembles into a $(PbSe)_{1.18}(TiSe_2)_1$ unit cell upon annealing.[6] Samples were annealed on a hot plate at 350°C in a nitrogen atmosphere. Electron-probe microanalysis (EPMA) was used to determine the composition of the thin film samples.[7] Specular X-ray diffraction data were collected using a Bruker D8 Discover diffractometer with Cu Kα radiation.

Thin film specimens for electrical transport properties were deposited on insulating fused silica substrates in order to minimize the influence of the substrate on the measurements. The films were patterned in a standard cross geometry using a shadow mask. Four-probe electrical resistivity (ρ) was measured from 20 K to 300 K in a custom closed-cycle He cryo-system using the van der Pauw technique.[8] Electrical leads were attached using silver epoxy. Seebeck coefficient (*S*) was measured using a differential technique, by determining the slope of applied temperature difference vs. measured voltage difference, corrected for the Seebeck coefficients (*S*) of the copper-constantan thermocouple leads. All reported electrical transport data correspond to the in-plane direction.

VII.4. Results and Discussion

Sample precursors were prepared in two deposition cycles to synthesize a precursor which yields a sample after annealing that is crystallographically and compositionally in agreement with the previously reported turbostratically disordered $([PbSe]_{1.16})(TiSe_2)$.[6] Once a parameter-space close to optimal was found,[96] the depositions were fine-tuned by varying the elemental layer thicknesses of the precursor, which changes the compositions of the precursors. The full width at half maximum of the (002) Bragg reflection was used between depositions as a fast indicator of 1:1 sample quality. Data collected on the samples prepared for this study that formed the 1:1 compound are summarized in Table VII.1.

Low angle diffraction patterns are shown in Figure V.1 and indicate little variation is present within deposition cycles. The small variation of critical angle from 0.62 to 0.67 degrees in 2-theta shows little change in density and no correlation was able to be drawn between small shifts in critical angle and composition. Fitting of the high-frequency Keissig oscillations to the Bragg equation modified for refractive contributions results in film thicknesses within 2.5 nm of the targeted values of 50 nm for set 1 and 35 nm for set 2. The angle at which the Kiessig fringes can no longer be resolved is an indicator of the roughness of the films. The increased smoothness seen in the second set of samples is due to diffraction data being collected from samples on a Si substrate as opposed to fused quartz. The changes in rate of decay of the Kiessig fringes between samples is most-likely due to a variance in different substrate's native oxide thicknesses. The first Bragg Peak is seen in all low-angle scans. The peak centers of gravity vary little from 7.27 degrees, corresponding to a d-spacing of 12.15 angstroms and the 001 reflection of the 1:1 ferecrystal.

Table VII.1. Summary of all samples as well as data from the previously reported 1:1 compound. Samples from the first deposition cycle, set a, were deposited in order from a1 to a9. Samples from the second deposition, set b, were deposited in order from b1 to b4.

Sample	c-lattice parameter (Å)	Carrier Density (cm^{-3})	Composition		
			Pb/Ti	Pb/Se	Ti/Se
a1	12.181	2.12E+21	0.95	0.36	0.38
a2	12.173	1.76E+21	1.05	0.39	0.37
a3	12.181	2.04E+21	0.88	0.33	0.38
a4	12.167	1.72E+21	1.10	0.38	0.35
a5	12.169	1.71E+21	0.99	0.37	0.37
a6	12.181	1.72E+21	1.07	0.38	0.36
a7	12.170	1.82E+21	0.96	0.36	0.37
a8	12.176	1.86E+21	0.95	0.37	0.38
a9	12.173	2.10E+21	0.98	0.36	0.36
b1	12.188	1.44E+21	0.92	0.40	0.44
b2	12.193	1.07E+21	1.16	0.46	0.40
b3	12.199	1.16E+21	1.08	0.43	0.40
b4	12.194	1.29E+21	0.91	0.40	0.43
Moore 2012[6]	12.174	2.10E+21	1.16	0.37	0.32

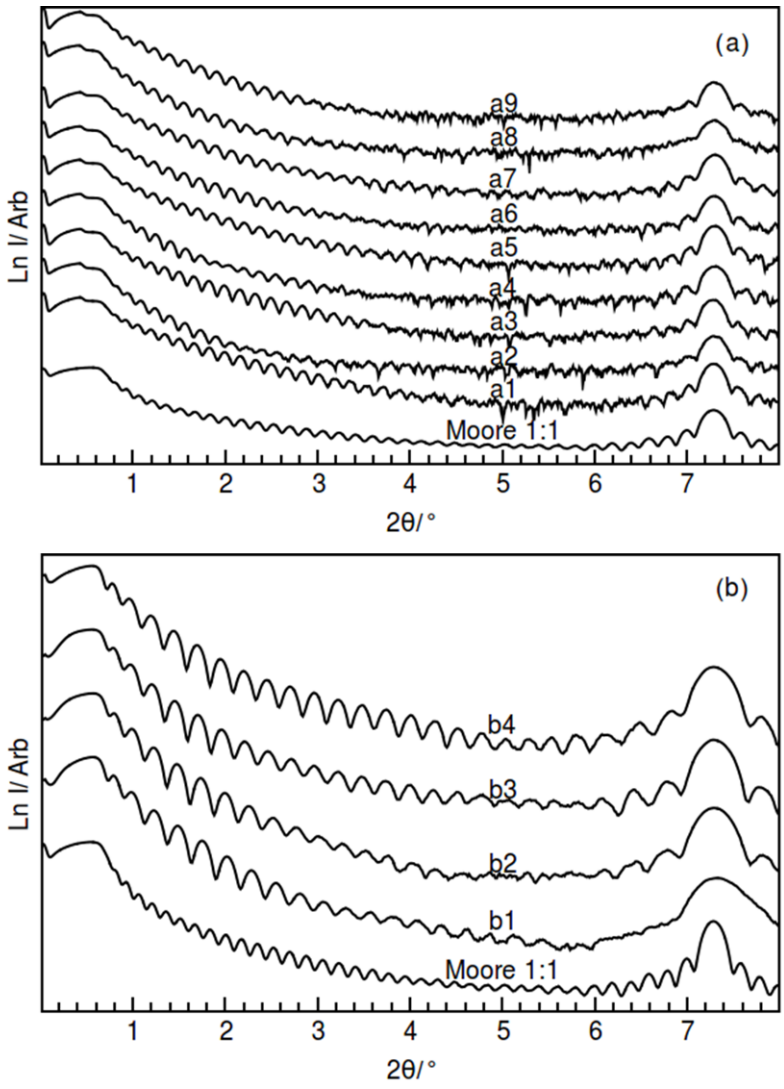

Figure VII.1. Low-angle diffraction patterns collected from samples. Data from the Moore 1:1 compound are shown as the bottom curve in each. (a) Set A. The first loss of intensity near the critical angle is a substrate artifact. The critical angle is taken from the second loss. (b) Set B. The apparent amplitude difference is due to the stacking. The range of normalized data is comparable for all samples.

The high angle diffraction patterns (Figure VII.2) from both sets of sample also show little variation between samples or deposition cycles. The *c*-lattice parameters of all the samples are within 0.01 Angstroms of the average value and within 0.25% of the previously reported value for the $([PbSe]_{1.16})(TiSe_2)$ ferecrystal. This small change in *c*-lattice parameter correlates weakly with composition changes, trending with the

measured metal (Pb, Ti) to Se ratio. The increased FWHM of the samples from the second deposition cycle is due to fewer layers in the (00*l*) direction in which the crystallite size is limited by the thickness of the film. The lack of any (*hkl*) reflections with $h, k \neq 0$ in an out-of-plane geometry is characteristic of ferecrystal samples due to the crystallographic alignment of the samples with the substrate. The similarity of the diffraction patterns suggests a similar average structure for all of the samples. There is some variation in the relative intensities of peaks throughout both sets of samples, with the largest variations within 50% of the average relative intensity for each peak. These changes in relative intensity suggest a variation in the occupancy of specific locations reflecting the different compositions of the precursors.

Electrical measurements are more sensitive to impurity phases or local crystalline defects than x-ray measurements. Prior literature suggests charge transport occurs mainly in the conduction band of the transition metal dichalcogenide constituent. We expect changes in impurity and defect concentration would alter the carrier density of the semimetallic $TiSe_2$. Table VII.1 contains the room temperature resistivity of the samples. The composition and resistivity data from both sets of samples cluster in nearby but discrete regions of parameter space, distinct also from the previously published compound. The variation of the extrema from the average value is ±40% within sample set A and ±30% within sample set B. There is a factor of 2 difference between the averages of the resistivity values of the two data sets, with the extrema from the entire experiment spanning a 400% change. The resistivity values were found to trend with the Pb/Se ratio, as shown in Figure VII.3. The variation in room temperature resistivity (400%), however, is smaller than that reported for different single crystals of misfit layer

compounds (500-700%). This is somewhat surprising, as the MLC crystals were grown under nearly equilibrium conditions while the self-assembly of our precursors is a kinetic process. This suggests that in the self-assembly, some of the excess elements are clustered in inclusions rather than being dispersed as local defects throughout the film. The larger variation between depositions also suggests that it would be better to make samples with different m and n in the same set to correlate nanoarchitecture with properties.

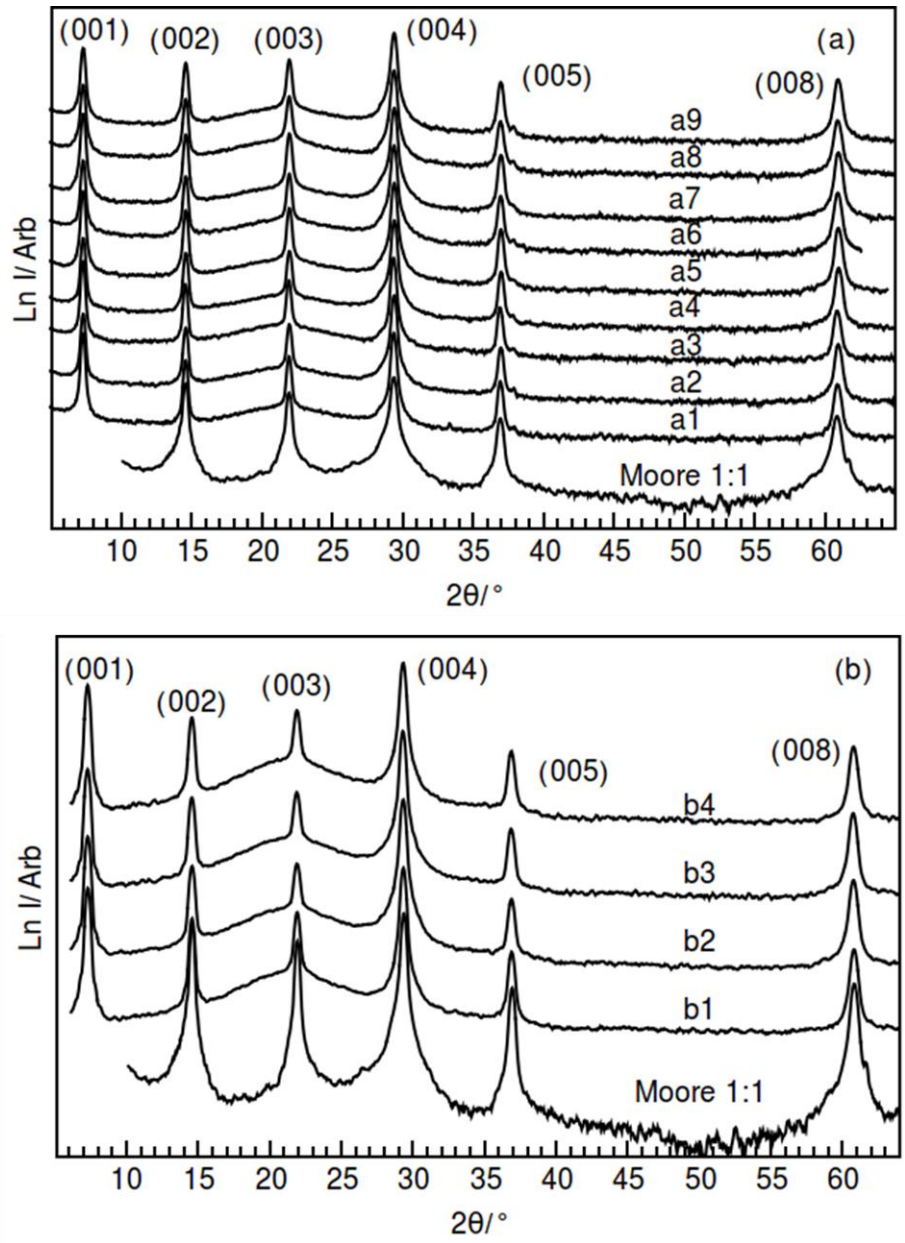

Figure VII.2. High angle specular diffraction patterns collected from samples in (a) set A and (b) set B. Data from the Moore 1:1 compound are shown for comparison as the bottom curve in each pane. The apparent difference in scales is due to a reduced range in the pane with fewer curves.

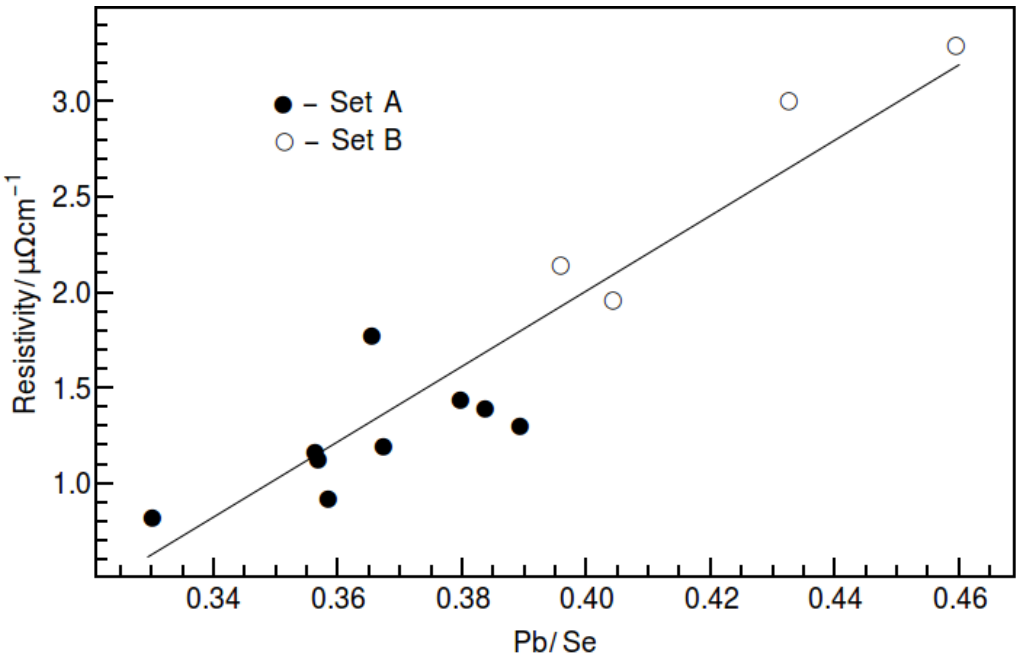

Figure VII.3. Sample resistivity values cluster in two regions for the two sample sets and trend with Pb/Se ratio. The line is provided as a guide to the eye.

Temperature dependent resistivity data, collected for most of the compounds studied, are shown in Figure V.4. The temperature dependence is very similar for all samples and indicates metallic behavior. The temperature dependence of the electrical resistivity can be modeled using the Bloch-Grüneisen equation as expected for a metal,

$$\rho(T) = \rho_0 + \Re\left(\frac{T}{\theta_D}\right)^5 \int_0^{\frac{\theta_D}{T}} \frac{z^5}{(e^z - 1)(1 - e^z)} dz$$

where ρ_0 is the residual resistivity, $\Re$ is the electron-phonon interaction constant, and θ_D is the debye temperature. The very weak temperature dependence indicates a small electron phonon interaction constant, reflecting the lack of long range order found for compounds prepared by self-assembling designed precursors. This disorder, and the resultant lack of phonons, results in the low lattice thermal conductivity of ferecrystals. The variation of the residual resistivity with both sample set and composition is similar to that of the room temperature values, discussed above. There is evidence for a slight

upturn in the resistivity at the lowest temperatures measured, but this upturn is smaller than previously reported.

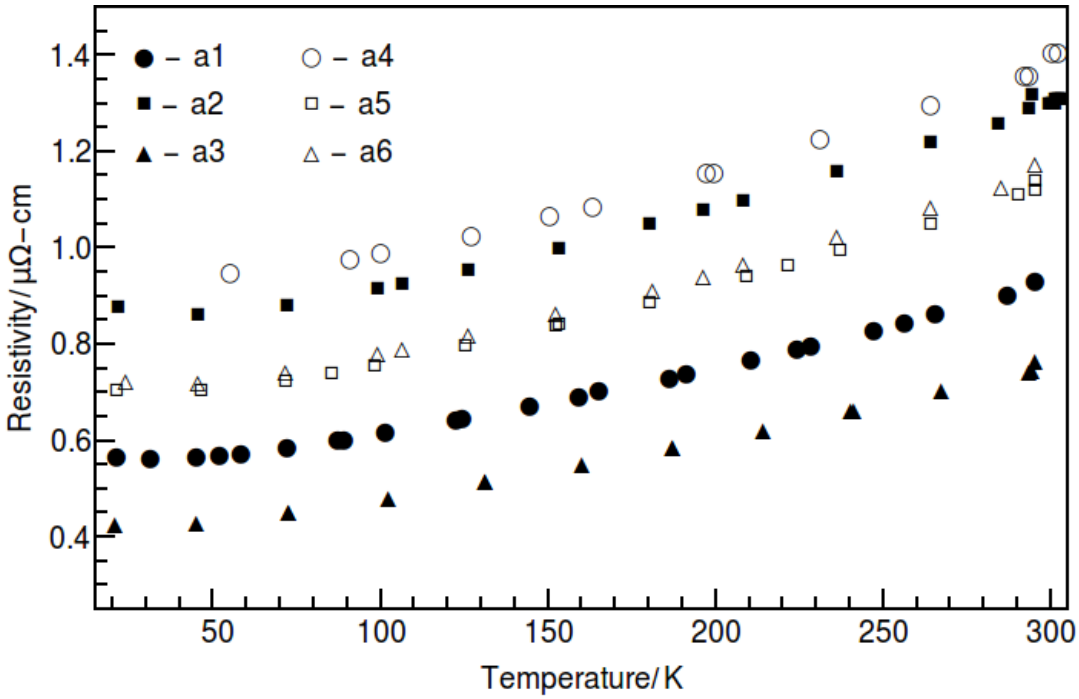

Figure VII.4.Variable temperature resistivity data for select ferecrystal samples from set A. Curvature is very similar in all cases, with the value differences in magnitude roughly scaling with carrier concentration.

To gain further information on the electrical properties, Hall coefficients were measured at room temperature for all samples. All samples exhibit a negative Hall coefficient indicating conduction via electrons, which is consistent with prior suggestions of charge donation to $TiSe_2$ from PbSe.[6] Following prior literature reports, the Hall coefficients were converted to carrier concentration assuming a single band model.[3] Carrier concentrations are reported for all samples in Table VII.1 and are shown as a function of temperature on a subset of samples (Figure VII.5). Room temperature carrier concentration for each deposition varies by 15% from the average value and there is a factor of 1.5 between sets. Carrier concentration has a linear downward trend with cation

impurity, suggesting reduced donation of charge into the dichalcogenide layer. The variation of the carrier concentration with temperature may be a consequence of assuming a single band model to calculate carrier concentrations. A change in charge transfer with temperature would be expected and lead to the observed weak temperature dependence.

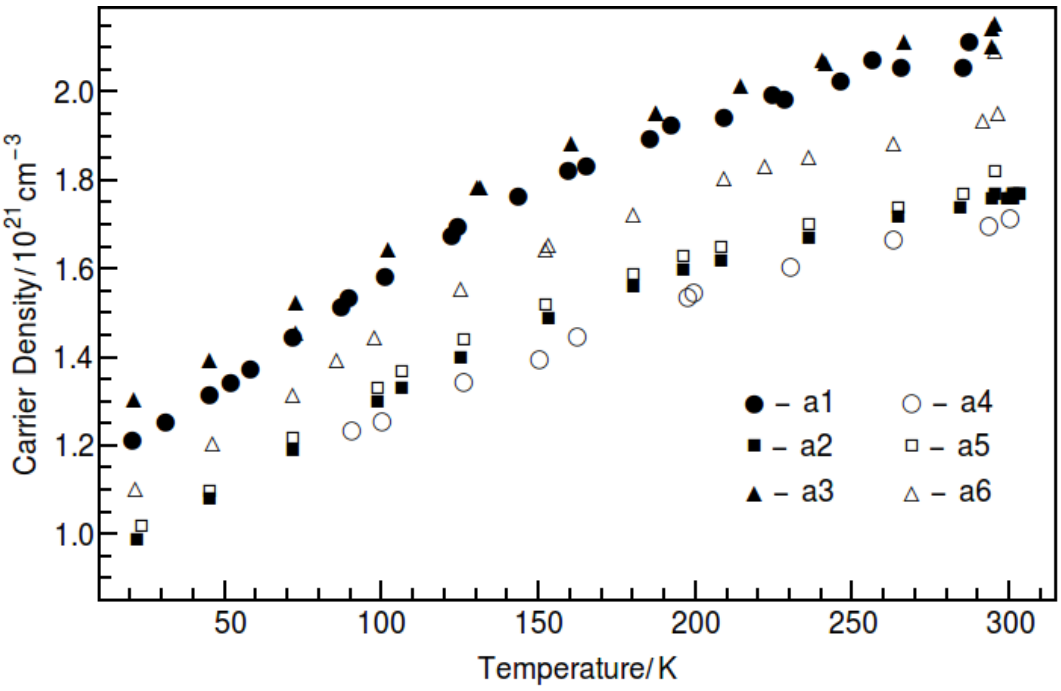

Figure VII.5. Carrier concentration as a function of temperature for a subset of samples. The gentle change is typical of a metallic band structure.

Hall mobilities calculated from carrier concentration and resistivity measurements vary between 1.8 and 3.8 $cm^2V^{-1}s^{-1}$. The mobility increases with carrier concentration, which is unusual for doping because dopant atoms usually cause scattering. However, this is consistent with charge donation from PbSe to $TiSe_2$, where conduction occurs in a location spatially separated from the dopant. The mobility decreases as the Pb/Se ratio increases.

Seebeck coefficients were all negative, consistent with Hall coefficient in indicating that electrons are the majority carrier. The magnitude of the Seebeck coefficients vary by about 2.5 μV/K within a set of samples with the values of each set clustered around averages 5 μV/K apart. As expected, the magnitude of the Seebeck coefficient increases as carrier density is reduced. Assuming a parabolic band with acoustic scattering, the effective mass can be determined from the Pisarenko relationship,[10]

$$\alpha = \frac{8\pi^2 k_B^2}{3eh^2} m^* T \left(\frac{\pi}{3n}\right)^{\frac{3}{2}}$$

Where α is the Seebeck voltage, k_B is the Boltzmann constant, e is the elementary charge, h is Planck's constant, m^* is the effective mass, T is the absolute temperature, and n is the carrier concentration. The average carrier mass was found to be $4.4m_e$ and $3.6m_e$ for sets A and B respectively, both lower than calculated from data on the previously reported 1:1 compound ($5.5m_e$). Figure VII.6 graphs the correlation between the Seebeck coefficient and the carrier concentration at 295K. The Seebeck coefficient is relatively insensitive to the Hall determined carrier concentration. The solid curves show the values expected from the Pisarenko relationship for the minimum, maximum, and average effective masses. The lowest effective masses correspond to samples with a high cation (Pb, Ti)/Se ratio. The changes in m^* reflect the shortfall of assuming a single band model to obtain carrier concentration or that the band becomes more disperse with increased impurity concentration. Additional investigations will be required, both to understand modulation doping and how to use it in band structure engineering of ferecrystal compounds.

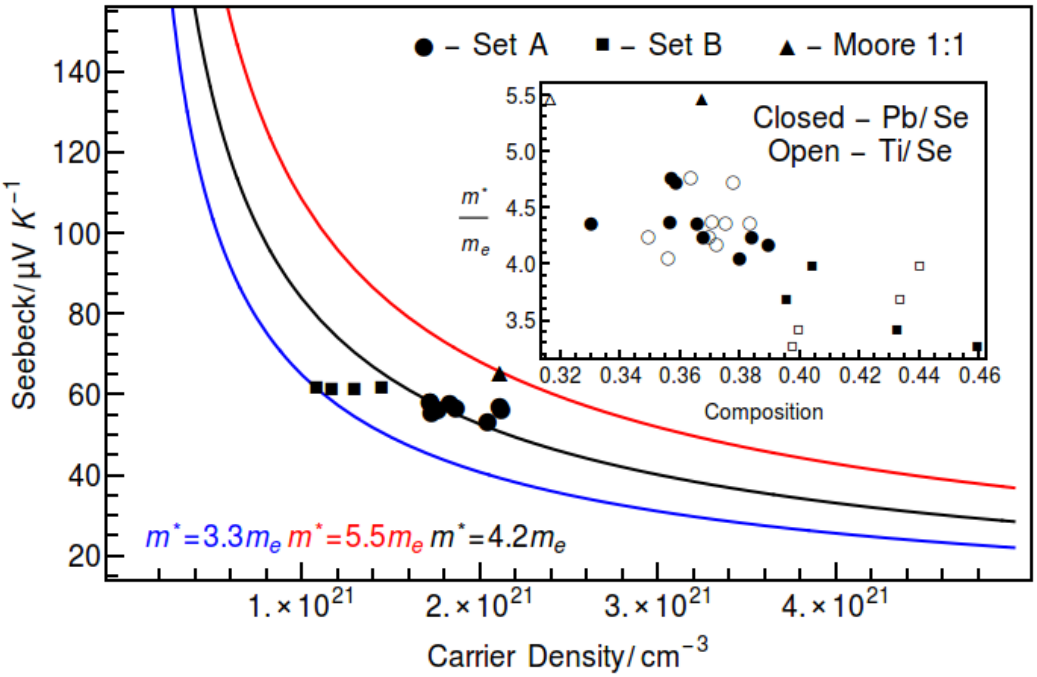

Figure VII.6. Room temperature carrier density plotted against Seebeck coefficients for all samples. The solid curves indicate the expected relationship for different effective masses assuming a single rigid parabolic band.

VII.5. Conclusion

$([PbSe]_{1.16})_1(TiSe_2)_1$ forms over a range of initial precursor parameters resulting in a very narrow range of *c*-axis lattice parameters, suggesting a narrow phase width for this compound. The resistivity was found to vary by a factor of two, with the change correlating with the Pb/Se ratio. The Seebeck coefficient was consistent within a set of samples prepared in the same deposition cycle. The unusual temperature dependence of the carrier concentration and unusual variation in the effective mass calculated from the Seebeck coefficients and the carrier concentration suggest that using a single band approximation to convert Hall coefficients to carrier concentration may be a poor assumption. The small change in electrical properties between ferecrystal samples relative to the large difference between reports of single crystals of misfit layered compounds, especially within a set of samples in the same deposition cycle, is

encouraging for future experiments that explore how properties vary as compounds with different values of n and m are prepared.

CHAPTER VIII

MODIFYING A CHARGE DENSITY WAVE TRANSITION BY MODULATION DOPING: FERECRYSTALLINE COMPOUNDS $([Sn_{1-x}Bi_xSe]_{1.15})_1(VSe_2)_1$ WITH $0 \leqq X \leqq 0.66$.

VIII.1. Authorship Statement

Matthias Falmbigl is the primary author of the following paper. This work was published in the Journal of Materials Chemistry C in 2015, volume 3, pages 12308-12315. I performed high resolution aberration corrected STEM measurements which confirmed the absence of Bi-Bi antiphase boundaries and the observation of very large grains.

VIII.2. Introduction

Quasi-2 dimensional transition metal dichalcogenides, and in particular nanosheets of these layered materials are currently subject to intense theoretical and experimental investigations due to their versatile and outstanding properties ranging from insulating to superconducting.[1–5] Many of these research efforts have focused on VSe_2 due to the appearance of a charge density wave (CDW) transition in the bulk compound.[6,7] The investigation of a dimensionality effect on the CDW going from bulk to monolayers[8] led to the discovery of the size dependence of the charge density wave transition temperature first in $TiSe_2$[9] and later also in $TaSe_2$[10] and VSe_2[11,12] and unconventional ferromagnetic properties.[12,13] A controlled manipulation of the charge density wave transition is crucial for potential applications in electro-optical switches, memory and spintronic devices[12,14,15] as

well as low-power information processing[16] and data storage devices.[17] In bulk VSe_2 this is challenging to accomplish, because the charge density wave transition is extremely sensitive to any manipulation of the structure. Slight deviations from the ideal stoichiometry resulting in interstitial V-atoms for $V_{1+x}Se_2$ lead to a rapid suppression of the CDW.[18] Also partial substitution of vanadium by isovalent Nb,[19] Fe- and Ti-doping[20] or Fe intercalation[21] result in a suppression of the charge density wave transition.

Recently we have demonstrated that the charge density wave transition in ferecrystalline compounds $([SnSe]_{1.15})_m(VSe_2)_1$ is strongly enhanced and stabilized against structural defects.[22–25] Ferecrystals are thin film intergrowth compounds of alternating staggered rocksalt-like and transition metal dichalcogenid layers, which exhibit extensive rotational disorder between the constituents.[26] The analogous $([BiSe]_{1+d})_1(VSe_2)_1$ ferecrystal was recently reported, which had no charge density wave and a negative Hall coefficient rather than the positive Hall coefficient observed for $([SnSe]_{1.15})_m(VSe_2)_1$ compounds.[27] The interwoven superstructure of two distinct constituents and the presence of rotational disorder among them provide a unique opportunity for indirect (modulation) doping of the VSe_2 constituent. Partial substitution of the Sn by Bi in $([Sn_{1-x}Bi_xSe]_{1.15})_1(VSe_2)_1$ should in a simple picture result in electron donation from bismuth into the VSe_2-layer. The charge density wave transition provides an extremely sensitive inherent probe to any changes in the electronic structure of the VSe_2 constituent of the ferecrystal. This approach to indirect doping with electrons might open a new pathway to optimizing the charge density wave

transition for specific applications. However, earlier studies on misfit layer compounds[28,29] and ferecrystals[27,30] containing BiX, with X = S or Se, demonstrated that the behavior of Bi within the com- pounds depends strongly on structural features as well as the transition metal of the dichalcogenide layer and no general prediction is possible.

In this study we present the influence of Bi-doping on the structure and electrical properties of the ferecrystalline compounds $([Sn_{1-x}Bi_xSe]_{1.15})_1(VSe_2)_1$ with $0 \leq x \leq 0.66$. Interestingly, the Bi- substitution causes systematic structural changes in both constituents of the intergrowth compounds revealing that the interlayer interaction varies with the Bi-content. The electrical properties demonstrate that small Bi-contents cause a strong enhancement of the charge density wave transition, whereas at higher substitution levels the minority charge carriers steming from the $Sn_{1-x}Bi_xSe$ layer contribute significantly to the properties of the compounds and the electrical properties resemble those of bulk VSe_2. This is the first report of intentional modulation doping of a material with a charge density wave, which results in a change of majority carrier type for the compound with the highest bismuth content. Modulation doping *via* substitution in the rock salt layer modifies the charge density wave transition in these compounds, which is of great importance for any future applications.

VIII.3. Experimental

Physical vapor deposition was utilized to form the thin film samples used in this study in a vacuum deposition chamber evacuated to a base pressure of 10^{-7} mbar before deposition.[31] An effusion cell was used to evaporate Se (Alfa Aesar, 99.999 at%

purity) and three thermionics electron beam guns were used to evaporate Sn (Alfa Aesar, 99.98 at% purity), V (Alfa Aesar, 99.7 at % purity) and Bi (Alfa Aesar, 99.99 at% purity). Substrates, (100) oriented silicon wafers, were positioned approximately 25 cm above the sources on a motorized carousel. Pneumatically powered shutters positioned between the sources and substrates were utilized to control the amount of time each element had for deposition onto the substrate. A LabView program positioned the substrates on top of the diff erent source elements, controlled the shutter opening times and the layer sequence. A quartz microbalance crystal monitor system was used to control deposi- tion rates. Se, V, and Sn were deposited at 0.5 Å s^{-1}, 0.4 Å s^{-1}, and 0.4 Å s^{-1}, respectively. For Bi deposition rates of 0.2 Å s^{-1} and 0.4 Å s^{-1} were used depending on the targeted Bi-content. The deposition for each sample was carried out in layers by repeatedly depositing a sequence of Se–Bi–Sn–Se–V forming the initial precursors. A thickness of 50 nm was targeted for the resultant thin films. The precursors were annealed on a hot plate in nitrogen atmosphere (0.5 ppm of O_2) at 400 1C for 20 minutes, which allowed the precursors to self-assemble into the desired $([Sn_{1-x}Bi_xSe]_{1.15})_1(VSe_2)_1$ products. In order to deter- mine the amount of each element required to produce a precursor that self assembles into a $([Sn_{1-x}Bi_xSe]_{1.15})_1(VSe_2)_1$ ferecrystalline compound after annealing, extensive calibration of deposition parameters described elsewhere was required.[22] Electron probe microanalysis (EPMA) on a CAMECA SX-50 was used to analyze the composition of the thin films before and after annealing, using wavelength dispersive spectrometers (WDS) utilizing a special thin film technique.[32]

Both, X-ray reflection (XRR) and X-ray diffraction (XRD) data were obtained on a Bruker D8 Discover diffractometer using Cu-Ka radiation (λ = 1.54185 Å). A y–2y locked coupled scan geometry was used to gather XRR data between 0 and 101 in 2y and XRD data between 6 and 651 in 2y for the precursors as well as the annealed samples in the (00*l*) direction. In-plane X-ray diffraction was carried out for selected samples on a Rigaku SmartLab equipped with a Cu-Ka radiation source in the (*hk*0) direction of the samples from 25 to 1001.

High resolution scanning transmission electron microscopy (HRSTEM) was carried out on an aberration-corrected FEI Titan (300 kV incident beam) at Pacific Northwest National Laboratory. The preparation of selected samples for HRSTEM was performed utilizing a FEI Helios Nanolab D600 Dual Beam focused ion beam (FIB). Samples for electrical measurements (electrical resistivity and Hall coefficient) were synthesized using a shadow mask to deposit films in a 1 cm by 1 cm cross shape on fused silica substrates. Indium and copper-wires were used for contacting, and the in-plane sheet resistance and Hall voltage were measured in van der Pauw geometry. The resulting electrical resistivity and Hall coefficients were calculated using the corresponding film thicknesses, extracted from XRR data. The measurements were conducted between 20 and 295 K on a LabView controlled closed cycle helium transport measurement system. For Hall measurements magnetic fields from 0 to 1.6 T were applied. The Seebeck coefficient was measured at room temperature using Cu/Constantan thermocouples and a Peltier cooler to generate a temperature gradient of 0.5 K.

VIII.4.Results and Discussion

The synthesis of the compounds was carried out using the modulated elemental reactants technique.[33] The deposition parameters from the synthesis of the parent $([SnSe]_{1+d})_1(VSe_2)_1$ compound[22–24] were used as a starting point and the targeted alloys were synthesized by continuously decreasing the deposition time for Sn and proportionately increasing the deposition time for Bi. After depositing a first set of calibration samples, of which the composition was determined by EPMA and the layer thickness by XRR, the deposition parameters were adjusted accordingly in order to synthesize compounds with varying Bi/Sn-ratio and thicknesses close to the targeted *c*-lattice para- meter. An annealing study was performed to define the best annealing conditions by dividing a precursor into several pieces and annealing each piece at a different temperature for a period of 20 minutes. X-ray diffraction scans were collected to follow the evolution of the samples, and representative scans are shown in Figure VIII. 1. All peaks can be indexed to (00*l*) reflections of the compound resulting from the highly preferred orientation perpendicular to the substrate surface. The as deposited scan contains the first five (00*l*) reflections suggesting that there is already considerable order in the as deposited precursor. There is no change in the diffraction pattern after annealing at 100 1C. Beginning at 200 1C a systematic increase of the intensity and decrease in width is observed for the Bragg-peaks as the annealing temperature increases indicating superlattice formation. Annealing at 500 1C results in reflections from impurity phases, intensity loss in all reflections of the ferecrystal seen most distinctly in the (007) peak, and an increase in the peak width. These changes all indicate the beginning of the

decomposition of the superlattice. The decrease in the repeating thickness as a function of annealing temperature, evident *via* the shift of the maxima to higher angles, is related to the formation of the super- lattice and loss of Se during the annealing process. The composition measured by EPMA changes only marginally up to 400 1C, suggesting that until this temperature the *c*-axis lattice parameter decreases as a result of the more efficient packing of atoms as the precursor self-assembles into the targeted compound. The decrease in Se content and increase in oxygen above 400 1C indicate the decomposition of the sample at higher temperatures due to evaporation losses of Se and oxidation of the sample even in a nitrogen atmosphere with less than 1 ppm O2

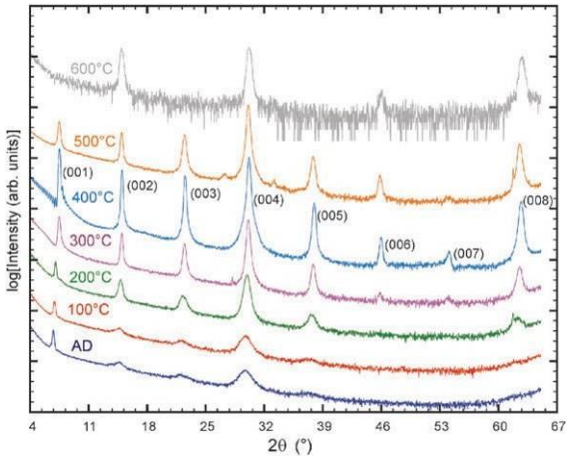

Figure VIII. 1 Specular X-ray diff raction of ([Sn0.4Bi0.6Se]1+d)1(VSe2)1 at temperatures indicated above the X-ray patterns with intensity plotted on a log scale to highlight weak reflections. AD means ‘‘as deposited’’

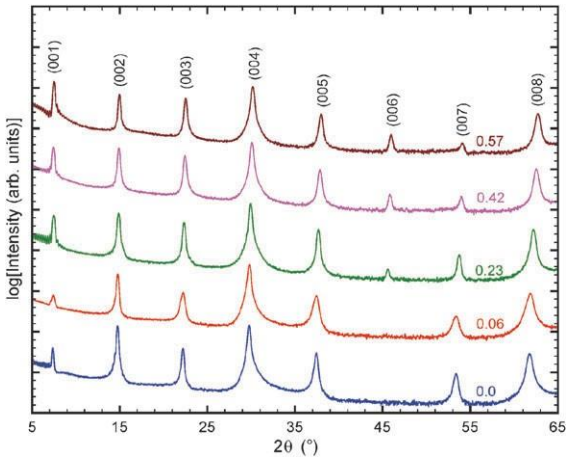

Figure VIII. 2 Specular X-ray diff raction patterns of ([Sn1−*x*Bi*x*Se]1+d)1(VSe2)1 compounds with diff erent Bi-contents. The intensity is plotted on a log scale to highlight weak intensity reflections.

In Figure VIII. 2 the specular X-ray diff raction patterns of compounds ([Sn1-*x*Bi*x*Se]1+d)1(VSe2)1 with 0 ≤ *x* ≤ 0.57 are dis- played. All peaks can be indexed to the corresponding (00*l*) reflections of the superlattice. The systematic change of intensities, especially for the (001), (006) and (007) Bragg-reflections, demonstrates the continuous change of the structure upon Sn substitution by Bi. The Bragg positions systematically shift to higher angles indicating a decrease of the *c*-axis lattice parameter with increasing Bi-content. Figure VIII. 3 shows a nearly linear relationship between Bicontent and *c*-lattice parameter, as expected from Vegard's law. The negative slope is consistent with the diff erence in the *c*-axis lattice parameters of the two unsubstituted rocksalt structured constituents of the misfit layer compounds ([SnSe]1.16)1(NbSe2)1, SnSe (*c* = 0.614 nm)[34] and ([BiSe]1.10)1(NbSe2)1, BiSe (*c* = 0.592 nm),[35] respectively. For ferecrystalline compounds of ([SnSe]1.15)*m*(VSe2)1 a thickness of 0.576(2) nm was extrapolated for the SnSe constituent from the systematic change in the *c*-axis lattice parameter with *m*.[23] The

change in the *c*-axis lattice parameter from 1.203(1) $([SnSe]_{1.15})_1(VSe_2)_1$ nm to 1.179 nm in the analogous $([BiSe]_{1+d})_1(VSe_2)_1$ ferecrystal suggests a thickness 35 of 0.55(2) nm for the thickness of the BiSe. This is close to the thickness of 0.56(2) nm for the BiSe constituent reported for $([BiSe]_{1.10})_m(NbSe_2)_n$.[36] Extrapolation of the linear fit to $x = 1$ results in a *c*-axis lattice parameter of 1.172(7) nm, which is which is smaller but close to the observed value of 1.179 nm for $([BiSe]_{1+d})_1(VSe_2)_1$ reported previously.[27] The Bi-content and the (Bi + Sn)/V-ratio together with the corresponding *c*-axis lattice parameters for each sample are given in Table VIII. 1.

In-plane X-ray diffraction reveals both independent lattice dimensions and different crystal symmetries for the two structurally distinct constituents (Figure VIII. 4), which is characteristic for ferecrystalline compounds.[37] The reflections can be indexed as (*hk*0) reflections for each of the constituents. For the Sn1-*x*Bi*x*Se constituent all peaks can be indexed to a square basal plane consistent with earlier reports for $([SnSe]_{1.15})_m(VSe_2)_1$ compounds.[23] Interestingly, this kinetically stable rocksalt-like layer has a different structure compared to bulk SnSe and BiSe, which crystallize in the orthorhombic GeS-type38 and the trigonal BiSe-type,39 respectively. Whereas alloying of the thermodynamically stable phases would require the existence of a two phase region, until $x = 0.57$ a continuous solid solution for the Sn1-*x*Bi*x*Se layer is observed. In contrast to $([BiSe]_{1+d})_m(T\text{-}Se_2)_n$ ferecrystals and misfit layer compounds, no indication for the presence of antiphase boundaries in the Sn1-*x*Bi*x*Se layer ($x = 0.4$) was found.[27,35,40,41] The peaks corresponding to the VSe_2 constituent can all be indexed to a hexagonal basal plane in agreement with the bulk 1T-structure[42] and the ferecrystalline

compounds ([SnSe]1.15)1(VSe2)*n*.24 Comparing the intensity ratio between the (110) peak of the VSe2 constituent and the (220) peak of the Sn1-*x*Bi*x*Se constituent a continuous decrease of the ratio as a function of the Bi-content is observed (0.80–0.43), which is expected assuming an electron density increase and hence a larger scattering power for the rocksalt-like constituent upon Sn-substitution by Bi. An interesting observation is the shift of the peak positions to lower angles for all VSe2 reflections (see Figure VIII. 5), even though the substitution is on the roc salt like constituent.

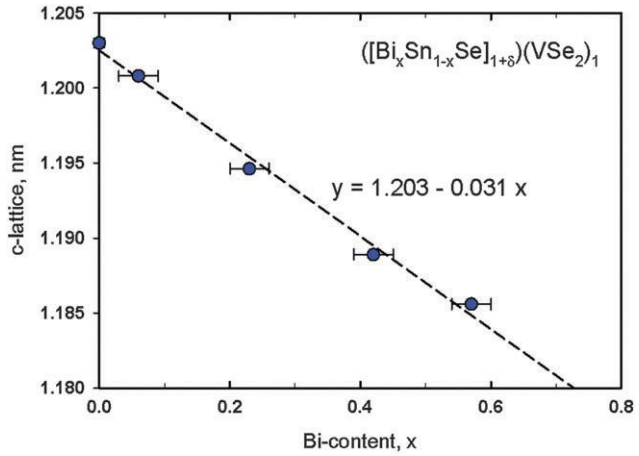

Figure VIII. 3 The *c*-axis lattice parameter as a function of Bi-content for ([Sn1−*x*Bi*x*Se]1+d)1(VSe2)1 compounds.

Table VIII. 1 Bismuth content (from EPMA) (*x*), *c*-axis lattice parameter, (Bi + Sn)/V-ratio (from EPMA), *a*-axis lattice parameters of the two constituents and calculated misfit parameter for ([Sn1−*x*Bi*x*Se]1+d)1(VSe2)1 compounds

Bi-content, x	c-axis lattice parameter, nm	(Bi + Sn)/V	a-axis lattice parameter ($Sn_{1-x}Bi_xSe$), nm	a-axis lattice parameter (VSe_2), nm	Misfit, 1 + d
0	1.203(1)	1.10	0.5935(2)	0.3414(2)	1.143
0.06(3)	1.2008(2)	1.20	0.6022(3)	0.3434(3)	1.127
0.23(2)	1.1946(1)	1.12	0.5999(2)	0.3456(2)	1.150
0.42(3)	1.1889(1)	1.26	0.5997(3)	0.3466(3)	1.157
0.57(3)	1.1856(1)	1.23	0.5996(2)	0.3475(2)	1.164

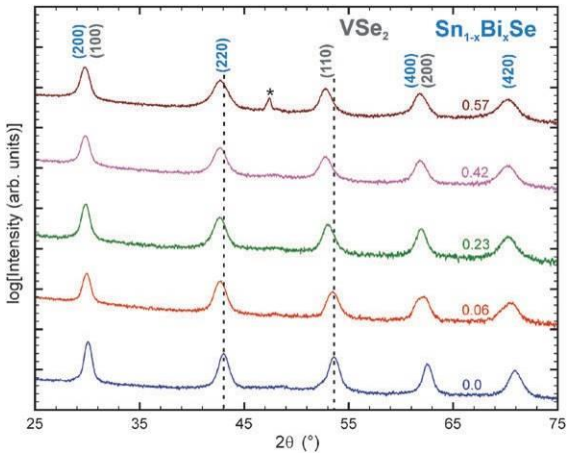

Figure VIII. 4 In-plane X-ray diff raction patterns of ([Sn1-*x*Bi*x*Se]1+d)1(VSe2)1 compounds with 0 r *x* r 0.57. The dashed vertical lines highlight the peak shift observed for the (110) reflection of the VSe_2 constituent and the (220) reflection on the rock salt constituent. The asterisk marks a stage peak.

In Figure VIII. 5 the area/formula unit (f.u.) for both constituents is plotted as a function of Bi-content. The area for the rocksalt like constituent increases abruptly on the addition of bismuth and then remains constant as it is further alloyed. Surprisingly, the area of the VSe2 constituent increases continuously although the atom substitution takes place in the other layer of the intergrowth compound. This observation might indicate a change in the electronic structure of the transition metal dichalcogenide layer due to charge transfer between the layers, which should correlate with the Bi-content. Due to the increase in area for dichalcogenide constituent the misshit parameter increases slightly as a function of the Bi-content, which is different from the end members of the misfit layer compound system ([MSe]1+d)1(NbSe2)1, where diff erent SnSe- and BiSe- based structures were

reported and the misfit decreases from 0.16 to 0.10.[34,35]

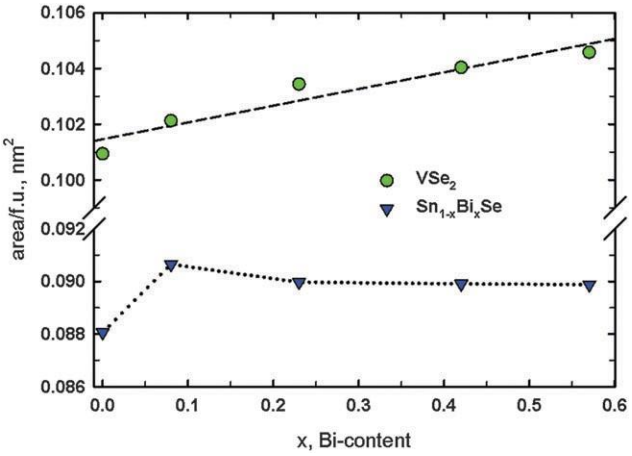

Figure VIII. 5 In-plane area/f.u. for both constituents of ([Sn1-*x*Bi*x*Se]1+d)1(VSe2)1 as a function of *x*.

Rietveld refinements of the specular X-ray diff raction paterns were conducted to gain some insight into the structural changes along the *c*-axis. A structural schematic and the refinement model are displayed in Figure VIII. 6a. Due to the limited number of reflections and the close spacing along the *c*-axis any attempt to split the atomic planes of the Bi, Sn and Se atoms 40 within the Sn1-*x*Bi*x*Se layer into three positions was unsuccessful. Hence, the Bi- and Sn-planes were constrained to the same position and for the compound with the highest Bi-content (*x* = 0.57) the lowest *R*-values were achieved by constraining all three atomic species to the same position (see ESI†). EPMA results were used as a starting point for the occupation and were refined at a later stage of the refinement essentially confirming the EPMA results for the Bi/Sn-ratio. Also the misfit between the constituents was very close to the misfit parameter calculated from the in-plane dimensions (see Table VIII. 1 and ESI†). The interplanar distances change systematically as a function of Bi-content within the intergrowth structure and are plotted in Figure

VIII. 6b. Most significantly, the puckering (Sn/Bi-Se) in the $Sn_{1-x}Bi_xSe$ layer decreases considerably upon Bi-doping and at the same time also the distance between the Se-planes within the rocksalt-like layer (Se–Se) increases leading in sum to a slight shrinkage of the layer thickness from 0.309 to 0.295 nm. As the puckering decreases, also the distance between the two constituents (Se–Sn/Bi) increases slightly. The drives, the system closer to an undistorted rock salt structure and would, in a simple picture, indicate a weaker interaction between the two layers. At the same time the interplanar distance between the V and Se planes within the VSe_2 constituent decreases continuously from 1.76 for x = 0t o 1.71 for x = 0.57. A similar decrease of the *c*/*a*-ratio was reported for nonstoichiometric and Li-intercalated VSe2, and was attributed to enhanced Coulomb repulsion in the V 3d-band due to electron donation from interstitial V or Li, respectively.[18,44]

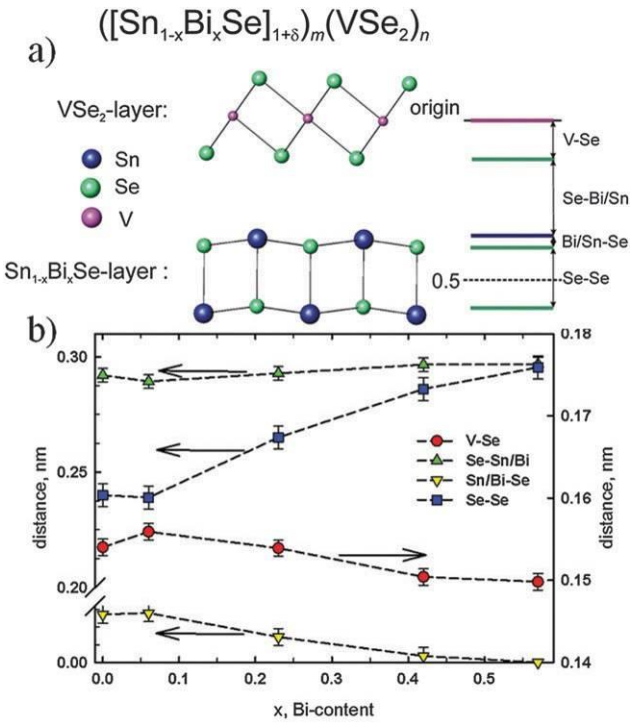

Figure VIII. 6 (a) Structural schematic and refinement model with the distances between the atomic planes along the *c*-direction of the ferecrystalline superlattice. (b) Change of the interplanar distances as a function of Bi-content from Rietveld refinements.

HAADF-STEM images are shown in Figure VIII. 7, where the bright double layers correspond to the Sn1-*x*Bi*x*Se constituent and the darker layers to the VSe2 constituent. Atomically abrupt inter- faces and the intended layering sequence are observed (Figure VIII. 7a). In Figure VIII. 7b, diff erent crystallographic orientations of the contituent layers can be identified confirming the presence of rotational disorder. In the Sn1-*x*Bi*x*Se constituent the observed contrasts arise from the crystallographic orientation and no sign for agglomeration of Bi-atoms in specific areas or anti- phase boundaries, as reported for BiSe based misfit layer compounds and ferecrystals,[27,35,40,41] was identified. The observed zone axes for both constituents are in agreement with the results from X-ray diff raction and confirm the presence of a rocksalt-like bilayer for Sn1-*x*Bi*x*Se with a homogeneous dis- tribution of

Sn and Bi atoms for the solid solution Sn0.6Bi0.4Se and the 1T-polytype (CdI2-type) with octahedral coordination of 20 the V-atoms in the VSe2-layer. An electron diff raction image of ([Sn0.6Bi0.4Se]1+d)1(VSe2)1 displayed in Figure VIII. S5 (ESI†) demon- strates the high degree of order along the *c*-direction and extensive streaking for (*hkl*) (with *h*, *k*, *l* a 0) reflections indicating extensive turbostratic disorder. For the Sn1-*x*Bi*x*Se even the slight puckering distortion consistent with Rietveld refinement results (Figure VIII. 6b) is evident in the (110) orientation. In one of the VSe2-layers an abrupt change of the crystal- lographic orientation indicating the polycrystalline nature of the intergrowth compounds within the *ab*-plane can be observed.

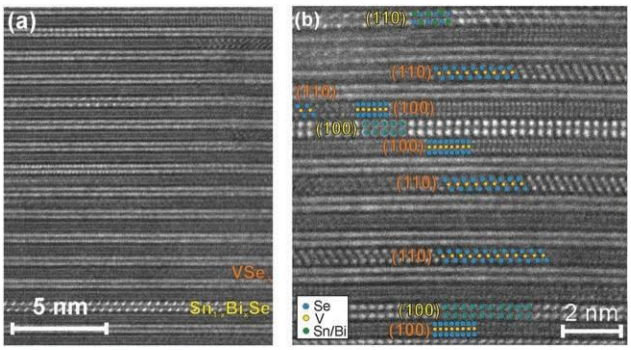

Figure VIII. 7 STEM images of ([Sn0.6Bi0.4Se]1+d)1(VSe2)1 showing (a) an overview of the sample along the *c*-direction, and (b) distinct crystallographic orientations in diff erent layers highlighting the rotational disorder.

In general all structural data clearly demonstrate that the alloy ($[Sn_{1-x}Bi_xSe]_{1+d}$)(VSe_2) with with 0 r *x* r 0.6 were successfully synthesized and that increasing the Bi-content results in a continuous change of the structure. Interestingly, not only the $Sn_{1-x}Bi_xSe$ layers, where the substitution takes place, but also the adjacent VSe_2 layers are affected, which is similar to the changes observed in the bulk structure on the both self- and Li- intercalation. In both cases the

presence of interstitial atoms results in electron donation into the V 3d-band, which causes a drastic reduction of the charge density wave transition. These observations are corroborated by theoretical calculations demonstrating the charge density wave instability is already suppressed by a slight decrease in the *c*/*a*-ratio of $VSe_{2.43}$.

VIII.4.1. Electrical Properties

The temperature dependent electrical resistivities and Hall coeffi cients of the ([Sn1-*x*Bi*x*Se]1+d)1(VSe2)1 compounds with $0 \leq x \leq 0.66$ are displayed in Figure VIII. 8 and 9, and reveal a significant alteration as a function of the Bi-content. The electrical resistivities of the compounds at or below $x = 0.2$ exhibit a resistivity anomaly with a sharp increase in resistivity around 100 K similar to the CDW-anomaly observed in ([SnSe]1.15)1(VSe2)1.[25] Above $x = 0.2$ the resistivity still increases, but there are changes in magnitude and shape which are dependent on the Bi-content. The charge could also be induced by structural changes and especially for higher doping levels a pseudo charge density wave state without long range order could be present.[45] A small amount of 6% of Bi enhances the anomaly, causing a factor of 3 increase in resistivity at the transition compared to about a factor of 2 change for the unalloyed $([SnSe]_{1.15})_1(VSe_2)_1$ compounds, which results in a shift of the charge density wave transition temperature[23, 24] increasing the Bi-content has no considerable effect on the transition temperature. The magnitude of the resistivity at room temperature first increases until x = 0.55 and then decreases again

revealing a complex trend upon increased Bi-substitution, which does not follow the expected behavior for an increased filling of the V 3d-band.

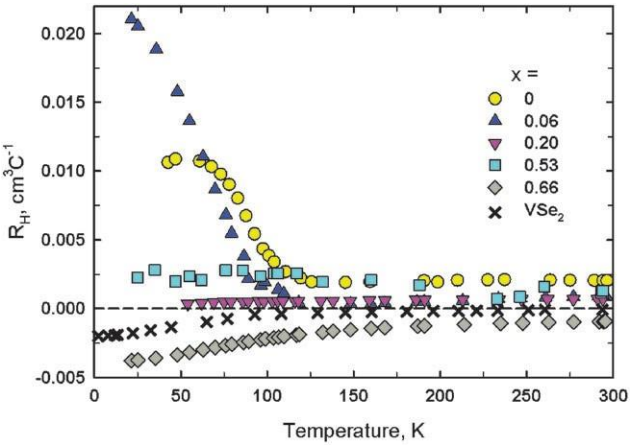

Figure VIII. 8 Resistivity of ([Sn1−*x*Bi*x*Se]1.15)1(VSe2)1 compounds as function of temperature. The inset displays the temperature dependence of the residual resistivity ratio (RRR).

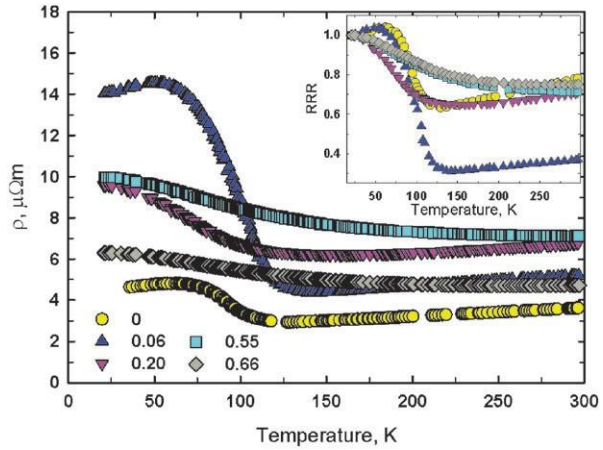

Figure VIII. 9 Hall coefficient, R_H, of ([Sn1−*x*Bi*x*Se]1.15)1(VSe2)1 as function of temperature. For comparison the Hall coefficient for bulk 1T-VSe2 is plotted.[6]

The changes in the Hall coefficients as a function of temperature and composition further highlight the significant changes observed in transport properties (see Figure VIII. 9). Only the sample with a Bi-content of 0.06 shows the rapid increase in the Hall coefficient found for ([SnSe]1.15)*m*(VSe2)1.[23] The number of

carriers/V-atom that are localized as the compound undergoes an apparent CDW transition increases dramatically from 0.5 for $x = 0$ to 3.7 carriers per V for $x = 0.06$. Assuming that only the VSe_2 layer is involved in the charge density wave transition, this change can only be explained by a shift in the Fermi-level due to charge transfer similar to alkali-metal intercalation.[46] At higher Bi-contents of 0.20 and 0.55, an almost temperature indepen- dent behavior of the Hall coeffi cient is observed and for a Bi content of 0.66 a change in sign from positive to negative is observed. Bulk VSe_2 also exhibits a negative Hall coefficient[6] and the temperature dependence of bulk VSe_2 is very similar to the compound with a Bi-content of 0.66 (see Figure VIII. 9). A similar change in the temperature dependence of the Hall coeffi cient results from increasing the thickness of the VSe_2 constituent, which was attributed to the loss of quasi 2-dimensionality for the dichalcogenide layer.[24] This suggests that Bi-doping might induce a stronger coupling between the VSe_2 layers through the $Sn_{1-x}Bi_xSe$ layer.

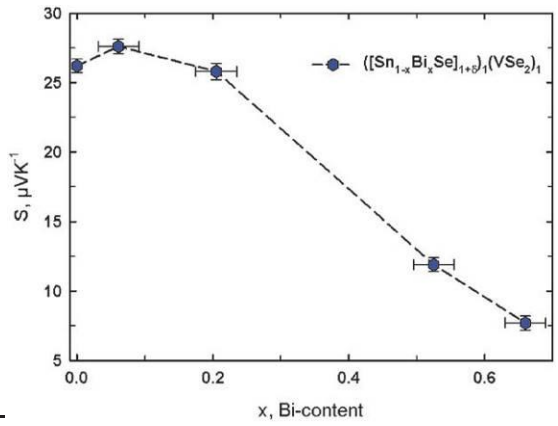

Figure VIII. 10 Seebeck coefficient, s, at room temperature for $([SnSe]_{1.15})_m(VSe_2)_1$ compounds as function of x

The Seebeck coefficient (*S*) at room temperature is positive for all samples in contrast to the change in sign observed for the Hall coeffi cient for a Bi-content greater than 0.55 (Figure VIII. 10). This clearly demonstrates contributions of both types of car- riers, holes and electrons, to the transport properties in the alloyed samples. The change of sign in the Hall-coeffi cient while *S* remains positive implies the presence of heavy holes and light electrons for ([Sn0.44Bi0.66Se]1.15)1(VSe2)1. The continuous decrease of the Seebeck coeffi cient as a function of Bi- content points toward an increase of the amount of light electrons, which is consistent with increasing carrier concentration and mobility in Bi-doped SnS thin films. Doping by 6–8% of Bi in SnS films causes an increase in carrier concentration by two to three orders of magnitude (to 10^{18} cm^{-3}) and a compar- ably high mobility of the electrons of B500 $cm^2V^{-1}s^{-1}$. [47]

The undoped ferecrystalline $([SnSe]_{1.15})_1(VSe_2)_1$ compound exhibits a hole concentration of 3×10^{21} cm^{-3} and a carrier mobility of 2 cm^2 V^{-1} s^{-1}. Considering these values the influence of minority charge carriers from the $Sn_{1-x}Bi_xSe$ constituent cannot be neglected for alloys with higher Bi-content.

Both, structural and electrical properties of the alloyed ([Sn1-*x*Bi*x*Se]1.15)1(VSe2)1 compounds, reveal a considerable influence on both layers in the intergrowth compounds upon Bi doping and suggest charge transfer between the constituents as well as the presence of two types of charge carriers at higher Bi-contents. The initial increase of the Seebeck coeffi cient, which depends on the first derivative of the

density of states as a function of energy at the Fermi level as well as the enhancement of the CDW transition observed for the compound with $x = 0.06$ are indications for the presence of charge transfer, and therefore the potential for modulation doping in ferecrystalline compounds. One way to explain the p-type con- duction of the initial $([SnSe]_{1.15})_1(VSe_2)_1$ is considering a split- ting of the V 3d-band similar to trigonal prismatically coordinated 2*H*-$NbSe_2$ and 2*H*-$TaSe_2$[48] and electron transfer from the SnSe-layer into the initially half-filled conduction band of the transition metal dichalcogenide layer. The density of state of VSe_2 was reported to closely resemble an electronic structure expected for trigonal prismatic coordination due to the abnormally large *c*/*a*-ratio.[43] Hence a similar band splitting could be induced by small amounts of charge transfer or reduced dimensionality, which is well known to influence the band structure of transition metal dichalcogenides.[1] Doping by 6% of Bi can cause a small shift in the Fermi-level towards a maximum in the density of states, which explains the significant increase in the number of carriers involved in the charge density wave transition (7 times more for $x = 0.06$ compared to $x = 0$), in which most likely only the VSe_2-layer participates. Further increasing the Bi-content results in significant changes in the electrical properties, with the loss of the abrupt change in the Hall coefficient with temperature. Above $x = 0.55$ clearly two types of carriers, light electrons steming from the $Sn_{1-x}Bi_xSe$ layer and heavy holes from the VSe_2-layer, are present at room temperature. However, the kink at 100 K in the temperature dependent Hall coefficient for the compound with $x = 0.66$ may be still due to a charge density wave transition, as it closely resembles the behavior reported

for the bulk compound (see Figure VIII. 9). Theoretical studies would be extremely helpful to unravel and understand the observed complex behavior in the ferecrystalline alloys $([Sn_{1-x}Bi_xSe]_{1.15})_1(VSe_2)_1$.

VIII.5. Conclusion

Alloys of $([Sn_{1-x}Bi_xSe]_{1.15})_1(VSe_2)_1$ compounds with $0 \leq x \leq 0.66$ were synthesized using the modulated elemental reactant technique. The *c*-axis lattice parameter decreases slightly upon Bi-substitution, whereas the *a*-axis lattice parameter of the VSe_2 constituent continuously increases. Together with structural changes investigated by Rietveld refinement, this observation clearly points toward changes in the electronic structure of both constituents of the intergrowth compounds. Indeed, a very complex scenario is observed for the electrical properties of these alloys as a function of the Bi-content. A small amount of Bi causes a dramatic increase in the charge density wave transition indicating a shift of the Fermi level toward a max- imum in the density of states. However, a further increase of the Bi-content results in a change of the electrical transport. Above $x = 0.55$ the diff erent signs of Hall and Seebeck coeffi- cient demonstrate the presence of two diff erent carrier types, light electrons and heavy holes. This study indicates that modulation doping within these ferecrystalline intergrowths opens a pathway for controlled tuning of properties such as a charge density wave transition, which is crucial for any future applications.

CHAPTER IX

THE SYNTHESIS, STRUCTURE, AND ELECTRICAL CHARACTERIZATION OF $(SnSe)_{1.2}TiSe_2$

IX.1. Authorship Statement

In the following chapters (IX-XII). I used the electron microscope to revealed new information about systems that were not predicted by bulk characterization methods. In the following chapter (IX) I found the first evidence of long range order in ferecrystals which was later found to be related to the close A and B lattice parameters of SnSe and TiSe2. The primary author of this manuscript is Devin Merrill. The paper was published in The European Journal of Inorganic Chemistry in 2015, issue 1, pages 83-91.

IX.2. Introduction

Over the last two decades the search for compounds with enhanced thermoelectric performance was motivated to a large degree by a paper by Hicks and Dresselhaus that predicted enhanced power factors for structures of reduced dimensionality and the phonon glass electron crystal concept introduced by Slack.[1-3] The power factor, $\alpha^2\sigma$, where α is the Seebeck coefficient and σ is the electrical conductivity, is typically optimized as a function of carrier concentration through doping, to give the largest thermoelectric figure or merit, zT. Most thermoelectric materials are semiconductors resulting in an optimized carrier concentration of typically around 10^{19} carriers cm^{-3}. While not directly conforming to the original idea put forth by Hicks, there are a number of layered materials that have unusually high Seebeck coefficients with

higher carrier concentrations ~10^{20} - 10^{21} carriers cm^{-3}. These include the layered cobalt oxides, Na_xCoO_2 and the misfit compound $[Ca_2\ CoO_3\ ]_{0.62}[CoO_2]$, and a number of compounds containing titanium dichalcogenide layers, $(MS)_{1+x}(TiS_2)_2$ (M.Pb, Bi, Sn), $Ti_{1+x}Se_2$, and Cu_xTiS_2.[4-6]

Titanium dichalcogenide TiX_2 compounds themselves exhibit interesting transport properties. $TiTe_2$ is generally agreed to be semimetallic, TiS_2 is generally agreed to be semiconducting and $TiSe_2$, while debated over the years, is thought to be a small bandgap semiconductor.[7-9] TiS_2 and $TiSe_2$ have anomalously large Seebeck coefficients, which has been attributed to an unusually large phonon drag effect.[10] While the binary compounds have thermal conductivities that are too large for them to be effective thermoelectric materials, recent reports have shown that inserting cations or incorporating structural layers into the van der Waal gaps reduces thermal conductivity while preserving the unusual electrical properties.[5,6,11,12] For the misfit layered TiS_2 containing compounds, the group of Koumoto has shown that changing the identity of the intercalated rock salt structure changes the amount of charge transfer.[5] There have only been three reports of misfit layered compounds containing $TiSe_2$. Crystalline $[(PbSe)_{1.16}]_1(TiSe_2)_2$ was reported to be a superconducting metal below 2.3 K by Giang, et al. Turbostratically disordered $[(PbSe)_{1.18}]_1(TiSe_2)_2$ and $[(PbSe)_{1.18}]_1(TiSe_2)_1$ were reported by Moore, et. al. to have a lower room temperature resistivity and a Seebeck coefficient that was almost double that of the crystalline analog reported previously.[13-15] The synthesis approach used by Moore, et al. opens opportunities to prepare both new compounds and different polymorphs of existing compounds within the $TiSe_2$ containing family of compounds.[14,15] Turbostratic disorder, a common feature of compounds

prepared using this approach, has been shown to result in remarkably low lattice thermal conductivities.[16,17] Since in the crystalline misfit sulfides reported by Wan the SnS containing compound had better thermoelectric performance than the lead analog, we were motivated to synthesize $(SnSe)_{1.2}TiSe_2$.[5] Here we present the synthesis of this new compound, its structure, and its electrical transport properties. The power factor was found to be almost a factor of two larger than reported for $(PbSe)_{1.18}TiSe_2$.[14] Reducing the carrier concentration, through doping of the SnSe layer or by incorporating a larger band gap partner for $TiSe_2$, are suggested as avenues to further increase the performance of these interesting materials.

IX.3. Experimental Section

Designed precursors containing modulated elemental reactants were synthesized in a custom built high vacuum system at pressures below 5×10^{-7} torr. Tin and titanium metal were deposited using electron beam guns and Se was deposited using an effusion cell, with rates maintained between 0.2-0.3 Å/s at the substrate and monitored by quartz crystal microbalances. Elemental layers were deposited in calibrated thicknesses in the sequence of Ti, Se, Sn, Se and repeated 43 times to give total film thickness of approximately 50 nm. Films were deposited on Si and fused silica substrates for structural and electrical measurements, respectively. Samples were annealed in a nitrogen atmosphere ($[O_2],[H_2O] \leq 0.7$ ppm) for 30 minutes at different temperatures to determine the optimum formation conditions.

X-ray reflectivity and diffraction measurements were conducted on a Bruker D8 Discover (Cu Kα radiation) and used to measure total film thickness and as-deposited repeat unit thickness, as well as to follow the self-assembly of the precursor into the

superlattice. Refinement of the atomic planes along the c axis was performed using the Rietveld method and the Full Prof Suite software package.[18] Composition was monitored with electron probe microanalysis (EPMA) using a Cameca SX50 to follow O, Se, Sn, and Ti content using a process described elsewhere.[19] Samples were cleaved in vacuum for XPS analysis by epoxying a post to the sample surface and knocking the post off in the sample introduction chamber. TEM cross-section Samples were prepared on a FEI Helios 600 Dual-Beam FIB with a Sidewinder ion column using methods developed by Schaffer et al .[40] High angle annular dark field scanning transmission electron microscopy (HAADF-STEM) images were obtained using an FEI Titan 80-300 TEM at 300keV. Temperature dependent resistivity and Hall effect measurements were performed in the van der Pauw geometry on cross-shaped samples deposited on quartz substrates using shadow masks. Lab built measurement systems were used for electrical characterization. Low temperature measurements were performed under high vacuum conditions (University of Oregon) and high temperature measurements were conducted in a 100mbar nitrogen environment (Fraunhofer Institute for Physical Measurement Techniques).

IX.4. Results and Discussion

The synthetic approach used to prepare the title compound requires that precursors are prepared which contain constituent layers with compositions close to the stoichiometry of the desired components to induce them to nucleate, and that the total amount of material deposited in each constituent layer is close to that required to form a structural unit of the desired constituent.[20-22] The deposition parameters for $TiSe_2$ that result in a one to two Ti:Se ratio and the proper thickness to form a single Se-Ti-Se

trilayer had been established previously, and were used as a starting point for the calibration.[14,15] The misfit parameter δ was initially estimated to be 0.20 using the analogous sulfide misfit layer compound[23] and was used as a target Sn:Ti ratio until the true value could be determined experimentally from the in-plane packing density calculated from the constituent lattice parameters. In order to establish the necessary deposition parameters to get the correct stoichiometric ratio of Sn to Ti, a series of films were created in which the thickness of the elemental Sn-Se precursor bilayer was varied while the previously determined $TiSe_2$ parameters were maintained. The resulting films were then analyzed with EPMA to determine the elemental composition.[19] The Sn:Se ratio was next optimized by varying the thickness of the elemental Se layer while maintaining the Sn parameter and checking composition with EPMA. Finally, while maintaining established elemental ratios, the thickness of the repeating unit was varied to be just slightly thicker than the c-lattice parameter of the target compound, which was determined by least squares refinement of superlattice diffraction observed in some of the annealed samples from the initial depositions. Samples prepared using the calibrated deposition parameters had the desired Sn:Ti ratio for the targeted misfit parameter. The Ti:Se and Sn:Se ratios were calibrated to be 3-5% selenium rich compared to the idealized 1:2 and 1:1 ratios respectively, to compensate for Se loss during the annealing process.

IX.4.1. Structural Analysis

The initial sets of samples were annealed at 350°C, the temperature determined to be optimal for the formation of the Pb analog.[14,15] Once precursors with correct composition and repeat unit thickness that formed the title compound on annealing at

350°C were prepared, 00*l* diffraction patterns were taken as a function of annealing temperature to probe the formation of the superlattice as a function of annealing conditions (Figure IX.1). The as-deposited precursor contains weak and broad low angle Bragg reflections due to the periodic electron density in the films. Intense, sharp peaks are not observed due to the composition gradients that likely exist across the mostly amorphous interfaces and local variations in the thickness of the elemental layers. As the annealing temperature increased, the superlattice reflections intensify and a clear decrease in the full width at half maximum (FWHM) of the Bragg peaks is observed as the temperature is increased from 200-350°C, which is consistent with the formation of the targeted compound. Maximum intensities are obtained for the 350°C annealed sample. A shoulder on the 004 peak begins to appear at 400°C, suggesting the growth of another phase, probably SnSe. At T > 400°C, the shoulder intensifies, unidentified phases grow in, and the diffraction peaks from the superlattice structure decay suggesting the decomposition of the target structure. From this study, 350° C was chosen as an optimal annealing temperature.

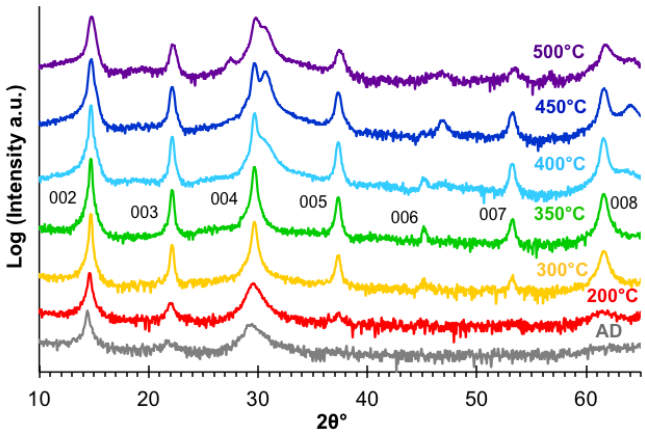

Figure IX.1: 00*l* Diffraction as a function of annealing temperature (offset for clarity). Observed superlattice maxima are indexed for the pattern at the optimum temperature (350°C)

During the calibration process, annealed films with a surprisingly large range of composition and precursor repeat unit thicknesses (summarized in Table IX.1) had diffraction patterns consistent with the target superlattice structure. The ratio of Sn to Ti varied between 1.0 and 1.39 and the thickness of the repeating unit in the precursor varied between 12.1 and 13.2 Å. The c-parameters varied little (12.04 Å to 12.08 Å), suggesting that there is a defined structure. One possible explanation is the occurrence of conformal inclusions, regions where one layer substitutes for the other, observed previously in MER synthesized films.[24] These conformal inclusions allow composition to be varied without a disruption of the long-range superlattice structure of the material. In an attempt to characterize the relative amount of the target product formed, the defect level of the structure and the variability of the layer stacking, the intensity of the 003 reflection (counts per seconds, CPS), the FWHM of the 003 reflection and the ratio of the 003 to 002 reflection intensities were tabulated (Table IX.1). The films can be sorted into two distinct groups. The first (Samples A-E, bold, Table IX.1) contains films that show high intensity, low FWHM, and a small range of 003/002 intensity ratios, suggesting the formation of a similar product in each case. Samples in the second group (Samples F-M, Table IX.1) have one or more of the following features: low intensity, larger FWHM, more variability in the ratio of 003/002 reflection intensities, and a wider range of annealed c-parameters. Since sample thickness and the sample area illuminated were held constant, the low intensity results from less superlattice material in the sample volume. The increase in the FWHM is likely caused by higher defect concentrations and/or smaller grain size. The larger range of the ratio of the 003 and 002 reflections is likely caused by different concentrations of volume defects,

regions where one layer substitutes for the other. It is clear that the formation of ferecrystalline products from the amorphous precursors is surprisingly robust and the details of the resulting defects formed require further investigation. For the remainder of this paper, however, we will focus our attention on the samples in group 1.

EPMA data was collected as a function of annealing temperature to determine if changes in the composition of the film with annealing time or temperature were responsible for the decrease in superlattice diffraction above 350°C. The atomic percent of oxygen increased from approximately 3% for as-deposited films, to 4-5% for films annealed at 350°C despite annealing in a nitrogen atmosphere with ~0.5 ppm oxygen. The oxygen signal in the as-deposited sample is in part due to the native oxide layer on the Si substrate. Additional oxygen in the as-deposited sample could come from incorporation during the deposition process or from surface oxidation after removal from the deposition chamber. To distinguish between surface oxidation and a distribution of oxygen throughout the sample, samples were cleaved in the XPS vacuum chamber and a comparison of the exfoliated regions to original surface regions was performed. The resulting spectra show that the original surface of the film had a strong oxygen signal, while the freshly exposed interior layers displayed no observable oxygen signal, suggesting that oxygen is not incorporated in the sample during deposition and surface oxidation is the major factor in the increase in oxygen level during annealing. Further support for surface oxidation comes from HAADF-STEM experiments, where 2-3 bilayers of SnSe could be identified adjacent to one another at the surface of the film, suggesting that $TiSe_2$ is oxidized in the uppermost unit cells, forming independent TiO_x and SnSe layers not associated with the intergrowth compound. At temperatures above

350°C, the oxygen content of the films increased dramatically to 15-20 atomic percent after annealing at 400°C, even though the annealing was done in an inert atmosphere, suggesting that there is sufficient energy at this temperature to overcome any kinetic barrier towards oxidation. The decomposition of $(SnSe)_{1+\delta}TiSe_2$ is therefore in part due to it's instability with respect to oxidation.

Table IX.1: Table of samples synthesized during the calibration process that displayed superlattice diffraction maxima. Composition is reported from EPMA and represents global film composition. The composition of the superstructure is given by the in-plane packing density of each constituent (calculated from in-plane lattice parameters below). Samples given in bold (A-E) are considered representative of the title compound.

Sample	Precursor c (Å)	Sn/Ti	Annealed c (Å)	FWHM (003)	Normalized Intensity (CPS-003)	003/002 Intensity Ratio
A	**12.1(1)**	**1.25(1)**	**12.04(1)**	**0.24**	**82.2**	**0.067**
B	**12.1(1)**	**1.20(1)**	**12.04(1)**	**0.25**	**61.3**	**0.070**
C	**12.4(1)**	**1.16(1)**	**12.05(1)**	**0.24**	**100.0**	**0.062**
D	**12.1(1)**	**1.25(1)**	**12.04(1)**	**0.26**	**80.1**	**0.064**
E	**13.2(1)**	**1.14(1)**	**12.04(1)**	**0.26**	**81.8**	**0.059**
F	12.5(1)	1.00(1)	12.06(1)	0.28	22.5	0.085
G	12.2(1)	1.21(1)	12.06(1)	0.27	17.2	0.145
H	12.1(1)	1.23(1)	12.04(1)	0.27	46.8	0.075
I	12.6(1)	1.13(1)	12.05(1)	0.38	16.8	0.166
J	12.7(1)	1.33(1)	12.05(1)	0.29	6.4	0.202
K	12.8(1)	1.15(1)	12.08(1)	0.78	0.9	0.088
L	12.3(1)	1.21(1)	12.04(1)	0.28	24.0	0.069
M	12.4(1)	1.39(1)	12.061(1)	0.68	13.1	0.050

A high quality θ/2θ diffraction scan of sample can be seen in Figure IX.2a. The films are highly textured, with the c-axis normal to the substrate, so diffraction data taken in the conventional θ/2θ geometry show only 00*l* diffraction maxima. The presence of Kiessig fringes (the high frequency oscillations between Bragg reflections) to relatively high two theta values suggests that the air/film and film/substrate interfaces are smooth and parallel. The Parratt relationship (inset Figure IX.2b) describes the extent to which these interfaces are parallel and smooth, where Δt is the film roughness, θ_c is the critical

angle, and θ_i represents the angle at which fringes can no longer be resolved.[25] Based off the pattern shown in Figure IX.2b, θ_i was estimated to be 7.5°, leading to a calculated roughness of 0.9 Å. This suggests that the top and bottom interfaces are very parallel and near atomically smooth. Further insight about the evolution of the film during annealing can be gained from the number of fringes appearing between Bragg reflections. In theory, the number of fringes (n_f) between Bragg reflections is $n_f = n_{r.u.} - 2$, where $n_{r.u}$, is the number of repeating units present in the film. In the pattern in Figure IX.2 $n_f = 39$, and in the designed precursor $n_{r.u.} = 43$, yielding $n_f = n_{r.u.} - 4$. This indicates that two of the deposited repeating units were lost, probably due to surface oxidation as suggested by the EPMA and XPS results, during the annealing process.

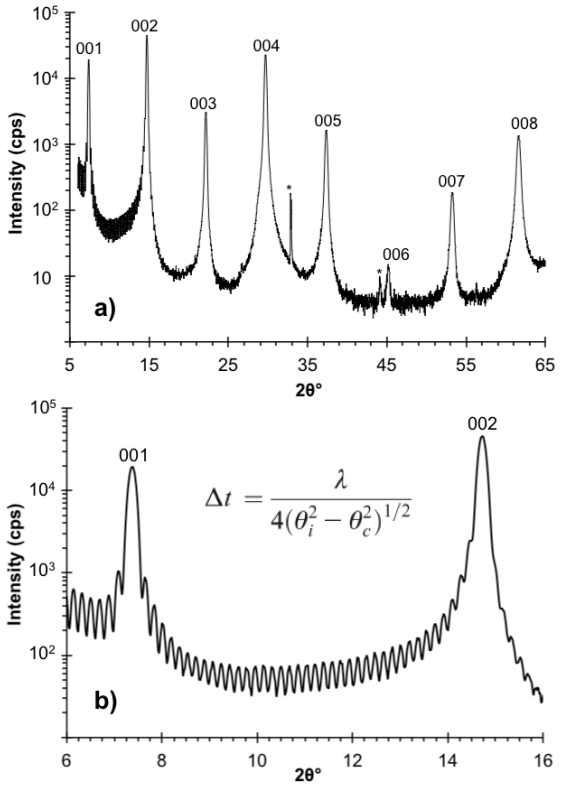

Figure IX.2: A diffraction pattern of sample A **(a)** displaying Kiessig fringes to more than 15° 2θ **(b)**. The Parratt relationship is inset. Superlattice maxima are indexed, * denotes substrate or stage peaks.

Cross-sectional HAADF-STEM data was obtained on sample A to probe the structure and the frequency of defects. The lower magnification image shown in Figure IX.3a clearly shows the alternating SnSe (bright) and $TiSe_2$ (dark) layers throughout the film, confirming the formation of the superlattice unit cell consisting of 1 structural unit of each constituent. Interestingly, there are several regions of higher order within the film that have not been observed previously in compounds synthesized by modulated elemental reactants. The bulk structures for each constituent compound can be seen in Figure IX.3b, and a higher magnification HAADF-STEM image of a particularly ordered region in Figure IX.3c. $TiSe_2$, like other dichalcogenides, consists of Se-Ti-Se trilayers with a van der Waal gap separating adjacent layers, The Se-Ti-Se layers are stacked in an a-b-c pattern resulting in Ti being octahedrally coordinated to 6 Se atoms. The Se-Ti-Se layers stack in an A-A stacking sequence, with the trilayers identically aligned in each layer, resulting in the 1T polytype.[26] The 110 zone axes observed in the STEM image shows that the Ti atoms are octahedrally coordinated.α-SnSe, the thermodynamically stable phase at room temperature and ambient pressure, crystallizes in the GeS structure, which is a distorted variant of the cubic rock salt structure.[27] In previously reported SnSe containing misfit layer compounds, SnSe is significantly distorted from the bulk structure, and was reported to have a = b, or a square basal-plane structure for single bilayers of SnSe.[20-22,28,29] In Figure IX.3c, both 100 and 110 zone axes are clearly visible, but the extent of the distortion cannot be determined from the images. The indices assigned in Figure IX.3c are consistent with the square basal plane SnSe and 1T-$TiSe_2$ structures reported for the constituents in previously reported misfit layer

compounds.[14,15,20-22,28,29] The images clearly confirm the independent constituent structures of the intergrowth compound.

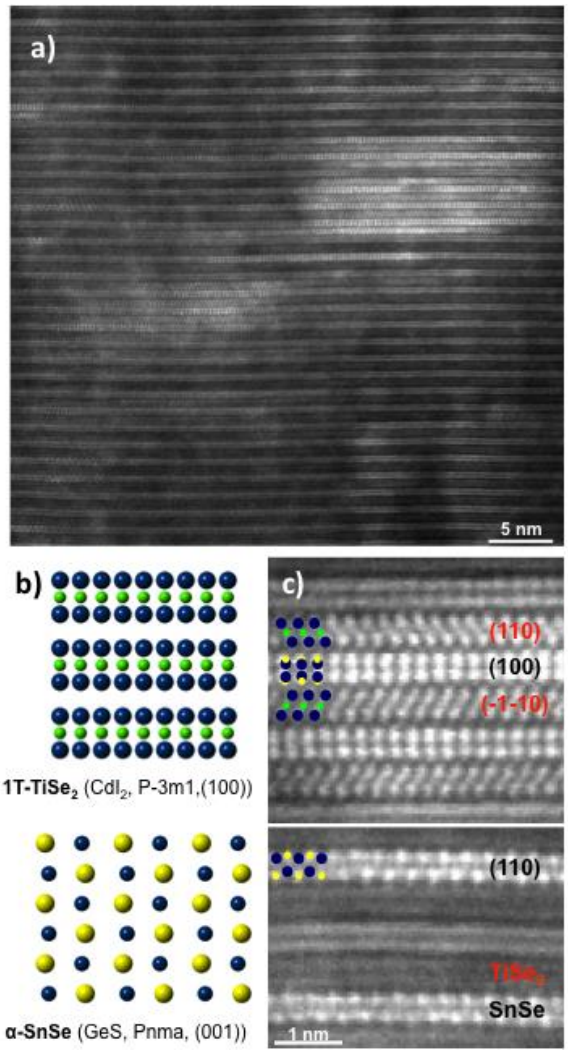

Figure IX.3: (a) Low magnification HAADF-STEM images displaying alternating layers of SnSe and $TiSe_2$ throughout the entirety of the film. **(b)** Bulk structures for the constituent compounds. **(c)** High magnification HAADF-STEM displaying two unique lattices intergrown. Crystal faces and structure representations are specified for hexagonal $TiSe_2$ and square-basal SnSe, as seen with other ferecrystal systems.

The presence of clearly defined crystallographic planes offers the opportunity to calculate the in-plane lattice parameters from the HAADF-STEM images. Line profiles in the hk0 direction were analyzed to determine the distance between atomic columns, from which the lattice parameters were calculated for each constituent, assuming a square

basal plane for SnSe and the CdI_2 structure for $TiSe_2$. The lattice parameters for both SnSe (a = 6.2(1)Å) and TiSe2 (a = 3.7(1) Å) are both within the error bars of those reported for other ferecrystalline and misfit layered compounds containing SnSe (generally a = 6.0 (1) Å)[20-22,28,29] or $TiSe_2$ (a = 3.55(5) Å).[13-15] The calculated misfit parameter, from our STEM derived lattice parameters was found to be 0.2, which is the same value previously reported for the analogous sulfide compound.[23]

Further details of the structure were obtained by refining the 00*l* diffraction pattern using the Rietveld method to determine the location of atomic planes in the c direction, as shown in Figure IX.4 and tabulated refinement parameters can bee seen in Table IX.2.[18] The refinement converged to a lattice parameter c = 12.050(1) Å, with residuals, R_F and R_B of 0.0159 and 0.00781 respectively. Further details of the results are tabulated and a depiction of the resulting model and the calculated distortions are given in Figure IX.4. Within the SnSe layer, the Sn and Se atoms are not in the same plane. This puckering of what would be a single 100 plane in an ideal rock salt structure is nearly double that observed in the PbSe layer in the $(PbSe)_{1.16}TiSe_2$ ferecrystal reported previously.[14] The 27 pm distortion is larger than that found in $[(SnSe)_{1.15}]_1[VSe_2]_1$ (19(3) pm) Sn-Se but smaller than that found in $[(SnSe)_{1.06}]_1[MoSe_2]_1$, (40(1)pm).[21,28] The refined distance between the Ti and Se planes in the $TiSe_2$ constituent (1.54Å) is significantly larger than the 1.45 Å reported for the analogous Pb compound.[14] The distance between the Se plane in $TiSe_2$ and the puckered Sn plane in the Sn-Se layers is 2.98 Å compared to 3.13 Å for the analogous distance reported for $(PbSe)_{1.16}TiSe_2$.[14] The model and the refined distances are all consistent with the conclusions drawn from the STEM images in Figure IX.3.

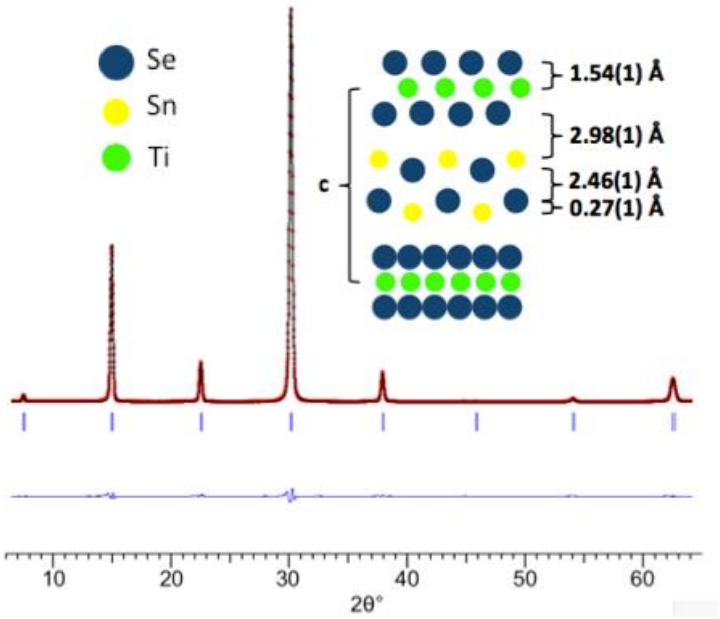

Figure IX.4: Rietveld refinement of sample A. The red dots represent the measured pattern, the black line the modeled intensity, the blue line the difference between experimental and calculated intenstity, and the blue ticks indicate the Bragg positions (only 00l). Spacings between interatomic planes in the c direction are also given.

IX.4.2. Electrical Characterization

Table IX.3 contains the room temperature transport data for both samples A and B studied here, and a summary of prior published values for both $TiSe_2$ and TiS_2 containing misfit layered compounds. The magnitude of the conductivity of samples A and B is consistent with that of a low conductivity metal, a semimetal or a heavily doped semiconductor. The magnitude is slightly higher than prior reported values for $TiSe_2$ containing misfit layer compounds and ferecrystals[13-15] but smaller by a factor of 3 than the values reported for TiS_2 containing misfit layer compounds.[5,30] In these prior reports, it was suggested that the TiX_2 layers dominate the electrical properties as substitution of Sn for isoelectronic Pb did not significantly alter the electrical properties.

Table IX.2: Refinement parameters for interatomic plane spacing along the c-axis associated with the fit plotted in Figure IX.4.

Compound Parameters	
Composition from refinement	$(SnSe)_{1.14}TiSe_2$
Radiation	Bruker D8, Cu
2θ range (degrees)	$6 \leq 2\theta \leq 65$
c (Å)	12.050(1)
Reflections in refinement	16
Number of variables	13
$R_F = \Sigma \mid F_o - F_c \mid / \Sigma F_o$	0.0160
$R_I = \Sigma \mid I_o - I_c \mid / \Sigma I_o$	0.0079
$R_{wP} = [\Sigma w_i \mid y_{oi} -$	0.0826
$R_P = \Sigma \mid y_{oi} - y_{ci} \mid / \Sigma \mid y_{oi} \mid$	0.0403
$R_e = [(N-P+C)/(\Sigma w_i y^2_{oi})]^{1/2}$	0.0186
$\chi^2 = (R_{wP}/R_e)^2$	19.7
Atom parameters	
Ti in 1a(0), B_{eq} (B_{iso})	
Occ.	1.0
Se1 in 2c (z), z	0.1268(1)
Occ.	1.0
Sn in 2c (z), z	0.3754(2)
Occ.	1.14(1)
Se2 in 2c (z), z	0.3977(3)
Occ.	1.14(1)

The resistivity as a function of temperature for samples A and B are shown in Figure IX.5, along with the isoelectronic $(PbSe)_{1.16}TiSe_2$ analog. The slight difference in resistivity between heating and cooling in the high temperature data for sample A is a consequence of surface oxidation of the top layers due to prolonged exposure to elevated temperatures, resulting in a slight decrease in the conducting film thickness. The resistivity shows relatively little temperature dependence, with the overall magnitude of the resistivity changing by less than a factor of two from 20 K to 295K, with a slight upturn at low temperatures. This change in the resistivity with temperature is a factor of 12 less than reported for $(PbSe)_{1.16}(TiSe_2)_2$ by Giang et. al,[13] and a factor of 5 and 10 less than that of $(PbS)_{1.16}TiS_2$ and $(SnS)_{1.20}TiS_2$ reported by Wiegers[30] respectively. The smaller -magnitude of the temperature dependence of the resistivity has been attributed to the turbostratic disorder observed in compounds synthesized from modulated elemental

reactants. The turbostratic disorder results in a very different phonon distribution and very low cross plane lattice thermal conductivities.[16,17] The room temperature electrical resistivity of $(SnSe)_{1.2}TiSe_2$ is a factor of two smaller than that reported for single crystals of $(PbSe)_{1.16}(TiSe_2)_2$,[13] suggesting that the decreased temperature dependence is not a result of a high residual resistivity, but rather due to less phonon scattering at higher temperatures. The upturn at low temperatures, found in all $TiSe_2$ containing intergrowths with significant rotational disorder between layers is thought to result from electron-electron correlations leading to weak localization.[33]

Table IX.3: Electrical properties of TiX_2 based compounds are shown. Those given in bold are compounds synthesized from modulated elemental reactants.

Material	σ_{ab} (S/cm)	n_e ($10^{21}cm^{-3}$)	α_{ab} ($\mu V/K$)	$\alpha^2\sigma$ **x**10^{-4} **(**W/K^2m)
Sample A	**660**	**2.0**	**-75**	**3.7**
Sample B	**860**	**2.4**	**-77**	**5.1**
$(PbSe)_{1.16}TiSe_2$[14]	**650**	**2.3**	**-66**	**2.8**
$(PbSe)_{1.16}(TiSe_2)_2$[15]	**360**	**-**	**-91**	**3.0**
$(PbSe)_{1.16}(TiSe_2)_2$[13]	50	-	-50	0.13
$(SnS)_{1.20}TiS_2$[30]	2000	1.8	-36	2.6
$(PbS)_{1.18}TiS_2$[30]	6300	3.8	-29	5.3
$(SnS)_{1.2}(TiS_2)_2$[5]	1700	1.9	-70	8.3
$(PbS)_{1.18}(TiS_2)_2$[5]	1900	2.4	-56	6.0
$(BiS)_{1.18}(TiS_2)_2$[5]	2700	5.3	-45	5.5
$TiSe_2$[31]	$1.0x10^{-3}$	-	+15	2.3 x 10-7
$Ti_{1.1}Se_2$(MER)[32]	280	3.4	-134	5.0
$Cu_{0.1}TiS_2$[6]	4000	3.7	-45	10
$Cu_{0.11}TiSe_2$[12]	3000	0.2	-50	8

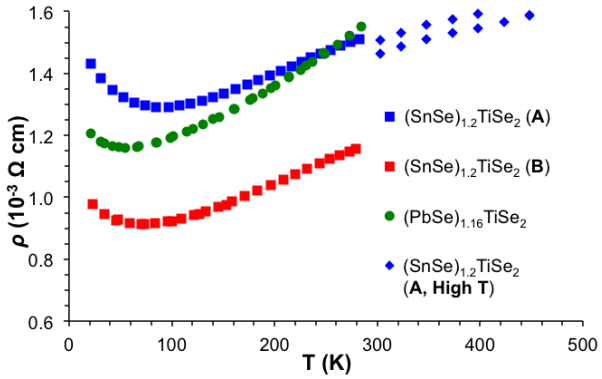

Figure IX.5: Temperature dependent resistivity for the compounds synthesized from modulated elemental reactants.

To further understand the electrical behavior of the $(SnSe)_{1.20}TiSe_2$ compounds, Hall effect measurements were performed. The Hall coefficients were found to be negative, indicating electrons are the majority charge carriers. Following previous reports, the carrier concentration was calculated using $R_H = 1/n_e e$ where n_e is the concentration of conducting electrons and e is the elementary charge (Figure IX.6 and IX.7). The carrier concentration measured for samples A and B are very similar to that reported for other isoelectronic $(MX)_{1+\delta}TiX_2$ intergrowth compounds. The carriers are thought to arise from the rock salt constituent donating electrons to the 3d band of the TiX_2 constituent, which is responsible for the majority of the conductivity.[34] The carrier concentration decreases linearly for the Sn compounds below room temperature, and are very similar in magnitude and behavior to the previously reported PbSe analog, synthesized by methods previously reported and measured for comparison (Figure IX.7a).[14] There is a significant increase in carrier concentration as the temperature is raised above 300 K, which may be a consequence of the thermal excitation of carriers or increased contribution from the carriers in the SnSe layer. The calculated single band mobility (Figure IX.7b) of the carriers in $(SnSe)_{1.2}TiSe_2$ and $(PbSe)_{1.18}TiSe_2$ have nearly

identical temperature dependent behavior and magnitudes, as may be expected for the isoelectronic systems. Similar temperature dependence was also found for $(BiSe)_{1.15}TiSe_2$ synthesized from modulated elemental reactants and reported elsewhere,[35] though the magnitude of the carrier concentration coincided with the addition of an extra carriers, consistent with reports of the TiS_2 compounds, and further suggesting that a $TiSe_2$ band is responsible for conduction.[5,14,35] The increase in mobility as temperature decreases is likely due to a decrease in in-plane phonon scattering and decreased magnitude of the atomic vibrations. The carrier mobility found in single crystals of the analogous sulfides is a factor of 3 larger. Prior studies on semiconducting $[(PbSe)_{1.0}]_m[MoSe_2]_n$ and $[(PbSe)_{1.0}]_m[WSe_2]_n$ compounds suggests that the mobility of $(SnSe)_{1.2}TiSe_2$ might be increased by extended low temperature annealing in a selenium partial pressure.[36,37]

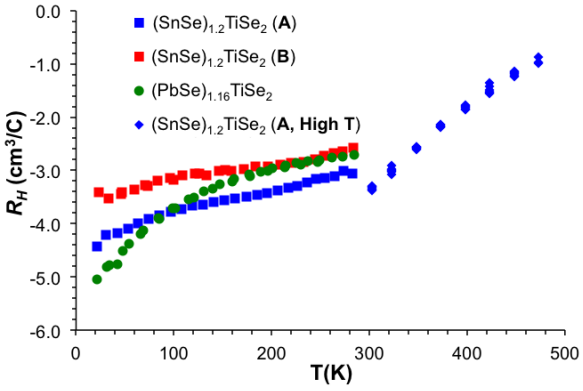

Figure IX.6: Temperature dependent Hall coefficient for the compounds synthesized from modulated elemental reactants.

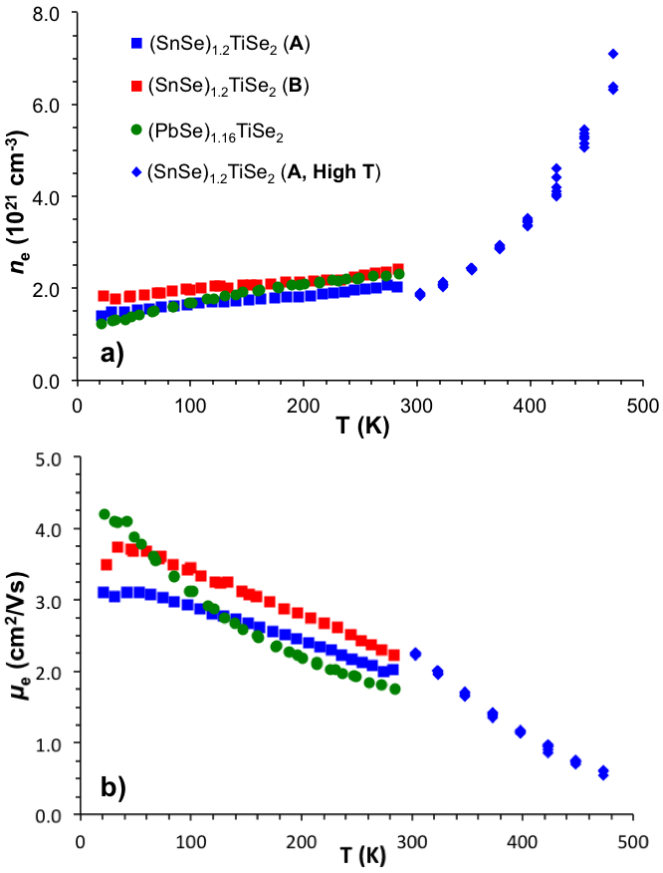

Figure IX.7: (a) Calculated carrier concentration (n_e) and **(b)** electron mobility (μ_e) based on a single band model, as a function of temperature.

The Seebeck coefficients (S) of samples A and B were -75 μVK^{-1} and -77 μVK^{-1} at room temperature, respectively. The negative sign of S agrees with the negative Hall coefficient, also indicating that electrons are the predominant charge carriers. The Seebeck coefficients of samples A and B are greater in magnitude than the -66 μVK^{-1} previously reported for the $(PbSe)_{1.16}TiSe_2$ ferecrystal just as S is larger in $(SnS)_{1.2}(TiS_2)_n$ than $(PbS)_{1.18}(TiS_2)_n$.[5,14,30] The Seebeck coefficients of the selenide compounds $(SnSe)_{1.2}TiSe_2$ and $(PbSe)_{1.16}TiSe_2$ are about than a factor of 2 higher than that reported for the sulfide compounds $(SnS)_{1.2}TiS_2$ and $(PbS)_{1.18}TiS_2$ with similar carrier concentrations.[30]

Formal valence arguments suggest that $(MX)_{1+\delta}TiX_2$ compounds should be semiconductors ($[M^{2+}X^{2-}]_{1+\delta}[Ti^{4+}X^{2-}_2]$). Prior literature explains the metallic behavior of these compounds as resulting from an overlap of the valence band of the MX constituent with the formally empty d band of TiX_2 leading to charge transfer from MX to TiX_2.[34] For the $(SnSe)_{1.2}TiSe_2$ compounds reported here, an average carrier concentration of 0.3 electron per Ti was calculated by considering the density of Ti atoms and assuming the Hall voltage can be converted to carrier concentration using a single band model where the carriers are in a Ti 3d conduction band. This value is approximately double of that reported for $(SnS)_{1.2}(TiS_2)_2$, as expected because the Sn/Ti ratio is half of that in $(SnSe)_{1.2}TiSe_2$.[5]

Figure IX.8 contains a schematic band structure diagram illustrating the proposed relative band energy and Fermi level of the two constituents and the stabilization of the material due to charge transfer. The energy contained in the capacitance resulting from electrons in the $TiSe_2$ layer and the corresponding number of holes left in the adjacent SnSe constituent is appreciable, between 7 and 9 kJ/mol depending on the value used for the distance of the charge separation (6 Å between the Ti layer in $TiSe_2$ to center of the SnSe layer or 4.5 Å from the Ti to the closest Sn/Se average plane position, respectively), the approximation used for permittivity (vacuum), and assuming a Madelung constant of 2 for the superlattice structure. This suggests that charge transfer between constituents may help explain the somewhat unexpected thermodynamic stability of the intergrowth compound compared to the individual constituents when prepared using solid-state synthesis methods.[34] The data presented here, in agreement with prior literature results,

show that electrons dominate the electrical conduction. This implies that the mobility of the holes in SnSe is significantly smaller than that of the electrons in $TiSe_2$.

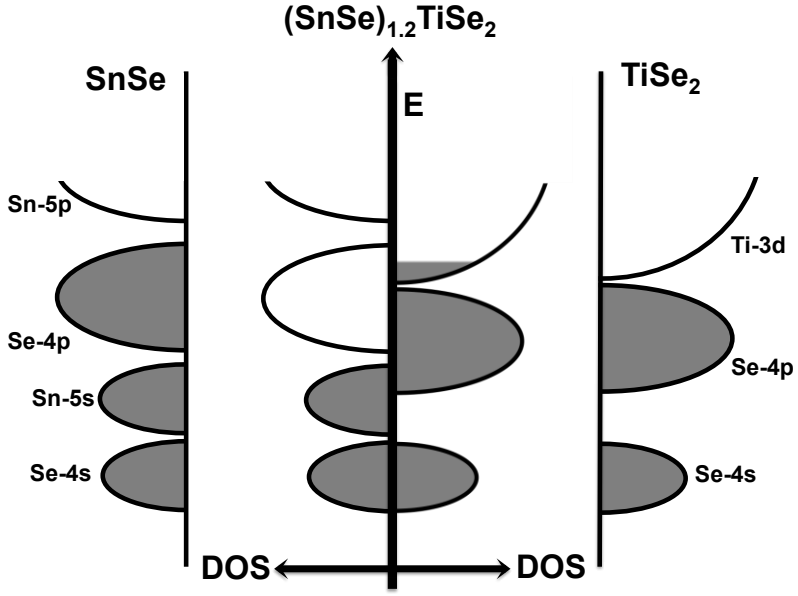

Figure IX.8: Proposed band structures of the constituent materials (left and right) and the ferecrystal product (center).

The effective mass of samples A and B were calculated to be 6.1 and 7.1 times that of a free electron from α and n_e measured at room temperature, respectively, assuming a single band and carrier type are responsible for conduction. The relationship used for the calculation is given below, where kB is Boltzmann's constant, e is the elementary charge, h is Planck's constant, m* is the effective mass, and T is temperature.[38]

$$\alpha = \frac{8\pi^2 {k_B}^2}{3eh^2} m^* T \left(\frac{\pi}{3n}\right)^{2/3}$$

As a first approximation, one can estimate the power factor as a function of n_e by assuming a constant effective mass and using the Pisarenko relationship.[39] Not surprisingly, lowering the carrier concentration in $(SnSe)_{1.2}TiSe_2$ should result in an

increased power factor. The proposed band diagram suggests that there are several mechanisms possible for lowering the carrier concentration in the material. A series of compounds $(SnSe)_{1+\delta}(TiSe_2)_n$ would lower the carrier concentration in each $TiSe_2$ layer as n increases, if the amount of charge transfer remains relatively constant. Substituting a monovalent cation for Sn^{2+} in the rocksalt layer would lower the amount of charge transfer, potentially without lowering the carrier mobility in the $TiSe_2$ layer.

IX.5. Conclusions

Intergrowth compounds represent an opportunity to study buried interfaces and the bonding between two different structures. The different band structures of the components provide opportunities to controllably adjust the properties of one material with one carrier type by choosing the other constituent to provide the correct band alignment and therefore provide carriers by charge transfer. In an ideal situation, the "donor" layer would contribute the amount of carriers required to maximize the power factor of a thermoelectric material, while not providing detrimental effects from the holes left after charge transfer. Such a system would effectively allow for a controlled doping with little or no effect on carrier mobility as demonstrated above.

CHAPTER X

TUNING ELECTRICAL PROPERTIES THROUGH CONTROL OF $TiSe_2$ THICKNESS IN $(BiSe)_{1+\delta}(TiSe_2)_n$ COMPOUNDS

X.1. Authorship Statement

The primary author of the following paper is Susannah Wood. The paper was published in Chemistry of Materials, Volume 27, issue 17, pages 6067-6076. For this work I used electron microscopy to identy the presence of Bi-Bi antiphase boundaries and provided confirmation that the targeted phase of BiSe had formed.

X.2. Introduction

Van der Waals heterostructures consisting of stacks of crystalline 2-dimensional (2-D) layers have recently garnered significant interest due to their unusual properties.[1] The vision is that by combining the unique crystal structures and properties of each layer in specific sequences within the heterostructure, "designer devices" with properties and performance that exceed that of the constituents can be achieved.[1] Tunable direct band gap materials have been predicted to result from stacking different metal disulfides and diselenides[2] and p-n junctions at van der Waals heterostructure interfaces have been experimentally characterized.[3] Charge transfer between constituent layers of a heterostructures has been shown to occur at ultrafast time scales.[4] Understanding how to control and modify the interaction between constituents within a heterostructure, including the extent of charge transfer, is essential for achieving the vision of designing optimized nanoscale devices. Systematic changes to a structural unit, a common approach to understand structure-function relationships in synthetic molecular chemistry, will be a

valuable tool both to understand and control properties in the emerging field of van der Waals heterostructures.

Ferecrystals are a subset of misfit layered compounds (MLC) with extensive turbostratic disorder between the constituents, which eliminates the structural distortions in the layers caused by the commensurate in-plane axis of MLCs. Ferecrystals are essentially heterostructure analogs of misfit layer compounds. They have the formula $[(MX)_{1+\delta}]_m[TX_2]_n$ (M = Pb, Sn, Bi, Sb, RE; T = transition metal; X = Se or Te). Ferecrystals are synthesized using modulated elemental reactants (MER), a method that uses low temperature annealing of layered precursors consisting of thin layers of the respective elements to access metastable compounds. Because of the short diffusion lengths, a large array of *m* and *n* values can be prepared and the sequence of the individual 2D layers can be controlled, resulting in structural isomers.[5] The ability to prepare sequences of compounds with controlled *n* and *m* values enables structure-property relationships to be investigated in more detail than previously possible.[6–8] Studies of SnSe-$TiSe_2$ and PbSe-$TiSe_2$ ferecrystals have shown that charge transfer occurs from the MSe layer to the TSe_2 layer.[9–11] $(BiSe)_{1+\delta}(TiSe_2)_1$ showed an increased carrier concentration compared to $(PbSe)_{1+\delta}(TiSe_2)_1$.[11,12]

This work describes the preparation of three new ferecrysals containing a BiSe bilayer: $(BiSe)_{1.14}(TiSe_2)_2$, $(BiSe)_{1.15}(TiSe_2)_3$, and $(BiSe)_{1.14}(TiSe_2)_4$. The c-lattice parameter and distortion of BiSe increases with each additional $TiSe_2$ layer in the heterostructure, with the refined position of atomic planes along the c-axis agreeing with the general structure proposed for the misfit layer compound analogs, $(BiSe)_x(TiSe_2)$ and

$(BiSe)_{1.15}(TiSe_2)_2$.[13,14] The differences in electrical resistivity temperature dependences between the crystalline misfit layer compounds and the heterostructure ferecrystals are attributed to different electron-phonon coupling resulting from the turbostratic disorder in the ferecrystals. The systematic change in resistivity in the heterostructures suggests that there is a constant amount of donated charge from the single BiSe layer regardless of the number of $TiSe_2$ layers, and this charge is distributed across the $TiSe_2$ layers. This behavior is similar to that reported for $(BiS)_{1+\delta}(TiS_2)_n$ compounds, where n = 1 and 2.[15,16] In general, the extent of charge transfer between constituents in $(BiX)_{1+\delta}(TX_2)_n$ misfit layer compounds where n = 1, 2 depends on the identity of the transition metal dichalcogenide.[15–17] The single crystal structure of, $(BiSe)_{1.08}(TaSe_2)$, was found to have a large in-plane supercell due to anti phase boundaries perpendicular to the a axis and the antiphase boundaries were used to explain the lack of charge donation from BiSe to $TaSe_2$.[18,19] STEM investigation of the compounds reported herein revealed evidence for similar anti phase boundaries approximately one third of the time. This may explain the reduced amount of charge transfer observed in this work relative to that previously reported for the $(BiSe)_{1.14}(TiSe_2)_1$ compound.

X.3. Experimental

Precursors designed to form the compounds $(BiSe)_{1+\delta}(TiSe_2)_n$, where $2 \leq n \leq 4$ were prepared in a custom-built physical vapor deposition system, with pressures below 5 x 10^{-7} Torr using the modulated elemental reactants (MER) method.[10–12] Elemental bismuth and titanium were deposited with Thermionics electron beam guns, while selenium was deposited with an effusion cell. Quartz crystal microbalances monitored deposition rates and the elements were deposited with a rate between 0.2-0.3 Å/s onto the

substrate. Layers of each element were deposited on silicon and fused silica substrates in the order of $(Ti\text{-}Se)_p$-Bi-Se, where *p* equals 2, 3, or 4, repeatedly to give a total film thickness of approximately 50 nm. Samples were annealed between 200-400°C in a nitrogen atmosphere with oxygen below 1.0 ppm for 30 minutes. Elemental compositions of as deposited and annealed samples were determined via electron probe microanalysis (EPMA) using a Cameca SX 50.[20]

X-ray reflectivity and cross-plane (00*l*) diffraction were measured on a Bruker D8 Discover (Cu Kα) diffractometer, equipped with a Göbel mirror. These scans were used to measure total film thickness, track as deposited repeat layer thickness, and follow the self-assembly of the precursors. The repeat layer thickness of the as deposited precursors was compared to an estimated *c*-axis lattice parameter based on the $TiSe_2$ thickness from the reported $[(PbSe)_{1+\delta}]_m(TiSe_2)_n$ ferecrystalline compounds[10,11] and the BiSe thickness based on the reported $[(BiSe)_{1+\delta}]_m(NbSe_2)_n$ compounds.[21] Off-specular, x-ray diffraction scans were acquired on a Rigaku Smartlab (Cu Kα) diffractometer and also on the Multi-Purpose General Scattering beamline 33-BM-C (λ = 1.2653 Å) at the Advanced Photon Source (APS), at Argonne National Laboratory. Rietveld refinements were performed on the cross-plane (*00l*) scans using the FullProf software suite.[22] In-plane (*hk*0) diffraction was collected at APS, 33-BM-C, and on a Rigaku Smartlab (Cu Kα) diffractometer for least-squares fits of the lattice parameters (*a* and *b*) of the constituents $TiSe_2$ and BiSe, using the WinCSD software package.[23] Area diffraction was collected at APS, 33-BM-C, using a Mar345 image plate detector with θ = 1.0°, 20 seconds exposure and 180 seconds acquisition time, and λ = 0.991842 Å.

Scanning transmission electron microscopy (STEM) cross-sections were prepared on an FEI Helios 600-Dual Beam focused ion beam (FIB) with a side winder ion column using backside milling methods[24] and wedge pre-milling methods.[25] High angle annular dark field scanning transmission electron microscopy (HAADF-STEM) was performed on a FEI Titan 80-300 TEM/STEM at 300 keV.

In-plane resistivity and Hall measurements were carried out in the van der Pauw geometry[26] using a custom-built measurement system under vacuum. Samples for these measurements were deposited on fused silica substrates. Electrical contacts were thin copper wires connected to the sample using indium. Samples were measured from 20 K to 295 K and magnetic fields up to 2 T were applied.

X.4. Result and Discussion

In the MER synthetic approach, the design and calibration of the precursor is critical to yield the targeted metastable products. By depositing elemental layers in the order $[Ti\text{-}Se]_p$-Bi-Se, where p equals 2, 3, or 4, we control the precursors' layering sequence to mimic the respective target products' final structure, minimizing the diffusion required to form the products. The $TiSe_2$ thickness from the reported $[(PbSe)_{1+\delta}]_n(TiSe_2)_m$ ferecrystalline compounds and the BiSe thickness based on the reported $[(BiSe)_{1+\delta}]_n(NbSe_2)_m$ compounds were used for the initial target repeat layer thickness.[10,11,21] The deposition parameters were scaled so that the repeat layer thickness was close to the targeted repeat layer thickness and the compositions were adjusted to match the targeted compounds. To evaluate the quality of the precursors, cross-plane XRR and XRD patterns were collected. The as-deposited precursors for the compounds

are significantly ordered, exhibiting Bragg diffraction to high angles, suggesting that the compounds begin to self assemble during the nominally room temperature deposition of the precursors (Figure X. 1). The optimum annealing conditions were determined by annealing pieces of a precursor designed to form $(BiSe)_{1+\delta}(TiSe_2)_2$ at different temperatures. The resulting diffraction patterns are shown in Figure X. 1.

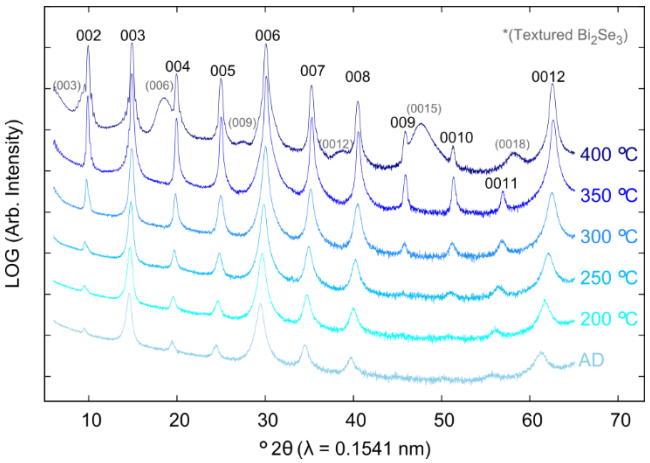

Figure X.20. A series of *00l* diffraction patterns for a precursor designed to form $(BiSe)_{1+\delta}(TiSe_2)_2$ collected as a function of annealing temperature (offset for clarity). All films were annealed for 30 minutes at the temperature indicated by the scan and the scans are offset by arbitrary amounts. The y-axis is log intensity to make weak reflections more apparent.

The positions of the *00l* reflections shift to higher 2θ with increasing annealing temperature as the repeating unit decreases in thickness. There is a systematic growth in intensity of the (*00l*) reflections as temperature is increased. For temperatures below 400 °C, only *00l* diffraction maxima are observed implying the films are highly textured. Above 350 °C, additional peaks appear and can be indexed to textured Bi_2Se_3. The maximum peak intensity, minimum full width at half maxima, and absence of impurity phases (Bi_2Se_3) were observed at 350°C, which was chosen as the optimal annealing temperature for all samples. This annealing temperature and time are consistent with that reported for $(BiSe)_{1.15}TiSe_2$.[12]

Diffraction patterns from $(BiSe)_{1+\delta}(TiSe_2)_2$, $(BiSe)_{1+\delta}(TiSe_2)_3$, and $(BiSe)_{1+\delta}(TiSe_2)_4$ samples are shown in Figure X. 2. All the Bragg reflections can be indexed as 00*l* reflections indicating the films are highly textured. The *c*-axis lattice parameters calculated from this indexing are contained in Table X. 1. The *c*-axis lattice parameter system- atically increases by 0.603(5) nm with each additional $TiSe_2$ layer. This is larger than the difference between the $(BiSe)_{1.13}(TiSe_2)$ and $(BiSe)_{1.15}(TiSe_2)_2$ MLC's reported by McQueen (0.594 nm).[14] This distance is close to the *c*-axis lattice parameter of 1T-$TiSe_2$ (0.6004 nm),[27] and the difference in *c*-axis lattice parameter between the previously reported $(PbSe)_{1.16}(TiSe_2)$ and $(PbSe)_{1.18}(TiSe_2)_2$ ferecrystals (0.608 nm).[10,11] The BiSe layer thickness obtained by extrapolating to $n = 0$ is 0.58(1) nm, This is similar to the BiSe thickness in ferecrystalline $[(BiSe)_{1.10}]_1(NbSe_2)_m$ compounds (0.59(2) nm)[21] and that reported for $(BiSe)_{1.13}(TiSe_2)$ and $(BiSe)_{1.15}(TiSe_2)_2$ misfit layer compounds (0.593 nm).[14]

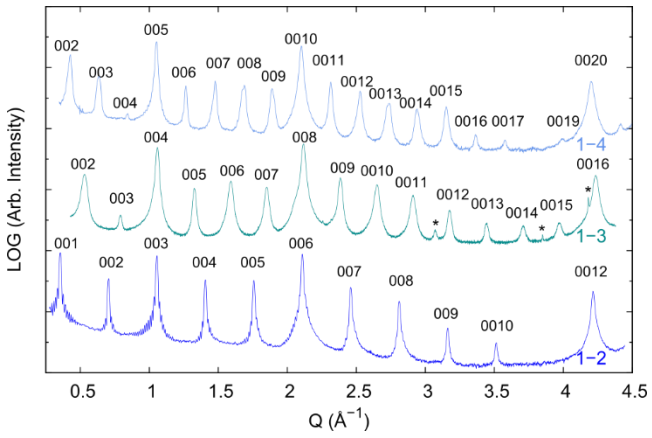

Figure X.2. X-ray diffraction patterns of $[(BiSe)_{1+\delta}]_1(TiSe_2)_n$ (1-*n*) samples. Compounds are crystallographically aligned with the c-axis normal to the substrate so all maxima can be indexed as 00*l* reflections. Diffraction patterns were collected using two different wavelengths and are shown as log intensity versus Q to make weak reflections visible. The scans are offset by arbitrary amounts. The asterisk (*) indicates peaks from the silicon substrate.

Grazing incidence diffraction patterns were collected (Figure X. 3) to characterize the in-plane structure of the constituents. All peaks can be indexed as (*hk*0) reflections of the two constituents. Only (*hk*0) reflections are observed due to the texture of the samples. For the $(BiSe)_{1+\delta}[TiSe_2]_3$ sample, weak reflections from crystallographically aligned Bi_2Se_3, are also present. The positions of the reflections did not change significantly as the number of $TiSe_2$ layers increased and were consistent with the reflections seen for $(BiSe)_{1.15}TiSe_2$.[12] The relative intensity of the $TiSe_2$ reflections increased as the number of $TiSe_2$ layers in the unit cell was increased and could be indexed using the CdI_2-type structure. The calculated *a*-axis lattice parameters for the $TiSe_2$ constituent of the *n* = 2 - 4 compounds are contained in Table X. 1.[23] The lattice parameters $TiSe_2$ were slightly larger than in the bulk structure (CdI_2-type, *a* = 0.3535 nm),[27] and similar to $TiSe_2$ reported in the ferecrystalline compound $(BiSe)_{1.15}TiSe_2$ (*a* =0.358(6) nm),[12] $(PbSe)_{1.16}(TiSe_2)$ (*a* = 0.3552(7) nm),[11] $(PbSe)_{1.18}(TiSe_2)_2$ (*a* = 0.3568(2) nm),[10] and $(SnSe)_{1.2}(TiSe_2)$ (*a* = 0.37(1) nm).[9] The Bragg reflections for BiSe were indexed using the orthorhombic space group *Pcmn*, in contrast to the bulk structure of BiSe, which crystallizes in its own trigonal structure type with an *a*-lattice parameter of 0.415(2) nm.[28] The *a* and *b* lattice parameters (Table X. 1) compared well with the published $(BiSe)_{1.15}TiSe_2$ ferecrystalline compound (*a* = 0.4562(2) nm and *b* = 0.4242(1) nm).[12] The calculated misfit parameters were the same as reported for the misfit layer

compound $(BiSe)_{1.15}TiSe_2$ and within the expected range for misfit layer compounds (Table X. 1).[15]

Table X. 1. Lattice parameters and misfit parameters for the $(BiSe)_{1+\delta}(TiSe_2)_n$ compounds investigated.

Compound	*Repeat Thickness*	*$TiSe_2$ (CdI_2 –type)*	*BiSe (Pcmn)*	
	c (nm)	*a* (nm)	*a* (nm)	*b* (nm)
$(BiSe)_{1.14}(TiSe_2)_2$ (1-2)	1.7909 (1)	0.3568(2)	0.4554(1)	0.4235(1)
$(BiSe)_{1.15}(TiSe_2)_3$ (1-3)	2.3741(1)	0.3583(1)	0.4559(4)	0.4243(1)
$(BiSe)_{1.14}(TiSe_2)_4$ (1-4)	2.9941 (1)	0.3565(2)	0.4562(2)	0.4232(1)

X.5. Electrical Properties

Temperature dependent resistivity data for the series of compounds is compared to the published ferecrystal and misfit layer compound analogs in Figure X. 8.[12,14] For the compounds reported in this study, the electrical properties were measured from samples synthesized using the same equipment cycle; this minimizes differences in composition and defeat density.[30,31] As seen in Figure X. 8.

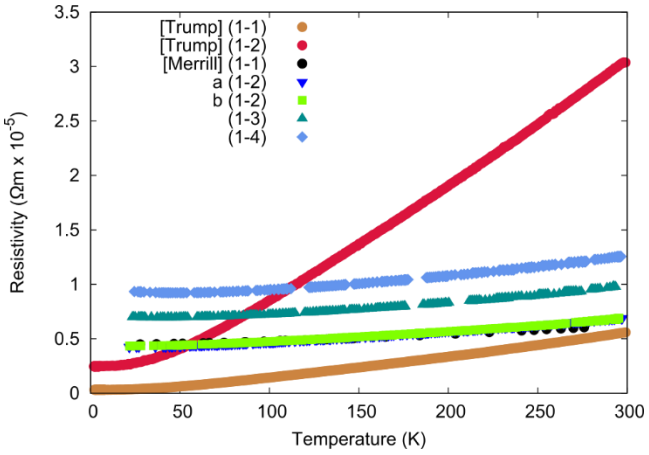

Figure X.3. Temperature-dependent resistivity of the $[(BiSe)_{1+\delta}]_1(TiSe_2)_n$ (1-n) ferecrystalline compounds is compared to the published temperature dependent resistivity for the ferecrystal $(BiSe)_{1.15}TiSe_2$,[12] and MLC $(BiSe)_{1.13}TiSe_2$ and $(BiSe)_{1.15}(TiSe_2)_2$.[14]

The temperature dependent resistivity of two different samples of the ferecrystalline compound $(BiSe)_{1.14}(TiSe_2)_2$ are the same within experimental error, demonstrating the reproducibility of the electrical measurements within adeposition cycle. The magnitude of resistivity of these compounds is consistent with a low conductivity metal or a semimetal. While both the ferecrystal $(BiSe)_{1.14}(TiSe_2)_2$ and the MLC compound $(BiSe)_{1.15}(TiSe_2)_2$ have the same magnitude of resistivity, the compound synthesized using the MER technique shows a significantly smaller temperature dependence. To understand this difference, the data was fit to the Bloch-Grüneisen equation. The Bloch-Grüneisen equation describes metallic resistivity:

$$\rho(T) = \rho_0 + \Re\left(\frac{T}{\theta_D}\right)^5 \int_0^{\theta_D/T} \frac{z^5}{\left(e^z - 1\right)\left(1 - e^{-z}\right)} dz \quad (1)$$

where ρ_0 is the residual resistivity, $\Re$ is the electron-phonon interaction constant, and θ_D is the Debye temperature.[32] Fits to the Bloch-Grüneisen equation revealed a 6-7 times stronger electron-phonon interaction in the MLC compound, $(BiSe)_{1.15}(TiSe_2)_2$, compared to the analogous ferecrystalline compound, $(BiSe)_{1.14}(TiSe_2)_2$, a consequence of the rotational disorder in the ferecrystalline polymorph (SI, Figure X. S4). A similar difference between the electron-phonon interaction in misfit layer compounds and ferecrystalline compounds was observed in $(PbSe)_{1.16}(TiSe_2)_2$ and $(PbSe)_{1.18}(TiSe_2)_2$.[10,11] While the Bloch-Grüneisen equation provides valuable insight into the difference in electron-phonon interactions, this equation does not account for the slight upturn in the resistivity data at low temperatures. While this upturn is less prominent than in the $(PbSe)_{1.18}(TiSe_2)_2$ and $(SnSe)_{1.2}(TiSe_2)$ ferecrystal analogs,[9,10] it indicates that electron-

electron correlations and localization of carriers occurs in these BiSe-$TiSe_2$ containing polymorphs.[33]

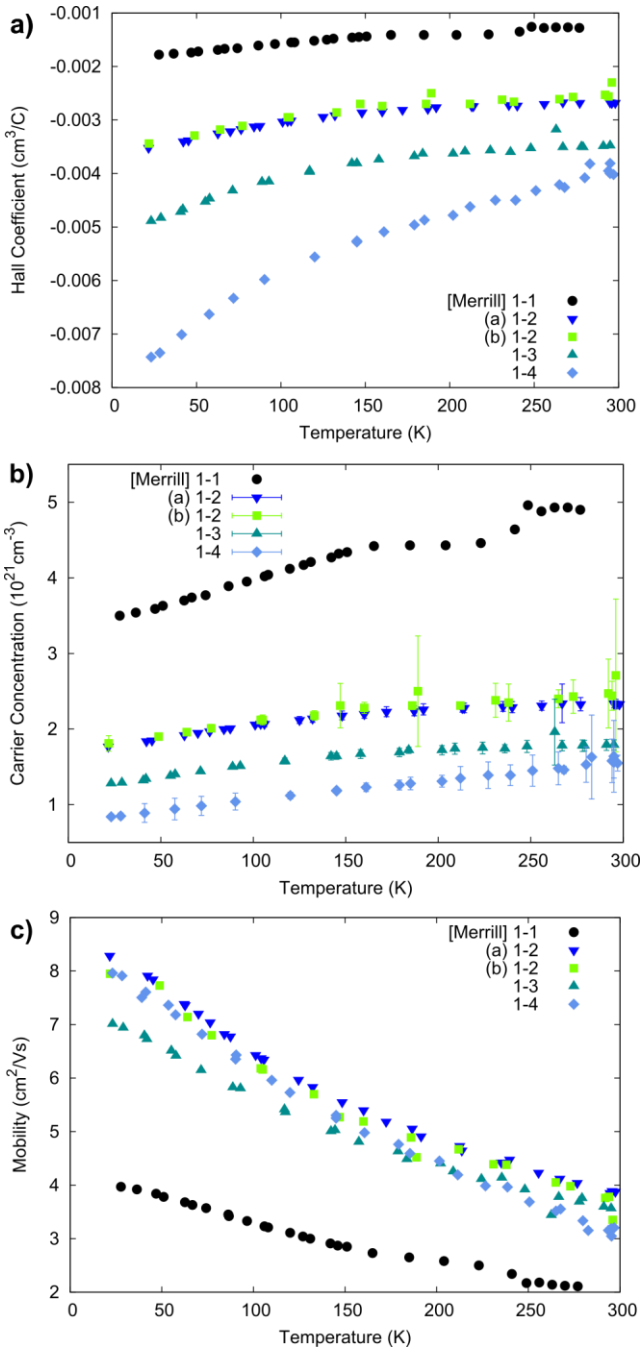

Figure X.4. Temperature-dependent a) Hall Coefficients, b) carrier concentrations, and c) mobilities. a) Temperature-dependent Hall Coefficients for the ferecrystalline compounds $[(BiSe)_{1+\delta}]_1(TiSe_2)_n$ (1-*n*) are compared to the previously published ferecrystal $(BiSe)_{1.15}TiSe_2$.[12] b) Temperature-dependent carrier concentration calculated using a single band model for the ferecrystalline compounds $[(BiSe)_{1+\delta}]_1(TiSe_2)_n$ (1-*n*) including previously published $(BiSe)_{1.15}TiSe_2$.[12] c) Temperature-dependent mobilities calculated using a single band model for synthesized from the ferecrystals including previously published $(BiSe)_{1.15}TiSe_2$.[12]

The systematic increase in the resistivity and the similarity of temperature dependence as the number of $TiSe_2$ layers increases from 2 to 4 for the ferecrystals reported here, invites comparison to bulk 1T-$TiSe_2$, the eventual end member of this series where $n = \infty$. At room temperature, pristine, bulk 1T-$TiSe_2$ has a reported resistivity between 1×10^{-5} Ωm and 15.6×10^{-5} Ωm.[14,34,35] The room temperature resistivity values of the ferecrystals reported here reasonably converge to the reported room temperature resistivity. However, the temperature dependence of these compounds differs significantly from bulk 1T-$TiSe_2$, which exhibits a broad feature below 200 K attributed to the onset of a charge density wave (CDW).[14,34–38] There is no analogous feature in the temperature-dependent resistivity of the reported compounds that suggests the presence of a CDW. This is consistent with prior reports of $TiSe_2$ containing crystalline MLCs[14,16,39] and the ferecrystalline analogs.[9–12] Historically, the absence of CDW in MLCs has been explained by the structural distortion of the TX_2 layer due to long range periodic interaction between the constituents.[15] To our knowledge, the only misfit layer compounds to exhibit a charge density wave are tin vanadium selenide ferecrystals, due to turbostratic disorder and low dimensionality of the dichalogenide.[40–43] In bulk 1T – $TiSe_2$, the CDW is formed by electron-phonon coupling and can be suppressed by increases in the carrier concentration.[38,44]

To investigate the absence of the CDW and whether the increase in resistivity with increased $TiSe_2$ layers is due to a change in carrier concentration or carrier mobility, temperature-dependent Hall coefficient were measured and compared to the previously published ferecrystal $(BiSe)_{1.15}(TiSe_2)$ (Figure X. 9a).[12] The Hall coefficients for the samples are negative, indicating that electrons are the majority carrier type. Electrons were also found to be the carriers in the ferecrystal analogs $(SnSe)_{1.2}(TiSe_2)$,[9] $(PbSe)_{1.18}(TiSe_2)_2$,[10] and for the analog $(MS)_{1+x}(TiS_2)_2$ (M = Pb, Bi, Sn) misfit layer compounds.[16] For the $(BiSe)_{1+\delta}(TiSe_2)_n$ compounds, there is a systematic increase in magnitude of the Hall coefficient as the number of layers of $TiSe_2$ increases. Assuming a single band model, the Hall coefficient is inversely proportional to the carrier concentration and carrier concentrations calculated using a single band model are compared to the previously published ferecrystal $(BiSe)_{1.15}(TiSe_2)$ in Figure X. 9b.[12] The carrier concentration decreases as the temperature decreases for all samples and decreases with each additional layer of $TiSe_2$. The carrier concentration agrees well with the high temperature carrier concentration reported by Wan for the misfit layer compound $(BiS)_{1.2}(TiS_2)_2$.[16] The carrier concentration for all the reported ferecrystals was found to be an order of magnitude higher than bulk selenium-deficient $TiSe_{2-x}$;[38] This may explain the absence of CDWs in these materials, despite similar room temperature resistivity values. Temperature dependent mobility determined from resistivity measurements and from Hall measurements are compared to the previously published ferecrystal $(BiSe)_{1.15}(TiSe_2)$ in Figure X. 9c.[12] The mobility of carriers increases as the temperature decreases for all compounds. The similarity of mobility suggests that the $TiSe_2$ is the conducting layer in all of these compounds. Similar values for the mobility of the

compounds prepared here would not be expected assuming a rigid band model since the carrier concentration changes. A rigid band model is an oversimplification, however, as the structure of the constituents change as n is increased. The mobility of the published ferecrystal $(BiSe)_{1.15}(TiSe_2)$ is lower than the ferecrystalline compounds investigated here. This is likely due to a slight difference in composition and defeat density.[30,31] Neglecting the previously published $(BiSe)_{1.15}(TiSe_2)$, the difference in temperature dependent resistivity is due to differences in the carrier concentration.

Previous work with $(BiX)_{1+\delta}(TX_2)_n$ misfit layer compounds indicates that the amount of charge transfer between (BiX) and the (TX_2) constituents depends on the transition metal in the dichalcogenide, and that the anti phase distortion in BiX also depends on the amount of charge transfer. A lack of electron donation from BiX layers to the NbX_2 layer is reported, while electron donation is suggested to occur from the BiS layers to the CrS_2 layers[15] and from the BiSe layers to $CrSe_2$ layers.[17] As seen in Figure X. 9b, the carrier concentration decreases with each additional layer of $TiSe_2$ suggesting that BiSe acts as an electron donor, and $TiSe_2$ acts as an electron acceptor, as previously suggested in literature for $BiX\text{-}TiX_2$ containing intergrowths.[9,15,16] In the misfit layer compound $(BiS)_{1.2}(TiS_2)_2$, 0.45 carriers (electrons) per Ti atom are received from the BiS layer.[16] To investigate how charge is transferred between constituent layers, the carrier concentration was normalized to the number of Bi atoms per unit volume and to the number of Ti atoms per unit volume (Figure X.s 10a and 10b, respectively). While there is a systematic trend for the overall carrier concentration, this trend does not persist when the carrier concentration is normalized to the number of Bi atoms. Instead the carriers donated per Bi atom is approximately the same for the ferecrystal compounds

$(BiSe)_{1.14}(TiSe_2)_2$, $(BiSe)_{1.15}(TiSe_2)_3$, and $(BiSe)_{1.14}(TiSe_2)_4$. For all compounds the number of carriers per Bi atom decreases as the temperature decreases.

A systematic trend in the total carrier concentration is also observed when the carrier concentration is normalized to the number of Ti atoms per unit volume. The number of carriers systematically decreases as the number of $TiSe_2$ layers increases. If a constant number of carriers is transferred from the BiSe layer into the $TiSe_2$ layers and just distributed over an increasing number of $TiSe_2$ layers (n), then the following equation should hold:

$$cc_{Ti,tot} = cc_{Ti,i} + \frac{1.15 cc_{Bi}}{n} \quad (2)$$

where $cc_{Ti,tot}$ is the total number of carrier per Ti atom, $cc_{Ti,i}$ the number of intrinsic $TiSe_2$ carriers per $TiSe_2$ atom, and cc_{Bi} is the amount of donated carriers from the BiSe layer per Ti atom (Figure X. 10c). As seen in Figure X. 10c, this simple model appears to apply for the ferecrystalline compounds $(BiSe)_{1.14}(TiSe_2)_2$, $(BiSe)_{1.15}(TiSe_2)_3$, and $(BiSe)_{1.14}(TiSe_2)_4$. At both room temperature and 20 K approximately 0.35 carriers per Bi atom are donated into the conduction band of $TiSe_2$.

To further characterize the carriers in the material, room temperature Seebeck coefficients of the ferecrystalline compounds $(BiSe)_{1+\delta}(TiSe_2)_n$ were measured (Table X.2). The negative sign of the Seebeck coefficients indicates that electrons are the charge carriers in the ferecrystalline compounds, which is consistent with the sign of the Hall coefficients (Figure X. 9a). The magnitude of the Seebeck coefficient increases with the number of $TiSe_2$ layers,

Table X.2. Seebeck Coefficients of $(BiSe)_{1+\delta}(TiSe_2)_n$ at room temperature.

Compound	Seebeck Coefficient (μV/K)
$(BiSe)_{1.14}(TiSe_2)_2$ (1-2)	-65
$(BiSe)_{1.15}(TiSe_2)_3$ (1-3)	-68
$(BiSe)_{1.14}(TiSe_2)_4$ (1-4)	-80

which is consistent with the decrease in carrier concentration. For metals, under a single parabolic band and assuming energy independent scattering, the Seebeck coefficient is given by:

$$\alpha = \frac{8\pi^2 k_B^2}{3eh^2} m^* T \left(\frac{\pi}{3n}\right)^{2/3} \quad (3)$$

where n is the carrier concentration and m^* is the effective mass of the carrier.[45] Equation 3 was used to calculate the effective mass of the electron for each ferecrystalline compound $(BiSe)_{1+\delta}(TiSe_2)_n$ (n = 2 – 4) yielding a value of 5-6 m_e. This compares well with the effective carrier mass for the MLC $(BiS)_{1.2}(TiS_2)_2$ (6.3 m_e).[16]

X.6. Conclusions

The synthesis, structure, and electrical properties of three new heterostructures, $(BiSe)_{1.14}(TiSe_2)_2$, $(BiSe)_{1.15}(TiSe_2)_3$, and $(BiSe)_{1.14}(TiSe_2)_4$, consisting of a bilayer of BiSe and the trilayer $TiSe_2$ dichalogenide were discussed. The compounds were formed from designed precursors. With each additional $TiSe_2$ layer, the *c*-axis lattice parameter increased by 0.603(5) nm. The structure of the compounds suggests charge transfer occurs, which is confirmed by electrical transport measurements. All samples displayed a lower temperature dependence in the resistivity data than MLC compounds due to decreased electron-phonon coupling. As the number of $TiSe_2$ layers is increased, the

number of carriers are decreased while maintain the same carrier mobility and effective carrier mass. This suggests it might be possible to tune electrical properties by modulating the nanostructure of the heterostructures by controlling the charge transfer between constituents.

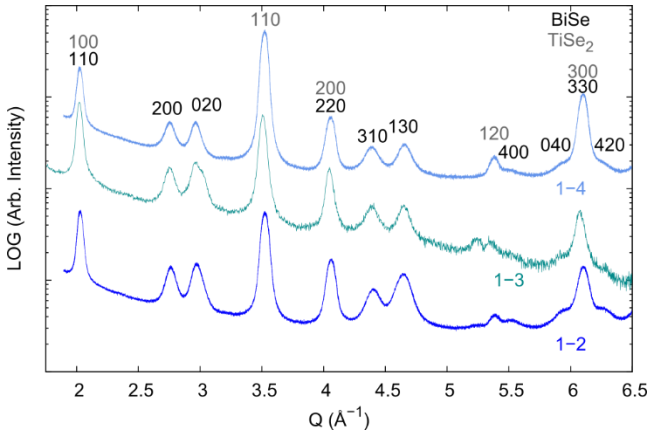

Figure X.5. In-plane (*hk0*) diffraction pattern of $[(BiSe)_{1+\delta}]_1(TiSe_2)_n$ (1-*n*) samples displaying Bragg peaks and associated indices from the independent lattice structures of both constituents. Diffraction patterns shown in q-space because they were collected using two different wavelengths, graphed using log intensity to make weak reflections visible and offset by arbitrary amounts. All films were annealed for 30 min at 350 °C.

Cross-sectional high angle annular dark field scanning transmission electron microscopy (HAADF-STEM) images were collected to further characterize the structure of these compounds (Figure X. 4). These images contain the expected layering sequences for $(BiSe)_{1.15}(TiSe_2)_2$, $(BiSe)_{1.14}(TiSe_2)_3$, and $(BiSe)_{1.15}(TiSe_2)_4$ (Figure X.s 4a-b, 4c, and 4d, respectively). The images of all three compounds contain brighter BiSe layers and by darker $TiSe_2$ layers separated by a van der Waals gap. The BiSe - $TiSe_2$ interface is atomically abruptness in all of the images. The image of $(BiSe)_{1.15}(TiSe_2)_2$ in Figure X. 4a contains both the substrate and the top carbon coating. The precursor of this sample

had 28 $[Ti\text{-}Se]_2$-Bi-Se layers as deposited while the image contains ~26 BiSe-$TiSe_2$-$TiSe_2$ repeats with additional material at the top and bottom of the sample.

Different crystal faces of each constituent are present both within a layer and between layers, reflecting the turbostratic disorder of the ferecrystalline structure. The overall stacking sequence is consistent across the samples. The 1T-polytype of $TiSe_2$ can be seen in regions of each of these compounds suggesting an octahedral coordination of the transition metal. While relatively defect free regions were chosen for HAADF-STEM images shown in Figure X. 4 of the $(BiSe)_{1.15}(TiSe_2)_2$, $(BiSe)_{1.14}(TiSe_2)_3$, and $(BiSe)_{1.15}(TiSe_2)_4$ films, there were regions where defects were observed.

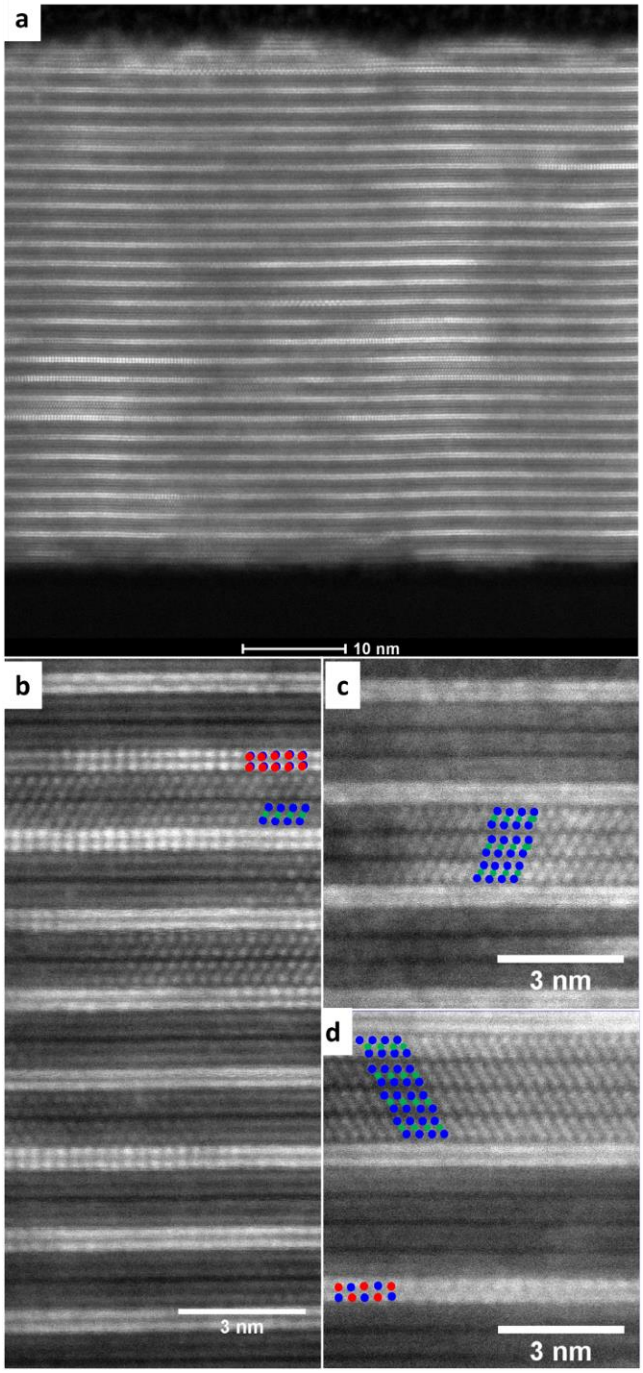
a
10 nm
b
3 nm
c
3 nm
d
3 nm

Figure X.6. Cross Sectional HAADF-STEM images: a) a full film cross-section showing alternating BiSe and $TiSe_2$ layers in $(BiSe)_{1.14}(TiSe_2)_2$ and rotational disorder between constituent layers, b) higher magnification image of a region of the $(BiSe)_{1.14}(TiSe_2)_2$ sample showing the 1-T polymorph of the $TiSe_2$ layer, c) higher magnification image of a region of the $(BiSe)_{1.15}(TiSe_2)_3$ with a grain boundary in the $TiSe_2$ layer, and d) a higher magnification image of a region of the $(BiSe)_{1.14}(TiSe_2)_4$ showing the 1T polymorph of the $TiSe_2$ layer and the rotational disorder between constituents.

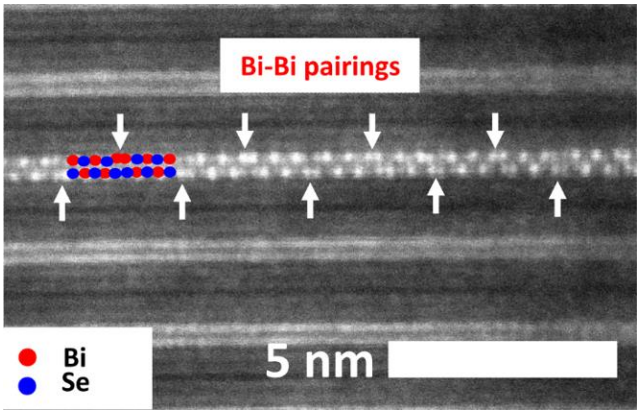

Figure X.7. High magnification cross sectional HAADF-STEM image of $(BiSe)_{1.14}(TiSe_2)_2$ showing the Bi-Bi bonded pairs resulting from the anti phase boundary are most visible along the (110) zone axis (rock salt setting) of the BiSe.

The presence of anti phase boundaries in single crystals of $(BiSe)_{1.10}NbSe_2$ and $(BiSe)_{1.09}TaSe_2$[18,19] lead us to search for these defects in the compounds discussed here. The Bi-Bi bonded pairs resulting from the anti phase boundary are most visible along the (110) zone axis (rock salt setting) of the BiSe. All HAADF-STEM images collected for these samples were examined for this defect in the (*110*) face. There were a total 25 of (110) faces observed. Of these 19 were clear enough to distinguish atomic columns. In 7 of these clear images, Bi-Bi pairing was clearly visible (Figure X. 5). This is the first time this distortion has been seen in $TiSe_2$ containing misfit compounds. As discussed by Wiegers,[15] the anti phase distortion does not alter the position or intensities of the parent face center cubic in-plane cell, so the diffraction data is consistent with the average local structure.

The STEM images were used to create models of the structures of $(BiSe)_{1.14}(TiSe_2)_2$, $(BiSe)_{1.15}(TiSe_2)_3$, and $(BiSe)_{1.14}(TiSe_2)_4$, along the c axis, which were then refined using the 00*l* diffraction data to obtain the distance between atomic planes along the *z*-axis (Figure X.6; Refinements SI, Figure.s S1-S3, Tables S1-S3)**.** The refinement of $(BiSe)_{1.14}(TiSe_2)_2$ converged to a c-lattice parameter of 17.9094(6) Å, which is larger than in the corresponding misfit layer compound (17.8103(1) Å).[14] Within the BiSe layer, the Bi and Se atoms were not in the same plane but were distorted by 19 pm from an ideal 001 plane. This distortion is similar to the distortion in SnSe in the ferecrystal $(SnSe)_{1.2}TiSe_2$ (27 pm).[9] There are two different refined Ti-Se distances (151 pm and 133 pm); different Ti-Se distances were also reported in the refinement of the atomic planes of $(PbSe)_{1.18}(TiSe_2)_2$.[10] These distances correspond to the distance from Ti to the Se plane bordering the BiSe layer and to the Se plane bordering the second $TiSe_2$ layer, respectively. The refinement of $(BiSe)_{1.14}(TiSe_2)_3$ converged to a c-lattice parameter of 23.7409(9) Å. Within the BiSe layer, the Bi and Se atoms are distorted by 29 pm from an ideal *00l* plane. While there are two different refined Ti-Se distances, these distances are more similar than the distances in $(BiSe)_{1.14}(TiSe_2)_2$. The 00*l* refinement of $(BiSe)_{1.14}(TiSe_2)_4$ converged to a c-lattice parameter of 29.940(2) Å. Within the BiSe layer, the Bi and Se atoms were not in the same the Se-Ti distance adjacent to BiSe larger than the distance adjacent to $TiSe_2$. This suggests an ionic interaction between the Bi cation in the rock salt and the Se anion in increases, the puckering distortion of the BiSe bilayer becomes larger. This increase in puckering leads to a larger distance between Bi atomic planes and a smaller distance between Se atomic planes within a BiSe layer, as the number of $TiSe_2$ layers increases. This also indicates a

stronger covalent interaction between the Bi in the rock salt like layer and the adjacent Se of the $TiSe_2$ layer.

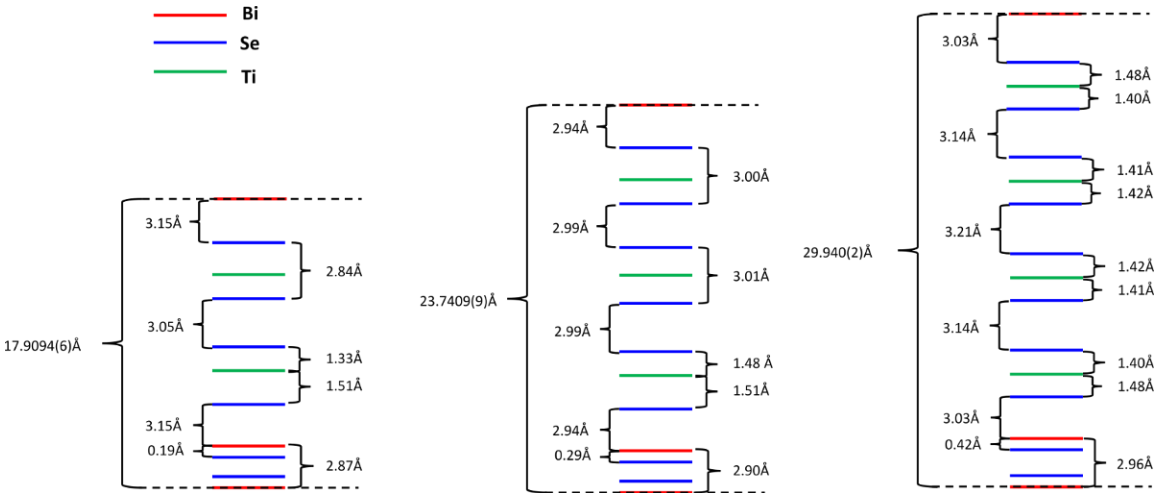

Figure X.8. Models for the refined atomic plane positions in $(BiSe)_{1+\delta}(TiSe_2)_2$, $(BiSe)_{1+\delta}(TiSe_2)_3$, and $(BiSe)_{1+\delta}(TiSe_2)_4$. The dashed lines indicate the unit cell. The models for the Rietveld refinement of *00l* diffraction patterns were based on the constituents BiSe and $TiSe_2$ as determined by *hk0* diffraction. For each compound Bi is puckered toward the dichalcogenide.

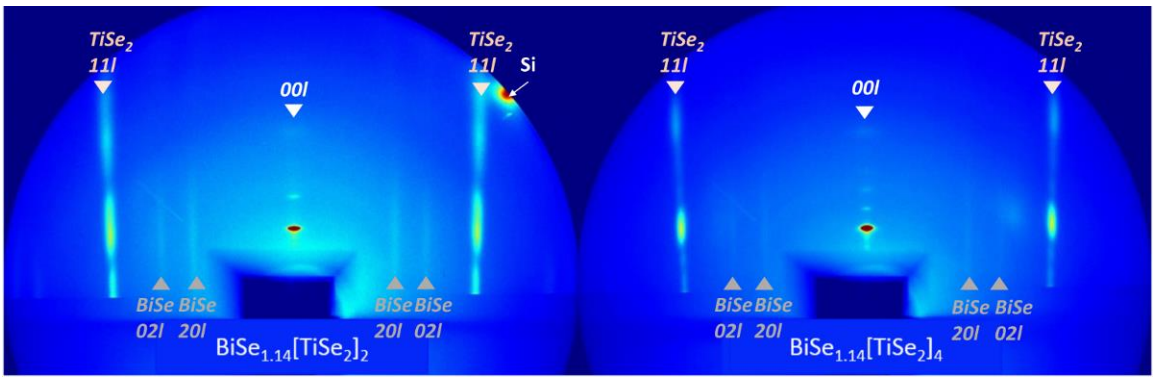

Figure X.9. Area X-ray diffraction data for $(BiSe)_{1.14}(TiSe_2)_2$ and $(BiSe)_{1.14}(TiSe_2)_4$ compounds indicate turbostratic disorder.

Table X. 3. Bi/Ti Ratio Measured by EPMA and Calculated from Misfit Parameter (δ)

Compound	Measured Bi/Ti using EPMA	Calculated Bi/Ti from fit of *hko* diffraction (δ)	Calculated Bi/Ti from refinement of *ool* diffraction (δ)
$(BiSe)_{1.14}(TiSe_2)_2$ (1-2)	0.44(5)	0.57	0.54
$(BiSe)_{1.15}(TiSe_2)_3$ (1-3)	0.33(1)	0.38	0.33

$(BiSe)_{1.14}(TiSe_2)_4$ (1-4)	0.23(1)	0.29	0.29

Area diffraction scans were collected to better understand the three dimensional structure of the films (Figure X. 7). Sharp reflections are observed along the 00*l* direction due to the regular and coherent spacing of the atomic planes along the *c*-axis. Diffuse scattering occurs along the *l* direction for $h+k \neq 0$. The broadening of these (hkl) reflections where $h+k \neq 0$ results from a shortened coherence length in the direction of the reflection, which was reflected in the rotational disorder of the different constituents observed in the STEM images. The sharp (*hk*0) reflections presented earlier in Figure X. 3 indicate that the individual layers have much larger in-plane coherence lengths. The combination of very broad *hkl* reflection but sharp 00*l* and *hk*0 reflections is consistent with turbostratically disordered layers.[29]

Area diffraction also provided additional insight into the structure of the constituent layers. The broad relatively intense reflections along the $TiSe_2$ (11*l*) direction result from the TiSe2 structure and do not reflect the c-axis of the compounds. The increased sharpness of this reflection for $(BiSe)_{1.15}(TiSe_2)_4$ compared to $(BiSe)_{1.15}(TiSe_2)_2$ results from a longer coherence length in this direction, which is consistent with the ordered 1T-polytype structure observed in the HAADF-STEM images where all layers within one block of $TiSe_2$ exhibit the same crystallographic orientation. The two weak broad maxima at lower angles along the (11*l*) direction result from incomplete destructive interference from the 4 layers in each block.

The ratio of bismuth to titanium in the compounds was measured using electron probe microanalysis and was also calculated based on the misfit parameter (Table X.3).

All compounds were found to be bismuth poor in comparison to the expected Bi/Ti ratio based on the misfit parameters. The misfit parameters were determined based on the in-plane lattice parameters of the constituents BiSe and $TiSe_2$ from the *hk*0 diffraction data. The misfit parameter was also determined from the Rietveld refinement of the 00*l* diffraction. While there appears to be a discrepancy in the Bi/Ti ratio, the EPMA measures of the average film composition and not necessarily the composition of the refined crystalline component. The presence of defects in the films, the material at the top and the bottom of the film, and the loss of one or more layers relative to the deposited precursor is consistent with the difference between Bi/Ti ratios measured using EPMA and calculated from lattice parameters. While there are defects in the films, the structure found from the refinement of the diffraction data is consistent with the local structure observed via HAADF-STEM within the respective uncertainties.

CHAPTER XI

TRANSPORT PROPERTIES OF VANADIUM DISELENIDE MONOLAYERS SEPARATED BY BILAYERS OF BISE

XI.1. Authorship Statement

The following paper was primarily prepared by Omar Hite. The paper was published in the Journal of Materials Research in 2015, volume 31, issue 7, pages 886-892. For this work, I performed STEM measurements which confirmed the targeted stacking motif and the presence of Bi-Bi antiphase boundaries.

XI.2. Introduction

Research on two dimensional atomic crystals and heterostructures has grown enormously in the last decade, sparked by the properties of monolayers being different than properties of the bulk, to become one of the leading sub-fields in condensed matter physics and materials science.[1,2] The wavefunction of a monolayer extends beyond its surface, decaying exponentially into the materials (or vacuum) both above and below it. The surface (if vacuum) or interface (in a heterostructure) interactions result in structural distortions, new phenomena, new physics and challenging chemistry. For example, MoS_2 transitions from an indirect to a direct band gap semiconductor,[3] the onset temperature of superconductivity in 2H-$NbSe_2$ decreases as the number of $NbSe_2$ layers is decreased and in extremely thin samples of $NbSe_2$ superconductivity no longer persists,[4] and ultrathin layers of PbSe distort from the bulk rock salt structure, with both a puckering distortion in and a pairing interaction between layers.[5] While stability issues have limited the ability

to prepare monolayer films of many materials via a cleaving approach,[6] the ability to reasonably predict the structure of potential heterostructures made from 2-D atomic constituents makes them attractive candidates for theoretical investigations that predict properties as a function of nanoarchitecture. There are already quite a few predictions of interesting properties reported in the literature.[7,8]

The interaction at the interfaces between monolayers also provides interesting experimental opportunities to both tailor existing properties and potentially obtain properties not found in either of the constituent materials. It has already been shown that the properties of graphene strongly depend on the substrate on which it is grown.[9] Ultra low thermal conductivity results from rotational disorder between layers.[11] Several reports of samples containing thin layers of VSe_2 differ with respect to the effect of layer thickness on the charge density wave that occurs at 100K in the bulk single crystals.[12] If prepared via liquid exfoliation, the CDW increases to 135 K[13] as thickness is reduced to 4-8 trilayers of VSe_2. In VSe_2 micromechanically exofoliated nanoflakes, the CDW onset temperature was reported to decrease to 81 K at 11.6 nm, the lowest thickness measured.[14] In turbostratically disordered single layers of VSe_2 separated by layers of SnSe prepared using a self-assembly approach, a CDW has been reported that has an opposite carrier type (holes) than the bulk (electrons),[15] which does not occur when the VSe_2 thickness is increased beyond a monolayer.[16] An understanding of how to control properties based on the interaction between layers is developing as more heterostructures and their properties are reported.

The change in carrier type and CDW reported for SnSe-VSe_2 heterostructures relative to bulk VSe_2 prompted us to prepare a new heterostructure consisting of

alternating layers of BiSe and VSe_2. BiSe was chosen as a companion layer due to the prior literature on BiSe-dichalcogenide misfit compounds, which showed that the transport properties of $(BiSe)_{1.10}NbSe_2$ and $(BiSe)_{1.09}TaSe_2$ are very similar to those of the analogous Sn compound.[17] Localization of the additional valence electron of the Bi within the BiX subsystem has been proposed as a reason for the similar transport properties.[18] The charge is localized in Bi-Bi bonds at anti-phase boundaries, which are thought to systematically occur due to the mutual accommodation of the lattice mismatch to form a commensurate structure.[17,19] We find that the VSe_2 layer(s) in a superlattice containing single layers of BiSe and VSe_2 is structurally similar to what was previously reported for $[(SnSe)_{1.15}]_1(VSe_2)_1$. The in-plane diffraction pattern and layer positions from Rietveld refinement of the specular diffraction pattern are consistent with BiSe having a rocksalt type structure. HAADF-STEM images, however, reveal extensive turbostratic disorder and the presence of anti-phase boundaries seen previously in BiSe containing misfit layer compounds. This suggests that the presence of anti-phase boundaries are not dependent on forming an ordered long range distortion of both constituent structures to form a coherent crystal. Despite the similarity of the structure of the VSe_2 single layers, no CDW is observed in the BiSe-VSe_2 heterostructure. The BiSe-VSe_2 heterostructure has a negative Hall coefficient, indicating n-type carriers predominate, which is similar to bulk VSe_2.[12] Since $[(SnSe)_{1.15}]_m(VSe_2)_1$ heterostructures have positive Hall coefficients, indicating that holes are the predominant carrier, the change of carrier type in the BiS -VSe_2 heterostructure prevents formation of the CDW.

XI.3. Experimental

The compound $[(BiSe)_{1+\delta}]_1(VSe_2)_1$ was synthesized using the modulated elemental reactants (MER) technique in a custom built high-vacuum physical vapor deposition chamber.[20] Elemental sources of Bi (99.995%) and V (99.8%), obtained from Alfa Aesar, were evaporated at a rate of 0.4 Å/s using Thermionics 3kW electron-beam guns onto (100) oriented Si wafers. Se (99.999%) was deposited at a rate of 0.5 Å/s utilizing a Knudsen effusion cell. Rates were monitored using quartz crystal monitors positioned 25 cm above the elemental sources. A custom-made LabView program controlled the rotation of the carousel with the mounted Si wafers over the desired elemental sources to obtain the desired deposition sequence. Pneumatically powered shutters allow a precise control of atomic composition based on the opening time of the shutter. The Se-Bi-Se-V layering sequence was repeated until a total thickness of 45-55 nm of the modulated precursor was obtained. To determine optimal annealing conditions for self-assembly the precursors were annealed between 200 °C - 550 °C for 20 minutes. X-ray diffraction, discussed below, was used to determine optimal temperature.

To form the ferecrystalline products, the precursors were annealed for 20 minutes in a N_2 glove box with oxygen content below 0.6 ppm and the resulting products characterized using X-ray scattering. X-ray diffraction (XRD) were performed to determine repeat unit thickness of the film. XRD measurements were performed on a Bruker D8 Discover diffractometer equipped with Cu Kα radiation, Göbel mirrors, and Bragg-Brentano optics geometry. Locked coupled θ-2θ scans were taken from 0-9° 2θ for XRR and 5-65° 2θ for XRD. Samples were prepared for STEM on a FEI Helios 600 dual-beam using methods developed by Schaffer *et al.*[21] High-angle Annular Dark-field Scanning Transmission Electron Microscopy (HAADF-STEM) images were taken on a

FEI Titan 80-300 FEG-TEM at the Center for Advanced Materials Characterization in Oregon (CAMCOR).

The Van der Pauw technique[22] was used to determine temperature-dependent resistivity and Hall coefficient of the sample in a temperature range of 20-295 K. Samples for electrical resistivity and Hall measurements were deposited on fused Quartz crystal slides. Using a shadow mask, a 1 cm x 1 cm cross geometry was deposited and indium contacts were placed on the points of the cross. By sourcing a current between two adjacent contacts and measuring the voltage on the remaining two contacts, an average sheet resistance at a fixed temperature can be found.

$$\rho = \frac{\pi d}{\ln 2} R_{Avg,Sheet} f$$

Resistivity, ρ, can be found by converting the average sheet resistance, R, into resistivity by using thickness (d) of the sample and the cross pattern symmetry (f). The Hall coefficient was also determined using the Van der Pauw technique by sourcing a current of 100 mA between two opposing contacts, applying a magnetic field of 0 - 1.6 T, and measuring the voltage induced by the magnetic field between the two remaining opposing contacts. The Hall coefficient, R_H, is the slope of the least squares fit for the measured voltage vs. applied magnetic field curve.

XI.4. Result and Discussion

The $[(BiSe)_{1+\delta}]_1[VSe_2]_1$ heterostructure was synthesized using modulated elemental reactants approach. In this approach, precursors consisting of a sequence of elemental layers are repeatedly deposited on a nominally room temperature substrate and then annealed to self-assemble the desired heterostructure. The sequence of elemental

layers, in this case Bi-Se-V-Se was chosen to resemble that in the targeted heterostructure. The relative thicknesses of the elemental layers in the Bi-Se bilayer was calibrated to yield a one to one stoichiometry and the absolute thickness was calibrated to yield two (100) monolayers of a rock salt structured BiSe. The relative thicknesses of the elemental layers in the V-Se bilayer was calibrated to yield a one to two stoichiometry and the absolute thickness was calibrated to a single layer of a Se-V-Se dichalcogenide structure. The precursors were deposited using a previously described deposition system.[20] Initial ratio of deposition thicknesses and absolute thicknesses both Bi-Se and V-Se elemental bilayers to obtain a bilayer layer of BiSe and a structural monolayer of VSe_2 were taken from previous studies.[15,23] The initial samples self-assembled in to the desired $[(BiSe)_{1+\delta}]_1[VSe_2]_1$ compound after annealing at 350°C for 20 minutes, but broader and less intense 00l diffraction maxima than seen in previous ferecrystals[11,15,25] were observed in a specular XRD scan. The lattice parameter was close, however, to the expected one, and only 00*l* reflections were observed in the specular scan, suggesting the formation of the desired compound crystallographically aligned with the *c*-axis perpendicular to the substrate. We varied the initial Bi composition in the BiSe component by 5% both above and below the ideal composition. The *c*-axis lattice parameter varied from 1.178(1) nm when Bi was deficient to 1.180(1) nm when there was excess Bi, and in both extremes the quality of XRD scans decreased, having larger line widths and less intensity than at the ideal composition. The Bi content that gave the largest intensity and smallest line-width was used in subsequent studies. The *c*-axis lattice parameters in all of the samples are smaller than the 1.203 Å observed for $[(SnSe)_{1.15}]_1(VSe_2)_1$.[15]

An annealing study was performed to determine optimal formation conditions and the resulting specular XRD scans are shown in Figure XI. 1. The as-deposited scan contains only broad (001) and (004) reflections. After 20 minutes of annealing at 250°C, the first six (00*l*) reflections are observed, indicating the self-assembly of the targeted heterostructure. The intensity of these reflections increases and the line width decreases with increasing annealing temperature until 500°C. After annealing at 550°C, the line-widths begin to broaden due to evaporation of the components. An annealing period of 20 minutes at 500°C was therefore chosen as the optimal annealing conditions.

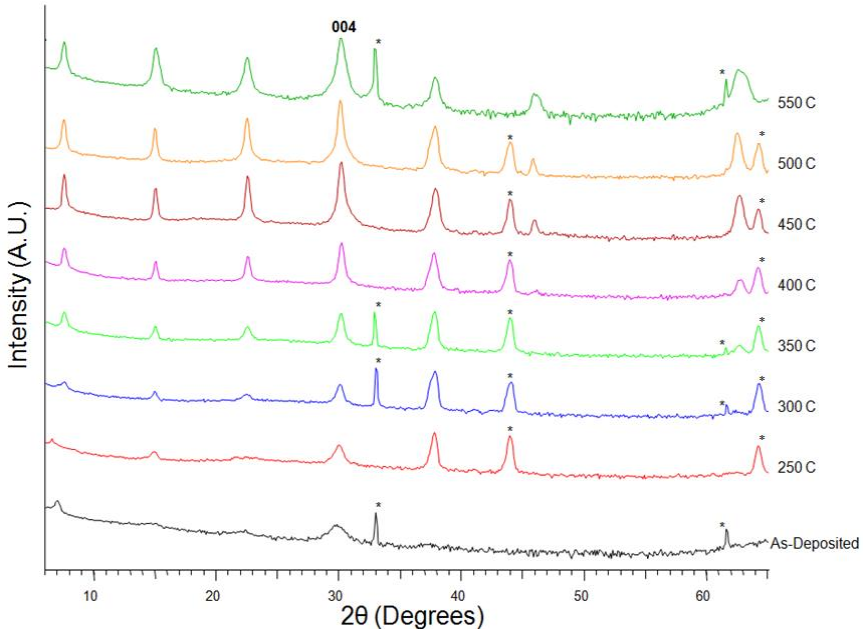

Figure XI.21. A series of diffraction scans collected as a function of annealing temperature, as indicated at the right side of the scans. All of the diffraction peaks from the sample can be indexed as (00*l*) reflections and the (004) reflection is indexed in the figure. Diffraction artifacts from the stage and Si substrate are marked with * symbols.

The specular diffraction pattern, Rietveld refinement and difference between them for the $[(BiSe)_{1+\delta}]_1[VSe_2]_1$ heterostructure are shown in Figure XI. XI.2. The refined position of the atomic planes along the *c*-axis of the refined structure is compared to the previously reported structure for $[(SnSe)_{1.15}]_1(VSe_2)_1$ in the image below the data. The

positions of the atomic planes are consistent with the expected heterostructure. The refined V-Se distance is 0.152(1) nm in the BiSe-VSe_2 heterostructure, which is very similar to the 0.152(1) nm reported for $[(SnSe)_{1.15}]_1(VSe_2)_1$.[15] The Bi and Se atoms in the BiSe layer are no longer in the same plane as would be expected for a rock salt structure, with the Bi closer to the Se layer in VSe_2 by 0.025(1) nm. This "puckering" distortion is smaller than most reported, which range between 0.020 - 0.060(1) nm in previously reported rock salt-dichalcogenide misfit structures.[18] In $[(SnSe)_{1.15}]_1(VSe_2)_1$, the Sn and Se planes are 0.034(1) nm apart,[15] while a puckering of 0.0293(1) nm[17] and 0.291(1) nm[19] have been reported in the misfit layer compound $(BiSe)_{1.09}TaSe_2$. A two selenium layers of the BiSe constituent are separated by 0.260(1) nm, which is slightly smaller than the 0.2751(1) nm and 0.2820(1) nm found by Zhou *et. al.*[17] in $(BiSe)_{1.09}TaSe_2$. This separation is much larger than the 0.24(1) nm found in $[(SnSe)_{1.15}]_1(VSe_2)_1$.[15] Gap between Bi layer of the BiSe and VSe_2 is 0.286(1) nm which is shorter than the 0.292(1) found in $[(SnSe)_{1.15}]_1(VSe_2)_1$.[15] In $(BiSe)_{1.09}TaSe_2$, a gap of 0.3232 nm is found between the BiSe and the Se plane of $TaSe_2$.[19]..... A gap of 0.289(1) nm was reported in a recent paper containing the structure of a BiSe-$NbSe_2$ heterostructure.[26] The refined model is consistent with the targeted BiSe-VSe_2 heterostructure.

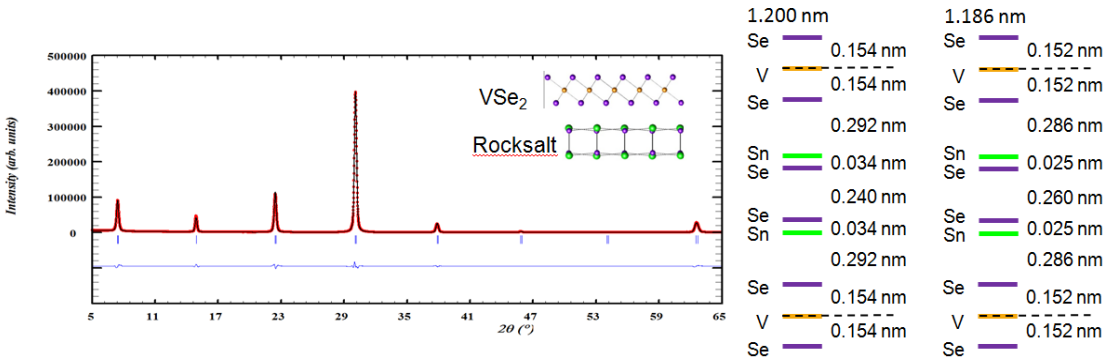

Figure XI.22: Rietveld refinement of the $[(BiSe)_{1+\delta}]_1[VSe_2]_1$ heterostructure determine the position of atomic planes along the c-axis. The model to the right shows projected positions of the atoms onto the c-axis and their relative distances.

To obtain additional information about the $[(BiSe)_{1+\delta}]_1[VSe_2]_1$ heterostructure, cross section HAADF-STEM images were collected and representative images are contained in Figure XI.3. The structure from the top to the bottom of the film, Figure XI3a, contains alternating layers of VSe_2 and BiSe consistent with the targeted heterostructure. Occasionally, there are missing layers of BiSe suggesting that the precursor used for this STEM sample was deficient in Bi. These missing layers of BiSe, which reduce the coherence of the structure perpendicular to the substrate, are the likely cause of the line broadening observed in the specular diffraction patterns as composition was varied. In higher resolution images, some of the layers are aligned along the [111] and [100]/[010] zone axes, but the majority of the layers are not, consistent with prior reports of extensive rotational disorder between layers for samples prepared using modulated elemental reactants.[24] Several images contained regions where some of the BiSe layers were aligned along a zone axis, as shown in Figure XI.3b. Clearly visible in these layers is a periodic anti-phase boundary, similar to that previously reported for $(BiSe)_{1.09}TaSe_2$.[17,19]

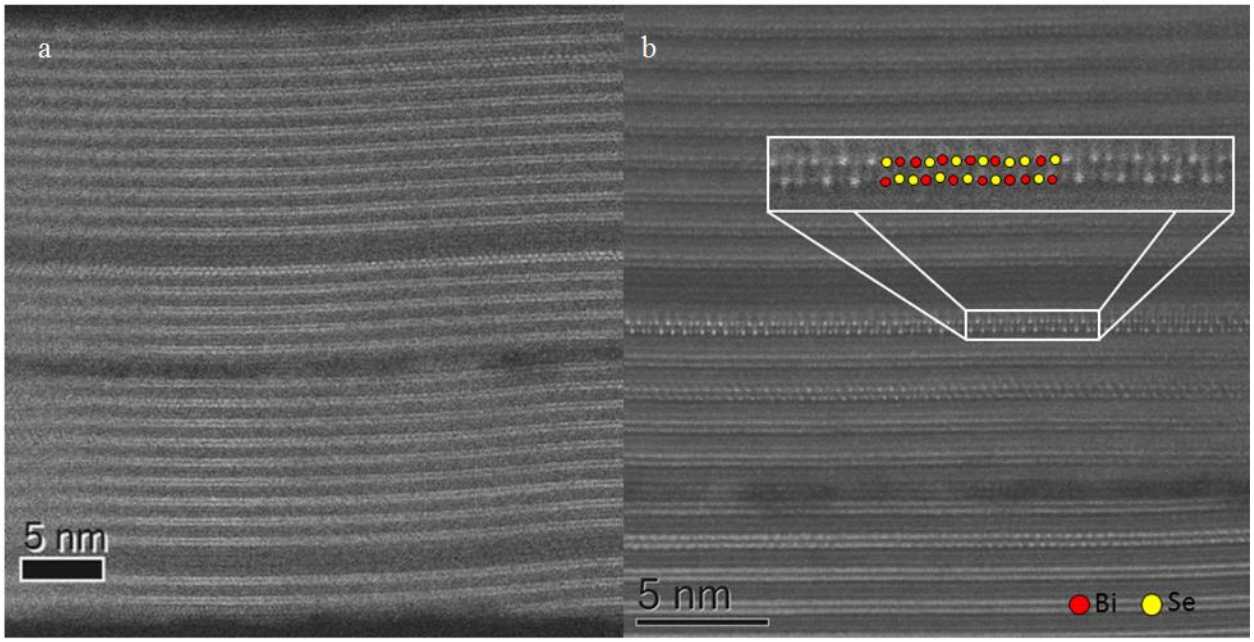

Figure XI.23. (a) Representative cross section HAADF-STEM images of the $[(BiSe)_{1+\delta}]_1[VSe_2]_1$ heterostructure. (b) Appearance of anti-phase boundaries apparent in BiSe bilayer.

Resistivity as a function of temperature is shown in Figure XI.4 for the $[(BiSe)_{1+\delta}]_1[VSe_2]_1$ heterostructure prepared in this study along with that of bulk VSe_2[12] and $[(SnSe)_{1.15}]_1(VSe_2)_1$.[15] The resistivity of the $[(BiSe)_{1+\delta}]_1[VSe_2]_1$ heterostructure looks like that of a metal both in magnitude and in its temperature dependence. It has a very similar room temperature resistivity as $[(SnSe)_{1.15}]_1(VSe_2)_1$[15] and 2.5 times higher resistivity than bulk VSe_2. It has a more temperature independent resistivity than bulk VSe_2, which is consistent with prior comparisons of heterostructures made using modulated elemental reactants with crystalline misfit layered compounds.[25] There is no evidence for the prominent charge density wave transition found for $[(SnSe)_{1.15}]_1(VSe_2)_1$[15] in the resistivity data for the $[(BiSe)_{1+\delta}]_1[VSe_2]_1$ heterostructure.

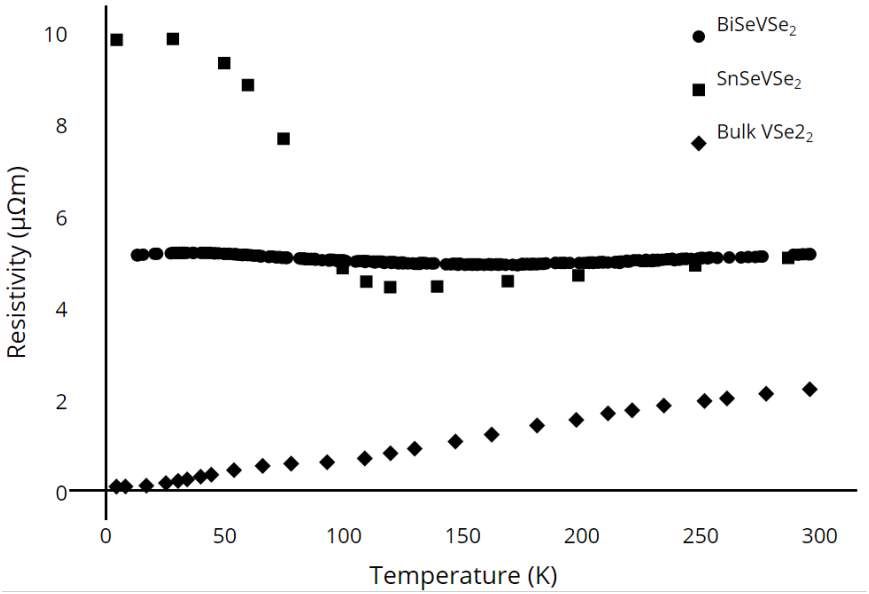

Figure XI.24. Resistivity data as a function of temperature for the $[(BiSe)_{1+\delta}]_1[VSe_2]_1$ heterostructure compared to that reported for VSe_2[12] and $[(SnSe)_{1.15}]_1(VSe_2)_1$.[15]

To obtain more information on the differences between the electrical properties of the $[(BiSe)_{1+\delta}]_1[VSe_2]_1$ heterostructure, Hall coefficients were measured as a function of temperature as shown in Figure XI. 5. The measured Hall coefficient for the $[(BiSe)_{1+\delta}]_1[VSe_2]_1$ heterostructure is negative, similar in magnitude and temperature dependence as that reported for bulk VSe_2[12] and for SnSe-VSe_2 heterostructures prepared with thicker VSe_2 layers.[16] This contrasts with the positive Hall coefficient previously reported for $[(SnSe)_{1.15}]_1(VSe_2)_1$.[15]

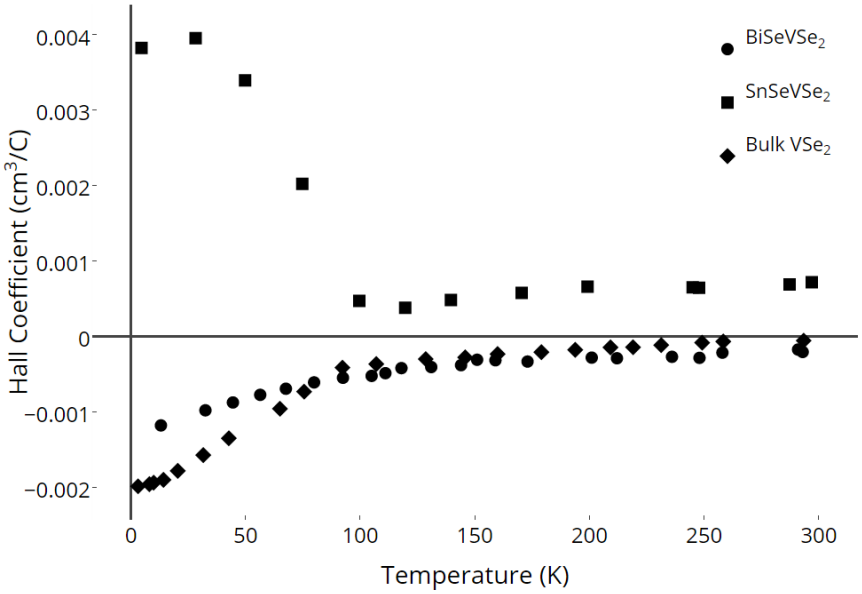

Figure XI.25. Hall coefficients as a function of temperature for the $[(BiSe)_{1+\delta}]_1[VSe_2]_1$ heterostructure compared to that reported for VSe_2[12] and $[(SnSe)_{1.15}]_1(VSe_2)_1$.[15]

The resistivity and Hall data reported here for the $[(BiSe)_{1+\delta}]_1[VSe_2]_1$ heterostructure is distinctly different than that reported for the analogous SnSe compound as shown in Figures XI.4 and XI.5. $[(SnSe)_{1.15}]_1(VSe_2)_1$[15] is a p-type conductor and has a significant increase in resistivity and in the Hall coefficient consistent with a charge density wave transition. The $[(BiSe)_{1+\delta}]_1[VSe_2]_1$ heterostructure is an n-type conductor and the temperature dependence of its Hall coefficient looks very similar to that of VSe_2. The higher resistivity of the the $[(BiSe)_{1+\delta}]_1[VSe_2]_1$ heterostructure likely results from a higher concentration of defects than the equilibrium grown single crystal of VSe_2.

There are several potential reasons for the difference in transport behavior between the $[(BiSe)_{1+\delta}]_1[VSe_2]_1$ and the $[(SnSe)_{1.15}]_1[VSe_2]_1$ heterostructures. One unlikely explanation is that the V centers of the VSe_2 layer in the $[(BiSe)_{1+\delta}]_1[VSe_2]_1$ heterostructure adopt a trigonal prismatic coordination rather than the expected octahedral coordination found in the $[(SnSe)_{1.15}]_1[VSe_2]_1$ heterostructure and in bulk

VSe_2. The similarity of the bond distances between the V and Se layers in both heterostructures argues against this, although there is no direct evidence for the coordination of the V in the VSe_2 layer. A second possibility is that a difference in the alignment of the electronic bands and the Fermi level of the SnSe and BiSe constituent with those of the VSe_2 monolayer results in a different amount of charge transfer. The distortion of both the SnSe and BiSe bilayers in the $[(MSe)_{1+\delta}]_1[VSe_2]_1$ heterostructures relative to their bulk structures indicates the importance of the interface in determining the structure and consequently the electronic structure. The periodic anti-phase boundary in the BiSe bilayer has been proposed by Wiegers to localize potential conduction electrons in Bi-Bi bonds at the anti-phase boundary in BiX containing misfit layer compounds as a means of rationalizing the trivalent nature of Bi determined from bond valence sum calculations with the similar electronic properties of analogous Sn containing misfit layer compound.[18] A higher conductivity of the BiSe layer relative to that of SnSe might electronically couple with the VSe_2 layers on either side of it more strongly, changing the electronic structure. The periodic changes in the interface potential resulting from the regular anti-phase boundaries in the BiSe layer might also prevent the formation of the CDW. The lack of CDW in crystalline misfit layer compounds has been proposed to result from the strong interaction between layers overwhelming the weaker electron-phonon interactions underlying charge density wave formation.

The modular design criteria inherent to heterostructures enables one to propose potential heterostructures to systematically test physical phenomena. For example, preparing a repeating structure consisting of a single structural unit of VSe_2-BiSe-$MoSe_2$-BiSe would maintain the same interfaces adjacent to the VSe_2 layer, but the

semiconducting $MoSe_2$ layer would reduce the through plane conductivity. If electron localization is the driving force for the formation of anti-phase boundaries in the BiSe bilayer, a VSe_2-BiSe-VSe_2-$M_{1-x}M'_xSe$ heterostructure where M and M' had different valences would enable the titration of the charge density. The changing charge density might also be expected to change the frequency of the anti-phase boundary. Comparing a VSe_2-BiSe heterostructure with a VSe_2-Bi_2Se_3 or a VSe_2-PbSe heterostructure would probe the effect of the anti-phase boundary on the CDW. Interest in heterostructures will continue to expand as theory and experiment are able to test ideas and concepts via systematic changes in nanostructure and nanoarchitecture.

XI.6. Conclusions

The single structural layer of VSe_2 in the $[(BiSe)_{1+\delta}]_1[VSe_2]_1$ heterostructure has very similar structural properties to that found in the analogous $[(SnSe)_{1.15}]_1[VSe_2]_1$ heterostructure, but the heterostructures have very different electrical properties. The $[(BiSe)_{1+\delta}]_1[VSe_2]_1$ heterostructure is metallic with electrons as majority carriers while the analogous $[(SnSe)_{1.15}]_1[VSe_2]_1$ heterostructure has holes as the majority carriers. The $[(SnSe)_{1.15}]_1[VSe_2]_1$ heterostructure has large resistance and Hall coefficient change with temperature as a consequence of a charge density wave transition, while the $[(BiSe)_{1+\delta}]_1[VSe_2]_1$ heterostructure has an almost temperature independent resistivity and a Hall coefficient sign (negative), magnitude and temperature dependence that is very similar to bulk VSe_2. The major structural difference between the two heterostructures is in the MSe constituent. The bilayer of SnSe adopts a rock salt structure while the BiSe bilayer has periodic anti-phase boundaries resulting in a larger *a*-axis lattice parameter. The anti-phase boundaries are thought to both localize electrons in Bi-Bi bonds and

potentially effectively scatter charge carriers, resulting in a low mobility. Systematic changes in heterostructure constituents and nanoarchitecture are suggested to further probe the effect of interfaces and charge transfer between constituents on properties.

CHAPTER XII

ANTIPHASE BOUNDARIES IN THE TURBOSTRATICALLY-DISORDERED MISFIT COMPOUND $(BiSe)_{1+\delta}NbSe_2$

XII.1. Authorship Statement

The following manuscript was prepared by Gavin Mitchison and published in Inorganic Chemistry in 2015, volume 54, pages 10309-10315. For this work I performed STEM measurements that highlighted the presence trigonal prismatic coordination in the $NbSe_2$ layer, of turbostratic disorder and of Bi-Bi antiphase boundaries.

XII.2. Introduction

Misfit layer compounds are materials with an interleaved structure of different 2-D constituents. The compounds are described by the general formula $[(MX)_{1+\delta}]_m(TX_2)_n$, where M = Sn, Pb, Bi, Sb, or a rare earth, X = S or Se, and T = Ti, V, Nb, Ta, and Cr.[1,2] The misfit parameter, δ, describes the ratio of in-plane unit cell areas between constituents. Parameters *m* and *n* are 1 and 1, 2, or rarely 3, respectively, and describe the number of layers of each constituent along the *c*-axis of the unit cell. The interactions between constituents result in structural distortions within and electronic interactions between the components. Hence the properties of the misfit compounds differ from those found in either constituent. Typically, MX layers adopt a distorted "rock salt-like" structure while the X-T-X dichalcogenide trilayer is similar to that found in the binary compounds. The compounds are usually partially commensurate, in that the sub-lattices of the compound constituents typically distort from bulk structures to adopt a common lattice parameter along one in-plane axis, but maintain distinct lattice parameters along the other in-plane axis.[1] The different constituents typically interact electronically

through charge transfer from one constituent to the other, usually from the MX layers into the TX_2 layers.[3] Misfit compounds with extensive turbostratic disorder between the constituents have incommensurate in-plane structures and have been called ferecrystals.[4] Despite the incommensurate lattices, electronic interaction through charge transfer between constituents still exists, and recent studies of $[(SnSe)_{1.16}]_m(NbSe_2)_n$ and $[(PbSe)_{1.14}]_m(NbSe_2)_n$ ferecrystals indicate that tunable charge transfer occurs as a function of *m* from the SnSe or PbSe layers into the $NbSe_2$ layers.[5,6]

While the interaction between the constituents are reasonably well understood for most misfit compounds, those containing BiX layers were initially puzzling. The physical properties of $[(BiX)_{1+\delta}]_m(TX_2)_n$ compounds with T = Ti are well explained by BiX donating approximately one electron per bismuth atom to the dichalcogenide.[7–9] Since δ is greater than 0, there is a compensating non-stoichiometry resulting in slightly less charge transfer than one electron per bismuth atom.[8] For $[(BiX)_{1+\delta}]_m(TX_2)_n$ compounds where T is a Group V transition metal, however, the carrier concentrations were found to be very similar to those in the analogous PbX and SnX compounds, suggesting that no or minimal charge transfer occurs.[3,10] The first clue towards resolving this contradiction was discovered by Wulff and co-workers,[11] who observed the presence of antiphase boundaries in the BiS sublattice of $(BiS)_{1.07}TaS_2$ misfit layer compound. Subsequent single crystal refinements by Gotoh et al[12] for the $(BiS)_{1.08}TaS_2$ misfit layer compound established that the BiS structure contains Bi-Bi bonds and S-S non-bonds (in one plane of the BiS bilayer) every 15.368(6) Å along the b-axis (perpendicular to the commensurate axis) of the crystal. The Bi-Bi distance is very close to the 3.1 Å observed in Bi metal, while the S-S distance is approximately 3.7 Å, much greater than the ~2 Å

typically observed in S-S bonding interactions.[13] First reported by Zhou et al[10] and later confirmed with an extensive single crystal refinement by Petricek et al,[14] the $(BiSe)_{1.09}TaSe_2$ misfit layer compound exhibits a modulated BiSe lattice with a 37.62 Å modulation periodicity. In the selenide compound, the antiphase boundaries alternate between layers in the BiSe bilayer in the direction perpendicular to the commensurate in-plane axis, hence the larger lattice parameter. In the Bi-containing misfit layer compound $(BiS)_{1.11}NbS_2$, Gotoh and co-workers[15] report the presence of the modulated BiS lattice with same repeat sequence as observed in the BiSe lattice in $(BiSe)_{1.09}TaSe_2$. In both the $(BiS)_{1.08}TaS_2$ and the $(BiSe)_{1.09}TaSe_2$ misfit layer compounds, the BiX lattice modulation also leads to a fully commensurate compound. For the $(BiS)_{1.11}NbS_2$ compound, the BiX modulation does not quite produce a fully commensurate compound, as the deviation in the subsystem lattice parameters from the commensurate ratio is small, but greater than the error of the measurement. The structural modulation observed in BiX-containing misfit layer compounds correlates with the lack of charge transfer from the BiX to the TX2 layers. A bond valence calculation by Petricek and co-workers[14] for the $(BiSe)_{1.09}TaSe_2$ misfit layer compound found that Bi is on average +3, similar to trivalent rare earth-containing misfit layer compounds. Their results indicate that the Bi-Bi bonding localizes the electrons from the trivalent Bi (on average), resulting in no significant electron donation into the $TaSe_2$ layers. Additionally, Pervov and Makhonina[16] speculate that the formation of Bi-Bi bonding pairs and Se-Se non-bonding pairs is related to strain between the BiX and TX_2 layers.

In this work, we chose to synthesize and study the $(BiSe)_{1+\delta}NbSe_2$ compound. Two structures have been reported for bulk BiSe: a stable trigonal phase and a metastable

cubic phase. Gaudin and co-workers[17] describe trigonal BiSe as a 2-D material consisting of two Se-Bi-Se-Bi-Se five-layer stacks and one Bi-Bi bilayer, with only van der Waals interactions between adjacent five-layer stacks. Semiletov[18] reports that a metastable face-centered cubic phase also exists. Reports of the properties of either BiSe phase are scant. Gobrecht and co-workers[19] report semi-metallic electrical transport properties of a "Bi_2Se_2" compound, which is consistent with theoretical calculations by Lind and colleagues.[20] In bulk, $NbSe_2$ consists of Se-Nb-Se trilayers separated by van der Waals gaps. The compound also displays several polytypes depending on the stacking arrangement of the layers, with all polytypes displaying hexagonal in-plane symmetry.[21] The electrical behavior is that of a p-type metal and some of the polytypes display charge density wave and superconducting transitions.[22] In the $(BiSe)_{1.10}NbSe_2$ misfit layer compound, both components distort from their parent structures to obtain a commensurate in-plane axis,[10] but the crystal structure of this misfit layer compound has not been reported.

Our goals in this study were to determine whether the structures would be incommensurate, if the BiSe would form antiphase boundaries, and whether the BiSe layers donate electrons to the $NbSe_2$ layers. Heideman and coworkers[23] previously reported the synthesis of many members of the $[(BiSe)_{1.10}]_m(NbSe_2)_n$ ferecrystal family, but did not investigate the in-plane structure or electrical transport properties of these compounds. Our results clearly demonstrate that the in-plane structures of the BiSe and $NbSe_2$ are not commensurate. HAADF-STEM images revealed extensive turbostratic disorder, consistent with a ferecrystalline misfit layer compound. A possible superstructure of the BiSe constituent was not observed in the in-plane XRD scans, but

cannot be excluded as a possibility due to the in-plane structural characteristics of ferecrystals, such as turbostratic disorder and small grain sizes.[10] However, the HAADF-STEM images revealed modulation of the BiSe layers similar to that reported for BiX-containing misfit layered compounds, which are clearly visible in the layers with grains oriented along the [110] zone axis. This suggests that strain between the BiX and TX_2 layers does not drive the formation of Bi-Bi bonding pairs and Se-Se non-bonding pairs. In-plane electrical resistivity and Hall coefficient measurements from 20 K to 295 K indicate p-type conductivity and no or minimal charge transfer from the BiSe layers into the $NbSe_2$ layers. This is consistent with the observation that the formation of Bi-Bi bonding pairs localizes electrons in the BiX layers and prevents charge transfer to the TX_2 layers.

XII.3. Experimental

Heideman et al[23] describe the synthesis of $[(BiSe)_{1.10}]_m[NbSe_2]_n$ ferecrystals using the Modulated Elemental Reactants method. In brief, ferecrystal precursors are formed by sequential layer-by-layer physical vapor deposition of the constituent elements. The precursors are then transferred through air to a dry, nitrogen-rich atmosphere (less than 1.0 ppm O_2) and annealed on a hot plate to self-assemble into the ferecrystal. In this work, precursors were simultaneously deposited onto both cleaved pieces of silicon wafers (Sumco, <100> orientation) and onto quartz slides (GM Associates). The quartz slides were shadow-masked to produce a 2 cm by 2 cm cross suitable for use with the van der Pauw technique for thin film electrical resistivity measurements. The raw materials used to form the precursors were bismuth needles (Alfa Aesar, 99.99% purity), a niobium slug (Alfa Aesar, 99.95% ex Ta purity), and selenium shot (Alfa Aesar, amorphous,

99.999% purity). Bismuth and niobium were evaporated at nominal rates of 0.4 and 0.2 Å/s, respectively, using 3 kW Thermionics e-Guns. Selenium was evaporated at 0.5 Å/s using a heated effusion cell. Nominal deposition rates were measured and controlled by quartz crystal microbalances dedicated to each element and positioned near the substrates. A LabVIEW program controls a motorized stage that drives the substrates over each source and opens and closes shutters for either a specific time delay (rate-controlled elements, Bi and Nb) or for a specific thickness interval (Se).

X-ray reflectivity ("XRR") measurements were collected on as-deposited and annealed films to obtain film thickness and smoothness using a Bruker D8 Discover Diffractometer with Cu Kα radiation. Specular X-ray diffraction ("XRD") scans were also taken for the annealed films. The crystal structure along the c-axis of the films was determined from a Rietveld refinement using the FullProf software package.[24] The *a*- and *b*-axis lattice parameters were determined using the WinCSD software package[25] from grazing incidence in-plane diffraction scans acquired using a Rigaku Smartlab Diffractometer with Cu K_α radiation. The structures of the compounds were confirmed by images acquired through High Angle Annular Dark Field imaging in a Scanning Transmission Electron Microscope ("HAADF STEM"), using an aberration-corrected FEI Titan (300 kV incident beam) at Pacific Northwest National Laboratory. Specimens for HAADF-STEM imaging were prepared using Ga+ Focused Ion Beam ("FIB") milling following a procedure similar to the Wedge-prep method described by Schaffer, et al.[26] Sample compositions were acquired from both Electron-Probe MicroAnalysis ("EPMA," Cameca SX-50) using a thin-film technique[27] and X-Ray Fluorescence ("XRF," Rigaku ZSX-II) measurements. Temperature-dependent electrical resistivity and Hall effect

measurements were taken between 12 and 295 K using the van der Pauw technique[28] on samples deposited onto quartz substrates.

XII.4. Result and Discussion

We made numerous precursors targeting the $(BiSe)_{1.10}NbSe_2$ ferecrystal with varied deposition parameters and annealing conditions in order to determine the optimal conditions for sample synthesis. The deposition parameters control the metal-to-metal ratio in the precursor and the amount of material in each layer, while the annealing conditions determine the kinetics for self-assembly into a ferecrystal. The precursor compositions and as deposited repeat thicknesses for these samples clustered around values that are reasonable for the formation of the targeted compound. Annealing the samples at 350 °C for 25 to 60 minutes typically resulted in self-assembly of crystalline layers, while annealing at higher temperatures (450 °C and above) resulted in evaporation of Bi from the sample and oxidation of the remaining Nb metal (despite the inert atmosphere), as determined from compositional EPMA measurements. After annealing the different precursors, we conducted specular XRR and XRD scans. The XRR scans indicated the total thicknesses of all annealed precursors were approximately 39 nm, as expected based on the number of repeat units deposited during precursor synthesis. The c-axis lattice parameters obtained for the highest quality samples, summarized in Table XII1, were approximately 1.210 nm, in good agreement with the 1.2048 to 1.2122 nm range reported previously for the ferecrystal and misfit layer compounds.[10,23,29]

Table XII.1. Sample numbers, annealing conditions, lattice parameters, and Bi/Nb atomic ratios for four different Bi-Nb ferecrystals.

Sample	Annealing T (°C), Time (min)	*c*-axis (nm)	BiSe *a*-axis (nm)	BiSe *b*-axis (nm)	$NbSe_2$ *a*-axis (nm)	In-Plane Misft	XRF Bi/Nb ratio	EPMA Bi/Nb ratio

1	350, 25	1.209(1)	0.446(1)	0.4207(9)	0.348(1)	1.12	1.16	1.17
2	350, 25	1.210(1)	0.4484(9)	0.4226(8)	0.348(1)	1.11	1.04	1.03
3	350, 25	1.211(2)	0.448(1)	0.424(1)	0.3496(7)	1.11	1.17	-
4	350, 60	1.209(3)	0.447(1)	0.4213(9)	0.3479(9)	1.11	1.17	-

Wiegers[1] states that interlayer charge transfer is correlated with a stronger interaction and hence shorter bond distance between the M atoms in MX and X in TX_2 than the interaction between M and X atoms in MX. We conducted a Rietveld refinement on the XRD pattern collected for sample 2, shown Figure XII. 26, in order to determine the atomic plane positions along the *c*-axis. Table XII.2 contains a summary of the refinement parameters. The refinement provided a *c*-axis lattice parameter of 1.2123(1) nm, similar to that obtained from lower quality specular diffraction scans. Assuming half the interlayer gap belongs to the BiSe layer and the other half belongs to the $NbSe_2$ layer, the BiSe layer and $NbSe_2$ layer thicknesses are 0.5972(1) and 0.615(1) nm, respectively. Although bulk BiSe typically adopts a trigonal phase, a cubic phase is known with a lattice parameter close to that which we observed, 0.599 nm.[18] The layer thicknesses reported for the BiSe in $(BiSe)_{1.10}NbSe_2$ misfit layer compounds are somewhat smaller, 0.582 to 0.5874 nm,[29,30] while the $NbSe_2$ layer is slightly larger, 0.6226 to 0.635 nm.[29–31] These differences can be attributed either to our assumption that the interlayer gap is split equally between the layers, or to the literature's assumption of bulk dichalcogenide trilayer thicknesses when estimating the MX bilayer thickness for the misfit layer compounds.

There is no structural refinement reported for the $(BiSe)_{1.10}NbSe_2$ misfit layer compound, so we compared our refinement results to those from compounds containing

one constituent or the other. The Nb-Se plane spacing we observed is 0.1627(3) nm, slightly smaller than typically reported for other $NbSe_2$-containing ferecrystals and misfit layer compounds, 0.1644(2) to 0.168 nm.[32–34] For the BiSe constituent, the puckering of Bi and Se atoms in the same layer, shown in Figure XII. 1 as 0.0375(4) nm, is within the 0.020 to 0.060 nm range common for misfit layer compounds in general.[1] Zhou[10] and Petricek[14] report values of 0.02929 nm and 0.02914 nm, respectively, for the puckering found in the $(BiSe)_{1.09}TaSe_2$ misfit layer compound. puckering effect, in which the Bi and Se atoms on the (001) faces of the BiSe constituent are not coincident on the same plane as they would be for a simple rock salt structure, is typically attributed to a slight attraction of the M atoms towards the Se atoms in the TSe_2 layers. The larger value we observed could be due to greater interaction between the Bi and Se of $NbSe_2$. We found the spacing between planes of Bi and Se atoms in different layers (still within the same bilayer) to be 0.2699(5) nm. Zhou[10] reports a range of slightly larger values, 0.2751 to 0.2820 nm, for the Bi-Se bond distances in the BiSe double layer in $(BiSe)_{1.09}TaSe_2$ that are approximately parallel to the *c*-axis of the crystal. The gap distance between the planes of Bi in BiSe and planes of Se in $NbSe_2$, 0.2986(8) nm, is much smaller than observed for $(BiSe)_{1.09}TaSe_2$ misfit layer compound,0.3232 nm,[14] which also suggests a greater interaction between layers.

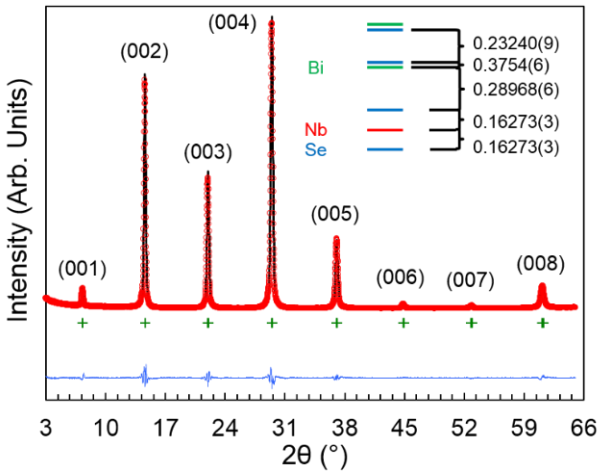

Figure XII. 26. Out-of-plane XRD pattern (Cu K_α source) for representative sample (red circles), calculated pattern from Reitveld refinement (black line), and difference between the experimental and simulated patterns (blue line). The numbers in parenthesis indicate the (00*l*) plane contributing to the observed reflection. The schematic represents the refined structure, with blue lines indicating a plane of Se atoms, red lines a plane of Nb atoms, and green lines a plane of Bi atoms. Dimensions in the schematic are given in nm.

Table XII.2. Refinement parameters for Rietveld refinement conducted on Sample 2 in space group $P\bar{3}m1$.

Parameter/Compound	
Composition from refinement	$[(BiSe)_{1.07}]_1(NbSe_2)_1$
Composition from EPMA	$[(BiSe)_{1.04}]_1(NbSe_2)_1$
Radiation	Bruker D8, Cu K_α
2θ range (degrees)	$3 \leq 2\theta \leq 65$
c (nm)	1.2123(1)
Reflections in refinement	8
Number of variables	12
$R_F = \Sigma \lvert F_o - F_c \rvert / \Sigma F_o$	0.0114
$R_I = \Sigma \lvert I_o - I_c \rvert / \Sigma I_o$	0.00922

$R_{wP}=[\Sigma w_i \lvert y_{oi}-y_{ci} \rvert^2/\Sigma w_i \lvert y_{oi} \rvert^2]^{1/2}$	0.0915
$R_P = \Sigma \lvert y_{oi}-y_{ci} \rvert /\Sigma \lvert y_{oi} \rvert$	0.0654
$R_e =[(N-P+C)/(\Sigma w_i y^2_{oi})]^{1/2}$	0.0474
$\chi^2 = (R_{wP}/R_e)^2$	3.722
Atom Parameters	
Nb in 1*a*(0)	
Occ.	1.0
Se1 in 2*c* (*z*), *z*	0.1342(2)
Occ.	2.0
Bi in 2*c* (*z*), *z*	0.3731(8)
Occ.	1.07(8)
Se2 in 2*c* (z), z	0.4043(2)
Occ.	1.07(8)

We also collected grazing incidence in-plane XRD patterns in order to determine the in-plane (*hk*0) lattice parameters of the samples. A representative in-plane diffraction scan from Sample 2 with indexed peaks corresponding to each constituent is shown in Figure XII. 27. All observed peaks but one could be assigned to (*hk*0) reflections by using a 3D space group with primitive rectangular basal plane symmetry for the BiSe constituent, *Pcmn* (similar to the approach employed by Merrill et al[8] for the BiSe in $[BiSe]_{1.15}TiSe_2$), and a space group with primitive hexagona basal plane symmetry for the $NbSe_2$ constituent, *P-3m1*. The one peak that could not be assigned, at 21.5 °*2θ*, was observed in all samples and may be a reflection, e.g. (010), that is classically forbidden in 3D for the space group used for the BiSe constituent. This reflection is allowed in the two

dimensional space group *pm* that would be expected for a single bilayer of BiSe, as it is extinguished only when two bilayers are present.

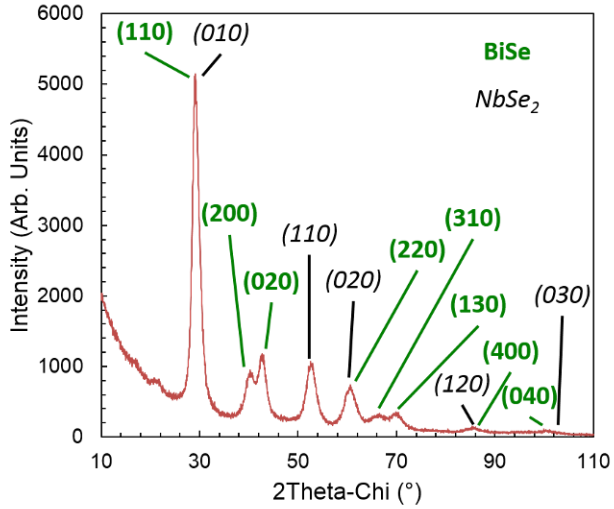

Figure XII. 27. In-plane XRD scan from Sample B. Peaks corresponding to the BiSe phase are labeled in green boldface. Peaks corresponding to the $NbSe_2$ phase are labeled in black italics. The broad reflections at angles greater than 75 °2θ were not used to determine in-plane lattice parameters.

The in-plane lattice parameters for all four samples are reported in Table XII. Unlike similar misfit layer compounds, the two constituents are entirely incommensurate with no common in-plane lattice parameters. The primitive *a*- and *b*-axis lattice parameters for the BiSe constituent in all the samples are around 0.447 and 0.423 nm, respectively. The *a*-axis lattice parameter is slightly less than Merrill et al report for the *a*-axis in their $(BiSe)_{1.15}TiSe_2$ ferecrystal, 0.4562(2) nm, but the *b*-axis parameter we found is very similar to their value of 0.4242(1) nm.[8] Conversion of our values to a face-centered lattice, as described by Falmbigl et al,[35] gives values from 0.631(1) to 0.634(1) and 0.5950(9) to 0.600(1) nm for *a* and *b*, respectively, which compare favorably with those reported for the $(BiSe)_{1.10}NbSe_2$ and $(BiSe)_{1.09}TaSe_2$ compounds, for which a = 0.6255-0.6270 nm and b = 0.5967-0.5983 nm.[10,14]

From Figure XII. 2, it is readily apparent that the $NbSe_2$ layers maintain their hexagonal in-plane symmetry. The *a*-axis lattice parameter for the $NbSe_2$ constituent for all of the samples was around 0.348(1) nm, within the range of values measured for different $NbSe_2$ polytypes, 0.344-0.353 nm.[21] Alemayehu et al[32] report a similar *a*-axis lattice parameter for the $NbSe_2$ constituent in the $(SnSe)_{1.16}NbSe_2$ ferecrystal, 0.3462 nm. The rectangular in-plane lattice parameters of the distorted $NbSe_2$ layers in the $(BiSe)_{1.10}NbSe_2$ misfit layer compound are 0.344 and 0.598 nm for *a* and *b*, respectively. Comparing the same rectangular area from the ferecrystal (a = 0.348 nm and b = 0.603 nm), the $NbSe_2$ area in the ferecrystal is approximately 2% larger than in the misfit layer compound. The difference may arise from a slight non-stoichiometry in the $NbSe_2$ layers due to small variances in ferecrystal precursor composition,[21,36,37] or from the turbostratic disorder and incommensurate nature of the interleaved and interacting layers. Based on the in-plane lattice parameters, the calculated misfit parameters for the four samples, shown in Table XII, fall within the range 1.11-1.12. The lack of a commensurate relationship between the BiSe and $NbSe_2$ layers leads to a slightly larger $NbSe_2$ basal plane area in the ferecrystal relative to the misfit layer compound, and hence a slightly larger misfit ratio.

To gain more structural information, we collected cross-sectional images using High-Angle Annular Dark Field Scanning Transmission Electron Microscopy. The HAADF-STEM images collected from the samples (see Figure XII. 28 for a representative image from Sample 2) show the layered structure expected in the *c*-axis, with alternating layers of BiSe (marked in green) and $NbSe_2$ (marked in red). The apparent waviness in the layers is probably due to sample dirft during image acquisition.

Different zone axes are apparent in different layers, indicating that the compounds are turbostratically disordered as is typical for ferecrystals [4]. Selected area electron diffraction images acquired for one of the samples (not shown) exhibited streaking along *l* except for sharp spots along the (00*l*) direction, which is also consistent with turbostratic disorder.

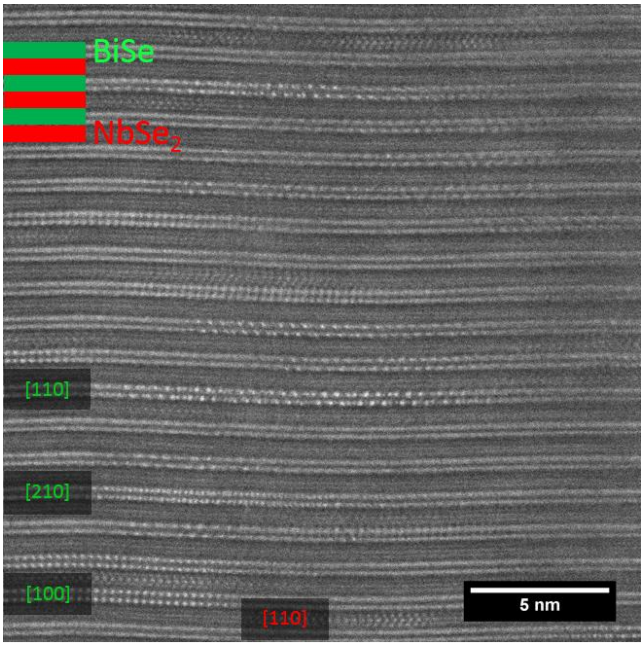

Figure XII. 28. Representative cross-sectional HAADF-STEM image. The colored boxes in the upper left corner indicate which layers correspond to which constituent. The indices refer to the zone axis of the grain to the right of the indices in that layer.

A close examination of the regions of the HAADF-STEM images containing [110] zone axes show that the majority of them contain periodic antiphase boundaries with an approximate repeat distance between Bi-Bi bonds of 1.52 nm. For convenience, we describe this direction as it would be for a rock salt-like face centered cubic lattice. The antiphase boundaries in BiX-containing misfit layer compounds were reported along the [100] or [010] directions. The [110] orientation provides adjacent atomic columns composed solely of Bi or Se atoms, making antiphase boundaries clearly visible in the

HAADF-STEM images. Figure XII. 29 contains a magnified image of one of these regions, in which the red arrows mark where the usual bright-dim sequence is periodically interrupted by a bright-bright sequence. These images are similar to what would be expected from Bi-containing selenide and sulfide misfit layer compounds with T = Nb and Ta.[1,10,14] The sequence is repeated with the same periodicity as observed in the misfit layer compound $(BiS)_{1.07}TaS_2$; approximately every third Bi atom is adjacent to another Bi atom. Examining all of the [110] zone axes in our STEM images, this structural motif was by far the one most commonly observed in our samples. Occasionally, we saw the repeat sequence characteristic of that reported for $(BiSe)_{1.09}TaSe_2$[14] with periodicity approximately 3.6 nm. Given that the ferecrystals are kinetically synthesized and that multiple modulation types are possible, it is perhaps not surprising that we observed both types. Since we did not observe any commensurate relationship between the BiSe and $NbSe_2$ constituents of the ferecrystal samples and we see periodic Bi-Bi bonding and Se-Se non-bonding characteristic of antiphase boundaries, the driving factor for the modulated BiSe structure cannot be lowering of the interfacial energy through achieving a commensurate lattice between BiSe and $NbSe_2$.

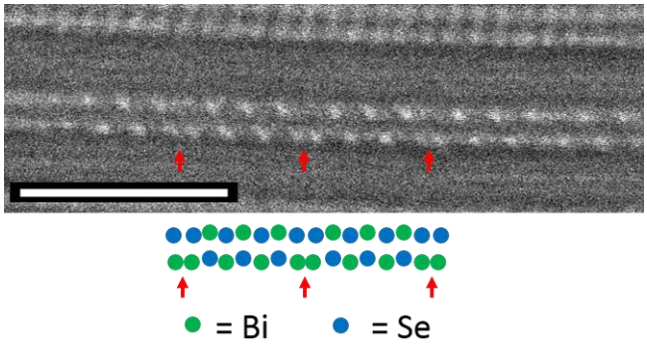

Figure XII. 29. A 110 zone axis (relative to a face centered cubic unit cell) showing antiphase boundaries approximately every 1.52 nm. The scale bar represents 2.5 nm. The

colored image below the HAADF-STEM image shows an idealized structural model. The red arrows indicate the observed antiphase boundaries.

The HAADF-STEM images also provide insight into whether or not the BiSe layers donate charge into the $NbSe_2$ layers. Py and Haering[38] observe that charge transfer due to Li intercalation into MoS_2 distorts the Mo atoms from trigonal prismatic to octahedral coordination. Alemayehu et al[6] also observe the presence of mixed trigonal prismatic and octahedral coordination of Nb in $[(SnSe)_{1+\delta}]_m NbSe_2$, for which charge transfer from SnSe to $NbSe_2$ was demonstrated. The vast majority of $NbSe_2$ grains oriented along the microscope zone axis in our HAADF-STEM images appeared to contain Nb in only trigonal prismatic coordination (easily visible as chevrons in certain $NbSe_2$ grains in Figure XII. 28). Only a few grains were observed in which the Nb appeared to be octahedrally coordinated (diagonal lines, none visible in Figure XII. 28). While by no means conclusive, the predominantly trigonal prismatic coordination environment for Nb in the $NbSe_2$ layers is consistent with the lack of charge transfer reported for the BiX-containing misfit layer compounds.

The in-plane electrical resistivity of the ferecrystals between 20 K and 295 K is shown in Figure XII. 30. The samples displayed a very weak, roughly linear decrease in resistivity as temperature is decreased. Three of the samples cluster closely together while Sample 3 has approximately double the resistivity and a slight increase in resistivity with temperature. This reflects the sensitivity of electrical properties to the structure and composition of the precursor and subsequent annealing conditions. This nearly temperature-independent resistivity behavior is typical for ferecrystals containing $NbSe_2$.[5,32] In comparison to the equivalent misfit layer compound (also shown in Figure XII. 5, labeled "MLC,"[10]), the ferecrystals were one to two orders of magnitude more

resistive due to higher residual resistivity values. This is contrary to other observations comparing ferecrystals containing $NbSe_2$ and the corresponding misfit layer compounds, in which the ferecrystal is typically less resistive than the misfit layer compound.[5,31,32] An exception is the semi-metallic $(BiSe)_{1.15}TiSe_2$ ferecrystal, which is also observed to be more resistive than its misfit layer compound counterpart.[8]

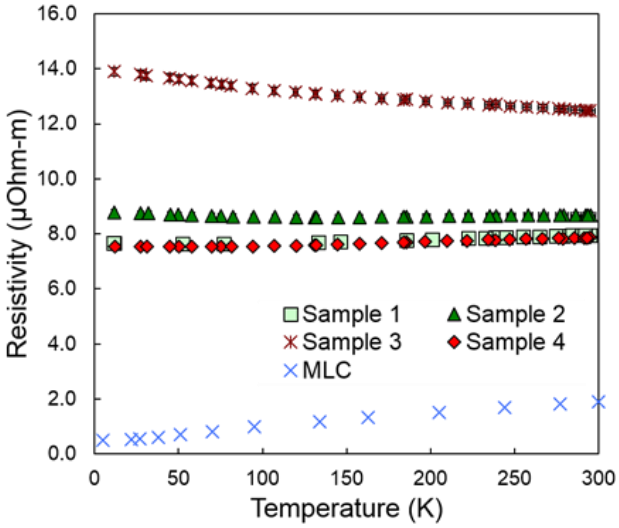

Figure XII. 30. Temperature-dependent electrical resistivities for four different Bi-Nb ferecrystals (measured in this work) and for the Bi-Nb misfit layered compound measured by Zhou and coworkers.[10] The error bars due to uncertainty in the measurements are about the size of each data point in the figure.

Van der Pauw Hall measurements were also collected as a function of temperature to determine if the increased resistivity of the ferecrystals relative to the misfit layer compounds results from a decrease in charge carriers or a smaller mobility. As shown in Figure XII. 31, the magnitude of the Hall coefficients for the Bi-Nb ferecrystals were similar to those observed for the misfit layer compound.[10] Assuming both materials have similar band structures, this indicates that both have comparable charge carrier concentrations. This suggests that the difference in resistivity is due to a lower carrier mobility for the ferecrystals. The lower carrier mobility might be due to the non-periodic

nature of the Bi-Bi bonds from plane to plane in the incommensurate ferecrystalline structure, which could scatter carriers more than would be expected in a commensurate structure. An alternate possibility is that the ferecrystals have smaller grain sizes and more defects than do the thermodynamically formed misfit layer compounds.

Unlike the misfit layer compound, in which the room temperature Seebeck coefficient was around -10 μV/K, we measured room temperature Seebeck coefficients of positive 2 to 3 μV/K for the ferecrystals. Zhou et al[10] attribute their observation of positive Hall coefficient and negative Seebeck coefficient to conduction via light holes and heavy electrons. However, our measurements indicate that holes are the dominant charge carrying species. Assuming then a single band model, we calculated for all of our samples 1.25 to 1.71 holes per Nb atom at room temperature. In theory, trigonal prismatic (2H, 3R) $NbSe_2$ has one hole per Nb atom, although defects such as excess Nb atoms in the van der Waals gaps between layers can reduce the number of holes per Nb atom to slightly less than one.[37] Typically for misfit layer compounds, slight charge transfer from divalent rock salt cations (e.g., Sn and Pb) is indicated by holes per Nb somewhat less than one (in the range 0.7-0.8), whereas for trivalent cations (lanthanides) the holes per Nb number drops to close to 0 (in the range 0.1 to 0.2).[1] Our calculated values greater than one suggests that our assumption of a single band model in which the conductivity is dominated by the $NbSe_2$ constituent is invalid. The similarity of our Hall coefficients to that measured for the misfit compound suggests, however, that similar charge transfer from BiSe to $NbSe_2$ occurs.

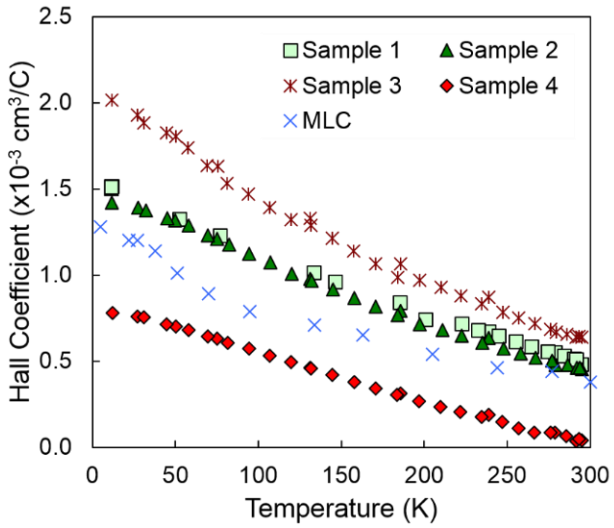

Figure XII. 31. Temperature-dependent Hall coefficients for four different Bi-Nb ferecrystals (measured in this work) and for the Bi-Nb misfit layer compound measured by Zhou and coworkers.[10]

XII.5. Conclusions

$(BiSe)_{1+\delta}NbSe_2$ compounds were prepared using modulated elemental reactant precursors. X-ray diffraction investigations indicated no epitaxial relationship exists between the BiSe and $NbSe_2$ layers. The BiSe *a*- and *b*-axis lattice parameters were similar to those observed for the misfit layer compound, while the $NbSe_2$ *a*-axis lattice parameter was slightly larger. HAADF STEM investigations revealed extensive turbostratic disorder between the constituent layers. The incommensurate structure observed for the ferecrystals prepared in this study is distinctly different than the fully commensurate misfit layer compounds prepared using conventional solid state synthesis techniques. Periodic antiphase boundaries were observed in STEM images down the [110] zone axis of the BiSe layers, similar to those reported previously for misfit layer compounds containing BiSe or BiS. Since the MER prepared samples do not have a commensurate structure, the BiSe antiphase boundaries cannot be due to coherency strain

between the constituent layers. Electrical transport measurements between 20 K and 295 K revealed a weaker temperature dependence and a higher residual resistivity for the ferecrystals than for the misfit layer compound. Both the Hall and the Seebeck coefficients were positive in sign. The electrical measurements suggest no charge transfer occurs from the BiSe layers to the $NbSe_2$ layers, which is consistent with observations of the structural modulation reported in the misfit layer compound literature for BiX-containing misfit layer compounds.

CHAPTER XIII

DESIGNED SYNTHESIS OF NEW VAN DER WAALS HETEROSTRUCTURES: THE POWER OF KINETIC CONTROLS

XIII.1. Authorship Statement

The general synthesis strategy using the MER method utilizes XRD to optimize peaks in diffraction patterns and composition using EPMA by tuning precursor layer thicknesses and annealing time and temperature until a targeted compound is made. Occasionally the targeted material was not formed, however, high quality diffraction patterns are collected which cannot be accurately solved without a reasonable starting model. In the following chapter I used scanning transmission electron microscopy to help solve the structures that formed which were quite unique from typical systems which interdigitate a rock salt structure with dichalcogenide layers. The primary author of this work, Matti Alemayehu used input from STEM-EDX and HAADF-STEM to corroborate XRD Reitveld refinement fits that suggested a partial form of the crystal structure for $GeSe_2$ was present in the interdigitated system. This paper was published in Angewandte Chemie International Edition in 2015, volume 54, pages 15468-15472.

XIII.2. Communication

*T*he discovery of graphene in 2004 and subsequent preparation of isolated monolayers of layered materials, such as *h*BN and transition-metal dichalcogenides, have had a profound effect on the fields of condensed-matter physics and materials science.[1–4] Mechanical exfoliation, chemical isolation, and van der Waals epitaxy via vapor deposition have all been shown to yield 2D structures.[3,5–9] The next big advance was the creation of heterostructures by stacking different 2D crystals on top of each other in a

chosen sequence, creating artificial materials.[10, 11] To form these van der Waals hetero- structures, two 3D van der Waals compounds (such as graphite, $MoSe_2$, $NbSe_2$, WSe_2 …) are typically cleaved at their van der Waals gap and placed on top of one another to form novel heterostructures. Heterostructures open a pathway to materials by design and offer potentially enhanced performance in many applications including energy conver- sion and storage, catalysis, sensing, and memory devices.[12–16] The major challenges in forming van der Waals hetero- structures were recently summarized by Geim and Grigor-ieva.[17] They provided "three rules of survival" to guide this growing field: 1) the parent 3D structure should have a melt- ing temperature above 10008C so that the 2D sheet is stable at room temperature, 2) the 3D structure must be chemically inert so that no decomposed surface layer forms in air or any other environment, 3) insulating and semiconducting 2D- crystals are more likely to be stable compared to metallic ones. Other challenges for scientists in this field include avoiding epitaxial relationships between the 2D structures and the substrate and precisely controlling the chosen sequence and thickness of the constituent layers of the heterostructure.

The modulated elemental-reactants (MER) technique provides a way to overcome these challenges. The MER approach precisely controls the layer sequence and nano- architecture of intergrowths of a transition-metal dichalcoge- nide and a rock salt structured constituent by using designed precursors where no epitaxial relationship between the constituents or the substrate exists.[18, 19] Herein we show the successful synthesis of heterostructures of VSe2 (metallic) and $GeSe_2$ (layered semiconductor with melting point of 7428C), which violate the survival rules outlined by Geim and Grigorieva. Bulk GeSe2 has a GeS_2-type crystal structure with *a*-, *b*-, *c*-lattice parameters

and b of 0.7016(5) nm, 1.6796(8) nm, 1.1831(5) nm and 90.65(5)8 respectively,[20] and was reported to have strong covalent bonding within the corrugated $GeSe_2$ sheets. Bulk VSe_2 crystallizes in a 1*T* polytype[21] and is among the most thoroughly investigated transition-metal dichalcogenides owing to its charge-density wave transition with an onset temperature of 100 K.[22–24] The different structure types makes intermixing of Ge and V less likely.[25] To our knowledge, GeSe2 has not been considered as a potential candidate for forming heterostructures.[17] As a member of the IV–VI family of semiconductors, bulk GeSe2 has a wide band gap (ca. 2.3 eV) and has potentially promising applications in electronics, optoelectronics, and renewable energy devices. There are limited reports of nanostructured $GeSe_2$ in the literature.[26–30]

To prepare the targeted intergrowth structures, we deposited specific sequences of bilayers of Ge and Se and bilayers of V and Se in 1:2 atomic ratios onto a silicon or quartz substrate via physical vapor deposition (PVD). An iterative calibration process was carried out to obtain 1:2 ratios of Ge and V to Se within each of the bilayers, and to obtain the targeted misfit ratio between these two different bilayers.[31] The precursors were self-assembled into the targeted metastable compounds by a short low-temperature annealing process (Figure XIII. 1 a). By varying the number of each of the bilayers deposited, the compounds VSe_2(*m*)–$GeSe_2$(*n*), where *m* = 2–4 and *n* = 1 and *m* = 3, *n* = 2, were synthesized. Throughout the manuscript we identify the compounds with a short-hand notation of (*m*,*n*) indicating the number of (VSe_2, $GeSe_2$) layers, respectively (Figure XIII. 1 a). Figure XIII. 1b shows the specular X-ray diffraction patterns of the compounds where *n* = 1–2 and *m* = 2–4, which contain only (00*l*)

reflections. The calculated *c*- lattice parameters increase by 0.609(2) nm per VSe2 layer, which is close to that reported for intergrowths of VSe_2 with rock salt structured constituents.[32] The $GeSe_2$ layer adds 0.670-(4) nm (i.e. the thickness of a $GeSe_2$ monolayer) to the *c*-lattice parameter of the (*m*,1) compounds. In the (3,2) compound, the thickness of the bilayer $GeSe_2$ was calculated to be 1.125-(6) nm, which is close to the *c*-lattice parameter of bulk GeSe2.[20]

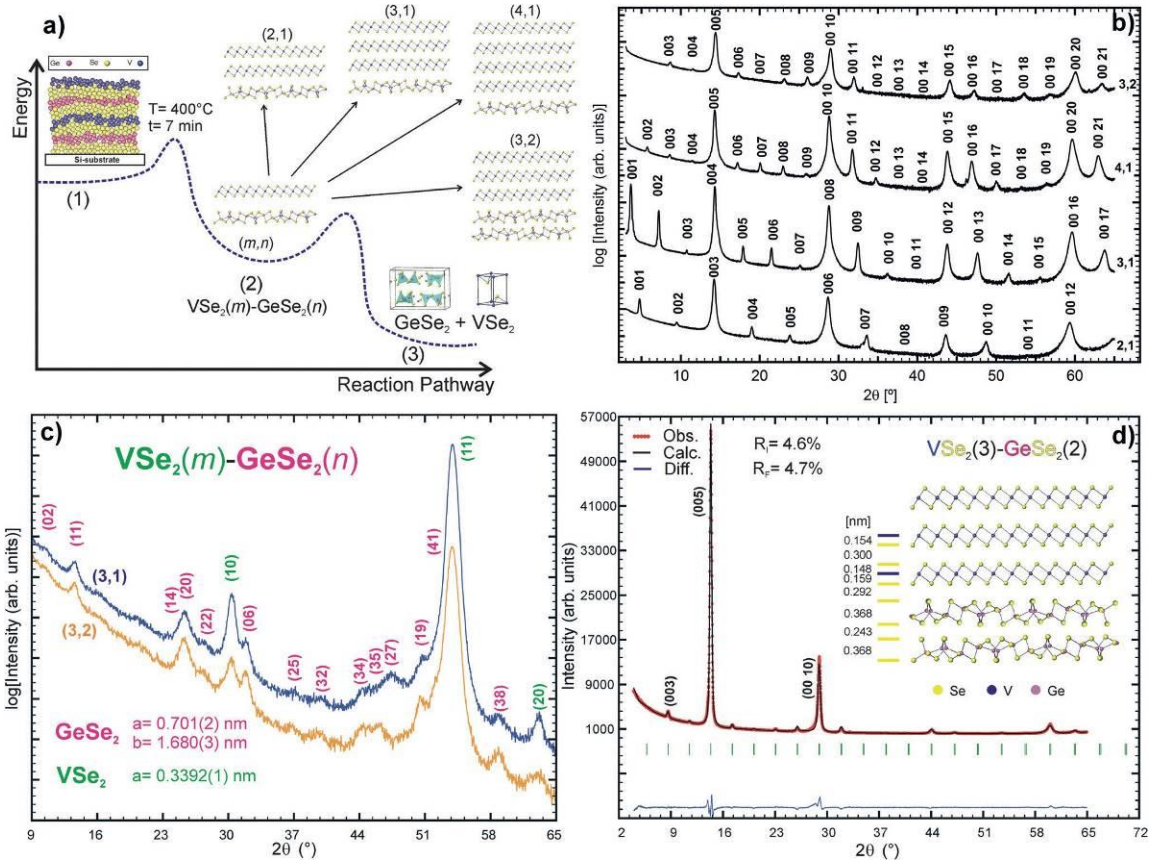

Figure XIII. 1. Structural information for the VSe_2–$GeSe_2$ heterostructures. a) Energetic requirements and reaction pathway for the formation of the VSe_2(m)–$GeSe_2$(n) heterostructures where m = 2–4 and n = 1–2. b) Specular X-ray diffraction patterns of VSe_2(m)–$GeSe_2$(n). c) In-plane X-ray diffraction patterns of VSe_2(3)–$GeSe_2$(1) and VSe_2(3)–$GeSe_2$(2). d) Rietveld refinement of VSe_2(3)–$GeSe_2$(2), the error of atomic plane distances is below 0.002 nm.

To gain more insight into the structural arrangement of the heterostructures, Rietveld refinements of the 00*l* reflections for the (3,1) and (3,2) compounds were conducted (Fig- ure 1 d). Fixing the atomic plane distances for the $GeSe_2$ to those found in the bulk compound, the atomic planes of the VSe_2 and the van der Waals gap distances between the layers were refined yielding the distances between atomic planes along the *c*-axis. The resulting van der Waals gaps are VSe_2–VSe_2: 0.300(2) nm; VSe_2–$GeSe_2$: 0.292(2) nm; and $GeSe_2$–$GeSe_2$: 0.243-(2) nm. The $GeSe_2$–$GeSe_2$ gap is larger than the bulk value (0.213 nm) [20] and the VSe_2–VSe_2 distance is similar to its bulk counterpart (0.297–0.306 nm)[21, 33] (Figure XIII. 1 d). These results indicate that the heterostructures contain monolayers of $GeSe_2$.

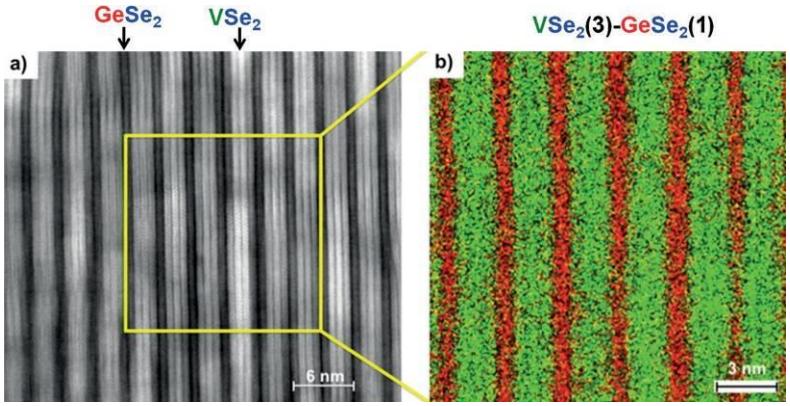

Figure XIII. 2. STEM image and an EDX map of the (3,1) heterostructure. a) STEM image of the VSe_2(3)–$GeSe_2$(1) compound with VSe_2 corresponding to the bright layers and $GeSe_2$ corresponding to the dark layers. b) EDX map of the area highlighted by the yellow square in (a). Ge red, V green.

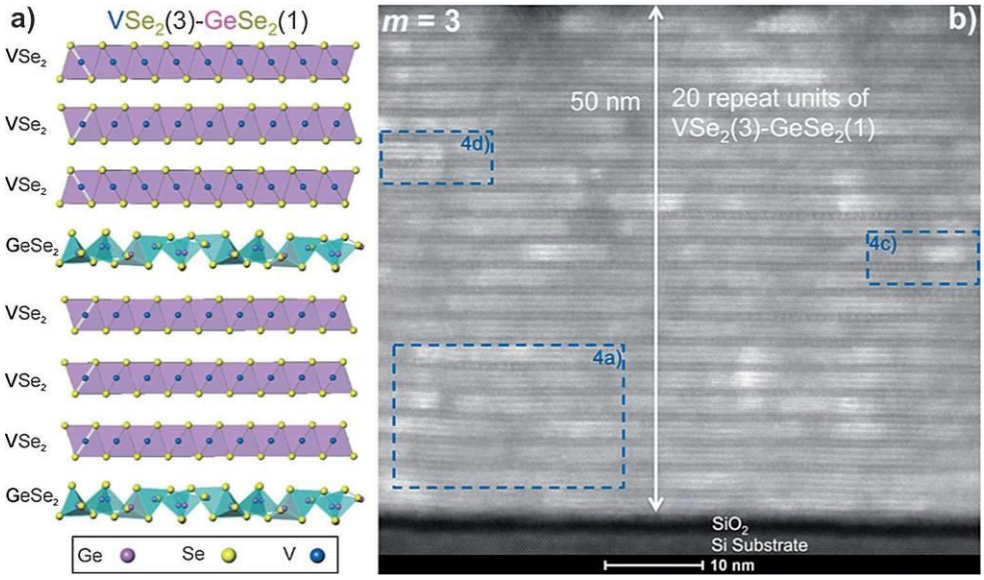

Figure XIII. 3. Superlattice structural representation and HAADF-STEM image of the (3,1) heterostructure. a) Two structural units of the VSe_2(3)–$GeSe_2$(1) compound highlighting rotational disorder indicated by white marks. b) HAADF-STEM image of VSe_2(3)–$GeSe_2$(1) with all the 20 consecutive structural units of the (3,1) compound. The highlighted areas labeled 4a, 4c, and 4d refer to the close up images in Figure XIII. 4.

In-plane X-ray diffraction supports the structural refinement, containing reflections consistent with the presence of independent crystal structures for both constituents. Indexing the reflections shows that specific planes of both constituents are parallel to one another and are crystallographically aligned to the substrate. The in-plane lattice parameters, given in Figure XIII. 1 c, are in good agreement with those of the bulk compounds, [20, 33] which supports the interpretation of minimal cation intermixing across the interfaces. The lattice mismatch along the *a*- and *b*-axis and different in-plane geometries (hexagonal and monoclinic) reinforce that this synthesis technique does not require an epitaxial relationship between the constituents.

Further confirmation of the formation of distinct VSe_2 and $GeSe_2$ layers is provided by transmission electron microscopy. Figure XIII. 2a shows a high-angle

annular dark field (HAADF) scanning transmission electron microscopy (STEM) image of VSe_2(3)–$GeSe_2$(1) showing the clearly distinguishable layers. The corresponding energy dispersive X-ray spectroscopy (EDX) maps for Ge and V in Figure XIII. 2b demonstrate the strong partitioning of the cations to their specific layers.

Additional insights concerning the structure of these new compounds containing thin slabs of $GeSe_2$ are provided by the HAADF-STEM images of the (3,1) heterostructure shown in Figure XIII. 3 and Figure XIII. 4. In Figure XIII. 3 b, a cross-sectional view of the entire film is presented with a total film thickness of 50 nm corresponding to 20 structural units. Continuous stacking of three VSe_2 layers (bright in Figure XIII. 3 b) followed by a single $GeSe_2$ layer (dark in Figure XIII. 3 b) is found throughout the sample, without any stacking defects and with atomically sharp interfaces between the constituents. Several different crystallographic orientations between subsequent layers were found indicating rotational disorder. Similar disorder was found in previous compounds synthesized via the MER technique.[18]

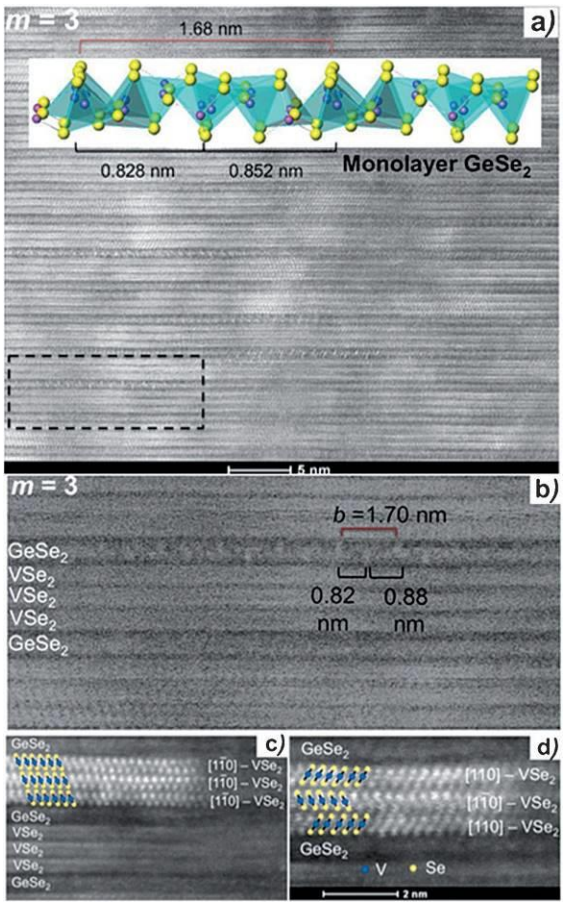

Figure XIII. 4. HAADF-STEM images of the (3,1) heterostructure. a) A monolayer $GeSe_2$ structure with a section that contains the $GeSe_2$ structure shown. b) An enlargement of Figure XIII. 4a illustrating the [100] orientation of the $GeSe_2$ structure. An enlargement of Figure XIII. 3b where the same (c) or different (d) VSe_2 orientations are observed.

Figure XIII. 4a highlights a region of the STEM image with a [100] zone axis orientation of $GeSe_2$, and the *b*- lattice parameter of 1.70(5) nm, which is consistent with the in-plane X-ray diffraction discussed above. The periodicities of the observed intensity modulations are consistent with those expected from a [100] oriented slice of the bulk structure (see inset of Figure XIII. 4 a). This supports our assertion that a monolayer of $GeSe_2$ is incorporated into these new compounds. Regions of the VSe_2 layers down the [110] zone axis are consistent

with a Se-V-Se trilayer with V in octahedral coordination (Figure XIII. 4 c). A close inspection of the VSe_2 layers contains regions that are not stacked as expected for a 1*T*-polytype (Figure XIII. 4 d). To our knowledge this has never been observed before, and highlights the rotational disorder between layers in these new compounds.

All the VSe_2–$GeSe_2$ heterostructures exhibit metallic behavior, agreeing with theoretical calculations by Terrones that predict metal–semiconductor heterostructures to exhibit metallic behavior.[34] A significant change of the magnitude as well as the temperature dependence of the resistivity is observed as the ratio of the constituents is varied (Figure XIII. 5 a). The resistivity increases with the content of $GeSe_2$ per repeat unit as would be expected for a larger amount of the semiconducting component. All of the compounds exhibit an anomaly, which changes in magnitude and onset temperature systematically with the amount of $GeSe_2$ per repeat unit. The magnitude of the anomaly is much larger than the charge-density wave transition observed in bulk VSe_2 or any reported VSe_2 nanostructures. For the (2,1) compound, an increase in the resistivity by a factor of two is observed, which is higher than reported for the charge density wave in VSe_2 containing intergrowth compounds.[32]

To get deeper insight into the observed changes in electrical resistivity, Hall effect measurements were con- ducted (Figure XIII. 5 b). While bulk VSe_2 has a small negative Hall coefficient at room temperature, owing to its nearly half filled d-band, all the VSe_2–$GeSe_2$ compounds have a positive Hall coefficient at room temperature suggesting charge transfer from $GeSe_2$ to VSe_2 has occurred.

The Hall coefficient of bulk VSe_2 becomes increasingly negative with an abrupt change in slope at the charge-density wave onset temperature of 100 K.[22] The Hall coefficients of the (3,1) and (4,1) com- pounds linearly decrease as temperature is decreased, changing sign at about 175 K with a change in slope at 150 K and 100 K, similar to that of bulk VSe_2 respectively. These changes correlate with the observed increases in resistivity at around 130 K and 100 K observed in the (3,1) and (4,1) compounds respectively. The change in sign of the Hall coefficient indicates that both electrons and holes contribute to the conductivity. The sign of RH for the (2,1) compound remains positive throughout the temperature range investigated and shows a sharp increase at the same temperature where the resistivity increases, also suggesting that carriers are localized as would be expected in a charge-density wave. This evolution, as the thickness of the VSe_2 constituent layer decreases, highlights the sensitivity of properties to the nanoarchitecture of the layering sequence. Examining RH for the (3,2) compound allows us to begin to separate the effect of constituent thickness from the ratio of constituents. The sign of RH is positive but an order of magnitude smaller than observed for the (2,1) compound. There is a smooth increase by an order of magnitude in RH as temperature is decreased between 150 K and 100 K. Again, the change in RH corresponds to the observed increase in the resistivity. Comparing the Hall coefficients at low temperatures reveals electrons and holes as majority carrier types for the heterostructures with n/m ratio below and above 0.35 respectively (Figure XIII. 5 c). This further indicates

that with increasing content of $GeSe_2$, the electronic structure of the heterostructures is significantly altered from that of bulk VSe_2.[35]

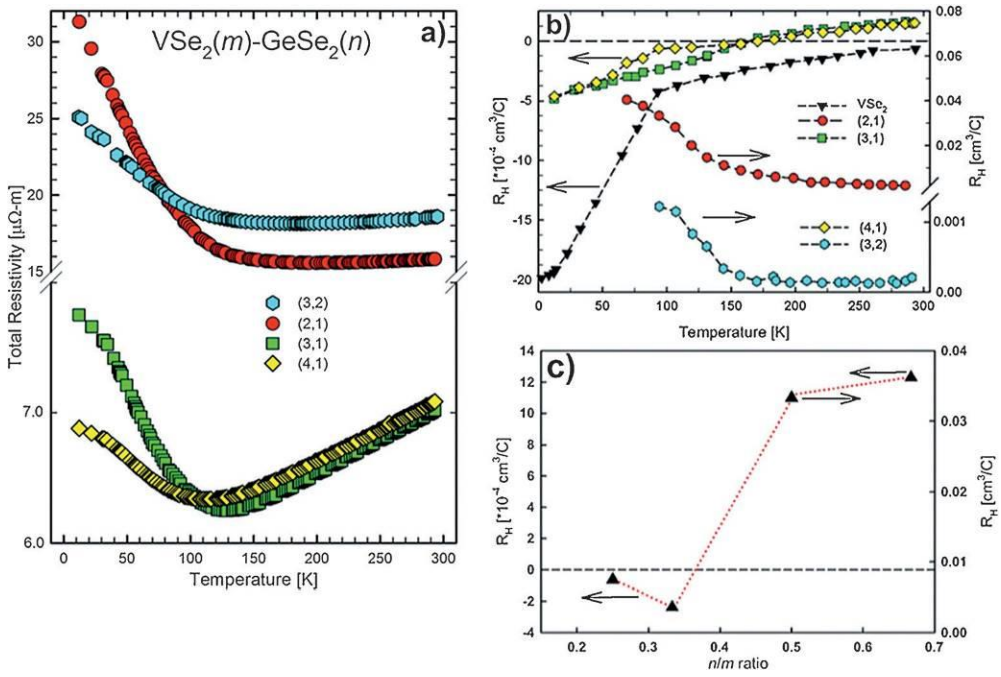

Figure XIII. 5. Electrical transport properties of VSe_2(m)–$GeSe_2$(n) where m = 2–4 and n = 1 or 2. a) Temperature- dependent resistivity. Note: the break in the y-axis. b) Temperature dependent Hall coefficient. Note: the scale change in the y-axis. c) Hall coefficient at 95K as a function of n/m ratio.

In conclusion, metalsemiconductor heterostructures were synthesized via the MER technique. Different crystal structures were incorporated into the heterostructure to avoid the pitfall of intermixing of cations in heterostructures with the same crystal structures. The precise control afforded by the synthesis technique allowed the formation of the first monolayer of $GeSe_2$ ever reported. The transport properties show systematic changes as a function of both VSe_2 and $GeSe_2$ content. Compared to bulk VSe_2 the charge density wavelike transition is strongly enhanced and the transition temperature and magnitude of this anomaly can be tuned by varying the layering sequence. This example demonstrates that the MER technique provides a powerful alternative to other

synthesis methods and allows several present limitations to a set of materials accessible for van der Waals heterostructures to be overcome, such as cation intermixing across constituents, epitaxial relationships, restriction to semiconducting and insulating constituents, and formation of a limited number of sheets of the heterostructure compounds.

XIII.3. Experimental Section

We used the modulated elemental reactant (MER) technique to synthesize the compounds reported via physical vapor deposition. The sequential deposition technique which requires an extensive calibration is described in detail elsewhere.[36]

Specular and in-plane X-ray diffraction measurements were performed on a Bruker AXS D8 diffractometer and Rigaku SmartLab equipped with CuK*a* (0.154 nm) radiation, respectively. High angular annular dark field scanning transmission electron microscopy (HAADF-STEM) samples were prepared on an FEI Helios Nano- lab 600 Dual Beam focused ion beam (FIB) using a method developed by Schaffer et al.[37] HAADF-STEM imaging was per- formed on an FEI Titan 80–300. EDS analyses were conducted using a probe-corrected FEI Titan G2 80–200, operated at 200 keV and equipped with a SuperX large area windowless X-ray detector array. Transport property measurements were conducted using a standard van der Pauw technique to acquire the in-plane electrical resistivity and Hall coefficient of the compounds in a temperature range of 10– 295 K.

CHAPTER XIV

KINETICALLY CONTROLLED SITE-SPECIFIC SUBSTITUTIONS IN HIGHER ORDER HETEROSTRUCTURES

XIV.1. Authorship Statement

In the following chapters (XIV-XVIII), quaternary systems, alloy systems, and partial alloy systems were synthesized. Observing the composition distribution after self-assembly of precursors is difficult with bulk techniques. STEM-EDX and STEM-HAADF analysis were employed to corroborate bulk methods which, together, described the resulting structure and composition distribution of the products. In the following manuscript authored by Devin Merrill, I used qualitative EDX intensity analysis to corroborate the interpretation that a solid solution was formed in bilayers of PbSe-SnSe rocksalt structured alloys. This paper was published in Chemistry of Materials in 2015, volume 27, pages 4066-4072.

XIV.2. Introduction

Perhaps the most common technique used to optimize or tune the properties of solids is to make a chemical substitution. For example, in thermoelectric materials solid solutions between two isostructural compounds are used to both lower thermal conductivity and to control carrier concentrations, resulting in improved zT values relative to the end members.[1] Substitutions are also a common method used to probe physical properties in the search for their fundamental underpinnings. Examples include superconducting compounds and magnetic materials, where substitutions have been used to probe the interaction that leads to the superconducting state and to explore magnetic coupling mechanisms between different sites, respectively.[2-6] In the electronics industry,

trace amounts of an element are added to electronically dope semiconductors, for example As, P or B into silicon, to control material properties. Carrier concentrations increase as the doping concentration increases, with a subsequent decrease in carrier mobility due to increased impurity scattering. Typically substitutions are done during synthesis or crystal growth, where the high process temperatures enhance the incorporation of the substituting atom due to entropic considerations. However, these same high temperatures lead to random substitutions distributed across potential sites controlled by the segregation coefficients of each site at the temperatures used.

Preparing desired solid solutions or tuning carrier concentration by doping becomes more challenging as solids become more complex - either structurally, in the number of constituent elements, or if a concentration gradient of the dopant is desired. For example, doping Si is rather straightforward with high activation percentages of 0.5 or more, due to preferred substitutions of dopants on lattice sites rather than other locations such as inclusions or defects.[7] Similar controlled substitutions in ternary and higher order tetrahedrally-based semiconductors, such as $CuInSe_2$, become more difficult as substitutions can occur in multiple sites and many different defects can form.[8-10] Higher order compounds with different structural motifs, such as misfit layer compounds that contain interleaved layers of a rock salt structured constituent with a transition metal dichalcogenide,[11] provide an even greater challenge. Processing conditions can also make substitutions difficult. While Si can be doped from a melt, where the segregation coefficients are known, growth conditions involving heterogeneous intermediates are difficult to control.[7] For example, compounds grown as single crystals via vapor transport reactions are notoriously difficult to dope, as the partition function between the vapor and

solids are usually not known and the kinetics of the transport reaction are different for different elements.[12] As a result of these synthetic limitations, site specific alloys of complex materials, such as misfit layer compounds, remain relatively unexplored.

A potential solution to this challenge is provided by the modulated elemental reactant method. Modulated elemental reactants have been used to prepare many new misfit layer compounds and the nanoarchitecture of the precursor has been shown to be preserved in the self assembly of the targeted kinetically-stable product.[13-15] This synthetic approach has also been shown to provide a route to prepare solid solutions within just the transition metal dichalcogenide constituent, suggesting promise for control of material properties on a finer scale than previously possible in these compounds.[16] The literature on misfit layer compounds discusses them as being related to intercalation compounds,[11,17-19] with the rock salt (MX) constituent donating charge to the dichalcogenide (TX_2) and electrical transport occurring mainly in the TX_2 constituent. It should be possible to test this hypothesis by preparing solid solutions of the MX constituent. In principle, if the MX constituent contributes significantly to the conduction, then making a solid solution should decrease the overall mobility. However, if the TX_2 constituent dominates the conduction, the mobility should not be affected by the solid solution.

Here we report the synthesis of the alloyed intergrowth compounds $(Pb_xSn_{1-x}Se)_{1+\delta}TiSe_2$ using modulated elemental reactants. The compounds are shown to form a solid solution in the rock salt structured constituent over the entire range of $0 \leq x \leq 1$, confirmed via X-ray diffraction and electron microscopy experiments. The transport properties are also characterized and Hall mobility shows that the alloying of $Pb_xSn_{1-x}Se$

actually increases carrier mobility, providing direct evidence for conduction occurring mainly in the dichalcogenide constituent in misfit layer compounds. This suggests that modulation doping, i.e. adding doping atoms to the rock salt structured layer of a misfit compound, would be an effective approach to varying carrier concentration without decreasing mobility.

XIV.3. Experimental

Amorphous layered precursors containing modulated elemental reactants were deposited in a custom built high-vacuum chamber at pressures lower than 5×10^{-7} torr. The elemental layers were deposited sequentially, in the order Ti, Se, Pb, Sn, Se, and repeated 42 times for ease of characterization. The deposition parameters were calibrated in a process described in detail elsewhere,[13] and were refined as discussed below. Si substrates were used for structural characterization. All samples were annealed in a N_2 atmosphere ($[O_2,H_2O] \leq 0.7$ ppm) for 30 minutes at 350°C, unless otherwise specified.

Structural characterization was carried out using X-ray diffraction (XRD) and X-ray reflectivity (XRR), electron probe microanalysis (EPMA), and electron microscopy techniques. Standard $\theta/2\theta$ and in-plane geometry XRD measurements were performed on a Bruker D8 Discover diffractometer and Rigaku SmartLab diffractometer, respectively (Cu Kα radiation). Standard geometry measurements were used to characterize the total film thickness (XRR) and the superlattice structure (XRD). In-plane geometry XRD was used to obtain structural information about the individual constituents. Composition data were obtained using EPMA via a thin-film technique described elsewhere.[20]

High angle annular dark field scanning transmission electron microscopy (HAADF-STEM) and energy dispersive X-ray spectroscopy (EDX) measurements were

conducted using an aberration corrected FEI Titan G2 80-200 STEM equipped with *ChemiSTEM*™ technology. The STEM was operated at 200keV, 18.1 mrad convergence angle, 110 mm camera length, and approximately 0.1 nA of current using a 50 μm condenser aperture. EDX spectrum images were acquired with a 2.3 ms dwell time per pixel integrated over multiple drift-corrected frames. Thin cross-section lamellae were prepared on an FEI Helios 600i Dual-Beam FIB using wedge premilling methods.[21] EDX signal intensity profiles were extracted for Sn, Pb, Ti, and Se at energy windows of 3.34-3.99 keV, 2.23-2.56 keV, 4.37-4.67 keV, and 1.30-1.57 keV, respectively.

Transport measurements were conducted on samples deposited through a shadow mask onto fused quartz substrates. All measurements were performed on a lab-built system between 20 and 290 K, with measurements being made during both cooling and heating to identify any hysteresis. Film thicknesses were previously measured with XRR and contacts were made with pressed indium. Resistivity measurements were performed using the van der Pauw method[22,23] in a standard cross geometry while sourcing a current of ≤ 0.1mA. Hall effect measurements were made while sourcing 0.1 mA and were performed in the same cross geometry by measuring induced voltage while varying a perpendicular magnetic field between 0-16 kG. Carrier concentration and mobility calculations assume conduction via a single carrier and band.

XIV.4.Result and Discussion

The compounds in this study were prepared using the modulated elemental reactants synthesis approach. This method relies on controlling local compositions to control reaction kinetics. To prepare the targeted alloy intergrowth compounds requires that precursor films have different regions corresponding to the compositions of the

constituents with thickness of each region close to that of the targeted structural unit. For the $Pb_xSn_{1-x}Se$, the structural unit is a bilayer with a rock salt like structure. For the $TiSe_2$, the structural unit is a Se-Ti-Se trilayer with Ti octahedrally coordinated by Se. Initial deposition parameters were taken from the prior synthesis of the parent SnSe and PbSe containing compounds and scaled to prepare the three alloy compositions.[24,25] These initial precursors were annealed at the optimum temperature for the parent compounds (350°C) and x-ray diffraction patterns were collected to confirm that the targeted compounds formed. The ratio of Pb to Sn was modified slightly based on EPMA data until the targeted compositions were obtained. The thickness of the Pb/Sn layer was then adjusted until a maximum intensity and minimum line width of 00*l* reflections was obtained without any detectable impurity phases.

An annealing study was performed on the nominally x = 0.5 precursor to determine the optimal temperature for the formation of the alloys. Figure XIV.1 contains diffraction patterns collected as a function of temperature. The as-deposited sample shows broad, low intensity 00*l* reflections due to the repeating electron density in the precursor. As the temperature was gradually increased up to 350°C, the reflections narrow, increase in intensity, and higher order 00*l* reflections appear indicating the formation of the desired superstructure. The maximum intensity and minimum line width was observed in the 350°C diffraction pattern. Above 350°C, the line widths increase, intensities of the 00*l* reflections decrease, and unidentified reflections are observed, suggesting the decomposition of the targeted compound and the formation of additional phases. 350°C was also found to be the optimal annealing temperature for the end members, and was therefore used for all of the samples in this study.

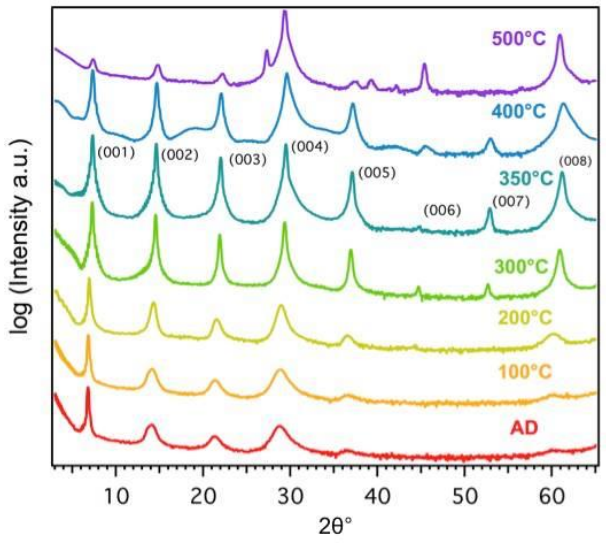

Figure XIV.1: The evolution of the diffraction pattern during the self assembly of an as-deposited precursor designed to nominally form $(Pb_{0.5}Sn_{0.5}Se)_{1+\delta}TiSe_2$. The 00*l* indices for the superlattice reflections are given above the 350°C scan.

XIV.4.1. Structural Properties

To track changes in lattice parameters as a function of Sn substitution for Pb, 00*l* diffraction patterns for both the alloys and end members were collected, and are shown in Figure XIV.2. Due to the layered nature of the compound, the films display a high level of texturing, with the c-axis normal to the substrate surface. All the diffraction maxima can be indexed as 00*l* reflections of the targeted alloyed superlattices, with no observable impurity phases or phase segregation. Qualitatively, the peaks shift continuously as a function of x from one end member to the other, which is especially obvious at higher angles (Figure XIV.2b). The c lattice parameters calculated from the patterns (Table XIV.1, inset Figure XIV.2b) vary linearly as a function of the measured global composition, following Vegard's law.[26] The (007) reflection shows the largest variation in intensity between the two end members and its normalized intensity varies systematically

with composition, resulting from the change in scattering power of the rock salt cation as a function of x, also supporting the formation of the targeted solid solution in the $Pb_xSn_{1-x}Se$ constituent (Figure XIV.2b).

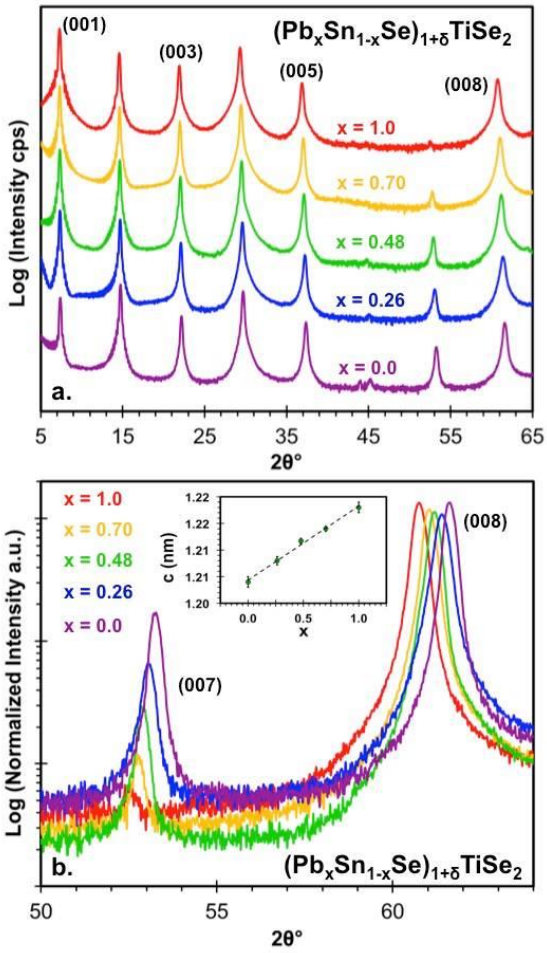

Figure XIV.2: (a) The 00*l* diffraction pattern of the five $(Pb_xSn_{1-x}Se)_{1+\delta}TiSe_2$ compounds prepared in this investigation (offset for clarity), the peaks can be indexed to the superlattice (out-of-plane) structure. **(b)** A close up of the (007) and (008) reflections, showing the systematic shift in the position of the reflections and the systematic change in the intensity of the (007) reflection of the different compounds as x is varied. The inset shows the change in the lattice parameter as a function of composition.

Table XIV.1: A summary of the measured composition and lattice parameter for the targeted $(Pb_xSn_{1-x}Se)_{1+\delta}TiSe_2$ compounds. The measured oxygen content partially results from the SiO_2 layer on the top of the substrate and is not used in calculating x.

Target Composition (x)	Fractional [O] Composition	Fractional [Se] Composition	Fractional [Ti] Composition	Fractional [Sn] Composition	Fractional [Pb] Composition	Measured Composition (x)	c-axis lattice parameter (nm)
1.0	0.04	0.59	0.18	0.00	0.19	1.00	1.218(1)
0.75	0.03	0.57	0.18	0.07	0.16	0.70	1.2140(5)
0.50	0.03	0.59	0.18	0.10	0.10	0.48	1.2117(5)
0.25	0.03	0.57	0.18	0.16	0.06	0.26	1.2080(8)
0.0	0.01	0.58	0.19	0.22	0.00	0.00	1.204(1)

The constituent structures can be characterized independently and the in-plane diffraction patterns of the compounds are shown in Figure XIV.3a.[13-16,24,25] All of the reflections can be indexed as *hk*0 reflections from the expected constituent structures. For $TiSe_2$, the indexed reflections in Figure XIV.3a are consistent with CdI_2 structure of bulk 1-T $TiSe_2$ and other $TiSe_2$-containing intergrowth compounds.[24,25,27-29,] The *a*-axis lattice parameters for the $TiSe_2$ constituent of the five compounds were calculated using a least squares fit and the space group *P-3m1*, (Table XIV.2). The $TiSe_2$ lattice parameter does not systematically vary with composition changes in the rocksalt-like layer and is consistent with that measured for other $TiSe_2$ containing misfit compounds and is close to that of bulk $TiSe_2$, further supporting the targeted site-specific substitution.[24,25,27-29] The remaining peaks in the patterns could be indexed to a rocksalt-like structure as labeled in Figure XIV.3a. The PbSe structure (x = 1) can be fit using a 2-D rocksalt structure (*p4gm*), with a square basal plane where a = b = 0.6125(2) nm. This agrees well with the lattice parameter reported previously.[24,27,28,29] The *hk*0 patterns for the SnSe structure (x = 0) shows a distortion from the square basal plane that can be fit using 2-D space group *p2gg*. This reduction in symmetry was not resolvable in the previously reported STEM data.[25] The reduced symmetry allows for the identification of all split reflections and yields an *a*-axis lattice parameter of 0.6094(3) nm and a *b*-axis lattice parameter of 0.5974(4) nm.

The intermediate compositions vary between the end members, with the lattice parameters decreasing and in-plane distortion increasing as a function of x (Figure XIV.3b and Table XIV.2). Both the a and b lattice parameters of the MSe constituent display Vegard's law behavior within error, and the in-plane area of the 2-D lattice along with the resulting calculated misfit parameter (the difference in in-plane packing density that results from incommensurate constituent lattices, represented by the 1+δ ratio of constituent formula units) can be seen plotted in Figure XIV.4 as a function of composition. The clear identification of all maxima observed in the patterns, the strong correlation between lattice parameter and measured global composition, and the lack of any impurity phases supports the conclusion drawn from the 00*l* diffraction that a $Pb_xSn_{1-x}Se$ solid solution of the rock salt constituent forms across the entire range of $0 \leq x \leq 1$. While the bulk $Pb_xSn_{1-x}Se$ solid solution has a miscibility gap such that the x = 0.26 and x = 0.48 compositions would be expected to disproportionate into Sn rich and Pb rich compounds, the kinetic approach used here provides a route to a single-phase metastable $Pb_xSn_{1-x}Se$ bilayer constituent. This solid solution behavior is perhaps not unexpected, as the structure of the rock salt bilayers is significantly different from the bulk constituents.[30]

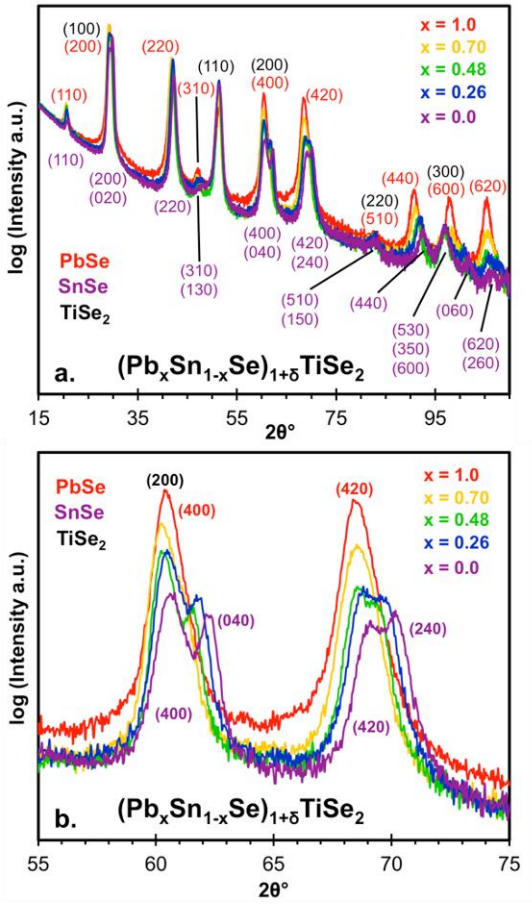

Figure XIV.3: (a) In-plane diffraction patterns of the five $(Pb_xSn_{1-x}Se)_{1+\delta}TiSe_2$ compounds prepared in this investigation. All peaks can be indexed to *hk*0 reflections of the constituent structures. **(b)** A close up of two reflections that clearly show the rectangular in plane distortion of the rock salt constituent as it becomes more Sn rich.

Table XIV.2: In-plane lattice parameters for both constituents of $[(Pb_xSn_{1-x}Se)_{1+\delta}]TiSe_2$ and the calculated misfit parameter (1+δ).

x	$Pb_xSn_{1-x}Se$ *a* (nm)	$Pb_xSn_{1-x}Se$ *b* (nm)	$TiSe_2$ *a* (nm)	1+δ
1.0	0.6125(2)	0.6125(2)	0.3542(3)	1.158(3)
0.70	0.6116(8)	0.6073(7)	0.3550(4)	1.173(6)
0.48	0.6132(9)	0.6040(9)	0.3556(4)	1.183(6)
0.26	0.6110(9)	0.6010(9)	0.3547(6)	1.187(7)
0.0	0.6094(3)	0.5974(4)	0.3562(6)	1.207(5)

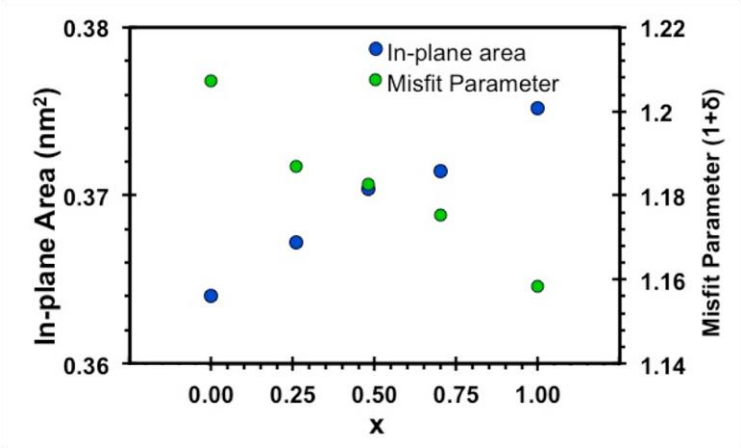

Figure XIV.4: In-plane area of the PbxSn1-xSe constituent unit cell and the calculated misfit parameter, which results from the incommensurate constituent lattices. The error for both data sets is smaller than the markers for each point.

Additional evidence for the structure of the two constituents was obtained from HAADF-STEM data, with a representative example (x = 0.26) shown in Figure XIV.5a. The image contains two constituent phases, with identifiable zone axes for a single phase rocksalt-like $Pb_xSn_{1-x}Se$ layer (brighter) and the octahedrally-coordinated CdI_2 structure expected for $TiSe_2$ (darker), consistent with the published parent compounds and the fits used in the *hk*0 diffraction data above. Turbostratic disorder is also observed, as is common in the kinetically stabilized class of compounds, synthesized from modulated elemental reactants.[13-16,24,25,29] EDX spectra images were also collected to qualitatively confirm the formation of the targeted constituents, and a map of the same representative region is shown in Figure XIV.5b. The Spectra confirm the presence of Pb, Sn, and Se in the MX layer identified by STEM, further supporting the formation of a solid solution. The repeating unit is clearly resolved, and in some regions, the individual Se and Ti layers in the Se-Ti-Se trilayers expected for $TiSe_2$ can be seen. Spectra were integrated along the a-b plane to give intensity profiles in the c direction to assess the variation in relative local compositions with alloying. A representative sample area and the resulting

profiles for the three alloy compounds are shown in Figure XIV.6, with Se removed for clarity. The systematic variations in intensities for each elemental signal correspond quite well with the expectations from the EPMA and XRD results across the compositional series. In some cases the bilayer of the MX structure can even be resolved, providing further support for the presence of bilayers of a $Pb_xSn_{1-x}Se$ alloy separated by $TiSe_2$ trilayers.

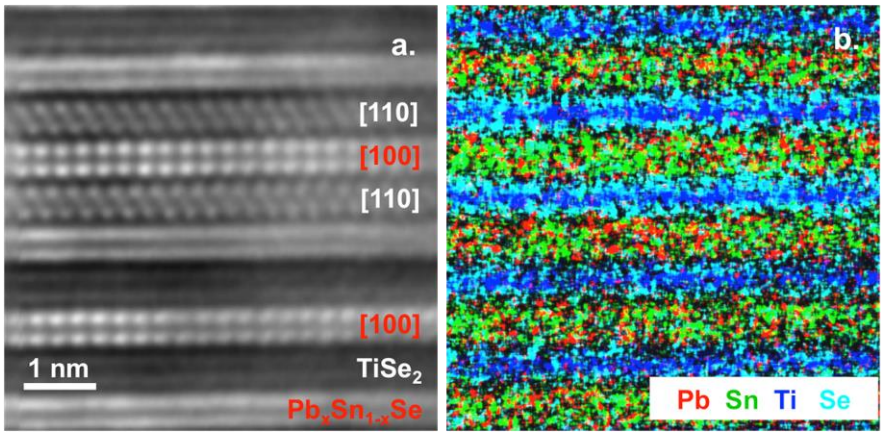

Figure XIV.5: (a) HAADF-STEM data of a representative region (x = 0.26) showing superlattice structure. Visible zone axes are labeled for each constituent and **(b)** the corresponding EDX map, with Se-Ti-Se trilayers clearly visible.

XIV.4.2. Electrical Transport Properties

Electrical transport measurements in the in-plane direction were conducted to understand the effect of the targeted substitution on the electronic structure of the compounds. The temperature dependent resistivity data for the mixed cation compounds can be seen in Figure XIV.7 along with that previously published for the two end-members.[24,25] The magnitude of the resistivity is that of a poor metal and surprisingly the lowest resistivity was found for the tin-rich alloys. The magnitudes are similar to those reported previously for other PbSe-$TiSe_2$ and SnSe-$TiSe_2$ containing layered compounds

in the literature.[24,25,28,29] Given the isovalent nature of the substitution, and the variation seen in the Sn end member shown in Figure XIV.7, the magnitudes measured on the compounds reported here likely fall within the reproducibility of samples. The very small temperature dependence of the intermediate compounds is very similar to that found for the parent compounds, suggesting a weak electron-phonon interaction. The presence of turbostratic disorder and the subsequent lack of phonons with a cross-plane component has been suggested as a cause of the small electron-phonon coupling.[25,29]

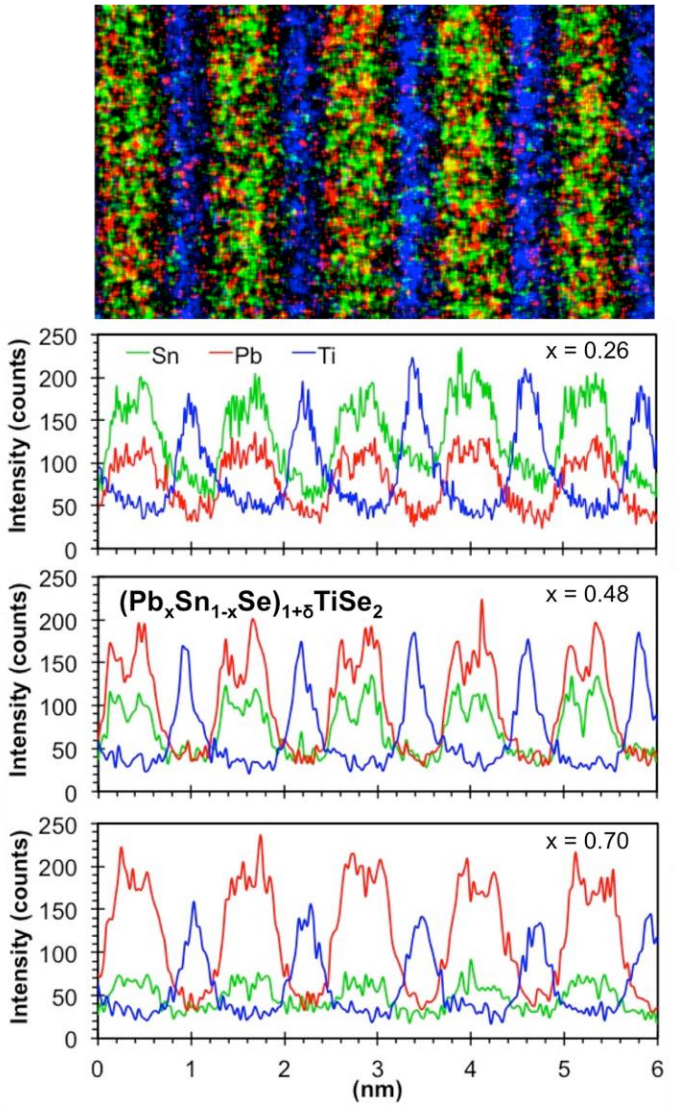

Figure XIV.6: top - EDX map for the x = 0.70 sample with the Se signal removed for clarity. The bottom three graphs provide integrated intensity profiles for the three alloy compounds. Pixel resolution varies depending on the magnification used for the profile, but the compositionally distinct layers are clearly resolved for all three samples.

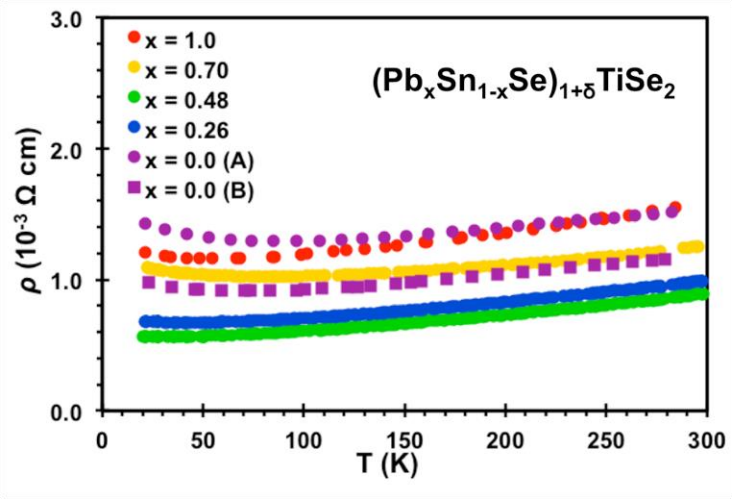

Figure XIV.7: Temperature dependent resistivity. The magnitudes of the resistivity for all compounds fall within the range expected from sample to sample variation. The (A) and (B) labels for the two x = 0 data sets refer to two separate preparations of nominally the same sample, as previously reported.[25]

The Hall coefficient (R_H) was measured to be negative for all compounds, as reported for the parent compounds and other TiX_2 based misfit type compounds,[24,25,28,29,31,32] suggesting electrons are the majority carrier. Carrier concentration was calculated for each of the compounds assuming a single band model (Figure XIV.8). The number of carriers calculated from R_H for the misfit type compounds here and in prior reports is far greater than those reported for bulk TiX_2 compounds, which has been attributed to charge transfer between constituents.[24,25,28,29,31,32] The carrier concentrations decrease linearly with decreasing temperature, which could be a result of carrier localization or a consequence of assuming a single band model. The calculated carrier concentration decreases with increasing Pb content and hence with decreasing misfit parameter. The trend in the carrier concentration is consistent with charge transfer from the rock salt layer to the $TiSe_2$, the magnitude of which would be expected to scale with the misfit parameter and the resulting change in stoichiometry between the two constituents. The

spread of the values for the two $SnSe_{1.21}TiSe_2$ compounds prepared during different deposition runs indicate that the trend is at the limit of our resolution, given the sample to sample variation.[25] This lack of a strong variation in the carrier concentration as a function of x is not surprising considering the isovalent substitution of Pb for Sn.

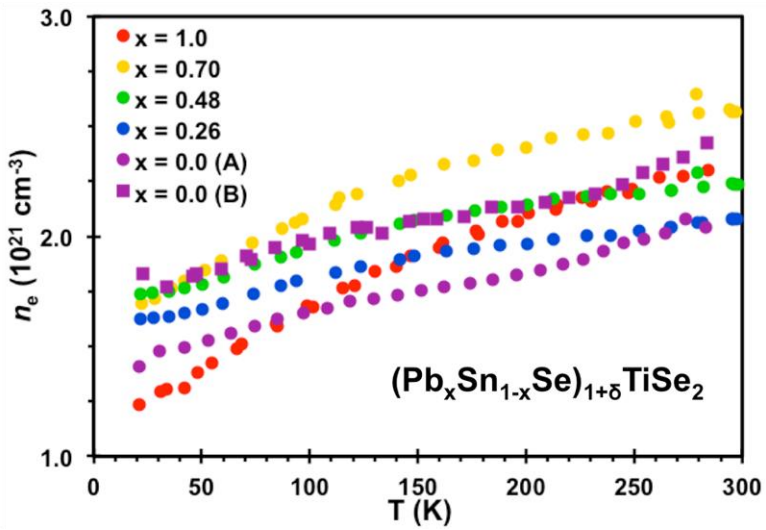

Figure XIV.8: Carrier concentration calculated from the Hall coefficient, assuming a single band model.

From the carrier concentration and resistivity, the Hall mobility was calculated for the different samples and displayed in Figure XIV.9. The highest mobility is found for the Sn rich alloys. In general, the mobility of charge carriers is influenced by defects, the presence of the interface between the constituents and by electron/phonon interactions cause by atomic displacement in the lattice due to thermal vibrations. At low temperatures, the density of impurities and defects determines the mean free path of charge carriers, and therefore mobility. Previously prepared solid solutions of both SnSe and PbSe material systems have shown decreased mobility, as expected, because the disorder present in the solid solution reduces the mean free path.[33,34] In the compounds

presented here, the disorder in the rock salt layer would be expected to significantly decrease Hall mobility if the free carriers are conducting through states in the $Pb_xSn_{1-x}Se$ layer. However, the magnitude of the mobility is equal or greater than the end members, suggesting that little charge transport occurs through the $Pb_xSn_{1-x}Se$ constituent. This mobility data provides direct evidence that electrons in the $TiSe_2$ constituent are responsible for conduction, supporting the general assumption that the dichalcogenide constituent dominates the electrical transport in misfit layer compounds.[11,17-19] We speculate that the increase in mobility for the alloys might result from preferential site occupancy by Sn and Pb, which could reduce interfacial scattering. This would imply surface segregation might occur in compounds with thicker, alloyed layers of the rock salt constituent.

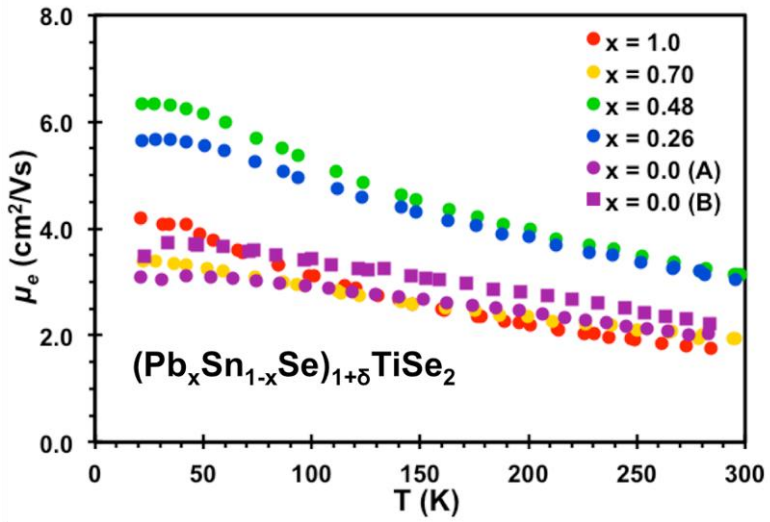

Figure XIV.9: Hall mobility calculated from resistivity and carrier concentration. The magnitude of the mobility either remains constant or increases for the mixed cation compounds, providing the first direct evidence for the conduction mechanism in the compounds.

XIV.5. Conclusions

$(Pb_xSn_{1-x}Se)_{1+\delta}TiSe_2$ compounds were successfully synthesized from modulated elemental reactants over the entire range of $0 \leq x \leq 1$, demonstrating that controlled substitution of the rocksalt cation site in a misfit layer compound is possible. The superlattice and constituent lattice parameters vary according to Vegard's law, supporting the formation of a solid solution. HAADF-STEM and EDX also support the conclusions drawn from the X-ray diffraction data. The mobility of the intermediate compounds is equal or greater than that of the end members, providing direct evidence that conduction of electrons in the $TiSe_2$ constituent is the mechanism of conduction in this family of compounds. If the appropriate substitutions can be identified, it may be possible to tune the Fermi energy in the MX layer to control charge transfer, carrier concentration and the subsequent properties of the material, without negatively impacting carrier mobility in the TX_2 structural unit. Such a modulation doping approach in a nanoscale composite material could provide a method for optimizing contradictory single-phase properties in complex materials applications, such as thermoelectric devices. More broadly, the ability to prepare complex materials with site-specific substitutions at lower reaction temperatures suggests that the use of designed precursors that target specific local compositions could enable more efficient doping of semiconducting compounds.

CHAPTER XV

THE SYNTHESIS OF MULTI-CONSTITUENT HETEROSTRUCTURES FROM DESIGNED AMORPHOUS PRECURSORS

XV.1. Authorship Statement

The following manuscript was prepared by Devin Merrill and Duncan Sutherland. For this project, I used HAADF-STEM to identify the presence of $SnSe_2$ layers in place o fthe originally targeted material, SnSe. In addition, STEM-EDX was used to qualitatively observe the separation of $SnSe_2$ and PbSe by $TiSe_2$ layers. Some migration of Sn into the PbSe layer was observed. This work has not yet been published.

XV.2. Communication

The number of unique properties discovered in single layer materials like graphene[1] and other 2-dimensional systems such as transition metal dichalcogenides have increased tremendously in the last decade.[2-4] The opportunity to design and control properties via the stacking of 2-D layers in heterostructures has further increased the interest in this field.[5] The ability to predict the structure of multiple constituent heterostructures has enabled theorists to predict combinations of constituents with enhanced properties relative to those of the bulk constituents or isolated individual 2-D layer.[6] It has been proposed that graphene monolayers separated by high k dielectric materials might result in new materials with high superconducting critical temperatures, similar to the behavior observed between loosely coupled planes in copper oxide superconducting materials.[5,7,8] Novel optical properties in heterostructures of TX_2

compounds where T = Mo and W and X = S and Se have been predicted,[9] and the observed variation in electronic structure based on the number of adjacent TX_2 layers suggests further opportunity for material design.[2,6,10] There have also been a limited number of experimental demonstrations of enhanced properties of complex structures built from 2-D materials. Intercalation of atomic or molecular species has been used to adjust properties, such as superconductivity in Ca intercalated graphene,[11] and increased T_c in superconducting TaS_2.[12] Tuning both constituents and the interaction between constituents show promise for engineering properties tuned for specific applications.[5,13]

Synthetic challenges have prevented the broader exploration of higher order heterostructures. Approaches to large area films of single constituent 2-D materials are being developed using a variety of techniques, for example the recent work on the synthesis of 2-D MoS_2,[14] but it is generally not possible to use them sequentially to prepare heterostructures containing chemically different 2-D materials.[5] The most common approach to preparing heterostructures involves the cleaving of monolayers from bulk crystals or films with adhesive tape. The individual layers are then sequentially stacked together to form a heterostructure. This is a challenging approach, which requires layers to be individually manipulated. Only a few groups have developed the necessary expertise to successfully prepare multiconstituent films. Without pristine starting materials and formation conditions, the integrity of the film and its properties may also be compromised. The stability of the isolated 2-D constituents prepared by cleaving also presents challenges, as recently highlighted Geim et al.[5] New approaches are needed to enable the preparation of heterostructures containing layers that may not be stable on

their own and that can be used to prepare homogenous multiconstituent 2-D structures over large areas.

Here we show that a kinetic approach for the synthesis of heterostructures enables the preparation of 3 constituent heterostructures in the $[(PbSe)_{1+\delta}]_m(TiSe_2)_n[(SnSe_2)_{1+\gamma}]_m(TiSe_2)_n$ family of compounds with a variety of m and n values by controlling the local composition and nanoarchitecture of designed amorphous precursors. To our knowledge, this is the first reported heterostructure containing $SnSe_2$ and among the first three-constituent heterostructures to be reported. Although structurally analogous to the thermodynamically stable misfit layer chalcogenide compounds[15] and the closely related tubular superstructures[16] including SnS-SnS_2 reported by Radovsky, et al,[17] the turbostratically-disordered products reported here consist of crystallographically independent layers with different constituent structures.

The samples were prepared by depositing elemental layers in sequences resembling the structure of the desired products,[18,19] for example a Pb-Se-Ti-Se-Sn-Se-Ti-Se sequence was used as a precursor for $[(PbSe)_{1+\delta}]_m(TiSe_2)_n[(SnSe_2)_{1+\gamma}]_m(TiSe_2)_n$. Individual elemental layer thicknesses were adjusted based on composition data from electron probe microanalysis[20] and the repeat unit thickness determined from X-ray reflectivity to contain the correct number of atoms for the targeted constituent. The precursors were intentionally deposited with ~5% excess Se to compensate for losses during annealing.[21,22] An annealing study was conducted and 275°C was established as the optimal temperature for formation. This temperature is lower than previously reported for $[(MSe)_{1+\delta}]_m(TiSe_2)_n$ compounds (M=Sn or Pb), or alloyed $[(Pb_xSn_{1-x}Se)_{1+\delta}]_m(TiSe_2)_n$ compounds.[21-24] Extended annealing above 275°C results in selenium loss and

interdiffusion of the Sn and Pb layers to form the random alloy $[(Pb_xSn_{1-x}Se)_{1+\delta}]_m(TiSe_2)_n$.[22]

Figure XV.1 contains the diffraction patterns resulting from annealing different precursors at 275°C for 15 minutes. All the diffraction maxima can be indexed as (00*l*) reflections indicating that the compounds are crystallographically aligned with their *c*-axis perpendicular to the substrate. The *c*-axis lattice parameters and in-plane lattice parameters for each of the constituents in the compounds derived from the data in Figure XV.1 and Figure XV.2 are summarized in Table XV.1. The systematic changes in the *c*-axis lattice parameter as a function of *m* and *n* enable us to calculate the average thickness of the constituent layers. The thickness of a $TiSe_2$ layer was calculated to be 0.613 nm, which is larger than the thickness of the repeating Se-Ti-Se layer found in bulk $TiSe_2$ (0.6008 nm),[25] and the thickness of $TiSe_2$ layers found in ferecrystals (0.603 nm).[26] The sum of the thicknesses of the $SnSe_2$ and PbSe layers is 1.217 nm which is slightly lower than the sum of the bulk *c*-axis lattice parameters reported in the literature for $SnSe_2$ and PbSe (1.226 nm).[27,28] A structural model inferred from the changes in c-axis lattice parameter and the HAADF STEM data discussed below containing layers with thicknesses given by the m and n values reproduce the observed intensity patterns in the 00*l* diffraction patterns.

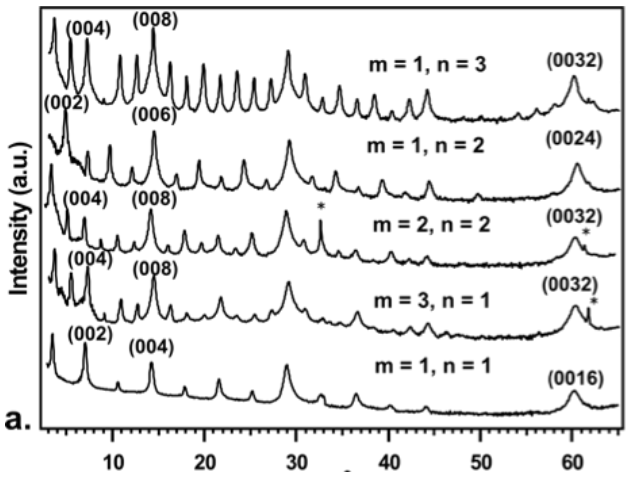

Figure XV.32: a. Out-of-plane (00*l*) diffraction patterns for compounds with different layering schemes. Indices are shown in parentheses above for selected reflections.

Table XV.1: Lattice Parameters obtained from the in and out of plane diffraction measurements.

m	n	Superstructure *c*-lattice parameter (nm)	PbSe *a*-axis lattice parameter (nm)	$TiSe_2$ *a*-axis lattice parameter (nm)	$SnSe_2$ *a*-axis lattice parameter (nm)
1	3	4.91 (1)	0.6115 (4)	0.357 (1)	0.377 (1)
1	2	3.66 (1)	0.607 (3)	0.353 (2)	0.374 (2)
2	2	4.87 (2)	0.606 (3)	0.354 (2)	0.376 (3)
3	1	4.90 (2)	0.6119 (2)	0.354 (1)	0.380 (1)
1	1	2.46 (1)	0.607 (2)	0.353 (3)	0.376 (1)

Diffraction experiments using in-plane geometry were collected to characterize the independent crystal lattices of the constituent materials, and the resulting patterns of three of the compounds are contained in Figure XV.2. Due to the textured nature of the film, only *hk*0 reflections of the independent constituent structures are present in the patterns. The lattice parameters calculated for the PbSe and $TiSe_2$ constituents (Table XV.1) are consistent with previously reported compounds, and display no clear trends as a function of the layering scheme. The PbSe constituent can be indexed using the 2-D rocksalt structure (*p*4*gm*), resulting in an *a*-axis lattice parameter ranging between

0.606(3) - 0.612(1) nm. This in-plane lattice parameter is slightly smaller than those reported for PbSe containing misfit compounds (0.614-0.620 nm) and agrees with previously reported PbSe containing ferecrystals (0.603-0.618 nm).[29] $TiSe_2$ reflections can be fit using the CdI_2 structure (*P*-3*m*1) with an *a*-axis lattice parameter that varies between 0.353(3) nm and 0.357(1) nm, also consistent with previous reports of ferecrystals (0.354-0.356 nm) containing $TiSe_2$ layers.[21-24,26] The remaining reflections can be indexed to a hexagonal CdI_2 structure (*P*-3*m*1) with the calculated *a*-axis lattice parameter varying between 0.374(2) nm and 0.380(1) nm for the heterostructures shown in Figure XV.2. These in-plane lattice parameters are close to the reported *a*-axis lattice parameter of bulk $SnSe_2$ of 3.81(1) nm.[27].

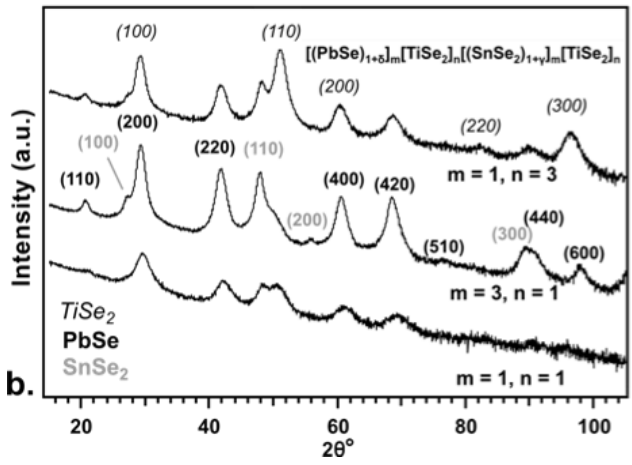

Figure XV.2 in- plane (*hk*0) diffraction patterns for compounds with different layering schemes. Indices are shown in parentheses above for selected reflections.

High angle annular dark field scanning transmission electron microscopy (HAADF-STEM) and energy dispersive x-ray spectroscopy (EDX) mapping experiments were performed to obtain further structural and compositional information on the heterostructures formed. Representative images for the m = 1, n = 3 compound, shown in Figures 3a and b, support the formation of 3 unique constituents. Figure XV.3a contains a

consistent repeating structure throughout the entirety of the film, with blocks of $TiSe_2$ separating the $SnSe_2$ and PbSe constituents. Higher magnification images like Figure XV.3b, show 3 unique constituents with different zone axes in different layers resulting from the turbostratic disorder between constituents. The brightest layers, corresponding to high Z, contain regions with the expected zone axes of a rocksalt-like structure. This is consistent with the formation of a PbSe layer. The layers with the lowest intensity correspond to the 3 layer thick regions of $TiSe_2$ (CdI_2 structure) expected from the precursor structure. In the region displayed in Figure XV.3b, many identifiable zone axes in the $TiSe_2$ layers are clearly defined. While only a 1T stacking was observed in previous $[(PbSe)_{1+\delta}]_m(TiSe_2)_n$ ferecrystals,[26] here we see several layers in which one of the layers in the $TiSe_2$ block has a different orientation, perhaps reflecting the asymmetry of the environment between the PbSe and $SnSe_2$ constituents, and the low formation temperatures. The intermediate z-contrast layers correspond to the single layer of the $SnSe_2$ constituent, which also has a CdI_2 structure type. The unique Z-contrast of the three layers, and observed patterns of the zone axes corroborate the formation of three unique constituent structures suggested by the diffraction data.

EDX maps (Figure XV.3c) show the variation of the local composition and support the structural assignments made from the HAADF-STEM images. The EDX data suggests that little intermixing is occurring, with the constituent layers remaining unique. The slight upturn in Sn signal in the Pb layer suggests that some Sn atoms may have been incorporated into the PbSe layer. The $SnSe_2$ and $TiSe_2$ layers do not appear to intermix though they have the same structure. The large difference between the in-plane lattice

parameters of these two constituents probably makes Sn/Ti substitutions enthalpically unfavorable.

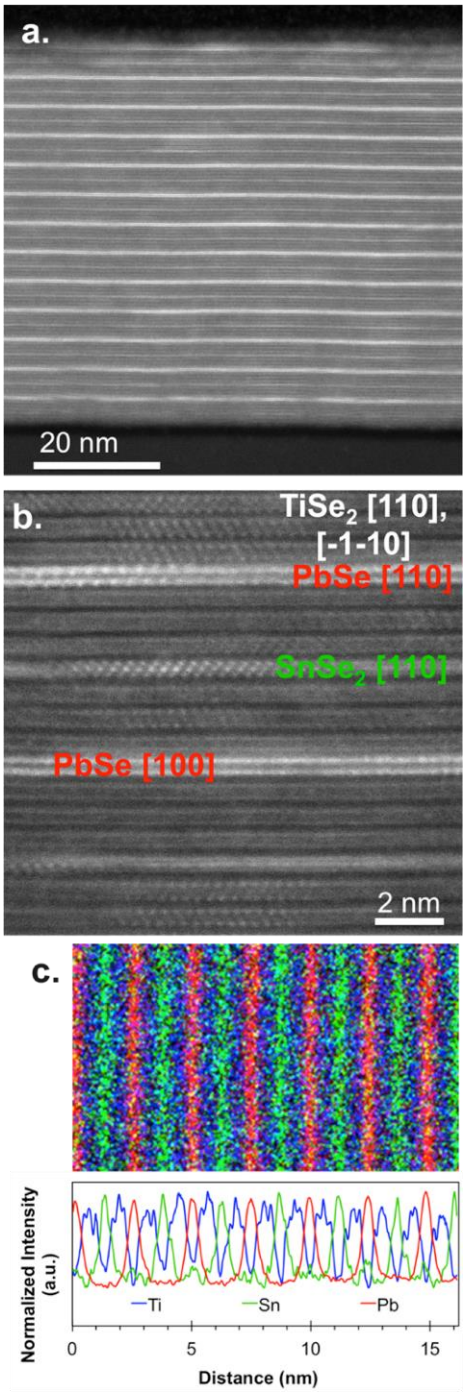

Figure XV.33: HAADF-STEM of the m = 1, n = 3 compound at low (a) and high (b) magnification, where the expected crystal faces for the constituents are observed. The EDS mapping data and the corresponding integrated profile can be found in pane c.

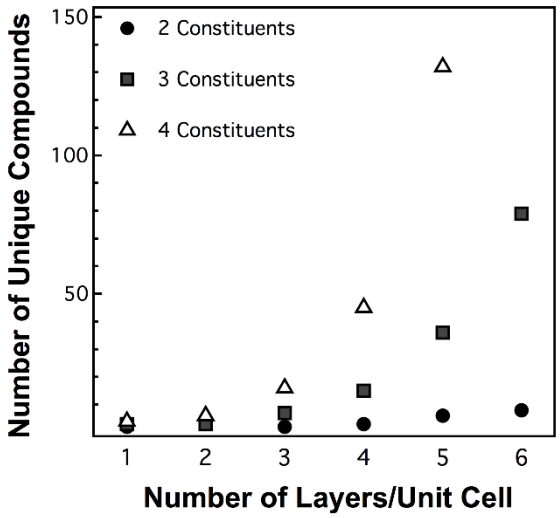

Figure XV.4: The calculated number of unique compounds based on the number of constituent layers, and the number of layers in the unit cell.

The ability to vary the sequence of layers in the precursor to self assemble specific higher order heterostructures enables systematic investigations of structure-property relationships in these complex materials. Systematic studies combined with theory to understand the fundamental interactions will be needed to guide optimization of properties and performance of devices containing heterostructures, since the number of possible configurations increases rapidly as the number of constituents increase (Figure XV.4). The total number of uniquely layered compounds for varying constituents for up to a total of 20 constituent layers per unit cell was calculated using necklace combinatorics[30] and subtracted out the repeats that occur from the factors of larger unit cells. The total number of compounds for n = 20 increases from almost 60,000 with two constituents to over 130 million with three constituents and to over 35 billion with four constituents. This illustrates the need to fundamentally understanding the interactions

between constituents and how these interactions effect structure and properties to predict how properties evolve with nanoarchitecture. The ability to prepare specific heterostructures with known structure will enable predictions to be experimentally tested, enhancing the feedback between experiment and theory.

XV.3. Experimental Section

Samples were synthesized in a custom-built physical vapour deposition system, as described elsewhere.[21-24] Pressures were maintained below $5x10^{-7}$ torr during the deposition, and rates were held between 0.1-0.3 Å/s at the substrate and monitored with quartz-crystal microbalances. Annealing was done in a N_2 environment ($[O_2,H_2O] \leq 0.8$ ppm). Out-of-plane and in-plane diffraction measurements were conducted on a Bruker D8 Discover and a Rigaku SmartLab diffractometer, respectively (Cu Kα). HAADF-STEM measurements were conducted at Pacific Northwest National Laboratory using a probe aberration-corrected Titan 80-300™ STEM and EDX maps were acquired using a probe aberration corrected JEOL ARM200CF.

CHAPTER XVI

SYNTHESIS AND CHARACTERIZATION OF QUATERNARY MONOLAYER THICK $MoSe_2$/SnSe/$NbSe_2$/SnSe HETEROJUNCTION SUPERLATTICES

XVI.1. Authorship Statement

Chapter XVI was published in Chemistry of Materials, volume 27, pages 6411-6417 in 2015. I performed microscopy measurements and the STEM-EDX used to verify the presence of a quaternary system and minimal mixing of the dichalchogenide layers. Richard Westover is the primary author of the manuscript.

XVI.2. Introduction

Heterostructures containing different layers of 2-D crystals interleaved with one another in defined order have attracted considerable interest as they provide a potentially broad platform where ideas for exceptional performance or new functionalities can be theoretically tested with reasonable assumptions about structure.[1-12] A key driver for this interest is the high probability that it will be possible to experimentally verify predictions. While initially the focus was on graphene-based heterostructures, there is increasing interest in preparing systems using other 2-D materials such as hexagonal BN and transition metal dichalcogenides (TMDs). Recent work includes the prediction that van der Waals crystals, containing alternate layers of MoS_2 and WS_2, will have optical and electronic properties distinct from its individual components[8] and the prediction of piezoelectricity in systems where different 2-D constituents are layered.[9] The use of TMD nanostructures such as ultra-thin films or nanoparticles has recently improved the properties of TMDs dramatically. Semiconducting TMDs, such as MoS_2 and $MoSe_2$, are currently being investigated for numerous applications (electrochemical sensors,[10]

supercapacitors,[11] photovoltaics,[12] and as catalysts for water splitting reactions).[13-14] While bulk MoS_2 shows limited utility as a hydrogen evolution reaction (HER) catalyst- due to low conductivity and high onset voltage[13] -its performance is greatly improved by incorporating MoS_2 nanoparticles onto the surface of reduced graphene oxide sheets.[14] The observation that the properties of 2-D materials often differ from those of the bulk compounds will continue to be an important motivation to synthesize and study heterostructures.

While techniques exist for the synthesis of heterostructures, their preparation remains a challenge. One approach has been the cleaving and stacking of individual layers. While this technique has led to the formation of many new and exciting structures, it is an exacting task only done by a few groups with very low yield.[1-7] Additionally, metallic layers have generally been found to be unstable in ambient atmosphere.[1] Epitaxy provides another approach for the synthesis of heterostructures. Koma has shown that it is possible to grow TMD superlattices via MBE, coining the term van der Waals epitaxy due to the weak bonding between constituent layers.[15-17] While this technique has produced films of exceptional quality, van der Waals epitaxy of superlattices is challenging for several reasons. The weak interlayer attraction tends to the formation of island structures rather than coherent monolayers. MBE becomes increasingly difficult as the number of constituents increases, requiring separate sets of growth conditions for each. Frequently it is not possible to grow both B on A and A on B. In addition, if the two constituents are thermodynamically miscible, increased interdiffusion occurs as the modulation wavelength of the superlattice decreases.[18-19] Significant analytical challenges arise when attempting to determine the extent of interdiffusion as precise compositional

analysis of single layers is non-trivial. Preparing multi constituent heterostructures is experimentally challenging.

Here we demonstrate that the modulated elemental reactant (MER) method is viable for the formation of ordered systems containing three different structural constituents. To the best of our knowledge, there have been no reports of crystalline misfit layer compounds with three distinct constituents. The compound with a formula of $(SnSe)_{1+\delta}(MoSe_2)_{1+\gamma}(SnSe)_{1+\delta}(NbSe_2)_1$ was targeted from a precursor with an initial structure containing a repeating sequence of elemental layers in the order Sn|Se|Mo|Se|Sn|Se|Nb|Se, as illustrated in Figure XVI.1. The targeted compound is a "worst case" synthetic challenge because compounds with alloyed transition metal dichalcogenide layers, $(SnSe)_{1+\delta}(Nb_{1-y}Mo_y)Se_2$, readily form[20] and the single bilayer-thick SnSe layer is only a 0.6 nm barrier to the mixing of the transition metals during self-assembly of the precursor into the desired superstructure. Due to the interdiffusion of miscible heterostructures synthesized by both normal and van der Waals epitaxy, and the reported miscibility of $NbSe_2$ and $MoSe_2$,[21] interdiffusion of the dichalcogenides is difficult to avoid. The extent of the interdiffusion was evaluated by comparing structural as well as electrical properties to the $(SnSe)_{1+\delta}(Nb_xMo_{1-x})Se_2$ ferecrystal alloys reported previously.[20] We estimate a stoichiometry of $(SnSe)_{1.16}([Mo_{0.9}Nb_{0.1}]Se_2)_{1.06}(SnSe)_{1.16}$ $([Nb_{0.9}Mo_{0.1}]Se_2)$ for the prepared compound. This suggests that MER provides a general route to the synthesis of van der Waals heterostructures. The ability of MER to prepare heterostructures with several constituents in designed arrangements greatly expands the range of theoretical predictions which can be experimentally tested.

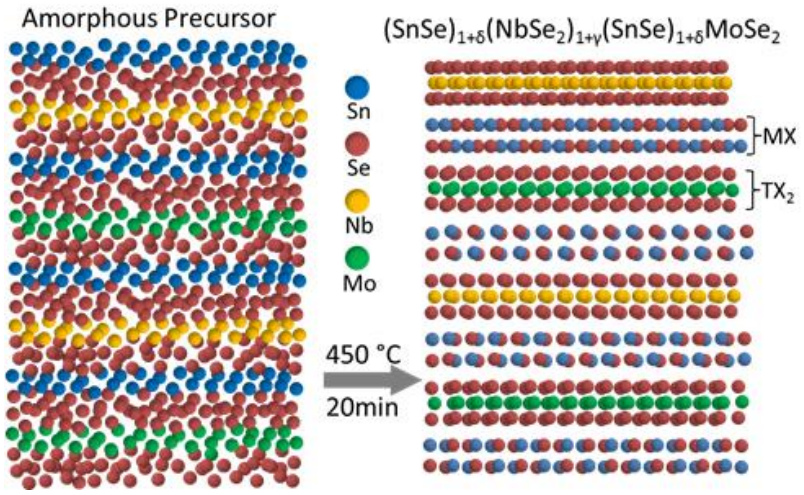

Figure XVI.1. (a) Synthesis schematic for $(SnSe)_{1+\delta}(MoSe_2)_{1+\gamma}(SnSe)_{1+\delta}(NbSe_2)_1$. The as deposited precursor is depicted on the left with the self-assembled ferecrystal on the right.

XVI.3. Experimental

The $(SnSe)_{1+\delta}(MoSe_2)_{1+\gamma}(SnSe)_{1+\delta}(NbSe_2)_1$ samples were self-assembled from carefully designed modulated precursors prepared using a custom-built physical vapor deposition system.[22] A vacuum system with dual turbo and cryo pumps allowed depositions at pressures as low as 10^{-8} torr. Mo (99.95% purity), Nb (99.8% purity), Sn (99.999% purity) and Se (99.5% purity) acquired from Alfa Aesar were used as elemental sources. Metal sources were evaporated at rates of approximately 0.2 Å/s for Mo and Nb and 0.4 Å/s for Sn, using Thermionics 3 kW electron beam guns. Se was evaporated using a custom built Knudsen effusion cell at a rate of about 0.5 Å/s. Deposition rates were monitored with INFICON Xtal quartz microbalance monitors. Substrates were mounted on a rotating carousel controlled by a custom designed LabVIEW program, which positioned the sample over the desired source. Pneumatically powered shutters between the elemental sources and the substrates controlled the exposure time of the samples to the elemental flux. Repetition of this process allowed the modulated

precursors to be built up layer-by-layer until reaching a desired thickness between 500 and 600 Å. This thickness was chosen for convenience. Films thicker than ~300 nm become less crystallographically aligned due to cumulative roughness. Films containing a single repeating unit are difficult to characterize. The precursors were annealed on a hotplate under inert conditions with O_2 < 0.6 ppm in a N_2 drybox.

Compositions of the modulated precursors and ferecrystal samples were determined by electron probe micro-analysis (EPMA) on a Cameca SX-100. Acceleration voltages of 7, 12, and 17 keV were used to collect intensities. Composition was then calculated from the film and substrate as a function of acceleration voltage as described previously.[23]

Total thickness and repeating unit thickness were monitored by high resolution X-ray reflectivity (XRR) and X-ray diffraction (XRD) performed on a Bruker D8 Discover diffractometer, equipped with a Cu K_α X-ray source and Göbel mirror optics. *ab*-plane lattice parameters were determined from in-plane Synchrotron X-ray diffraction performed at the Advanced Photon Source (APS), Argonne National Laboratory (beamline 33BM).

Transmission electron microscopy (TEM) cross-section, lift-out samples were prepared and analyzed at the Center for Advanced Materials Characterization in Oregon (CAMCOR) High-Resolution and Nanofabrication Facility. Scanning transmission electron microscopy (STEM) samples were prepared using an FEI NOVA Nanolab Dual Beam FIB equipped with Side winder ion column and performed on a FEI 80-300 kV Titan equipped with a Fischione Model 3000 Annular Dark Field (ADF) detector. All images were collected at 300 kV.

Electrical measurements were obtained from samples deposited on quartz slides in a 1 x 1 cm cross-pattern defined by a shadow mask. Temperature dependent resistivity and Hall effect measurements were performed using the van der Pauw technique as described previously.[24]

XVI 4. Results and Discussion

The targeted compounds were prepared from compositionally modulated precursors with appropriate compositions, layering sequence, and layer thicknesses which were subsequently annealed to self-assemble the desired structure. The calibrations for the parent ternary compounds, $(SnSe)_{1.04}MoSe_2$ and $(SnSe)_{1.16}NbSe_2$ have been previously reported,[25,26] and were used as a starting point to form the initial quaternary $(SnSe)_{1+\delta}(MoSe_2)_{1+\gamma}(SnSe)_{1+\delta}(NbSe_2)_1$ ferecrystal. The calibration process for the quaternary $(SnSe)(NbSe_2)_z(SnSe)(MoSe_2)_{z'}$ precursor involved scaling the precursor for $(SnSe)_{1.04}MoSe_2$ to compensate for the misfit between the ternary compounds. The procedure followed was similar to that described previously for two-constituent systems.[24]

The annealing conditions required to form the $(SnSe)_{1+\delta}([Mo_xNb_{1-x}]Se_2)_{1+\gamma}$ $(SnSe)_{1+\delta}([Nb_xMo_{1-x}]Se_2)$ ferecrystal were determined by annealing the precursor at temperatures ranging from 300 to 500 °C for 20 min in 50 °C increments. The resulting diffraction scans are shown in Figure XVI.2. In the as-deposited sample, the first few diffraction peaks are visible but there is considerable broadening of the higher order peaks (Figure XVI..2a). This indicates that the as-deposited sample lacks long-range order. At 300°C, additional (00*l*) reflections are apparent and increase in intensity with increased annealing temperature. A maximum intensity with minimum full width at half

maximum (FWHM) is reached at 450°C, as shown in Figures IV.3a and IV.3b. Above 450°C, peaks broaden and lose intensity due to the metastable nature of the product. Consequently, 450°C was chosen as the annealing temperature for this system.

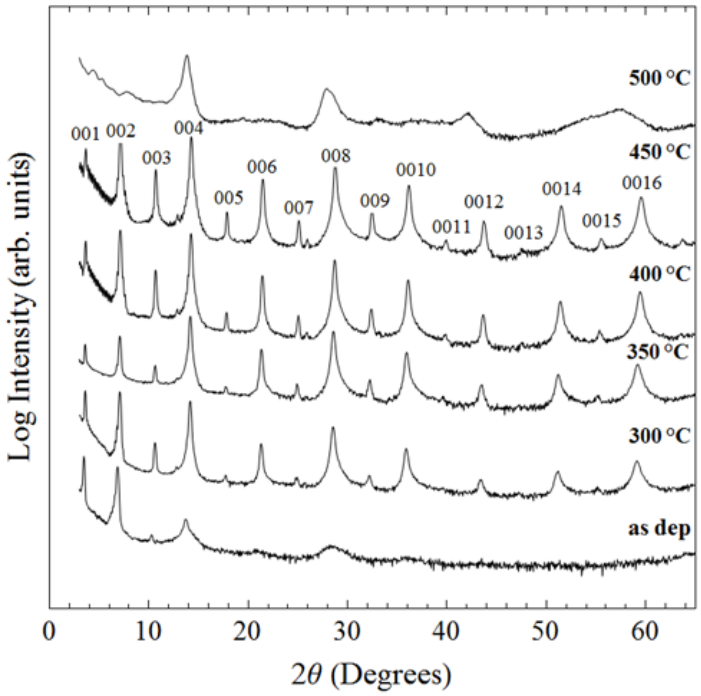

Figure XVI.2. Specular XRD patterns of $(SnSe)_{1+\delta}([Mo_xNb_{1-x}]Se_2)_{1+\gamma}(SnSe)_{1+\delta}$ ($[Nb_xMo_{1-x}]Se_2$) annealed at temperatures ranging from 300 to 500 °C. The (00*l*) indices are shown above the scan taken after annealing at 450°C.

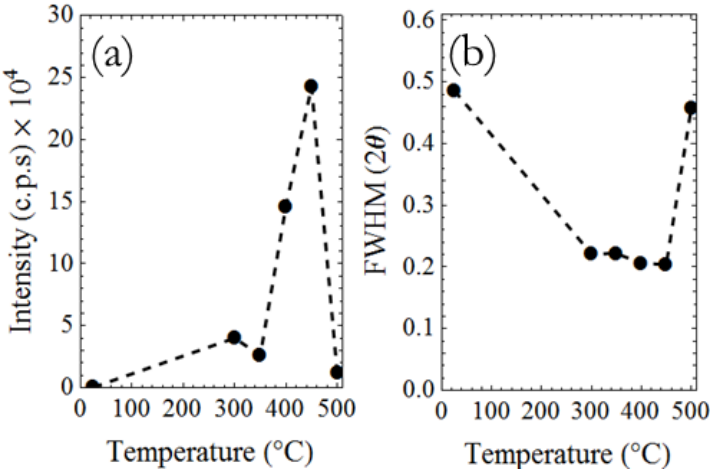

Figure XVI.3. (a) Change in the intensity of the (004) reflection with temperature. (b) Change in the FWHM of the (004) reflection with temperature.

The amorphous $(Sn|Se)(Nb|2Se)_z(Sn|Se)(Mo|2Se)_{z'}$ precursor clearly self-assembles into the ferecrystalline product; however, interdiffusion of the dichalcogenide metals across the SnSe may occur resulting in a structure better described by $(SnSe)_{1+\delta}(Nb_xMo_{1-x}Se_2)_{1+\gamma}(SnSe)_{1+\delta}(Mo_xNb_{1-x}Se_2)$, where x represents the extent of intermixing between the resulting Nb-rich and Mo-rich dichalcogenide constituents. This interdiffusion is often seen in superlattices with miscible constituents and increases as the superlattice period decreases.[18-19] It is analytically difficult to determine the exact composition of individual layers within the structure. The specular X-ray diffraction pattern of $(SnSe)_{1+\delta}([Mo_xNb_{1-x}]Se_2)_{1+\gamma}(SnSe)_{1+\delta}([Nb_xMo_{1-x}]Se_2)$, shown in Figure XVI..4, contains (00*l*) superlattice peaks not seen in the X-ray pattern of the $(SnSe)_{1.13}(Nb_{0.51}Mo_{0.49})Se_2$ alloy ferecrystal published previously,[20] indicating that the c-axis lattice parameter has approximately doubled in size. This implies that the sample has Nb-rich and Mo-rich regions as described by the above formula. Figure XVI..4 also shows the Rietveld refinement of the 00*l* data, which gives the positions of the planes of atoms along the c direction. The c-lattice parameter obtained is 2.484(2) nm, which is close to that expected from the sum of the two parent compounds, $(SnSe)_{1.04}MoSe_2$ and $(SnSe)_{1.16}NbSe_2$.[25,26] As the electron density differences between Mo and Nb are slight, only differing by a single electron, the extent of intermixing cannot rigorously be determined using this method, but a best fit was obtained assuming a negligible amount of interdiffusion. The distances between the plane of transition metal atoms and the planes of selenium atoms in the Se-T-Se trilayers were determined to be 1.65(2) and

1.61(2) Å, which match well with the published values of 0.16(1) and 0.1644(2) nm for the $(SnSe)_{1.04}MoSe_2$ and $(SnSe)_{1.16}NbSe_2$ parent ferecrystals.[25,26] The distance between the dichalcogenide selenium atoms and the neighboring rock salt atoms were determined to be 0.302(2) and 0.296(2) nm, which also match well with the published values for the $(SnSe)_{1.04}MoSe_2$ and $(SnSe)_{1.16}NbSe_2$ parent compounds of 0.31(1) and 0.2906(1) nm respectively. The total thickness of the rock salt bilayer, 0.318 nm, is close to that found in the parent compounds 0.30(2) nm for $(SnSe)_{1.04}MoSe_2$ and 0.316(1) nm for $(SnSe)_{1.16}NbSe_2$). The Rietveld refinement also revealed information regarding the puckering of the rock salt layers arising from interlayer attraction. During the refinement, however, we found that the puckering values were unstable, varying greatly with changes in the composition or misfit parameter used in the fit. While the puckering of the rock salt on the $NbSe_2$ side was found to be 0.05(2) nm, closely matching the value of 0.045(1) nm found for the $(SnSe)_{1.16}NbSe_2$ parent compound, the puckering of the SnSe on the $MoSe_2$ side was 0.07(2) nm. This is somewhat larger than that found in typical ferecrystals and may be indicative of stronger interlayer interaction, but also could be due to defects.

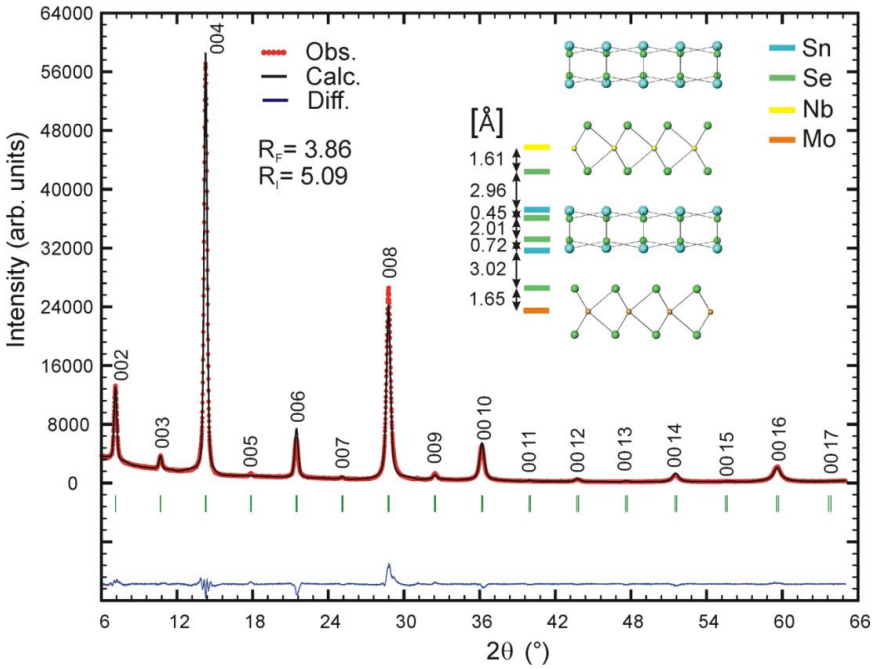

Figure XVI.4. Rietveld refinement of the $(SnSe)_{1+\delta}([Mo_xNb_{1-x}]Se_2)_{1+\gamma}(SnSe)_{1+\delta}([Nb_xMo_{1-x}]Se_2$. Experimental data are in black and the fit to the data in red with the residuals below in blue. The inset shows the structure and distances obtained from the fit.

To gain additional structural information about the $(SnSe)_{1+\delta}([Mo_xNb_{1-x}]Se_2)_{1+\gamma}(SnSe)_{1+\delta}([Nb_xMo_{1-x}]Se_2)$ films, high-angle annular dark-field (HAADF) STEM images were obtained. Figure XVI.5a illustrates the long-range order and precise layering in the sample that result in the sharp diffraction pattern shown in Figure XVI.4. The alternating layering of SnSe bilayers with the dichalcogenide regions can be clearly seen. The coordination of the various atoms can be clearly seen in the Z-contrast STEM image expansions provided in Figure XVI.5b. The chevron structure observed in the dichalcogenide regions indicates trigonal prismatic coordination for the transition metals, while a rock salt structure is observed for the SnSe constituents. In Figure XVI.5a, the Z-contrast is insufficient to distinguish between the $MoSe_2$ and the $NbSe_2$ layers. Increasing the electron current and reducing the camera length allowed the Z-contrast of the image

to be further improved, but with a loss of atomic resolution. A HAADF intensity line profile, given in Figure XVI5c, clearly shows a difference in intensity for the two dichalcogenide layers. The contrast results from the slightly increased Z-value of Mo, as well as a reduced a-lattice parameter of $MoSe_2$ compared to $NbSe_2$, which increases the density of the $MoSe_2$ layer.

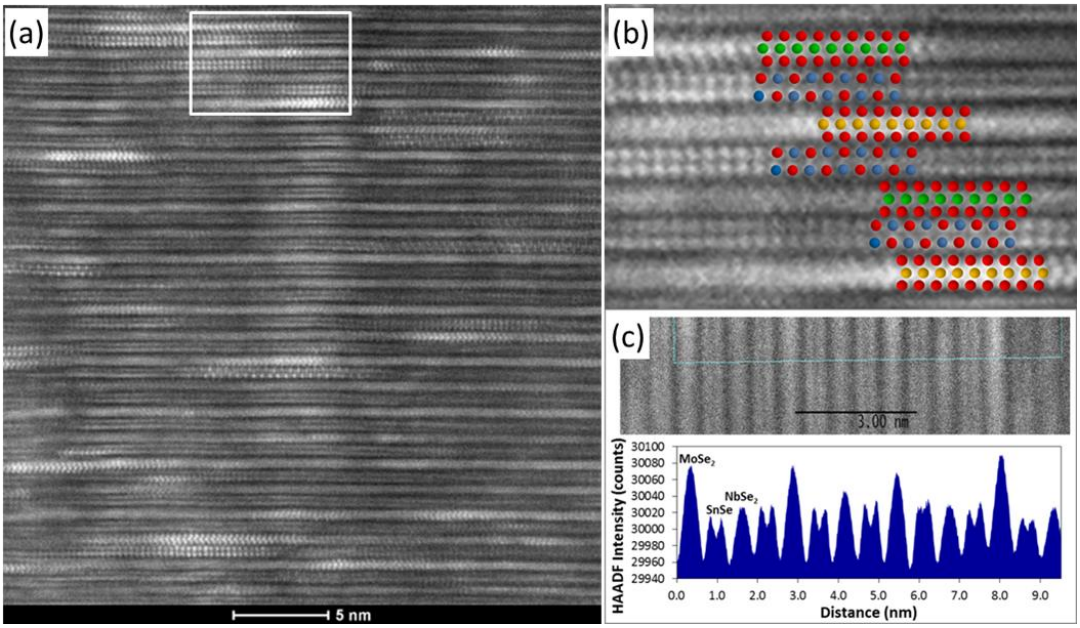

Figure XVI 5. (a) STEM image of $(SnSe)_{1+\delta}([Mo_xNb_{1-x}]Se_2)_{1+\gamma}(SnSe)_{1+\delta}([Nb_xMo_{1-x}]Se_2)$. (b) Expansions of different layers within part a showing the local coordination of the layers. (c) HAADF Intensity line profile for $(SnSe)_{1+\delta}([Mo_xNb_{1-x}]Se_2)_{1+\gamma}(SnSe)_{1+\delta}([Nb_xMo_{1-x}]Se_2$ film.

To further identify the different layers within the $(SnSe)_{1+\delta}([Mo_xNb_{1-x}]Se_2)_{1+\gamma}(SnSe)_{1+\delta}([Nb_xMo_{1-x}]Se_2)$ film, EDX line scans were also performed (Figure XVI.6). While the separation of the Mo, Nb, and Sn into distinct layers was observed, quantifying the amount of interdiffusion is difficult using EDX as it requires accurate measurement of the background signal of the instrument. The peak widths of the EDX signals are

determined by the excitation volume of the electron beam, resulting in widths that are broader than the 0.6 nm thicknesses of the individual layers. This limits our ability to determine the extent of mixing between adjacent layers.

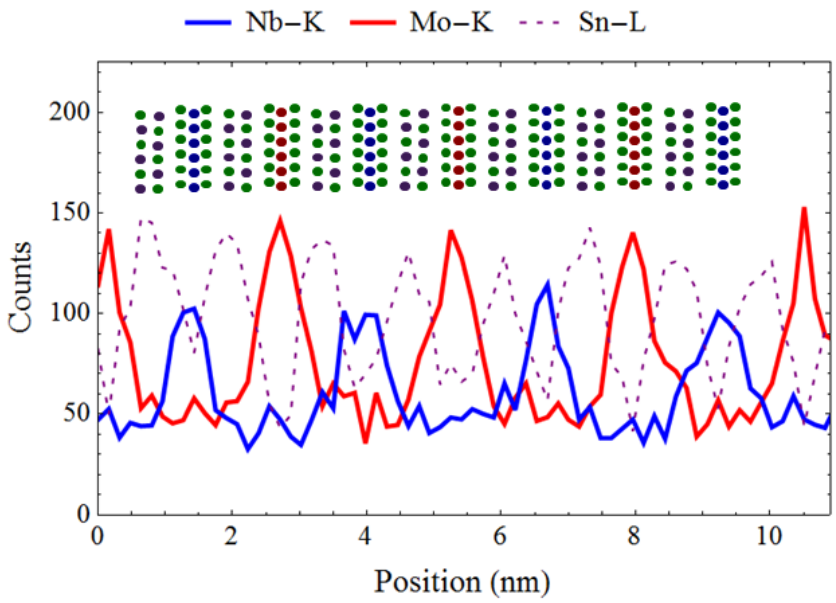

Figure XVI.6. EDX line scan of $(SnSe)_{1+\delta}([Mo_xNb_{1-x}]Se_2)_{1+\gamma}(SnSe)_{1+\delta}([Nb_xMo_{1-x}]Se_2)$. The Mo-K line (red), Nb-K line (blue) and the Sn-L line (purple dashed) are shown. Selenium omitted for clarity.

In order to study the in-plane structure of $(SnSe)_{1+\delta}([Mo_xNb_{1-x}]Se_2)_{1+\gamma}(SnSe)_{1+\delta}([Nb_xMo_{1-x}]Se_2)$, the *hk*0 diffraction pattern of the ferecrystal was collected and compared to those of the parent compounds (Figure XVI.7). *hk*0 diffraction scans, shown in Figure XVI.7a, exhibit diffraction maxima that can be attributed to a single SnSe rock salt structured constituent and the dichalcogenide structured constituents. The splitting of the dichalcogenide peaks indicates the presence of two distinct dichalcogenides. The dichalcogenide 110 reflection, expanded in Figure XVI.7b, shows diffraction maxima for the $(SnSe)_{1+\delta}([Mo_xNb_{1-x}]Se_2)_{1+\gamma}(SnSe)_{1+\delta}([Nb_xMo_{1-x}]Se_2)$ at positions between those of the $(SnSe)_{1.16}NbSe_2$ and $(SnSe)_{1.09}MoSe_2$ parent compounds. This change in the a-axis

lattice parameters could be a result of the different compositions of the dichalcogenides, electron transfer, or templating of the dichalcogenide layers through the rock salt. If different compositions are assumed to be the dominant cause for the splitting, the maximum extent of the interdiffusion in the $(SnSe)_{1+\delta}([Mo_xNb_{1-x}]Se_2)_{1+\gamma}(SnSe)_{1+\delta}([Nb_xMo_{1-x}]Se_2)$ can be estimated. As expected from Vegard's law, a linear relationship between composition and in-plane lattice parameter was found previously in a study of $(SnSe)_z(Nb_xMo_{1-x})Se_2$ ferecrystal alloys.[20] Using this data, we estimate a maximum value for the amount of interdiffusion of 12 ± 2%, which agrees with our estimate from the Rietveld refinement and is comparable to MBE grown epitaxial superlattices with periods in this range.[18-19] This would give a formula of $(SnSe)_{1.16}([Mo_{0.9}Nb_{0.1}]Se_2)_{1.06}(SnSe)_{1.16}([Nb_{0.9}Mo_{0.1}]Se_2)$ for the compound.

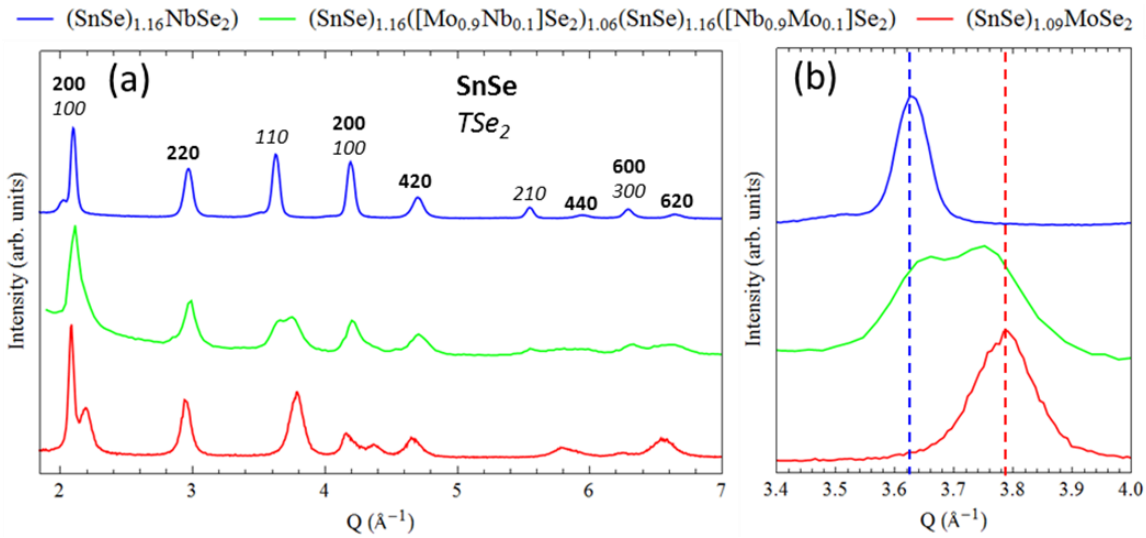

Figure XVI.7. (a) In-plane (*hk*0) XRD pattern of $(SnSe)_{1+\delta}([Mo_xNb_{1-x}]Se_2)_{1+\gamma}(SnSe)_{1+\delta}([Nb_xMo_{1-x}]Se_2)$ compared to the $(SnSe)_{1.16}NbSe_2$ and $(SnSe)_{1.09}MoSe_2$ parent compounds. Indices for the SnSe are given in bold, while those of the TSe_2 (where T = Mo and/or Nb) are given in italics. (b) Expansion of the TSe_2 110 region.

Electrical resistivity vs. temperature for the $(SnSe)_{1.16}([Mo_{0.9}Nb_{0.1}]Se_2)_{1.06}(SnSe)_{1.16}([Nb_{0.9}Mo_{0.1}]Se_2)$ ferecrystal shows that it is metallic with an order of

magnitude higher resistivity than that of $(SnSe)_{1.16}NbSe_2$ and two orders of magnitude lower than $(SnSe)_{1.09}MoSe_2$ (Figure XVI8a). The resistivity shows a slight increase with decreasing temperature previously observed in Nb-rich $(SnSe)_{1+\delta}(Nb_xMo_{1-x})Se_2$ ferecrystal alloys. Since the SnSe rock salt and Mo-rich dichalcogenide layers are expected to be semiconducting, the majority of charge conduction is expected to be through the Nb-rich dichalcogenide layers. By assuming all of the current travels in the Nb rich layer, the resistivity of the $(SnSe)_{1.16}([Mo_{0.9}Nb_{0.1}]Se_2)_{1.06}(SnSe)_{1.16}$ $([Nb_{0.9}Mo_{0.1}]Se_2)$ ferecrystal can be used to estimate the degree of intermixing.

The $(SnSe)_{1.16}([Mo_{0.9}Nb_{0.1}]Se_2)_{1.06}(SnSe)_{1.16}([Nb_{0.9}Mo_{0.1}]Se_2)$ ferecrystal has fewer Nb-rich dichalcogenide layers than the $(SnSe)_{1+\delta}(Nb_xMo_{1-x})Se_2$ ferecrystal alloys which must be accounted for in comparing the resistivity's. Normalization of the resistivity by multiplying by the amount of the c-axis lattice parameter of the unit cell contributed by the Nb-rich dichalcogenide layer allows these numbers to be compared. Figure XVI.8b shows the linear relationships of the normalized room temperature and low temperature (45K) resistivity vs x for the Nb-rich $(SnSe)_{1+\delta}(Nb_xMo_{1-x})Se_2$ ferecrystal alloys with x = 0.76, 0.81, and 1. Assuming the change in resistivity is primarily a result of interdiffusion, rather than charge transfer, the normalized electrical resistivity of the $(SnSe)_{1+\delta}([Mo_xNb_{1-x}]Se_2)_{1+\gamma}(SnSe)_{1+\delta}([Nb_xMo_{1-x}]Se_2)$ ferecrystal should follow this same relationship. This allows a second, independent estimate of the interdiffusion in addition to the value obtained by diffraction. Fitting the room temperature and low temperature

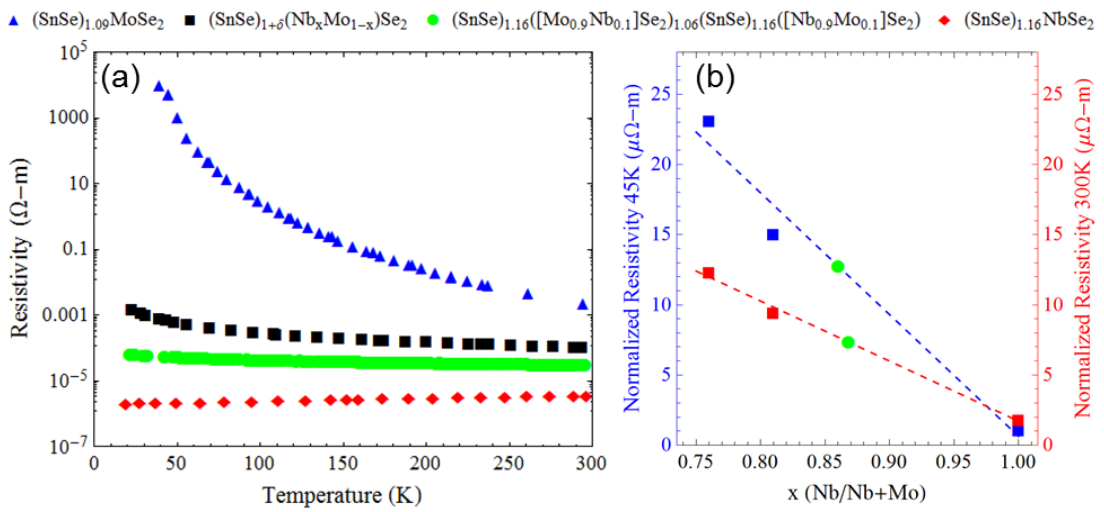

Figure XVI.8. (a) Electrical resistivity vs. temperature of $(SnSe)_{1.16}([Mo_{0.9}Nb_{0.1}]Se_2)_{1.06}$ $(SnSe)_{1.16}([Nb_{0.9}Mo_{0.1}]Se_2)$ (green circles), $(SnSe)_{1.03}MoSe_2$ (blue triangles), $(SnSe)_{1.13}$ $([Nb_{0.5}Mo_{0.5}]Se_2)$ (black squares) and $(SnSe)_{1.16}NbSe_2$ (red diamonds). (b) Normalized room temperature (red squares) and 45K (blue squares) resistivity vs. x for the $(SnSe)_z$ $(Nb_xMo_{1-x})Se_2)$ ferecrystal alloys compared to the $(SnSe)_{1+\delta}([Mo_xNb_{1-x}]Se_2)_{1+\gamma}(SnSe)_{1+\delta}$ $([Nb_xMo_{1-x}]Se_2)$ (green circles).

resistivity of the $(SnSe)_{1+\delta}([Mo_xNb_{1-x}]Se_2)_{1+\gamma}(SnSe)_{1+\delta}([Nb_xMo_{1-x}]Se_2)$ compound to the lines given by the alloys (Figure XVI.8b) gives interdiffusion estimates of 13 ± 2% and 14 ± 4% respectively. These are in close agreement to the interdiffusion estimate of 12 ± 2% obtained from diffraction. Charge transfer, which may be occurring, would cause these numbers to be overestimated, making them a reasonable upper limit to the amount of interdiffusion occurring.

To investigate the extent of the possible charge transfer, Hall coefficient measurements of the $(SnSe)_{1+\delta}([Mo_xNb_{1-x}]Se_2)_{1+\gamma}(SnSe)_{1+\delta}([Nb_xMo_{1-x}]Se_2)$ compound were performed. A positive Hall coefficient of $3.2(1) \times 10^{-3}$ cm^3C^{-1} was measured, indicating that holes are the majority carrier. Using a single band model results in a calculated carrier concentration of $2.0(1) \times 10^{21}$ cm^{-3}, or 0.6 holes per Nb atom in the compound. This is significantly less than the nearly one hole per Nb atom reported for

$([SnSe]_{1.16})_1(NbSe_2)_1$, but very close to the 0.6 holes per Nb reported for $([SnSe]_{1.16})_2(NbSe_2)_1$.[27] The additional SnSe layer in $([SnSe]_{1.16})_2(NbSe_2)_1$ relative to $([SnSe]_{1.16})_1(NbSe_2)_1$ results in a significantly reduced number of carriers per Nb atom, presumably due to increased charge transfer from the SnSe. The similarity between the Hall coefficient of $([SnSe]_{1.16})_2(NbSe_2)_1$ and $(SnSe)_{1+\delta}([Mo_xNb_{1-x}]Se_2)_{1+\gamma}(SnSe)_{1+\delta}$ $([Nb_xMo_{1-x}]Se_2)$ suggests that charge transfer is also occurring between SnSe and the dichalcogenide layers.

XVI.5. Conclusion

We have successfully prepared the compound $(SnSe)_{1.16}([Mo_{0.9}Nb_{0.1}]Se_2)_{1.06}$ $(SnSe)_{1.16}([Nb_{0.9}Mo_{0.1}]Se_2$ through the self-assembly of a layered precursor of the formula Sn|Se|Mo|Se|Sn|Se|Nb|Se. Analysis by XRD and STEM indicates distinct Mo and Nb rich dichalcogenide layers with interleaved SnSe between them. This represents the first example of a three component ferecrystal and illustrates the utility of the MER technique in the preparation multiple component heterostructures. The ability to control local composition through the use of designed precursors allowed the interdiffusion of the two dichalcogenide constituents to be evaluated by comparison of structural and electrical properties to the $(SnSe)_{1+\delta}(Nb_xMo_{1-x})Se_2$ random alloys. It is expected that the amount of interdiffusion will decrease as the SnSe layer thickness is increased. The ability to form multiple component thin films via the MER method greatly increases the number of compounds that can be prepared, and will enable theoretical predictions and proposed thin film device strategies to be tested.

CHAPTER XVII

SYNTHESIS OF A FAMILY OF $([SnSe]_{1+\delta})_m([\{Mo_xNb_{1-x}\}Se_2]_{1+\gamma})_1$ $([SnSe]_{1+\delta})_m(\{Nb_xMo_{1-x}\}Se_2)_1$ HETEROJUNCTION SUPERLATTICES (WHERE m = 0, 1, 2, 3 AND 4)

XVII.1. Authorship Statement

Chapter XVII was published in the European Journal of Inorganic Chemistry in 2016, pages 1225–1231.I performed microscopy measurements, HAADF-STEM and EDX, to identify the degree of intermixing between the Nb and Mo layers. Richard Westover is the primary author of the manuscript.

XVII.2. Introduction

Since the isolation of graphene in 2004[1] there has been great interest in two-dimensional materials which often exhibit different properties than in the bulk compound.[2,3] In recent years, researchers have prepared two-dimensional heterostructures by stacking different two-dimensional materails.[4-10] The layering of different two-dimensional materials to form heterostructures provides the ability to optimize properties by taking advantage of the qualities of each material. It also allows properties to be systematically tuned by varying the nanoarchitecture. Numerous applications have been suggested, including electrical sensors,[11] supercapacitors,[12] photovoltaics[13] and water splitting reactions.[14,15] Despite their enormous potential, however, systematic studies of the properties of multi-component heterostructures are hindered by synthetic challenges.

The synthesis of two-dimensional heterostructures is often accomplished through the cleaving of bulk crystals, followed by the physical stacking of individual layers.

While this process has led to films with exciting properties, it is a tedious and difficult technique.[5-9] Additionally, the requirement that films be stable as monolayers limits the number of two-dimensional materials that can be stacked using this technique. Metallic monolayers are thought to be generally unstable under ambient conditions.[4] In addition to physical stacking, synthesis of heterostructures can also be accomplished through epitaxy. Koma and coworkers demonstrated epitaxial growth of transition metal dichalcogenide (TMD) superlattices, coining the term van der Waals epitaxy due to weak interlayer bonding.[16,17] Epitaxy, however, becomes increasingly difficult as the number of constituents increases because new and mutually compatible growth conditions must be found for each additional constituent. It is often not possible to find mutually compatible conditions to grow both B on A as well as A on B. In addition, interdiffusion occurs during growth if layers are miscible.[18,19] Another method for the formation of two-dimensional heterostructures is the modulated elemental reactants (MER) technique. This approach has been used to prepare families of related structures, allowing systematic studies of properties as a function of nanoarchitecture.[20] Rather than epitaxy, MER relies on a diffusion constrained self-assembly of compositionally modulated amorphous precursors to form kinetically stable films. Families of related compounds are prepared by changing the layering scheme of the precursors.[21, 22]

Herein we report the synthesis of a family of related $([SnSe]_{1+\delta})_m([NbSe_2]_{1+\gamma})_1([SnSe]_{1+\delta})_m(MoSe_2)_1$ heterojunction superlattices (with m = 0 - 4), whose structures are schematically illustrated in Figure XVII.1. Systematically increasing the thickness of the SnSe layers interleaved between $MoSe_2$ and $NbSe_2$ constituents decreases the extent of

interdiffusion of the miscible dichalcogenide layers. When m = 0 the miscible dichalcogenide layers interdiffused leading to about 20% alloying. When m = 1, approximately 10% of the transition metals diffused into the neighboring layer, forming $(SnSe)_{1.16}([Mo_{0.9}Nb_{0.1}]Se_2)_{1.06}(SnSe)_{1.16}([Nb_{0.9}Mo_{0.1}]Se_2)$ rather than the targeted compound $(SnSe)_{1.16}(MoSe_2)_{1.06}(SnSe)_{1.16}(NbSe_2)$.[23] Herein we show that increasing m to 2 reduces the alloying to about 5% and the extent of alloying became less than our experimental approaches could determine (less than 1%) when m = 3 or 4. The electrical transport properties of the $([SnSe]_{1+\delta})_m([NbSe_2]_{1+\gamma})_1([SnSe]_{1+\delta})_m(MoSe_2)_1$ (m = 0 - 4) compounds show evidence of reduced alloying with increased m as well as charge transfer from the SnSe layers previously observed in the $([SnSe]_{1+\delta})_m(NbSe_2)_1$ (m = 1 - 8) compounds.[20] Comparison of the electrical transport properties with the $([SnSe]_{1+\delta})_m(NbSe_2)_1$ (m = 1 - 8) compounds also provides insight into the electronic interactions between the $MoSe_2$ and $NbSe_2$ constituents, indicating little to no charge transfer occurs. The ability to prepare 3-component quaternary heterojunctions with designed structures greatly expands the number of parameters that can be used to understand how nanoarchitecture affects both structure and properties, which increases the ability to tune and optimize properties.

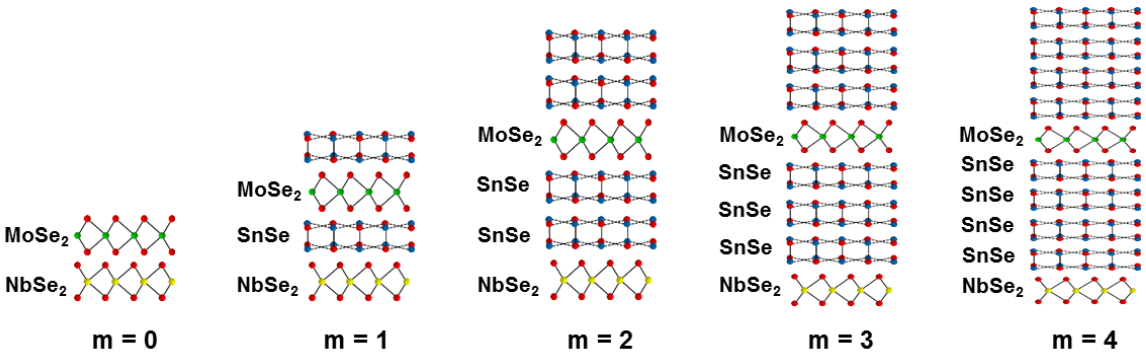

Figure XVII.1. Illustration of the change in the dichalcogenide separation through modification of the stacking sequence of $([SnSe]_{1+\delta})_m([\{Mo_xNb_{1-x}\}Se_2]_{1+\gamma})_1([SnSe]_{1+\delta})_m$ $(\{Nb_xMo_{1-x}\}Se_2)_1$ ferecrystals (with m = to 0 - 4).

XVII.3. Experimental

The compositionally modulated amorphous precursors were formed in a custom-built physical vapor deposition system. A dual turbo and cryo vacuum pump system allowed depositions at pressures of 10-7 torr. Tin (99.999 % purity), niobium (99.8 % purity) and molybdenum (99.95 % purity) obtained from Alpha Aeasar were deposited using Thermionics 3kW electron beam guns. Se (99.5 % purity) was deposited using a custom-built Knudson effusion cell. Precursors were built-up layer by layer following a designed layering scheme until a thickness of about 42 nm was reached. Thickness and deposition rates were monitored and controlled using quartz crystal microbalances. Following formation of the precursors sample were annealed in a nitrogen atmosphere (O_2 < 0.6 ppm) at 450 C for 20 min to ensure self-assembly into the ferecrystalline products.

X-ray diffraction and reflectivity measurements, performed on a bruker D8 discover (CuKα radiation), were used to determine repeating unit and total film thickness respectively. Grazing incidence in-plane (*hk*0) X-ray diffraction, performed on a Rigaku Smartlab X-ray diffractometer with CuKα radiation (λ = 0.15418 nm), was used to characterize the in-plane structure of the films.

Samples for high angle annular dark field scanning transmission electron microscopy (HAADF-STEM) imaging were prepared at the Center for Advanced Materials Characterization in Oregon (CAMCOR) High-Resolution and Nanofabrication Facility.

Samples were prepared using an FEI NOVA Nanolab Dual Beam FIB equipped with Side winder ion column. (HAADF-STEM) images were obtained at the Environmental Molecular Sciences Laboratory at the Pacific Northwest National Laboratory (PNNL).

Compositions of the modulated precursors and ferecrystal samples were measured by electron probe micro-analysis (EPMA) on a Cameca SX-100. Intensities were collected at acceleration voltages of 7, 12, and 17 keV allowing composition to be calculated from the film and substrate as a function of acceleration voltage using a previously described approach.[29]

Samples for electrical transport measurements were deposited on quartz slides in a 1 x 1 cross pattern defined by a shadow mask. Electrical resistivity and hall coefficient measurements were performed using a van der Pauw geometry as previously described.[30]

XVII.4. Results and Discussion

The synthesis of compounds via MER relies on the formation of compositionally modulated amorphous precursors, which closely mimic the stoichiometry and structure of the desired products, resulting in self-assembly upon mild annealing. Careful calibration of the deposition parameters used in the formation of the precursors is required to ensure formation of the desired product as has been previously described.[23] For the synthesis of the $([SnSe]_{1+\delta})_m([NbSe_2]_{1+\gamma})_1([SnSe]_{1+\delta})_m(MoSe_2)_1$ (m = 0 - 4) the deposition parameters determined previously for the m = 1 compound were used as a starting point for the compounds with m = 0, 2, 3, and 4.[24] Precursors for the compounds $([SnSe]_{1+\delta})_m([NbSe_2]_{1+\gamma})_1([SnSe]_{1+\delta})_m(MoSe_2)_1$ (m = 0 - 4) were prepared by depositing a repeating sequence of elemental layers m × [Sn|Se]|Mo|Se|{m × [Sn|Se]}|Nb|Se onto silicon wafers

(Table XVII.1). Each layer sequence was repeated until the total thickness of the film reached about 42nm. X-ray reflectivity patterns of the precursors showed the expected systematic increase in the repeating thickness as *m* was increased.

Table XVII.1. The precursor structure, targeted structure and elemental ratios, both targeted and measured, of the $([SnSe]_{1+\delta})_m([MoSe_2]_{1+\gamma})_1([SnSe]_{1+\delta})_m(NbSe_2)_1$ compounds.

Precursor Structure	Targeted Structure	Se/(Sn+Mo+Nb)		Sn/(Mo+Nb)		Mo/Nb	
		Target	Found	Target	Found	Target	Found
Mo-Se + Nb-Se	$([MoSe_2]_{1.06})_1(NbSe_2)_1$	2.00	2.0(1)	0.00	0.00	1.08	1.1(1)
1(Sn-Se) + Mo-Se + 1(Sn-Se) + Nb-Se	$([SnSe]_{1.17})_1([MoSe_2]_{1.06})_1$ $([SnSe]_{1.17})_1(NbSe_2)_1$	1.47	1.4(1)	1.13	1.2(1)	1.08	1.1(1)
2(Sn-Se) + Mo-Se + 2(Sn-Se) + Nb-Se	$([SnSe]_{1.17})_2([MoSe_2]_{1.06})_1$ $([SnSe]_{1.17})_2(NbSe_2)_1$	1.31	1.3(1)	2.23	2.3(1)	1.08	1.1(1)
3(Sn-Se) + Mo-Se + 3(Sn-Se) + Nb-Se	$([SnSe]_{1.17})_3([MoSe_2]_{1.06})_1$ $([SnSe]_{1.17})_3(NbSe_2)_1$	1.23	1.2(1)	3.35	3.4(1)	1.08	1.2(1)
4(Sn-Se) + Mo-Se + 4(Sn-Se) + Nb-Se	$([SnSe]_{1.17})_4([MoSe_2]_{1.06})_1$ $([SnSe]_{1.17})_4(NbSe_2)_1$	1.18	1.2(1)	4.46	4.5(1)	1.08	1.2(1)

Annealing these amorphous precursors for 20 minutes at 450°C in an N_2 atmosphere[23] resulted in an increase in both the number of specular (00*l*) XRD reflections and their intensity. An increasing number of Bragg reflections were observed for samples with increasing numbers of SnSe layers, indicating the unit cell size increased (Figure XVII.2). For each sample, all maxima could be indexed as (00*l*) reflections, indicating that the samples are crystographically aligned to the substrate. The *c*-axis lattice parameters, given in Table XVII.2, increase linearly as *m* is increased. The slope yields an average thickness of a single SnSe bilayer of 0.580(1) nm. This is consistent with the literature values of SnSe bilayer thicknesses in 1:1 misfit layer compounds, which range between 5.78 and 0.599 nm.[27] The slope is also consistent with changes in the c-axis lattice parameter with SnSe thickness observed in previous studies of the ferecrystal

families $([SnSe]_{1.16})_m(NbSe_2)_1$ and $([SnSe]_{1.04})_m(MoSe_2)_1$ (0.577(5)[20] and 0.589(1)[28] respectively). This suggests that the $([SnSe]_{1+\delta})_m([\{Mo_xNb_{1-x}\}Se_2]_{1+\gamma})_1([SnSe]_{1+\delta})_m(\{Nb_xMo_{1-x}\}Se_2)_1$ compounds which share a similar structure. The measured atomic compositions of the ferecystals, given in Table XVII.1, are similar to the stoichiometry's of the targeted compounds and systematically vary as expected from the layer sequences of the precursors.

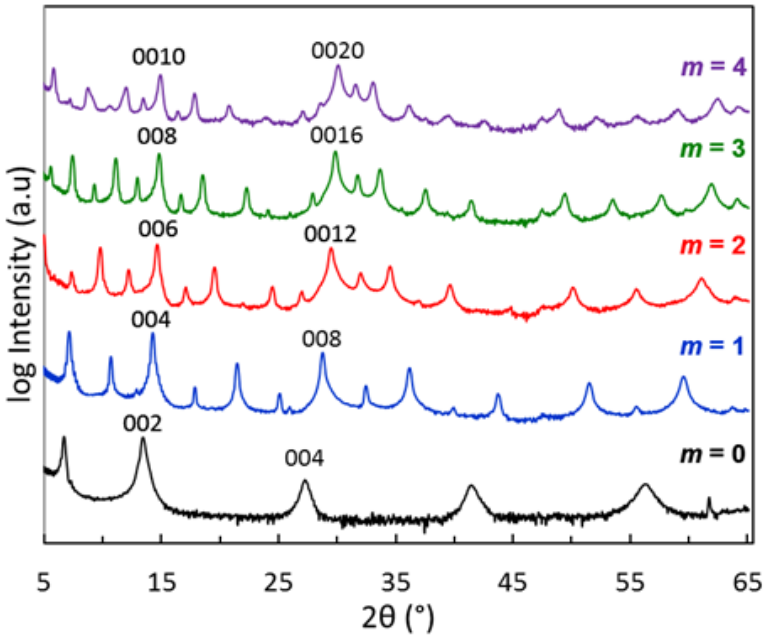

Figure XVII.2. Locked-coupled (00*l*) XRD patterns of $([SnSe]_{1+\delta})_m([\{Mo_xNb_{1-x}\}Se_2]_{1+\gamma})_1$ $([SnSe]_{1+\delta})_m(\{Nb_xMo_{1-x}\}Se_2)_1$ ferecrystals (with m = to 0 - 4).

Further insight into the structure of the $([SnSe]_{1+\delta})_m([\{Mo_xNb_{1-x}\}Se_2]_{1+\gamma})_1$ $([SnSe]_{1+\delta})_m(\{Nb_xMo_{1-x}\}Se_2)_1$ ferecrystals was obtained from high-angle annular dark-field scanning transmission microscopy (HAADF STEM) images. Figure XVII.3 shows a representative image of the sample with m = 2. The image agrees with the interpretation of the specular diffraction patterns. All of the zone axes imaged reflect trigonal prismatic

coordination of the metal in the dichalcogenide layers with each dichalcogenide layer interleaved with two rock salt bilayers. The individual layers are distinct and parallel and exhibit the turbostratic disorder typical of ferecrystals.

Table XVII.2. The lattice parameters and formulas estimated from in-plane X-ray diffraction for the $([SnSe]_{1+\delta})_m([MoSe_2]_{1+\gamma})_1([SnSe]_{1+\delta})_m(NbSe_2)_1$ compounds.

m	*c*-axis lattice parameters (nm)	a-b axis lattice parameters (nm)				Formula predicted from *hk*0 X-ray diffraction
		SnSe (a)	SnSe (b)	$NbSe_2$	$MoSe_2$	
0	1.311(1)	-	-	0.343(1)	0.334(1)	$([\{Mo_{0.9}Nb_{0.1}\}Se_2]_{1.06})_1$ $(\{Nb_{0.8}Mo_{0.2}\}Se_2)_1$
1	2.476(1)	0.4225(1)	0.4222(1)	0.3447(5)	0.3342(5)	$([SnSe]_{1.16})_1([\{Mo_{0.90}Nb_{0.10}\}Se_2]_{1.06})_1$ $([SnSe]_{1.16})_1(\{Nb_{0.87}Mo_{0.13}\}Se_2)_1$
2	3.637(1)	0.4279(1)	0.4239(1)	0.3458(5)	0.3343(5)	$([SnSe]_{1.17}]_2([\{Mo_{0.89}Nb_{0.11}\}Se_2]_{1.07}]_1$ $([SnSe]_{1.17})_2[\{Nb_{0.95}Mo_{0.05}\}Se_2)_1$
3	4.791(1)	0.4292(1)	0.4238(1)	0.3462(5)	0.3334(5)	$([SnSe]_{1.17})_3([MoSe_2]_{1.08})_1$ $([SnSe]_{1.17})_3(NbSe_2)_1$
4	5.951(1)	0.4302(1)	0.4233(1)	0.3458(5)	0.3329(5)	$([SnSe]_{1.17})_4([MoSe_2]_{1.08})_1$ $([SnSe]_{1.17})_4(NbSe_2)_1$

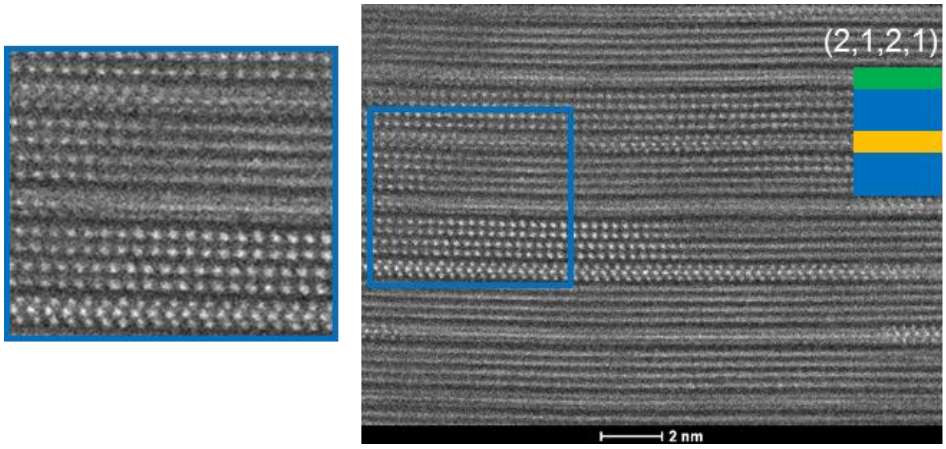

Figure XVII.3. HAADF-STEM images of $([SnSe]_{1+\delta})_m([\{Mo_xNb_{1-x}\}Se_2]_{1+\gamma})_1$ $([SnSe]_{1+\delta})_m(\{Nb_xMo_{1-x}\}Se_2)_1$samples with m = 2 and 4. Se_2 Different orientations of the individual constituents are highlighted.

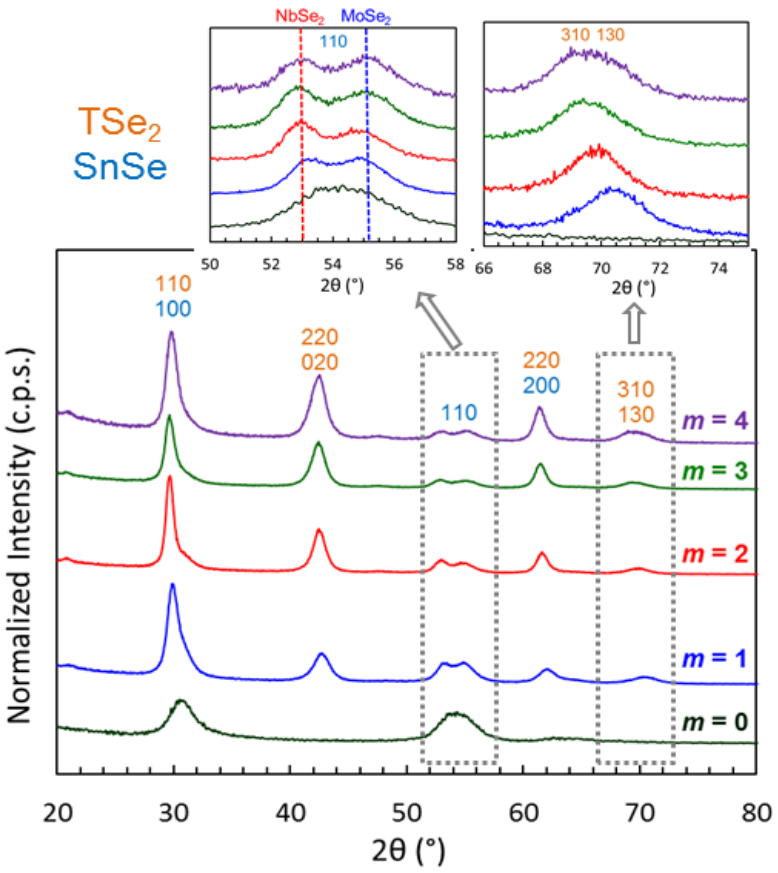

Figure XVII.4. In-Plane (*hk*0) XRD $([SnSe]_{1+\delta})_m([\{Mo_xNb_{1-x}\}Se_2]_{1+\gamma})_1([SnSe]_{1+\delta})_m$ ($\{Nb_xMo_{1-x}\}Se_2$) ferecrystals (with m = to 0-4) compared to the $([SnSe]_{1.16})_1(NbSe_2)_1$ and $([SnSe]_{1.09})_1(MoSe_2)_1$ parent compounds. Insets show the expansion of the TSe_2 110 and SnSe 310/130 regions.

In-plane diffraction patterns were collected to determine the in-plane structure of the reported compounds. All maxima can be indexed as (*hk*0) reflections of the respective SnSe, $NbSe_2$ and $MoSe_2$ constituents. The SnSe reflections show a slight broadening with increasing thickness of the SnSe layers (see the inset of Figure XVII.4) indicating a symmetry reduction to a rectangular in-plane unit cell similar to that observed previously in $([SnSe]_{1+\delta})_m(NbSe_2)_1$ (m = 1 - 8) compounds.[20] Rectangular in-plane lattice constants are given in Table XVII.2 and range from 0.422 to 0.430 nm, matching well the magnitude and following the same trend as those found for the $([SnSe]_{1+\delta})_m(NbSe_2)_1$ compounds. Dichalcogenide (*hk*0) reflections for both the $NbSe_2$ and $MoSe_2$ constituents

can be observed in all samples, as can be clearly seen in the inset expansion of the (110) reflection in Figure XVII.4). The *a*-axis lattice parameters (Table XVII.2) all lie between those of the $([SnSe]_{1.16})_1(NbSe_2)_1$ and $([SnSe]_{1.09})_1(MoSe_2)_1$ parent compounds of 0.3462(1)[20] and 0.3320(1) nm[28] respectively. For the $m = 0$ compound the dichalcogenide peaks are closer together, resulting in considerable overlap between dichalcogenide peaks. This is likely due to alloying between the miscible constituents. With the addition of increasing numbers of SnSe layers the dichalcogenide (*hk*0) reflections separate and become closer to the positions of the parent compounds (Figure XVII.4). Using the Vegard's law relationship determined previously for the $(SnSe)_{1.16\text{-}1.09}(Nb_xMo_{1-x})Se_2$ alloys[29] allows us to estimate the alloying between the dichalcogenides. This yields a stoichiometry of $([\{Mo_{0.9}Nb_{0.1}\}Se_2]_{1.06})_1(\{Nb_{0.8}Mo_{0.2}\}Se_2)_1$ for the $m = 0$ compound. The *a*-axis lattice parameters approach those of the parent compounds as the number of SnSe layers is increased, indicating a decrease in the amount of alloying (Figure XVII.5). Samples with one and two SnSe layers give estimates for the interdiffusion from Vegard's law of about 10%. Addition of three or more SnSe layers causes the estimated interdiffusion to be lowered below detectable limits. Estimated formulas for each compound are given in Table XVII.2.

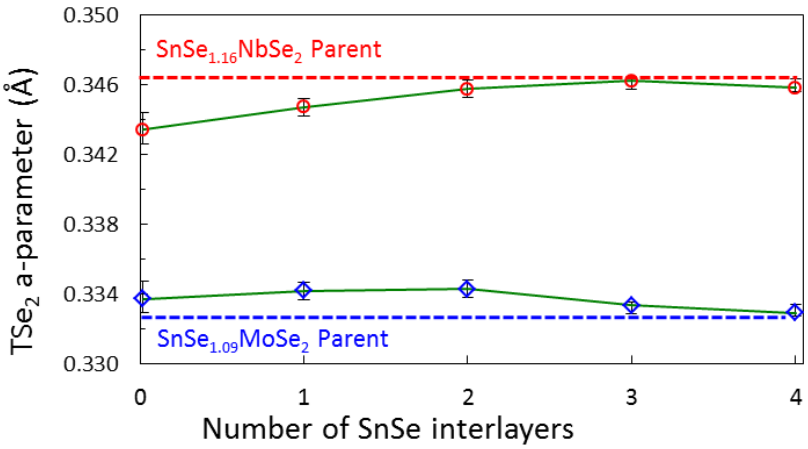

Figure XVII.5. TSe_2 *a*-axis lattice parameter is graphed versus the number of SnSe bilayers. The Mo-rich constituent is given by blue triangles, the Nb-rich constituent by red circles. The red and blue horizontal lines depict the *a*-parameters of the $SnSe_{1.16}NbSe_2$ and $SnSe_{1.09}MoSe_2$ parent compounds respectively.

The electrical transport properties of the $([SnSe]_{1+\delta})_m([\{Mo_xNb_{1-x}\}Se_2]_{1+\gamma})_1$ $([SnSe]_{1+\delta})_m(\{Nb_xMo_{1-x}\}Se_2)_1$ ferecrystals is dominated by the conductivity of the Nb-rich TSe_2 constituent, similar to previously investigated $([SnSe]_{1+\delta})_m(NbSe_2)_1$[20] compounds and Nb-rich $(SnSe)_{1.16-1.09}(Nb_xMo_{1-x})Se_2$ alloys.[29] The resistivity vs. temperature behavior (Figure XVII.6) shows an increase in resistivity with decreasing temperature with the ρ/ρ_{300K} value rising with *m* to reach a value of 2.8 for the $m = 4$ compound. This effect was also observed for the Nb-rich $(SnSe)_{1.16-1.09}(Nb_xMo_{1-x})Se_2$ alloys[29] and $([SnSe]_{1+\delta})_m(NbSe_2)_1$ compounds[20] with *m* greater than 6. For the $([SnSe]_{1+\delta})_m(NbSe_2)_1$ compounds, this effect was attributed to charge transfer from the SnSe layers into the $NbSe_2$ layers. Its onset at lower *m* values in the $([SnSe]_{1+\delta})_m$ $([\{Mo_xNb_{1-x}\}Se_2]_{1+\gamma})_1([SnSe]_{1+\delta})_m(\{Nb_xMo_{1-x}\}Se_2)_1$ ferecrystals may be evidence of alloying of the dichalcogenides with small numbers of SnSe interlayers. This is supported by the resistivity behavior of the $([\{Mo_{0.9}Nb_{0.1}\}Se_2]_{1.06})_1(\{Nb_{0.8}Mo_{0.2}\}Se_2)_1$ ($m = 0$) compound which shows similar behavior to the $(SnSe)_{1.16-1.09}(Nb_xMo_{1-x})Se_2$ ($x = 0.76$)

compound previously reported.[29] The localization of carriers appears to be related to the separation of the conducting $NbSe_2$ rich layers by semiconducting layers of either SnSe or $MoSe_2$, and increases as this thickness is increased.

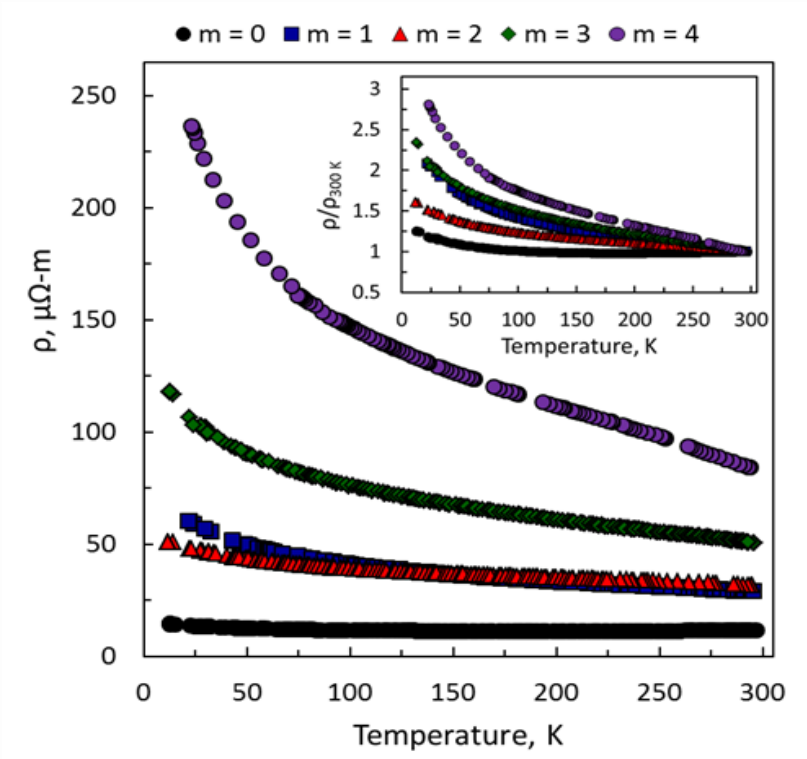

Figure XVII.6. Resistivity vs. temperature for the $([SnSe]_{1+\delta})_m([\{Mo_xNb_{1-x}\}Se_2]_{1+\gamma})_1$ $([SnSe]_{1+\delta})_m(\{Nb_xMo_{1-x}\}Se_2)_1$ compounds with m = 0-4. The inset shows the resistivity ratio ρ/ρ_{295K}.

The room temperature resistivity (Figure XVII.7a) shows a gradual increase with increasing SnSe layers as a result of an increased contribution of the semiconducting SnSe. If the majority of charge conduction occurs through the conducting $NbSe_2$ layers, we can extract the resistance of this conducting layer by assuming that it is in parallel with high resistance layers of $SnSe/MoSe_2$ (Figure XVII.7b). The reduction in the normalized room temperature resistivity with increasing thickness of SnSe from *m* = 0 to 2, results from the decrease in alloying of the dichalcogenide layers. The increase in room

temperature normalized resistivity observed for the $([SnSe]_{1+\delta})_m(NbSe_2)_1$ compounds from $m = 2$ to $m = 4$, is thought to result from increased charge transfer from the SnSe.

Temperature dependent Hall measurements, shown in Figure XVII.8, reveal positive Hall coefficients for all samples, indicating that holes are the majority carriers. There is a systematic increase in the Hall coefficient with increased *m* suggesting that average carrier concentration is decreasing as the thickness of SnSe increases. The Hall coefficient decreases with temperature for m = 0. The Hall coefficient increases with temperature for $m = 1 – 3$, as observed previously for the $([SnSe]_{1+\delta})_m(NbSe_2)_1$ compounds.[20] The Hall coefficient for the $m = 4$ compound decreases at low temperatures followed by an increase above 100K. This complex behavior suggests that multiple bands are likely involved and that the interaction between the constituents changes as a function of nanoarchitecture.

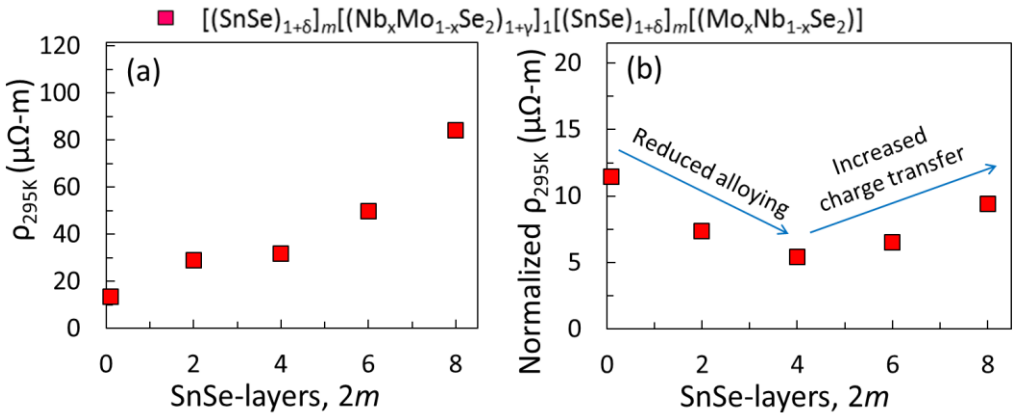

Figure XVII.7. (a) Room temperature resistivity and normalized room temperature resistivity (b) vs. the number of SnSe layers in $([SnSe]_{1+\delta})_m([\{Mo_xNb_{1-x}\}Se_2]_{1+\gamma})_1([SnSe]_{1+\delta})_m$ $(\{Nb_xMo_{1-x}\}Se_2)_1$ compounds with m = to 0-4. (b) Normalized room temperature resistivity (red squares).

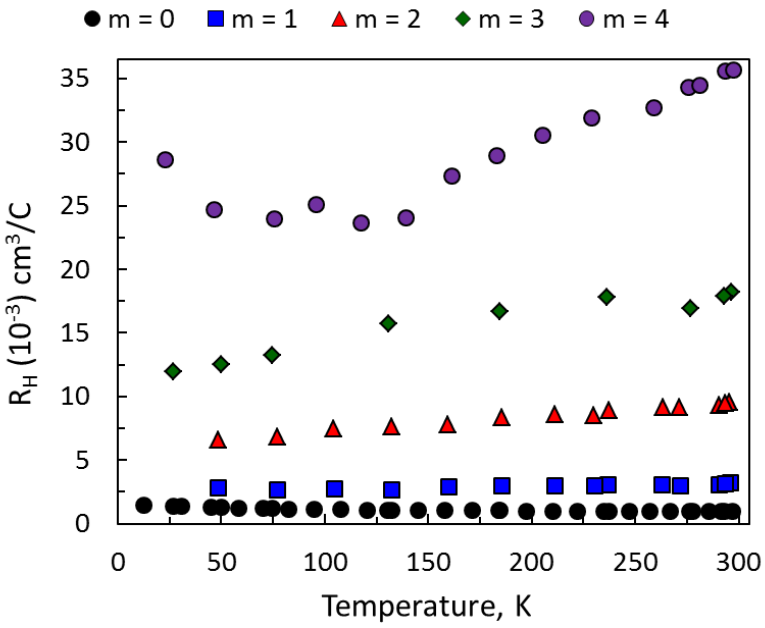

Figure XVII.8. Temperature dependent Hall coefficients measured for the $([SnSe]_{1+\delta})_m([\{Mo_xNb_{1-x}\}Se_2]_{1+\gamma})_1([SnSe]_{1+\delta})_m(\{Nb_xMo_{1-x}\}Se_2)_1$ compounds with m = to 0-4.

A rough estimate of the temperature dependent carrier concentrations can be obtained from the Hall coefficients using the single-band approximation (Figure XVII.9). A reduction in the carrier concentration is observed for increasing m as a result of the increased proportion of semiconducting SnSe layers in the samples. A slight increase in carrier concentration vs. temperature is observed for samples with m = 1-4, which was also observed in the $([SnSe]_{1+\delta})_m(NbSe_2)_1$ system[20] and was attributed to possible limitations of the single band model, energy dependence of the Hall scattering factor, or a change in charge transfer between constituents with temperature.

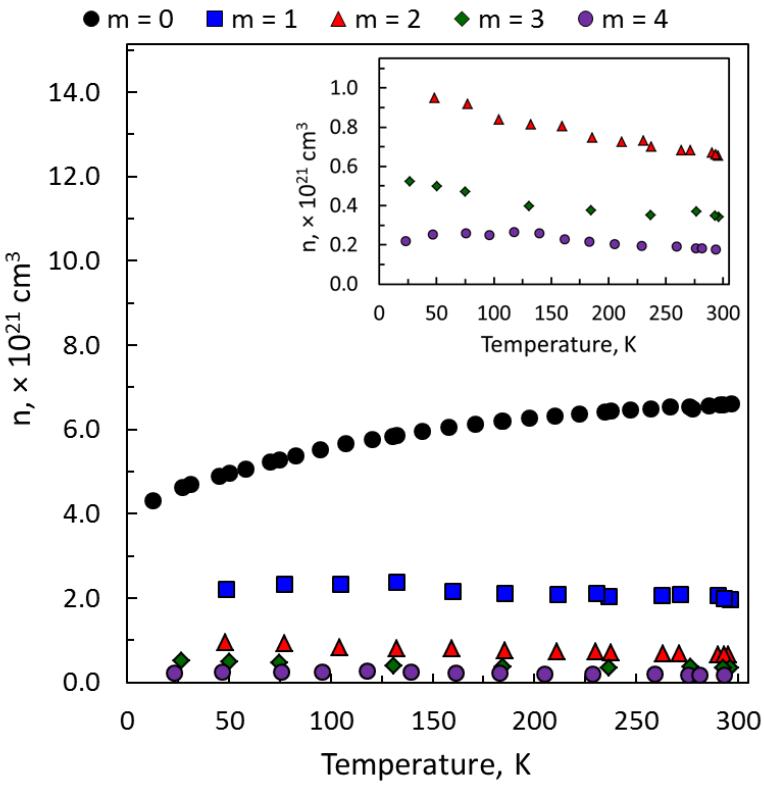

Figure XVII.9. Temperature dependent carrer concentrations calculated using a single band model for the $([SnSe]_{1+\delta})_m([\{Mo_xNb_{1-x}\}Se_2]_{1+\gamma})_1([SnSe]_{1+\delta})_m(\{Nb_xMo_{1-x}\}Se_2)_1$ compounds.

Temperature dependent mobility values calculated assuming a single band model for the *m* = 0 compound decrease slightly with temperature as expected for a metallic-type sample. For the *m* = 1-4 compounds, however, the mobility increases with temperature, suggesting carriers are localized as the temperature is decreased. The absolute values of the room temperature mobility for the $([SnSe]_{1+\delta})_m([\{Mo_xNb_{1-x}\}Se_2]_{1+\gamma})_1([SnSe]_{1+\delta})_m(\{Nb_xMo_{1-x}\}Se_2)_1$ compounds increase with increasing *m* and are lower than those found for the $([SnSe]_{1+\delta})_m(NbSe_2)_1$ compounds.[20] The lower values for the mobility for small m values are probably a consequence of increased scattering due to Mo alloying with the $NbSe_2$ layers.

Assuming the transport is dominated by the niobium rich layer, we can calculate the number of carriers per niobium atom in the $Mo_xNb_{1-x}Se_2$ layer by assuming all the carriers are in this layer and dividing by the number of calculated Nb atoms per cm^3 (Figure XVII.10). Charge transfer from the Se 4p band of the SnSe into the half-filled band formed by the Nb d_z^2 orbitals is thought to decrease the number of holes as *m* increases.[28] Comparing the number of carriers per Nb atom in the $Mo_xNb_{1-x}Se_2$ layer with data for previously reported $([SnSe]_{1+\delta})_m(NbSe_2)_1$ compounds containing the same number of SnSe layers per $NbSe_2$ layer suggests that there is little or no charge transfer between the $NbSe_2$ and $MoSe_2$ constituents.

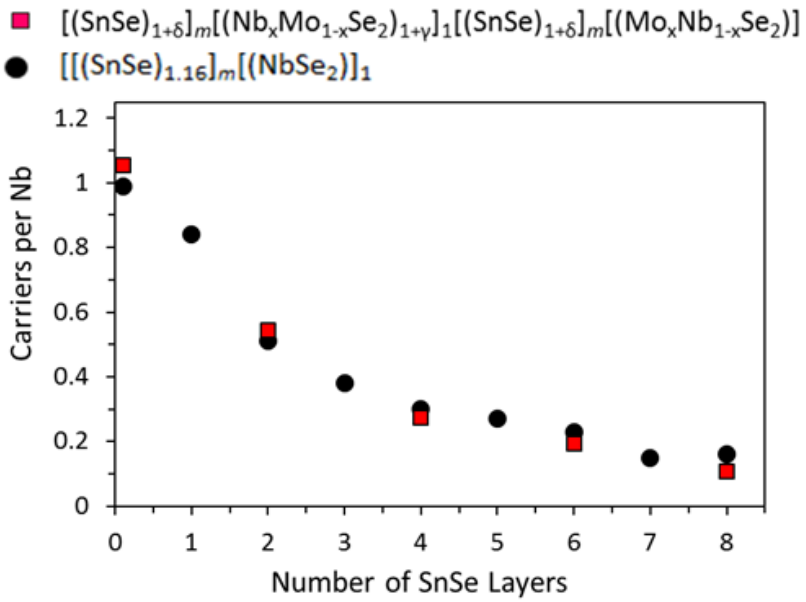

Figure XVII.10. Holes per Nb with increasing numbers of SnSe layers for the $([SnSe]_{1+\delta})_m([\{Mo_xNb_{1-x}\}Se_2]_{1+\gamma})_1([SnSe]_{1+\delta})_m(\{Nb_xMo_{1-x}\}Se_2)_1$ (red squares) compared to the $([SnSe]_{1.16})_m(NbSe_2)_1$ (black circles).

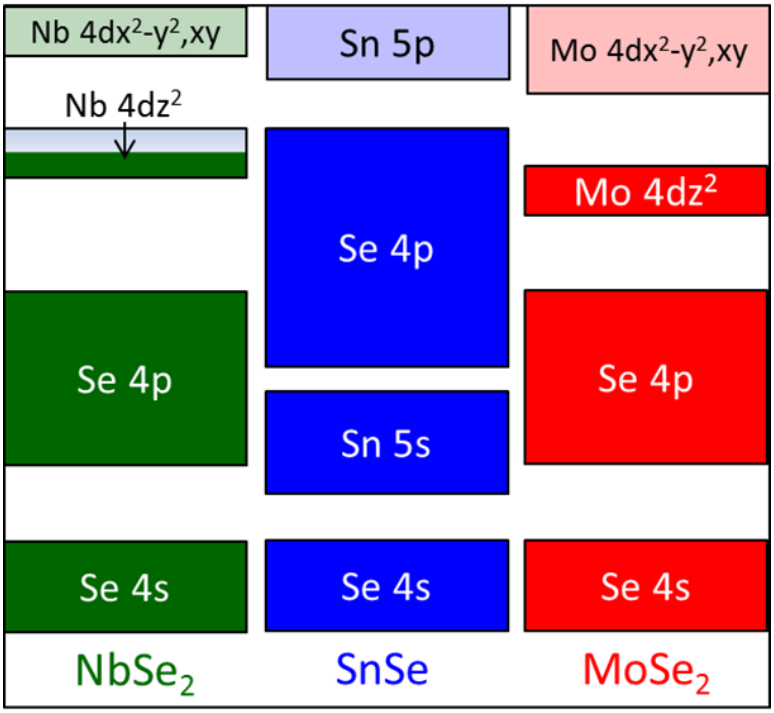

Figure XVII.11. Band alignment diagram of the $NbSe_2$ (green), SnSe (blue), and $MoSe_2$ (red) systems.

A proposed band alignment diagram for $NbSe_2$, SnSe, and $MoSe_2$ is given in Figure XVII.11. Charge transfer from the SnSe layer to the $NbSe_2$ layer observed in the $([SnSe]_{1+\delta})_m(NbSe_2)_1$ compounds[20] has been proposed to occur due to the Se 4p band of the SnSe layer, which lies at a higher energy than the half-filled Nb $4d_z^2$ band. The lack of charge transfer between the $MoSe_2$ and $NbSe_2$ layers may be due to the filled Mo $4d_z^2$ being at lower energy than the corresponding Nb $4d_z^2$ band. The Fermi level would then reside within the Nb 4dz2 band and within the band gap of the $MoSe_2$ layer.

XVII.5. Conclusion

We have reported the successful synthesis of a family of $([SnSe]_{1+\delta})_m([\{Mo_xNb_{1-x}\}Se_2]_{1+\gamma})_1([SnSe]_{1+\delta})_m(\{Nb_xMo_{1-x}\}Se_2)_1$ heterojunction superlattices with *m* = 0 - 4). Characterization of the compounds by XRD and HAADF-STEM confirmed the

formation of individual dichalcogenide layers, which are distinct and parallel, interleaved with a systematically increasing number of distorted rock salt bilayers. Comparison of the in-plane X-ray diffraction patterns to those of the $(SnSe)_{1.16-1.09}(Nb_xMo_{1-x})Se_2$ alloys allowed the extent of alloying between the miscible $MoSe_2$ and $NbSe_2$ constituents to be estimated. Alloying, which was about 20% at $m = 0$, is systematically reduced to less than 1% as m is increased to 3 and 4. Electrical transport measurements of the $([SnSe]_{1+\delta})_m([\{Mo_xNb_{1-x}\}Se_2]_{1+\gamma})_1([SnSe]_{1+\delta})_m(\{Nb_xMo_{1-x}\}Se_2)_1$ compounds with $m = 0$ - 4 is consistent with the extent of dichalcogenide alloying decreasing with increasing m. Comparison of the electrical transport properties to those of the $([SnSe]_{1+\delta})_m(NbSe_2)_1$ (m = 1 - 8) compounds suggests that there is little or no charge transfer between the $MoSe_2$ and $NbSe_2$ layers. The ability to form families of related three component heterostructure thin films greatly expands the number of compounds that can be created, allowing systematic study of complex interlayer interactions.

CHAPTER XVIII

SELF-ASSEMBLY OF DISIGNED PRECURSORS: A ROUTE TO CRYSTALLOGRAPHICALLY ALIGNED NEW MATERIALS WITH CONTROLLED NANOARCHITECUTURE

XVIII.1. Authorship Statement

Chapter XVIII contains material published in the Journal of Solid State Chemistry in 2016, doi:10.1016/j.jssc.2015.08.018. I performed electron microscopy and EDX measurements. Richard Westover is the primary author of the manuscript.

XVIII.2. Introduction

New synthetic methods have been critical both to advance scientific understanding as well as to advance technology. Traditional approaches have historically focused on using thermodynamic control to make desired products, for example growing doped silicon crystals from a melt of fixed composition. Phase diagrams were determined to understand the thermodynamic relationships between compounds. Kinetic control, typically achieved by controlling temperature as a function of time, was used to influence the microstructure. The search for new materials focused on finding reaction conditions where new compounds would be thermodynamically stable. High temperature synthesis and the growth of new materials from melts were commonly used to overcome slow solid state diffusion rates and to form single crystals for structure determination. New compounds and new phenomena are discovered whenever new approaches are developed, such as vapor transport reactions in the 1960's,[1,2] or new adaptations, such as the use of low temperature fluxes,[3,4] are explored. A grand challenge in the field of materials discovery is the development of approaches to predict new structures and the

properties associated with specific compositions, and the development of approaches that will enable their synthesis. Historically, serendipity played a significant role in most new discoveries as unexpected compounds formed in reaction mixtures.

An example of a new crystal growth technique that has significantly advanced both scientific understanding and technology is the development of molecular beam epitaxy (MBE). In the 1960's there was much interest in producing new semiconducting materials with specific compositions and specific doping profiles required for new devices. The development of MBE by Arthur and Cho,[5-10] was a significant breakthrough because it enabled new materials to be created with known structure and designed composition modulations. The MBE process involves directing a flux of the respective elements at a heated substrate with the goal of controlling the surface equilibrium. The temperature of the substrate controls the surface diffusion rates, such that atoms can find favorable surface sites, and the desorption rates of different species. The relative fluxes of the sources to the surface control the surface composition by balancing the arrival rates with the desorption rates. Done correctly, and when the lattice mismatch between the film and the substrate is slight, the process results in the growth of solids with the structure of the substrate but composition controlled by the fluxes of reactants. Composition gradients can be kinetically trapped via the epitaxial growth process, because the volume diffusion rates at the temperatures used are small compared to the surface diffusion rates. MBE growth has yielded new materials with exceptional properties, as materials with designed structural sequences can be prepared with very low defect levels due to low growth temperatures. An example of an exceptional property resulting from MBE growth is very high mobility values produced when dopants are incorporated in a layer that then donates

the resulting carriers to another layer in the grown structure. This process is referred to as modulation doping.[11] The lack of dopant atoms in the transport layer, which normally scatter the charge carriers, results in the exceptionally high mobility values. These new materials have led to the discovery of new phenomena including the fractional Hall effect.[12,13]

The ability to anticipate structures that could be prepared via MBE resulted in theoretical predictions of new phenomena, which resulted in new technologies. Light emitting diodes (LED) are one example where predictions were made about the materials properties and architectures required to observe the emission of light from a diode. Once the phenomenon was observed, predictions were made about how to optimize efficiency and how to produce white light from a LED. MBE practitioners determined how to grow and optimize the predicted structures and the resulting LED technology continues to be enhanced today. An important implication is that synthesis routes that yield materials with predictable structures and compositions enhance synergies between theory and experiment. Starting with reasonable assumptions about structure makes calculations easier and enables extrapolations from existing data, both of which facilitate transforming ideas into technologies.

There is currently significant interest in two-dimensional materials, particularly (2-D) - single structural units that are not epitaxially connected to the structure of the substrate, and the stacking of these layers to make 2-D heterostructures, because of the promise of properties that do not exist in the bulk materials or that are enhanced in the heterostructure relative to the bulk or the individual 2-D constituents. The layer-by-layer design provides clear structural starting points for theory, and the surface states present in

these 2-D layers have resulted in novel classes of materials such as topological insulators - materials that are bulk insulators but whose surfaces contain conducting states. There is a growing list of potential constituents accompanied by criteria to evaluate stability of potential 2-D layers that have yet to be tried. Heterostructures are an ideal class of materials for the materials genome project to explore materials by design because of their defined starting structure.

Approaches to preparing individual 2-D layers have been developing over time. Initially the preparation was based on the effective but technically challenging cleaving of bulk crystals followed by searching for single constituent layers. More recently, recipes have been developed to prepare individual layers on specific substrates by reaction of surface layers or growth from vapor phase precursors. Examples of materials prepared to date via these recipes include MoS_2,[14,15] WS_2,[16-17] Silicene[18-20] and ZrS_2,[21] all materials with anisotropic structures. Preparing 2-D heterostructures is much more challenging, as the growth techniques developed for individual 2-D layers are typically not compatible with the sequential growth of one constituent on top of another. Indeed the most common approach to making heterostructures has been the cleaving and stacking of individual layers, which has been described as being analogous to building with Lego blocks. While this technique has yielded many new and exciting structures, it is an exacting task only done by a few groups with very low yield[22-27] and is limited to small sample areas. It is also limited to those compounds that can be cleaved into a single layer thick 2-D layer and that are stable as an atomically thick layer. Geim has suggested three criteria for stability based on existing data.[28] He suggests that 1) the parent 3D structure should have a melting temperature above 1000 °C so that the 2D sheet is stable

at room temperature, 2) the 3D structure must be chemically inert so that no decomposed surface layer forms in air or any other environment, and 3) that insulating and semiconducting 2D-crystals are more likely to be stable compared to metallic ones. There is a need for a flexible synthesis approach that is scalable, enables constituents to be layered without epitaxial relationships between layers, and that is applicable to a wide variety of constituents.

XVIII.3. Modulated Elemental Reactants

The modulated elemental reactant (MER) synthesis approach has been developed over the last two decades at the University of Oregon and is based on controlling local composition and diffusion lengths to control the kinetics of phase formation. The initial concept was that by depositing sequential elemental layers, the layer thicknesses could be reduced such that the layers would mix at low enough temperatures that mixing would be complete before interfacial nucleation could occur. This is illustrated schematically in Figure XVIII.1. The initial ratio of layer thicknesses would control the composition of the amorphous intermediate formed. It was shown that the composition of the amorphous intermediate could control the subsequent nucleation process enabling compounds to be formed kinetically even if they are not thermodynamically stable at the reaction conditions.[30] A high level of selectivity can be achieved. By designing precursors that closely mimic the local composition and structure of targeted compounds, diffusion lengths are greatly reduced relative to more traditional synthetic approaches, which allows much lower reaction temperatures and shorter times to be used then conventional methods. The combination of mild annealing conditions and the ability to easily modify

the precursor structure allows numerous metastable compounds to be formed, which cannot be accessed using other techniques.[31-35]

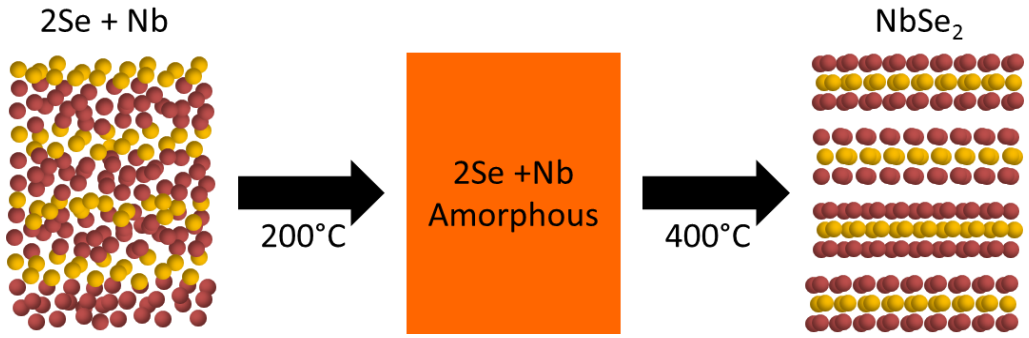

Figure XVIII.1. Schematic of a layered precursor showing the interdiffusion of the layers to form an amorphous intermediate and the subsequent nucleation of the targeted compound.

The structural complexity of products can be increased by adding additional layers with different compositions, leading to the formation of new layered solids containing constituents with different structures. These new compounds can be prepared by combining the precursor layering schemes for single component systems. The structure and composition of each layer is controlled by the composition and thickness of the layer in the precursor. Variations to the layering scheme (nanoarchitecture) of the product can be achieved by simply changing the layering scheme of the precursor. This is illustrated in Figure XVIII.2, where the center structures can be combined to yield three different families of layered structures containing two constituents each. The thickness of each block can be individually controlled as well as the order of the layers, resulting in over 20,000 distinct nanoarchitectures for n and m less than 10. [36] The three constituents can also be combined into one heterostructure, either by alloying the constituents that have a common structure, [37] to form a random (A,B)C alloy, or by preparing three component heterostructures with distinct layers of each constituent forming an ordered

ABAC alloy. These two possibilities provide access to a large number of new compounds, many more than one would like to make, so the challenge is to understand how properties change as the constituent thicknesses, order, and composition are varied to accelerate the search for the optimum properties for a particular application. In the following sections we outline how this approach can be used to prepare increasingly complex compounds with the structure of the initial precursor controlling the nucleation of individual layers and the resulting nanoarchitecture of the final product.

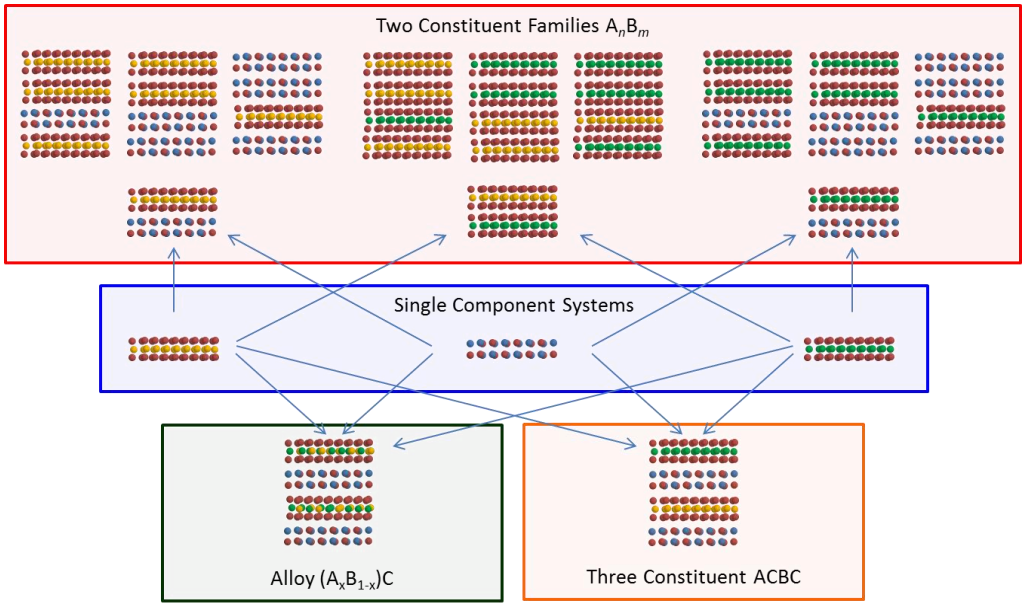

Figure XVIII.2. The blue box shows the thinnest structural units of three representative binary constituents, the outside two with a transition metal dichalcogenide structure (TSe2 and T'Se2) and the middle one a rock salt structure (MSe) with two (001) planes. The second row in the red box displays the three simplest binary heterostrutures, (MSe)1(TSe2)1, (TSe2)1(T'Se2)1 and(MSe)1(T'Se2)1. The top row shows the three compounds with the next smallest repeating units, A1B2, A2B2 and A2B1, illustrating how the constituents can be assembled with different individual thicknesses and, for thicker repeats, different orders of assembly. The bottom row contains a schematic of compounds where the dichalcogenides have been allowed to form the compound (MSe)1(T1 - *x*T'*x*Se2)1 (green box). The thickness of each constituent can be controlled as shown in the top row for the pure dichalcogenides. The image on the bottom left (orange box) shows an ordered alloy, where the three components form the (MSe)1(TSe2)1(MSe)1(T'Se2)1 compound. The A, B, and C components can be combined in different thicknesses and sequences to make a very large number of unique

nanoarchitectures. (For interpretation of the references to color in this figure legend, the reader is referred to the web version of this article.)

XVIII.3.1. Single Component Systems

The simplest materials to form by MER are compounds containing multiple elements but only one structure or type of material, for example a binary rock salt structure or transition metal dichalcogenide structure. These single constituent systems are the building blocks of the more complex materials to be discussed later. The synthesis of these single constituent systems has provided insights into the formation mechanism as the layered precursor system interdiffuses and ideally nucleates into the desired structures. The interdiffusion of the thin elemental layers in the precursors was shown in the early 1980's to be a low temperature route to amorphous alloys.[38] These mechanistic insights are useful in understanding the evolution and resulting structure and properties of more complex systems containing several constituents. The calibration schemes used for these simple component systems are also applied in the design of the precursors required to form more complex materials.

Calibration of the modulated precursors for single component systems consists of two basic steps. The first step is to adjust the relative deposition times of each element to ensure the desired composition. In a binary system, two elements are deposited typically holding the deposition time of one constituent constant while systematically varying the deposition time of the other. By holding the deposition time of Se constant while that of the Nb is incrementally changed a linear relationship between the atomic ratio of the elements and the ratio of the deposition times results with the slope related to the proportionality factor between the deposition rates measured by the quartz crystal

monitors and the actual deposition rates at the sample surface. Scaling deposition times of all sources equally, yields the same composition but different repeat thicknesses. This enables the deposition time corresponding to the desired Nb/Se composition ratio to be interpolated, which can then be scaled to deposit a specific thickness of a desired composition. Typically, a 3–5% excess of selenium is used to compensate for losses during annealing of the precursors to transform them into the targeted products.

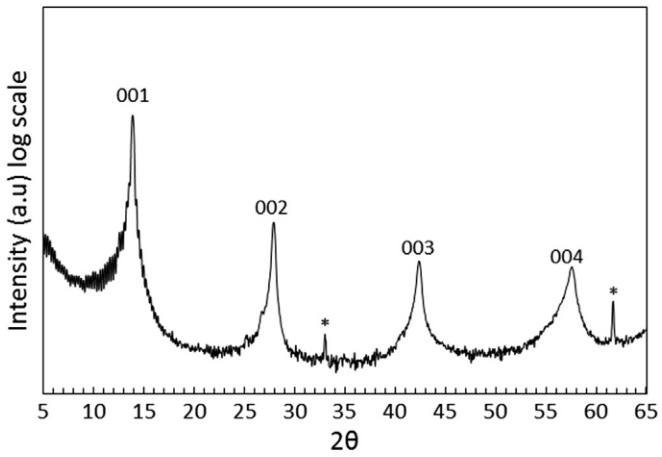

Figure XVIII. 3. Diffraction pattern of NbSe2 formed at 400 °C by annealing a precursor containing Nb/Se elemental bilayers. The y *axis* is log intensity to highlight low intensity diffraction maxima. Only the 00*l*reflections are observed due to the textured nature of the product. Substrate peaks are indicated with an asterisk.

Once the composition of the precursor is correct, it is crucial that the thickness of the layering is thin enough that the layers interdiffuse before interfacial nucleation occurs. This is the second step in the calibration. Low temperature annealing causes inter- diffusion, and if the layers are thin enough this results in an amorphous intermediate with a constant composition. The aver- age composition has a large impact on what crystallizes as nu- cleation is controlled by local composition. Figure XVIII. 3 contains a dif- fraction pattern of a sample with a Nb to Se composition ratio of one to two after

annealing at 400 °C. The intensity of the peaks depends on both the percent of the precursor that has crystallized as well as the extent of preferred alignment of the crystallites. The sharpness of the diffraction peaks reflects the size of coherently scattering crystalline domains. As shown in Figure XVIII. 4, the intensity of the peaks of the assembled ferecrystal are sensitive to composi- tion, presumably due to a combination of a reduced amount of product crystallized and the reduced size of the crystallites with increasing deviations of the precursor from the composition cor- responding to the stoichiometry of the crystallizing compound. This is presumably caused by the increasing non-stoichiometry at the growing crystallites as the excess element is excluded from the growing crystal. This variation in intensity provides an additional guide when optimizing the correct composition and thickness of the precursor.

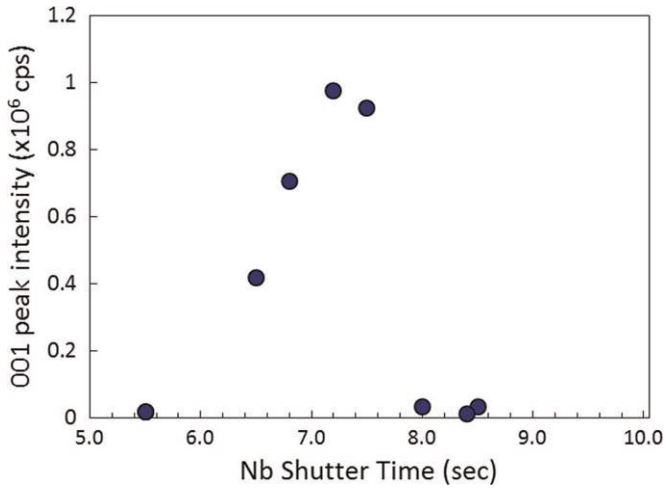

Figure XVIII. 4. The intensity of the first observed 00*l* reflection of $NbSe_2$, formed at 400 °C, as a function of time that the shutter was open depositing Nb at a constant rate. The maximum in the intensity corresponds to the precursor with a 1:2 ratio of Nb to Se.

The goal of the second calibration step is to optimize the thickness of the repeating sequence of elemental layers in a way that each deposited layer evolves into a single

structural unit of the targeted constituent, for example, a single Mo/Se bilayer would evolve into one Se–Mo–Se trilayer. The thickness of a single repeating sequence of deposited atomic layers can be determined from an analysis of the X-ray reflectivity (XRR) pattern of the precursor. The XRR patterns contains Bragg reflections from the repeating sequence of layers and Kiessig fringes, which result from the interference pattern from the front and back of the film and intensity from the incomplete destructive interference of the finite number of layers. A plot of monolayer thickness versus deposition time allows the deposition times that correspond to a desired repeat thickness to be determined. If the correct repeat thickness is used, then the number of repeats in the precursor is equal to the number of repeats in the final product. For example Figure XVIII. 5 contains an NbSe2 sample in which 58 repeats were deposited giving a product with 58 repeating units by XRR. Having calibrated the thickness in this manner, the number of repeating structural units in the crystalline sample is precisely controlled by changing the number of repeats in the precursor. Samples containing from 2 to 80 repeating structural units have been prepared using this method [39].

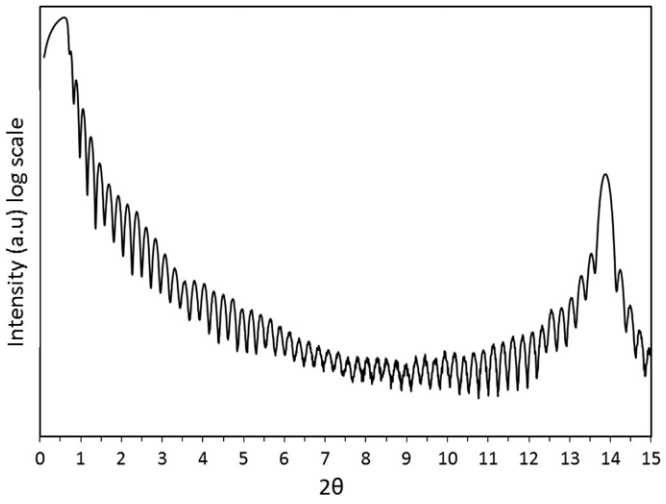

Figure XVIII. 5. An XRR pattern of a sample containing 58 repeating NbSe2 trilayers, formed at 400 °C, from a precursor containing 58 repeating Nb–Se bilayers in the repeating precursor.

The preparation of metastable crystalline compounds is a challenge and requires control of both nucleation and growth of the targeted compound. The preparation method described above has turned out to be effective for the synthesis of metastable crystalline samples with varying chemical compositions that cannot be obtained applying classical approaches [40–43]. The key for the success of the method is a drastic reduction of the diffusion length to some nm or even down to few Å. As a consequence in- terdiffusion, nucleation and crystallization occur at low tempera- tures compared to classic approaches of preparing of inorganic solids [44–46].

XVIII.4. Two Component Systems

The calibration of a precursor designed to form a two-compo- nent compound follows the same logical process used for the single component precursor, but the additional constituent adds additional elements that need to be calibrated, requiring more steps. The calibration of the relative compositions and thicknesses of all of the layers in the repeating sequence of elemental layers for two component systems is made easier if the deposition para- meters for each of the constituents have already been in- dependently calibrated. In this case, the first step in the calibration is to adjust the relative amount of each of the constituents. The relative amounts depends on the different entities being layered, as there will be a misfit in area between the constituents that depends on the crystal faces of the constituents that are adjacent to one another and the unit cell parameters. This results in a factor1þδ, where δ is the so called misfit parameter, reflecting the differences, or mismatch, of the lattice parameters of the adjacent planes at

the interface between the two constituents giving rise to different numbers of formula units per area. When making deri- vatives of known compounds containing two different con- stituents, the desired ratio is simply the reported misfit parameter for the two constituents. When attempting to create new com- pounds between two constituents that have not been layered before, assumptions about the adjacent crystal phases are made and the bulk lattice parameters are used to calculate misfits. The second step in the calibration is to prepare samples at the desired composition ratios by holding the deposition times of one con- stituent constant while those of the other are systematically scaled. Plotting the composition ratio versus the deposition time of the varied constituent yields a calibration curve from which the deposition time yielding the desired atomic ratio for the elements can be determined. The third step is to scale thickness of two constituents so that the layers deposited for each constituent yields a single crystallographic unit.

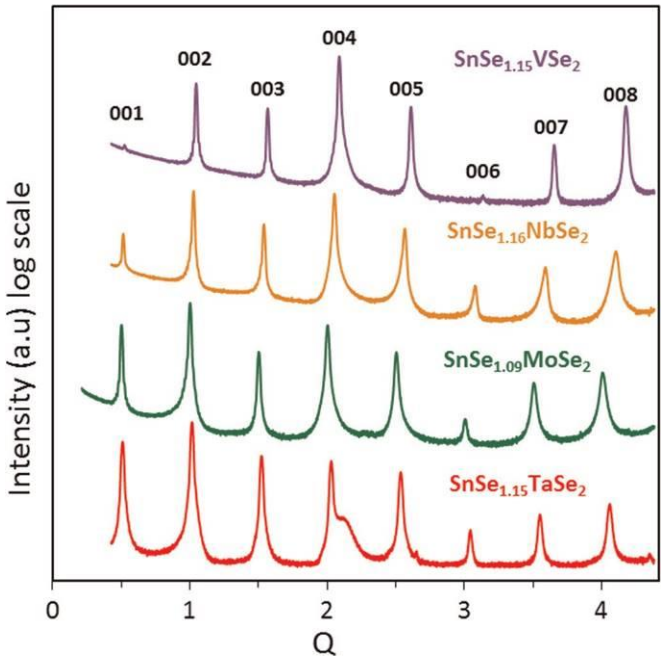

Figure XVIII. 6. Specular diffraction scans of $[(SnSe)_{1.15}]_1(VSe_2)_1$, $[(SnSe)_{1.16}]1(NbSe_2)_1$, $[(SnSe)_{1.09}]_1(MoSe_2)_1$, and $[(SnSe)_{1.15}]_1(TaSe_2)_1$. All of the diffraction peaks are

00lreflections, and the indices for each reflection are indicated above the scan of the $[(SnSe)_{1.15}]_1(VSe_2)_1$ sample. All samples were annealed at 400 °C for 20 min The following example illustrates the process. In the calibration of the SnSe–$NbSe_2$ system, the difference in area between the (001) planes of SnSe and the (001) planes of $NbSe_2$ is 1.16 obtainedeither from the known misfit compound or by using the lattice parameters of the bulk compounds as an estimate. To find the ratio of deposition times to obtain this Sn/Nb ratio, the Nb and Se de- position times of the $NbSe_2$ constituent are held constant while the deposition times of the Sn and Se precursor layers for the SnSe component are systematically scaled. A plot of the Sn/Nb ratio vs. the amount of time the Sn shutter is open results in a linear re- lationship for the specific deposition rates and geometry used. This experimental relationship enables the deposition time that gives a Sn/Nb ratio equal to the known misfit parameter for this com- pound to be determined. After the appropriate composition is achieved, scaling the deposition times of all elements together to achieve the thickness such that layers in the precursor evolve into single structural units of each constituent completes the calibration. If the thicknesses were correct for each of the single component systems, the thickness after scaling the compositions are usually pretty close for the two component system, which simplifies this step.

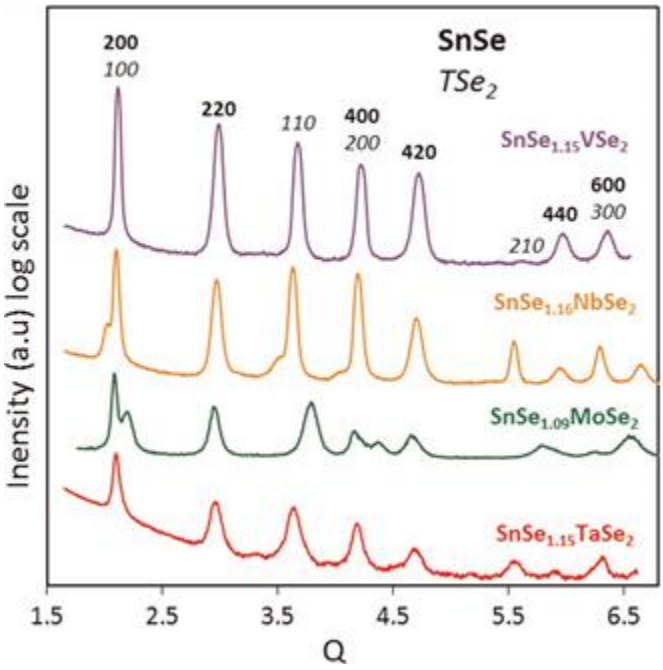

Figure XVIII. 7In-plane diffraction scans of $([SnSe])_{1.15})_1(VSe_2)_1$, $([SnSe])_{1.16})_1(NbSe_2)_1$, $([SnSe])_{1.09})_1(MoSe_2)_1$, and $([SnSe])_{1.15})_1(TaSe_2)_1$. All of the diffraction peaks can be indexed as (*hk*0) reflections of the two constituents. The indices for each reflection are indicated above the scan of the $([SnSe]_{1.15})_1(VSe_2)_1$ sample

Using different single component systems as building blocks, a variety of two component systems can quickly be calibrated, precursors prepared, and precursors

annealed to form targeted compounds. For example, Figure XVIII. 6 contains the specular diffraction patterns for four different $[(SnSe)_{1+\delta}]_1(TSe_2)_1$ compounds with T¼ V, Nb, Mo and Ta. The specular diffraction patterns for all of these compounds are similar, but the intensities of the 00*l*re¯ections vary mainly due to the different scattering factors for the transition metals in the dichalcogenide component. The *c*-axis lattice parameters of all of the compounds are similar and can be thought of as the sum of the thickness of two (001) planes of SnSe and a Se–T–Se trilayer. Figure XVIII. 7 contains the in-plane X-ray diffraction patterns of the same four $[(SnSe)_{1+\delta}]_1(TSe_2)_1$ compounds with T¼ V, Nb, Mo and Ta. The reflections in the in-plane diffraction scans of these compounds can be indexed as two families of reflections, each arising from one of the constituents. The in-plane lattice parameters of SnSe do not vary as much as the in-plane *a*- axis lattice parameter of the transition metal dichalcogenides, leading to the different misfit parameters. In contrast to the crystalline misfit compounds prepared at high temperature which typically have one commensurate in-plane axis, the in-plane lat- tice parameters of the constituents in the compounds prepared using the MER approach remain incommensurate. Figure XVIII. 8 contains a representative high angle annular dark field scanning transmission microscopy (HAADF-STEM) image of $[(SnSe)_{1.15}]_1(VSe_2)_1$. The im- age shows the regular stacking of the two constituent layers and the random rotational disorder between layers. Due to this ex- tensive random rotational disorder found in all the misfit layer compounds prepared using the MER approach, the term "ferecrystal", from the Latin "fere" meaning almost, has been created to describe them.

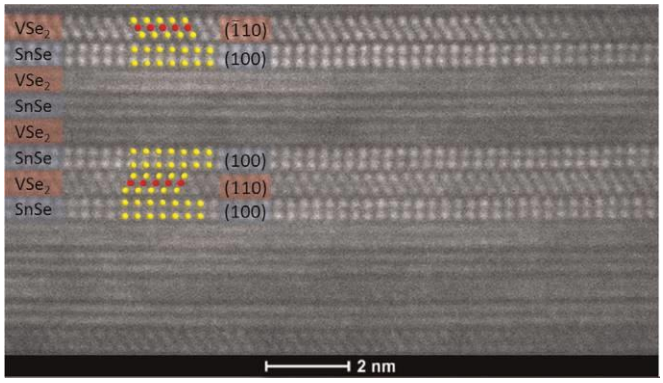

Figure XVIII. 8 Cross sectional HAADF STEM image of $([SnSe]_{1.15})_1(VSe_2)_1$

In addition to these four compounds, many other members of these $[(SnSe)_1](TSe)$ families compounds have been prepared as well as quite a few additional families as summarized in Table XVIII 1. Several ferecrystals containing two different dichalcogenides have been prepared, although the extent of intermixing of the transition metals was not determined, because it is very difficult to experimentally determine the extent of alloying. Two different dichalcogenide–M_2Te_3 systems have been investigated to date, with a large range of different thicknesses of the two constituents. There is an atomically abrupt structural change between the constituents, and the chemical difference between the two structures results in an abrupt composition change as well. The same is true for the dichalcogenide–rock salt compounds, for which the largest number of compounds have been prepared and the most extensive structural studies have been conducted. To our knowledge, this approach has not been tried on other constituents, except for one report of the formation of intergrowths of $CoSb_3$ and $IrSb_3$ [47]. While a superlattice was observed, it was not crystallographically aligned with the substrate, making structural characterization challenging. The data suggests that this synthesis

approach provides a promising avenue to prepare ferecrystalline materials with a wide variety of different structures.

Table XVIII 1. A summary of the different families of compounds that have been prepared utilizing the MER technique.

Compounds	References
Dichalcogenide-Dichalcogenide	
$[(TiSe_2)_{1+\delta}](NbSe_2)$	48-51
$\{[(VSe_2)_n]_{1.06}(TaSe_2)_m\}_z$	52,53
Dichalcogenide-M_2Te_3	
$[(TiTe_2)_{1.36}]_x[Bi_2Te_3]_y$	54,55
$[(TiTe_2)_{1+\delta}]_x[Sb_2Te_3]_y$	56-58
M_2Te_3 - M'_2Te_3	
$[Sb_2Te_3/(Bi,Sb)_2Te_3$	59-61
Rock salt - Dichalcogenide	
$[(SnSe)_{1.15}]_m(VSe_2)_n$	62-65
$[(SnSe)_{1.16}]_m(NbSe_2)_n$	66-71
$[(SnSe)_{1.09}]_m(MoSe_2)_n$	72-75
$[(SnSe)_{1.15}]_m(TaSe_2)_n$	76,77
$[(SnSe)_{1.20}]_m(TiSe_2)_n$	78,79
$[(PbSe)_{1.15}]_m(TiSe_2)_n$	80-82
$[(PbSe)_{1.10}]_m(NbSe_2)_n$	83,84
$[(PbSe)_{1.00}]_m(MoSe_2)_n$	85-89
$[(PbSe)_{1.12}]_m(TaSe_2)_n$	90
$[(PbSe)_{0.99}]_m(WSe_2)_n$	91-93
$[(BiSe)_{1.15}]_m(TiSe_2)n$	94
$[(BiSe)_{1.10}]_m(NbSe_2)_n$	95
$[(CeSe)_{1.14}]_m(NbSe_2)_n$	95
$[(PbTe)_{1.17}]_m(TiTe_2)_n$	96

For any intergrowth of two constituents, there is a large number of compounds that can be formed by varying the layer sequence. For example, there are two distinct structural isomers that contain three layers of each constituent A_3B_3 and $A_2B_2A_1B_1$. Both of these compounds will have the same overall composition and approximately the same *c*-axis lattice

parameter, but different superstructures. When there are three layers of one constituent and two of another, there are also two distinct isomers, A_3B_2 and $A_2B_1A_1B_1$. As the number of layers increases, so does the number of potential structural isomers. When there are four layers of each constituent, there are 6 distinct structural isomers, A_4B_4, $A_3B_3A_1B_1$, $A_3B_2A_1B_2$, $A_2B_3A_2B_1$, $A_2B_2A_1B_1A_1B_1$, and $A_2B_1A_1B_2A_1B_1$. When there are 10 layers of each constituent, there are over 4700 possible distinct structural isomers. As illustrated in Figure XVIII.9, for n and m both equal to ten or less, there are over 20,000 distinct structural isomers that can be formed that might be expected to have different physical properties.

$m \backslash n$	1	2	3	4	5	6	7	8	9	10
1	1	1	1	1	1	1	1	1	1	1
2	1	1	2	2	3	3	4	4	5	5
3	1	2	2	4	5	6	8	10	11	14
4	1	2	4	6	10	14	20	26	35	44
5	1	3	5	10	15	26	38	57	79	110
6	1	3	6	14	26	46	76	122	183	275
7	1	4	8	20	38	76	132	232	375	600
8	1	4	10	26	57	122	232	432	750	1272
9	1	5	11	35	79	183	375	750	1384	2494
10	1	5	14	14	110	275	600	1272	2494	4735

Figure XVIII. 9 The number of possible structural isomers for a given AmBn stoichiometry are given in each of the boxes. The shading of the boxes reflects the rapid increase in the number of isomers as m and n increase.

XVIII.5.Adding Additional Complexity

There are several ways to add complexity beyond that found with two binary constituents. One approach is to alloy one or both of the constituents. Another would be to layer three different constituents, two of which have the same structure to form an

ordered intergrowth. A third approach would be to layer three constituents all of which have different structures. In each of these cases, the composition and structure of each constituent and the interaction between constituents will affect physical properties. The following sections discuss strategies to prepare the required precursors for each of these approaches with experimental examples.

XVIII.5.1. Preparing Random Alloys

Alloying a particular constituent within a multilayer containing two or more compounds in the repeating structure is based on controlling local composition in the specific layer within the precursor that will evolve into the constituent being alloyed.[37] The composition control is accomplished via calibrations similar to what was discussed earlier. There are at least two different approaches based on the number of sources used. The elements to be alloyed in the targeted constituent can be deposited from one source, which is an alloy itself, or the elements can be deposited from different sources, and composition changed by increasing the amount of one element deposited while decreasing the other by the same amount.

Preparing an alloyed constituent using an alloy source is straightforward if the elements are miscible and have similar deposition characteristics. Depositing from an (A,B) alloy source can allow (A,B)C alloys to be synthesized with only minor adjustments to the calibrations of the parent compounds discussed earlier. $(SnSe)_z$ $(Nb_xMo_{1-x})Se_2$ alloys, which were recently reported, are one example. One complication of this approach is that the vapor and the melt will have different compositions, and the composition of the vapor as a function of the composition of the melt may not be known. This difference in composition also results in the composition being deposited from the

alloy source changing with the amount of time the source has been depositing. This is illustrated in Figure XVIII.10 where the composition of $(SnSe)_z(Nb_xMo_{1-x})Se_2$ samples made by the deposition of Nb/Mo alloy sources results in samples with a lower Nb content than the deposition source. Subsequent samples made with the same deposition source, shown in Figure XVIII.11, have increasing Nb content as the source becomes depleted in Mo.

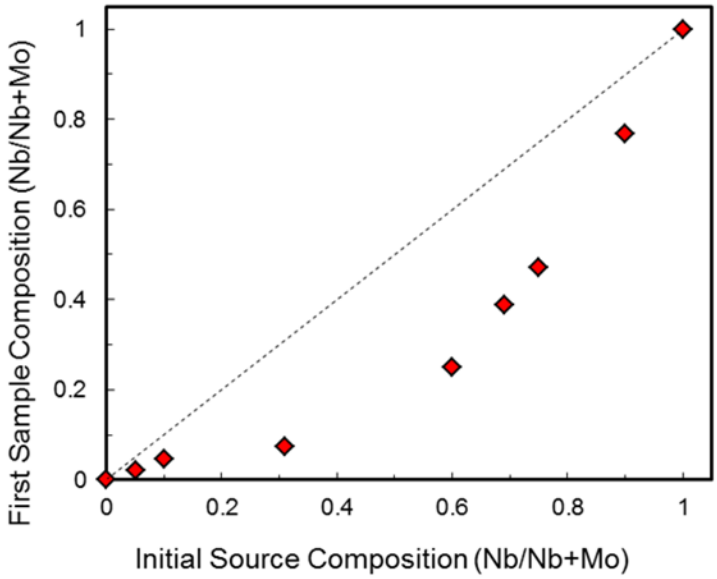

Figure XVIII.10. The difference between the initial source composition and the composition of the first sample made from that source, showing the preferential deposition of Mo.

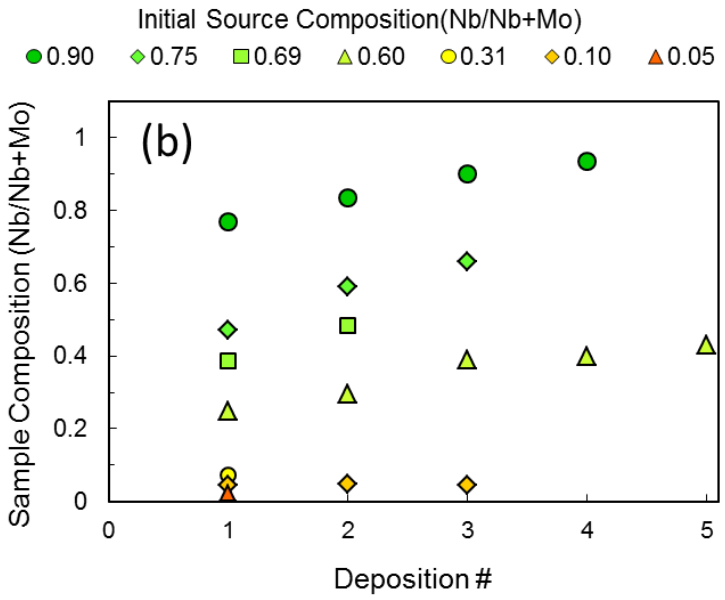

Figure XVIII.11. Plot of the change in the composition of samples as samples are sequentially made from a specific source. The samples become more Nb rich as the source becomes depleted in Mo.

A second approach is using two different deposition sources to create the alloy, which enables alloys to be made of systems where the elements either do not alloy or have vastly different partial pressures over a melted alloy. Depositing fractions of layers using the calibrations of the original components as starting points works even for systems with very different deposition characteristics such as vanadium and tantalum in the alloy system $(SnSe)_{1+\delta}(V_xTa_{1-x})Se_2$. Holding the non-alloyed constituent constant, the deposition time of the elements in the constituent that are being alloyed are varied as relative fractions of the calibrated parent compounds. As shown in Figure XVIII.12, a linear relationship occurs between relative shutter times and relative compositions of the alloys, allowing the preparation of alloys with precisely controlled compositions.

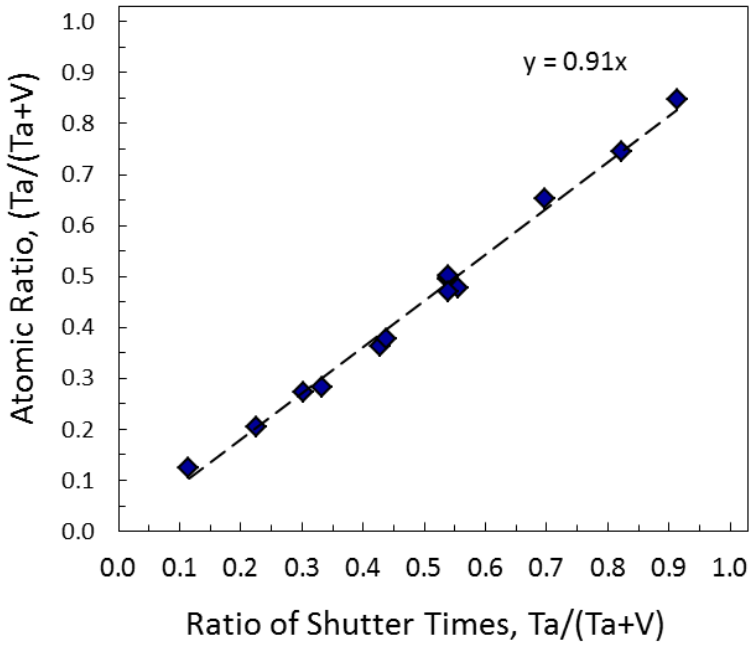

Figure XVIII.12. The change in the atomic percent of Ta in a sample containing an alloyed $(Ta_{1-x}V_x)Se_2$ layer graphed versus the change in the percent of time the shutter of Ta was open divided by the total time that the shutters of Ta and V were opened.

Detecting that one constituent has been alloyed and determining the composition of the alloyed layer is an experimental challenge Specular XRD of the $(SnSe)_{1+\delta}(Ta_xV_{1-x})Se_2$ system shows systematic changes in relative peak intensities (Figure XVIII. 13) and in the position of reflections as *x* goes from 0 to 1. The systematic shift to lower angles of the Bragg peaks with increasing substitution of V by Ta indicates an increase in the lattice parameter in the *c* direction. As shown in Figure XVIII. 14, the *c*-axis lattice parameter increases linearly as the amount of Ta is increased, as expected from Vegard's law due to the larger size of Ta. The *c*-axis lattice parameter, however, is the sum of the thicknesses of the SnSe and dichalcogenide constituents, so additional data

are re- quired to confirm that the alloying is limited to the dichalcogenide layer.

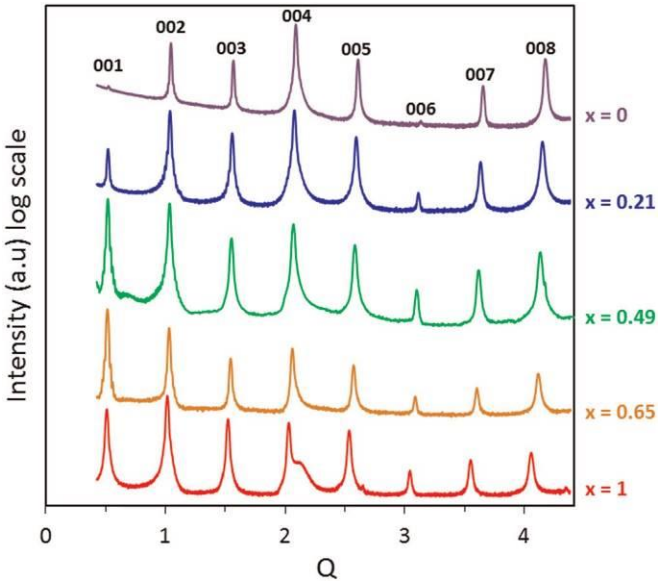

Figure XVIII. 13. Specular X-ray diffraction scans of a series of $(SnSe)_{1-\delta}(Ta_xV_{1-x})Se_2$ compounds formed at 400°C. The diffraction peaks shift slightly to lower angles as x is increased, indicating an increase in the c-axis lattice parameter. The 00l indices are shown above the top diffraction scan.

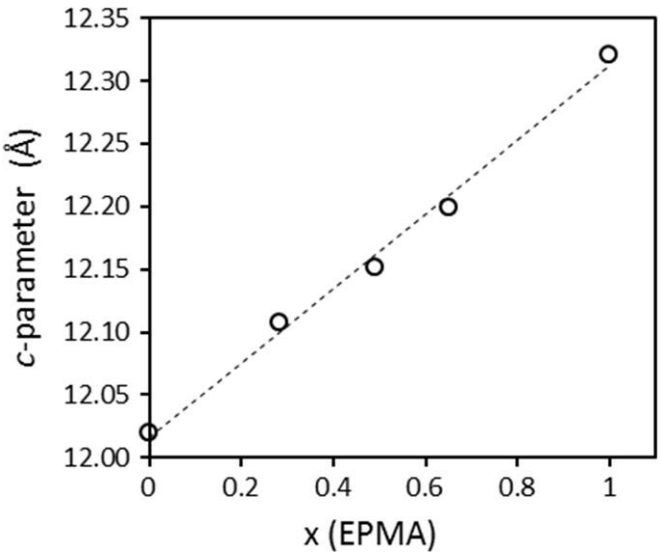

Figure XVIII. 14. The calculated c-axis lattice parameter for a series of (SnSe)1 þ δ(TaxV1 - x)Se2 compounds plotted as a function of x. The linear increase in the c-axis lattice parameter with increasing x is expected from Vegard's law.

In-plane XRD scans of the (SnSe)1 þ δ(Ta*x*V1 - *x*)Se2 compounds, shown in Figure XVIII. 15, provide information about in-plane structure of both constituents, enabling us to determine how the structure of each constituent changes as a function of *x*. The relative intensities of the *hk*0 reflections change as the vanadium content increases. For example, the intensity of the (210) reflection of the dichalcogenide decreases relative to the (110) reflection. The relative positions of the peaks also change as a function of *x*, indicating changing in-plane lattice parameters of both the SnSe and Tax $V_{1-x}Se_2$ constituents. Figure XVIIIs. 16 and 17 show the change in the *a*-axis lattice parameters of SnSe and $Ta_xV_{1-x}Se_2$ respectively. The *a*-axis lattice parameters of both compounds increase linearly as *x* in- creases to 0.65. The *a*-axis lattice parameters for *x* ¼ 1, the $SnSe_{1.15}TaSe_2$ sample, are smaller than expected from the trends observed as *x* increases, due to a change in the coordination of the transition metal in the dichalcogenide from octahedral for the V rich samples to trigonal prismatic coordination for Ta in $TaSe_2$. This is consistent with prior results reported for alloying of VSe2 and TaSe2. The change in the lattice parameter of SnSe is likely due to changes in charge transfer with the

dichalcogenide as the co- ordination changes. Changes in the lattice parameter of SnSe have been observed both as a function of the thickness of the SnSe layer, and as the

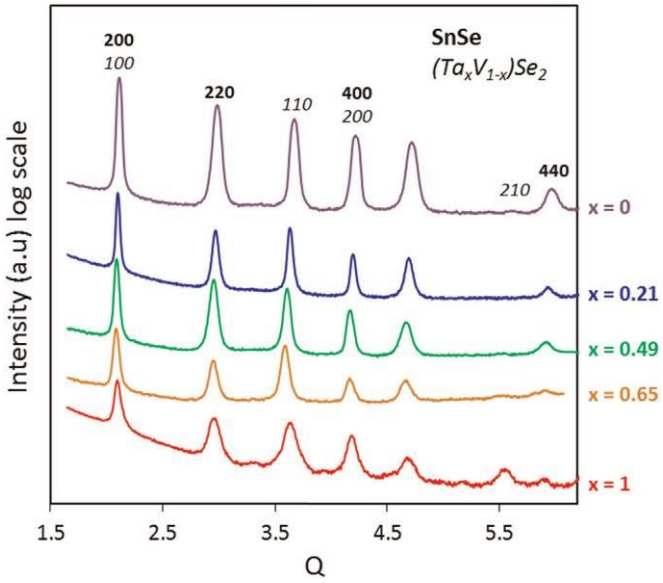

dichalcogenide constituent has been varied [97].

Figure XVIII. 15. In-plane X-ray diffraction scans of a series of $(SnSe)_{1-\delta}(Ta_xV_{1-x})Se_2$ com- pounds formed at 400 °C. The diffraction peaks shift as x is increased, indicating changes in the a-axis lattice parameter of both constituents. The (hk0) indices are shown above the top diffraction scan with the indices for SnSe indicated in bold.

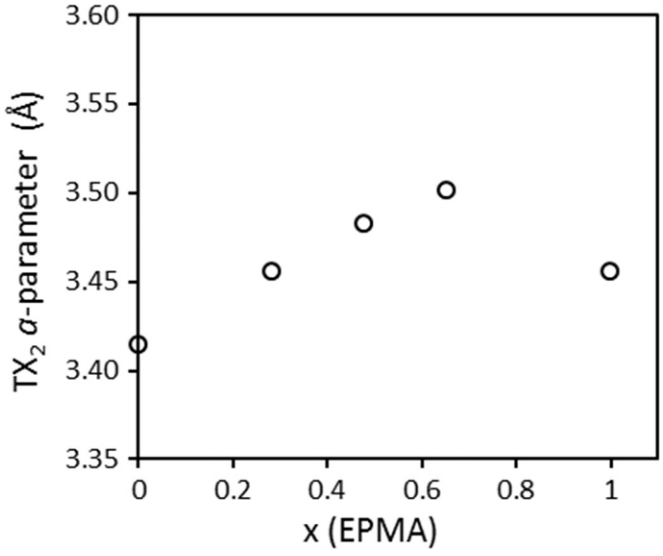

Figure XVIII. 16. The calculated a-axis lattice parameter for the $(Ta_xV_1\text{-}x)Se_2$ constituent plotted as a function of x. The linear increase in the a-axis lattice parameter with increasing x is expected from Vegard's law due to the larger size of Ta relative to V. The

small a-axis lattice parameter for x ¼ 1 results from a change from octahedral coordination for x ¼ 0.8 to trigonal prismatic coordination when x ¼ 1.

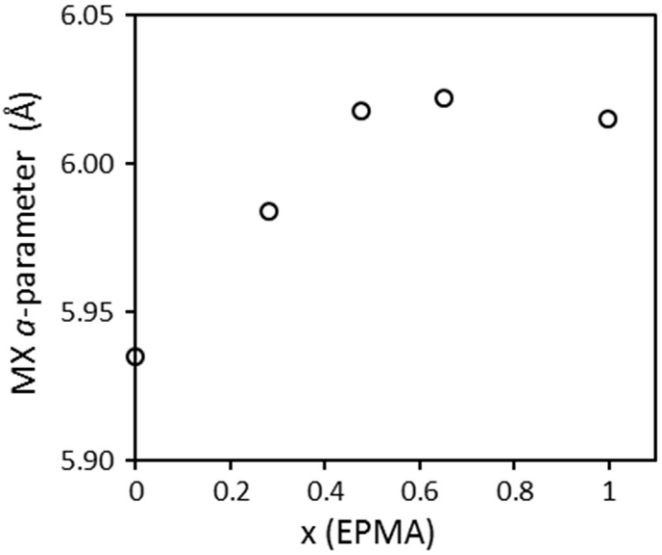

Figure XVIII. 17. The calculated a-axis lattice parameter for the SnSe constituent plotted as a function of x.

To our knowledge, there have not been any solid solution studies of misfit layered compounds reported due to both difficulties in their synthesis and in the analysis of their diffraction patterns. There are only three systems involving alloying of constituents using the MER approach reported, including that of $(SnSe)_{1-\delta}(Ta_xV_{1-x})Se_2$ reported here. The synthesis and properties of $[(TiTe_2)_{1-\delta}]x[(Bi_{2-x}Sb_x)_2Te_3]_y$ alloys was reported by Mortensen et al. [57] the rock salt constituent was alloyed in $([Pb_xSn_{1-x}]Se)_z$ $TiSe_2$ [98], and the transition metal constituent was alloyed in $(SnSe)_z(Nb_xMo_{1-x})Se_2$ [37].

XVIII.6.Ordered ABAC Alloys

Ordered AmBnCp or more complex sequences of three compounds, such as $A_mB_nC_pB_q$, where A, B and C are compounds containing three compositionally different

constituents, three structurally different constituents or a mix of these can be prepared expanding the calibration procedure described above. If the calibrated deposition parameters for two component systems containing the constituents are known, the process is straight forward. The desired atomic ratios of the relative layers are based on known or estimated misfit parameters derived from the structures of the constituents. The first step in the calibration is to prepare a sequence of samples with varying amount of the third component while holding the known parameters for the two component system fixed. Interpolating the resulting curve enables the deposition parameters that yield the correct overall stoichiometry to be determined as shown in Figure XVIII. 18 for the $([SnSe]_{1+\delta})_m$ $(NbSe_2)_n([MoSe_2]n)_{1.06}$ system. A second step of scaling of all layers simultaneously may be required to ensure appropriate thickness of the precursor. This is not usually necessary, however, as the calibration of the simpler systems is usually accurate enough to produce the desired precursors. If the disordered alloys have already been made by sequential deposition, as in the case of (SnSe)1+δ(TaxV1-x)Se2 described above, then the deposition times giving the appropriate metal ratios are already known and can be used for the disordered alloys.

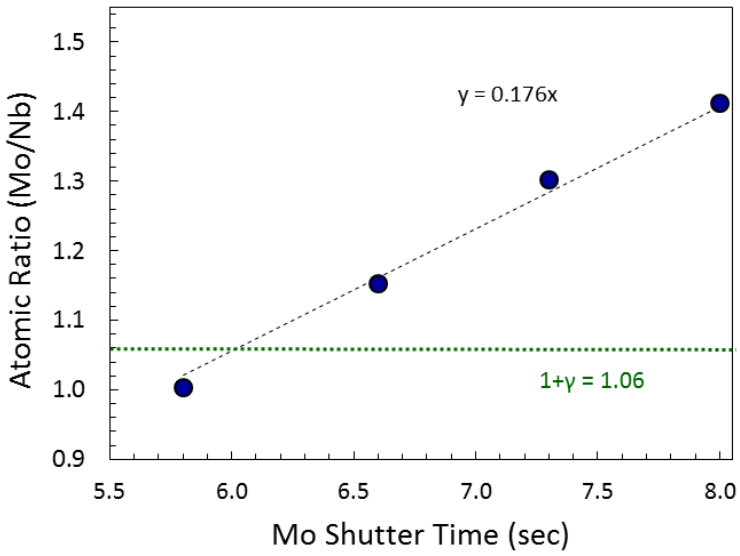

Figure XVIII. 18. A graph of the Mo to Nb ratio as a function of the time the Mo shutter was open while the Nb shutter time was held constant. The dotted green line describes the misfit between the NbSe2 and the MoSe2 constituents and the intercept with the experimental line provides the time the Mo shutter needs to be held open to achieve this composition.

The formation of an ordered alloy can be seen from the additional 00/reflection in the specular diffraction pattern due to the increased size of the unit. Figure XVIII. 19 compares the specular diffraction patterns of the $(SnSe)_{1-\delta}(Ta_{0.5}V_{0.5})Se_2$ random alloy and the ordered compound $(SnSe)_{1-\delta}(VSe_2)_{1-\gamma}(SnSe)_{1-\delta}TaSe_2$. A total of 80 layers were used for the compounds, 40 repeat units for the A(B,C) random alloys and 20 repeat units for the ABAC alloys, making both films approximately 50 nm thick. A doubling of the unit cell compared to the $(SnSe)_{1-\delta}(Ta_{0.5}V_{0.5})Se_2$ is indicative of the formation of an ordered $A_mB_nC_pB_q$ alloy with the general for- mula of $(SnSe)_{1-\delta}([Ta_xV_{1-x}]Se_2)_{1-\gamma}(SnSe)_{1-\delta}$ ([V*y*Ta1 - *y*]Se2)1 where the degree of intermixing of the dichalcogenide layers must be determined before the formula for the new compound is known.

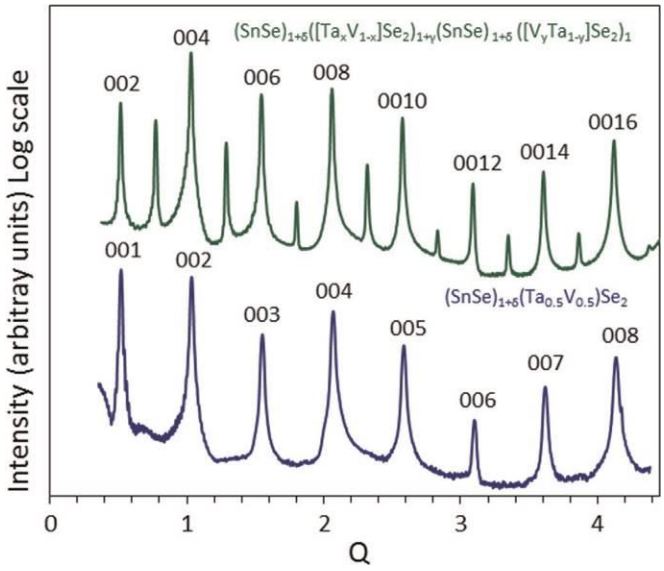

Figure XVIII. 19. A comparison of the diffraction patterns of $(SnSe)_{1-\delta}(Ta_{0.5}V_{0.5})Se_2$ and $(SnSe)_{1-\delta}(VSe_2)_{1-\gamma}(SnSe)_{1-\delta}TaSe_2$ formated at 400 °C. The doubling of the number of reflections results form a doubling of the *c*-axis lattice parameter

The extent of intermixing between the dichalcogenide layers is difficult to determine experimentally. One estimate of the extent of intermixing can be obtained from the in-plane lattice parameters of the constituents. Figure XVIII. 20 contains the in-plane X-ray diffraction pattern of the nominally $(SnSe)_{1-\delta}(VSe_2)_{1-\gamma}(SnSe)_{1-\delta}TaSe_2$ compound. The aplitting of the dichalcogenide peaks, which would be expected for pure VSe_2 and $TaSe_2$ constituents, is not observed. This suggests that the mixing is significant, larger than 20% from the linewidths of the reflections and the change in the lattice parameters of the $(SnSe)_{1\ þδ}TaSe_2$ alooys discussed earlier.

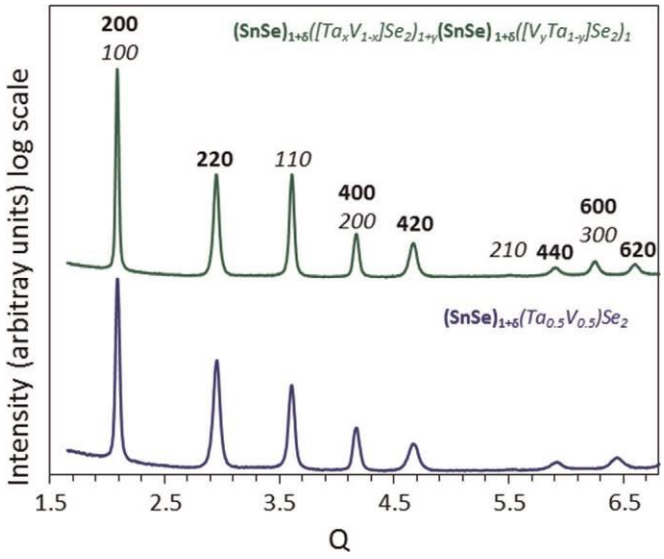

Figure XVIII. 20. In-plane diffraction of the nominally (SnSe)1 þδ(VSe2)1 þ γ(SnSe)1 þ δTaSe2 compound (green) to determine the extent of intermixing. The indices of the (hk0) reflections are given above the top diffraction scan, with those in bold the indices for SnSe reflections and those in italic for the dichalcogenide constituents. The pattern of the (SnSe)1þ δ(VSe2)1þ γ(SnSe)1þ δTaSe2 (blue) is provided for comparison. (For interpretation of the reference to color in this figure legend, the reader is referred to the web version of this article.)

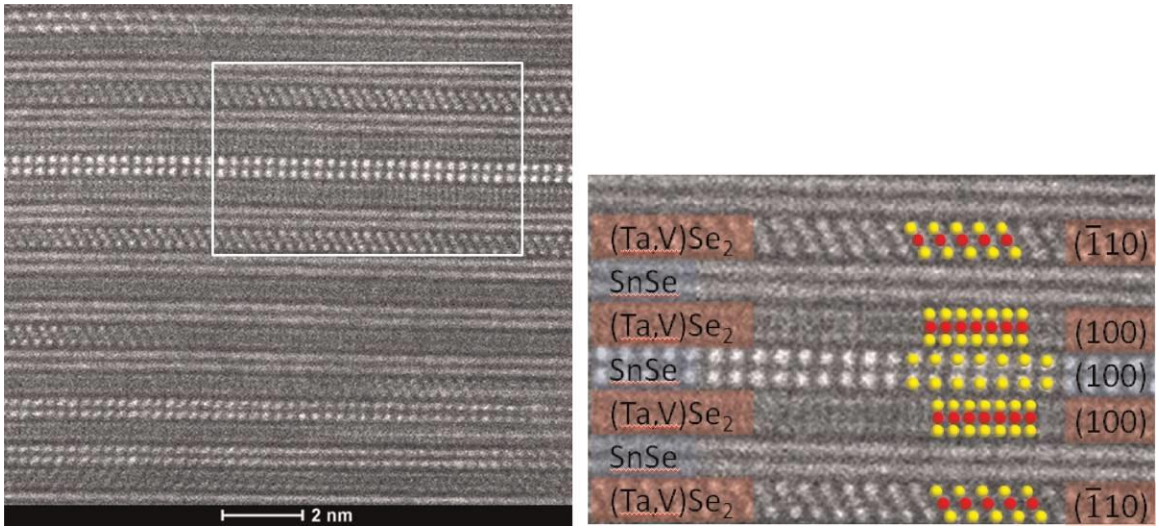

Figure XVIII. 21. High resolution HAADF STEM image of the nominal (SnSe)1 þ δ(VSe2)1 þ γ(SnSe)1 þδTaSe2 compound shows the local structure. The different zone axes in different layers result from rotational disorder which is typical for layered compounds prepared using the MER technique.

To obtain additional information on the structure, HAADF- STEM images were collected and shown in Figure XVIII. 21. The structure consists of alternating layers of a

dichalcogenide and rock salt structure in distinct parallel layers. Multiple orientations of each constituent can be seen due to the turbostratic disorder between layers. The coordination of the dichalcogenide atoms in both layers is octahedral, which agrees with what would be expected if the TaSe2 layer contains at least 20% vanadium. If there was no al- loying between the layers, the TaSe2 layer would be expected to have trigonal prismatic coordination. An intensity difference would be expected between the VSe2 and TaSe2 layers due to the difference between the atomic numbers of the transition metals, but only a small intensity difference is observed. This, combined with the observed octahedral coordination and the X-ray diffrac- tion results indicates significant intermixing of the dichalcogenide layers. The data suggests that a more accurate representation of the nominally (SnSe)1 þ δ(VSe2)1 þ γ(SnSe)1 þ δTaSe2 compound is [(SnSe)1.15]1([Ta*x*V1 - x]Se2)1[(SnSe)1.15]1([V*y*Ta1 - *y*]Se2)1 to account for intermixing and alloying of the dichalcogenide layers.

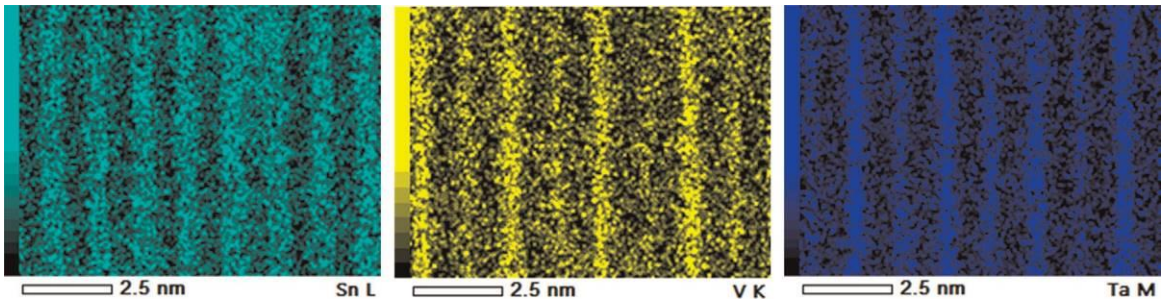

Figure XVIII. 22. EDX maps of a region the $[(SnSe)_{1.15}]_1([Ta_xV_{1-x}]Se_2)_1[(SnSe)_{1.15}]_1([V_yTa_{1-y}]Se_2)_1$ compound. The data is consistent with the HAADF STEM images, with alternating layers of SnSe and the transition metal dichalcogenide. The vanadium and tantalum intensities oscillate out of phase with one another, suggesting alternating layers of a tantalum rich and a vanadium rich dichalcogenide

A more direct measure of the distribution of the V and Ta atoms between the dichalcogenide layers was obtained via EDX maps of the $(SnSe)_{1.15}([Ta_xV_{1-x}]Se_2)_1(SnSe)_{1.15}([V_yTa_{1-y}]Se_2)_1$ compound, which are shown in Figure XVIII. 22. The

EDX images show alternating regions of brighter and lesser intensity for the V and Ta regions indicating Ta-rich and V-rich dichalcogenide regions, which is consistent with the specular diffraction data.

EDX line scan (Figure XVIII 23) of $[(SnSe)_{1.15}]_1([Ta_xV_{1-x}]Se_2)_1[(SnSe)_{1.15}]_1([V_yTa_{1-y}]Se_2)_1$ allow the extent of inter- diffusion to be estimated. If x is equal to y, then the ratio of the areas of the V peaks in the V-rich layer and the Ta-rich layer should equal the ratio of the Ta peak areas. With this assumption, x can be calculated from the V peak area in the V rich layer divided by the sum of the areas of the V peaks in both layers. The same calculation can be done using the Ta signal, giving an estimate of the error and the validity of the assumption. Calculating the areas of the peaks using Gaussian fits, a value for x of 0.68(5) was ob- tained. The relatively large uncertainty comes from the difficulty of choosing a value for the background signal for both of the EDX energies. The quantification is consistent with estimates from the other approaches discussed above.

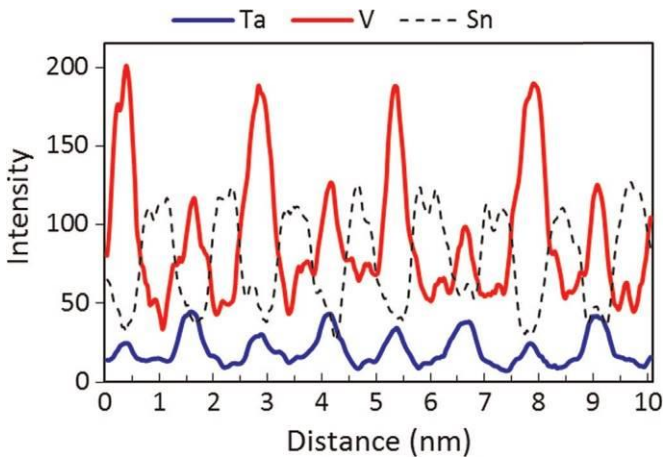

Figure XVIII. 23. EDX line scans of$[(SnSe)_{1.15}]_1([Ta_xV_{1-x}]Se_2)_1[(SnSe)_{1.15}]_1([V_yTa_{1-y}]Se_2)$ compound. The out of phase oscillation of the Ta and V layers indicates alternating V and Ta rich dichalcogenide layers

The data collected on the $[(SnSe)_{1.15}]_1([Ta_x V_{1-x}]Se_2)_1[(SnSe)_{1.15}]_1([V_yTa_{1-y}]Se_2)_1$ compound illustrates the challenges in limiting the interdiffusion of layers during the self- assembly of the MER precursor into the targeted compound. This case was chosen as a "worst case" scenario, with two metals that form a complete solid solution as dichalcogenides and only a single bilayer of SnSe separating the two of them. One would anticipate a reduction in the amount of mixing of the layers as a result of separating the constituents by thicker rock salt layers and by reducing either the time or temperature of the annealing required to self-assemble the product from the precursor. Changing the identity of the rock salt buffer layer might also reduce the amount of interdiffusion. Choosing components that are less miscible or using three different structural elements would be additional approaches to limit the amount of mixing. More knowledge of the mechanism of the transformation of the pre- cursor to the final product would be useful to identify approaches to better control the final compositions of the constituent layers.

XVIII.7. Electrical Properties

Adding complexity to the structure of the layered compounds provides an additional avenue to control properties. Figure XVIII. 24a contains electrical resistivity data for the six $(SnSe)_{1-\delta}(Ta_xV_{1-x})Se_2$ alloys prepared in this investigation. The absolute values of the room temperature resistivity is that expected for a metal, agreeing with prior reports of the analogous dichalcogenide alloys reported by DiSalvo et al. [29], but the

magnitude of the resistivity is higher due to the interfaces and SnSe bilayer which would not expected to contribute significantly to the conductivity [99]. Figure XVIII. 24b plots room temperature resistivity vs. *x* which has a linear relationship up to *x*¼0.85. The resistivity of the *x*¼1 compound is smaller than expected from the extrapolation of this trend, due to the change in coordination of the dichalcogenide from octahedral to trigonal prismatic in the pure $TaSe_2$ end member. The temperature dependent resistivity measurements show a suppression of the charge density phenomenon previously reported for $(SnSe)_{1.15}VSe_2$ at doping levels above *x* ¼ 0.12. This is in agreement with previously reported findings for the $(Ta_zV_{1-x})Se_2$ transition metal dichalgegenide alloys[29]. The general increase in the resistivity at lower temperatures apparent in the alloys reported here was also observed in the TMD alloys. Temperature dependent Hall coefficient measurements, shown in Figure XVIII. 21c, suggest complex behavior. The charge density wave in $(SnSe)_{1.15}VSe_2$ is clearly evident withan abrupt increase in the Hall coefficient for this compound. The suppression of the charge density wave with substitution of Ta for V results in essentially temperature independent Hall coefficients for all of the other compounds except the alloy with 0.49. This compound shows a change in the sign of the Hall coefficient changing at 134 K and a continuously decreasing Hall coefficient. Additional studies will be required to understand the complex behavior of this alloy Table 1.

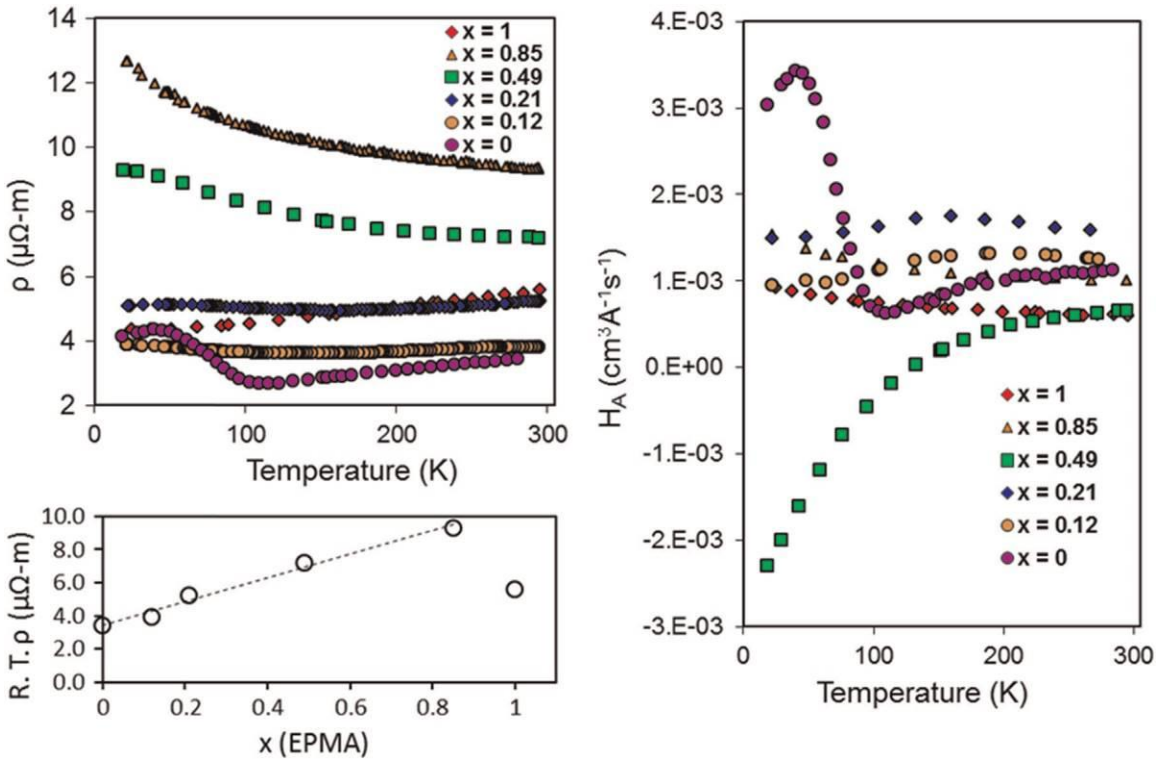

Figure XVIII.24. Electrical transport properties of the $(SnSe)_{1+\delta}(Ta_xV_{1-x})Se_2$ compounds as a function of x. (a)Temperature dependent resistivity. (b) Room temperature resistivity as a function of x. (c) Temperature dependent Hall coefficient.

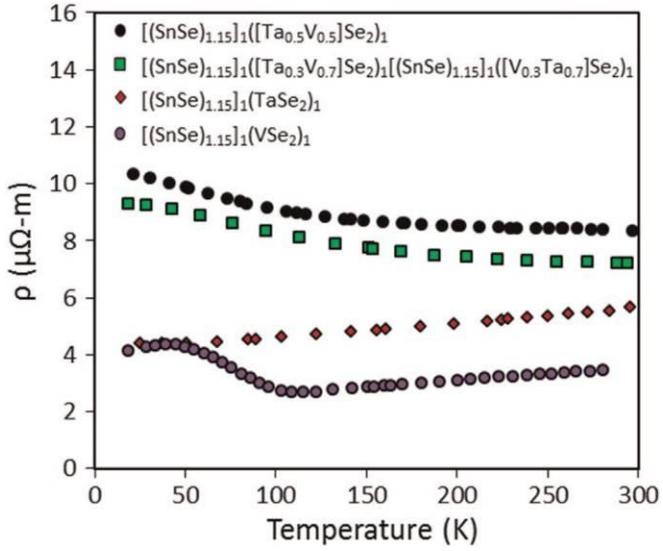

Figure XVIII.25. Temperature dependent resistivity of the $[(SnSe)_{1.15}]_1([Ta_{o.3}V_{0.7}]Se_2)_1[(SnSe)_{1.15}]_1([V_{0.3}Ta_{0.7}]Se_2)_1$ compound and the related compounds$[(SnSe)_{1.15}]_1(VSe_2)_1$,$[(SnSe)_{1.15}]_1(TaSe_2)_1$and $[(SnSe)_{1.15}]_1([Ta_{0.5}V_{0.5}]Se_2)_1$.

Figure XVIII. 25 contains the temperature dependence of the electrical resistivity of the ordered alloy with the targeted composition $[(SnSe)_{1.15}]_1(VSe_2)_1[(SnSe)_{1.15}]_1(TaSe_2)_1$ along with that measured for $[(SnSe)_{1.15}]1(VSe_2)_1$, $[(SnSe)_{1.15}]_1(TaSe_2)_1$ and $[(SnSe)_{1.15}]_1([Ta_{0.5}V_{0.5}]Se_2)_1$.The ordered alloy has a slightly higher resistivity than that of the disordered alloy and a similar temperature dependence, consistent with the extensive Interdiffusion of the dichalcogenide constituents dis- cussed earlier. The sharp change in resistivity at low temperature, attributed to a charge density wave in $SeSe_{1.15}VSe_2$ is not present in the ordered alloy. Using the compositional results of the EDX scans, both the magnitude and temperature dependence can be modeled by $[(SnSe)_{1.15}]_1([Ta_{0.7}V_{0.3}]Se_2)_1$ and $[(SnSe)_{1.15}]_1([Ta_{0.3}V_{0.7}]Se_2)_1$ layers in parallel.

XVIII. 8. Summary and Conclusions

This manuscript summarizes the current status of the MER synthetic approach. Accessing a homogeneous amorphous state via low temperature annealing of a nanolayered precursor enables metastable compounds to preferentially nucleate, controlled by the composition of the amorphous intermediate. Self-assembly of more complex designed precursors through MER provides a method to systematically design materials with designed nanoarchitecture. Once a targeted intergrowth compound is prepared, additional related compounds with different constituent layer thicknesses and/or different layering sequences can be synthesized simply by changing the layering scheme in the precursor. This permits structure–function relationships to be systematically tested, as over 20,000 compounds, including structural isomers, can be prepared with each pair of constituents when the thick- nesses of the constituents is 10 repeat units or less.

Adding additional constituents to make more complex systems is straightforward since the synthesis of simpler systems serves as a starting point for the necessary calibrations. The ability to use three or more different components greatly expands the potential complexity of the compounds prepared. For an intergrowth of three or more constituents, the number of additional compounds that can be formed by varying the layer sequence is extremely large.

There is much to understand about the structure of the defined thickness constituent layers and how the layers interact electronically with one another. These interactions will control thermal, electronic and magnetic properties. The ability to anticipate the structure of so many potential compounds provides an opportunity for theory to predict both new properties and the nanoarchitectures where optimal performance will be observed. The ability to scale this approach to prepare films over large areas on a variety of substrates will facilitate the development of devices to exploit unique or exceptional properties that are discovered.

CHAPTER XIX

NON-UNIFORM COMPOSITION PROFILES IN INORGANIC THIN FILMS FROM AQUEOUS SOLUTIONS

XIX.1. Authorship Statement

In the prior studies with ferecrystals, the atoms have arranged into a 2D crystalline structure. Here we look at amorphous thin films which have been deposited using a solution precursor. Prior microscopy guided the assumption that the films were homogeneous and smooth. The results were acquired from a TEM which is dominated by phase contrast. Making interpretations from TEM images of small composition and density changes are difficult to do. Here we were able to corroborate some results from XRR modeling using STEM which is an incoherent imaging mode and the image intensities can be directly interpreted. To acquire data from unpatterned HafSOx, special methods were designed to prepare the samples using the FIB. This work was published in ACS Applied Materials & Interfaces in 2016, volume 8, pages 667-672. Kurtis Fairley is the primary author of the manuscript.

XIX.2. Introduction

Inorganic coatings are ubiquitous in modern technology. While the majority of inorganic coatings are made via high-vacuum processes (e.g. sputtering, evaporation, atomic layer deposition), there has long been an interest in preparing dense, smooth inorganic coatings using a solution route. Perhaps the most widely studied solution route to thin films is the sol-gel method, which generally employs non-aqueous solvents.[1] This method has been used to prepare films with varying degrees of porosity and a wide range of pore sizes. Sol-gel-derived monoliths and films can generally be described as porous

rigid oxide networks in which the pores are filled with liquid or gas.[1,2] More recently, Keszler and coworkers have developed a 'Prompt Inorganic Condensation' (PIC) aqueous route to prepare ultra-smooth amorphous inorganic films with a variety of cations by controlling the condensation process.[3–10] This method allows the preparation of dense oxide films with near-atomic surface smoothness, presumably due to the surface tension of the water-based solution during spin coating.[3,10] Film thicknesses can easily be controlled via the concentration of the solution and the physical parameters used to spin the films. Thin films made via PIC have been incorporated into thin-film transistors using spin coating and low temperature annealing to obtain devices that meet or exceed the performance of conventional vapor-deposited devices.[5,11–15] PIC films prepared from solutions of hafnium oxychloride dissolved in sulfuric acid (HafSOx) with added peroxide have been shown to function as ultra-high resolution resists, patternable with electron beam or extreme ultraviolet radiation.[16,17] These resists enable patterning with minimum linewidths and edge roughnesses superior to those obtainable using organic resist materials using conventional lithography techniques. These advantages are expected to become even more important for extreme ultraviolet (EUV) lithography in next generation semiconductor manufacturing.[18]

For solution-processed films, developing a fundamental understanding of the chemistry occurring in each processing step is critical for improving film morphology and performance.[19–23] In the case of inorganic metal oxide films (using sol-gel or PIC), processing steps include: film deposition (via spin coating or dip coating), a "soft bake" to drive off excess solvent, and higher temperature annealing to facilitate counterion removal and condensation. In the sol-gel process, evaporation of organic solvent

molecules and simultaneous hydrolysis reactions at relatively low temperatures lead to a stiff inorganic network, and subsequent drying occurs via evaporation from pores.[24] By contrast, in the aqueous PIC route, evaporation of solvent (water) involves considerably more energy due to hydrogen bonding and increased solvent/solute interaction strength. The loss of water leads to condensation reactions that directly link the inorganic species as their concentration increases.[12]

Although fundamentally different chemistries occur in the various methods used to prepare inorganic films, drying and densification models generally assume the resulting films are homogeneous.[24] However, there are a few previous studies that show inhomogeneities in sol-gel- derived multilayer films observable by TEM[25] or X-ray reflectivity (XRR).[26,27] Denser surface 'crusts' in single layer films have also been observed via ellipsometry in sol-gel silica coatings[28] and by XRR in PIC aluminum oxide phosphate films.[29] The nature of these inhomogeneities, whether due to density variations or compositional inhomogeneity, has not been determined. This prompted us to undertake a systematic study of density and composition gradients in PIC-prepared films using multiple techniques.

In this paper we present XRR data on a diverse set of films made using PIC with different metal precursor solutions. The three material systems investigated were selected based on their ability to form dense, smooth, amorphous thin films. Films comprised of multiple layers yielded XRR patterns inconsistent with those expected for homogeneous films, suggesting a general phenomenon of density or composition gradients in the individual layers of PIC-derived films. Using HafSOx as a model system, single and multilayer films annealed at different temperatures were examined using XRR, cross-

sectional high-angle annular dark-field scanning transmission electron microscopy (HAADF-STEM), and medium energy ion scattering (MEIS). These techniques reveal the evolution of density and compositional inhomogeneity in the films during processing. They suggest a thin, dense surface 'crust' forms during spin coating, presumably because the reactants near the surface dehydrate faster than the interior of the film. This surface 'crust' persists during subsequent low temperature annealing, but surprisingly does not increase in thickness. Because the performance of photoresists has been shown to be very sensitive to processing conditions,[22] controlling the inhomogeneity in HafSOx films may be an important avenue towards improving performance in ultra-high resolution resist applications. More generally, the presence of a dense surface layer may affect the kinetics of film formation, as well as the final properties of metal oxide films derived using PIC. Therefore, understanding and controlling the formation of the surface layer is important for tailoring the evolution and properties of films made using this method.

XIX.3. Experimental

$InGaO_x$ and AlO_x Precursor Solution Preparation: A 2.00 M total metal concentration (6:7 In:Ga) solution of $In(NO_3)_3 \bullet xH_2O$ (Sigma Aldrich, 99.9% In) and $Ga(NO_3)_3 \bullet xH_2O$ (Alfa Aesar, 99.999% Ga) and a 1.70 M metal concentration solution of $Al(NO_3)_3 \bullet 9H_2O$ (Alfa Aesar, 98% Al) were electrochemically treated to reduce nitrate counterion concentrations according to previously reported methods.[30,31] Water content of the indium and gallium nitrate hydrate salts was determined through calcination of the salts to form the oxide and back calculation of the hydrate content (~5 and ~8 H_2O for the indium and gallium nitrate hydrate salts, respectively). Both solutions were diluted to

0.25 M (total metal concentration) with 18 MΩ nanopure water and filtered through 0.45 μm PTFE filters.

$Hf(OH)_{4-2x-2y}(O_2)_x(SO_4)_y \cdot zH_2O$ (HafSOx) Precursor Solution Preparation: A 1.00 M stock solution of $HfOCl_2 \cdot 8H_2O$ (Alfa Aesar, 98% Hf) was prepared by dissolution and dilution with 18 MΩ nanopure water. Solutions for spin coating were prepared by mixing 2.000 N H_2SO_4(aq) (VWR) and 30 wt% H_2O_2(aq) (EMD Millipore) followed by the addition of $HfOCl_2$(aq).[32] The final solution was diluted using 18 MΩ water to a concentration of 0.105 M sulfuric acid, 0.45 M hydrogen peroxide, and 0.15 M Hf. The 4-coat multilayer was synthesized from a solution without peroxide to decrease the solubility of the film, allowing for a lower annealing temperature to prevent subsequent layers from dissolving the previous.[17]

$InGaO_x$, AlO_x, and HafSOx Film Preparation: N-type, Sb-doped silicon substrates (0.008-0.02 Ω cm) received surface treatments using a MΔRCH cs-1701 plasma cleaner running on O_2 plasma at 30% O_2 in N_2 using 150 W for 60 s immediately before spin coating. Films were prepared by filtering the solutions through a 0.45 μm filter and spin-coating at 3000 rpm for 30 s. The HafSOx thin films were subjected to a one minute anneal at either 80 °C for a single layer or 180 °C for the multilayer samples. The $InGaO_x$ and AlO_x multilayer films were annealed at 450 °C for 20 min per coat followed by a final 60 min anneal at 450 °C. All films were annealed on a preheated, calibrated hot plate.

XRR patterns were obtained on a Bruker D8 discover (Cu k_α radiation). Sample alignment was checked to ensure that the incident and exit angle were equal and that the

sample was in the center of the goniometer. Alignment procedures involved iteratively performing rocking curves and z (height) scans to ensure the above criteria were met.[33] Fits of the XRR data were performed using the BEDE Refs software package, which creates a population of solutions based on an initial model and uses a genetic algorithm to minimize residuals.[34] Once the best fit was achieved, the models were perturbed to confirm that the model was not a local minimum. Films were initially fit as a single film, to determine the average density and total film thickness. For single coat films, the model was then split in half, with each half allowed to vary thickness and density independently to improve the fit. A gradient was also added to the fit, as the abruptness of the interface was unknown. Comparison of the difference between the simulated and experimental data (i.e. residuals) over a constant range allows for the quantitative comparison of the fits for a single data set. Comparison of residuals between different data sets requires a more detailed analysis, as the noise inherent in the experimental data contributes differently to the residuals for each data set. Multilayer films were modeled similarly; each coat was split into a two-layer unit and each layer was allowed to vary independently in thickness and density (all coats assumed to be identical).

For scanning transmission electron microscopy (STEM) investigations, a thin cross-section sample was prepared from a section of the film using an in-situ lift-out process on a FEI Helios 600 equipped with a Sidewinder ion column and a Quorum cryo stage.[35] Steps were taken to avoid exposure of the beam-sensitive film while imaging with the SEM and sputtering with the focused ion beam (FIB). Prior to loading the sample in the FIB-SEM, the sample was coated with a 30 nm protecting layer of evaporated carbon. A second 1.5 μ m thick protecting layer of FIB-induced carbon was

deposited over the area of interest using a 2 keV accelerating voltage (<5 nm stopping range in evaporated carbon). The lift-out and thinning process was carried out using a 500 eV accelerating voltage on the electron beam to minimize the interaction volume of the beam (<9 nm interaction depth). After completing the lift-out, the sample remained 1.5 μ m thick to assure no beam interaction had taken place. The sample was then cooled to -170 °C throughout the thinning process. The FIB accelerating voltages used were lowered as the thickness decreased, 30 keV (1.5 to 0.5 μ m), 5 keV (500 to 100 nm), and 2 keV (100 to 40 nm). During thinning the sample was monitored using low dose electron beam conditions to reduce risk of exposure and excessive heat (periodic single frames using 500 eV, 90 pA, 500 ns dwell per pixel, 50 um horizontal field width, 1024x768 pixels). The thin sample (approx. 40 nm thick), was warmed slowly overnight in the FIB-SEM vacuum chamber to ambient temperature. High-angle annular dark-field (HAADF) STEM imaging was completed on a FEI Titan at 300 keV (0.245 m camera length, 10 μ s dwell, 2048x2048 pixels, 0.6 nA current) at -175°C with a Gatan single-tilt cryo-transfer holder.

Medium energy ion scattering (MEIS), a high resolution version of Rutherford backscattering (RBS), was performed at the Rutgers MEIS facility using 130 keV protons as the incident ion.[36]

XIX.4. Result and Discussion

Four-coat samples of $InGaO_x$, AlO_x, and HafSOx were prepared using PIC as described above and examined by XRR (Fig. 1). For all samples, the XRR patterns consist of regular Kiessig fringes with a pattern of varying intensity. Figure XIX.2a

contains a schematic of two potential structures of these films, one that is homogeneous and one that contains a repeating structure of four layers (coats) where each layer has an identical non-uniform electron density gradient. Figure XIX.2b contains the simulated XRR patterns for these two films. Since XRR is very sensitive to variations in electron density, small (1%) differences in electron density can be detected. The simulated XRR pattern for a homogeneous single film shows a characteristic systematic decay in the Kiessig fringe intensity with increasing diffraction angle. The simulated XRR pattern of the film with a repeating inhomogeneous layered structure contains a characteristic modulation of the Kiessig fringe decay, with more intense diffraction maxima corresponding to the thickness of the individual layers resulting from the coherent scattering of the electron density profiles in each layer. Between these more intense maxima are n-2 smaller maxima, where n is the number of coats, resulting from incomplete destructive interference. All of the multilayer films prepared via PIC have XRR patterns (Fig. 1) characteristic of films consisting of repeating layers of non-uniform electron density profiles, inconsistent with those expected for homogeneous films. This suggests that this inhomogeneity is a general characteristic of PIC solution-deposited thin films. We elected to study the effects of this phenomenon in more detail for the HafSOx system.

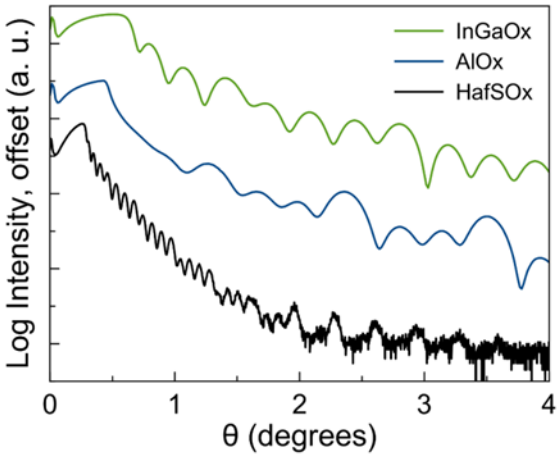

Figure XIX.1. XRR patterns of 4-coat films of $InGaO_x$, AlO_x, and HafSOx without peroxide (top to bottom, respectively). The patterns are offset for clarity.

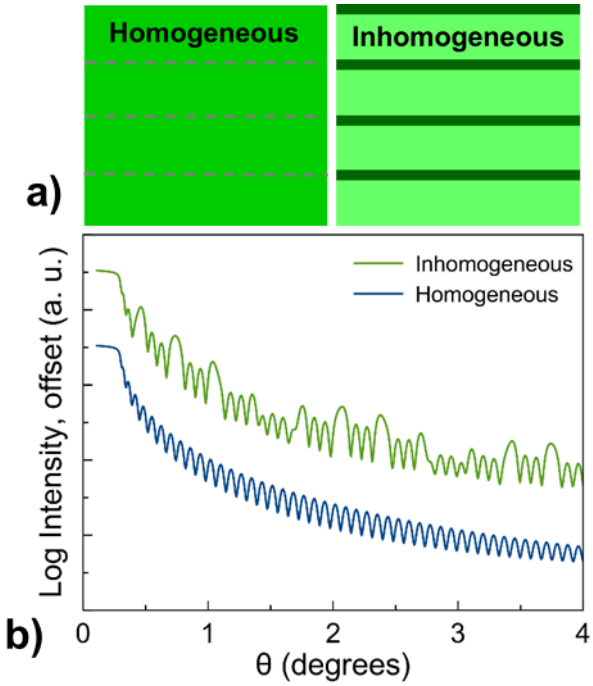

Figure XIX.2. (a) A schematic representation of two simple structures of a 4-coat stack, one in which each coat is homogeneous and one where each coat has the identical inhomogeneous electron density. (b) The simulated XRR data for the two cases shown in (a).

In Figure XIX.3., we model the XRR data of the 4-coat HafSOx film assuming that each deposited coat consists of a bilayer: a 'bulk' layer and a surface layer. The

density and thickness of the bulk and surface layers were allowed to freely vary in order to obtain the best possible fit. It was also assumed that all four coats were identical as a simple, first approximation. This model is not quantitative, as the actual structure is more complex due to the different thermal treatment for each layer. Within these constraints, the best fits were obtained with a thin surface layer (or 'crust') in each coat with a higher electron density than the underlying bulk layer. Attempts to perturb the models to give a bulk layer of higher density than the surface layer resulted in low quality fits. Although this model is an oversimplification, it indicates that the films have a higher density surface region within each deposited layer.

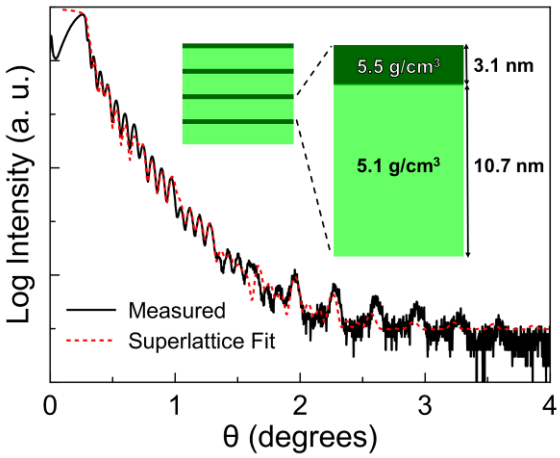

Figure XIX.3. The raw and modeled XRR data of a 4-coat multilayer of HafSOx without peroxide annealed at 180 °C for 1 minute.

A single coat film was also investigated to determine if the 'crust' is inherent in each coat or whether it is induced by the processing conditions used to make the 4-coat multilayer. To match the processing of the 4-coat multilayer, the film was annealed at 180 °C. XRR data for the single coat film was modeled both as a homogeneous single

layer film and as a bilayer separated by a gradient. For the latter model, the surface and bulk layer were allowed to freely vary in thickness and electron density (Figure XIX.4).

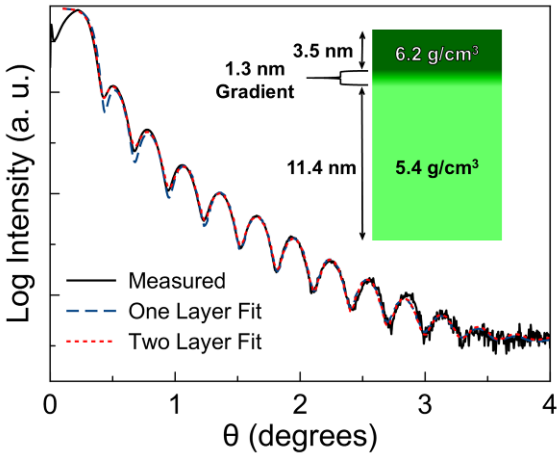

Figure XIX.4. XRR data for a single coat film without peroxide annealed at 180 °C for 1 minute. The data was modeled as a homogeneous single layer and as a bilayer with a thin, dense surface layer and a less dense bulk layer separated by a density gradient. The addition of the surface 'crust' improved the agreement between the model and the data, especially in the first three observed minima in the XRR pattern.

Between the two models, the two-layer model with a thin, denser ‘crust’ has a 20% reduction in the residuals as compared to the single layer model when both models are allowed to search for the minimum using the genetic algorithm and modeling procedure described above. Perturbing the models from the fits to find better solutions was unsuccessful, indicating the refined fits represent global minima. In XRR, the density values are derived from the critical angle, which is directly related to electron density. In order to obtain density in g cm^{-3}, the composition of the film must be assumed. Therefore, the density values of the layers should be viewed as being approximate, as they depend on the model used. The modeling suggests the best description of the film within the applied modeling constraints is that of a less electron-dense layer topped by a thin, higher electron density ‘crust’. These are probably separated by a thin gradient region between

the surface and bulk layers, which was included in the model of the single coat films. This two-layer model with a thin, dense 'crust' therefore qualitatively agrees well with the modeling of the individual coats in the 4-coat film, which was previously discussed. Not surprisingly, the simple model assuming four identical bilayers does not quantitatively match the model used for the single coat films, where the addition of a gradient layer increases the density of the surface layer. In both models, a denser surface 'crust' and less dense bulk layer are required to obtain good fits.

Since it has previously been reported that peroxide-containing HafSOx films used for lithography were homogeneous,[17] new films containing peroxide were prepared to test whether the crusts observed above also occur when peroxide is added. These peroxide-containing films were also used to examine the effect of annealing temperature. In order to replicate HafSOx films used for patterning, a single coat film containing peroxide was annealed to the soft-bake temperature of 80 °C for XRR studies. As seen in Figure XIX.5, not only does the bilayer model give a better fit to the data, but the residuals are reduced by 50% when the model is allowed to create two layers separated by a gradient. This supports the formation of a 'crust' in films containing peroxide, even at the low soft bake temperatures used for lithography.

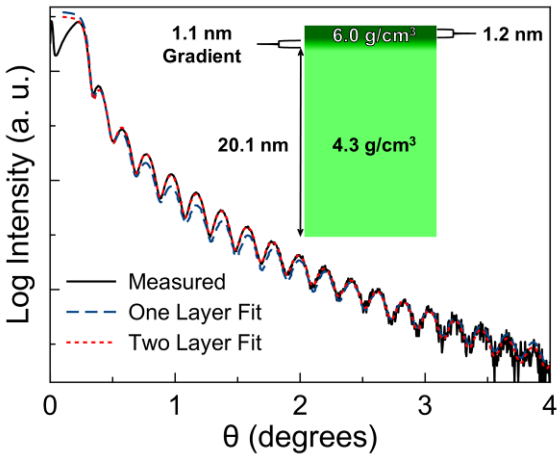

Figure XIX.5. XRR data for a single coat film containing peroxide annealed at 80 °C for 1 minute. The data was modeled as a homogeneous single layer and as a bilayer consisting of a thin, dense surface layer and a less dense bulk layer separated by a density gradient. The addition of the surface 'crust' improved the agreement between the model and the data, especially with respect to the minima in the XRR pattern between 0.8 and 2 degrees.

XRR studies reveal electron density gradients and periodicity (in multilayers), but do not reveal the source of the density gradients (i.e. whether they are due to density variations of a single chemical composition or a chemical gradient). Additional information on the HafSOx films was obtained using HAADF-STEM. Cross sections of a single coat film containing peroxide were prepared with care to maintain its condition prior to exposure, and a representative cryo–HAADF STEM image is shown in Figure XIX.6a. The image reveals a bright thin band at the top of the sample indicating an increased density of heavy atoms at the surface. Integration of the average HAADF signal intensity over the highlighted area in Figure XIX.6a provides a two-dimensional plot of the heavy atom density profile across the film (Figure XIX.6b). This indicates that, in addition to concentration of heavy atoms at the surface of the film, there is also a slight increase of heavy atom density near the bottom of the film. This data provides direct

evidence that there is electron density inhomogeneity within the films and supports the two-layer XRR model used above.

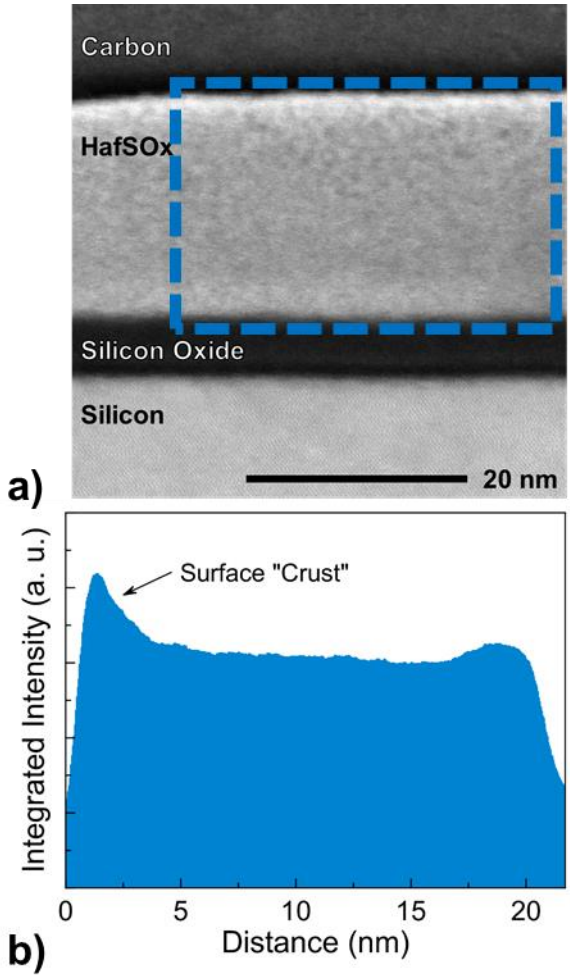

Figure XIX.6. (a) HAADF-STEM image of the cryo-FIB cross-section of a single layer HafSOx film containing peroxide annealed at 80 °C for 1 minute, and (b) the heavy atom density profile of the film obtained by integrating the intensity of the pixels in the boxed region in (a).

In order to obtain information about chemical inhomogeneity, medium energy ion scattering (MEIS) data was collected as a function of annealing temperature and time. MEIS, a low energy, high-resolution version of Rutherford backscattering (RBS), is a quantitative technique. The experiment directly measures the number of backscattered

ions of each mass. Using calibrated instrumental parameters and well-established cross sections, these can be converted into areal densities. Further, the ions lose energy as they travel through the film, with the amount of energy loss being a measure of the distance traveled. The width of a peak in an MEIS spectrum is therefore a measure of the thickness of the corresponding layer and its integrated area yields a direct quantitative areal density (atoms/cm^2). The highest energy peak results from protons backscattered from the heaviest atom (i.e. Hf) in the film. The areal density can be converted into a thickness if the bulk density is known (e.g. from XRD), and, conversely, the density can be determined if one has an alternative measure of thickness (e.g. from TEM). Because there is some uncertainty in the water content of the HafSOx films (which depends on processing conditions, film history, temperature, and gas phase partial pressures during characterization), precise comparisons between different samples is challenging. Nevertheless, the relative density changes from MEIS in the film as a function of depth are quite meaningful.

Hafnium segregation to, or densification at, the surface is readily apparent from the raw MEIS data (Figure XIX.7.). If Hf were distributed uniformly throughout the film, the highest energy peak (corresponding to Hf) would have a 'flat' plateau. However, the intensity of the Hf MEIS peaks is greatest at the highest detected energy (at the surface) and is decreased at lower energies (further below the surface). This is consistent with the increased intensity in the HAADF-STEM image at the surface due to an increased concentration of heavy atoms (i.e. Hf). It is also readily apparent in the MEIS spectra that the film thickness decreases (with corresponding increase in density) as the annealing temperature is increased (Figure XIX.7b). Qualitatively, the MEIS data is consistent with

the results obtained from XRR and STEM investigations. All three techniques indicate the presence of a Hf-enriched denser surface 'crust' in all HafSOx films reported in this work (annealed from 80 to 300 °C, with or without peroxide).

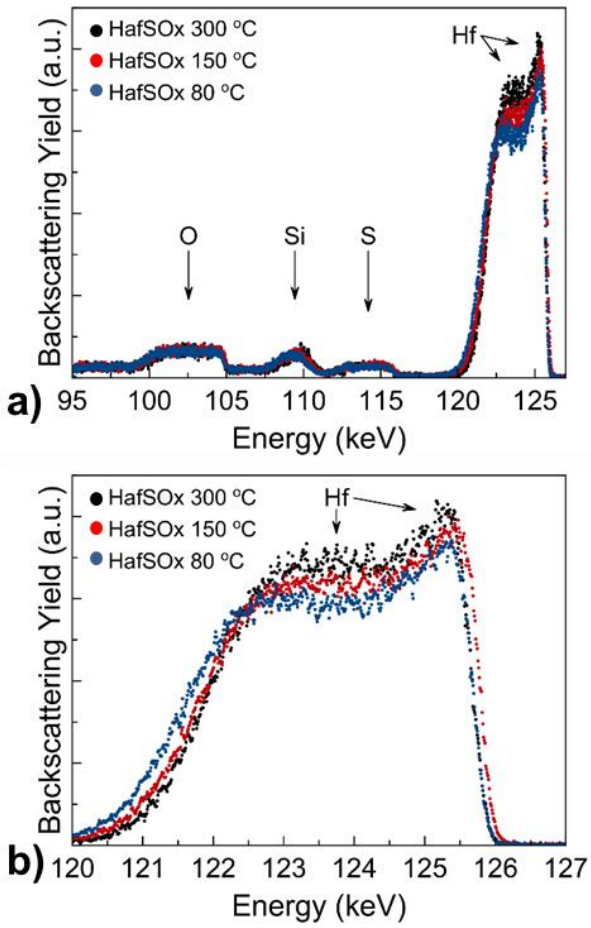

Figure XIX.7. (a) MEIS data collected on a HafSOx film containing peroxide annealed for 3 minutes at 80 °C (blue), 5 minutes at 150 °C (red) and 5 minutes at 300 °C (black). (b) An expansion of the Hf area, which visually demonstrates the total film thickness decreases with increasing annealing temperature while the average density increases. The peak at 125 keV indicates that all of the films have a surface layer with higher Hf density.

XIX.5. Summary

The data presented suggests that films prepared from aqueous solutions via the PIC process are inhomogeneous in composition and density throughout their thickness.

For HafSOx films, a dense region forms at the surface after a low temperature anneal. This may result from enhanced evaporation of solvent at the surface of the film, increasing concentration and resulting in condensation reactions between the Hf-containing moieties to yield a dense surface layer on the film. Presumably this acts as a diffusion barrier, leading to the lower density observed in the bulk of the film. We postulate that the slow rate of water diffusion through the 'crust' relative to the rate of diffusion within the 'bulk layer' of the film prevents the formation of density gradients in the bulk of the film during subsequent annealing. In the case of HafSOx, the denser surface layer may influence the patterning resolution and contrast obtainable with this system. It may be possible to control the density and/or thickness of the surface 'crust' by adjusting annealing conditions (e.g. temperature, atmosphere, ramp rate) and to correlate changes with patterning metrics. We also show that 'crust' formation is quite general for PIC processed films and that the density inhomogeneities in single coats result in periodic density gradients in multilayer films, which may affect film properties such as electrical conductivity or breakdown voltage. In the case of multimetal-component oxides deposited from solutions of mixed metal cations, the chemical composition profiles are expected to be more complicated and dependent on a number of factors (e.g. metal solubility and diffusion rate differences). Determining chemical composition gradients at the nanoscale would enable the development of a mechanistic picture of the chemistry occurring during film formation and provide avenues to design chemical inhomogeneities to obtain enhanced properties. The determination of chemical composition gradients at the nanoscale, however, remains a major analytical challenge. Ultimately, understanding

and controlling film inhomogeneities will provide an additional tool to modify the physical and chemical properties of films prepared using the PIC approach.

CHAPTER XX

LOW VOLTAGE PATTERING OF HafSOx: EFFECTS OF VALTAGE ON RESOLUTION, CONTRAST, AND SENSITIVITY

XX.1. Authorship Statement

In the previous chapter, low voltages were used to reduce the interaction volume of the electron beam to less than 7 nm to avoid exposing the cross-section of the lamella. Here we use the same strategy to expose a thin film by concentrating the deposited dose at the surface of the film where the beam resist resides. This strategy enabled a large decrease in incident dose and therefore pattern much more quickly. I provided the general concept of this project and provided the theoretical arguments for the application of low voltage patterning. I performed STEM measurements of the patterned lines which proved that ultrathin features were patterned. Kurtis Fairley is the primary author of this paper. This work is not yet published.

XX.2. Introduction

Improvements in scanning electron microscope (SEM) technology have led to overall performance enhancements across a broad range of common accelerating voltages, including those less than 5 keV.[1] The use of magnetic immersion lenses and stage deceleration have significantly reduced the impacts of aberrations associated with low energy (1-5 keV) beams.[2] This has been vital for studying biological samples in which beam damage is a serious concern. Modern cold-field emission sources, monochromators, and better lenses have improved the low-energy beam performance even further.[1] These performance enhancements have led to an explosion of SEM use in the biological world, in which beam damage at high voltages has traditionally been a

limiting factor.[3] More recently, these advances have been applied to electron beam lithography.[3,4,5]

Electron beam lithography (EBL) performed using an SEM operating at high accelerating voltages, 30 keV and above, has been used extensively for the patterning of densely packed features with critical dimensions less than 10 nm.[6] High accelerating voltages reduce the spot size of the beam and penetrate deep into thick, dense films to fully expose them.[7] Significant work has also been done to optimize the chemistry of the EBL resists for enhanced sensitivity at these voltages.[6] However, high accelerating voltages create several problems for EBL that are exacerbated with the use of thin (tens of nm) films. A significant portion of the energy of the beam passes through the resist and is buried deep in the substrate instead of reacting with the resist.[8] These electrons heat and damage the sample directly beneath the beam and diminish lateral resolution due to long-range proximity effects from secondary electrons.[9] It has been shown in several high resolution resists that decreasing the accelerating voltage leads to an increase in the sensitivity of the target resist.[8,10,11] Due to the enhanced sensitivity, the time required to pattern the resist is dramatically decreased, enabling patterning of larger, more intricate structures while avoiding vacuum damage through drying or condensation effects in sensitive films. If the beam energy is reduced too much, however, the beam interaction volume may become smaller than the film thickness. This is a problem for full exposure, but has been shown to lead to interesting 3-D stepped structures in positive tone resists.[12] For thin inorganic resists, this suggests that reducing the accelerating voltage to an optimal value may lead to a substantial decrease in patterning time with full resist exposure and minimal impact on lateral resolution.

In this work, we investigate the patterning sensitivity and contrast of HafSOx,[13–16] a negative-tone inorganic electron beam resist, at primary beam energies of 2-30 keV, and the lateral resolution of the resist by patterning at 10 keV. HafSOx was chosen as a model inorganic resist because films of this resist are thin and dense. Consistent with reports for other thin inorganic resists, the sensitivity of HafSOx increased dramatically as the beam energy decreased. We were able to use a 10 keV beam energy to produce sub 10 nm lines without any loss in line edge roughness using only half the dose required at 30 keV. Monte Carlo simulations predict sensitivity enhancements with decreased beam energy in good agreement with our experimental observations. The simulations also suggest that patterning at beam energies less than 10 keV may still enable patterning of sub-20 nm feature sizes or better as film thickness decreases. This work has implications for improving the throughput of EBL with existing thin inorganic resists while maintaining high lateral resolution.

XX.3. Experimental

A 1 M stock solution of $HfOCl_2 \bullet 8H_2O$ (Alfa Aesar) was prepared by dissolution and dilution with 18 MΩ nanopure water. Solutions for spin coating were prepared by mixing 2 N H_2SO_4(aq) (VWR) and 30 wt% H_2O_2(aq) (EMD Millipore) followed by the addition of $HfOCl_2$(aq). The final solution was diluted using 18 MΩ water to a concentration of 0.105 M sulfuric acid, 0.45 M hydrogen peroxide, and 0.15 M hafnium. N-type, Sb-doped silicon substrates (0.008-0.02 Ω-cm) received surface treatments using a MΔRCH cs-1701 plasma cleaner running on O_2 plasma at 30% O_2 in N_2 using 150 W for 60 s immediately before spin coating. To obtain more reliable ellipsometry measurements, 100 nm thermally grown oxide silicon substrates were used and treated

with SC1 (5 parts 18 MΩ water, 1 part 29% ammonium hydroxide, 1 part 30% hydrogen peroxide) at 80 °C for 30 minutes before plasma cleaning. Films were prepared by filtering the solutions through a 0.45 μm filter and then spin-coating at 3000 rpm for 30 s. The HafSOx thin films were then subjected to a one minute anneal at 80 °C as a soft bake to densify the films.

HafSOx films prepared as described above were patterned in an FEI Helios 600i DualBeam either manually or by using FEI's automation program, iFast. Arrays of 200x200 μm^2 boxes spaced 400 μm apart were patterned with accelerating voltages of 2, 5, 10, 20, or 30 kV at a pitch of 60 nm and a dwell time of 100 ns. The number of beam passes across a pattern controlled the dose,

$$Dose = \frac{N \times I \times t}{p_x^{\,2}} \qquad (1)$$

where N is the number of passes, I is the beam current in μA, t is the dwell time in s, and p_x is the pitch in the X and Y directions, measured in cm. The beam current was measured prior to each experiment using a Faraday cup standard. Films were developed at room temperature in 25 wt% tetramethylammonium hydroxide (TMAH, Alfa Aesar) for 1 min and thoroughly rinsed with 18 MΩ water, followed by a post development hard bake at 300 °C for 3 min.

Data was taken on a J.C. Woollam VASE Ellipsometer with focusing probes installed to reduce the ellipsometric spot size to 60 μm. Each patterned box was measured at three angles, 55°, 60°, and 65°, with 8 second acquisitions at each angle. The resist was modeled as a Cauchy film on 100 nm SiO_2. All measurements had an MSE value below 10. The squares patterned with doses below the turn-on dose allow the contrast and sensitivity to be calculated by the number of partially patterned squares. A trend line is

drawn between the points that lie between a normalized thickness of 0.2 and 0.8, with 1 being completely patterned, striking the x-axis at d_0 and providing a y value of 1 at d_{100}. The slope of the trend line is used to calculate the contrast of the resists and d_{100} is defined as the sensitivity.

HafSOx films were prepared as described above and patterned using an FEI Helios 600i DualBeam. A 10 kV beam with a current of 7.7 pA was used to pattern high resolution line arrays. An immersion lens was used to decrease the spot size of the probe, lensing through the sample for better resolution. To focus the beam without exposing the resist or moving the stage from the target location, a 2 μm tall platinum-carbon pillar 50 nm in diameter was created by using the electron beam to decompose a platinum-containing gas precursor, $MeCpPtMe_3$. Individual platinum grains were used to confirm the final focus and stigmation without exposing any of the surrounding material. The horizontal field width was set to 61.4 μm, and the pattern was then generated from a bitmap using iFast. The pitch, set by the bitmap pixel size, was set at 10 nm, but only a single pass per line was used to allow for the highest resolution.

Following exposure, the resolution arrays described above were developed using the same procedure as described for the dose arrays and subsequently imaged with the SEM. High magnification, high resolution images were obtained (1.484 pixels per nm) and analyzed using the freely available ImageJ software. The images were converted to binary format, and the average line widths for six of the lines in the array were obtained over a 700 nm length of each line. The line width roughness was calculated as three sigma of the standard deviation in the line width measurements for each line. The reported average line width and line width roughness were calculated by averaging the

values obtained for each line. The line edge roughness was calculated in a similar fashion. The top and bottom edge positions were determined for each line, then the top and bottom line edge roughness was calculated as three times the standard deviation in the line edge position. These values were then averaged for each line. The line edge roughness we report was obtained by averaging the line edge roughnesses measured for all six distinct lines.

We calculated the point spread functions ("PSFs") of 2, 5, 6, 10, 20, and 30 keV primary beam energies in 22 nm thick soft-baked HafSOx films using the Monte Carlo software CASINO v3.2.0.4.[17] The PSFs represent the implanted energy distribution in the resist as a function of radial distance from the beam irradiation spot.[8] We initially assumed an unexposed film density of 4.3 g/cm^3, with a 100 nm SiO_2 (1.74 g/cm^3) layer and an infinitely thick Si substrate beneath the resist. We also tested a range of film thicknesses (20 – 24 nm) and densities (4.0 – 4.6 g/cm^3) at each energy in order to understand how the simulation results might change with potential experimental variations. All simulations were conducted using a 1 nm beam spot size and 100,000 electrons. The beam PSFs were calculated from the implanted energy distributions summed radially over the depth of the resist layer. The default electron-sample models in the software were used.

Cross-sectional images of developed HafSOx lines were acquired using high-angle annular dark field imaging in a scanning transmission electron microscope (HAADF STEM, FEI Titan, 300 kV incident beam). The specimens for cross-sectional imaging were prepared using Ga^+ focused ion beam (FIB) milling and following a procedure similar to the Wedge-prep method described by Schaffer et al.[18]

XX.4. Result and Discussion

Arrays of 200 μm squares were patterned in HafSOx using doses from 1 μC/cm^2 to 1 mC/cm^2 and accelerating voltages from 2 keV to 30 keV to determine the turn-on dose in the resist at each voltage. Planar SEM images (see Figure XX. 1 for an example) were used to identify the approximate turn-on dose for the resist by observing when patterned material no longer remained after development. The images showed no defects, such as voids or ridges, in the exposed films. Such defects would lead to errors in the ellipsometry measurements used to quantify the thickness of the films to determine sensitivity and contrast. Several arrays were also created using an immersion lens to confirm there was no impact on the sensitivity when high-resolution patterns were created. The patterned square edge length was reduced to 80 μm for these arrays due to a reduction in the maximum horizontal field width allowed with the immersion lens active. The immersion lens did not impact the sensitivity or contrast when patterning the resist.

FIGURE XX.1. SEM image of an example dose array

The sensitivity and contrast are both excellent measures of the quality of a resist. Films with high sensitivity require less energy and time to pattern, allowing for patterning using instruments that are more economically accessible. Films with high contrast enable close packing of patterned features and sharp sidewalls due to the high separation between patterned and unpatterned material. The completely patterned squares are 9 nm thick and give a baseline for sensitivity calculations. The sensitivity of the film linearly increases (decrease of the d_{100} value) with decreasing accelerating voltage, as shown in Figure XX. 2. At 2 keV the time required for full resist exposure is almost an order of magnitude less than at 30 keV, the beam energy at which high resolution lines in HafSOx were previously reported.[13]

At all accelerating voltages, the contrast values are greater than two. The contrast initially decreases as the accelerating voltage used to pattern the material decreases at 10 keV, but the contrast then recovers at 2 keV. This could be due to the tradeoff from losing the narrow "neck" of the interaction volume at high voltages and reducing the entire "tear drop" that interacts with the film. In the middle where the contrast decreases, the interaction volume is in a regime in the middle and gains no benefit from the narrow interaction volume "neck" or "tear drop" interaction with the film (Figure XX. 2)

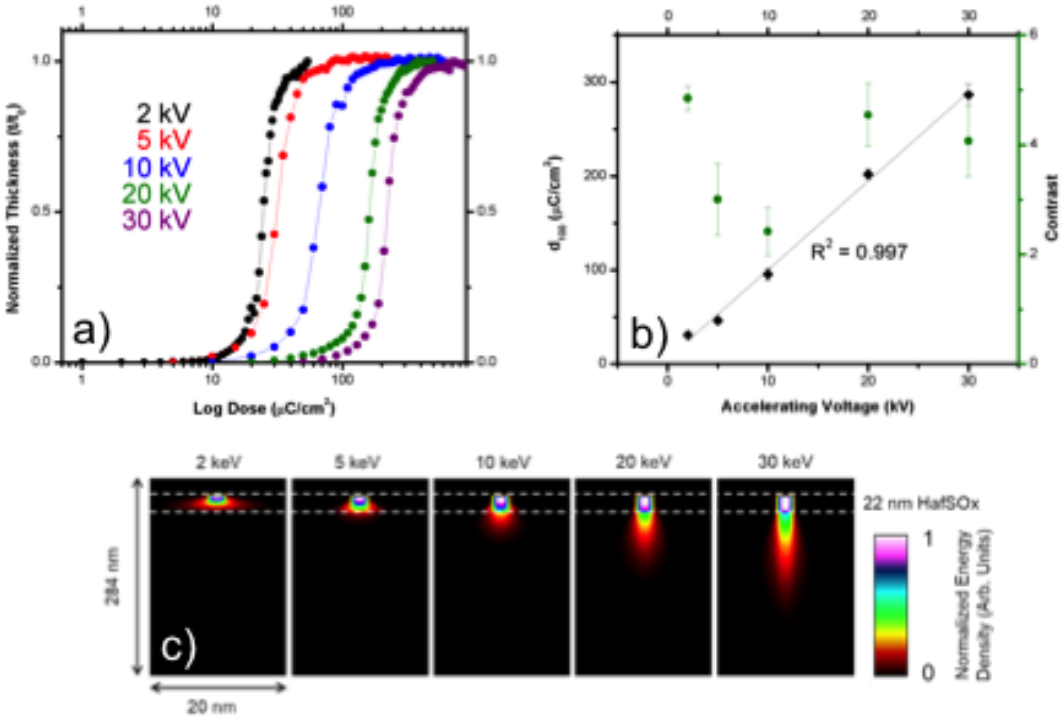

FIGURE XX.2. a) Plotted contrast curves for varying accelerating voltages and b) the dependence of contrast and d_{100} on accelerating voltage. c) Modeled interaction volumes for the corresponding voltages showing the retraction of the "tear drop" to the film.

While high sensitivity and high contrast are important requirements for an E-beam resist, the ability to pattern at high resolution is essential in order to outperform the myriad of well-established low resolution organic resists. To understand the interaction volume of the beam used to pattern the contrast curves and gain insight into the resolution, Monte Carlo simulations were used to model secondary electrons within the film and substrate. As expected from previous results with other resists,[8,11] decreasing the accelerating voltage leads to the containment of more electrons within the resist. To further grasp how the beam energy at different voltages is implanted radially within the film, PSF analysis was used. The normalized PSFs of the beam for 2, 5, 10, 20, and 30 keV primary beam energies are shown in Figure XX. 3. The PSF for each beam was

normalized to the total energy deposited in the resist by that beam. Because the sensitivity of the resist changes greatly with primary beam energy, this allows a more accurate comparison of how the energy is distributed radially throughout the resist. Integrating the area under each unnormalized PSF provides an estimate for the total amount of energy deposited in the resist. In Figure XX. 4, we show the sensitivity enhancement relative to 30 keV calculated from our simulations and from our experimental data from the turn-on dose curves. The trend in our simulation results is similar to the trend in our experimental observations: the resist sensitivity increases at an increasing rate as the beam energy decreases. For beam energies 10 keV and greater, the simulated and experimental data match closely where there is little beam spread. At lower energies, the theoretical and experimental data start to differ. This may be due to the effective dose applied during the simulation. For 100,000 electrons into a 1 nm spot, the applied dose is 1.02×10^{6} $\mu C \cdot cm^{-2}$, about three orders of magnitude larger than the range of d_{100} values for energies investigated experimentally. The large number of electrons is necessary for accurate Monte Carlo performance, but leads to excessively large applied doses, especially for the lower accelerating voltages. Furthermore, the simulations do not take into account the cross-linking, oxygen evolution, and other changes that occur within the resist layer during lithographic exposure, but rather assume the film density and thickness do not change.[19] Thus, while the simulation sensitivity enhancement shows qualitatively the same trend as observed in the experimental data, it should not be surprising that the exact values differ.

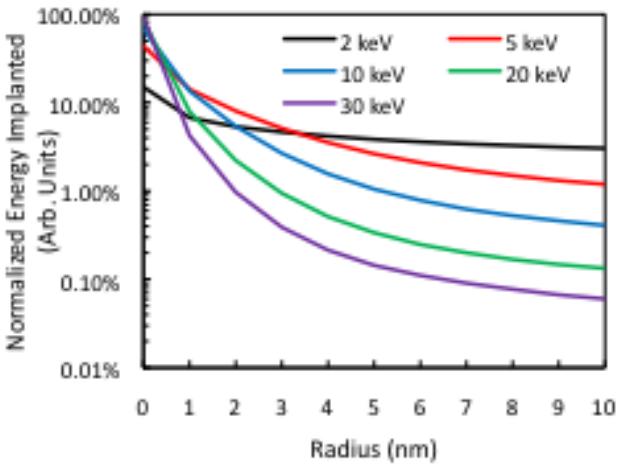

FIGURE XX.3. Simulated normalized PSFs for 2, 5, 6, 10, 20, and 30 keV primary beam energies in a 22 nm thick HafSOx resist.

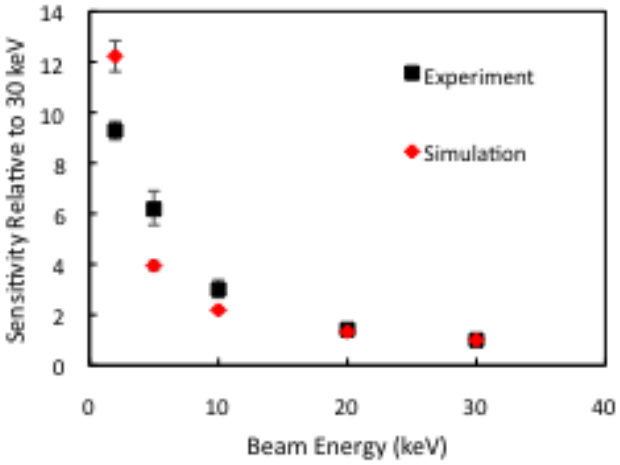

FIGURE XX.4. Simulated and experimental sensitivity enhancement as a function of beam energy, relative to 30 keV. For the experimental data points, the error bars reflect the uncertainty in the calculation of d_{100}. For the simulated data points, the error bars reflect the sensitivity of the model to small changes in film thickness and composition relative to the assumed values.

The normalized PSFs in Figure XX. 3 also give some indication of the possible lateral resolution that could be achieved as the beam energy is decreased. As expected, the energy deposited by a 30 keV beam is deposited within a very narrow region through the resist. As the beam energy is decreased, the width of the region in which energy is

deposited increases. We expect the area in which the majority of the beam's energy is deposited will correlate with the area in which the film is actually exposed. The width of the exposed region does not scale linearly with beam energy, but increases rapidly as the beam energy is decreased below 10 keV. Our average line width measurements (vide infra) indicate that at 10 keV the exposure radius of the beam is approximately 4 nm. From our simulations, this radius corresponds to approximately 99% of the total energy deposited in the resist by the 10 keV beam. Assuming that 99% of the deposited energy corresponds to the threshold between patterned and unpatterned resist at other beam energies as well, the simulation results imply that even a 5 keV primary beam may enable patterning of sub-20 nm features with a 4-6x reduction in patterning time relative to patterning at 30 keV.

To test the resolution of HafSOx at low accelerating voltages, line arrays were created with varying pitch. When patterning with small horizontal field widths, three artifacts produced by the limitations of the instrumentation arose that impeded high-resolution measurements. See supplementary material at [URL will be inserted by AIP Publishing] for examples and explanations of these artifacts. As a result, we could only test the lateral resolution using a 10 keV or greater beam energy. At 10 keV, high resolution lines were produced with line widths of 8.9(3) nm spaced 35 nm apart, as shown in Figure XX. 5. The dose used to create these lines was 488 $\mu C/cm^2$, resulting in a nearly a twofold reduction in the time previously required at 30 keV to create the same patterns. As measured from a plan view image, the line width roughness of the 8.9(3) nm lines was 2.5(3) nm and the line edge roughness was 2.6(3) nm, very similar to previously reported 30 keV patterning of HafSOx.[13] These results show that high-

resolution lines can be patterned using accelerating voltages less than 30 keV in less time while maintaining the same low roughness and critical dimensions.

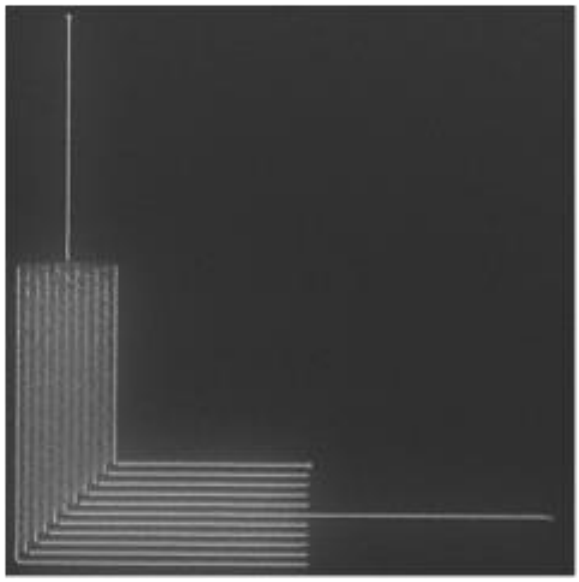

FIGURE XX.5. SEM images of patterned 9 nm lines at 10 keV.

After obtaining plan view images of the lines to obtain the line edge and width roughness, cross-sectional STEM gave further supporting measurements of the line height and width. HAADF-STEM images (Figure XX. 6) of a line array patterned at 10 keV show the height of each HfO_2 line, 9 nm, is identical to the film thicknesses determined for the dose arrays after exposure and development using ellipsometry. The images also show a 8.5 nm full width at half maximum (FWHM) for the lines. There is a 1-2 nm residual film between each of the lines that remains after processing, as seen in prior HafSOx studies.[13] The lines are spaced 30 nm apart from each other in an array of 11 lines, giving tight packing along with the high resolution. However, the moderate contrast leads to rounded edges instead of an ideal top hat shape. The contrast curves indicate that 10 keV accelerating voltage should produce the lowest resolution lines with

the highest roughness. This is most likely due to the fact that it does not have as small a spot size nor as small an interaction volume seen at higher and lower voltages, respectively.

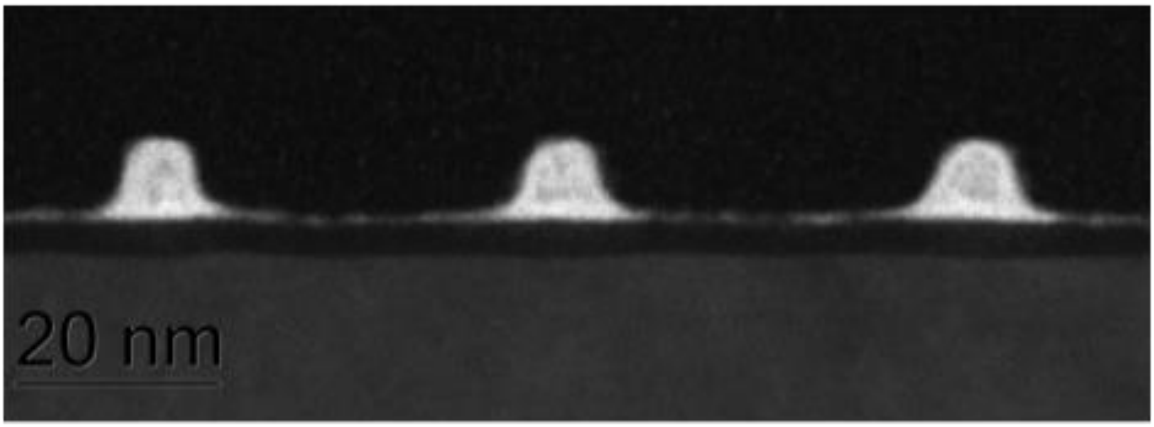

FIGURE XX.6. STEM cross-section images of high resolutions lines patterned using 10 keV primary beam energy.

For a 22 nm thick HafSOx resist, 10 keV beam energy appears to provide an acceptable compromise between high-resolution patterning and increased resist sensitivity. At very low beam energies, such as 2 keV, the lateral resolution is expected to be much worse than at 30 keV because more lateral scattering of the primary beam occurs in the resist. However, a 1-2 keV beam may still enable high resolution patterning in thinner resists (thicknesses around 5 nm from our simulations), where only the "neck" of the interaction volume is in the resist.

Since inorganic resists, such as HafSOx, can be spin coated to varying thicknesses, we also simulated the effects of resist thickness using a 10 keV incident beam (Figure XX. 7). Decreasing the resist thickness provides an effect similar to increasing the primary beam energy. More of the energy is deposited immediately in the vicinity of the beam irradiation spot for a thinner resist than for a thicker resist. However,

decreasing the resist thickness also leads to less total energy deposited in the resist and a corresponding decrease in the resist sensitivity. These results imply that as inorganic resists are made thinner, the ability to go to lower accelerating voltages and faster processing becomes more feasible without any loss in resolution.

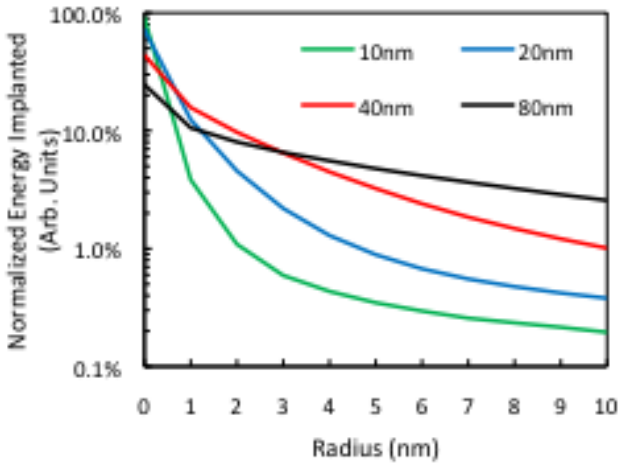

FIGURE XX.7. Percentage of total energy deposited in the resist as a function of radius from the beam irradiation spot for HafSOx films of different thicknesses.

Our simulations indicate that the resist sensitivity increases strongly as the primary beam energy is reduced, in good agreement with our experimental observations. Additionally, our simulations indicate for a 22 nm thick HafSOx resist, 10 keV appears to provide a compromise between good lateral resolution (sub-10 nm) and high throughput (2-3x relative to 30 keV patterning).

XX.5. Conclusion

With modern advances in microscopy, accelerating voltages less than 30 keV can still enable high resolution and low roughness in the patterned thin inorganic E-beam resists. Our results show that reducing the accelerating voltage of the primary beam to 10 keV or less dramatically increases the sensitivity of a HafSOx resist and still enables high-resolution patterning. Sub 10 nm lines were produced using 10 keV in half the time

required at 30 keV. Further reductions in process time may be achievable once hardware challenges are overcome. These results suggest EBL should no longer try to maximize the voltage of the incoming electrons, but instead match the energy required to penetrate only as deep as the thickness of the resist.

CHAPTER XXI

HAADF STEM SIGNAL INTENSITY ANALYSIS METHOD FOR EXTRACTING STRUCTURAL INFORMATION FROM COMPLEX THIN FILMS

XXI.1. Authorship Statement

The following manuscript was submitted to a special issue of Science and Technology in 2016. I performed the STEM measurements and worked with Gavin Mitchison, the primary author, to develop the data processing methods described.

XXI.2. Introduction

Thin films are used extensively in devices as key components in modern technologies, including thin-film transistors [1], photovoltaic films [2], and gas sensing devices [3]. Crystalline and amorphous inorganic thin films are traditionally produced using various vapor-deposition methods [4–6]. Solution-processing is more cost-effective and environmentally friendly than competing vacuum-deposition techniques [7]. Therefore, solution-cast amorphous inorganic oxide films are currently being investigated as thin, tunable dielectric layers and are also of interest for electron beam lithography resists and optoelectronic devices [8–14]. Deposition techniques that use water-based solutions in particular reduce environmental impacts and energy usage, and the resulting films require only minimal thermal processing [8,14–16].

As thin film thicknesses are reduced towards the 2-D limit and device complexity increases [17,18], more sophisticated techniques and analysis methods are needed to characterize the structures created. For traditionally prepared vapor-deposited films, the interface structure that dominates ultrathin films is sensitive to deposition conditions and

can be drastically different relative to the "bulk" structure of the film [19–21]. Similarly, solution-cast amorphous films are conventionally assumed to be compositionally homogeneous even when “thick” films are produced by layering multiple coats upon one another [22–24]. However, Fairley and co-workers recently reported that a variety of solution-cast stacked inorganic films all formed interfacial layers between each coat [25]. Fairley et. al also showed that single-coat films are not homogeneous, and generally have a denser surface layer relative to the bulk film. Understanding the origin of the variations in film density and structure at interfaces and rationally tuning processing conditions to optimize performance for both crystalline and non-crystalline films requires accurate film density and local composition information.

High angle annular dark field scanning transmission electron microscopy (HAADF STEM) is a useful technique for investigating structural information at the atomic scale [26–28]. Recent advancements in hardware and simulations have enabled extraction of quantitative atomic-level structural details in crystalline and nanocrystalline specimens [29–32]. Statistical analysis methods for analyzing the intensity distributions in ADF STEM images have been applied during quantitative analysis of atomic columns in nanocrystalline particles [28,30–33]. These approaches have also been used to extract interface structures from epitaxially grown crystalline intergrowths [21,34]. To our knowledge, these approaches have not been applied to estimate and understand the inhomogeneity of amorphous thin films.

In this paper, we develop an analysis method to identify statistically significant intensity variations in STEM signals by taking advantage of the asymmetry present in most thin films inherent in their preparation. This analysis method uses the difference in

signal variation parallel and perpendicular to the substrate to determine the extent of inhomogeneity. We first illustrate the application of our proposed method using HAADF STEM images obtained from a vapor-deposited multicomponent semi-crystalline heterostructure containing many different zone axis orientations such that it lacks the long-range order associated with a crystal. The obvious chemical asymmetry and changes in the signal distribution readily reveal the presence of multiple constituent structures in the heterostructure. Averaging signals over a large region results in reasonable estimations for the locations of planes of atoms, which provide a valuable initial model for a Rietveld refinement of X-ray diffraction data. Second, we apply this method to an amorphous multiple-coat solution-cast film where the magnitude of the intensity differences reflects the extent of inhomogeneity. The result HAADF STEM intensity profiles may provide a useful starting point for modeling X-ray reflectivity data of these solution-cast amorphous oxide films. Our analysis of the amorphous film suggests that the interfacial regions between layers may arise due to chemical interactions between the layers, such as migration of heavier atoms from the surrounding film, during the spin-casting or film formation process.

XXI.3. Experimental

The films in this study were prepared using previously reported techniques. The synthesis of the three-component $[(SnSe)_{1.16}]_2(MoSe_2)_{1.06}[(SnSe)_{1.16}]_2(NbSe_2)_1$ heterostructure and its structural characterization via X-ray diffraction was described previously [35]. The amorphous lanthanum zirconium oxide (LZO) film was prepared via spin-coating using an aqueous solution process similar to that reported previously for aluminum phosphate oxide [36]

and lanthanum aluminum oxide [16]. A Si substrate was prepared with a 5 min sonication in Decon Labs Contrad-70 solution followed by rinsing with 18.2-MΩ H2O, spin-drying, and a 1 min oxygen plasma etch using a Plasma Etch, Inc. PE-50 Benchtop Plasma Cleaner set to maximum power. The spin-cast (3000 rpm, 30 s) solution was a filtered (0.2 μm PTFE syringe filter) 0.25 M solution (total metal concentration, 1:1 La:Zr) comprising $La(NO_3)_3•6H_2O$ (Alfa Aeser, 99.9%) and $ZrO(NO_3)_2•nH_2O$ (Sigma-Aldrich, 99%) in 18.2 MΩ H_2O. Each coat of the four-coat film was annealed in air on a calibrated hot plate at 450 °C (starting at 125 °C with a 25 °C/min ramp) for 10 min, followed by a final 1 h anneal of the final 4-coat sample at 450 °C.

Specimens for HAADF STEM imaging were prepared from representative films using an FEI Helios 600 DualBeam instrument and following a procedure similar to the Wedge-Prep method described by Schaffer and co-workers [37]. HAADF STEM images for the heterostructure sample were collected at Pacific Northwest National Laboratory using a JEOL ARM 200CF S/TEM operating at 200 keV. HAADF STEM images for the LZO sample were obtained using an FEI Titan 300 keV TEM operating in STEM mode at the Center for Advanced Materials Characterization in Oregon (CAMCOR). Image analysis was conducted using scripts written in IPython and incorporating functions from the Hyperspy hyperspectral data analysis library [38,39]. When preparing histograms of signal intensity deviation, we employed the suggestion of Scott [40] for determining the optimal bin width for data-based histograms.

Additional characterization of the *00l* structure of the heterostructure sample was performed using a Rigaku Smartlab diffractometer with Cu Kα radiation. WinPLOTR

was used to perform the Rietveld refinement [41]. The refinement was conducted using space group *P -3 m 1* with the mirror plane on Mo.

XXI.4. Results and Discussion

We first illustrate our analysis method using a three-component nanolaminate heterostructure. Visual inspection of a representative HAADF STEM image of the $[(SnSe)_{1.16}]_2(MoSe_2)_{1.06}[(SnSe)_{1.16}]_2(NbSe_2)_1$ heterostructure, shown in Figure XXI. 34, is sufficient to determine both inhomogeneity perpendicular to the substrate and relative homogeneity of the film parallel to the substrate. The *c*-axis of the sample, which is perpendicular to the substrate, consists of two rocksalt-like bilayers of SnSe alternatingly interleaved with monolayers of $MoSe_2$ and $NbSe_2$ [35]. The self-assembly of the film from an amorphous precursor results in turbostratic disordering and small grain sizes within each layer, which are visible throughout Figure XXI. 34 as different zone axis alignments in different regions of the image. These features are characteristic of heterostructures prepared using this self-assembly technique, which has lead them to be called ferecrystals, from the Latin *fere*, meaning “almost” [42].

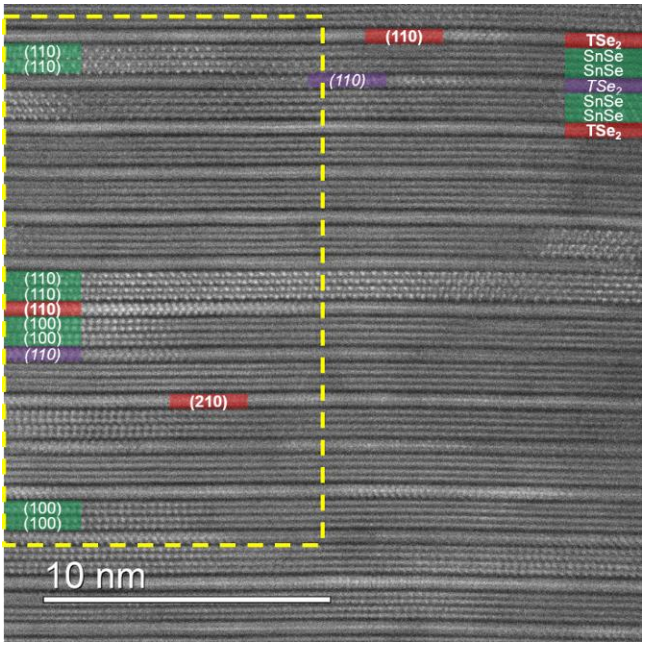

Figure XXI. 34. Representative HAADF STEM image from the $[(SnSe)_{1.16}]_2(MoSe_2)_{1.06}[(SnSe)_{1.16}]_2(NbSe_2)_1$ heterostructure. The $MoSe_2$ and $NbSe_2$ monolayers cannot be visually distinguished from one another, and are labeled as TSe_2 using red and purple boxes. The SnSe layers are indicated in green. Zone axes in selected regions are labeled for each constituent. The yellow box marks the region selected for analysis.

The first step in the analysis method is to determine the noise level in the HAADF signal by evaluating the deviation in mean HAADF intensity for each column of pixels in the image, which we refer to as the horizontal intensity deviation profile. The raw horizontal intensity deviation profile for the region outlined in yellow in Figure XXI. 1 is shown in Figure XXI. 35a. The variations we see in the raw intensity profile result from a variety of factors, including small thickness changes in the sample due to curtaining or other sample preparation artifacts [43], zone axis alignment and channeling effects [33], or potential chemical variations. The larger integrated intensity on the left side of the box results from more of the grains in the individual layers being aligned along zone axes. By applying a broad median filter (the solid line in Figure XXI. 2a) and subtracting this background signal from the data, we obtained the high frequency variation of the

integrated intensity (Figure XXI. 2b). The distribution of background corrected horizontal HAADF intensity deviations is shown in Figure XXI. 35c. The distribution is centered at approximately zero and appears symmetric. Figure XXI. 35d compares the effect of increased sampling size on the standard deviation of the horizontal intensity distribution relative to a normal distribution. The standard deviation of the intensity distribution decreases similarly as $1/\sqrt{n}$ as the box width (sampling size), *n*, is increased, suggesting that the high frequency variation in the horizontal intensity profile is due to noise. The difference between the observed and simulated curves may be due to the size of the smoother relative to real features, such as atomic columns and grains, which affect contrast in the image.

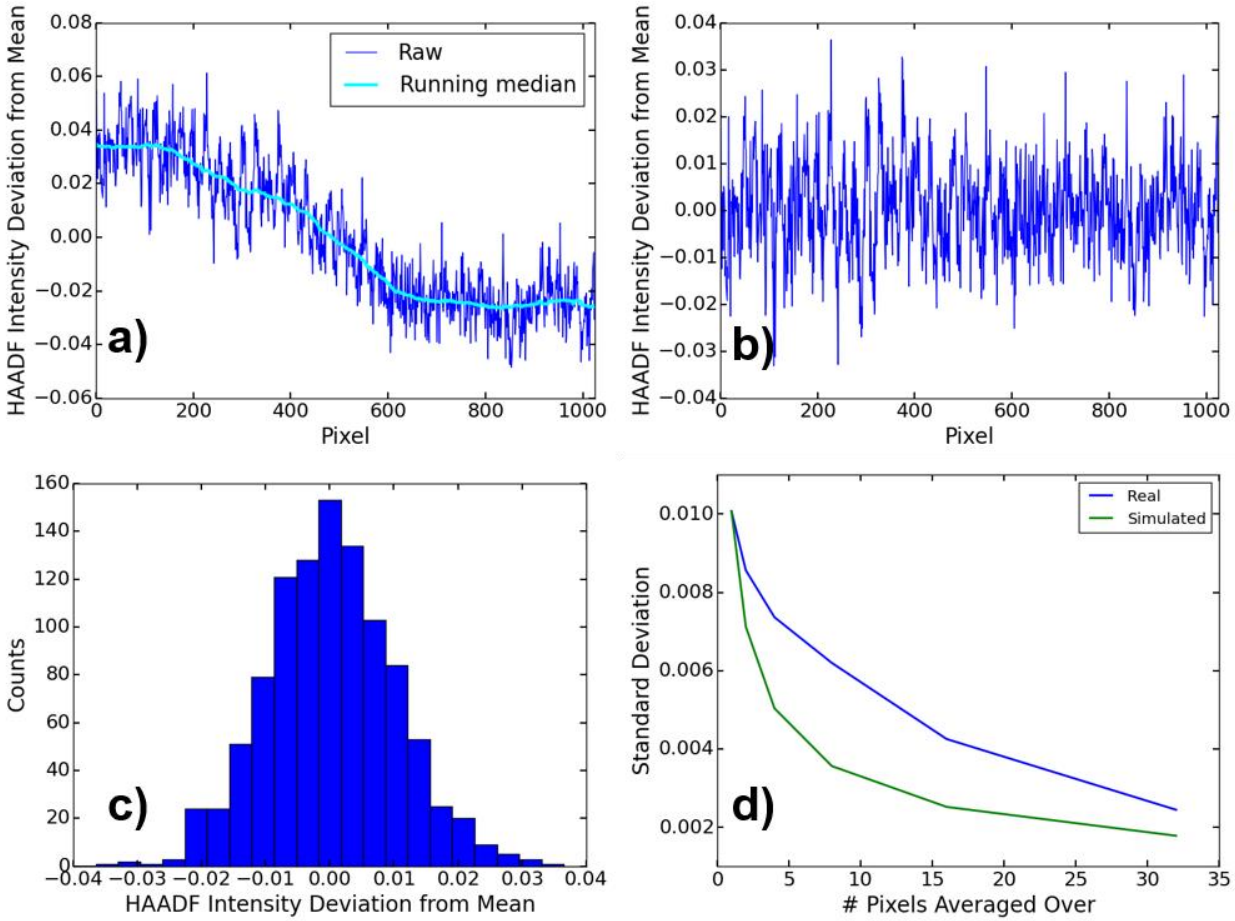

Figure XXI. 35. Horizontal intensity deviation analysis. **(a)** Shows the raw horizontal intensity deviation profile and 155-pixel running median smoother. (**b)** Shows the resulting background subtracted horizontal intensity deviation profile, in which the running median values have been subtracted from the raw profile. **(c)** Shows the distribution of intensity deviations relative to the mean. **(d)** Shows how the distribution width (standard deviation) depends on the box size that is scanned across image.

The variation of the raw vertical HAADF intensities is significantly larger than that observed in the horizontal direction due to the layered structure of the sample. Figure XXI. 3a contains a plot of the difference in the mean HAADF intensity for each *row* of pixels relative to the mean intensity for the whole image, and a periodic series of intensity maxima are observed on top of a varying background. The periodic series of intensity maxima reflect the positions of planes of atoms, with the different intensities reflecting the different chemical compositions of the layers. As with the variation in the horizontal

intensity signal, channeling contrast due to layer orientations relative to a zone axis provides a large contribution to the varying HAADF signal intensity. In order to remove this effect, we use the same running median filter that is much broader, 155 pixels, than the interesting feature sizes in this axis of the film to obtain an estimation of the background (the light blue line in Figure XXI. 3a). The background-subtracted vertical intensity deviation from the mean is shown in Figure XXI. 36b, and a repeating pattern of intensities consistent with four rock salt structured planes of SnSe, a $MoSe_2$ trilayer, 4 four rock salt structured planes of SnSe, and an $NbSe_2$ trilayer, is observed. There is even a slight difference in HAADF scattering intensities between alternating dichalcogenide layers, seen in Figure XXI. 36b, which is not noticed upon visual inspection of the image in Figure XXI. 34. This reflects the slight scattering difference between the $NbSe_2$ and $MoSe_2$ layers. The distribution of signal intensity deviation from the image mean is shown in Figure XXI. 36c, showing that the vertical intensities vary by a factor of 10 more than the horizontal intensity averages (the green superimposed distribution). The vertical intensity deviation distribution does not appear to be normally distributed. The distribution width decreases with increasing sample size at a much slower rate than would be expected for a randomly distributed signal (Figure XXI. 3d). This indicates that the variation in the signal reflects chemical differences between regions, as expected from the layered structure.

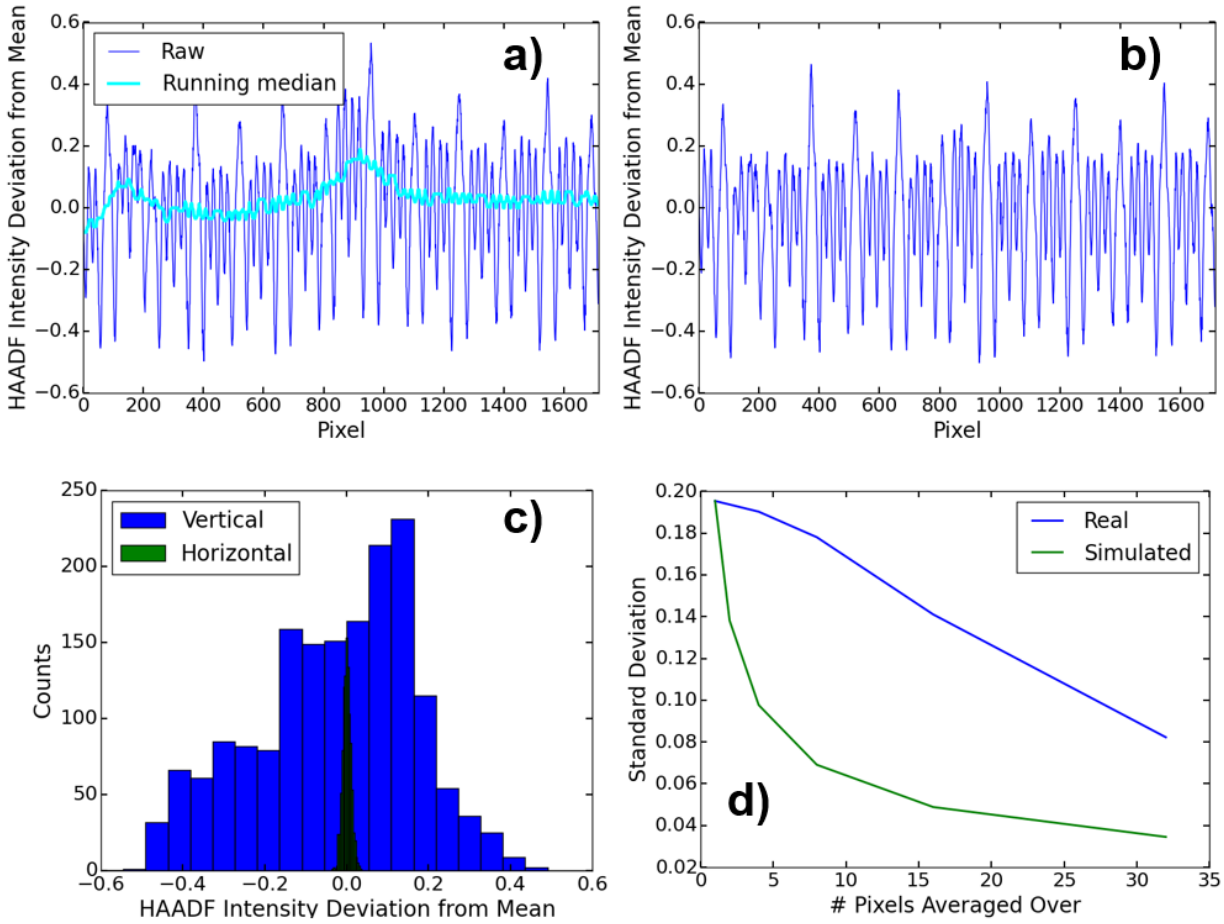

Figure XXI. 36. Vertical intensity deviation analysis. **(a)** Shows the raw vertical intensity deviation profile and 155-pixel running median smoother. **(b)** Shows the resulting background subtracted vertical intensity deviation profile, in which the running median values have been subtracted from the raw profile. **(c)** Shows the distribution of intensity deviations relative to the mean after background subtraction. For comparison, the horizontal distribution is the same as shown in Figure XXI. 35c. (**d)** Shows how the distribution width (standard deviation) depends on the box size that is scanned vertically across image.

While HAADF STEM is inherently a tool for examination of local structure in a material, it can also be used in conjunction with other techniques, such as X-ray diffraction (XRD), to determine the global structure of the material. Refinement of XRD data requires a starting structural model that usually is based on intuition and developed during the refinement process. A starting model grounded in data could be determined from the vertical intensity deviation profile shown in Figure XXI. 36b, which clearly

provides information regarding positions of atomic planes within the image. Numerous factors, such as sample drift and sample alignment, lead to low confidence in atomic plane position estimates determined from a single line scan or single image alone. However, averaging estimates from multiple images taken in different locations is expected to provide greater confidence in atomic plane positions. We extracted vertical intensity deviation profiles from the image shown in Figure XXI. 34 and four other images, used Gaussian peak fitting to determine peak locations with sub-pixel accuracy, and averaged the results to obtain initial estimates for the z-coordinate of each atomic plane in the heterostructure, as shown in Figure XXI. 37a. These values were then used to construct a model for refining X-ray diffraction data from the sample.

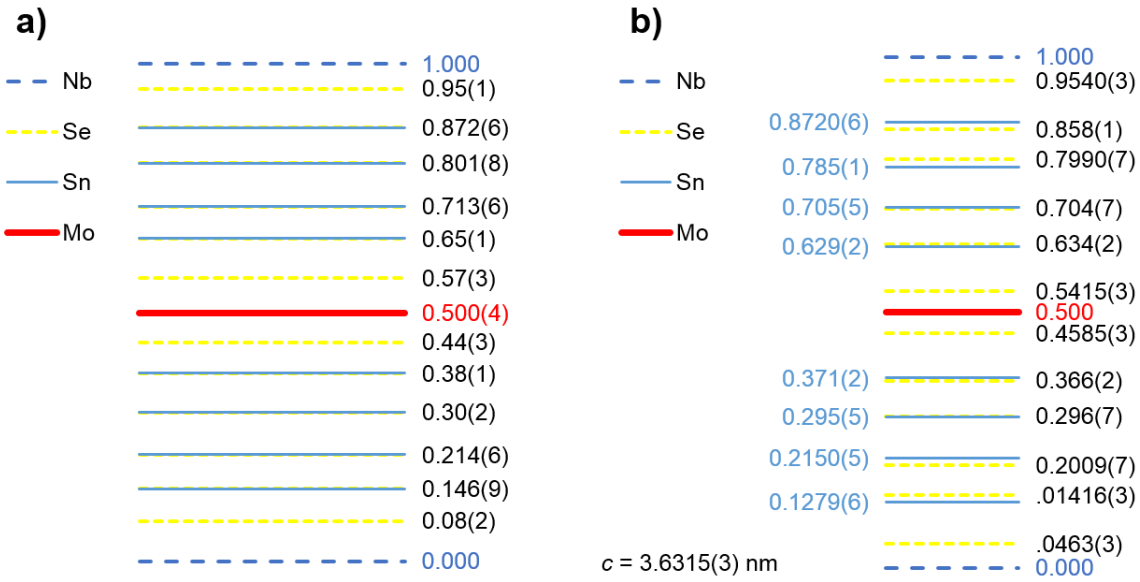

Figure XXI. 37. **a)** Atomic plane z-coordinates determined using HAADF STEM data. The uncertainty in the atomic plane positions comes from the 95% confidence interval from the combined image measurements. The Sn and Se layers in the SnSe layers could not be distinguished in the HAADF images. **b)** Refined atomic plane z-coordinates obtained after performing a Rietveld refinement of diffraction data using the coordinates in (a) as a starting point.

The refined atomic plane positions from the X-ray diffraction data (Figure XXI. 4b) are all very similar to the initial STEM model. The "puckering" effect of Sn and Se in the rock-salt layers reported in the literature for similar heterostructure samples [42] is not resolved in the HAADF images, but is revealed by the Rietveld refinement. The majority of refined atomic plane positions are within the confidence limits of the plane positions estimated from the HAADF images. The most notable change is in the positions of the Se atoms in the TSe_2 layers. The HAADF estimates placed most of these planes farther from the Nb or Mo atoms than the x-ray refinement and prior literature reports of similar structures [44]. However, the confidence intervals for these estimates were relatively large, such that the refined positions are still within the confidence limits of the estimated positions. Much of this error likely came from the reduced sample size of images available for accurately resolving the Mo or Nb and adjacent Se atomic columns. Additionally, no drift compensation was performed on slow-scan images. While the Sn/Se plane positions could be determined from grains both on- and off-zone axis and at relatively low magnifications, the Se and Mo or Nb planes can only be distinguished for on-axis grains and only at higher magnifications. The refinement results are also consistent with refined interplanar distances in the parent compounds and a related heterostructure [44]. Interestingly, the refinement gives more "puckering" of the Sn and Se atoms in the rock salt block adjacent to the $NbSe_2$ layers than in the rock salt block adjacent to the $MoSe_2$ layers. Wiegers speculates that the amount of puckering in the rock salt layer is correlated to the magnitude of interlayer interactions [45]. Stronger puckering of Sn towards $NbSe_2$ than towards $MoSe_2$ suggests a greater interaction between the SnSe and $NbSe_2$ layers than between the SnSe and $MoSe_2$ layers, which is consistent with

trends in the measured electrical properties of this family of heterostructures [35]. However, interpretation of the refinement results should still be undertaken cautiously, as estimating the amount of Mo and Nb intermixing in each TSe_2 layer from refining atom occupancies is difficult. Future refinements that incorporate STEM EDS data treated in a similar manner could provide independent confirmation of this result.

In order to demonstrate the general utility of this approach, we also applied the same HAADF intensity analysis method described above to a representative HAADF STEM image of an amorphous four-coat LZO film to extract information regarding the homogeneity of this sample (Figure XXI. 38). Although the majority of the LZO film appears homogeneous, three distinct horizontal lines are visible that appear slightly brighter than the surrounding material. These lines correspond to interfaces between each of the four coats used to prepare the film. As was done for the nanolaminate heterostructure described above, we first obtained the noise level of the signal by examining the horizontal intensity deviation distribution. Although the horizontal axis of the film is assumed to be chemically homogeneous, we observed some intensity variation in this axis, similar to that observed for the heterostructure sample. In this case, the signal variation is likely due to variations in the sample thickness due to curtaining artifacts created during sample preparation [43], which are visible in wider field of view images. Accordingly, we again used a broad 155-pixel running median filter to determine the horizontal axis background. The background-subtracted horizontal intensity deviation profile is shown in Figure XXI. 39a, in which all of the variation appears to be high frequency noise.

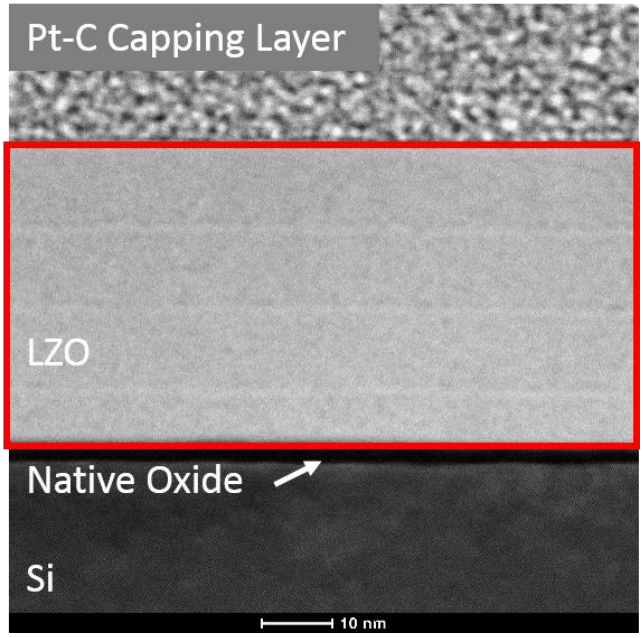

Figure XXI. 38. Representative HAADF STEM image from an amorphous solution-cast four layer LZO film. The red box represents the region of the image that was used for analysis.

In the vertical direction, the background appears to increase nearly linearly from the top to the bottom of the film. This could suggest an approximately linear density gradient through the vertical axis of the film leading to increased electron scattering. However, the sample was thinned from the top down, so the background increase may also be due to a gradient in sample thickness produced as an artifact of sample preparation. While there may or may not be chemical implications from the background intensity gradient, we applied the same size running median filter used for the horizontal direction to define the background level. Figure XXI. 39b shows the background-subtracted vertical intensity deviation profile, in which the brighter interface layers are clearly visible. The intensity deviation distributions for both the horizontal and vertical scan directions are shown in Figure XXI. 39c. The horizontal distribution appears approximately normal, with a relatively narrow width while the vertical distribution

appears much broader than the horizontal distribution, and contains a significant fraction of high-intensity deviations. The effect of sampling size on distribution width for both scan directions is shown in Figure XXI. 39d. The horizontal distribution width decays with a dependence on *n* similar to that expected for a normal distribution, which suggests that the horizontal variation is due solely to noise in the signal. Once again, the difference between the observed and simulated curves may arise from smaller variations in signal intensity that are not captured by the broad running median filter. The vertical distribution width decays at a slower rate than does the horizontal distribution width, suggesting that the variation observed in the vertical axis is outside the noise level in the signal.

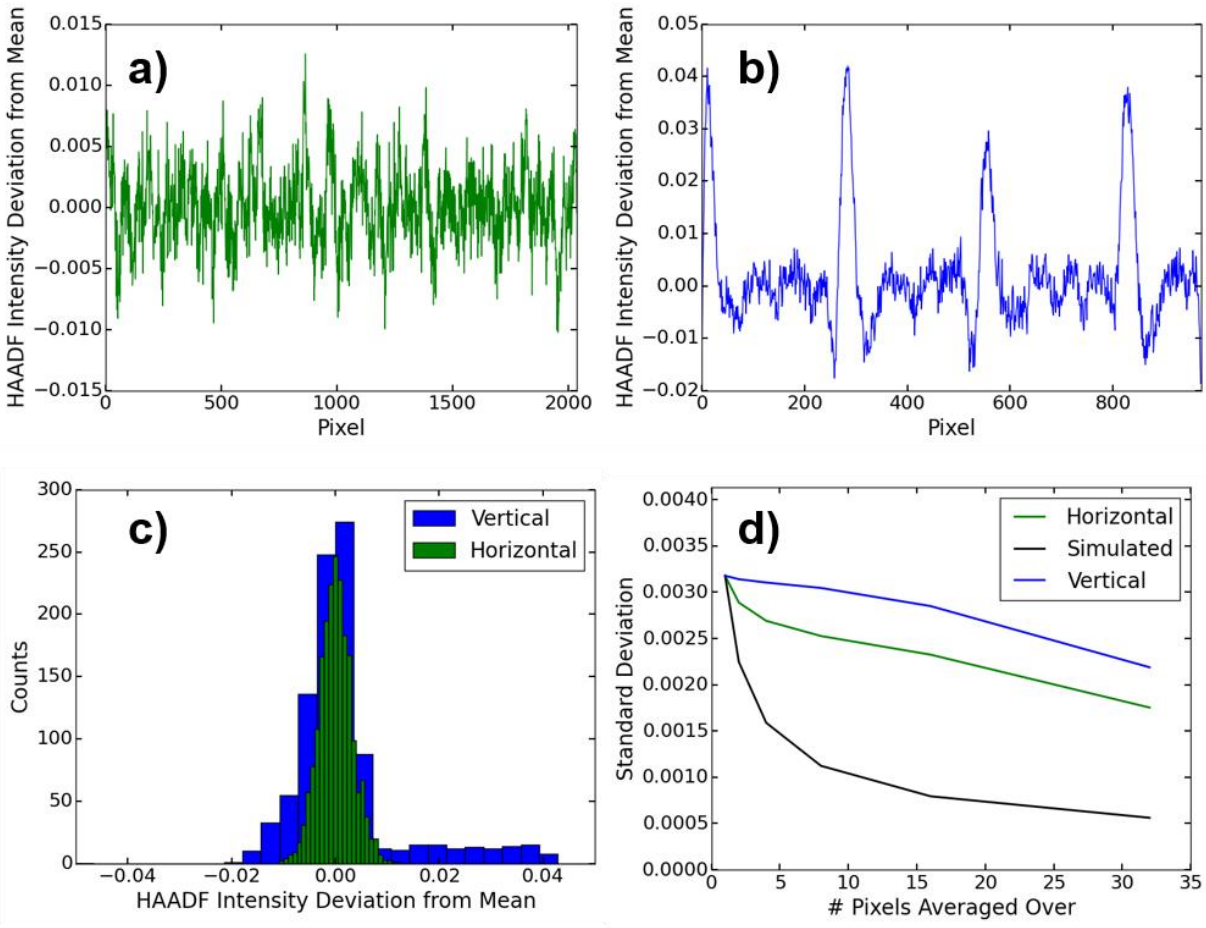

Figure XXI. 39. Horizontal and vertical intensity deviation analysis for LZO film using scanned boxes. **(a)** Background-subtracted horizontal intensity deviation profile. **(b)** Background-subtracted vertical intensity deviation profile. **(c)** Horizontal and vertical deviation distributions. **(d)** Effect of box size on distribution width for horizontal and vertical deviation profiles. The vertical distribution widths have been scaled down to match the range of horizontal distribution widths for convenient comparison.

Our analysis results have interesting implications for the LZO film and other solution-cast amorphous inorganic films. The lack of well-defined structure in these materials makes characterization using conventional techniques difficult. Previous XRR model fits to other metal oxide solution-cast films required assuming details of the interface structure relative to that of the bulk film [25]. We observe here decreased intensity immediately adjacent to each high intensity interfacial layer, a feature which was not anticipated. This suggests that strongly scattering species may be depleted from

either side to form the interfacial layer. The decreased intensities are only observed for the internal layers in the film and not at the substrate-film interface, suggesting that application of subsequent coats leads to a chemical interaction between layers. The interaction may occur during spin coating, perhaps due to a possible partial dissolution of the base layer from the spreading solution above it, or possibly due to diffusion that occurs during film annealing. However, HAADF intensities alone are insufficient to determine the chemistry at these interfacial layers. A similar analysis approach using X-ray energy dispersive spectroscopy maps and STEM may provide a more complete understanding and better information for modeling X-ray reflectivity data from amorphous oxide single- and multiple-coat films.

XXI.5. Summary

We have developed a method for analyzing HAADF STEM images of complex thin film materials that takes advantage of their inherent asymmetry to extract local structural information from the films. The method uses simple running median filters for background subtraction and a comparison of signal intensity deviations from the mean in both the vertical and horizontal directions to assess the presence of inhomogeneity in the film. For complex crystalline or partially-crystalline heterostructures, the analysis method yields reasonable estimates for the positions of atomic planes. These positions can then be used as a starting model for refinements of global structural data (such as XRD) to accelerate solving the *c*-axis structure of the material. For an amorphous, multiple-coat, solution-cast metal oxide film that is difficult to characterize using other techniques, the analysis method determined the relative density differences at interfaces formed during processing. This information will be useful for further determining the local structure and

composition of these films in complement to other techniques, such as X-ray reflectivity, that require accurate starting models to fit data.

CHAPTER XXII

ELEMENT SEGREGATION IN 2D HETEROSTRUCTURES $[(Pb_{1-X}Sn_x)_{1+\delta}]_n(TiSe_2)_1$ QUANTIFIED BY STEM-EDX

2D materials and their integration into heterostructures with emergent properties different from the bulk constituents is developing into a powerful concept to create new materials.[1,2] Properties can be tuned by controlling nanoarchitecture - the choice of constituent(s), the layering sequence and layer thicknesses, and the substrate used. For example, recent synthesis of borophene monolayers on a gold substrate illustrated the importance of long-range interactions between the borophene and the substrate as a tool to tune both structure and properties.[3] Graphene films on hexagonal boron nitride substrates have been found to have much larger carrier mobility than when they are on silicon oxide substrates.[4] FeSe monolayer films deposited on strontium titanate have higher superconducting critical temperatures than FeSe films on other substrates due to charge transfer from the substrate.[5] The structure of rock salt structured 2D layers have also been found to vary systematically with thickness and also with the dichalcogenide constituent they are layered with in heterostructures.[6–8] These examples demonstrate how low dimensional systems provide unique opportunities to put atoms in unusual bonding arrangements, resulting in optimized and/or emergent physical properties.

The large change in surface to volume ratio of both 2D layers and constituents in heterostructures can result in significant differences in structure and composition from that observed in bulk phase diagrams. A significant experimental challenge is how to observe and quantify the structure and composition of the 2D layers in heterostructures.

Here we demonstrate that both structure and composition can change with thickness, using high angle annular dark field scanning transmission electron microscopy (HAADF STEM) and energy dispersive X-ray spectroscopy (STEM EDX) to measure structural changes and to observe and quantify segregation at interfaces of 2D layers. By changing the structure of the precursors that self-assemble into the heterostructures and through theoretical calculations, we show that the observed segregation is driven by thermodynamics rather than by the kinetics of the synthetic pathway.

We prepared 2D monolayers of $TiSe_2$ interdigitated with 2D layers of rock salt structured alloys ($Pb_{1-x}Sn_xSe$) from designed precursors as described previously[9,10] by varying the thickness of the rock salt layer. Figure XXII.1 contains both HAADF STEM images and STEM EDX maps of a $TiSe_2/Pb_{1-x}Sn_xSe$ intergrowth containing a single rock salt layer with 6 planes of atoms within a matrix of alternating monolayers of $TiSe_2$ and bilayer thick rock salt layers. Intensity differences are apparent between the 6 planes of the $Pb_{1-x}Sn_xSe$ layers in the HAADF STEM image, with the outer layers brightest. The STEM EDX maps qualitatively show that the outermost layers are systematically enriched in Pb and depleted in Sn, the next layer is depleted in Pb and enriched in Sn, and the innermost layers have intermediate concentrations of Pb and Sn. For the regions with bilayer thick rock salt layers, lattice parameters determined from both in-plane X-ray diffraction and the STEM-EDX indicate that a solid solution is formed. This agrees with a prior study, which indicated that for a bilayer, a solid solution of $Pb_{1-x}Sn_xSe$ forms across the entire composition range even though the bulk phase diagram contains a miscibility gap.[10] The HAADF-STEM image also indicates that the six planes shown in Figure XXII.1 are not evenly spaced, but self-organize into pairs with longer distances

between pairs. This clearly demonstrates that 2D layers can stabilize structures and compositions not observed in the bulk 3D structures.

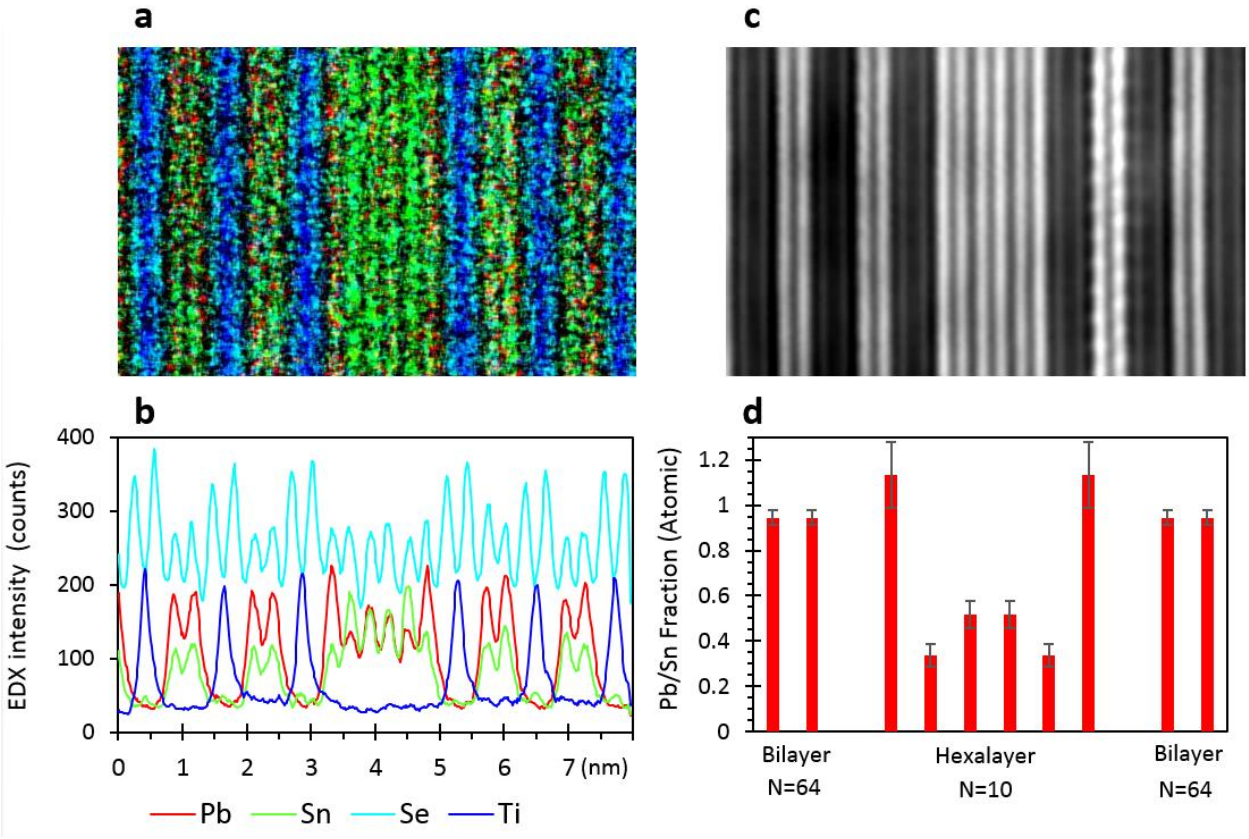

Figure XXII.1. (a) EDX map of this area indicating the non-uniform distribution of Pb and Sn in the 6 rock salt atomic planes. (b) Integrated intensity of the respective elemental signals smoothed with a 5 pixel moving average showing the average distribution of elements. (c) HAADF STEM image of a rock salt hexalayer surrounded by $[(Pb_xSn_{1-x}Se)_{1+\delta}]_1(TiSe_2)_1$ layers. (d) Bar graph indicating the quantified atomic ratio of Pb/Sn for the different atomic layers with error bars indicating the 99% confidence interval for each of the measurements. The ratios were determined using 6 different spectrum images and the average measured composition for the layers indicated.

Quantifying compositional changes in atomic planes and small volumes to determine absolute composition is challenging due to delocalization of signal[11–13], the unknown proportionality between counts and composition[14] and the small signal to noise ratio[15]. Our approach was to first determine an average background for each

spectroscopic peak by averaging the data in the entire area scanned, which provided a consistent background subtraction with small statistical uncertainty. We determined the sensitivity factors correlating EDX counts with composition[14] by using end member compounds as standards. The accuracy of the spatial variation of the EDX-determined compositions is limited by the counting statistics, which vary with the size of the area analyzed. X-ray spectrometer counting statistics are Poissonian in nature, such that the standard deviation (σ) of detected counts is approximately equal to $\sqrt{n}$ (n = counts)[16]. Binning the data over different size areas and scanning the areas over the hyperspectral image after analysis allows us to compare the statistically expected standard deviations from multiple data bin sizes and locations, which may reveal deviations from the average value through aberrations from the expected statistics. Larger bin sizes are expected to have a larger standard deviation in raw peak intensity due to more counts, but the relative standard deviation will decrease as the bin size increases because the linear increase in counts outpaces the square root increase in standard deviation. For example, examining the composition within each of the $[(Pb_xSn_{1-x}Se)_{1+y}]_1(TiSe_2)_1$ repeats of the area mapped, we found that variations in Pb composition were distributed normally, with large areas (1.3 nm x 16.0 nm) providing a standard deviation of σ = 0.4% and smaller areas (1.3 nm x 1.3 nm) resulting in the expected larger standard deviation (σ = 0.9%). This is in agreement with X-ray diffraction data[10] and in contrast to what is expected from the bulk phase diagram, which indicates that they are immiscible[17].

The 3 bilayers thick $Pb_xSn_{1-x}Se$ regions, however, have qualitatively different compositions in different atomic planes (Figure XXII.1b) such that the outermost layers are enriched in lead. The segregation of Pb to the surface layer must decrease the entropy

of the system and create an internal strain within the rock salt layer, suggesting there must be an enthalpic stabilization. The data analysis approach described above along with Gaussian peak fitting,[18] discussed below, allows us to quantify the compositional changes within each atomic plane (Figure XXII.1d), with the differences between the average composition in each atomic plane larger than the measured statistical deviation. The average composition of the 3 bilayer thick regions is enriched in Sn due to the 4 inner atomic planes having higher Sn compositions. A small difference in the Sn composition of these 4 inner layers is also found, at the limits of the statistical analysis. The outermost layer has a slightly higher Pb concentration than the adjacent $[(Pb_xSn_{1-x}Se)_{1+y}]_1(TiSe_2)_1$ layers. This statistics based approach enhances the ability to quantify miscibility, surface segregation, and the formation of complex heterostructures on the atomic scale, especially relative to the common qualitative practice of examining EDX intensity as a function of position across a line scan.

It is not clear if the segregation observed in the 3 bilayer thick regions is a kinetic phenomenon resulting from a variation in local precursor composition, or whether Sn in the inner layers and Pb in the outer layer is a more thermodynamically stable arrangement. To provide some insight to the observed segregation of Pb to the outer layers and Sn to the inner layers, DFT calculations were initially performed on isolated blocks of $Pb_xSn_{1-x}Se$. For single rock salt bilayers, we observe the structure relaxes such that the layers are puckered with cations on the outside and Se on the inside, agreeing with the position of these planes determined from Rietveld analysis of 00*l* diffraction data[19,20] For an isolated 3 bilayer stack of $Pb_xSn_{1-x}Se$, a series of calculations were done with either Pb or Sn in the outer layer using an initial structure whose composition profile

replicates the EDX map illustrated in Fig 1. We varied the composition of Pb in the system from 33 at% to 66% and also compared the extrema of pure 3 bilayer SnSe and PbSe. In the calculation, we observe a square in plane unit cell with a = 0.61 nm, in agreement with the experimental in-plane diffraction data that indexes to a square in-plane unit cell with a = 0.6095(1) nm. The calculations indicate that Sn is favored to be on the outside layer, but increasing the composition of lead in the bilayer results in a smaller energy difference between having Sn or Pb at the interface. The blue curve in Figure XXII.2 shows the composition dependence of this energy difference, which indicates that tin is preferred at the vacuum interface although the magnitude of the difference decreases as the percentage of lead increases. The computational models used that replicate these compositions are found in the supplementary figures.

The *in vacuo* calculation is not directly comparable with the experiment, as the dichalcogenide $TiSe_2$ layer is not included in these calculations and the energy of the idealized structures may also be unduly influenced by the strain of the perfectly ordered structures, with the outer bilayers containing Pb on the outside and Sn on the inside significantly higher in energy than the pure Sn and Pb bilyers found in the model with Pb only on the inside bilayer. Repeating the calculation with a $TiSe_2$ layer between a 3 bilayer thick (Pb,Sn)Se rock salt structured block we observe that lead segregation is preferred at the interface, reversing the trend of stability compared to the *in vacuo* calculation and agreeing with the experimental observation. With the $TiSe_2$ layer, Pb on the outside layer is lower in energy than Sn on the outside by a difference of 350 meV/nm^2 because its higher van der Waals polarizability and lower electronegativity compared to Sn leads to a stronger interaction between the two constituent structures.

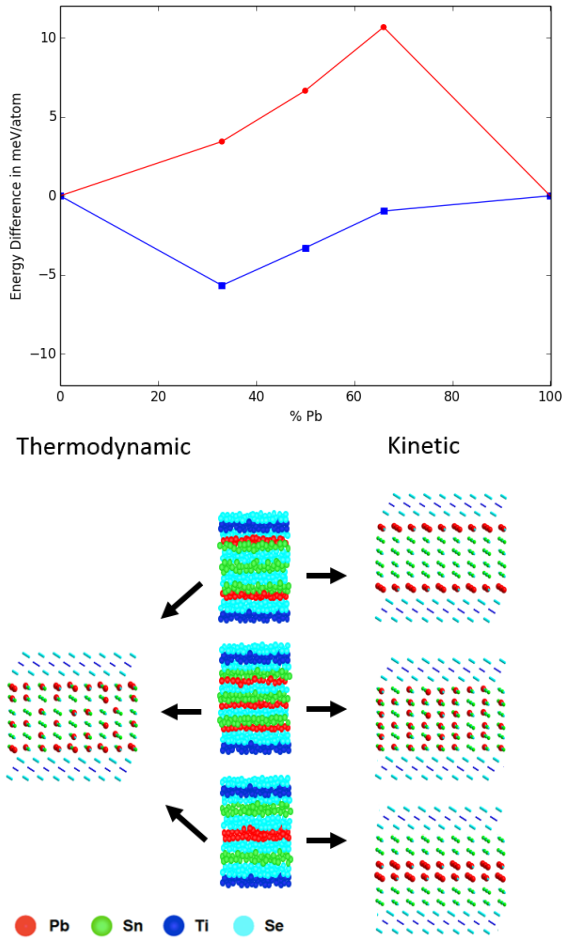

Figure XXII.2. Left: The calculated energy difference between computational models having Pb or Sn segregated to the interface as a function of composition of the $[(Pb_x Sn_{1-x}Se)]_3$ layer. A positive energy difference indicates the preference of Pb segregation to the interface. The blue curve is for vacuum isolated 6 layer thick rock salt structured layers and Sn segregation to the interface is thermodynamically preferred. Repeating the calculation now with a $TiSe_2$ layer between the rock salt layers (red curve), reverses this tendency and Pb preferentially occupies the interface as seen in the experimental data. The extremums are the pure PbSe and SnSe phases. Right: Schematic structures of 3 precursors with different initial distributions of Pb and Sn. The structures on the right would be expected if diffusion is limited and kinetics dominates. The structure on the left would be expected if the segregation lead to the surface is thermodynamically driven and accessible under the annealing conditions.

To determine if the segregation is a result of kinetic limitations induced by the diffusion limited synthesis approach or as a consequence of differences in

thermodynamic stability, three different $[(Pb_{1/3}Sn_{2/3}Se)_{1+\delta}]_3(TiSe_2)_1$ precursors were prepared as shown schematically on the right hand side of Figure XXII.2. If the initial structure of the precursor is maintained in the final product, this would support the distribution of Pb and Sn being a kinetic effect. If the products formed from the three different precursors have the same distributions of Pb and Sn after annealing, this would indicate that the distribution is a thermodynamic effect. A HAADF STEM image of the annealed product formed from the precursor with Sn and Pb homogenously distributed is shown in Figure XXII.3a. This image is representative of all of the annealed precursors, with the final compounds having the same basic structure consisting of six monolayer thick blocks of rock salt interleaved between single trilayers of $TiSe_2$. Zone axes consistent with [110] and [100] orientations of a rock salt structured layer, labeled in Figure XXII.3a, were seen in all of the three samples. Zone axes consistent with [110] and [100] orientations of a CdI_2 structure type were also observed in all of the samples (labeled in Figure XXII.3a), consistent with the structure expected for $TiSe_2$. The samples all displayed the characteristic rotational or turbostratic disorder between the layers previously reported for samples prepared from precursors in this manner. The HAADF-STEM contrast suggests the higher Z Pb and Sn atoms are present in the rocksalt structure, and that the darker CdI_2-structured layer contains the low Z Ti atoms.

A STEM EDX map showing the final distribution of Sn and Pb from the precursor that had Pb deposited in the middle layer is shown in Figure XXII.3b. The EDX map, which is representative of data of the self-assembled products from all three precursors, confirms the formation of distinct $Pb_xSn_{1-x}Se$ and $TiSe_2$ phases indicated by the HAADF images. Qualitatively, the changes in the measured raw intensity for the

different elements indicate enhanced Pb concentration in the atomic planes adjacent to the interfaces, which was observed for all of the precursors.The overall cation occupancy of the $Pb_xSn_{1-x}Se$ layers in the samples resulting from the three precursors, determined from STEM EDX using the same analysis procedure described earlier, is 63±2% Sn (and 37±2% Pb), where the uncertainty is expressed as the 99% confidence interval. The statistical error bars are likely a result of slight variations in precursor composition and the 0.5% EDX error. The measured compositions suggest that the rock salt structure is homogenous in the in-plane direction. The stoichiometry of each of the self-assembled products determined from the quantification is $[(Pb_{0.37}Sn_{0.63}Se)_{1.17}]_3(TiSe_{2.00})_1$, with a standard deviation of ±1% in repeat composition, which is consistent with electron microprobe data and the common deposition parameters used to prepare them.

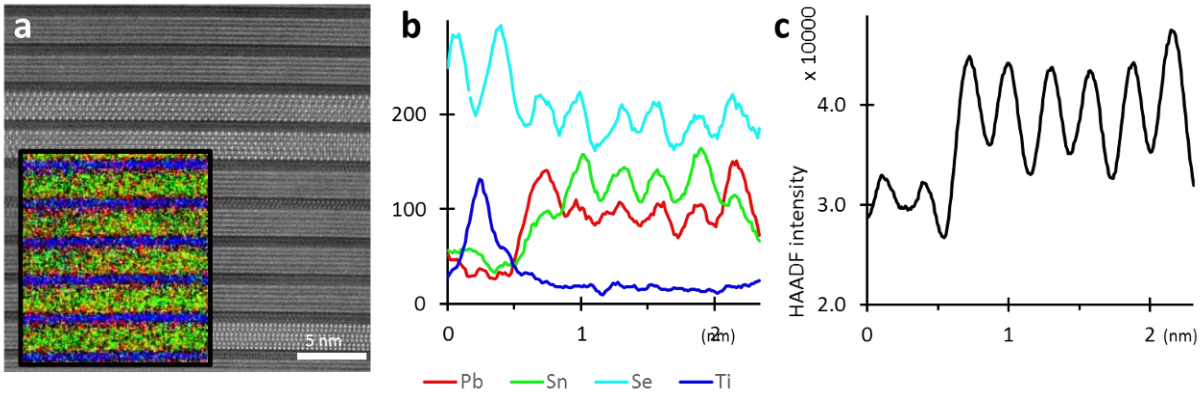

Figure XXII.3. (3a) A representative HAADF-STEM image and the corresponding EDX map (inset) for the heterostrucure formed from the disperse precursor (center precursor in the schematic on the right in Figure XXII.2). Crystallographic alignment of the expected phases is observed. (3b) The integrated EDX intensity profile of the heterostrucure formed from the precursor with Pb in the middle layer. After annealing, all precursors exhibited approximately the same intensity profile indicating that the same compositional heterostructure is forming with Pb at the interface. (3c) HAADF-STEM average intensity plot.

While HAADF STEM and STEM EDX techniques provide a window into the local structure of the heterostructures, X-ray diffraction (XRD) provides an overview of the global average structure. Typically, Rietveld refinements of XRD data are conducted by trying different initial models generated from intuition, but using the experimental positions of the atomic layers as a starting point for Rietveld refinements would be a significant improvement. The variation in HAADF-STEM intensity, averaged over an entire layer, is shown in Figure XXII.3c. Fitting Gaussian functions to the intensity variations enables the position of each of the intensity maxima to be determined. As shown previously, the position of the maxima correspond to the position of the atomic planes, which can be determined to relatively high precision by averaging the intensity profiles from multiple layers (see HAADF Initial Z column in Table XXII.). The refinement based on HAADF STEM-determined plane positions alone, however, is challenging because compositional variations from layer to layer in the rock salt block cannot be elucidated from HAADF intensities and because the limited number of *00l* reflections makes finding the global minimum difficult by limiting the number of parameters that can be allowed to independently vary. Having the relative ratio of the constituents in each layer, in addition to the atomic plane positions, would improve the starting point for the Rietveld refinement and could potentially reduce the number of parameters that need to be refined.

One potential way to obtain composition information as a function of position would be to use the STEM-EDX data. Quantifying the STEM-EDX data at the atomic scale, however, is complicated by beam channeling and dechanneling that depends on crystallographic orientations (on or off zone axes), sample thickness (which changes the

intensity and the width of the EDX signal as a function of the incident electron beam position)[11–13], and potentially residual amorphous surface layers from FIB milling of the sample (which could increase the background signal). For a rotationally disordered or off zone axis films, nonlinear excitation has been theoretically shown to be less significant than on-zone-axis alignments where channeling effects occur[21]. Gaussian peak fitting the spatial intensity distribution for each element has been previously shown by Lu *et.al.* to reasonably estimate the local signal for thin lamellae[18] providing a strategy to threshold complicated background intensities.

Table XXII.1. Atomic plane Z-coordinates relative to Ti atomic plane and atomic plane occupancies determined from analysis of HAADF and EDS data (initial Z's and Occ's) and values obtained from a Rietveld refinement of X-ray diffraction data using the initial *Z*'s and Occ's as model inputs. The refinements were conducted using space group *P -3 m 1* with the mirror plane halfway through the hexalayer. HAADF initial occupancies were estimated from the measured compound stoichiometry. For ease of comparison, Occupancies of Pb and Sn are expressed as fraction of nearest Se plane occupancy, assuming full Se occupancy. Both refinements converged to a *c* axis lattice parameter of 2.3862(2) nm, which is consistent with the 2.38(1) nm determined from both HAADF and EDS data. For further refinement details, the reader is referred to the supplemental information.

Atom	HAADF Initial Z	HAADF Refined Z	EDX Initial Z	EDX Refined Z	HAADF Initial Occ	HAADF Refined Occ	EDX Initial Occ	EDX Refined Occ
Ti	0	0	0	0	1	1	1	1
Se1	0.063(5)	0.0637(1)	0.066(3)	0.0637(1)	2	2	2	2
Pb1	0.193(3)	0.1930(1)	0.191(3)	0.1894(1)	0.34(1)	0.339(1)	0.41(3)	0.412(1)
Sn1	0.193(3)	0.1930(1)	0.196(3)	0.1944(1)	0.66(1)	0.661(1)	0.59(3)	0.588(1)
Se2	0.193(3)	0.1930(1)	0.197(3)	0.1954(1)	1.00	1.00	1.00	1.00
Se3	0.312(1)	0.3129(1)	0.313(5)	0.3118(1)	1.00	1.00	1.00	1.00
Sn2	0.312(1)	0.3129(1)	0.314(5)	0.3128(1)	0.66(1)	0.663(3)	0.80(1)	0.804(2)
Pb2	0.312(1)	0.3129(1)	0.317(3)	0.3158(1)	0.34(1)	0.337(3)	0.20(1)	0.196(2)
Pb3	0.439(1)	0.4401(1)	0.438(4)	0.4362(1)	0.34(1)	0.332(1)	0.23(2)	0.211(1)
Sn3	0.439(1)	0.4401(1)	0.441(3)	0.4392(1)	0.66(1)	0.668(1)	0.77(2)	0.789(1)
Se4	0.439(1)	0.4401(1)	0.445(7)	0.4432(1)	1.00	1.00	1.00	1.00

We independently tested the validity of this method on the calibrated alloy system[10], $(Pb_xSn_{1-x}Se)_{1+\delta}TiSe_2$, and found that the quantified intensities from Gaussian peak fitting scaled consistently over numerous measurements within statistical error. We then applied these methods to analyze the three $[(Pb_{0.37}Sn_{0.63}Se)_{1.17}]_3(TiSe_2)_1$ samples, using our experimental sensitivity factors determined from the calibrated alloy system. To get statistically meaningful composition information from each atomic plane, we laterally summed the EDX intensity over the entire spectrum image and then averaged those intensities for each repeating unit along the *c*-axis, creating a collapsed intensity versus distance (perpendicular to the substrate) curve; examples are shown in Figure

XXII.1b and 3b. Gaussian profile fits were used to quantify the signal and to also locate the center of each plane's compositional distribution. The average Pb/Sn composition ratio for the 6 planes was 0.43 (Pb occupancy, 30% ±4%), which is within error of the targeted bulk ratio of 0.50 (Pb occupancy, 33.3%) but in slight disagreement with the average composition determined above from summing over large areas. The EDX data suggested symmetry in the plane positions and composition ratios about the center (unoccupied) plane, Z=0.5, of the six rock salt layers, so only half are necessary to describe the structure. Table 1 contains the estimated Pb and Sn fractional occupancies (assuming Pb + Sn = Se = 1) determined from the Pb/Sn EDX composition ratios for half of the six rock salt layers (EDX Initial Occ's). The refined fractional occupancies (EDX Refined Occ's) are the same within error as those determined from the Pb/Sn EDX composition ratios. The specific values in Table 1 are from the dispersed precursor sample, which are the same within error of the averages from all three samples. The three samples from the different precursors have very similar composition profiles across the six rock salt planes, with enhanced Pb composition in the outer most layers and enhanced Sn composition in the inner layers, with the variation between the compositions of the interior layers being at the edge of being statistically significant at the 99% confidence interval. This indicates that the segregation of cations within the 6 atomic planes of the rock salt structure is a thermodynamic, rather than a kinetic, effect.

Much like HAADF-STEM, STEM-EDX is an incoherent imaging mode and signal intensity corresponds directly to the structure of the sample.[12] Therefore, the Gaussian peak positions from the data analysis also leads to average atomic plane positions for each of the elements of the sample, as summarized in Table 1 (EDX Initial

Z's), providing both atomic plane positions and compositions that can then be used as an initial model for the global structure using Rietveld refinement. The positions obtained from a Rietveld refinement using the STEM-EDX data as a starting point are contained in Table XXII.1 (EDX Refined Z's), and are very close to the EDX numbers and reach near the minimum possible difference between experiment and simulation based on the profiles used. The observed 0.152(1) nm separation between the Ti plane and the adjacent Se planes within the $TiSe_2$ constituent is slightly longer than the 0.145(3) nm distance found in the $[(PbSe)_{1.16}]_1TiSe_2$ ferecrystal[19], but is consistent with the 0.154(1) nm distance in the $[(SnSe)_{1.2}]_1TiSe_2$ ferecrystal[20] and the 0.153(1) nm interplanar distance found in bulk $TiSe_2$. Rock salt cation displacement towards the Se plane of the dichalcogenide layer, referred to as "puckering," ranges from 0.020 nm to 0.060 nm in the relatively few atomic level structures that have been previously determined.[16-23] The refinement based on the EDX data indicates some degree of puckering of the rock salt planes, with the magnitude of puckering dependent on the cation identity The Sn atoms pucker much less than the Pb atoms, 0.002(3) to .010(3) nm depending on the layer, which is much less than the 0.027(1) nm puckering reported for $[(SnSe)_{1.2}]_1TiSe_2$ ferecrystal. The degree of puckering of the Pb planes , 0.010(3) to 0.017(3) nm is similar to the 0.015(3) nm reported for $[(PbSe)_{1.16}]_1TiSe_2$ ferecrystal.[19] The differences may be due to the thicker rock salt layer and the fact that it is an alloy. The average Pb to Se *c*-axis distance within the rock-salt structure (0.292(2) nm) is close to the 0.306 nm observed in PbSe[22] while the corresponding Sn to Se distance is shorter, 0.280(2) nm, which is consistent with the 0.2744(3) - 0.2793(2) nm in bulk SnSe and reflects the size difference between the cations. A value of 0.300(2) nm was obtained for the distance

between the closest atomic planes of the rock salt and dichalcogenide constituents, which is consistent with prior studies of crystal structures of lead- and tin-containing ferecrystals.[19] The consistency of the interatomic plane distances between different samples, between the EDX and Rietveld analysis, and with prior studies shows the utility in using the local structure as a starting point to model the global structure. The experimental EDX determined local positions and compositions were critical to refine the global diffraction pattern of these complex heterostructures. While HAADF data alone could also be used to provide an initial starting model, the refined structure obtained does not indicate any puckering or segregation in the rock salt layers, contrary to the EDX data.

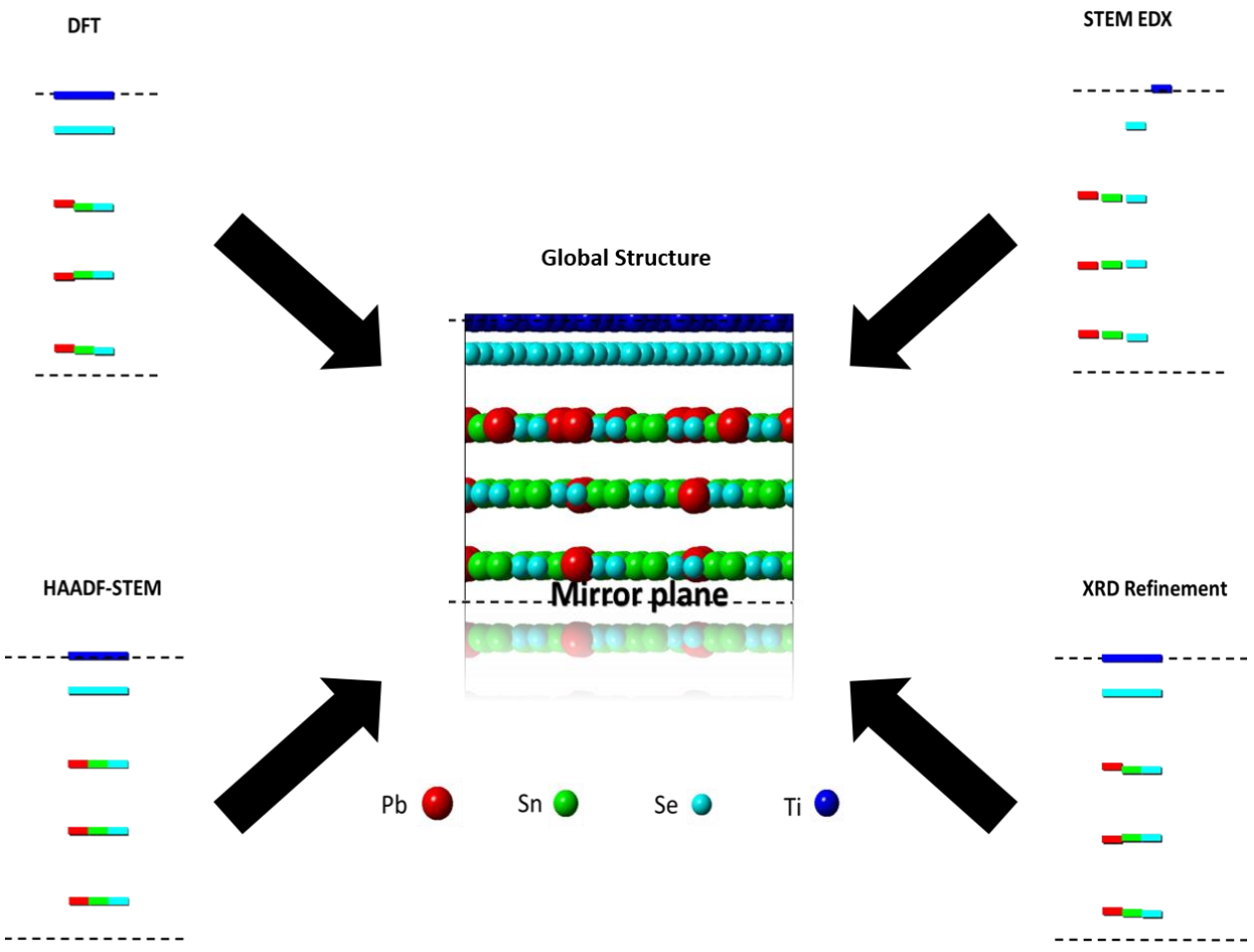

Figure XXII.4. Determining the global structure of complex layered 2D materials is best achieved through a combination of inputs from theory, microscopy, and XRD.

Figure XXII.4 shows how theory, HAADF-STEM, STEM-EDX and XRD were all used in concert in this investigation to unravel the structure of $[(Pb_{0.34}Sn_{0.66}Se)_{1.17}]_3(TiSe_2)_1$ samples. Determining global structures is particularly challenging for heterostructures that do not contain long-range order in all directions and this.investigation illustrates the importance of combining multiple experimental datasets with theoretical calculations to determine the structure. By applying statistical analysis methods to STEM-EDX data, we show that reasonably precise values can be obtained for local composition and the position of atomic planes. As research into 2D materials

continues and synthetic methods enable the formation of more complex heterostructures, we expect that determining accurate structural information will require the development of additional theoretical and statistical experimental approaches.

This investigation demonstrates that ultrathin layers can adopt a structure that is different from the bulk and that the distribution of elements in an alloy can vary from that expected from the bulk phase diagram. Initial STEM EDX observations of 3 bilayer-thick $Pb_xSn_{1-x}Se$ regions within nominally $[(Pb_xSn_{1-x}Se)_{1+y}]_1(TiSe_2)_1$ heterostructures showed unanticipated Pb segregation layers. Theoretical calculations indicate that the segregation is not expected to occur in a vacuum-isolated 3 bilayer thick model structure, but is thermodynamically favored to occur when the $Pb_xSn_{1-x}Se$ layers are interdigitated with $TiSe_2$ monolayers due to a stronger interaction between PbSe and $TiSe_2$ than that between SnSe and $TiSe_2$. This illustrates the importance of conducting theoretical calculations of 2D and ultrathin materials in the context their surroundings and not isolated in vacuum. STEM EDX data obtained on three $[(Pb_{0.34}Sn_{0.66}Se)_{1.17}]_3(TiSe_2)_1$ samples prepared from layered precursors with different initial distributions of Pb and Sn showed that the Pb segregation was thermodynamic favorability rather than kinetic phenomena. Statistical analysis of the microscopy data allowed precise determination of *c*-axis atomic plane positions and plane occupancies from local structure information, which were shown to be a good model for the global structure through Rietveld refinement of diffraction data.

REFERENCES CITED

Chapter I

(1) Novoselov, K. S.; Geim, A. K.; Morozov, S. V.; Jiang, D.; Zhang, Y.; Dubonos, S. V.; Grigorieva, I. V.; Firsov, A. A. *Science (80-.).* **2004**, *306*, 666–669.

(2) Novoselov, K. S.; Jiang, D.; Schedin, F.; Booth, T. J.; Khotkevich, V. V; Morozov, S. V; Geim, a K. *Proc. Natl. Acad. Sci. U. S. A.* **2005**, *102* (30), 10451–10453.

(3) Novoselov, K. S.; Geim, A. K.; Morozov, S. V; Jiang, D.; Katsnelson, M. I.; Grigorieva, I. V; Dubonos, S. V; Firsov, A. A. *Nature* **2005**, *438* (7065), 197–200.

(4) Mak, K. F.; Lee, C.; Hone, J.; Shan, J.; Heinz, T. F. *Phys. Rev. Lett.* **2010**, *105* (13), 2–5.

(5) Wang, H.; Zhang, C.; Chan, W.; Tiwari, S.; Rana, F. *Nat. Commun.* **2015**, *6*, 17–20.

(6) Enyashin, A. N.; Ivanovskii, A. L. *Phys. Status Solidi Basic Res.* **2011**, *248* (8), 1879–1883.

(7) Alducin, D.; Myers, B. D.; Liu, X.; Fisher, B. L. Synthesis of Borophenes: Anisotropic, Two-Dimensional Boron Polymorphs. **2015**, *350* (6267), 1513–1516.

(8) Bampoulis, P.; Zhang, L.; Safaei, a; van Gastel, R.; Poelsema, B.; Zandvliet, H. J. W. *J. Phys. Condens. Matter* **2014**, *26* (44), 442001.

(9) Gupta, A.; Sakthivel, T.; Seal, S. *Prog. Mater. Sci.* **2015**, *73*, 44–126.

(10) Blake, P.; Hill, E. W.; Castro Neto, A. H.; Novoselov, K. S.; Jiang, D.; Yang, R.; Booth, T. J.; Geim, A. K. *Appl. Phys. Lett.* **2007**, *91* (6), 2007–2009.

(11) Geim, A. K.; Grigorieva, I. V. *Nature* **2013**, *499* (7459), 419–425.

(12) Ponomarenko, L. a.; Geim, a. K.; Zhukov, a. a.; Jalil, R.; Morozov, S. V.; Novoselov, K. S.; Grigorieva, I. V.; Hill, E. H.; Cheianov, V.; Falko, V.; Watanabe, K.; Taniguchi, T.; Gorbachev, R. V. *Nat. Phys.* **2011**, *7* (12), 958–961.

(13) Britnell, L.; Gorbachev, R. V.; Jalil, R.; Belle, B. D.; Schedin, F.; Mishchenko, a.; Georgiou, T.; Katsnelson, M. I.; Eaves, L.; Morozov, S. V.; Peres, N. M. R.; Leist, J.; Geim, a. K.; Novoselov, K. S.; Ponomarenko, L. a. *Science (80-.).* **2012**, *335* (6071), 947–950.

(14) Wang, H.; Yu, L.; Lee, Y. H.; Shi, Y.; Hsu, A.; Chin, M. L.; Li, L. J.; Dubey, M.; Kong, J.; Palacios, T. *Nano Lett.* **2012**, *12* (9), 4674–4680.

(15) Haigh, S. J.; Gholinia, a.; Jalil, R.; Romani, S.; Britnell, L.; Elias, D. C.; Novoselov, K. S.; Ponomarenko, L. a.; Geim, a. K.; Gorbachev, R. *Nat. Mater.* **2012**, *11* (9), 764–767.

(16) J. C. Meyer; A. K. Geim; M. I. Katsnelson; Novoselov, K. S.; T. J. Booth; S. Roth. *Nature* **2007**, *446* (1), 60–63.

(17) Gass, M. H.; Bangert, U.; Bleloch, A. L.; Wang, P.; Nair, R. R.; Geim, A. K. *Nat. Nanotechnol.* **2008**, *3*, 676–681.

(18) Ci, L.; Song, L.; Jin, C.; Jariwala, D.; Wu, D.; Li, Y.; Srivastava, A.; Wang, Z. F.;

Storr, K.; Balicas, L.; Liu, F.; Ajayan, P. M. *Nat. Mater.* **2010**, *9* (5), 430–435.

(19) Batson, P. E. *Nature* **1993**, *366* (23/30), 727–728.

(20) Medlin, D. L.; Snyder, G. J. *Jom* **2013**, *65* (3), 390–400.

(21) Tong, W.; Yang, H.; Moeck, P.; Nandasiri, M. I.; Browning, N. D. *Acta Mater.* **2013**, *61* (9), 3392–3398.

(22) Medlin, D. L.; Yang, N. Y. C. *J. Electron. Mater.* **2012**, *41* (6), 1456–1464.

(23) Lee, M. *X-Ray Diffraction for Materials Research*; Apple Academic Press, Inc: Oakville, 2016.

(24) Haider, M.; Hartel, P.; Müller, H.; Uhlemann, S.; Zach, J. *Philos. Trans. A. Math. Phys. Eng. Sci.* **2009**, *367* (1903), 3665–3682.

(25) Sawada, H.; Sasaki, T.; Hosokawa, F.; Suenaga, K. *Phys. Rev. Lett.* **2015**, *114* (16), 6–10.

(26) Merrill, D. R.; Moore, D. B.; Bauers, S. R.; Falmbigl, M.; Johnson, D. C. *Materials (Basel).* **2015**, *8* (4), 2000–2029.

(27) Fister, L.; David, C. *J. Am. Chem. Soc.* **1992**, *114*, 4639–4644.

(28) Atkins, R.; Wilson, J.; Zschack, P.; Grosse, C.; Neumann, W.; Johnson, D. C. *Chem. Mater.* **2012**, *24* (23), 4594–4599.

(29) Heideman, C.; Nyugen, N.; Hanni, J.; Lin, Q.; Duncombe, S.; Johnson, D. C.; Zschack, P. *J. Solid State Chem.* **2008**, *181* (7), 1701–1706.

(30) Heideman, C. L.; Tepfer, S.; Lin, Q.; Rostek, R.; Zschack, P.; Anderson, M. D.;

Anderson, I. M.; Johnson, D. C. J. Am. Chem. Soc.. **2013**, 135, 11055-62.

(31) Krivanek, O. L.; Mooney, P. E. *Ultramicroscopy* **1993**, *49* (1-4), 95–108.

(32) Cowley, J. M.; Moodie, a. F. *Acta Crystallogr.* **1957**, *10* (10), 609–619.

(33) Goodman, P.; Moodie, a. F. Beam *Acta Crystallogr. Sect. A* **1974**, *30* (2), 280–290.

(34) Cliff, G.; Lorimer, G. W. *J. Microsc.* **1975**, *103* (2), 203–207.

(35) Oxley, M. P.; Varela, M.; Pennycook, T. J.; Van Benthem, K.; Findlay, S. D.; D'Alfonso, A. J.; Allen, L. J.; Pennycook, S. J. *Phys. Rev. B - Condens. Matter Mater. Phys.* **2007**, *76* (6), 1–8.

(36) D'Alfonso, A. J.; Freitag, B.; Klenov, D.; Allen, L. J. *Phys. Rev. B - Condens. Matter Mater. Phys.* **2010**, *81* (10), 2–5.

(37) Allen, L. J.; D'Alfonso, A. J.; Freitag, B.; Klenov, D. O. *MRS Bull.* **2012**, *37* (01), 47–52.

(38) Lu, P.; Romero, E.; Lee, S.; MacManus-Driscoll, J. L.; Jia, Q. *Microsc. Microanal.* **2014**, *20* (06), 1782–1790.

(39) Lu, P.; Zhou, L.; Kramer, M. J.; Smith, D. J. *Sci. Rep.* **2014**, *4*, 3945.

(40) Lugg, N. R.; Kothleitner, G.; Shibata, N.; Ikuhara, Y. *Ultramicroscopy* **2015**, *151*, 150–159.

(41) Kirk, E. C. G.; Williams, D. A.; Ahmed, H. *Inst. Phys. Conf. Ser.* **1989**, *100* (7), 501–506.

(42) Giannuzzi, L. A.; Stevie, F. A. *Introduction to Focused Ion Beams: Instrumentation, Theory, Techniques and Practice*; Springer: New York, 2005.

(43) Schaffer, M.; Schaffer, B.; Ramasse, Q. *Ultramicroscopy* **2012**, *114*, 62–71.

(44) Haider, M.; Uhlemann, S.; Schwan, E.; Rose, H.; Kabius, B. *Nature* **1998**, *392* (6678), 768–769.

(45) Batson, P. E.; Dellby, N.; Krivanek, O. L. *Nature* **2002**, *418* (6898), 617–620.

(46) Muller, D. A.; Fitting Kourkoutis, L.; Murfitt, M.; Song, J. H.; Hwang, H. Y.; Silcox, J.; Dellby, N.; Krivanek, O. L. *Science (80-.).* **2008**, *319*, 1073–1076.

Chapter II

(1) Kirk, E. C. G.; Williams, D. A.; Ahmed, H. *Inst. Phys. Conf. Ser.* **1989**, *100* (7), 501–506.

(2) Overwijk, M. H. F.; Heuvel, F. C. van den; Bulle-Lieuwma, C. W. T. Novel *J. Vac. Sci. Technol. B Microelectron. Nanom. Struct.* **1993**, *11* (6), 2021.

(3) Ishitani, T.; Umemura, K.; Ohnishi, T.; Yaguchi, T.; Kamino, T. *J. Electron Microsc. (Tokyo).* **2004**, *53* (5), 443–449.

(4) Mayer, J.; Giannuzzi, L. a; Kamino, T.; Michael, J. *MRS Bull.* **2007**, *32* (5), 400–407.

(5) Schwarz, S. M.; Kempshall, B. W.; Giannuzzi, L. a; Mccartney, M. R. *Microsc. Soc. Am.* **2003**, *9* (Suppl 2), 116–117.

(6) Buxbaum, a; Schampers, R.; Bolt, J.-J. *Microsc. Microanal.* **2009**, *15* (S2), 334–

335.

(7) Welz, S.; Browning, N.; Minor, A. *Microsc. Microanal.* **2005**, *11* (S02), 834–835.

(8) Vieweg, B. F.; Butz, B.; Peukert, W.; Klupp Taylor, R. N.; Spiecker, E. *Ultramicroscopy* **2012**, *113*, 165–170.

(9) Hosaka, S. *J. Vac. Sci. Technol.* **1978**, *15* (5), 1712.

(10) Tagg, M. A.; Smith, R.; Walls, J. M. *J. Mater. Sci.* **1986**, *21* (1), 123–130.

(11) Altmann, F.; Young, R. J. *J. Micro/Nanolithography, MEMS, MOEMS* **2014**, *13* (1), 011202.

(12) Burnett, T. L.; Kelley, R.; Winiarski, B.; Contreras, L.; Daly, M.; Gholinia, A.; Burke, M. G.; Withers, P. J. *Ultramicroscopy* **2016**, *161*, 119–129.

(13) Yamaguchi, H. *J. Vac. Sci. Technol. B Microelectron. Nanom. Struct.* **1985**, *3* (1), 71.

(14) Young, R. J. *J. Vac. Sci. Technol. B Microelectron. Nanom. Struct.* **1993**, *11* (2), 234.

(15) Krinsley, D.; Ditto, J.; Langworthy, K.; Dorn, R. I.; Thompson, T. *Phys. Geogr.* **2013**, *34* (3), 159–173.

(16) Clarke, J. J. In *Proc. SPIE 9636, Scanning Microscopies*; Postek, M. T., Newbury, D. E., Platek, S. F., Maugel, T. K., Eds.; Monterey, CA, 2015.

(17) Langworthy, K. A.; Krinsley, D. H.; Dorn, R. I. *Earth Surf. Process. Landforms*

2010, *35* (13), 1615–1620.

(18) Larson, P. H.; Dorn, R. I. *Phys. Geogr.* **2012**, *33* (2), 165–182.

(19) Krinsley, D. H.; Dorn, R. I.; DiGregorio, B. E.; Langworthy, K. A.; Ditto, J. *Geomorphology* **2012**, *138* (1), 339–351.

(20) Dorn, R. I. *Rock Coatings*; Elsevier: Amsterdam, 1998.

(21) Paradise, T. R. T. R. *Spec. Pap. Soc. Am.* **2005**, *390* (0), 39–49.

(22) *Stone Decay in the Architectural Environment*; Turkington, A. V., Ed.; The Geological Society of America: Boulder, 2005.

(23) Krinsley, D.; Dorn, R. I.; DiGregorio, B. *Astrobiology* **2009**, *9*, 551–562.

(24) Spilde, M. N.; Melim, L. A.; Northup, D. E.; Boston, P. J. *Geology* **2013**, *41* (2), 263–266.

(25) Liu, T.; Broecker, W. S. *Geology* **2008**, *36* (5), 403–406.

(26) Dorn, R. I. Parsons, A. J., Abrahams, A., Eds.; Springer: Amsterdam, 2009.

(27) Schaffer, M.; Schaffer, B.; Ramasse, Q. *Ultramicroscopy* **2012**, *114*, 62–71.

(28) Fairley, K. C.; Merrill, D. R.; Woods, K. N.; Ditto, J.; Xu, C.; Oleksak, R. P.; Gustafsson, T.; Johnson, D. W.; Garfunkel, E.; Herman, G. S.; Johnson, D. C.; Page, C. J. *ACS Appl. Mater. Interfaces* **2015**.

Chapter III

(1) Lin, Q.; Smeller, M.; Heideman, C. L.; Zschack, P.; Koyano, M.; Anderson, M. D.; Kykyneshi, R.; Keszler, D. A.; Anderson, I. M.; Johnson, D. C. *Chem. Mater.* **2010**, *22*, 1002–1009.

(2) Rouxel, J.; Meerschaut, A.; Wiegers, G. A. *J. Alloys Compd.* **1995**, *229*, 144–157.

(3) Wiegers, G. A. *Prog. Solid State Chem.* **1996**, *24*, 1 – 139.

(4) Noh, M.; Johnson, C. D.; Hornbostel, M. D.; Thiel, J.; Johnson, D. C. *Chem. Mater.* **1996**, *8*, 1625–1635.

(5) Oosawa, Y.; Gotoh, Y.; Akimoto, J.; Tsunoda, T.; Sohma, M.; Onoda, M. *Jap. J. Appl. Phys.* **1992**, *31*, 1096–1099.

(6) Noh, M.; Thiel, J.; Johnson, D. C. *Adv. Science* **1995**, *270*, 1181–1184.

(7) Kalläne, M., Rossnagel, K., Marczynski-Bühlow, M., Kipp, L., Starnberg, H., & Stoltz, S. *Phys. Rev.* ***2008****. 100*(6)

(8) Harris, F. R.; Standridge, S.; Feik, C.; Johnson, D. C. *Ange. Chem.* **2003**, *42*, 5296–9.

(9) Atkins, R.; Wilson, J.; Zschack, P.; Grosse, C.; Neumann, W.; Johnson, D. C.; David, C. *Chem. Mater.* **2012**, 24, 4594-4599.

(10) Mavrokefalos, A.; Lin, Q.; Beekman, M.; Seol, J. H.; Lee, Y. J.; Kong, H.; Pettes, M. T.; Johnson, D. C.; Shi, L. *Appl. Phys. Letters* **2010**, *96*, 181908.

(11) Kiessig, H. *Naturswiss*. **1930**, 18, 847-8

(12) Wainfan, N.; Parratt , L.G. *J Appl. Phys*. **1960,** 31, 1331

(13) Heideman, C.; Nyugen, N.; Hanni, J.; Lin, Q.; Duncombe, S.; Johnson, D. C.; Zschack, P. *J. Solid State Chem.* **2008**, *181*, 1701–1706.

(14) Nguyen, N. T.; Howe, B.; Hash, J. R.; Liebrecht, N.; Zschack, P.; Johnson, D. C. *Chem. Mater.* **2007**, *06*, 1923–1930.

(15) Nguyen, N. T.; Howe, B.; Hash, J. R.; Liebrecht, N.; Johnson, D. C. *Adv. Mater.* **2006**, *18*, 118–122.

(16) Lin, Q.; Heideman, C. L.; Nguyen, N.; Zschack, P.; Chiritescu, C.; Cahill, D. G.; Johnson, D. C. *Euro. J. Inorg. Chem.* **2008**, *2008*, 2382–2385.

(17) Van der Pauw, L. J. *Phil. Tech. Rev.* **1958**, 220–224.

(18) Das, V. D.; Bhat, S. *Phys. Rev. B.* **1989**, *40*, 7696 – 7703.

(19) Hirahara, E.; Murakami, M. *J. Phys. Soc. Japan* **1954**, *9*, 671 – 681.

(20) Edwards, J. S. Electrical conduction in niobium selenide, Simon Fraser University, 1971.

(21) Fister, L.; Li, X. M.; McConnell, J.; Novet, T.; Johnson, D. C. *J. Vac. Sci. T.* **1993**, *11*, 3014–3019.

Chapter IV

(1) Stein, A.; Keller, S. W.; Mallouk, T. E. *Science*, **1993**, 24, 1558−1564.

(2) DiSalvo, F. J. *Pure Appl. Chem*. **2000**, 72, 1799−1807.

(3) DiSalvo, F. J. *Science* **1990**, 247, 649−655.

(4) Wiegers, G. A. *Prog. Solid State Chem*. **1996**, 24, 1−139.

(5) Gotoh, Y.; Onoda, M.; Akimoto, J.; Goto, M.; Oosawa, Y. *Jpn. J. Appl. Phys., Part 1* **1993**, 32, 760−762.

(6) Wiegers, G. A.; Zhou, W. Y. *Mater. Res. Bull.* **1991**, 26, 879−885.

(7) Rouxel, J.; Meerschaut, A.; Wiegers, G. A. *J. Alloys Compd.* **1995**, 229, 144−157.

(8) Schäfer, H. *Angew. Chem., Int. Ed.* **1971**, 10, 43−50.

(9) Giang, N.; Xu, Q.; Hor, Y. S.; Williams, A. J.; Dutton, S. E.; Zandbegen, H. W.; Cava, R. *J. Phys. Rev. B* **2010**, 82 (2), 024503/1−024503/5.

(10) Kalikhman, V. L.; Lobova, T. A.; Pravoverova, L. L. *Neorg. Mater.* **1973**, 9 (6), 923−926.

(11) Kalikhman, V. L.; Kasiyan, I. M.; Mikailyuk, I. P. *Poroshkovaya Metalluriya (Kiev)* **1973**, 11, 75−79.

(12) Kalikhman, V. L.; Pravoverova, L. L. *Neorg. Mater.* **1974**, 10 (7),1190−1194.

(13) Delphine, M. S.; Jayachandran, M.; Sanjeeviraja, C.; Almusallam, A. W. *Int. J. Chem. Technol. Res.* **2011**, 3, 846−852.

(14) Bougouma, M.; Guel, B.; Segato, T.; Legma, J. B.; Delplancke-Ogletree, M.-P. *Bull. Chem. Soc. Ethiopia* **2008**, 22, 225−236.

(15) Chiritescu, C.; Cahill, D. G.; Nguyen, N.; Johnson, D.; Bodapati, A.; Keblinski, P.; Zschack, P. *Science* **2007**, 315, 351−353.

(16) Chiritescu, C.; Cahill, D. G.; Heideman, C.; Lin, Q.; Mortensen, C.; Nguyen, N. T.; Johnson, D.; Rostek, R.; Böttner, H. *J. Appl. Phys*. **2008**, 104, 033533.

(17) Heideman, C.; Nyugen, N.; Hanni, J.; Lin, Q.; Duncombe, S.; Johnson, D. C.; Zschack, P. *J. Solid State Chem.* **2008**, 181, 1701−1706.

(18) Lin, Q.; Smeller, M.; Heideman, C.; Zschack, P.; Koyano, M.; Anderson, M. D.; Kykyneshi, R.; Keszler, D. A.; Anderson, I. M.; Johnson, D. C. *Chem. Mater.* **2010**, 22, 1002−1009.

(19) Moss, S.; Noh, M.; Jeong, K. H.; Kim, D. H.; Johnson, D. C. *Chem. Mater.* **1996**, 8, 1853−1857.

(20) Heideman, C. L.; Rostek, R.; Anderson, M. D.; Herzing, A. A.; Anderson, I. M.; Johnson, D. C. *J. Electron. Mater.* **2010**, 39 (9), 1476−1481.

(21) Lin, Q.; Heideman, C. L.; Nguyen, N.; Zschack, P.; Chiristescu, C.; Cahill, D. G.; Johnson, D. C. Eur. *J. Inorg. Chem.* **2008**, 15, 382−2385.

(22) Beekman, M.; Cogburn, G.; Heideman, C.; Rouvimov, S.; Zschack, P.; Neumann, W.; Johnson, D. C. *J. Electron. Mater.* **2012**, 41,1476−1480.

(23) Atkins, R.; Wilson, J.; Zschack, P.; Grosse, C.; Neumann, W.; Johnson, D. C. *Chem. Mater*. **2012**, 24 (23), 4594−4599.

(24) Vegard, L. *Z. Phys.* **1921**, 5, 17−26.

(25) Denton, A. R.; Ashcroft, N. W. *Phys. Rev. A* **1991**, 43, 3161−3164.

(26) Donovan, J. J.; Tingle, T. N. *J. Microsc. Soc. Am.* **1996**, 2, 1−7.

(27) Heideman, C.; Nyugen, N.; Hanni, J.; Lin, Q.; Duncombe, S.; Johnson, D. C.; Zschack, P. *J. Solid State Chem.* **2008**, 181, 1701−1706.

(28) Lin, Q.; Smeller, M.; Heideman, C. L.; Zschack, P.; Koyano, M.; Anderson, M. D.; Kykyneshi, R.; Keszler, D. A.; Anderson, I. M.; Johnson, D. C. *Chem. Mater.* **2010**, 22, 1002−1009.

(29) Nguyen, N. T.; Berseth, P. A.; Lin, Q.; Chiritescu, C.; Cahill, D. G.; Mavrokefalos, A.; Shi, L.; Zschack, P.; Anderson, M. D.; Anderson, I. M.; Johnson, D. C. *Chem. Mater.* **2010**, 22, 2750−2756.

(30) Lide, D. R., Ed.;*CRC Handbook of Chemistry and Physics*, 84th ed.; CRC Press: **2003**.

(31) Mukhopadhyay, N. K.; Weatherly, G. C. *Mater. Sci. Eng., A* **2001**, 304−306, 855−859.

(32) Carson, K. R.; Rudee, M. L. *J. Vac. Sci. Technol.* **1970**, 7, 573−576.

Chapter V

(1) Fister, L.; Li, X.; McConnell, J.; Novet, T.; Johnson, D.C. *Journal of Vacuum Science and Technology A* **1993**, 11, 3014-3019.

(2) T. Roisnel, J. Rodriguez-Carvajal, *Mater. Sci. Forum* 118 (2001) 378-381.

(3) Phung T.; Jensen J.; Johnson D. C.; Donovan J. J.; McBurnett, B. G. *X-ray Spectrom.*, 2008, 37, 608-614.

(4) C. Grosse, R. Atkins, H. Krimse, A. Mogilatenko, W. Neumann, D. C. Johnson, *J. All. Comp.*, 2013, 579, 507-515.

(5) T. Chattopadhyay, J. Pannetier, H. G. von Schnering, *Z. Kristallogr*. (1985), 170, 29-32.

(6) C. S. Yadav, A. K. Rastogi, *Solid State Comm.* (2010), 150, 648-651.

(7) Atkins, R.; Disch, S.; Jones, Z.; Haeusler, I.; Grosse, C.; Fischer, S.F.; Neumann, W.; Zschack, P.; Johnson, D.C. Synthesis, structure, and electrical properties of a new tin vanadium selenide. *Journal of Solid State Chemistry* 2013, 202, 128-133.

(8) Atkins R.; Dolgos M.; Fiedler A.; Grosse C.; Fischer S. F.; Rudin S. P.; Johnson, D. C., *Chem. Mater.* 2014, 2862-2872.

(9) Matthias Falmbigl, Andreas Fiedler, Ryan E. Atkins, Saskia F. Fischer, David C. Johnson, *Nano Lett.*, (2015), 15(2), 943-948.

(10) M. Beekman, C. L. Heideman, D. C. Johnson, *Semicond. Sci. Technol.* 2014, 29, 064012.

(11) K. S. Novoselov, A. K. Geim, S. V. Morozov, D. Jiang, M. I. Katsnelson, I. V. Grigorieva, S. V. Dubonos, A. A. Firsov, *Nature* (2005) 438, 197-200.

(12) K. S. Novoselov, A. K. Geim, S. V. Morozov, D. Jiang, Y. Zhang, S. V. Dubonos, I. V. Grigorieva, A. A. Firsov. *Science* (2004) 306, 666-669.

(13) Golberg, Y. Bando, Y. Huang, T. Terao, M. Mitome, C. Tang, C. Zhi, *ACS Nano* (2010) 4(6), 2979-2993.

(14) Chhowalla M., Shin H.-S., Eda G., Li L.-J., Loh K.-P., Zhang H., *Nature Chemistry*, 2013, 5, 263-275.

(15) P. Miro, M. Audiffred, T. Heine, *Chem. Soc. Rev.* (2014), 43, 6537.

(16) A. A. Balandin, S. Ghosh, W. Bao, I. Calizo, D. Teweldebrhan, F. Miao, C. N. Lau, *Nano Lett.* (2008), 8(3), 902-907.

(17) C. Lee, X. Wei, J. W. Kysar, J. Hone, *Science* (2008), 321, 385-388.

(18) G. Eda, H. Yamaguchi, D. Voiry, T. Fujita, M. Chen, M. Chhowalla, *Nano Lett.* (2011), 11, 5111-5116.

(19) X. Hong, J. Kim, S. F. Shi, Y. Zhang, C. Jin, Y. Sun, S. Tongay, J. Wu, Y. Zhang, F. Wang, *Nature Nanotechnol.* (2014), 9, 682-686.

(20) Y. Ma, Y. Dai, M. Guo, C. Niu, Y. Zhu, B. Huang, *ACS Nano,* (2012), 6(2), 1695-1701.

(21) M. Callandra, I. I. Mazin, F. Mauri, *Phys. Rev. B,* (2009), 80, 241108.

(22) Y. Ge, A. Y. Liu, *Phys. Rev. B,* (2012), 86, 104101.

(23) P. Goli, J. Khan, D. Wickramaratne, R. K. Lake, A. A. Balandin, *Nanoletters*, 2012, 12, 5941-5945.

(24) J. Yang, W. Wang, Y. Liu, H. Du, W. Ning, G. Zheng, C. Jin, Y. Han, N. Wang, Z. Yang, M. Tian, Y. Zhang, *Applied Physics Letters*, 2014, 105, 063109.

(25) Di Salvo F. J., Moncton D. E., Waszczak J. V., *Phys. Rev. B*, 1976, 14, 4321.

(26) Craven, R. A., Di Salvo F. J., Hsu, F. S. L., *Solid State Comm*. (1978), 25, 39-42.

(27) J. Rouxel, A. Meerschaut, G. A. Wiegers, *J. All. Compnd*. (1995), 229, 144-157.

(28) M. B. Alemayehu, G. Mitchson, J. Ditto, B. E. Hanken, M. Asta, D. C. Johnson, *Chem. Mat.* (2014), 26(5), 1859-1866.

(29) M. B. Alemayehu, M. Falmbigl, K. Ta, C. Grosse, R. D. Westover, S. R. Bauers, S. F. Fischer D. C. Johnson, *Chem. Mat*. (2015), 27(3), 867-875.

(30) L. F. Schneemeyer, M. J. Sienko, *J. Phys. Chem. Solids* (1980), 41, 929-933.

(31) H. Mutka, *Physics and Chemistry of Materials with Low-Dimensional Structures*. (1999), 22, 153-184.

(32) J. Rigoult, C. Guidi-Morosini, A. Tomas, P. Molinie, *Acta Cryst.* (1982), B38, 1557-1559.

Chapter VI

(1) Fister, L.; Li, X.; McConnell, J.; Novet, T.; Johnson, D.C. *Journal of Vacuum Science and Technology A* **1993**, 11, 3014-3019.

(2) Atkins, R.; Disch, S.; Jones, Z.; Haeusler, I.; Grosse, C.; Fischer, S.F.; Neumann, W.; Zschack, P.; Johnson, D.C. *Journal of Solid State Chemistry* 2013, 202, 128-133.

(3) T. Roisnel, J. Rodriguez-Carvajal, Mater. Sci. Forum 118 (2001) 378-381.

(4) Phung T.; Jensen J.; Johnson D. C.; Donovan J. J.; McBurnett, B. G. X-ray Spectrom. 2008, 37, 608-614.

(5) Atkins R.; Dolgos M.; Fiedler A.; Grosse C.; Fischer S. F.; Rudin S. P.; Johnson, D. C., Chem. Mater. 2014, 26, 2862-2872.

(6) Heideman C.; Nguyen N.; Hanni J.; Lin Q.; Duncombe S.; Johnson D. C.; Zschack P., J. Solid State Chem. 2008, 181, 1701-1706.

(7) Platteeuw J. C.; Meyer, G.; Transactions of the Faraday Society 1956, 52, 1066-1073.

(8) Akselrud L.; Grin Y.; J. Appl. Crystallogr. 2014, 47, 803-805.

(9) Long J.A. P.; Vuorelainen Y.; Kouvo O.; American Mineralogist 1963, 48, 33-41.

(10) Rigoult J.; Guidi-Morosini C.; Tomas A.; Molinie P.; Acta Cryst. 1982, B38, 1557-1559.

(11) Falmbigl M.; Alemayehu M. B.; Merrill D. R.; Beekman M.; Johnson D. C.; Crystal Research and Technology 2015, DOI: 10.1002/crat.201500019.

(12) Grosse C.; Atkins R.; Kirmse H.; Mogilatenko A.; Neuann W.; Johnson D. C.; J. Alloys Compnd. 2013, 579, 507-515.

(13) Schneemeyer L. F.; Stacy A.; Sienko M. J.; Inorg. Chem. 1980, 19, 2659-2662.

(14) Bayard M.; Sienko M. J.; Journal Solid State Chem. 1976, 19, 325-329.

(15) Eaglesham D. J.; Withers R. L.; Bird D. M.; J: Phys. C: Solid State Phys. 1986, 19, 359,367.

(16) Giambattista B.; Slough C. G.; McNairy W. W.; Coleman R. V. Phys. Rev. B 1990, 41(14), 10082-10103.

(17) Zunger A.; Freeman A. J.; Phys. Rev. B 1979, 19(12), 6001-6009.

(18) H. N. S. Lee, M. Garcia, H. McKinzie, A. Wold, J. Solid State Chem. (1970), 1, 190-194.

(19) L. Hernan, J. Morales, J. Pattanayak, J. L. Tirado, J. Solid State Chem. 1992, 100, 262.

(20) L. Hernan, J. Morales, L. Sanchez, J. L. Tirado, Solid State Ionics, 1992, 58,179.

(21) L. Hernan, P. Lavela, J. Morales, J. Pattanayak J. L. Tirado, Mater. Res. Bull. 1991, 26, 1211.

(22) C. Barriga, P. Lavela, J. Morales, J. Pattanayak, J. L. Tirado, Chem. Mater. 1992, 4, 1021.

(23) C. Barriga, P. Lavela, J. Morales, J. L. Tirado, Solid State Ionics, 1993, 63-65, 450.

(24) B. A. Trump, K. J. T. Livi, T. M. McQueen, J. Solid State Chem. 2014, 209, 6-12.

(25) E. Rost, L. Gjertsen, Z. Anorg. Allg. Chem. 1964, 328, 299-308.

(26) M. Falmbigl, D. Putzky, J. Ditto, M. Esters, S. Bauers, F. Ronning, D. C. Johnson, ACS Nano 2015, submitted.

Chapter VII

(1) Stein, A.; Keller, S.; Mallouk, T. *Science.* **1993**, *259*, 1558–1564.

(2) S.M.Sze. *Semiconductor Devices Physics and Technology*; Zobrist, W., Ed.; John Wiley and Sons, 2002.

(3) Wiegers, G.; Haange, R. *Eur. J. Solid State Inorg. Chem.* **1991**. *28*, 1071-1078.

(4) Harris, F. R.; Standridge, S.; Johnson, D. C. *J. Am. Chem. Soc.* **2005**, *127*, 7843–7848.

(5) Lin, Q.; Smeller, M.; Heideman, C. L.; Zschack, P.; Koyano, M.; Anderson, M. D.; Kykyneshi, R.; Keszler, D. A.; Anderson, I. M.; Johnson, D. C. *Chem. Mater.* **2010**, *22*, 1002–1009.

(6) Moore, D.; Stolt, M.; Atkins, R.; Sitts, L.; Jones, Z.; Disch, S.; Beekman, M.; Johnson, D. *Emerg. Mater. Res.* **2012**, *1*, 292–298.

(7) Phung, T.; Jensen, J.; Johnson, D. C.; Donovan, J. J.; McBurnett, B. G. *X-Ray Spectrom.* **2008**, *37*, 608–614.

(8) Van der Pauw, L. J. *Philips Tech. Rev.* **1958**, *20*, 220–224.

(9) Moore, D. B.; Sitts, L.; Stolt, M. J.; Beekman, M.; Johnson, D. C. *J. Electron. Mater.* **2012**, *42*, 1647–1651.

(10) Snyder, G.; Toberer, E. *Nat. Mater.* **2008**, *7*, 105–114.

Chapter VIII

(1) M. Chhowalla, H.-S. Shin, G. Eda, L.-J. Li, K.-P. Loh and H. Zhang, *Nat. Chem.*, 2013, 5, 263–275.

(2) H. Terrones and M. Terrones, *J. Mater. Res.*, 2014, 29, 373–382.

(3) C. Tan and H. Zhang, *Chem. Soc. Rev.*, 2014, 44, 2713–2731.

(4) H. Yuan, H. Wang and Y. Cui, *Acc. Chem. Res.*, 2015, 48, 81–90.

(5) R. Lv, J. A. Robinson, R. E. Schaak, D. Sun, Y. Sun, T. E. Mallouk and M. Terrones, *Acc. Chem. Res.*, 2015, 48, 56–64.

(6) M. Bayard and M. J. Sienko, *J. Solid State Chem.*, 1976, 19, 325–329.

(7) C. F. van Bruggen and C. Haas, *Solid State Commun.*, 1976, 20, 251–254.

(8) F. Li, K. Tu and Z. Chen, *J. Phys. Chem. C*, 2014, 118, 21264–21274.

(9) P. Goli, J. Khan, D. Wickramaratne, R. K. Lake and A. A. Balandin, *Nano Lett.*, 2012, 12, 5941–5945.

(10) R. Samnakay, D. Wickramaratne, T. R. Pope, R. K. Lake, T. T. Salguero and A. A. Balandin, *Nano Lett.*, 15, 2965–2973.

(11) J. Yang, W. Wang, Y. Liu, H. Du, W. Ning, G. Zheng, C. Jin, Y. Han, N. Wang, Z. Yang, M. Tian and Y. Zhang, *Appl. Phys. Lett.*, 2014, 105, 063109.

(12) K. Xu, P. Chen, X. Li, C. Wu, Y. Guo, J. Zhao, X. Wu and Y. Xie, Angew. Chem., Int. Ed., 2013, 52, 10477–10481.

(13) Y. Ma, Y. Dai, M. Guo, C. Niu, Y. Zhu and B. Huang, ACS Nano, 2012, 6, 1695–1701.

(14) N. Ogawa and K. Miyano, Appl. Phys. Lett., 2002, 80, 3225–3227.

(15) J. Renteria, R. Samnaky, C. Jiang, T. R. Pope, P. Goli, Z. Yan, D. Wickramaratne, T. T. Salguero, A. G. Khitun, R. K. Lake and A. A. Balandin, J. Appl. Phys., 2014, 115, 034305.

(16) J. Khan, C. M. Nolen, D. Teweldebrhan, D. Wickramaratne, R. K. Lake and A. A. Balandin, Appl. Phys. Lett., 2012, 100, 043109.

(17) D. Mihailovic, D. Dvorsek, V. V. Kabanov, J. Demsar, L. Forro and H. Berger, Appl. Phys. Lett., 2002, 80, 871–873.

(18) L. F. Schneemeyer, A. Stacy and M. J. Sienko, Inorg. Chem., 1980, 19, 2659–2662.

(19) L. F. Schneemeyer and M. J. Sienko, J. Phys. Chem. Solids, 1980, 41, 929–933.

(20) F. J. diSalvo and J. V. Wasczak, J. Phys., Colloq., 1976, 4, 157.

(21) C. S. Yadav and A. K. Rastogi, J. Phys.: Condens. Matter, 2008, 20, 465219.

(22) Atkins, S. Disch, Z. Jones, I. Haeusler, C. Grosse, F. Fischer, W. Neumann, P. Zschack and D. C. Johnson, J. Solid State Chem., 2013, 202, 128–133.

(23) Atkins, M. Dolgos, A. Fiedler, C. Grosse, S. F. Fischer, P. Rudin and D. C. Johnson, Chem. Mater., 2014, 26, 2862–2872.

(24) M. Falmbigl, A. Fiedler, R. E. Atkins, S. F. Fischer and D. C. Johnson, Nano Lett., 2015, 15, 943–948.

(25) M. Falmbigl, D. Putzky, J. Ditto, M. Esters, S. R. Bauers, F. Ronning and D. C. Johnson, ACS Nano, 2015, 9, 8440–8448.

(26) M. Beekman, C. L. Heideman and D. C. Johnson, Semicond. Sci. Technol., 2014, 29, 064012.

(27) O. K. Hite, M. Nellist, J. Ditto, M. Falmbigl and D. C. Johnson, J. Mater. Res., 2015, submitted.

(28) G. A. Wiegers, Prog. Solid State Chem., 24, 1–139.

(29) K. Harada and T. Ohtani, J. Jpn. Soc. Powder Powder Metall., 2008, 55, 185–191.

(30) D. R. Merrill, D. B. Moore, M. N. Coffey, A. W. Jansons, M. Falmbigl and D. C. Johnson, Semicond. Sci. Technol., 2014, 29, 064004.

(31) L. Fister, X. Li, J. McConnell, T. Novet and D. C. Johnson, J. Vac. Sci. Technol., A, 1993, 11, 3014–3019.

(32) T. Phung, J. Jensen, D. C. Johnson, J. J. Donovan and B. G. McBurnett, X-ray Spectrom., 2008, 37, 608–614.

(33) M. Noh. J. Thiel and D. C. Johnson, Adv. Mater., 1996, 8, 596–599.

(34) G. A. Wiegers and W. Y. Zhou, Mater. Res. Bull., 1991, 26, 879–885.

(35) W. Y. Zhou, A. Meetsma, J. L. de Boer and G. A. Wiegers, Mater. Res. Bull., 1992, 27, 563–572.

(36) C. Heideman, N. Nguyen, J. Hanni, Q. Lin, S. Duncombe, D. C. Johnson and P. Zschack, J. Solid State Chem., 2008, 181, 1701–1706.

(37) M. Falmbigl, M. B. Alemayehu, D. R. Merrill, M. Beekman and D. C. Johnson, Cryst. Res. Technol., 2015, 6, 464–472.

(38) T. Chattopadhyay, J. Pannetier and H. G. von Schnering, Z. Kristallogr., 1985, 170, 29–32.

(39) A. A. Sher, I. P. Odin and A. V. Novoselova, Russ. J. Inorg. Chem., 1986, 31, 435–437.

(40) S. R. Wood, D. R. Merrill, M. Falmbigl, D. B. Moore, J. Ditto, M. Esters and D. C. Johnson, Chem. Mater., 2015, 27, 6067–6076.

(41) V. Petˇr´ıˇcek, I. Cisarova, J. L. de Boer, W. Zhou, A. Meetsma, G. A. Wiegers and S. van Smaalen, Acta Crystallogr., Sect. B: Struct. Sci., 1993, 49, 258–266.

(42) G. Rigoult, C. Guidi-Morosini, A. Tomas and P. Molinie, Acta Crystallogr., 1982, B38, 1557–1559.

(43) A. Zunger and A. J. Freeman, Phys. Rev. B: Condens. Matter Mater. Phys., 1979, 19, 6001–6009.

(44) A. B. Beal and W. Y. Liang, J. Phys. C: Solid State Phys., 1973, 6, L482.

(45) U. Chatterjee, J. Zhao, M. Iavarone, R. Di Capua, J. P. Castellan, G. Karapetrov, C. D. Malliakas, M. G. Kanatzidis, H. Claus, J. P. C. Ruff , F. Weber, J. van Wenzel, J. C. Campuzano, Osborn, M. Randeria, N. Trivedi, M. R. Norman and Rosenkranz, Nat. Commun., 2015, 6, 6313.

(46) A. H. Reshak and S. Auluck, Phys. B, 2004, 349, 310–315.

(47) A. Gowri Manohari, S. Dhanapandian, C. Manoharan, K. Santhosh Kumar and T. Mahalingam, Mater. Sci. Semicond. Process., 2014, 17, 138–142.

(48) H. N. S. Lee, M. Garcia, H. McKinzie and A. Wold, J. Solid State Chem., 1970, 1, 190–194.

Chapter IX

(1) Hicks, L.; Dresselhaus, M. *Phys. Rev. B* 1993, *47*, 727–731.

(2) Slack GA., CRC Handbook of Thermoelectrics, ed. DM Rowe, Boca Raton, FL: CRC Press (1995) ISBN 0-8493-0146-7.

(3) Nolas, GS; Morelli, DT; Tritt, TM. *Annu. Rev. Mater. Sci*. **1999**, *29*, 89–116.

(4) Terasaki, I.; Sasago, Y.; Uchinokura, K. *Phys. Rev. B* **1997**, *56*, 685–687.

(5) Wan, C.; Wang, Y.; Wang, N.; Koumoto, K. *Materials (Basel).* **2010**, *3*, 2606–2617.

(6) Guilmeau, E.; Bréard, Y.; Maignan, a. *Appl. Phys. Lett.* **2011**, *99*, 052107.

(7) de Boer, D.; Bruggen, C. Van; Bus, G. *Phys. Rev. B* **1984**, *29*, 6797.

(8) Klipstein, P.; Bagnall, A. *J. Phys. C …* **1981**, *14*, 4067–4081.

(9) Rasch, J.; Stemmler, T.; Müller, B.; Dudy, L.; Manzke, R. *Phys. Rev. Lett.* **2008**, *237602*, 2–5.

(10) R. D. Barnard. Thermoelectricity in Metals and Alloys (Wiley, New York, **1972**).

(11) Bhatt, R.; Basu, R.; Bhattacharya, S.; Singh, A. *Appl. Phys. A* **2013**, 465–470.

(12) Bhatt, R.; Bhattacharya, S.; Patel, M.; Basu, R.; Singh, A.; Sürger, C.; Navaneethan, M.; Hayakawa, Y.; Aswal, D. K. *J. Appl. Phys.* **2013**, *114*, 114509.

(13) Giang, N.; Xu, Q.; Hor, Y.; Williams, A.; Dutton, S.; Zandbergen, H.; Cava, R. *Phys. Rev. B* **2010**, *82*, 1–5.

(14) Moore, D. B.; Stolt, M. J.; Atkins, R.; Sitts, L.; Jones, Z.; Disch, S.; Matt, B.; Johnson, D. C. *Emerg. Mater. Res.* **2012**, *1*, 292–298.

(15) Moore, D. B.; Beekman, M.; Disch, S.; Zschack, P.; Häusler, I.; Neumann, W.; Johnson, D. C. *Chem. Mater.* **2013**, *25*, 2404–2409.

(16) Chiritescu, C.; Cahill, D. G.; Nguyen, N.; Johnson, D.; Bodapati, A.; Keblinski, P.; Zschack, P. *Science* **2007**, *315*, 351–353.

(17) Chiritescu, C.; Cahill, D. G.; Heideman, C.; Lin, Q.; Mortensen, C.; Nguyen, N. T.; Johnson, D.; Rostek, R.; Böttner, H. *J. Appl. Phys.* **2008**, *104*, 033533.

(18) Roisnel, T.; Rodríquez-Carvajal, J. *Mater. Sci. Forum* **2001**, *378-381*, 118–123.

(19) Phung, T.; Jensen, J.; Jonshon, D.; Donovan, J.; McBurnett, B. *X-Ray Spectrom.* **2008**, *37*, 608–614.

(20) Heideman, C.; Nyugen, N.; Hanni, J.; Lin, Q.; Duncombe, S.; Johnson, D. C.; Zschack, P. *J. Solid State Chem.* **2008**, *181*, 1701–1706.

(21) Atkins, R.; Disch, S.; Jones, Z.; Haeusler, I.; Grosse, C.; Fischer, S. F.; Neumann, W.; Zschack, P.; Johnson, D. C. *J. Solid State Chem.* **2013**, *202*, 128–133.

(22) Atkins, R.; Wilson, J.; Zschack, P.; Grosse, C.; Neumann, W.; Johnson, D. C. *Chem. Mater.* **2012**, *24*, 4594–4599.

(23) Wiegers, G.; Meetsma, A. *J.Phys. Condens. Matter* **1991**, 2603.

(24) Grosse, C.; Atkins, R.; Kirmse, H.; Mogilatenko, A.; Neumann, W.; Johnson, D. C. *Alloy. Compd.* **2013**, *579*, 507–515.

(25) Parratt, L. *Phys. Rev.* **1954**, *95*, 359–362.

(26) Greenaway, D. L.; Nitsche, R. *J. Phys. Chem. Solids* **1965**, *26*, 1445–1458.

(27) Chattopadhyay, T.; Pannetier, J.; von Schnering, H. *J. Phys. Chem. Solids* **1986**, *47*, 879–885.

(28) Beekman, M.; Cogburn, G.; Heideman, C.; Rouvimov, S.; Zschack, P.; Neumann, W.; Johnson, D. C. *J. Electron. Mater.* **2012**, *41*, 1476–1480.

(29) Smeller, M. M.; Heideman, C. L.; Lin, Q.; Beekman, M.; Anderson, M. D.; Zschack, P.; Anderson, I. M.; Johnson, D. C. *Zeitschrift für Anorg. und Allg. Chemie* **2012**, *638*, 2632–2639.

(30) Wiegers, G.; Haange, R. *Eur. J. Solid State Inorg. Chem.* **1991**, *28*, 1071–1078.

(31) Di Salvo, F. J.; Moncton, D. E.; Waszczak, J. V. *Phys. Rev. B* **1976**, *14*, 4321.

(32) Moore, D. B.; Sitts, L.; Stolt, M. J.; Beekman, M.; Johnson, D. C. *J. Electron. Mater.* **2012**, *42*, 1647–1651.

(33) Altshuler, B.; Khmel'Nitzkii, D.; Larkin, A.; Lee, P. *Phys. Rev. B* **1980**, *22*, 5142–5153.

(34) Wiegers, G. A. *Prog. Solid St. Chem.* **1996**, *24*, 1–139.

(35) Merrill, D. R.; Moore, D. B.; Coffey, M. N.; Jansons, A. W.; Falmbigl, M.; Johnson, D. C. *Semicond. Sci. Technol.* **2014**, *29*, 064004.

(36) Heideman, C. L.; Johnson, D. C. *Semicond. Sci. Technol.* **2014**, *29*, 064007.

(37) Lin, Q.; Tepfer, S.; Heideman, C.; Mortensen, C.; Nguyen, N.; Zschack, P.; Beekman, M.; Johnson, D. C. *J. Mater. Res.* **2011**, *26*, 1866–1871.

(38) Blatt FJ. Physics of electronic conduction in solids. New York: McGraw-Hill; 1968. p. 210.

(39) Snyder, G.; Toberer, E. *Nat. Mater.* **2008**, *7*, 105–114.

(40) Schaffer, M.; Schaffer, B.; Ramasse, Q. *Ultramicroscopy* **2012**, 114, 62–71.

Chapter X

(1) Geim, A. K.; Grigorieva, I. V. *Nature* **2013**, *499*, 419–425.

(2) Terrones, H.; López-Urías, F.; Terrones, M. *Sci. Rep.* **2013**, *3*, 1549.

(3) Lee, C.-H.; Lee, G.-H.; van der Zande, A. M.; Chen, W.; Li, Y.; Han, M.; Cui, X.; Arefe, G.; Nuckolls, C.; Heinz, T. F.; et al. *Nat. Nanotechnol.* **2014**, *9*, 676–681.

(4) Hong, X.; Kim, J.; Shi, S.-F.; Zhang, Y. Y.; Jin, C.; Sun, Y.; Tongay, S.; Wu, J.; Zhang, Y. Y.; Wang, F. *Nat. Nanotechnol.* **2014**, *9*, 1–5.

(5) Esters, M.; Alemayehu, M. B.; Jones, Z.; Nguyen, N. T.; Anderson, M. D.; Grosse, C.; Fischer, S. F.; Johnson, D. C. *Angew. Chemie* **2015**, *127*, 1130–1134.

(6) Alemayehu, M. B.; Mitchson, G.; Ditto, J.; Hanken, B. E.; Asta, M.; Johnson, D. C. *Chem. Mater.* **2014**, *26*, 1859–1866.

(7) Alemayehu, M. B.; Falmbigl, M.; Ta, K.; Grosse, C.; Westover, R. D.; Bauers, S. R.; Fischer, S. F.; Johnson, D. C. *Chem. Mater.* **2015**, *27*, 867–875.

(8) Alemayehu, M. B.; Ta, K.; Falmbigl, M.; Johnson, D. C. *Nanoscale* **2015**, *7*, 7378–7385.

(9) Merrill, D. R.; Moore, D. B.; Ditto, J.; Sutherland, D. R.; Falmbigl, M.; Winkler, M.; Pernau, H.-F.; Johnson, D. C. *Eur. J. Inorg. Chem.* **2015**, *2015*, 83–91.

(10) Moore, D. B.; Beekman, M.; Disch, S.; Zschack, P.; Häusler, I.; Neumann, W.; Johnson, D. C. *Chem. Mater.* **2013**, *25*, 2404–2409.

(11) Moore, D. B.; Stolt, M. J.; Atkins, R.; Sitts, L.; Jones, Z.; Disch, S.; Beekman, M.; Johnson, D. C. *Emerg. Mater. Res.* **2012**, *1*, 292–298.

(12) Merrill, D. R.; Moore, D. B.; Coffey, M. N.; Jansons, A. W.; Falmbigl, M.; Johnson, D. C. *Semicond. Sci. Technol.* **2014**, *29*, 064004.

(13) Oosawa, Y.; Gotoh, Y.; Akimoto, J.; Onoda, M. *J. Alloys Compd.* **1991**, *176*, 319–327.

(14) Trump, B. A.; Livi, K. J. T.; McQueen, T. M. Series. *J. Solid State Chem.* **2014**, *209*, 6–12.

(15) Wiegers, G. A. *Prog. Solid State Chem.* **1996**, *24*, 1–139.

(16) Wan, C.; Wang, Y.; Wang, N.; Koumoto, K. *Materials (Basel).* **2010**, *3*, 2606–2617.

(17) Clarke, S. M.; Freedman, D. E. *Inorg. Chem.* **2015**, *54*, 2765–2771.

(18) Zhou, W. Y.; Meetsma, A.; de Boer, J. L.; Wiegers, G. A. *Mater. Res. Bull.* **1992**, *27*, 563–572.

(19) Petříček, V.; Cisarova, I.; de Boer, J. L.; Zhou, W.; Meetsma, A.; Wiegers, G. A.; van Smaalen, S. *Acta Crystallogr. Sect. B Struct. Sci.* **1993**, *49*, 258–266.

(20) Phung, T. M.; Jensen, J. M.; Johnson, D. C.; Donovan, J. J.; McBurnett, B. G. *X-Ray Spectrom.* **2008**, *37*, 608–614.

(21) Heideman, C.; Nyugen, N.; Hanni, J.; Lin, Q.; Duncombe, S.; Johnson, D. C.; Zschack, P. *J. Solid State Chem.* **2008**, *181*, 1701–1706.

(22) Roisnel, T.; Rodríquez-Carvajal, J. *Materials Science Forum*, 2001, *378-381*, 118–123.

(23) Akselrud, L.; Grin, Y. *J. Appl. Crystallogr.* **2014**, *47*, 803–805.

(24) Kang, H.-J.; Kim, J.; Oh, J.; Back, T.; Kim, H. *Microsc. Microanal.* **2010**, *16*, 170–171.

(25) Schaffer, M.; Schaffer, B.; Ramasse, Q. *Ultramicroscopy* **2012**, *114*, 62–71.

(26) Pauw, L. J. van der. *Philips Res. Reports* **1958**, *13*, 1–9.

(27) McTaggart, F.; Wadsley, A. *Aust. J. Chem.* **1958**, *11*, 445.

(28) Gobrecht, H.; Boeters, K.-E.; Pantzer, G. *Zeitschrift für Phys.* **1964**, *177*, 68–83.

(29) Warren, B. E. *Phys. Rev.* **1941**, *59*, 693–698.

(30) Bauers, S. R.; Moore, D. B.; Ditto, J.; Johnson, D. C. *J. Alloys Compd.* **2015**, *645*, 118–124.

(31) Merrill, D.; Moore, D.; Bauers, S.; Falmbigl, M.; Johnson, D. *Materials (Basel).* **2015**, *8*, 2000–2029.

(32) Ziman, J. M. *Electrons and Phonons: The Theory of Transport Phenomena in Solids*, 1st ed.; Clarendon Press: Oxford, 1960.

(33) Altshuler, B. L.; Khmel'nitzkii, D.; Larkin, A. I.; Lee, P. A. *Phys. Rev. B* **1980**, *22*, 5142–5153.

(34) Di Salvo, F. J.; Moncton, D. E.; Waszczak, J. V. *Phys. Rev. B* **1976**, *14*, 4321–4328.

(35) Kusmartseva, A. F.; Sipos, B.; Berger, H.; Forró, L.; Tutiš, E. *Phys. Rev. Lett.* **2009**, *103*, 236401.

(36) Woo, K. C.; Brown, F. C.; McMillan, W. L.; Miller, R. J.; Schaffman, M. J.; Sears, M. P. *Phys. Rev. B* **1976**, *14*, 3242–3247.

(37) Li, G.; Hu, W. Z.; Qian, D.; Hsieh, D.; Hasan, M. Z.; Morosan, E.; Cava, R. J.; Wang, N. L. *Phys. Rev. Lett.* **2007**, *99*, 2–5.

(38) Bhatt, R.; Bhattacharya, S.; Basu, R.; Ahmad, S.; Chauhan, a. K.; Okram, G. S.; Bhatt, P.; Roy, M.; Navaneethan, M.; Hayakawa, Y.; et al. Enhanced *ACS Appl. Mater. Interfaces* **2014**, *6*, 18619–18625.

(39) Giang, N.; Xu, Q.; Hor, Y. S.; Williams, A. J.; Dutton, S. E.; Zandbergen, H. W.; Cava, R. J. *Phys. Rev. B* **2010**, *82*, 024503.

(40) Atkins, R.; Disch, S.; Jones, Z.; Haeusler, I.; Grosse, C.; Fischer, S. F.; Neumann, W.; Zschack, P.; Johnson, D. C. *J. Solid State Chem.* **2013**, *202*, 128–133.

(41) Atkins, R.; Dolgos, M.; Fiedler, A.; Grosse, C.; Fischer, S. F.; Rudin, S. P.; *Chem. Mater.* **2014**, *26*, 2862–2872.

(42) Falmbigl, M.; Fiedler, A.; Atkins, R. E.; Fischer, S. F.; Johnson, D. C. *Nano Lett.* **2015**, *15*, 943–948.

(43) Falmbigl, M.; Putzky, D.; Ditto, J.; Esters, M.; Bauers, S. R.; Ronning, F.; Johnson, D. C. *ACS Nano* [Online early access]. DOI: 10.1021/acsnano.5b03361. Published Online: 14 July 2015. http://pubs.acs.org/doi/abs/10.1021/acsnano.5b03361 (accessed 10 Aug 2015).

(44) Bhatt, R.; Basu, R.; Bhattacharya, S.; Singh, A.; Aswal, D. K.; Gupta, S. K.; Okram, G. S.; Ganesan, V.; Venkateshwarlu, D.; Surgers, C.; et al. *Appl. Phys. A* **2013**, *111*, 465–470.

(45) Snyder, G. J.; Toberer, E. S. *Nat. Mater.* **2008**, *7*, 105–114.

Chapter XI

(1) A.K. Geim: Science. 324(5934), 1530 (2009).

(2) Q.H. Wang, K. Kalantar-Zadeh, A. Kis, J.N. Coleman, M.S. Strano: Nat. Nanotechnol. 7(11), 699–712 (2012).

(3) H. Wang, H. Yuan, S.S. Hong, Y. Li, Y. Cui: Chem. Soc. Rev. 44(9), 2664-2680 (2015).

(4) M.S. El-Bana, D. Wolverson, S. Russo, G. Balakrishnan, D.M. Paul, S.J. Bending: Supercond. Sci. Technol. 26(12), 125020 (2013).

(5) M.D. Anderson, C.L. Heideman, Q. Lin, M. Smeller, R. Kokenyesi, A. a. Herzing, I.M. Anderson, D.A. Keszler, P. Zschack, D.C. Johnson: Angew. Chemie - Int. Ed. 52(7), 1982-1985 (2013)

(6) A.K. Geim, I. V. Grigorieva: Nature. 499(7459), 419-425 (2013).

(7) Q. Zeng, H. Wang, W. Fu, Y. Gong, W. Zhou, P.M. Ajayan, J. Lou, Z. Liu: Small. 11(16), 1868-1884 (2015).

(8) X. Qian, J. Liu, L. Fu, J. Li: Science. 346(6215), 1344-1347 (2014).

(9) W. Yang, G. Chen, Z. Shi, C.-C. Liu, L. Zhang, G. Xie, M. Cheng, D. Wang, R. Yang, D. Shi, K. Watanabe, T. Taniguchi, Y. Yao, Y. Zhang, G. Zhang: Nat. Mater. 12(9), 792-797 (2013).

(10) Y. Gong, S. Lei, G. Ye, B. Li, Y. He, K. Keyshar, X. Zhang, Q. Wang, J. Lou, Z. Liu, R. Vajtai, W. Zhou, P.M. Ajayan: Nano Lett. (2015). doi: 10.1021/acs.nanolett.5b02423.

(11) C.L. Heideman, S. Tepfer, Q. Lin, R. Rostek, P. Zschack, M.D. Anderson, I.M. Anderson, D.C. Johnson: J. Am. Chem. Soc. 135(30), 11055-11062 (2013).

(12) M. Bayard, M.J. Sienko: J. Solid State Chem. 19(4), 325-329 (1976).

(13) K. Xu, P. Chen, X. Li, C. Wu, Y. Guo, J. Zhao, X. Wu, Y. Xie: Angew. Chem. Int. Ed. Engl. 52(40), 10477-10481 (2013).

(14) J. Yang, W. Wang, Y. Liu, H. Du, W. Ning, G. Zheng, C. Jin, Y. Han, N. Wang, Z. Yang, M. Tian, Y. Zhang: Appl. Phys. Lett. 105(6), 063109 (2014).

(15) R. Atkins, S. Disch, Z. Jones, I. Haeusler, C. Grosse, S.F. Fischer, W. Neumann, P. Zschack, D.C. Johnson: J. Solid State Chem. 202, 128-133 (2013).

(16) M. Falmbigl, A. Fiedler, R.E. Atkins, S.F. Fischer, D.C. Johnson: Nano Lett. 15(2) 943-948 (2015).

(17) W.Y. Zhou, A. Meetsma, J.L. de Boer, G.A. Wiegers: Mater. Res. Bull. 27, 563-572 (1992).

(18) G.A. Wiegers: Prog. Solid State Chem. 24, 1-139 (1996).

(19) V. Petříček, I. Cisarova, J.L. de Boer, W. Zhou, a. Meetsma, G. a. Wiegers, S. van Smaalen: Acta Crystallogr. Sect. B Struct. Sci. 49(2), 258-266 (1993).

(20) L. Fister:. J. Vac. Sci. Technol. A. 11(6), 3014 (1993).

(21) M. Schaffer, B. Schaffer, Q. Ramasse: Ultramicroscopy. 114, 62-71 (2012).

(22) V. Der Pauw: Philips Tech. Rev. 26, 220-224 (1958).

(23) C. Heideman, N. Nyugen, J. Hanni, Q. Lin, S. Duncombe, D.C. Johnson, P. Zschack: J. Solid State Chem. 181(7), 1701-1706 (2008).

(24) C. Grosse, R. Atkins, H. Kirmse, A. Mogilatenko, W. Neumann, D.C. Johnson: J. Alloys Compd. 579, 507-515 (2013).

(25) M.B. Alemayehu, M. Falmbigl, C. Grosse, K. Ta, S.F. Fischer, D.C. Johnson: J. Alloys Compd. 619, 816-868 (2015).

(26) G. Mitchson, M. Falmbigl, J. Ditto, D.C. Johnson, Inorganic Chemistry. DOI: 10.1021/acs.inorgchem.5b01648, Published Online 14 October 2015.

Chapter XII

(1) Wiegers, G. A. *Prog. Solid State Chem.* **1996**, *24*, 1–139.

(2) Rouxel, J.; Meerschaut, A.; Wiegers, G. A. *J. Alloys Compd.* **1995**, *229*, 144–157.

(3) Wiegers, G. A. *J. Alloys Compd.* **1995**, *219*, 152–156.

(4) Beekman, M.; Heideman, C. L.; Johnson, D. C. *Semicond. Sci. Technol.* **2014**, *29*, 064012.

(5) Alemayehu, M. B.; Mitchson, G.; Hanken, B. E.; Asta, M.; Johnson, D. C. *Chem. Mater.* **2014**, *26*, 1859–1866.

(6) Alemayehu, M. B.; Falmbigl, M.; Ta, K.; Grosse, C.; Westover, R. D.; Bauers, S. R.; Fischer, S. F.; Johnson, D. C. *Chem. Mater.* **2015**, *27*, 867–875.

(7) Wan, C.; Wang, Y.; Wang, N.; Koumoto, K. *Materials (Basel).* **2010**, *3*, 2606–2617.

(8) Merrill, D. R.; Moore, D. B.; Coffey, M. N.; Jansons, A. W.; Falmbigl, M.; Johnson, D. C. *Semicond. Sci. Technol.* **2014**, *29*, 064004.

(9) Trump, B. a.; Livi, K. J. T.; McQueen, T. M. *J. Solid State Chem.* **2014**, *209*, 6–12.

(10) Zhou, W.; Meetsma, A.; de Boer, J. L.; Wiegers, G. A. *Mater. Res. Bull.* **1992**, *27*, 563–572.

(11) Wulff, J.; Meetsma, A.; Haange, R. J.; de Boer, J. L.; Wiegers, G. A. *Synth. Met.* **1990**, *39*, 1–12.

(12) Gotoh, Y.; Onoda, M.; Akimoto, J.; Goto, M.; Oosawa, Y. *Jpn. J. Appl. Phys.* **1992**, *31*, 3946–3950.

(13) Knop, O.; Boyd, R. J.; Choi, S. C. *J. Am. Chem. Soc.* **1988**, *110*, 7299–7301.

(14) Petříček, V.; Cisarova, I.; de Boer, J. L.; Zhou, W.; Meetsma, A.; Wiegers, G. A.; van Smaalen, S. *Acta Crystallogr. Sect. B Struct. Sci.* **1993**, *49*, 258–266.

(15) Gotoh, Y.; Akimoto, J.; Goto, M.; Oosawa, Y.; Onoda, M. *J. Solid State Chem.* **1995**, *116*, 61–67.

(16) Pervov, V. S.; Makhonina, E. V. *Russ. Chem. Rev.* **2000**, *69*, 481–489.

(17) Gaudin, E.; Jobic, S.; Evain, M.; Brec, R.; Rouxel, J. *Mater. Res. Bull.* **1995**, *30*, 549–561.

(18) Semiletov, S. A. *Tr. Instituta Krist. Akad. Nauk SSSR* **1954**, *10*, 76–83.

(19) Gobrecht, H.; Boeters, K.-E.; Pantzer, G. *Zeitschrift fur Phys.* **1964**, *177*, 68–83.

(20) Lind, H.; Lidin, S.; Häussermann, U. *Phys. Rev. B.* **2005**, *72*, 1–8.

(21) Kadijk, F.; Jellinek, F. *J. Less-common Met.* **1971**, *23*, 437–441.

(22) Berthier, C.; Molinie, P.; Jerome, D. *Solid State Commun.* **1976**, *18*, 1393–1395.

(23) Heideman, C.; Nyugen, N.; Hanni, J.; Lin, Q.; Duncombe, S.; Johnson, D. C.; Zschack, P. *J. Solid State Chem.* **2008**, *181*, 1701–1706.

(24) Roisnel, T.; Rodriguez-Carvajal, J. *Mater. Sci. Forum* **2001**, *378-381*, 118–123.

(25) Akselrud, L. G.; Grin, Y. *J. Appl. Crystallogr.* **2014**, *47*, 803–805.

(26) Schaffer, M.; Schaffer, B.; Ramasse, Q. *Ultramicroscopy* **2012**, *114*, 62–71.

(27) Phung, T. M.; Jensen, J. M.; Johnson, D. C.; Donovan, J. J.; Mcburnett, B. G. *X-Ray Spectrom.* **2008**, *37*, 608–614.

(28) Van der Pauw, L. J. *Philips Tech. Rev.* **1958**, *20*, 220–224.

(29) Gotoh, Y.; Onoda, M.; Uchida, K.; Tanaka, Y.; Iida, T.; Hayakawa, H.; Oosawa, Y. *Chem. Lett.* **1989**, 1559–1562.

(30) Oosawa, Y.; Gotoh, Y.; Onoda, M. *Chem. Lett.* **1989**, 1563–1566.

(31) Oosawa, Y.; Gotoh, Y.; Akimoto, J.; Tsunoda, T.; Sohma, M.; Onoda, M. *Jpn. J. Appl. Phys.* **1992**, *31*, 1096–1099.

(32) Alemayehu, M. B.; Falmbigl, M.; Grosse, C.; Ta, K.; Fischer, S. F.; Johnson, D. C. *J. Alloys Compd.* **2015**, *619*, 861–868.

(33) Wiegers, G. A.; Zhou, W. Y. *Mater. Res. Bull.* **1991**, *26*, 879–885.

(34) Oosawa, Y.; Gotoh, Y.; Akimoto, J.; Sohma, M.; Tsunoda, T.; Hayakawa, H.; Onoda, M.; V, E. S. B. *Solid State Ionics* **1994**, *67*, 287–294.

(35) Falmbigl, M.; Alemayehu, M. B.; Merrill, D. R.; Beekman, M.; Johnson, D. C. *Cryst. Res. Technol.* **2015**, *50*, 464-472.

(36) Andreeva, O. N.; Braude, I. S.; Mamalui, A. A. *Phys. Met. Metallogr.* **2012**, *113*, 888–892.

(37) Lee, H. N. S.; McKinzie, H.; Tannhauser, D. S.; Wold, A. *J. Appl. Phys.* **1969**, *40*, 602.

(38) Py, M. A.; Haering, R. R. *Can. J. Phys.* **1983**, *61*, 76–84.

Chapter XIII

(1) K. Novoselov, D. Jiang, Proc. Natl. Acad. Sci. USA 2005, 102, 10451 – 10453.

(2) K. S. Novoselov, A. K. Geim, S. V. Morozov, D. Jiang, Y. Zhang, S. V. Dubonos, I. V. Grigorieva, A. A. Firsov, Science 2004, 306, 666 – 669.

(3) A. Koma, K. Ueno, K. Saiki, J. Cryst. Growth 1991, 111, 1029 – 1032.

(4) P. Mir6, M. Audiffred, T. Heine, Chem. Soc. Rev. 2014, 43, 6537 – 6554.

(5) M. Chhowalla, H. S. Shin, G. Eda, L.-J. Li, K. P. Loh, H. Zhang, Nat. Chem. 2013, 5, 263 – 275.

(6) Y. Shi, H. Li, L.-J. Li, Chem. Soc. Rev. 2015, 44, 2744 – 2756.

(7) C. Tan, H. Zhang, Chem. Soc. Rev. 2015, 44, 2713 – 2731.

(8) Y. Min, G. D. Moon, C.-E. Kim, J.-H. Lee, H. Yang, A. Soon, U. Jeong, J. Mater. Chem. C 2014, 2, 6222.

(9) H. Wang, F. Liu, W. Fu, Z. Fang, W. Zhou, Z. Liu, Nanoscale 2014, 6, 12250 – 12272.

(10) T. Niu, A. Li, Prog. Surf. Sci. 2015, 90, 21– 45.

(11) X. Huang, C. Tan, Z. Yin, H. Zhang, Adv. Mater. 2014, 26, 2185 – 2203.

(12) R. Lv, J. Robinson, R. Schaak, Acc. Chem. Res. 2015, 48, 56– 64.

(13) M. Pumera, Z. Sofer, A. Ambrosi, J. Mater. Chem. A 2014, 2, 8981 – 8987.

(14) A. B. Kaul, J. Mater. Res. 2014, 29, 348 – 361.

(15) H. Yuan, H. Wang, Y. Cui, Acc. Chem. Res. 2015, 48, 81– 90.

(16) M. Osada, T. Sasaki, Adv. Mater. 2012, 24, 210 – 228.

(17) A. K. Geim, I. V. Grigorieva, Nature 2013, 499, 419 – 425.

(18) M. Beekman, C. L. Heideman, D. C. Johnson, Semicond. Sci. Technol. 2014, 29, 064012.

(19) D. B. Moore, M. Beekman, S. Disch, D. C. Johnson, Angew. Chem. Int. Ed. 2014, 53, 5672 – 5675; Angew. Chem. 2014, 126, 5778 – 5781.

(20) G. Dittmar, H. Schaefer, Acta Crystallogr. Sect. B 1976, 32, 2726 –2728.

(21) J. Rigoult, C. G. Morosini, A. Tomas, P. Moline, Acta Crystallogr. Sect. B 1982, 38, 1557 – 1559.

(22) M. Bayard, M. J. Sienko, J. Solid State Chem. 1976, 19, 325 – 329.

(23) L. F. Schneemeyer, A. Stacy, M. J. Sienko, Inorg. Chem. 1980, 19, 2659 – 2662.

(24) C. F. van Bruggen, C. Haas, Solid State Commun. 1976, 20, 251 – 254.

(25) C. Mande, R. N. Tatil, A. S. Nigavekar, Nature 1966, 211, 5048.

(26) S. Asanabe, J. Phys. Soc. Jpn. 1961, 16, 1789.

(27) Y. Zhang, H. Li, L. Jiang, H. Liu, C. Shu, Y. Li, C. Wang, Appl. Phys. Lett. 2011, 98, 113118.

(28) M. Nath, A. Choudhury, C. Rao, Chem. Commun. 2004, 1, 2 – 3.

(29) X. Wang, B. Liu, Q. Wang, W. Song, X. Hou, D. Chen, Y. Cheng, G. Shen, Adv. Mater. 2013, 25, 1479 – 1486.

(30) H. S. Im, Y. R. Lim, Y. J. Cho, J. Park, E. H. Cha, H. S. Kang, J. Phys. Chem. C 2014, 118, 21884 – 21888.

(31) L. Fister, D. C. Johnson, J. Am. Chem. Soc. 1992, 114, 4639 – 4644.

(32) M. Falmbigl, A. Fiedler, R. E. Atkins, S. F. Fischer, D. C. Johnson, Nano Lett. 2015, 15, 943 – 948.

(33) E. Hoschek, W. Klemm, Z. Anorg. Allg. Chem. 1939, 242, 49– 62.

(34) H. Terrones, M. Terrones, J. Mater. Res. 2014, 29, 373 – 382.

(35) A. Zunger, Phys. Rev. B 1979, 19, 6001 – 6009.

(36) M. B. Alemayehu, K. Ta, M. Falmbigl, D. C. Johnson, J. Am. Chem. Soc. 2015, 137, 4831 – 4839.

(37) S. Schaffer, B. Schaffer, Q. Ramasse, Ultramicroscopy 2012, 114, 62 – 71.

Chapter XIV

(1) Snyder, G. J.; Toberer, E. S. Complex Thermoelectric Materials. *Nat. Mater.* **2008**, *7*, 105–114.

(2) Stewart, G. R. Superconductivity in Iron Compounds. *Rev. Mod. Phys.* **2011**, *83*.

(3) Orenstein, J.; Millis, A. J. Advances in the Physics of High-Temperature Superconductivity. *Science.* **2000**, *288*, 468–474.

(4) Havinga, E. E.; Damsma, H.; van Maaren, M. H. Oscillatory Dependence of Superconductive Critical Temperature on Number of Valency Electrons in Cu3Au-Type Alloys. *J. Phys. Chem. Solids* **1970**, *31*, 2653–2662.

(5) Pickett, W. E.; Singh, D. J. Electronic Structure and Half-Metallic Transport in the $La_{1-x}Ca_xMnO_3$ System. *Phys. Rev. B* **1996**, *53*, 1146–1160.

(6) Li, C.; Hu, Q.; Yang, R.; Johansson, B.; Vitos, L. Magnetic Ordering and Physical Stability of $X_2Mn_{1+X}Sn_{1-X}$ (X = Ru, Os, Co, Rh, Ni, Pd, Cu, and Ag) Heusler Alloys from a First-Principles Study. *Phys. Rev. B* **2013**, *88*, 014109.

(7) Wolf, S.; Tauber, R. N. *Silicon Processing for the VLSI Era - Volume 1: Process Technology*; Second ed.; Lattice Press: Sunset Beach, CA, **2000**; pp. 1–32.

(8) Park, J.-S.; Yang, J.-H.; Ramanathan, K.; Wei, S.-H. Defect Properties of Sb- and Bi-Doped $CuInSe_2$: The Effect of the Deep Lone-Pair S States. *Appl. Phys. Lett.* **2014**, *105*, 243901.

(9) Cahen, D.; Abecassis, D.; Soltz, D. Doping of $CuInSe_2$ Crystals: Evidence for Influence of Thermal Defects. *Chem. Mater.* **1989**, 202–207.

(10) Chen, S.; Walsh, A.; Gong, X. G.; Wei, S. H. Classification of Lattice Defects in the Kesterite Cu_2ZnSnS_4 and $Cu_2ZnSnSe_4$ Earth-Abundant Solar Cell Absorbers. *Adv. Mater.* **2013**, *25*, 1522–1539.

(11) Wiegers, G. A. Misfit Layer Compounds: Structure and Physical Properties. *Prog. Solid St. Chem.* **1996**, *24*, 1–139.

(12) Schafer, H. *Chemical Transport Reactions*; Academic Press: New York, 1964.

(13) Atkins, R.; Wilson, J.; Zschack, P.; Grosse, C.; Neumann, W.; Johnson, D. C. Synthesis of $[(SnSe)_{1.15}]_m((TaSe_2)_n$ Ferecrystals: Structurally Tunable Metallic Compounds. *Chem. Mater.* **2012**, *24*, 4594–4599.

(14) Heideman, C.; Nyugen, N.; Hanni, J.; Lin, Q.; Duncombe, S.; Johnson, D. C.; Zschack, P. The Synthesis and Characterization of New $[(BiSe)_{1.10}]_m[NbSe_2]_n$, $[(PbSe)_{1.10}]_m[NbSe_2]_n$, $[(CeSe)_{1.14}]_m[NbSe_2]_n$ and $[(PbSe)_{1.12}]_m[TaSe_2]_n$ Misfit Layered Compounds. *J. Solid State Chem.* **2008**, *181*, 1701–1706.

(15) Heideman, C. L.; Tepfer, S.; Lin, Q.; Rostek, R.; Zschack, P.; Anderson, M. D.; Anderson, I. M.; Johnson, D. C. Designed Synthesis, Structure, and Properties of a Family of Ferecrystalline Compounds $[(PbSe)_{1.00}]_m(MoSe_2)_n$. *J. Am. Chem. Soc.* **2013**, *135*, 11055–11062.

(16) Westover, R.; Atkins, R.; Ditto, J. J.; Johnson, D. C. Synthesis of $[(SnSe)_{1.16-1.09}]_1[(Nb_xMo_{1-x})Se_2]_1$ Ferecrystal Alloys. *Chem. Mater.* **2014**, *26*, 3443–3449.

(17) Wiegers, G. a. Charge Transfer between Layers in Misfit Layer Compounds. *J. Alloys Compd.* **1995**, *219*, 152–156.

(18) Rouxel, J.; Meerschaut, a.; Wiegers, G. a. Chalcogenide Misfit Layer Compounds. *J. Alloys Compd.* **1995**, *229*, 144–157.

(19) Meerschaut, A. Misfit Layer Compounds. *Curr. Opin. Solid State Mater. Sci.* **1996**, *1*, 250–260.

(20) Phung, T.; Jensen, J.; Jonshon, D.; Donovan, J.; McBurnett, B. Determination of the Composition of Ultra-thin Ni-Si Films on Si: Constrained Modeling of Electron Probe Microanalysis and X-ray Reflectivity Data. *X-Ray Spectrom.* **2008**, *37*, 608–614.

(21) Schaffer, M.; Schaffer, B.; Ramasse, Q. Sample Preparation for Atomic-Resolution STEM at Low Voltages by FIB. *Ultramicroscopy* **2012**, *114*, 62–71.

(22) van der Pauw, L.J. A method of measuring specific resistivity and Hall effect of discs of arbitrary shape. *Philips Research Reports*. **1958,** *13*, 1–9.

(23) van der Pauw, L. J. A method of measuring the resistivity and Hall coefficient on lamellae of arbitrary shape. *Philips Tech. Rev.* **1958**, 20, 220.

(24) Moore, D. B.; Stolt, M. J.; Atkins, R.; Sitts, L.; Jones, Z.; Disch, S.; Matt, B.; Johnson, D. C. Structural and Electrical Properties of $(PbSe)_{1.16}TiSe_2$. *Emerg. Mater. Res.* **2012**, *1*, 292–298.

(25) Merrill, D. R.; Moore, D. B.; Ditto, J.; Sutherland, D. R.; Falmbigl, M.; Winkler, M.; Pernau, H.; Johnson, D. C. The Synthesis, Structure, and Electrical Characterization of $(SnSe)_{1.2}TiSe_2$. *Eur. J. Inorg. Chem.* **2015**, 83–91.

(26) Vegard, L. Die Konstitution der Mischkristalle und die Raumfüllung der Atome. *Zeitschrift für Physik* **1921** *5*, 1, 17–26.

(27) Greenaway, D. L.; Nitsche, R. Preparation and Optical Properties of IV-VI2 Chalcogenides Having the CdI2 Structure. *J. Phys. Chem. Solids* **1965**, *26*, 1445–1458.

(28) Giang, N.; Xu, Q.; Hor, Y.; Williams, A.; Dutton, S.; Zandbergen, H.; Cava, R. Superconductivity at 2.3 K in the Misfit Compound (PbSe)1.16(TiSe2)2. *Phys. Rev. B* **2010**, *82*, 1–5.

(29) Moore, D. B.; Beekman, M.; Disch, S.; Zschack, P.; Häusler, I.; Neumann, W.; Johnson, D. C. Synthesis, Structure, and Properties of Turbostratically Disordered (PbSe) 1.18 (TiSe 2) 2. *Chem. Mater.* **2013**, *25*, 2404–2409.

(30) Corso, S. D.; Liautard, B.; Tedenac, J. C. The Pb-Sn-Se system: Phase equilibria and reactions in the PbSe-SnSe-Se subternary *J. Phase Equilibria* **1995**, *16*, 308–314.

(31) Wiegers, G.; Haange, R. Electrical Transport Properties of the Misfit Layer Compounds $(SnS)_{1.20}TiS_2$ and $(PbS)_{1.18}TiS_2$. *Eur. J. solid state Inorg. Chem.* **1991**, *28*, 1071–1078.

(32) Wan, C.; Wang, Y.; Wang, N.; Koumoto, K. Low-Thermal-Conductivity $(MS)_{1+x}(TiS_2)_2$ (M = Pb, Bi, Sn) Misfit Layer Compounds for Bulk Thermoelectric Materials. *Materials (Basel).* **2010**, *3*, 2606–2617.

(33) Hohnke, D. K.; Kaiser, S. W. Epitaxial PbSe and $Pb_{1-x}Sn_xSe$: Growth and Electrical Properties. *J. Appl. Phys.* **1974**, *45*, 892–897.

(34) Chen, C.-L.; Wang, H.; Chen, Y.-Y.; Day, T.; Snyder, J. Thermoelectric Properties of P-Type Polycrystalline SnSe Doped with Ag. *J. Mater. Chem. A* **2014**, *2*, 11171–11176.

Chapter XV

(1) Geim, A. K.; Novoselov, K. S. Nat. Mater. 2007, 6, 183–191, and reference therein.

(2) Wang, Q. H.; Kalantar-Zadeh, K.; Kis, A.; Coleman, J. N.; Strano, M. S. Nat. Nanotechnol. 2012, 7, 699–712.

(3) Lv, R.; Robinson, J. a; Schaak, R. E.; Sun, D.; Sun, Y.; Mallouk, T. E.; Terrones, M. Acc. Chem. Res. 2015, 48, 56–64.

(4) Heine, T. Acc. Chem. Res. 2015, 48, 65–72.

(5) Geim, a K.; Grigorieva, I. V. Nature 2013, 499, 419–425 and references therein.

(6) Zeng, Q.; Wang, H.; Fu, W.; Gong, Y.; Zhou, W.; Ajayan, P. M.; Lou, J.; Liu, Z. Small 2015, 11, 1868–1884.

(7) Kastner, M.; Birgeneau, R.; Shirane, G.; Endoh, Y. Rev. Mod. Phys. 1998, 70, 897–928.

(8) Orenstein, J.; Millis, A. J. Science (80-.). 2000, 288, 468–474.

(9) Terrones, H.; López-Urías, F.; Terrones, M. Sci. Rep. 2013, 3, 1549.

(10) Lee, H. S.; Min, S. W.; Chang, Y. G.; Park, M. K.; Nam, T.; Kim, H.; Kim, J. H.; Ryu, S.; Im, S. Nano Lett. 2012, 12, 3695–3700.

(11) Yang, S.-L.; Sobota, J. a; Howard, C. a; Pickard, C. J.; Hashimoto, M.; Lu, D. H.; Mo, S.-K.; Kirchmann, P. S.; Shen, Z.-X. Nat. Commun. 2014, 5, 3493.

(12) Murphy, D. W. J. Chem. Phys. 1975, 62, 967.

(13) Fang, H.; Battaglia, C.; Carraro, C.; Nemsak, S.; Ozdol, B.; Kang, J. S.; Bechtel, H. A.; Desai, S. B.; Kronast, F.; Unal, A. A.; et al. Proc. Natl. Acad. Sci. U. S. A. 2014, 111, 6198–6202.

(14) Lin, Y.-C.; Lu, N.; Perea-Lopez, N.; Li, J.; Lin, Z.; Peng, X.; Lee, C. H.; Sun, C.; Calderin, L.; Browning, P. N.; et al. ACS Nano 2014, 8, 3715–3723.

(15) Wiegers, G. A. Prog. Solid St. Chem. 1996, 24, 1–139.

(16) Tenne, R. Recent. Front. Phys. 2013, 9, 370–377.

(17) Radovsky, G.; Popovitz-biro, R.; Tenne, Chem. Mater. 2012, 24, 3004–3015.

(18) Atkins, R.; Wilson, J.; Zschack, P.; Grosse, C.; Neumann, W.; Johnson, D. C. Chem. Mater. 2012, 24, 4594–4599.

(19) Heideman, C. L.; Tepfer, S.; Lin, Q.; Rostek, R.; Zschack, P.; Anderson, M. D.; Anderson, I. M.; Johnson, D. C. J. Am. Chem. Soc. 2013, 135, 11055–11062.

(20) Phung, T.; Jensen, J.; Jonshon, D.; Donovan, J.; McBurnett, B.. X-Ray Spectrom. 2008, 37, 608–614.

(21) Merrill, D. R.; Moore, D. B.; Ditto, J.; Sutherland, D. R.; Falmbigl, M.; Winkler, M.; Pernau, H.; Johnson, D. C. Eur. J. Inorg. Chem. 2015, 83–91.

(22) Merrill, D. R.; Sutherland, D. R.; Ditto, J.; Bauers, S. R.; Falmbigl, M.; Medlin, D. L.; Johnson, D. C. Chem. Mater. 2015, 27, 4066–4072.

(23) Moore, D. B.; Stolt, M. J.; Atkins, R.; Sitts, L.; Jones, Z.; Disch, S.; Matt, B.; Johnson, D. C. Emerg. Mater. Res. 2012, 1, 292–298.

(24) Moore, D. B.; Beekman, M.; Disch, S.; Zschack, P.; Häusler, I.; Neumann, W.; Johnson, D. C. Chem. Mater. 2013, 25, 2404–2409.

(25) Riekel, C. J. Solid State Chem. 1976, 17, 389–392.

(26) Bauers, S. R.; Merrill, D. R.; Moore, D. B.; Johnson, D. C. J. Mater. Chem. C 2015. 3, 10451-10458.

(27) Pałosz, B.; Salje, E. J. Appl. Crystallogr. 1989, 22, 622–623.

(28) Oosawa, Y.; Gotoh, Y.; Akimoto, J.; Tsunoda, T.; Sohma, M.; Onoda, M. Jpn. J. Appl. Phys. 1992, 31, 1096−1099.

(29) Falmbigl, M.; Alemayehu, M. B.; Merrill, D. R.; Beekman, M.; Johnson, D. C. Cryst. Res. Technol. 2015, 50, 464–472 and references therein.

(30) Faticoni, T. G. Combinatorics: An Introduction; John Wiley & Sons, 2014.

Chapter XVI

(1) Geim, A. K.; Grigorieva, I. V. *Nature* **2013**, 499, 419−425.

(2) Ponomarenko, L. A.; Geim, A. K.; Zhukov, A. A.; Jalil, R.; Morozov, S. V.; Novoselov, K. S.; Grigorieva, I. V.; Hill, E. H.; Cheianov, V. V.; Fal'ko, V. I.; Watanabe, K.; Taniguchi, T.; Gorbachev, R. V. *Nat. Phys.* **2011**, 7, 958−961.

(3) Dean, C.; Young, A. F.; Wang, L.; Meric, I.; Lee, G.-H.; Watanabe, K.; Taniguchi, T.; Shepard, K.; Kim, P.; Hone, J. *Solid State Commun.* **2012**, 152, 1275−1282.

(4) Yoon, J.; Park, W.; Bae, G.-Y.; Kim, Y.; Jang, H. S.; Hyun, Y.; Lim, S. K.; Kahng, Y. H.; Hong, W.-K.; Lee, B. H.; Ko, H. C. *Small* **2013**, 9, 3295−3300.

(5) Roy, T.; Tosun, M.; Kang, J. S.; Sachid, A. B.; Desai, S. B.; Hettick, M.; Hu, C. C.; Javey, A. *ACS Nano* **2014**, 8, 6259−6264.

(6) Choi, M. S.; Lee, G.-H.; Yu, Y.-J.; Lee, D.-Y.; Lee, S. H.; Kim, P.; Hone, J.; Yoo, W. J. *Nat. Commun*. **2013**, 4, 1624.

(7) Hong, X.; Kim, J.; Shi, S.-F.; Zhang, Y.; Jin, C.; Sun, Y.; Tongay, S.; Wu, J.; Zhang, Y.; Wang, F. *Nat. Nanotechnol.* **2014**, 9, 682−686.

(8) Kosmider, K.; Fernández-Rossier, J. *Phys. Rev. B*: *Condens. Matter Mater. Phys.* **2013**, 87, 075451.

(9) Duerloo, K.-A. N.; Ong, M. T.; Reed, E. J. *J. Phys. Chem. Lett.* **2012**, 3, 2871−2876.

(10) Wu, S.; Zeng, Z.; He, Q.; Wang, Z.; Wang, S. J.; Du, Y.; Yin, Z.; Sun, X.; Chen, W.; Zhang, H. *Small* **2012**, 8, 2264−2270.

(11) Cao, L.; Yang, S.; Gao, W.; Liu, Z.; Gong, Y.; Ma, L.; Shi, G.; Lei, S.; Zhang, Y.; Zhang, S.; Vajtai, R.; Ajayan, P. M. *Small* **2013**, 9, 2905−2910.

(12) Bernardi, M.; Palummo, M.; Grossman, J. C. *Nano Lett*. **2013**, 13, 3664−3670.

(13) Tributsch, H.; Bennett, J. C. *J. Electroanal. Chem.* **1977**, 81, 97−111.

(14) Li, Y.; Wang, H.; Xie, L.; Liang, Y.; Hong, G.; Dai, H. *J. Am. Chem. Soc.* **2011**, 133, 7296−7299.

(15) Koma, A.; Sunouchi, K.; Miyajima, T. *Microelectron. Eng.* **1984**, 2, 129−136.

(16) Koma, A.; Sunouchi, K.; Miyajima, T. *J. Vac. Sci. Technol., B:* **1985**, 3, 724.

(17) Parkinson, B. A.; Ohuchi, F. S.; Ueno, K.; Koma, A. *Appl. Phys. Lett.* **1991**, 58 (5), 472.

(18) Schuller, I. K. *Phys. Rev. Lett.* **1980**, 44 (24), 1597−1600.

(19) Kim, H.; Meng, Y.; Rouviére, J.-L.; Isheim, D.; Seidman, D. N.; Zuo, J.-M. *J. Appl. Phys.* **2013**, 113, 103511.

(20) Westover, R. D.; Atkins, R. A.; Ditto, J.; Johnson, D. C. *Chem. Mater.* **2014**, 26, 3443−3449.

(21) Kalikhman, V. L.; Lobova, T. A.; Pravoverova, L. L. *Neorg. Mater.* **1973**, 9, 923−926.

(22) Atkins, R.; Wilson, J.; Zschack, P.; Grosse, C.; Neumann, W.; Johnson, D. C. *Chem. Mater.* **2012**, 24 (23), 4594−4599.

(23) Donovan, J. J.; Tingle, T. N. *Microsc. Microanal.* **1996**, 2, 1−7.

(24) Heideman, C.; Nyugen, N.; Hanni, J.; Lin, Q.; Duncombe, S.; Johnson, D. C.; Zschack, P. *J. Solid State Chem.* **2008**, 181, 1701−1706.

(25) Beekman, M.; Heideman, C. L.; Johnson, D. C. *Semicond. Sci. Technol.* **2014**, 29, 064012.

(26) Alemayehu, M. B.; Falmbigl, M.; Grosse, C.; Ta, K.; Fischer, S.F.; Johnson, D. C. *J. Alloys Compd.* **2015**, 619, 861−868.

(27) Alemayehu, M. B.; Falmbigl, M.; Ta, K.; Grosse, C.; Westover, R. D.; Bauers, S. R.; Fischer, S. F.; Johnson, D. C. *Chem. Mater.* **2015**, 27, 867−875.

Chapter XVII

(1) Novoselov K S; Geim A K; Morozov S V; Jiang D; Zhang Y; Dubonos S V; Grigorieva I V; Firsov A A From Science (New York, N.Y.) (**2004**), 306(5696), 666-9.

(2) Castro Neto, A.; Guinea, F.; Peres, N. M. R.; Novoselov, K. S.; Geim, A. K. *Rev. Mod. Phys*. **2009**, 81, 109−162.

(3) Wilson, J. A.; Yoffe, A. D. *Adv. Phys*. **1969**, 18 (73), 193-335.

(4) Geim, A. K; I. V. Grigorieva, I. V. *Nature*, **2013**, 499, 419-425.

(5) Ponomarenko, L. A.; Geim, A. K.; Zhukov, A. A.; Jalil, R.; Morozov, S. V.; Morozov, Novoselov, K. S.; Grigorieva, I. V.; Hill, E. H.; Cheianov, V. V.; Fal'ko, V. I.; Watanabe, K.; Taniguchi, T.; Gorbachev, R. V. *Nature Phys.Lett.* **2011**, 7, 958–961.

(6) Dean, C.; Young, A. F.; Wang, L. Meric. I.; Lee,G.-H.; Watanbe, K.; Taniguchi, T.; Shepard, K; Kim, P.; Hone. J. *Solid State Comm.* **2012**, 152, 1275-1282.

(7) Yoon, J.; Park, W.; Bae, G.-Y.; Kim, Y.; Jang, H. S.; Hyun, Y.; Lim, S. K.; Kahng, Y. H.; Hong, W.-K.; Lee, B. H.; Ko, H. C. *Small*, **2013**, 9, 3295−3300.

(8) Roy, T.; Tosun, M.; Kang, J. S.; Sachid, A. B.; Desai, S. B.; Hettick, M.; Hu, C. C.; Javey, A. *ACS Nano*, **2014**, 8, 6259−6264.

(9) Choi, M. S.; Lee, G.-H.; Yu, Y.-J.; Lee, D.-Y.; Lee, S. H.; Kim, P.; Hone, J.; Yoo, W. J. *Nat. Commun.* **2013**, 4, 1624.

(10) Hong, X.; Kim, J.; Shi, S.-F.; Zhang, Y.; Jin, C.; Sun, Y.; Tongay, S.; Wu, J.; Zhang, Y.; Wang, F. *Nat. Nanotechnol.* **2014**, 9, 682−686.

(11) Wu, S.; Zeng, Z.; He, Q.; Wang, Z.; Wang, S. J.; Du, Y.; Yin, Z.; Sun, X.; Chen, W.; Zhang, H. *Small*, **2012**, 8, 2264–2270.

(12) Cao, L.; Yang, S.; Gao, W.; Liu, Z.; Gong, Y.; Ma, L.; Shi, G.; Lei, S.; Zhang, Y.; Zhang, S. Vajtai, R.; Ajayan P. M. *Small*, **2013**, 9, 2905–2910.

(13) Bernardi, M.; Palummo, M.; Grossman, J. C. *Nano Lett.* **2013**, 13, 3664–3670.

(14) Tributsch H.; Bennett, J. C. *J. Electroanal. Chem.* **1977**, 81, 97–111.

(15) Li, Y.; Wang, H.; Xie, L.; Liang, Y.; Hong G.; Dai, H. *J. Am. Chem. Soc.* **2011**, 133, 7296–7299.

(16) Koma, A.; Sunouchi K.; Miyajima, T. *Microelectron. Eng.* **1984**, 2, 129–136.

(17) Koma, A.; Sunouchi, K.; Miyajima, T. *J. Vac. Sci. Technol. B*. **1985**, 3 724-724.

(18) Schuller, *Phys. Rev. Lett*. **1980**, 44, 24, 1597-1600.

(19) Kim, H.; Meng, Y.; Rouviére, J.-L.; Isheim, D.; Seidman, D. N. *J. App. Phys.* **2013**, 113, 103511.

(20) Alemayehu, M.B.; Falmbigl, M.; Ta, K.; Grosse, C.; Westover, R. D.; Bauers, S. R. Fischer, S. F.; Johnson, D. C. *Chem. Mater.* **2015**, 27, 867–875.

(21) Beekman, M.; Heideman, C. L.; Johnson, D. C. *Semicond. Sci.Technol*. **2014**, 29, 064012.

(22) Moore, D. B.; Beekman, M.; Disch, S.; Johnson, D. C. *Angew.Chem., Int. Ed. Engl*. **2014**, 53, 5672−5.

(23) Westover, R. D.; Ditto, J.; Falmbigl, M.; Hay, Z. L.; Johnson, D. C. *Chem. Mater.* **2015**, 27, 6411-6417.

(24) Donovan, J. J.; Tingle, T. N. *J. Microsc. Soc. Am.* **1996**, 2, 1–7.

(25) Heideman, C.; Nyugen, N.; Hanni, J.; Lin, Q.; Duncombe, S.; Johnson, D.C.; Zschack, P. *J. Solid State Chem.* **2008**, 181, 1701–1706.

(26) Westover, R.D.; Atkins, R.E.; Falmbigl,M.; Ditto, J. J.; Johnson, D.C. *J. Solid State Chem.* **2015**, doi:10.1016/j.jssc.2015.08.018, ahead of print.

(27) Okazaki, A.; Ueda, I. *J. Phys. Soc. Jpn.* **1956**, 11, 470.

(28) Beekman, M.; Cogburn G.; Heideman, C. Rouvimov, S.; Zschack, P; Neumann, W.; Johnson, D. C. *J. Electronic. Mater.* **2012**, 41,(6) 1476-1480.

(29) Westover, R.D.; Atkins, R.A.; Ditto, J.; Johnson, D.C. *Chem. Mater*. **2014**, 26, 3443–3449.

(30) Wiegers, G. A. *Prog. Solid State Chem.***1996**, 24, 1−139.

Chapter XVIII

(1) H. Schäfer., Angew. Chem. Int. Ed. 10 (1971) 43–50.

(2) H. Schäfer, Chemical Transport Reactions, *Academic Press, New York*, 1964.

(3) T.J. McCarthy, M.G. Kanatzidis, Inorg. Chem. 34 (5) (1995) 1257–1267.

(4) M.G. Kanatzidis, Curr. Opin. Solid State Mater. Sci. 2 (1997) 139–

149.

(5) J.R. Arthur, J.J. LePore, J. Vac. Sci. Technol. 6 (1969) 545.

(6) J.R. Arthur, J. Appl. Phys. 39 (1968) 4032.

(7) A.Y. Cho, F.K. Reinhart, J. Appl. Phys. 45 (1974) 1812.

(8) A.Y. Cho, Appl. Phys. Lett. 19 (1971) 467.

(9) A.Y. Cho, J. Appl. Phys. 42 (1971) 2074.

(10) A.Y. Cho, J.R. Arthur, Prog. Solid State Chem. 10 (1975) 157–191.

(11) R. Dingle, H.L. Störmer, A.C. Gossard, W. Wiegmann, App. Phys. Lett. 33 (7) (1978) 665–667.

(12) H.L. Störmer, D.C. Tsui, A.C. Gossard, J.C.M. Hwang, Physica B 117/118 (2) (1983) 688–690.

(13) D.C. Tsui, H.L. Störmer, A.C. Gossard, Phys. Rev. Lett. 48 (1982) 1559.

(14) Y. Yu, C. Li, Y. Liu, L. Su, Y. Zhang, L. Cao, Sci. Rep. 3 (2013) 1866, http://dx.doi. org/10.1038/srep01866.

(15) K.M. McCreary, A.T. Hanbicki, J.T. Robinson, E. Cobas, J.C. Culbertson, A. L. Friedman, G.G. Jernigan, B.T. Jonker, Adv. Funct. Mater. 24 (41) (2014) 6449–6454.

(16) S.J. Yun, S.H. Chae, H. Kim, J.C. Park, J.H. Park, G.H. Han, J.S. Lee, S.M. Kim, H. M. Oh, J. Seok, ACS Nano 9 (5) (2015) 5510–5519.

(17) Y. Zhang, Y. Zhang, Q. Ji, J. Ju, H. Yuan, J. Shi, T. Gao, D. Ma, M.

Liu, Y. Chen, ACS Nano 7 (10) (2013) 8963–8971.

(18) A. Fleurence, R. Friedlein, T. Ozaki, H. Kawai, Y. Wang, Y. Yamada-Takamura, Phys. Rev. Lett. 108 (2012) 245501.

(19) L. Meng, Y. Wang, L. Zhang, S. Du, R. Wu, L. Li, Y. Zhang, G. Li, H. Zhou, W. A. Hofer, H. Gao, Nano Lett. 13 (2) (2013) 685–690.

(20) D. Chiappe, E. Scalise, E. Cinquanta, C. Grazianetti, B.V.D. Broek, M. Fanciulli, M. Houssa, A. Molle, Adv. Mater. 24 (2014) 2096–2101.

(21) M. Zhang, Y. Zhu, X. Wang, Q. Feng, S. Qiao, W. Wen, Y. Chen, M. Cui, J. Zhang, C. Cai, J. Am. Chem. Soc. 137 (22) (2015) 7051–7054.

(22) L.A. Ponomarenko, A.K. Geim, A.A. Zhukov, R. Jalil, S.V. Morozov, K. Novoselov, I.V. Grigorieva, E.H. Hill, V.V. Cheianov, V.I. Fal'ko, K. Watanabe, Taniguchi, R.V. Gorbachev, Nat. Phys. 7 (2011) 958–961.

(23) C. Dean, A.F. Young, L. Wang, I. Meric., G.-H. Lee, K. Watanbe, T. Taniguchi, K. Shepard, P. Kim, J. Hone., J. Solid State Commun. 152 (2012) 1275–1282.

(24) J. Yoon, W. Park, G.-Y. Bae, Y. Kim, H.S. Jang, Y. Hyun, S.K. Lim, Y.H. Kahng, W.–K. Hong, B.H. Lee, H.C. Ko, Small 9 (2013) 3295–3300.

(25) T. Roy, M. Tosun, J.S. Kang, A.B. Sachid, S.B. Desai, M.

Hettick, M.C.C. Hu, A. Javey, ACS Nano 8 (2014) 6259–6264.

(26) M.S. Choi, G.–H. Lee, Y.–J. Yu, D.–Y. Lee, S.H. Lee, P. Kim, J. Hone, W.J. Yoo, Nat. Commun. 4 (2013) 1624.

(27) X. Hong, J. Kim, S.–F. Shi, Y. Zhang, C. Jin, Y. Sun, S. Tongay, J. Wu, Y. Zhang, F. Wang, Nat. Nanotechnol. 9 (2014) 682–686.

(28) A.K. Geim, I.V. Grigorieva, Nature 499 (2013) 419–425.

(29) F.J. Di Salvo, J.A. Wilson, B.G. Bagley, J.V. Waszczak, Phys. Rev. B 12 (6) (1975) 2220–2236.

(30) T. Novet, D.C. Johnson, J. Am. Chem. Soc. 113 (1991) 3398–3403.

(31) N. Pienack, W. Bensch, Angew. Chem. Int. Ed. 50 (9) (2011) 2014–2034.

(32) M.D. Hornbostel, E.J. Hyer, J.P. Thiel, D.C. Johnson, J. Am. Chem. Soc. 119 (1997) 2665–2668.

(33) M.D. Hornbostel, E.J. Hyer, J.H. Edvalson, D.C. Johnson, Inorg. Chem. 36 (1997) 4270–4274.

(34) S.L. Stuckmeyer, H. Sellinschegg, M.D. Hornbostel, D.C. Johnson, Chem. Mater. 10 (4) (1998) 1096–1101.

(35) J.R. Williams, D.C. Johnson, Inorg. Chem. 41 (2002) 4127–4130.

(36) M. Esters, M. Alemayehu, Z. Jones, N.T. Nguyen, M.D. Anderson, C. Grosse, S. Fischer, D.C. Johnson, Angew. Chem. 54 (2015) 1130–1134, http://dx.doi.org/ 10.1002/anie.201409714.

(37) R.D. Westover, R.A. Atkins, J. Ditto, D.C. Johnson, Chem. Mater. 26

(2014) 3443–3449.

(38) E.J. Cotts, W.J. Meng, W.L. Johnson, Phys. Rev. Lett. 57 (1986) 2295.

(39) N.T. Nguyen, P.A. Berseth, Q. Lin, C. Chiritescu, D.G. Cahill, A. Mavrokefalos, L. Shi, P. Zschack, M.D. Anderson, I.M. Anderson, D.C. Johnson, Chem. Mater. 22 (2010) 2750–2756.

(40) M.D. Hornbostel, E.J. Hyer, J.P. Thiel, D.C. Johnson, J. Am. Chem. Soc. 119 (1997) 2665–2668.

(41) R. Williams, M. Johnson, D.C. Johnson, J. Am. Chem. Soc. 123 (2001) 1645.

(42) J.R. Williams, D.C. Johnson, Inorg. Chem. 41 (2002) 4127.

(43) A.L.E. Smally, M.L. Jespersen, D.C. Johnson, Inorg. Chem. 43 (2004) 2486.

(44) M. Behrens, R. Kiebach, W. Bensch, Inorg. Chem. 45 (2006) 2704.

(45) M. Behrens, J. Tomforde, E. May, R. Kiebach, W. Bensch, D. Häußler, W. Jäger, J. Solid State Chem. 179 (2006) 3330.

(46) M. Regus, G. Kuhn, S. Mankovsky, H. Ebert, W. Bensch, J. Solid State Chem. 196 (2012) 100.

(47) J.R. Williams, A.L.E. Smalley, H. Sellinschegg, C. Daniels-Hafer, J. Harris, M. B. Johnson, D.C. Johnson, J. Am. Chem. Soc. 12 (34) (2003) 10335–10341.

(48) M. Noh, D.C. Johnson, Angew. Chem. 35 (1996) 2666–2669.

(49) H.-J. Shin, K. Jeong, M. Noh, D.C. Johnson, S.D. Kevan, T.

Warwick., J. Appl. Phys. 81 (1997) 7787–7792.

(50) H.–J. Shin, K. Jeong, D.C. Johnson, S.D. Kevan, M. Noh, T. Warwick., J. Korean Phys. Soc. 30 (1997) 575–579.

(51) M. Noh, G. Elliott, D.C. Johnson, Chem. Mater. 12 (2000) 2894 290.

(52) N.T. Nguyen, B. Howe, J.R. Hash, N. Liebrecht, P. Zschack, D.C. Johnson, Chem. Mater. 19 (8) (2007) 1923–1930.

(53) N.T. Nguyen, B. Howe, J.R. Hash, N. Liebrecht, D.C. Johnson, Adv. Mater. 18 (2006) 118–122.

(54) F.R. Harris, S. Standridge, D.,C. Johnson, J. Am. Chem. Soc. 127 (21) (2005) 7843–7848.

(55) F.R. Harris, S. Standridge, C. Feik, D.C. Johnson, Angew. Chem. Int. Ed. 42 (43) (2003) 5296–5299.

(56) B.A. Schmid, R. Rostek, C. Mortensen, D.C. Johnson, Proceedings of the 24th International Conference on Thermoelectrics, Clemson, USA, June 2005, pp. 255–257.

(57) C. Mortensen, M. Beekman, D.C. Johnson, Sci. Adv. Mater. 3 (2011) 639–645.

(58) C. Chiritescu, D.G. Cahill, C. Mortensen, D. Johnson, P. Zschack, J. Appl. Phys. 106 (7) (2009) 073503/1–073503/5.

(59) J.D. König, M. Winkler, S. Buller, W. Bensch, U. Schürmann, L. Kienle, H. Böttner, J. Electron. Mater. 40 (2011) 1266–1270.

(60) J.D. König, H. Böttner, J. Tomforde, W. Bensch, Proceedings of the

26th In- ternational Conference on Thermoelectronics, Jeju, South Korea, 2007, pp. 395.

(61) M. Winkler, X. Liu, J.D. König, L. Kerste, H. Böttner, W. Bensch, L. Kienle, J. Electron. Mater. 41 (6) (2012) 1322–1331.

(62) R. Atkins, S. Disch, Z. Jones, I. Häeusler, C. Grosse, S.F. Fischer, W. Neumann, P. Zschack, D.C. Johnson, J. Solid State Chem. 202 (2013) 128–133, http://dx. doi.org/10.1016/j.jssc.2013.03.008.

(63) R. Atkins, M. Dolgos, A. Fiedler, C. Grosse, S.F. Fischer, S.P. Rudin, D.C. Johnson, Chem. Mater. 26 (2014) 2862–2872, http://dx.doi.org/10.1021/cm5004774.

(64) M. Falmbigl, A. Fiedler, R.E. Atkins, S.F. Fischer, D.C. Johnson, Nano Lett. 15 (2) (2015) 943–948, http://dx.doi.org/10.1021/nl503708j.

(65) R. Atkins, S. Disch, Z. Jones, I. Haeusler, C. Grosse, S.F. Fischer, W. Neumann, P. Zschack, D.C. Johnson, J. Solid State Chem. 202 (2013) 128–133.

(66) M.B. Alemayehu, M. Falmbigl, C. Grosse, K. Ta, S. Fischer, D.C. Johnson, J. Alloy. Compd. 619 (2015) (2015) 861–868.

(67) M. Alemayheu, M. Falmbigl, K. Ta, S. Bauers, D.C. Johnson, Chem. Mater. 27 (2015) 867–875.

(68) M.B. Alemayehu, K. Ta, M. Falmbigl, D.C. Johnson, Nanoscale 7 (2015) 7378–7385.

(69) M.B. Alemayehu, K. Ta, M. Falmbigl, D.C. Johnson, J. Am. Chem. Soc. 137 (2015) 4831–4839.

(70) M.B. Alemayehu, M. Falmbigl, K. Ta, D.C. Johnson, Chem. Mater. 27 (6) (2015) 2158–2164.

(71) M.B. Alemayehu, M. Falmbigl, K. Ta, D.C. Johnson, ACS Nano 9 (2015) 4427–4434.

(72) M. Beekman, S. Disch, S. Rouvimov, D. Kasinathan, K. Koepernik, H. Rosner, P. Zschack, W.S. Neumann, D.C. Johnson, Angew. Chem. Int. Ed. 52 (2013) 13211–13214.

(73) N.S. Gunning, J. Feser, M. Beekman, D.G. Cahill, D.C. Johnson, J. Am. Chem. Soc. 137 (27) (2015) 8803–8809, http://dx.doi.org/10.1021/jacs.5b04351.

(74) M. Ludemann, O.D. Gordan, D.R.T. Zahn, M. Beekman, R. Atkins, D.C. Johnson, Langmuir 30 (27) (2014) 8209–8214.

(75) N.S. Gunning, J. Feser, M. Falmbigl, M. Beekman, D.G. Cahill, D.C. Johnson, Semicond. Sci. Technol. 29 (2014) 124007.

(76) C. Grosse, R. Atkins, H. Kirmse, A. Mogilatenko, W. Neumann, D.C. Johnson, J. Alloy. Compd. 579 (2013) 507–515.

(77) R. Atkins, J. Wilson, P. Zschack, C. Grosse, W. Neumann, D.C. Johnson, Chem. Mater. 24 (23) (2012) 4594–4599.

(78) D.R. Merrill, D.B. Moore, S. Bauers, M. Falmbigl, D.C. Johnson, Materials 8 (2015) 2000–2029.

(79) D.R. Merrill, D.B. Moore, J. Ditto, D.R. Sutherland, M. Falmbigl, M. Winkler, H.–F. Pernau, D.C. Johnson, Eur. J. Inorg. Chem. 2015 (1) (2015) 83–91.

(80) D.B. Moore, M.J. Stolt, R. Atkins, L. Sitts, Z. Jones, S. Disch, M. Beekman, D. C. Johnson, Emerg. Mater. Res. 1 (2012) 292–298.

(81) S.R. Bauers, D.B. Moore, J. Ditto, D.C. Johnson, J. Alloy. Compd. 645 (5) (2015) 18–124, http://dx.doi.org/10.1039/c5tc015.

(82) D.B. Moore, M. Beekman, S. Disch, P. Zschack, I. Hausler, W. Neumann, D. C. Johnson, Chem. Mater. 25 (12) (2013) 2404–2409.

(83) M.B. Alemayehu, G. Mitchson, J. Ditto, B.E. Hanken, M. Asta, D.C. Johnson, Chem. Mater. 26 (2014) 1859–1866.

(84) M. Esters, M.B. Alemayehu, Z. Jones, N.T. Nguyen, M.D. Anderson, C. Grosse, S. F. Fischer, D.C. Johnson, Angew. Chem. Int. Ed. 54 (4) (2015) 1130–1134.

(85) M.M. Smeller, C.L. Heideman, Q. Lin, M.D. Anderson, P. Zschack, I.M. Anderson, D.C. Johnson, Z. Anorg. Allg. Chem. 638 (2012) 2632–2639.

(86) C.L. Heideman, S. Tepfer, Q. Lin, R. Rostek, P. Zschack, M.D. Anderson, I. M. Anderson, D.C. Johnson, J. Am. Chem. Soc. 135 (30) (2013) 11055–11062.

(87) C. Heideman, D.C. Johnson, Semicond. Sci. Technol. 29 (2014) 064007.

(88) M.D. Anderson, C.L. Heideman, M. Smeller, R. Kykyneshi, A.A. Herzing, I. M. Anderson, D.A. Keszler, P. Zschack, D.C. Johnson, Ang. Chem. Int. Ed 52 (2013) 1–5.

(89) C.L. Heideman, R. Rostek, M.D. Anderson, A.A. Herzing, I.M. Anderson, D. C. Johnson, J. Electron. Mater. (39 (9) (2010) 1476–1481.

(90) C. Heideman, N. Nyugen, J. Hanni, Q. Lin, S. Duncombe, D.C. Johnson, P. Zschack, J. Solid State Chem. 181 (2008) 1701–1706.

(91) A. Mavrokefalos, Q. Lin, M. Beekman, J.H. Seol, Y.J. Lee, H. Kong, M.T. Pettes, D. C. Johnson, L. Shi, App. Phys. Lett. 96 (18) (2010) 181908/1–181908/3.

(92) Q. Lin, S. Tepfer, C. Heideman, C. Mortensen, N. Nguyen, P. Zschack, M. Beekman, D.C. Johnson, J. Mater. Res. 26 (2011) 1866–1871.

(93) Q. Lin, M. Smeller, C.L. Heideman, P. Zschack, M. Koyano, M.D. Anderson, R. Kykyneshi, D.A. Keszler, I.M. Anderson, D.C. Johnson, Chem. Mater. 22 (3) (2010) 1002–1009.

(94) D.R. Merrill, D.B. Moore, M.N. Coffey, A.W. Jansons, M. Falmbigl, D.C. Johnson, Semicond. Sci. Technol 29 (6) (2014) 064004/1–064004/6 6.

(95) C. Heideman, N. Nyugen, J. Hanni, Q. Lin, S. Duncombe, D.C. Johnson, P. Zschack, J. Solid State Chem. 181 (7) (2008) 1701–1706.

(96) D.B. Moore, M. Beekman, S. Disch, D.C. Johnson, Angew. Chem. Int. Ed. 53 (22) (2014) 5672–5675.

(97) M. Falmbigl, M.B. Alemayehu, D.R. Merrill, M. Beekman, D.C.

Johnson, Crys. Res. Technol. 50 (6) (2015) 464–472

(98) D.R. Merrill, D.R. Sutherland, J. Ditto, S. Bauers, M. Falmbigl, D.L. Medlin, D. C. Johnson, Chem. Mater, 27, 2015 4066-4072

(99) G.A. Wiegers, Prog. Solid State Chem. 24 (1996) 1–139.

Chapter XIX

(1) Brinker, C. J.; Scherer, G. W. *Sol-Gel Science*: 1990, Academic Press: San Diego, CA, USA.

(2) Scherer, G. W. J. *Non. Cryst. Solids* 1992, 147-148, 363–374.

(3) Meyers, S. T.; Anderson, J. T.; Hong, D.; Hung, C. M.; Wager, J. F.; Keszler, D. A. *Chem. Mater.* 2007, 19, 4023–4029.

(4) Anderson, J. T.; Munsee, C. L.; Hung, C. M.; Phung, T. M.; Herman, G. S.; Johnson, D. C.; Wager, J. F.; Keszler, D. A. *Adv. Funct. Mater.* 2007, 17, 2117–2124.

(5) Meyers, S. T.; Anderson, J. T.; Hung, C. M.; Thompson, J.; Wager, J. F.; Keszler, D. A. *J. Am. Chem. Soc.* 2008, 130, 17603–17609.

(6) Jiang, K.; Zakutayev, A.; Stowers, J.; Anderson, M. D.; Tate, J.; McIntyre, D. H.; Johnson, D. C.; Keszler, D. A. *Solid State Sci.* 2009, 11, 1692–1699.

(7) Cowell, E. W.; Knutson, C. C.; Wager, J. F.; Keszler, D. A. *ACS Appl. Mater. Interfaces* 2010, 2, 1811–1813.

(8) Alemayehu, M.; Davis, J. E.; Jackson, M.; Lessig, B.; Smith, L.; Sumega, J. D.; Knutson, C.; Beekman, M.; Johnson, D. C.; Keszler, D. A. *Solid State Sci.* 2011, 13, 2037–2040.

(9) Jiang, K.; Anderson, J. T.; Hoshino, K.; Li, D.; Wager, J. F.; Keszler, D. A. *Chem. Mater.* 2011, 23, 945–952.

(10) Jiang, K.; Meyers, S. T.; Anderson, M. D.; Johnson, D. C.; Keszler, D. A. *Chem. Mater.* 2013, 25, 210–214.

(11) Kim, K. M.; Kim, C. W.; Heo, J. S.; Na, H.; Lee, J. E.; Park, C. B.; Bae, J. U.; Kim, C. D.; Jun, M.; Hwang, Y. K.; Meyers, S. T.; Grenville, A.; Keszler, D. A. *Appl. Phys. Lett.* 2011, 99, 2013–2016.

(12) Smith, S. W.; Wang, W.; Keszler, D. A.; Conley, J. F. *J. Vac. Sci. Technol. A Vacuum, Surfaces, Film.* 2014, 32, 041501.

(13) Plassmeyer, P. N.; Archila, K.; Wager, J. F.; Page, C. J. *ACS Appl. Mater. Interfaces* 2015, 7, 1678–1684.

(14) Keszler, D. A.; Anderson, J. T.; Meyers, S. T. *Oxide Dielectric Films for Active Electronics, In Solution Processing of Inorganic Materials.* Mitzi, D. B., Ed.; 2008, John Wiley & Sons, Inc.: Hoboken, NJ, USA.

(15) Nadarajah, A.; Wu, M. Z. B.; Archila, K.; Kast, M. G.; Smith, A. M.; Chiang, T. H.; Keszler, D. A.; Wager, J. F.; Boettcher, S. W. *Chem. Mater.* 2015, 27, 5587–5596.

(16) Telecky, A.; Xie, P.; Stowers, J.; Grenville, A.; Smith, B.; Keszler, D. A. *J. Vac. Sci. Technol. B Microelectron. Nanom. Struct.* 2010, 28, C6S19.

(17) Oleksak, R. P.; Ruther, R. E.; Luo, F.; Fairley, K. C.; Decker, S. R.; Stickle, W. F.; Johnson, D. W.; Garfunkel, E. L.; Herman, G. S.; Keszler, D. A. *ACS Appl. Mater. Interfaces* 2014, 6, 2917–2921.

(18) Ashby, P. D.; Olynick, D. L.; Ogletree, D. F.; Naulleau, P. P. *Adv. Mater.* 2015, 1–7.

(19) Vieu, C.; Carcenac, F.; Pepin, A.; Chen, Y.; Mejias, M.; Lebib, A.; Couraud, L.; Launois, H. *Appl. Surf. Sci.* 2000, 164, 111–117.

(20) Dobisz, E.; Brandow, S.; Bass, R.; Mitterender, J. *J. Vac. Sci Technol.* B 2000, 18, 107–111.

(21) Hasko, D.; Yasin, S.; Mumtaz, A. *J. Vac. Sci Technol. B* 2000, 18, 3441–3444.

(22) Sidorkin, V.; Grigorescu, A.; Salemink, H.; van der Drift, E. *Microelectron. Eng.* 2009, 86, 749–751.

(23) Grigorescu, A. E.; Hagen, C. W. *Nanotechnology* 2009, 20, 292001.

(24) Cairncross, R. A.; Schunk, P.; Chen, K. S.; Prakash, S. S.; Samuel, J.; Hurd, A.; Brinker, C. J. *Dry. Technol.* 1997, 15, 1815–1825.

(25) Teodorescu, V. S.; Blanchin, M. G. *TEM Study of the Sol-Gel Oxide Thin Films, In Microscopy: Advances in Scientific Research and Education*. 2014, FORMATEX: Madrid, Spain.

(26) Gutmann, E.; Meyer, D. C.; Levin, A. A.; Paufler, P. *Appl. Phys. A Mater. Sci. Process.* 2005, 81, 249–259.

(27) Brito, G. E. S.; Morelha, S. L.; Abramof, E. *Appl. Phys. Lett.* 2002, 80, 407–409.

(28) Loke, V. L. Y.; Riefler, N.; Mehner, A.; Prenzel, T.; Hoja, T.; Wriedt, T.; Mädler, L. *Thin Solid Films* 2013, 531, 93–98.

(29) Anderson, J. T.; Wang, W.; Jiang, K.; Gustafsson, T.; Xu, C.; Gafunkel, E. L.; Keszler, D. A. *ACS Sustain. Chem. Eng.* 2015, 3, 1081–1085.

(30) Carnes, M. E.; Knutson, C. C.; Nadarajah, A.; Jackson, M. N.; Oliveri, A. F.; Norelli, K. M.; Crockett, B. M.; Bauers, S. R.; Moreno-Luna, H. A.; Taber, B. N.; Pacheco, D. J.; Olson, J. Z.; Brevick, K. R.; Sheehan, C. E.; Johnson, D. W.; Boettcher, S. W. *Mater. Chem. C* 2014, 2, 8492–8496.

(31) Wang, W.; Liu, W.; Chang, I.-Y.; Wills, L. A.; Zakharov, L. N.; Boettcher, S. W.; Cheong, P. H.-Y.; Fang, C.; Keszler, D. A. *Proc. Natl. Acad. Sci.* U. S. A. 2013, 110, 18397–18401.

(32) Ruther, R. E.; Baker, B. M.; Son, J.-H.; Casey, W. H.; Nyman, M. *Inorg. Chem.* 2014, 53, 4234–4242.

(33) Phung, T. M.; Johnson, D. C.; Antonelli, G. A. *J. Appl. Phys.* 2006, 100, 1–7.

(34) Wormington, M.; Panaccione, C.; Matney, K. M.; Bowen, K. *Phil. Trans. R. Soc. Lond. A* 1999, 357, 2827–2848.

(35) Giannuzzi, L. A.; Stevie, F. A. *Introduction to Focused Ion Beams: Instrumentation, Theory, Techniques, and Practice*. 2005, Springer: New York, USA.

(36) Gustafsson, T.; Garfunkel, E.; Goncharova, L.; Starodub, D.; Barnes, R.; Dalponte, M.; Bersuker, G.; Foran, B.; Lysaght, P.; Schlom, D. G.; Vaithyanathan, V.; Hong, M.; Kwo, J. R. *Sci. Ser. II Math. Phys. Chem*. 2006, 220, 349–360.

Chapter XX

(1) J.R. Michael, Scanning 33, 147 (2011).

(2) D. Phifer, L. Tuma, T. Vystavel, P. Wandrol, and R.J. Young, Microsc. Today 17, 40 (2009).

(3) D.C. Bell and N. Erdman, editors , Low Voltage Electron Microscopy: Principles and Applications (Wiley, Published in association with the Royal Microscopical Society, Chichester, West Sussex, United Kingdom, 2013).

(4) M. Suga, S. Asahina, Y. Sakuda, H. Kazumori, H. Nishiyama, T. Nokuo, V. Alfredsson, T. Kjellman, S.M. Stevens, H.S. Cho, M. Cho, L. Han, S. Che, M.W. Anderson, F. Schüth, H. Deng, O.M. Yaghi, Z. Liu, H.Y. Jeong, A. Stein, K. Sakamoto, R. Ryoo, and O. Terasaki, Prog. Solid State Chem. 42, 1 (2014).

(5) H. Schatten, L.D. Sibley, and H. Ris, Microsc. Microanal. Off. J. Microsc. Soc. Am. Microbeam Anal. Soc. Microsc. Soc. Can. 9, 330 (2003).

(6) Y. Chen, Microelectron. Eng. 135, 57 (2015).

(7) F. Delachat, C. Constancias, J. Reche, B. Dal'Zotto, L. Pain, B. Le Drogoff, M. Chaker, and J. Margot, J. Vac. Sci. Technol. B Nanotechnol. Microelectron. Mater. Process. Meas. Phenom. 32, 06FJ02 (2014).

(8) V.R. Manfrinato, L.L. Cheong, H. Duan, D. Winston, H.I. Smith, and K.K. Berggren, Microelectron. Eng. 88, 3070 (2011).

(9) C.-H. Liu, P.C.W. Ng, Y.-T. Shen, S.-W. Chien, and K.-Y. Tsai, J. Vac. Sci. Technol. B Microelectron. Nanometer Struct. 31, 021605 (2013).

(10) D. Rio, C. Constancias, M. Saied, B. Icard, and L. Pain, J. Vac. Sci. Technol. B Microelectron. Nanometer Struct. 27, 2512 (2009).

(11) A. Tilke, M. Vogel, F. Simmel, A. Kriele, R.H. Blick, H. Lorenz, D.A. Wharam, and J.P. Kotthaus, J. Vac. Sci. Technol. B Microelectron. Nanometer Struct. 17, 1594 (1999).

(12) S.H. Oh, J.G. Kim, C.S. Kim, D.S. Choi, S. Chang, and M.Y. Jeong, Appl. Surf. Sci. 257, 3817 (2011).

(13) R.P. Oleksak, R.E. Ruther, F. Luo, K.C. Fairley, S.R. Decker, W.F. Stickle, D.W. Johnson, E.L. Garfunkel, G.S. Herman, and D.A. Keszler, ACS Appl. Mater. Interfaces 6, 2917 (2014).

(14) J.T. Anderson, C.L. Munsee, C.M. Hung, T.M. Phung, G.S. Herman, D.C. Johnson, J.F. Wager, and D.A. Keszler, Adv. Funct. Mater. 17, 2117 (2007).

(15) A. Telecky, P. Xie, J. Stowers, A. Grenville, B. Smith, and D.A. Keszler, J. Vac. Sci. Technol. B Microelectron. Nanometer Struct. 28, C6S19 (2010).

(16) J. Stowers and D.A. Keszler, Microelectron. Eng. 86, 730 (2009).

(17) H. Demers, N. Poirier-Demers, A.R. Couture, D. Joly, M. Guilmain, N. de Jonge, and D. Drouin, Scanning 33, 135 (2011).

(18) M. Schaffer, B. Schaffer, and Q. Ramasse, Ultramicroscopy 114, 62 (2012).

(19) J.K. Stowers, A. Telecky, M. Kocsis, B.L. Clark, D.A. Keszler, A. Grenville, C.N. Anderson, and P.P. Naulleau, in edited by B.M. La Fontaine and P.P. Naulleau (2011), pp. 796915–796915–11.

Chapter XXI

[1] Brotherton S 1995 *Semicond. Sci. Technol.* **721** 721–38

[2] Shah A, Torres P, Tscharner R, Wyrsch N and Keppner H 1999 *Science.* **285** 692–9

[3] Göpel W and Schierbaum K D 1995 *Sensors Actuators B Chem.* **26** 1–12

[4] Matsumura H 1998 *Jpn. J. Appl. Phys.* **37** 3175–87

[5] Presley R E, Munsee C L, Park C-H, Hong D, Wager J F and Keszler D A 2004 *J. Phys. D. Appl. Phys.* **37** 2810–3

[6] Liu M, Johnston M B and Snaith H J 2013 *Nature* **501** 395–8

[7] Johnson D C, Johnson D W, Wager J F and Keszler D A 2010 *CS MANTECH Conf. May* 3–6

[8] Alemayehu M, Davis J E, Jackson M, Lessig B, Smith L, Sumega J D, Knutson C, Beekman M, Johnson D C and Keszler D A 2011 *Solid State Sci.* **13** 2037–40

[9] Oleksak R P, Stickle W F and Herman G S 2015 *J. Mater. Chem. C* **3** 3114–20

[10] Oleksak R P and Herman G S 2014 *Proc. SPIE* **9048** 90483H

[11] Oleksak R P, Ruther R E, Luo F, Fairley K C, Decker S R, Stickle W F, Johnson D W, Garfunkel E L, Herman G S and Keszler D A 2014 *ACS Appl. Mater. Interfaces* **6** 2917–21

[12] Telecky A, Xie P, Stowers J, Grenville A, Smith B and Keszler D A 2010 *J. Vac. Sci. Technol. B Microelectron. Nanom. Struct.* **28** C6S19

[13] Smith S W, Wang W, Keszler D A and Conley J F 2014 *J. Vac. Sci. Technol. A Vacuum, Surfaces, Film.* **32** 041501

[14] Nadarajah A, Carnes M E, Kast M G, Johnson D W and Boettcher S W 2013 *Chem. Mater.* **25** 4080–7

[15] Nadarajah A, Wu M Z B, Archila K, Kasti M G, Smith A M, Chiang T H, Keszler D A, Wager J F and Boettcher S W 2015 *Chem. Mater.* **27** 5587–96

[16] Plassmeyer P N, Archila K, Wager J F and Page C J 2015 *ACS Appl. Mater. Interfaces* **7** 1678–84

[17] Novoselov K S, Jiang D, Schedin F, Booth T J, Khotkevich V V, Morozov S V and Geim a K 2005 *Proc. Natl. Acad. Sci. U. S. A.* **102** 10451–3

[18] Geim A K and Grigorieva I V 2013 *Nature* **499** 419–25

[19] Shibata N, Pennycook S J, Gosnell T R, Painter G S, Shelton W A and Becher P F 2004 *Nature* **428** 730–3

[20] Hanson M P, Bank S R, Zide J M O, Zimmerman J D and Gossard A C 2007 *J. Cryst. Growth* **301-302** 4–9

[21] Borisevich A Y, Chang H J, Huijben M, Oxley M P, Okamoto S, Niranjan M K, Burton J D, Tsymbal E Y, Chu Y H, Yu P, Ramesh R, Kalinin S V. and Pennycook S J 2010 *Phys. Rev. Lett.* **105** 1–4

[22] Anderson J T, Munsee C L, Hung C M, Phung T M, Herman G S, Johnson D C, Wager J F and Keszler D A 2007 *Adv. Funct. Mater.* **17** 2117–24

[23] Jiang K, Anderson J T, Hoshino K, Li D, Wager J F and Keszler D A 2011 *Chem. Mater.* **23** 945–52

[24] Jiang K, Meyers S T, Anderson M D, Johnson D C and Keszler D A 2013 *Chem. Mater.* **25** 210–4

[25] Fairley K C, Merrill D R, Woods K N, Ditto J, Xu C, Oleksak R P, Gustafsson T, Johnson D W, Garfunkel E, Herman G S, Johnson D C and Page C J 2016 *ACS Appl. Mater. Interfaces* **8** 667–72

[26] Häusler I, Atkins R, Falmbigl M, Rudin S P, Neumann W and Johnson D C 2015 *Zeitschrift für Krist.* **230** 45–54

[27] Pennycook S J and Nellist P D 2011 *Scanning Transmission Electron Microscopy*

[28] Krivanek O L, Chisholm M F, Nicolosi V, Pennycook T J, Corbin G J, Dellby N, Murfitt M F, Own C S, Szilagyi Z S, Oxley M P, Pantelides S T and Pennycook S J 2010 *Nature* **464** 571–4

[29] Eggeman A S, Krakow R and Midgley P A 2015 *Nat. Commun.* **6** 7267

[30] LeBeau J M and Stemmer S 2008 *Ultramicroscopy* **108** 1653–8

[31] Van Aert S, Batenburg K J, Rossell M D, Erni R and Van Tendeloo G 2011 *Nature* **470** 374–7

[32] Van Aert S, De Backer A, Martinez G T, Goris B, Bals S, Van Tendeloo G and Rosenauer A 2013 *Phys. Rev. B - Condens. Matter Mater. Phys.* **87** 1–6

[33] Macarthur K E E, D'Alfonso A J, Ozkaya D, Allen L J J, Nellist P D D, Alfonso A J D, Ozkaya D, Allen L J J and Nellist P D D 2015 *Ultramicroscopy* **156** 1–8

[34] Jarvis K A, Deng Z, Allard L F, Manthiram A and Ferreira P J 2011 *Chem. Mater.* **23** 3614–21

[35] Westover R D, Mitchson G, Ditto J J and Johnson D C 2016*Eur. J. Inorg. Chem.*

[36] Wiedle R A, Warner M, Tate J, Plassmeyer P N and Page C J 2013 *Thin Solid Films* **548** 225–9

[37] Schaffer M, Schaffer B and Ramasse Q 2012 *Ultramicroscopy* **114** 62–71

[38] de la Peña F, Burdet P, Ostasevicius T, Sarahan M, Nord M, Fauske V T, Taillon J, Eljarrat A, Mazzucco S, Donval G, Zagonel L F, Walls M and Iygr 2015 Hyperspy 0.8.2 10.5281/zenodo.28025

[39] Perez F and Granger B E 2007 *Comput. Sci. Eng.* **9** 21–9

[40] Scott D W *Biometrika* **66** 605–10

[41] Roisnel T and Rodriguez-Carvajal J 2001 *Mater. Sci. Forum* **378-381** 118–23

[42] Beekman M, Heideman C L and Johnson D C 2014 *Semicond. Sci. Technol.* **29** 064012

[43] Munroe P R 2009 *Mater. Charact.* **60** 2–13

[44] Westover R D, Ditto J, Falmbigl M, Hay Z L and Johnson D C 2015 *Chem. Mater.* **27** 6411–7

[45] Wiegers G A 1996 *Prog. Solid State Chem.* **24** 1–139

Chapter XXII

(1) Sutter, P.; Huang, Y.; Sutter, E. Nanoscale Integration of Two-Dimensional Materials by Lateral Heteroepitaxy. **2014**, No. 0001.

(2) Geim, A. K.; Grigorieva, I. V. *Nature* **2013**, *499* (7459), 419–425.

(3) Alducin, D.; Myers, B. D.; Liu, X.; Fisher, B. L. **2015**, *350* (6267), 1513–1516.

(4) Ni, G. X.; Wang, H.; Wu, J. S.; Fei, Z.; Goldflam, M. D.; Keilmann, F.;

Özyilmaz, B.; Neto, A. H. C.; Xie, X. M.; Fogler, M. M.; Basov, D. N. **2015**, *14* (September).

(5) Miyata, Y.; Nakayama, K.; Sugawara, K.; Sato, T.; Takahashi, T. **2015**, *14* (August), 775–780.

(6) Anderson, M. D.; Heideman, C. L.; Lin, Q.; Smeller, M.; Kokenyesi, R.; Herzing, A. A.; Anderson, I. M.; Keszler, D. A.; Zschack, P.; Johnson, D. C. *Angew. Chem. Int. Ed.* **2013**, *52*, 1982–1985.

(7) Beekman, M.; Disch, S.; Rouvimov, S.; Kasinathan, D.; Koepernik, K.; Rosner, H.; Zschack, P.; Neumann, W. S.; Johnson, D. C. *Angew. Chemie - Int. Ed.* **2013**, *52* (50), 13211–13214.

(8) Falmbigl, M.; Alemayehu, M. B.; Merrill, D. R.; Beekman, M.; Johnson, D. C. *Cryst. Res. Technol.* **2015**, *135* (30), 11055–11062.

(9) Fister, L.; David, C. *J. Am. Chem. Soc.* **1992**, *114*, 4639–4644.

(10) Merrill, D. R.; Sutherland, D. R.; Ditto, J.; Bauers, S. R.; Falmbigl, M.; Medlin, D. L.; Johnson, D. C. *Chem. Mater.* **2015**, *27* (11), 4066–4072.

(11) Oxley, M. P.; Varela, M.; Pennycook, T. J.; Van Benthem, K.; Findlay, S. D.; D'Alfonso, A. J.; Allen, L. J.; Pennycook, S. J. *Phys. Rev. B - Condens. Matter Mater. Phys.* **2007**, *76* (6), 1–8.

(12) D'Alfonso, A. J.; Freitag, B.; Klenov, D.; Allen, L. J. *Phys. Rev. B - Condens. Matter Mater. Phys.* **2010**, *81* (10), 2–5.

(13) Allen, L. J.; D'Alfonso, A. J.; Freitag, B.; Klenov, D. O. *MRS Bull.* **2012**, *37* (01),

47–52.

(14) Cliff, G.; Lorimer, G. W. *J. Microsc.* **1975**, *103* (2), 203–207.

(15) Parish, C. M.; Brewer, L. N. *Microsc. Microanal.* **2010**, *16* (3), 259–272.

(16) Williams, D. B.; Carter, C. B. *Transmission Electron Microscopy*, 2nd ed.; Springer: Newyork, 2009.

(17) Corso, S. D.; Liautard, B.; Tedenac, J. C. *J. Phase Equilibria* **1995**, *16* (4), 308–314.

(18) Lu, P.; Romero, E.; Lee, S.; MacManus-Driscoll, J. L.; Jia, Q. *Microsc. Microanal.* **2014**, *20* (06), 1782–1790.

(19) Moore, D. B.; Jones, Z.; Stolt, M. J.; Atkins, R.; Johnson, D. C. **2012**, *1*, 1–7.

(20) Merrill, D. R.; Moore, D. B.; Ditto, J.; Sutherland, D. R.; Falmbigl, M.; Winkler, M.; Pernau, H.-F.; Johnson, D. C. *Eur. J. Inorg. Chem.* **2015**, *2015* (1), 83–91.

(21) Lugg, N. R.; Kothleitner, G.; Shibata, N.; Ikuhara, Y. *Ultramicroscopy* **2015**, *151*, 150–159.

(22) Noda, Y.; Ohba, S.; Sato, S.; Saito, Y. *Acta Crystallogr. Sect. B Struct. Sci.* **1983**, *39* (3), 312–317.